INVESTIGATIONS OF THE MOVEMENT AND STRUCTURE OF D-REGION IONOSPHERIC IRREGULARITIES

By

W.K. HOCKING, B.Sc. (Hons)

A Thesis

presented for the degree of

DOCTOR OF PHILOSOPHY

at the

UNIVERSITY OF ADELAIDE

(Physics Department)

FEBRUARY 1981

VOLUME 1

To my parents

C O N T E N T S

Page

VOLUME I

Philosophy ix

Preface x

Acknowledgements xi

Summary xii

Table of Symbols xvi

CHAPTER I GENERAL REVIEW OF THE ATMOSPHERE WITH PARTICULAR EMPHASIS ON ALTITUDES OF 60-100 KM 1

1.1 Introduction 3

1.2 The Lower E and D regions 5

1.2.1 Basic Structure and Chemistry 5

1.2.2 Propagation of Radio Waves through the Ionosphere 9

1.2.3 D-region Absorption of Radio Waves, and the Winter Anomaly 11

1.3 D-region Dynamics 21

1.3.1 The Equations Governing the Atmosphere 21

1.3.2 Experimental Observations of Atmospheric Winds 22

1.3.3 Mesospheric Turbulence 28

1.4 Radio Wave Partial Reflections 35

1.4.1a Early Data 36

b Investigations of Echo Structure after 1962 41

c Layer Widths 46

d Rocket Comparisons 47

e Angular Spectrum 48

f Preferred Heights 50

g Amplitude Distributions 51

h Fading Times 53

i Conclusions of HF Results to about 1977 54

1.4.2 VHF Observations to 1977 57

CONTENTS Continued..... Page

CHAPTER II TURBULENCE - A GENERAL DISCUSSION 62

2.1 Warning 63

2.2 Description of Turbulence 65

2.2.1 The energy budget 65

2.2.2 Generation of Turbulence 70

2.2.3 The Spectrum, and important Turbulence parameters 74

a. The Spectrum 74

b. Eddy Transport 80

c. Equations involving important turbulence parameters 87

2.2.4 More careful treatment of ε, K 106

2.3 Correlation formulae, Structure functions, and some more rigorous theory 119

2.3.1 Theory 120

2.3.2 Estimation of C_n^2 126

2.4 Radar Scatter 141

2.4.1 Radar Equations 141

CHAPTER III INTRODUCTION, CALIBRATION, AND SOME PRELIMINARY OBSERVATIONS 148

3.1 Introduction 149

3.2 General Description of Technique 150

a. The Transmitter 150

b. Reception 151

c. Temporal Variations 153

d. Data Acquisition and Recording 154

e. Phase Recording 156

3.3 Calibration 160

3.3.1 Ground Characteristics 161

3.3.2 Techniques of Calibration 165

a. Definition of Units 165

b. Relating Measurements to Reflection Coefficients 168

c. Experimental Determination of Calibration Constants 172

d. Turbulent Scatter 173

CONTENTS Continued..... Page

CHAPTER III Continued

3.4 Some Simple Observations 176

3.5 The Field Sites 179

3.5.1 Buckland Park 179

3.5.2 Townsville and Woomera 186

CHAPTER IV ANGULAR AND TEMPORAL CHARACTERISTICS OF D-REGION SCATTERERS USING AMPLITUDE-ONLY DATA 187

4.1 Introduction 188

4.2 Investigations using time scales of the order of minutes 190

4.2.1 Temporal Variations 191

4.2.2 Angular spectra 197

4.2.3 O and X mode comparisons 201

4.2.4 Height fluctuations 205

(a) Upper limits of echoes 205

(b) Temporal height fluctuations 206

4.3 Short term temporal changes 212

4.3.1 Temporal fading 213

(a) Introduction 213

(b) Some theory to help interpretation 214

(c) Experimental 224

4.3.2 Height fluctuations 228

4.4 Spatial extent of scatterers 229

4.5 A review of VHF studies 231

4.5.1 Introduction 231

4.5.2 The scattered pulse profile 232

4.5.3 Experimental VHF observations 237

4.6 Water body refractive index profiles 250

CONTENTS Continued..... Page

CHAPTER V AMPLITUDE DISTRIBUTIONS 252

5.1 Introduction 253

5.2 Theory 254

5.2.1 Rice Distributions 254

5.2.2 The Rice Parameter 262

5.2.3 Removal of Noise from the Rice Parameter 267

5.3.4 Fitting the Data to the Distribution 269

5.3 Interpretation of Experimental Amplitude Distributions 271

5.3.1 Non-Rician Characteristics 271

5.3.2 Statistical Fluctuations of the Rice Parameter 277

5.3.3 Procedure for Determination of Specularity 280

5.4 Experimental Estimates of Specular to Random Scatter Ratios 283

5.4.1 The Distributions 283

5.4.2 Rejection Criteria 285

5.4.3 Results 287

CONTENTS Continued..... Page

VOLUME II

CHAPTER VI THE EFFECTS OF NOISE ON THE SIGNAL 292

6.1 Introduction 293

6.2 Notation and Assumptions 294

6.2.1 Notation 294

6.3 Complex Data 298

6.3.1 Determination of noise using complex data 298

6.4 Amplitude-only Sampling 301

6.4.1 Effect of noise on the data series 301

6.4.2 Effect of noise on the autocovariance 303

a. Introduction 303

b. Power (Intensity) analysis 304

c. Amplitude-only analysis 309

(i) Noise estimation 309

(ii) Autocovariance distortion 312

6.5 Experimental Results 318

6.6 Conclusions 322

CHAPTER VII OBSERVATIONS USING COMPLEX DATA 323

7.1 Introduction 324

7.2 Some Simple Observations 325

7.2.1 Short duration data (1-2 minutes) 325

7.2.2 Interpretation of short term data 327

7.3 Interpretation of Ionospheric scatter data 328

7.3.1 Simulation of beam broadening 328

7.3.2 More accurate estimates of expected spectral widths 335

7.3.3 Two unequal spectral peaks, and their effect on the auto-correlations. (OR the phase of the sum of two sine waves beating together) 342

CONTENTS Continued.... Page

CHAPTER VII Continued

7.4 Experimental data 347

7.4.1 Doppler winds 347

7.4.2 Spectral widths using the vertical beam 349

7.4.3 Spectral widths using the tilted beam 354

7.4.4 Theoretical spectra for anisotropic turbulence 357

7.4.5 Interpretation of spectral widths using tilted beam 362

7.4.6 The relative roles of gravity waves and turbulence in the mesosphere 373

7.5 Deconvolution 380

7.6 Conclusions 382

CHAPTER VIII COMPARISON OF PARTIAL REFLECTION PROFILES AND ROCKET MEASUREMENTS OF ELECTRON DENSITY 384

8.1 Introduction 385

8.2 Reflection of a radio pulse in a horizontally stratified ionosphere 386

8.2.1 Theory 386

a. Pulse convolution 386

b. Fourier procedure 388

8.2.2 Some Simple Applications 391

8.3 Analysis of simultaneous rocket and partial reflection measurements 393

8.3.1 Introduction 393

8.3.2 Experimental details 394

a. Technique 394

b. Results 396

8.3.3 Computer simulation of partial reflection height profile 400

8.3.4 Some extra observations of interest 404

a. Diffuse fluctuations in electron density measurements 404

b. Structure below 80 km 405

8.4 Conclusions 407

CONTENTS Continued....

		Page
CHAPTER IX	INVESTIGATION INTO THE GENERATION OF THE HF SCATTERERS	408
9.1	Introduction	409
9.2	Scatterer correlations with winds	410
9.2.1	Correlations between mean wind profiles and scattering layers	410
	a. Experimental observations	410
	b. Results from other references	413
9.2.2	Gravity wave effects in producing scattering layers	415
9.3	The relative roles of turbulence and specular scatter	420
9.3.1	Turbulence	420
9.3.2	Expected specular to isotropic scatter ratios	423
9.4	Conclusions	428
CHAPTER X	INVESTIGATIONS AT 6 MHz	429
10.1	Introduction	431
10.2	Experimental Results	433
10.2.1	Power profiles and temporal variations	433
10.2.2	Fading times and power spectra	438
10.3	Theoretical Interpretations	443
10.3.1	Theory and Interpretation	443
10.4	Conclusions	449
CHAPTER XI	DISCUSSION AND CONCLUSIONS	450
11.1	Introduction	451
11.2	Summary of Facts	452
11.3	Discussion	457
11.3.1	Discussion of doubtful points	457
	a. Production of turbulence	457
	b. Reasons for specular scatter	459
	c. Reasons for preferred heights	463
	d. Seasonal variations	465

CONTENTS Continued..... Page

CHAPTER XI Continued

11.3.2 The Author's View 466

11.4 Inconclusive results, future projects and schematic summary 468

APPENDICES

A. The Neutral Atmosphere, and the Ionosphere above 100 km

B. Propagation of radio waves through the Ionosphere

C. The Dynamical equations governing the Atmosphere

D. Angular and Temporal Characteristics of Partial Reflection from the D-Region of the Ionosphere

(A paper presented in Journal of Geophysical Research, 84, 845, (1979))

E. Computer program Specpol

F. Computer program Scatprf

G. Computer program Volscat

H. Co-ordinates of some Important Middle-Atmosphere Observatories (Past and Present)

BIBLIOGRAPHY

There is a saying which says that Scientists are people who are learning more and more about less and less, until one day each will know everything about nothing.

But it seems to me that to learn more and more about less and less, it is necessary to learn more and more about more and more. For even the smallest system contains a myriad of principles, when understood in its fullest complexity.

This philosophy is particularly appropriate for the work discussed in this thesis. The studies involved investigations into reflection processes from the upper Middle-Atmosphere. Yet to fully understand the processes requires understanding of many concepts; e.g. radio waves, turbulence, fluid dynamics, gravity waves, tides, magnetionic theory, photochemistry, chemistry, Solar-Terrestrial phenomena, meteors, global circulation, and rocket techniques, to name but a few.

W.K. HOCKING

PREFACE

To the best of the author's knowledge, this thesis contains no material previously published or written by another person, except where due reference is made in the text. It contains no material which has been submitted or accepted for the award of any other degree or diploma in any University.

(W.K. Hocking)

ACKNOWLEDGEMENTS

The work described in this thesis was carried out under the supervision of Drs. B.H. Briggs and R.A. Vincent, using the facilities of the Department of Physics, University of Adelaide. The advice and encouragement of both Dr. Briggs and Dr. Vincent were greatly appreciated throughout the project, and Dr. Elford also gave some helpful advice.

Invaluable technical assistance was provided by Neville Wild, Lindsay Hettner, Alex Didenko, Brian Fuller and Albert Robertson.

Other research students in the Radiophysics group also provided useful assistance. Discussions with Sue Ball proved extremely fruitful, as did conversations with Laurie Campbell, Ron Craig, Stuart Young and Iain Reid.

My thanks are also extended to Lyn Birchby, who performed her tasks as Data Assistant with excellence.

Sue Dolman, Pat Coe and Joyce Locke have clearly done an excellent job as typists, and Judy Laing's help in creating some of the diagrams in this thesis is gratefully acknowledged.

The author was in receipt of an Australian Commonwealth Post-Graduate award.

Most importantly, however, I would like to thank my parents for their continued support and encouragement throughout my academic career.

SUMMARY

Radiowaves (typically 2 to 50MHz i.e. HF and VHF radio bands) incident upon the ionosphere from below suffer weak partial reflection at altitudes between 50 and 100 km (the ionospheric D-region). These weak reflections are used to measure various parameters such as wind speeds and electron densities for the region. However, the mechanisms causing this scatter are not yet fully understood. The purpose of the work for this thesis was to obtain more information on the nature of these scatterers.

A wide variety of factors may be related to these scatterers, and so the first part of the first chapter is dedicated to a review of general properties of the D-region. This is followed by a more intensive review of previous investigations of D-region scatter characteristics.

Since turbulence may be important in relation to this scatter, the second chapter contains a review of turbulence. Some important formulae are presented, including some which are believed to be original.

Chapter III describes the equipment used for the investigations undertaken, and gives some preliminary observations, while Chapter IV discusses in detail many of the important general features of these scatterers. Chapter II can, in some ways, be considered as the most important chapter of the thesis. Observations were made near Adelaide, Australia (35°56'S, 138°30'E) and Townsville, Australia (19°40'S, 146°54'E), initially at frequencies close to 2MHz. Stratification of echoes was shown to occur. The first direct observations of the angular spectrum of the scatterers are also presented, and results agree with previous

indirect measurements. Scatter is generally quasi-isotropic above 80 to 85km, but quite "mirror-like" (Fresnel) below 75 to 80km. The temporal variation of echo strength was also monitored, and at times extremely strong, short-lived "bursts" were observed. This was particularly so for heights below about 80km, where power "bursts" up to 10 and 20 dB above the "normal" level could be seen. The observing equipment was fully calibrated, allowing absolute measurements of effective voltage reflection coefficients to be obtained.

Chapter IV also contains a review of VHF scatter observations by other authors, since VHF results complement HF results to some degree.

Investigations of the specularity of scatter by utilizing amplitude histograms are presented in Chapter V, and in particular the Rice distribution is extensively used. This may prove to be a controversial chapter, since it dismisses (with reasons) several investigations carried out by other authors. However, the author is confident of his results, particularly since they agree well with previous conclusions reached by studying the angular spectrum. It was found that scatter from below ≈80km is quite specular, whilst scatter from ≈80 to 90km appears to contain a mixture of specular and random quasi-isotropic scatter.

In all the observations, a knowledge of the background noise level is essential. For this reason, Chapter VI is dedicated to discussions of the determination of mean noise levels from observations of the signal. For cases in which both amplitude and phase are recorded this is quite simple, but the problem becomes somewhat more difficult when only amplitude is recorded. The presence of noise also distorts the auto-correlation function

if data is recorded as amplitude-only, and the form of this distortion is discussed. It is believed that much of the theory presented in Chapter VI is original work.

The use of equipment capable of recording both amplitude and phase simultaneously also provided a major advance in the understanding of these scatterers. Such equipment was installed at both the Townsville and Adelaide sites, and Chapter VII discusses results obtained. It is shown that the fading times observed are primarily related to beam-broadening, so these fading rates cannot be used directly for determination of turbulence parameters. However, some authors have attempted to make such measurements, and some controversy may result from a few of the statements in this chapter. It is also shown that observations taken with a tilted beam produce wider power spectra than those taken with a vertical beam. An explanation for this effect is presented, and it is believed that this is the first time that this explanation has been recognized. The explanation is related to 2-dimensional turbulence. The effect is used to derive turbulence parameters (eddy dissipation rate, eddy diffusion coefficient, outer scale), and it is believed that the first such useful measurements at HF are contained in this thesis. Estimates by other authors working at HF are believed to have been made using erroneous assumptions, and to have been adjusted to appear realistic by the manipulation of unknown constants to compatible values.

A comparison of partial reflections was also made with simultaneously recorded high resolution measurements of electron density made during a rocket flight at Woomera, Australia (30°45'S, 136°18'E), and the results are presented in Chapter VIII.

This comparison gave further insight into the nature of D-region scatter.

Chapter IX contains a more detailed search for mechanisms causing the scatter. The role of turbulence is discussed, and it is shown that this is unlikely to directly produce the observed scatter for heights below about 75 to 80km. However, this does not rule out indirect turbulence effects. Above 80 to 85km, turbulence is quite capable of producing a significant component of the observed scatter. The role of wind shears and gravity waves in producing these scatterers is also discussed. It appears that gravity waves may play an important role.

Towards the end of the work for this dissertation, facilities were installed at the Adelaide site to allow observations of the scatter at a frequency close to 6MHz. The ability to observe on two frequencies simultaneously proved extremely useful, and comparisons of 2 and 6MHz results are presented in Chapter X.

Although the exact nature of the scatterers is still not known, it is believed that this thesis has made some progress in understanding these scattering phenomena.

Table of Symbols.

The following table gives a brief summary of the symbols used in this thesis. Within any one section, the use of symbols is generally consistent; but different sections may on occasion use different sets of symbols. For example, sometimes "n" is used for refractive index, and sometimes"μ". I have tried to be fairly consistent, but this has not always been possible, especially when the diversity of topics covered is appreciated. Further, it is possible some symbols have been missed, particularly if they are used only a few times.

Not all the symbols are fully defined, either. For example, I write " θ = potential temperature," but do not explain the term "potential temperature". There is no room to fully define all symbols. Either see the text, or other references, for fuller definitions.

I. ROMAN

A: used at times to represent amplitude of return echoes (Prairs etc.).
Aeff = effective area for aerial array.

a: sometimes used as a constant.
a(t) = amplitude time series.

B : $\underline{B}$ = magnetic induction, $\underline{H}/\mu_o$.

C: Cp,Cv - specific heats at constant pressure, volume $\{=(\frac{dQ}{dT})p,v\}$.
C = speed of sound $(\gamma p_o/\rho_o)^{\frac{1}{2}}$.
$C_{\frac{1}{2}}, C_{0.5}$ = complex fading time.

c: c_p, c_v = specific heats at constant pressure, volume $\{=(\frac{dQ}{dT})p,v\}$.
c = speed of light (= 2.9979 x 10^8 m s^{-1} in a vacuum).
c = speed of sound (at times) $(=(\gamma p_o/\rho_o)^{\frac{1}{2}})$.

D: $D_\theta(\underline{r})$ = structure function (turbulence).
D = directivity of aerial array.

d: total differentiation, e.g. $\frac{d}{dt}$.

E: $\underline{E}$ = electric field.

e: e = charge of an electron (=1.602x10^{-19} Coulombs).
e_{ij} = strain tensor.

F: $\underline{F}$ = force; $\underline{F}$ = force per unit mass at times.

f: f = frequency; $\underline{f}$ = force per unit mass at times.

G: Gain of aerial array.

g: acceleration due to gravity ($\simeq$9.8m s^{-2} at ground level).

H: $\underline{H}$ = magnetic field = $\mu_o\underline{B}$.
H = scale height ($C^2/\gamma g$ for isothermal atmosphere).

Special Case:
$\underline{\mathcal{H}} = Z_o\underline{H}$ in appendix B where $\underline{H}$ = magnetic field of E-M radiation, and $Z_o = \sqrt{\mu_o/\varepsilon_o}$.

h: $\underline{h}$ = heat flux vector.

i: $\sqrt{-1}$ at times; $\underline{i}$ = unit vector parallel to x axis; i = current.

j: $\sqrt{-1}$ at times; $\underline{j}$ = unit vector parallel to y axis; j = current density.

K: K_e = dielectric constant = $\varepsilon/\varepsilon_o$.

$\underline{K}$ = complex wave-number (e.g. $K_z = k_z + j\frac{\gamma g}{2c^2}$)

K_{2M}, K_{*2M}, K_{2W}, K_{*2W}, K_{6M}, K_{*6M}, K_{T3}, K_{*T3} = calibration constants.

K_t, K_m = eddy diffusivities of heat, momentum.

k: $\underline{k}$ = unit vector parallel to z axis; k = Boltzmann's constant ($p=\rho kT$, where ρ may be in particles per unit mole, or mass per unit volume; in the latter case, use k_m).

$\underline{k}$ = wavenumber.

$\underline{k}$ = reciprocal scale in turbulence analysis.

L: $\underline{L}$ = absorption parameter

L = outer scale of turbulence (also L_m, L(m), L_o).

ℓ: ℓ = turbulence scales, $\frac{1}{k}$

M: M = potential refractive index gradient; M_e = potential refractive index gradient in ionosphere.

[M]= susceptibility matrix in analysis of E-M radiation propagating through ionosphere (Appendix B).

m: m_e = mass of electron.

N: N = concentration of electrons.

n: n = phase refractive index = $n_R + j\, n_I$

n = frequency (at times).

P: P = polar diagram function of array

P = constant in gravity wave analysis ($\frac{p'}{Pp_o} = \frac{\rho'}{R\rho_o} = \ldots$)

p: p = atmospheric pressure (possibly total, possibly perturbation)

p_o = background atmospheric pressure

p' = perturbation pressure.

Q: Q = heat content; Q = rate of heat transfer

R: R = reflection coefficient

R = gas constant in $p = \rho RT$, ρ in moles/unit volume;

R_{ij} = 2-point velocity correlation function (turbulence).

R_r = radiation resistance.

R = constant in gravity wave analysis ($\frac{p'}{Pp_o} = \frac{\rho'}{R\rho_o} = \ldots$)

R() = Fourier transform of reflection coefficient.

r: r = reflection coefficient.

S: S = entropy

s: s = entropy

T: T = temperature

t: t = time; t_* = time for turbulence to form.

U: $\underline{U}$ = wind velocity (often background wind velocity).

u: $\underline{u}$ = wind velocity (often perturbation velocity).

u = x component of wind velocity.

V: V = volume

$\underline{V}$ = wind velocity.

v: v = volume (at times).
v = phase velocity of wave
v_g = group velocity
$\underline{v}$ = fluid velocity or wind velocity (often perturbation component).
v = y component of wind velocity.

w: w = z component of wind velocity.

X: X = constant in gravity wave analysis ($\frac{Ux}{X} = \frac{p'}{Pp_o} = \ldots$)

x: x = horizontal cartesian co-ordinate (Eastward)
(x_1, x_2, x_3) = cartesian co-ordinates.

y: y = horizontal (Northward) cartesian co-ordinate
y(t) = amplitude time series

Z: $Z_o = \sqrt{\mu_o/\varepsilon_o}$ = impedance of free space.
Z = constant in gravity wave analysis (e.g. $\frac{u_z}{Z} = \frac{u_x}{X} \ldots$)

z: z = vertical cartesian co-ordinate.
z(t) = amplitude time series.

II. GREEK

α: α = angle (general).
α = angle between group and phase paths of ionospheric E-M wave.
α = constant in turbulence relation $E = \alpha\varepsilon^{2/3}k^{2/3}$.
α_{12}, α_{24} = Rice parameters (Ch. V).

Γ: Γ_g, Γ_a = adiabatic lapse rate.
Γ() = Γ function.

γ: γ = Cp/Cv.

Δ: used to indicate small steps, e.g. t + Δt.

δ: used to indicate small steps, e.g. t + δt.

ε: ε_o = permittivity of free space (= 8.85 x 10^{-12} Farad m^{-1})
ε = permittivity.
ε' = complex permittivity.
ε_R = receiver array efficiency.
ε_T = transmitter array efficiency.
ε = internal energy per unit volume for a fluid.
ε = energy generation per unit mass for turbulence (also at times used for energy dissipation rate)
ε_d = viscous energy dissipation rate (turbulence).
ε_g = bouyancy dissipation rate.

ζ: ζ = integration variable; ζ = space co-ordinate (especially when used in correlation functions).

η: L α $\cos^{\eta}\chi$ (absorption relation);
η = Kolmogoroff microscale;
η = total backscatter cross-section (= 4Πσ).

Θ: Θ = potential temperature.

θ: θ = angle (general) : particularly that from the vertical.
θ = general scalar (turbulence).
θ = potential temperature at times.

κ: κ' = dielectric constant = $\frac{\varepsilon'}{\varepsilon_o}$; κ = Re(κ').
κ, κ_t, κ_m = molecular diffusion coefficients of particles (density), temperature, momentum.

λ: λ = wavelength; λ = mean free path.

μ: μ = phase refractive index = $\mu_R + j\mu_I$, $j = \sqrt{-1}$.

μ_g = group refractive index.

μ_g' = $\mu_g \cos\alpha$ for E-M radiation propagating through ionosphere.

μ_o = permeability of free space = $4\pi \times 10^{-7}$ Henry m^{-1}

μ = permeability

μ = dynamic viscosity coefficient.

ν: ν = kinematic viscosity = μ/ρ.

ν_m = electron collision frequency with molecules.

Ξ: used as a "specular component" in Ch. VI.

ξ: often used as integration variable; ξ = space co-ordinate, especially when used in correlation functions.

π: π = 3.14159 = constant relating circumference and diameter of a circle.

ρ: ρ = density (possibly total, possibly perturbation)

ρ_o = background density, ρ' = perturbation density.

ρ_g = ground reflection coefficient.

$\rho()$ = autocorrelation function.

ρ_I = interpolated value of $\rho(\tau)$ i.e. spike removed.

Σ: Summation Symbol.

σ: σ_{ij} = stress tensor; σ = backscatter cross-section per unit steradian ($=\eta/4\pi$); σ = conductivity.

σ^2 = structure function of turbulence (at times).

τ: τ = time (especially used as time lag in correlation functions).

Φ: Φ = gravitational potential per unit mass.

ϕ: ϕ = angle in xy plane from x axis.

χ: χ = solar zenith angle; $\chi = \underline{\nabla}.\underline{u}$ in gravity wave analysis; χ = electron to neutral density ratio;

χ^2 = chisquare test parameter.

ψ: used as angle at times.

Ω: Ω = angular frequency at times (particularly that of Earth)

Ω_e = electron gyro-frequency = $\frac{eB}{m_e}$ rad m^{-1};

$\Omega = \underline{\omega} - \underline{k} \cdot \underline{U}$ = Doppler-shifted frequency of gravity wave moving with a wind, $\underline{U}$.

Ω = resistance.

ω: ω = angular frequency; ω_g = gravity wave cut-off in isothermal atmosphere; ω_a = acoustic cut-off.

ω_B = Brunt-Vaisala frequency = $[\frac{g}{\theta} \cdot \frac{d\theta}{dz}]^{\frac{1}{2}} = \{\frac{g}{T}[\frac{dT}{dz}+\Gamma_a]\}^{\frac{1}{2}}$

III. OTHERS

$\underline{\nabla}$(grad) = $\underline{i}\frac{\partial}{\partial x} + \underline{j}\frac{\partial}{\partial y} + \underline{k}\frac{\partial}{\partial z}$ (cartesian co-ordinates)

$\underline{\nabla}_k = \underline{i}\frac{\partial}{\partial k_x} + \underline{j}\frac{\partial}{\partial k_y} + \underline{k}\frac{\partial}{\partial k_z}$; (k_x, k_y, k_z) = wavenumber.

∂ = partial differentiation symbol.

$\frac{D}{Dt} = \frac{\partial}{\partial t} + \underline{v} \cdot \underline{\nabla}$.(also written $\frac{d}{dt}$ at times).
DAE = Differential Absorption Experiment.
PRD = Partial Reflection Drifts.
PRF = Pulse repetition frequency.
CW = continuous wave.
RF = radio-frequency.
IF = intermediate frequency.
PRAIR - Parameter of Reflection for Adelaide Ionospheric Reserach.
TIRP = Townsville Ionospheric Reflection Parameter.
CRO = Cathode-Ray Oscilloscope.
SWF = Short-wave fadeout.
RMS = Root mean square.
$\langle x \rangle$ = mean of x.
$\bar{x}$ = mean of x.

CHAPTER I

GENERAL REVIEW OF THE ATMOSPHERE WITH PARTICULAR EMPHASIS ON ALTITUDES OF 60-100KM

1.1 Introduction

1.2 The Lower E and D regions

1.2.1 Basic Structure and Chemistry

1.2.2 Propagation of Radio Waves Through the Ionosphere

1.2.3 D-region Absorption of Radio Waves, and the Winter Anomaly

1.3 D-region Dynamics

1.3.1 The Equations Governing the Atmosphere

1.3.2 Experimental Observations of Atmospheric Winds

1.3.3 Mesopheric Turbulence

1.4 Radio Wave Partial Reflections

1.4.1a Early Data

b Investigations of Echo Structure After 1962

c Layer Widths

d Rocket Comparisons

e Angular Spectrum

f Preferred Heights

g Amplitude Distributions

h Fading Times

i Conclusions of HF Results to about 1977

1.4.2 VHF Observations to 1977

Chapter I: General Review of the Atmosphere

When HF radio waves are transmitted vertically, they are often weakly reflected from regions of the atmosphere in the height regime 50 to 100km. The purpose of the work for this thesis was to give some insight into the physical causes for this weak scatter. Experiments were carried out at three stations in Australia; Adelaide (35°S, 138½°E), Townsville (19°S, 147°E), and Woomera (31°S, 136°E). A frequency close to 2MHz was used in all cases. At Adelaide, observations could also be made at 6MHz.

Determination of the nature of these scattering mechanisms is not simple, however. A general understanding of the atmosphere's chemistry and dynamics is necessary before significant progress can be made in this quest. Chapter I of this thesis attempts to provide such a background of information.

1.1 Introduction

The work contained in this dissertation discusses primarily the regions of the Earth's atmosphere between 60 and 100km above ground level. Studies are concentrated largely on determination of the mechanisms causing weak partial reflection of radio waves (2-50MHz) from this region. This would appear, then, to be quite a small topic. However, this is not the case. The reflections are quite important for a variety of ionospheric studies, including the measurement of winds in this region, and the measurement of electron densities. The various uses will be discussed in more detail later. But the fact remains that a clear interpretation of the results of experiments using these partial reflections is not possible until the nature of the scatterers is fully understood. Yet an understanding of these scatterers requires quite a general background of knowledge of the static and dynamic properties of the region in which they reside; and an understanding of the properties of this region requires in turn some degree of understanding of the properties of the rest of the atmosphere, for the region cannot be treated in isolation.

A complete discussion of the whole atmosphere would be an unrealistic proposal, particularly in a thesis of this type. A more than elementary understanding of the atmosphere is, however, essential. The approach taken in this thesis is to concentrate largely on the region 60-100km, and refer to other regions as the need arises. A brief review of the atmosphere as a whole is given in Appendix A. The appendix concentrates largely on atmospheric nomenclature, and the neutral atmosphere. A section on ion and electron distributions above 100km is also included. The discussion is of the type found in general text books on the ionosphere.

However, discussion on the 60-100km region's properties is felt to be of sufficient relevance to be included in the bulk of this introductory chapter. The techniques used to obtain the various results will not be discussed. Graph 1.2a, which may perhaps seem more appropriate to Appendix A, is included in this section because it shows well the transition from the structure below 100km to that above. Figures A2 and A3 given quite good summaries of the distribution of the important molecular and ionic species in the atmosphere, and a quick inspection of them is recommended.

1.2 The Lower E and D Regions

1.2.1 Basic Structure and Chemistry

Below the E region, a high proportion of the incident high energy ionizing solar radiation has been absorbed, and the ionization falls away. However, the Lyman-α (121.6nm) hydrogen line of emission from the Sun is extremely strong, and also suffers less absorption by O, O_2 and N_2 than many of the more energetic radiations, and indeed many of the longer wavelengths, too. (The atmosphere has by "chance" a window in the spectrum at 121.6nm). This L_α line then ionizes NO in the lower atmosphere (75-90km) to produce some degree of ionization. O_2 is also ionized, above about 85km, by UV, X rays (0.2-0.8nm), and Lyman β. A good diagram of the dominant ionizing radiations can be found in Ratcliffe (1972), Fig. 2.3. A more detailed discussion is to be found in Gnanalingam and Kane (1978), Fig. 3. For ease of reference, the production rates of Thomas (1971) are reproduced in Fig. 1.1. Below about 75km, Cosmic rays can produce a significant degree of ionization, and X-rays can be important during solar flares at these lower heights. Parameswaran et al. (1978) and Gnanalingam (1978) both give examples of D region dependence on 0.1-0.8nm X-rays.

In all cases, the electron concentrations are much greater by day. This is so even for Cosmic-ray produced 60-70km ionization, because the free electrons attach to neutral molecules at night. This attachment is very sensitive to photo dissociation, so as soon as the Sun rises the electrons become free quickly, and a rapid increase in electron density thus occurs at sunrise (with a similar rapid decrease at sunset). Higher up (about 80km), the build-up of electron density during the morning is a much slower process.

Electron precipitation (that is, dumping of high energy electrons from high in the thermosphere and plasmasphere) can also be a significant

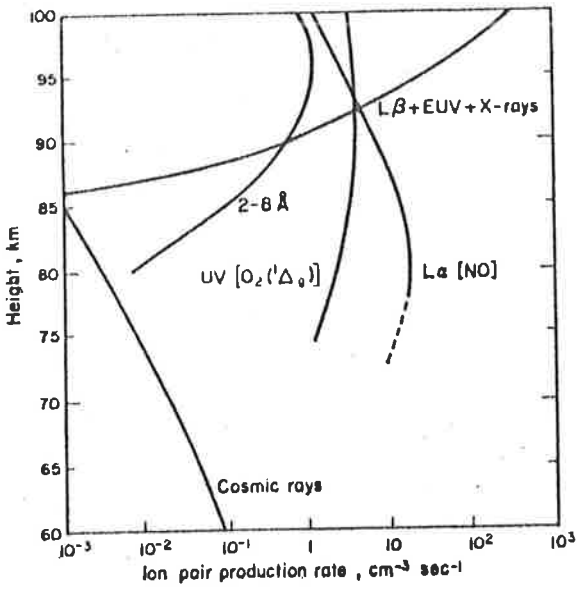

Fig. 1.1 Main production rates of electrons in the D region for quiet daytime conditions (after Thomas, 1971).

source of ionization - for example Montbriand and Belrose (1976); Chamberlain and Jacka (1979).

The rates of most recombination processes ensure that there are few free electrons at night, if there are no ionizing sources. However, a night time ionosphere does exist. The reasons for this are not fully clear, but several mechanisms have been proposed. Photo ionization by L_α and L_β radiation resonantly scattered around the Earth by the hydrogen Geocorona, is one suggestion (Tohmatsu and Wakai (1970) have shown photoionization by L_β could account for mid-latitude night-time E region electron densities). Ionization of NO by L_α, and of O_2 by L_β, are both effective. Thomas (1971), Fig. 10, gives typical night-time production rates. Chamberlain and Jacka (1979), have presented evidence that particle precipitation (electron precipitation especially) could have an effect at mid-latitudes at least equal in effect to the above processes. The suggestion is also made, from time to time, that direct meteoric ionization may be an important process, but little qualitative data to support this appears to exist. Certainly, however, metallic ions left by meteors can play important roles in the creation of some sporadic E layers (eg. Sinno, 1980).

Thomas (1971) is a good reference for an initial understanding of some of these important ionizing effects, although of course understanding of D region chemistry has improved since then. A more recent discussion is that of Torr and Torr (1979).

The role of water cluster ions in D region chemistry is quite significant, but other molecules also play important roles. Thomas (1976), has discussed the role of CO_2 in helping speed up the creation of some of these water clusters. $NO^+(H_2O)_n$ appears to be formed with the help of CO_2, and thence $H^+(H_2O)_n$. Thomas finds the reactions reasonably

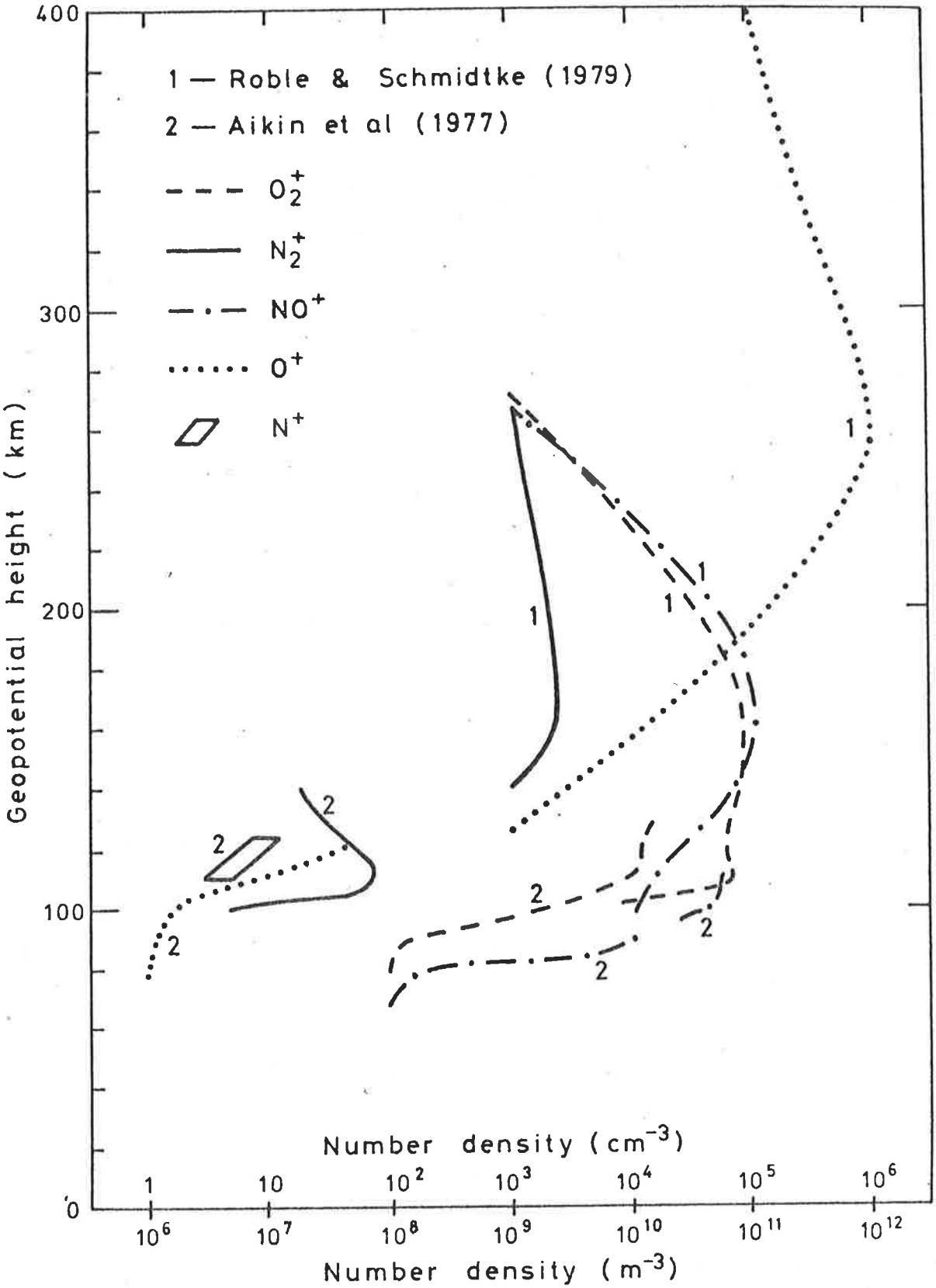

Fig. 1.2a Main ions in the upper ionosphere. The main ions are clearly O^+, O_2^+ and N_2^+, with O^+ dominating above about 200km.

Fig. 1.2b Lower ionosphere dominant ions. The situation in general can be described as an NO^+/O_2^+ dominance above 80km, and a water cluster ion dominance below about 75km.

This diagram does not include all the major ions, but is representative of them. The $H^+(H_2O)_4$ (also denoted as $H_3O^+(H_2O)_3$) curve of the warm wet model of Reid (1977) is typical of many of the H^+ water clusters, with a rapid decrease above about 75-80km. However, the dominant clusters vary with temperature and conditions. In Reid's models, $H^+(H_2O)_4$ and $H^+(H_2O)_3$ are the main clusters, but their concentrations and relative importance vary with water vapour content and temperature. The rocket flights of Aikin et al. (1977) suggested that $H_3O^+(H_2O)$ dominates, and $H_3O^+(H_2O)_3$ concentrations are somewhat weaker. H_3O^+ and $H_3O^+(H_2O)_2$ lie between $H_3O^+(H_2O)_3$ and $H_3O^+(H_2O)$ in the Aikin profiles.

Other clusters also exist, eg., $NO^+(H_2O)_n$. Reid's models showed the concentrations and shapes of the profiles of these species to be a little similar to those of the H^+ clusters; although the heights of the maxima, and the dominant ions, again changed with temperature and water vapour content. $NO^+(H_2O)_n$, n = 1 and 2, appeared to be the main members of the $NO^+(H_2O)_n$ series.

Other clusters such as NO^+CO_2 exist too (eg., Reid, 1977). This NO^+ profile due to Aikin et al. is a little abnormal, and this appears to be a day of anomalous Winter absorption. Such days have an unusually large concentration of NO^+ at 80 to 90km (with a corresponding lowering of the water cluster to NO^+ dominance height (transition height)), resulting in strong absorption of HF radio waves due to the associated increase in electron density.

The difference between the NO^+ profiles for the Reid cold dry, and Reid warm wet models is clearly quite significant, showing the sensitivity of the region to temperature and water vapour changes.

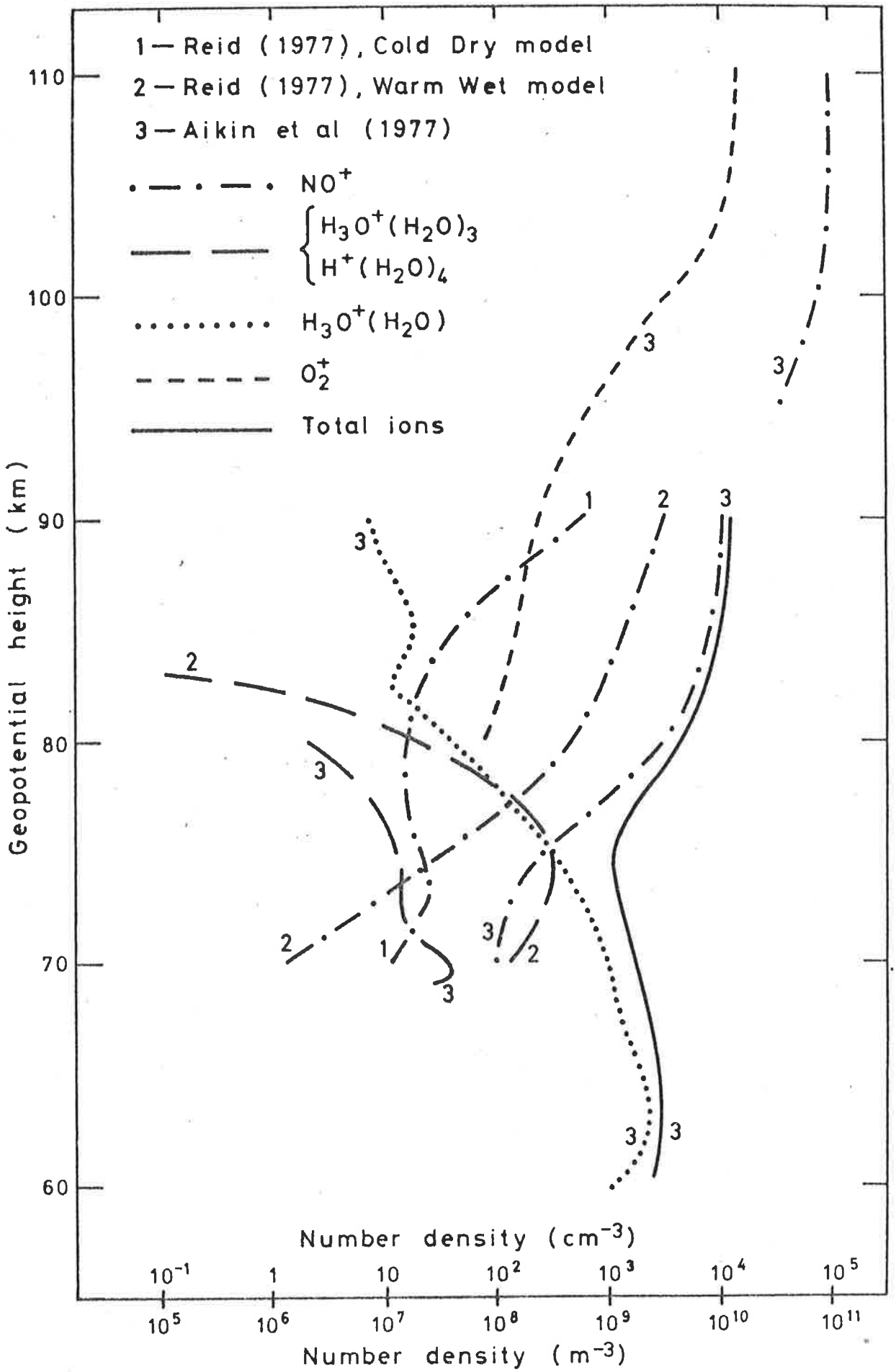
1 — Reid (1977), Cold Dry model
2 — Reid (1977), Warm Wet model
3 — Aikin et al (1977)
NO+
H3O+(H2O)3
H+(H2O)4
H3O+(H2O)
O2+
Total ions
Geopotential height (km)
110
100
90
80
70
60
Number density (cm−3)
10−1
1
10
10²
10³
10⁴
10⁵
Number density (m−3)
10⁵
10⁶
10⁷
10⁸
10⁹
10¹⁰
10¹¹

temperature dependent, and hence expects some degree of seasonal variation of the various profiles.

Fig. 1.3 shows some of the principle D region reactions (from Chakrabarty et al., 1978b). O_2^+ and NO^+ are the main ions formed by direct solar radiation, and the chemistry starts here. Reactions involving CO_2, H_2O, N_2, and OH then proceed from this point. The final state of the atmosphere is determined as the equilibrium of all these reactions. The concentrations of the various species can play an important role in this equilibrium, and the reactions can be extremely temperature dependent. Chakrabarty et al., (1978a) provides an example of comparisons of such calculations with experiment. Increases in densities of N, N_2 due to turbulent diffusion from higher up, and temperature changes, have both been invoked to explain increases in NO^+ densities (with corresponding electron increases) at 80-90km which are seen from time to time (Koshelov, 1979; Chakrabarty et al., 1978c). These increases in electron concentration give rise to higher than normal radio wave absorption, and occur particularly in winter, when the mesosphere is warmer. This phenomenon is called anomalous winter absorption, (or simply the winter anomaly) and will be discussed in more detail shortly.

Fig. 1.4 shows a typical D region electron density profile. The ledge at 80, 85km is a common feature of D region profiles, and can vary in height by 2 to 6km over a few hours (Trost, 1979). There is sometimes a small dip in electron density immediately under the ledge, (a little similar to that on 16 Jan.). Another feature of D region profiles is the presence of a maximum in electron density near 60km - perhaps a little similar to those in Fig. 1.4. This can sometimes be quite pronounced.

The ledge at 80-85km, and associated dip underneath, has been investigated theoretically by Chakrabarty et al. (1978c). They find

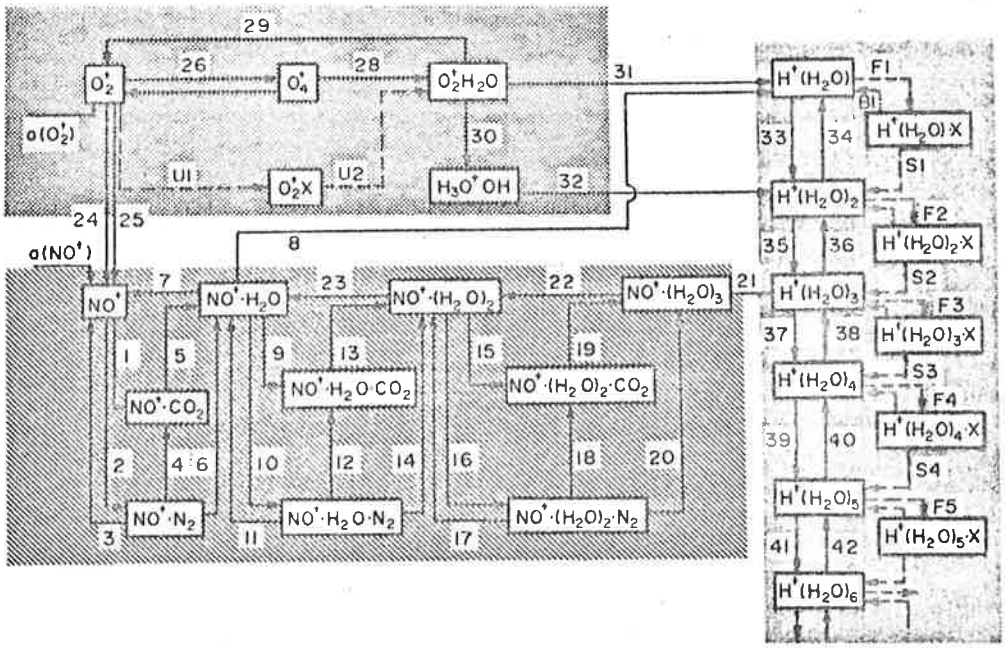

Fig. 1.3 Schematic of some of the major D region positive ion chemistry (from Chakrabarty et al., 1978a and 1978b).

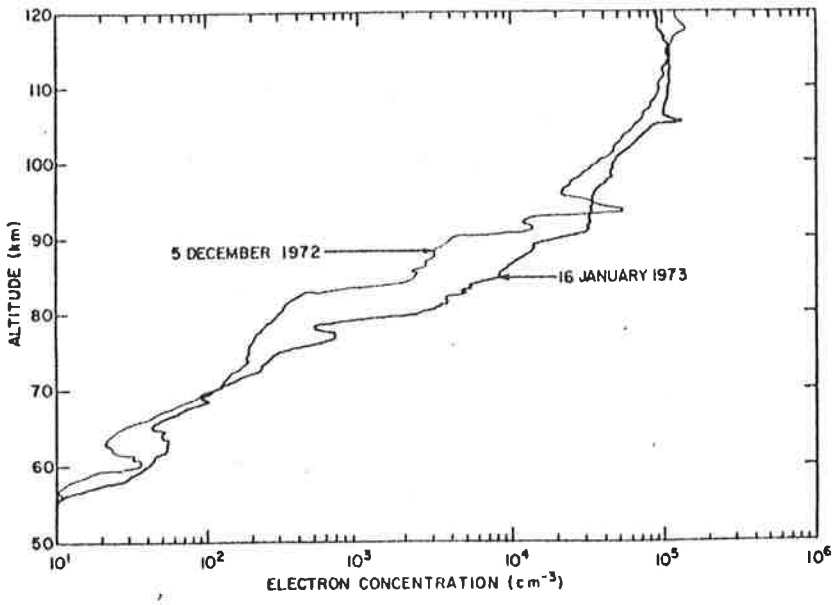

Fig. 1.4 Sample electron density profiles at Wallops Island (38°N, 75°W) from Smith et al. (1978). 5 Dec. is a normal day, and 16 Jan. a day of high absorption at 1.8MHz. The rapid increase in electron density at about 85, 80km (ledge) is a common feature. A small lip under the ledge, as on 16 Jan., also often occurs. A bulge in electron density at around 60 to 70km is also often seen, at least at mid-latitude in the Southern Hemisphere - particularly during sunspot minimum, since Galactic Cosmic Rays are at a maximum then (during sunspot maximum, the cosmic rays are in effect "blown away" by the solar wind - the so called "Forbush effect" eg., see Van Allen 1979). 1972-73 were near sunspot minimum. A reference for general profiles is Mechtly et al. (1972). McNamara (1979) also provides average D-region electron density profiles, though with very coarse resolution.

that they can simulate this ledge on purely chemical grounds. The height Hc of intersection of the $q(O_2)$ and q(NO) profiles (ion-electron production rates) is one important parameter. The q(NO) profile has a minimum value at about 85km, and when Hc is below this height, the ledge forms. The explanation of Chakrabarty et al. also explains the sudden decrease in hydronium ions associated with this ledge. The rise of temperature above the mesopause, and the decrease of total neutral particle density with height are the main causes of this hydronium ion decrease. The results form an extension of the work of Ferguson (1972), who first explained this fall off as being associated with the reaction $O_4^+ + O \rightarrow O_2^+ + O_3$.

The bulge near 60km is probably produced by Cosmic ray ionization.

The discussion thus far has related only to electrons and positive ion chemistry. However, negative ions certainly exist, often forming by the attachment of an electron to a neutral molecule (equation A2). Thomas (1971) has discussed these reactions to some degree. They can have important effects. It has already been seen, for example, how these ions form at low heights at night-time, thus reducing the number of night time free electrons at 60-70km. Koshelev (1979) also gives an example of D region negative ion chemistry. The most important ions are O^-, O_3^-, CO_3^-, NO_2^-, OH^-, O_2^-, O_4^-, CO_4^- and NO_3^-.

Other constituents not mentioned here can also affect D region chemistry - for example, mesospheric dust can play a role (eg., Parthasarathy 1976).

1.2.2 Propagation of Radio Waves Through the Ionosphere

The passage of radio waves through the ionosphere must, of course, be well understood before a clear understanding of the scatter mechanisms in that region can be obtained. For most problems in this thesis a simple ray theory is adequate. At high electron densities ray treatment is not valid, however, and a more complex "full wave solution" is necessary. A complete discussion of the propagation of electromagnetic radiation through an ionosphere is beyond the scope of this thesis, but some degree of understanding is essential. For this reason Appendix B has been included. The appendix firstly discusses the general case of radio wave propagation in a fairly non-mathematical context, and then goes on to discuss the particular case of the ionospheric D-region. The concept of wave groups, ray paths and the WKB approximation, and radio wave absorption are considered to some degree, with some of the more relevant full wave formulae being also given. Workers in ionospheric physics will be well familiar with these discussions, but for readers not directly involved in this field, the section may give a feel for the problems involved in radio wave propagation.

The role of radio wave absorption in the ionosphere has always been an important facet of ionospheric research. The studies of this phenomenon can lead to an understanding of some important processes in the ionosphere, and for this reason a fairly detailed review of D region absorption studies is included in the next section.

Absorption processes can also be used to calculate the D region electron density as a function of height. When a radio wave enters the ionosphere, its strength is attenuated due to absorption (Appendix B). This absorption is a function of electron density. If two radio waves are transmitted, each suffering a different degree of attenuation for a given electron density, then the ratio of absorption of the two waves

as a function of height of scatter can be used to obtain an estimation of the electron density profile. Usually, the two radio waves used are O and X modes on one frequency, although two different frequencies could also be used. This is the Differential Absorption Experiment (DAE), and it is discussed in a little more detail in Appendix B.

1.2.3 D Region Absorption of Radio Waves and the Winter Anomaly

Radio waves passing through the ionosphere are attenuated in amplitude due to the dissipation of some of their energy, thus heating the medium they pass through. The amount of absorption is directly related to the imaginary part of the refractive index, as seen in equation B15b, and this depends on the electron density, collision frequency, magnitude of the magnetic field, and the angle of the ray path to the magnetic field. The refractive index is best approximated by the Sen-Wyller formula, and examples are shown in Fig. B.1. Appendix B shows how the absorption of O and X modes can be compared to give the electron density as a function of height (the DAE). But the measurement of total D-region absorption forms quite an important experiment in itself.

How is this total absorption measured? A variety of techniques exist, and Dieminger (1978) has given a brief review. The three main groups of measurement are A1 (measurement of the amplitudes of pulses critically reflected from the ionosphere), A2 (measurement of the absorption of extra terrestial radio noise), and A3 (measurement of the field strength of sky wave signals at short distances and oblique incidence on frequencies suitable for obtaining absorption data). Another technique used is the measurement of the minimum frequency recorded on an ionosonde, but this technique has come under some doubt recently, particularly for high absorption (Kotadia and Gupta, 1976; Offermann 1979). All the techniques used have shortcomings. Those which rely on critical reflection from the ionosphere, for example, actually contain two types of absorption. Firstly there is the non-deviative absorption, which is the absorption which occurs in the passage through the D region to the height of reflection and back (for D region absorption measurements, the frequency is chosen such that the reflection height is in the E region

(or F region at night)). Secondly, absorption occurs during the reflection process, and this is called deviative absorption. Strictly, it is only the non-deviative absorption which is desired. The deviative absorption can be minimized by correct choice of the frequency used. Further, the reflection height will depend on the frequency used, and the total absorption naturally depends on this height. If in fact reflection is from low sporadic E (93-95km) the absorption can be underestimated (Smith et al., 1978). But for all the disadvantages, measurement of absorption by these techniques forms a cheap and extensive way to monitor the ionosphere. Offermann (1979) has given a good review of D region absorption, and mentions some references comparing ground based absorption measurements and rocket results. Provided care is used, the techniques show fair agreement with rocket data. The Journal of Atmospheric and Terrestrial Physics, Volume 41, Numbers 10/11, 1979 also provides some good papers on absorption experiments.

The actual parameter used in Al measurements of absorption is the L parameter,

$$L = 20 \log_{10}(E_0/E), \qquad (1.2.3.1)$$

where E is the field strength received at the ground, and E_0 the field strength which would have been received had there been no absorption. The practical calculation of L will be discussed in Chapter 3, with some results for Townsville, Australia (19°S).

The degree of absorption varies on a variety of time scales - daily, seasonally, and with sunspot cycle, for example. The daily variation is fairly predictable. One may expect ionization to be maximum at minimum solar zenith angle χ, since the Sun's radiation has less ionosphere to pass through, resulting in higher intensities in the D

region, and hence higher ionization production rates. Thus one expects small absorption in the early morning, increasing to around 1200hr to 1400hr, and then decreasing toward sunset as χ once again increases. However, the rate of change of absorption can vary. Sometimes the L parameter does increase to noon and then fall away quite smoothly, following a roughly $L = L_0 \cos^{\eta}\chi$ form. The value η varies, but is generally ~ 0.75, though it may be as low as 0.4 and as high as 1.4 (Dieminger, 1978). On other days, absorption increases rapidly after sunrise, achieves an approximately constant value for much of the day, and then decreases rapidly around sunset. At other times, absorption can show big increases, associated with solar flares. Such effects last a few hours, and are termed SWFs (Short Wave Fadeouts) corresponding to SFEs (solar flare effects). Some examples of all these effects will be seen in Chapter 3, and Dieminger (1968) has given further examples. Taubenheim (1962) provided a good discussion of some SWFs, and presented evidence that the effect was primarily due to X ray effects at wavelengths of 0.2 to 0.3nm. He felt the absorption was primarily due to an electron density increase around 70 to 75km, and that the ionization was due to a line emission of X rays around 0.2nm. Generally, SWFs are associated with X rays with wavelengths in the range 0.1 to 1.0nm. Taubenheim's 1962 paper gives some of the earlier references on this topic, and the paper by Offermann (1979), section 3, some later ones. Gnanalingam and Kane (1979) and Parameswaran et al. (1978) also show evidence of X ray (.1 - .8nm) effects on the D region .

With regard to solar cycle effects, absorption is generally larger in years of maximum sunspot activity, due to increased solar emissions at short wavelengths. SWFs also tend to be more common in sunspot maximum years, due to increased flare activity on the Sun. For example, Bremer and Singer (1977) showed some solar cylce effects, as did Beynon

and Williams (1976a). Schlegel et al. (1977) suggested evidence for a shorter term correlation of D region absorption and interplanetary solar magnetic fields. They suggested that this implied a Cosmic ray dependence, since galactic cosmic ray intensities are governed to some extent by the solar wind (Forbush effect; e.g. see Van Allen, 1979).

Another commonly observed departure from "normality" are the geomagnetic storm effects. At times there are large currents flowing in the auroral ionosphere called electrojets, caused by the influx of high energy particles from the Sun and outer ionosphere. These produce fluctuations in magnetometers on the ground, and a geomagnetic storm is said to be occurring. Associated with such activity it is frequently found that the D region can show greatly increased absorption. There is a delay between the magnetic storm and the D-region effects, generally of the order of 1-3 days (e.g. Beynon and Williams, 1976a). Evidence suggests that the effects are due to high energy electrons (up to 1000keV; e.g. Montbriand and Belrose, 1976) precipitating down from the higher regions of the ionosphere (magnetosphere and Van Allen Belts). The delay in time seems to depend largely on the spatial and temporal distributions of the precipitating electrons (Beynon and Williams, 1976a; Montbriand and Belrose, 1976; Wratt, 1977; Offermann, 1979). Dickinson and Bennett (1978) suggested that the effect occurs predominantly in the region 68-90km. They also showed that the ledge in electron density frequently seen at around 85km (see section 1.2.1) almost disappears on such days.

The seasonal variation in absorption provides one of the greatest D-region enigmas. One might expect the absorption to be maximum when χ is least, and least when χ is largest. Thus it could be expected that noon absorption (or, as a better measure, the value L_0 which is obtained by fitting $L = L_0 \cos^{\eta}\chi$ to a full day's data) would be maximum in summer,

and least in winter. However, this is not the case, particularly above 35° to 40° lattitude. Winter shows a dramatic increase in absorption. There is an increase in the overall mean absorption, and also particular days of extraordinarily high absorption (anomalous days) occur. This winter increase is commonly known as Winter Anomalous Absorption (or simply the Winter Anomaly). Fig. 1.5 shows this effect. Absorption increases upwards on the vertical axis. During summer months, the trend is roughly as expected (smooth curve), with maximum absorption during mid-summer, and less either side. But during winter, the mean absorption is much higher.

Offermann (1979) provides an extensive review of the winter anomaly, and to some extent the following discussion is based on that reference. The Journal of Atmospheric and Terrestrial Physics, Volume 40, Number 10/11, 1979, also contains results of an extensive set of absorption investigations.

There appears to be a lower latitude limit to anomalous absorption around 40°, as discussed, but this does not mean anomalous absorption does not occur at all for latitudes below 40°. Rather, its magnitude decreases significantly at 40°-50°(Schwentek, 1976), then flattens out somewhat below 40°. The effect still exists below 40°, however, right down to around 20° latitude, although with decreasing strength. There may in fact also be an increase in absorption as one moves equatorward from 20°, but this is true in summer as well as winter. Below about 10°, winter and summer absorption values are similar. Schwentek (1976), Fig. 2, provides an excellent illustration of these effects. For ease of reference, the graph is reproduced here as Fig. 1.6. Results also suggest that the effect is similar in both hemispheres. An upper latitude limit to the winter anomaly is harder to define, as auroral effects begin to disturb the D-region greatly, making days when winter anomaly can

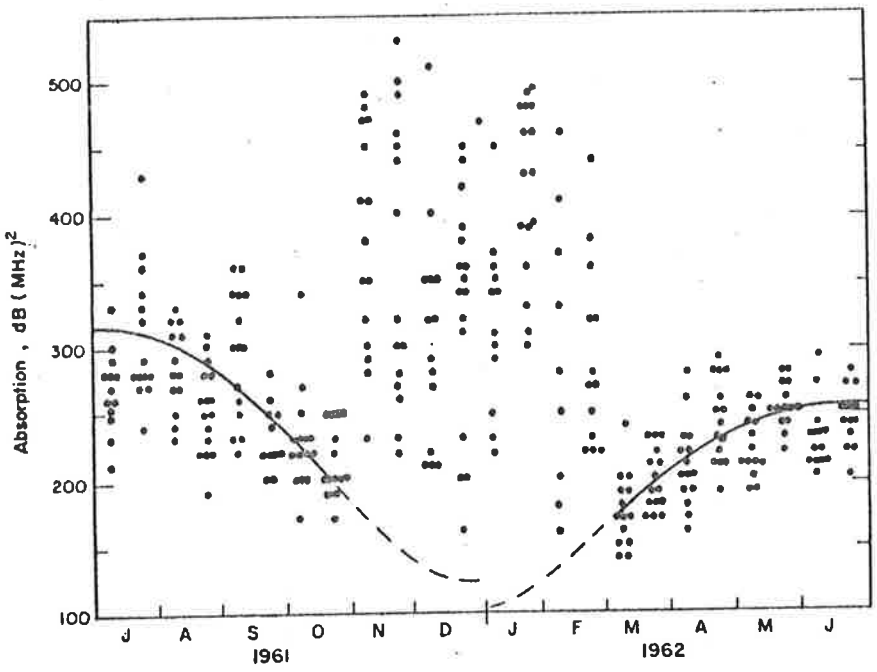

Fig. 1.5 Variation of the non-deviative absorption at noon for an effective frequency of 1MHz at vertical incidence between July 1961 and July 1962 as derived from measurements at 2.61MHz over a path of 295km (Northern hemisphere). The curves correspond to a $\cos^{0.75}\chi$ variation, the discrepancy between December 1961 and January 1962 being due to the change in the mean solar activity. The diagram comes from Thomas (1971), Fig. 15, and was originally due to Schewentek (1963).

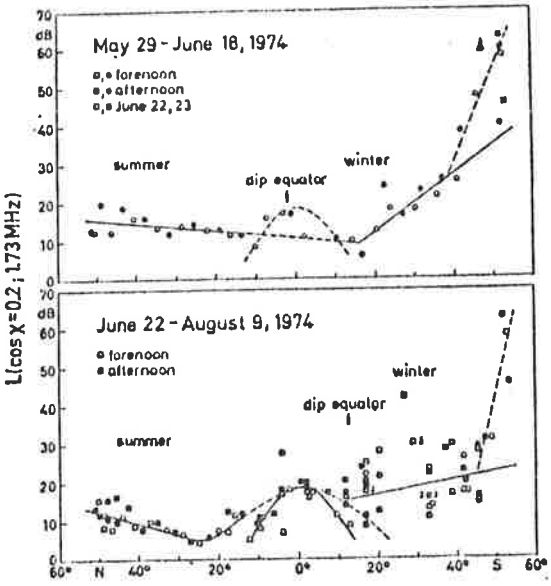

Fig. 1.6 Absorption L(cos χ = 0.2; 1.73MHz) as a function of geographic latitude. From Schwentek (1976). The data was taken on board a ship, so the two sets of data do not refer to the same longitudes. This is also why the dip equator appears at different latitudes in each case.

be studied rare. Ranta and Ranta (1977) have suggested a limit of 60°-65°, above which summer absorption is greater than winter (for example, see figure 4 of that reference). It also appears that the "erratic" part of the anomaly (that is, the occurrence of anomalous days of very high absorption) does not exist below about 40°, whereas the smoother winter increase (which Offermann calls the "normal" winter anomaly) does.

The latitudes mentioned above refer to geographic coordinates, and workers in this field appear to use such coordinates for their work. However, there may also be geomagnetic effects. Schwentek (1976) discussed this possibility, but, as seen in Fig. 1.6, the effect does seem to be geographic. The dip equator does not appear to be in a unique position relative to the absorption curves. Beynon and Williams (1976a), also feel the true winter anomaly is not strongly related to geomagnetic activity. (They do, however, claim to find a weak longitudinal dependence of the anomaly.)

It appears, particularly from rocket flights, that anomalous winter absorption occurs primarily due to increases in electron density (by a factor of typically 2 to 10 times) in the region 75-95km, with maximum enhancement around 80-83km (Beynon and Williams, 1976a, 1976b; Beynon et al., 1976; Smith et al., 1978). Smith et al. (1978) however, did find at least one case where the major effect appeared to be below 82km. Winter anomaly absorption is most pronounced at around 2.5MHz, and Beynon and Williams (1976a) suggest this is because the largest absolute electron density increases are at heights of greater than 90-95km. They feel the increases in electron density lower the height of reflection at frequencies less than about 2MHz, artificially depressing the absorption estimates on these lower frequencies. Above about 2.5 to 3MHz, absorption

simply falls off with increasing frequency (see Fig. B.1).

The spatial scale of the winter anomaly can be quite large. At times, correlations between places up to 1000 to 2000km apart can be observed (e.g. Schwentek, 1974; Offermann, 1979). Correlation up to 300km separation is frequently good.

One other feature of winter anomolous absorption is the occasional occurrence of regular oscillations in absorption (Offermann, 1979) which have periods typically in the range 7 to 14 days, and can appear coupled with ground pressures (Rose and Widdel, 1977; Offermann, 1979). These quasi-regular long period oscillations are possibly associated with a general class of planetary scale, long period oscillations called planetary waves (see later). Fraser (1977) claims to have found a correlation between the 30mb temperature and ionospheric absorption, each parameter having a period around 5 to 6 days. Brown and John (1979) also found correlations of oscillations, with periods 6 to 30 days, between the pressure oscillations at the surface, and the heights of electron isopleths in the E region, at times. Their work suggests that whether there is a correlation or not depends largely on stratospheric winds. Moderate eastward stratospheric winds allow propogation of planetary waves upward most easily, strong eastward winds inhibit propogation somewhat, and westward winds inhibit propogation greatly. Ebel (1978) also investigated quasi-regular periods in ionospheric absorption, and feels that, at times, planetary wave generation can occur in the thermosphere.

Explanations of the winter anomaly revolve largely around observed increases in NO^+ density during these events (e.g. Beynon et al., 1976: Aikin et al (1977): Offermann, 1979). Also associated with anomalous absorption is a lowering of the transition height from water cluster ion dominance below to NO^+ dominance above. This is generally about 83-85km,

but falls to heights around 77km during anomalous events (Fig. 1.2b). The general scheme appears to be that increases in NO molecular densities occur, resulting in higher electron densities. Offermann (1979) however, also suggests O_2 ($^1\Delta g$) concentrations may be increased also, allowing ionization of this species as well. However, few rocket flights measuring O_2 during anomalous absorption have been undertaken.

Explanations for the increase in NO density are based on either transport processes, or chemical changes through temperature dependence. The idea of NO produced in the auroral regions by particle precipitation and transported equatorward by meridional winds, is one which has been tested to some degree. Geller et al (1976), Wratt (1977), and Meek and Manson (1978), all claim to find correlations between increased electron densities and equatorward winds. However, a correlation between winds and absorption at a few places alone does not imply that the above mechanism is valid. The presence of zonal winds may mean that a particle starting at the auroral zone may never reach the lower latitudes (that is, the Lagrangian path lines may not link the auroral regions and equator). Offermann (1979) points out that preliminary results from Labitzke et al. suggest that there is no correlation between the ionospheric circulation and increased absorption.

The other major transport mechanism is that of transport from above. Koshelev (1979) has shown how variations in the turbulent eddy diffusion coefficient can result in transport of N and O species from greater heights, increasing the concentration of NO at 75 to 95km. If a temperature inversion exists at about 75 to 80km, this may prevent transport of these species any lower, resulting in a significant increase above. The possibility also exists for a temperature dependence of this diffusion coefficient (Zimmerman and Narcisi, 1970; Offermann, 1979).

Temperature dependences, with resulting chemical changes, form another line of explanation. Many of the reactions in the D region are strongly temperature dependent so small changes in temperature can have significant effects on chemical composition. The mesopause is warmer in winter than summer, and theory suggests that the warmer mesopause could result in increased NO densities (Offerman, 1979). Large temperature changes, of the order of 100K can occur in the D region within time scales of a day or so, and these could be correlated with anomalous absorption (Offermann, 1979). Theoretical results suggest temperature changes can dramatically affect NO densities (Reid, 1977; Koshelev, 1979).

Fig. 1.2b shows a quite dramatic change in NO densities for a cold dry atmosphere and a warm wet one, when the two NO curves of Reid are compared. Reid's results also explain the lowering of the transition height. Chakrabarty et al. (1978c) also claim to be able to explain this lowering of the transition height.

Reid's curves in Fig. 1.2b also illustrate to some degree the effect of changes in water vapour content, although the reader is referred to Reid's original paper for proper independent comparisons of temperature effects, and water vapour effects. The concentrations of H_2O, O, O_3, CO_2 and so forth can have important roles in the reaction rates in the D region (see Fig. 1.3). More accurate measurements of these quantities are important. Gadsden (1978) has pointed out possible errors in one method of water vapour determination.

Clearly, there are many possible factors which can affect D region absorption. There is still much work to be done, but based on present evidence, Offermann suggests the following scheme:

> "a strong temperature enhancement in the D-region is associated with increased downward turbulent transport of NO and O. This explains the high NO^+ and O_2 ($^1\Delta g$) densities measured, as O enhancements effect O_2 ($^1\Delta g$) increases via stronger O_3 production. At the same time both the high temperature and the

increased electron production rate act to decrease the water cluster ion formation. Furthermore the temperature inversion impedes the turbulent transport of water vapour from below, thus further decreasing the cluster formation."

1.3 D Region Dynamics

1.3.1 The Equations Governing the Atmosphere

Movements in the ionospheric D region are driven by a variety of forces - from seasonal winds to winds which oscillate in strength with regular periods, and right down to extremely small scale turbulence. Although studies of global winds do not form a major part of this thesis, an understanding of their main characteristics will still be necessary. Some of the smaller scale oscillations may turn out to be quite important in the studies presented here. Turbulence, it appears, is a crucial ingredient of the phenomena discussed in this work. For these reasons, then, a brief review of mesospheric dynamics will be given here, with the general tendency to place emphasis on the smaller scales. Turbulence will be discussed in some depth.

As with some other introductory aspects of the ionosphere, there is insufficient room to discuss the derivation of the equations of fluid dynamics, and their use in predicting atmospheric motions, in this chapter. A brief review is given in Appendix C. This section (1.3) of Chapter I will concentrate more on physically observed properties of the Earth's atmospheric dynamics.

Appendix C also contains a description of some of the important characteristics of gravity waves, planetary waves, and tides, with relevant references.

1.3.2 Experimental Observations of Atmospheric Winds

The general wind circulation of the Earth's Atmosphere, whilst not directly related to this thesis, should still be appreciated, as from time to time knowledge of atmospheric winds will be necessary.

Geller (1979) gives quite an extensive review of atmospheric dynamics, at least with regards to the mean winds, planetary waves, and temperature, of the middle atmosphere. Geller also gives an account of stratwarms - sudden warmings of the stratospheric temperature, with associated wind circulation breakdowns in the mesosphere. This aspect will not be discussed here. Groves (1976) provides quite a good review of atmospheric tides. Fig. 1.7 shows an approximate diagram of mean winds in the lower to middle Earth's atmosphere. Above 70km tidal oscillations frequently achieve amplitudes of 20 to 30ms^{-1} (e.g. Vincent and Stubbs, 1977), and amplitudes greater than 50ms^{-1} have been observed at Townsville, Australia (19°S) (R.A. Vincent, private communication). Hence the winds fluctuate greatly on a daily basis. Groves, Fig. 1 (1976), shows a good example of this, and it can be seen that tides become important above about 40 to 50km.

Evidence also exists at times for strong planetary wave activity at these heights, particularly with 2 and 5 day periods. Some mention of these has been made in Section 1.2.3. Muller and Nelson (1978) have shown evidence for a 2 day wave which peaks strongly in mid-summer (Northern hemisphere July-August). R.L. Craig (private communication) has shown the existence of an extremely strong ($\gtrsim$ 40ms^{-1} amplitude) quasi-2-day wave in the latter weeks of January at Adelaide (35°S, 138½°E) (Southern Hemisphere summer). The wave exists primarily in the meridional component - the zonal component is very weak for this wave. Various references to 5 day waves can be found in Muller and Nelson (1978) and Geller (1979). But for proper investigations, a world wide cooperative

Fig. 1.7 Approximate diagram of the mean atmospheric zonal (i.e. parallel to lines of latitude; EW) winds. Meridional winds (parallel to meridians of longitude; NS) tend to be somewhat weaker and less well defined (e.g. Groves, 1969). The top diagram comes from Geller (1979) and was originally due to Murgatroyd (1969).

Also shown are profiles of the mean winds for 35°S, winter and summer. Groves (1969) provides an alternative source for graphs of the mean atmospheric circulation, and points on these profiles above 70km come from that source (January is used for summer, June for winter).

Positive winds are eastward.

Notice in particular the strong westward jet at 60-70km in summer, and eastward jet at similar heights in winter (at Adelaide, this jet seems to be slightly higher, at 68 to 76km). The transition from winter to summer can be quite dramatic, taking place over only a few days, with strong wind reversals at around 70km. Such changes have been observed at Adelaide, September-October, 1979 (unpublished results). The strong winter to summer (and reverse) transition has also been observed in the phases of the semi diurnal tide (e.g. Schminder and Kurschner, 1978) at 90km. (Two phases are generally defined for tidal analysis - the hour of maximum northward wind, and hour of maximum eastward wind.)

It may also be worth bearing in mind that much of the data in this diagram was actually obtained using Northern hemisphere observing stations, and assuming the Southern hemisphere to be similar. Hopefully in the future more genuine Southern hemisphere measurements can also be used in the compilation of such diagrams.

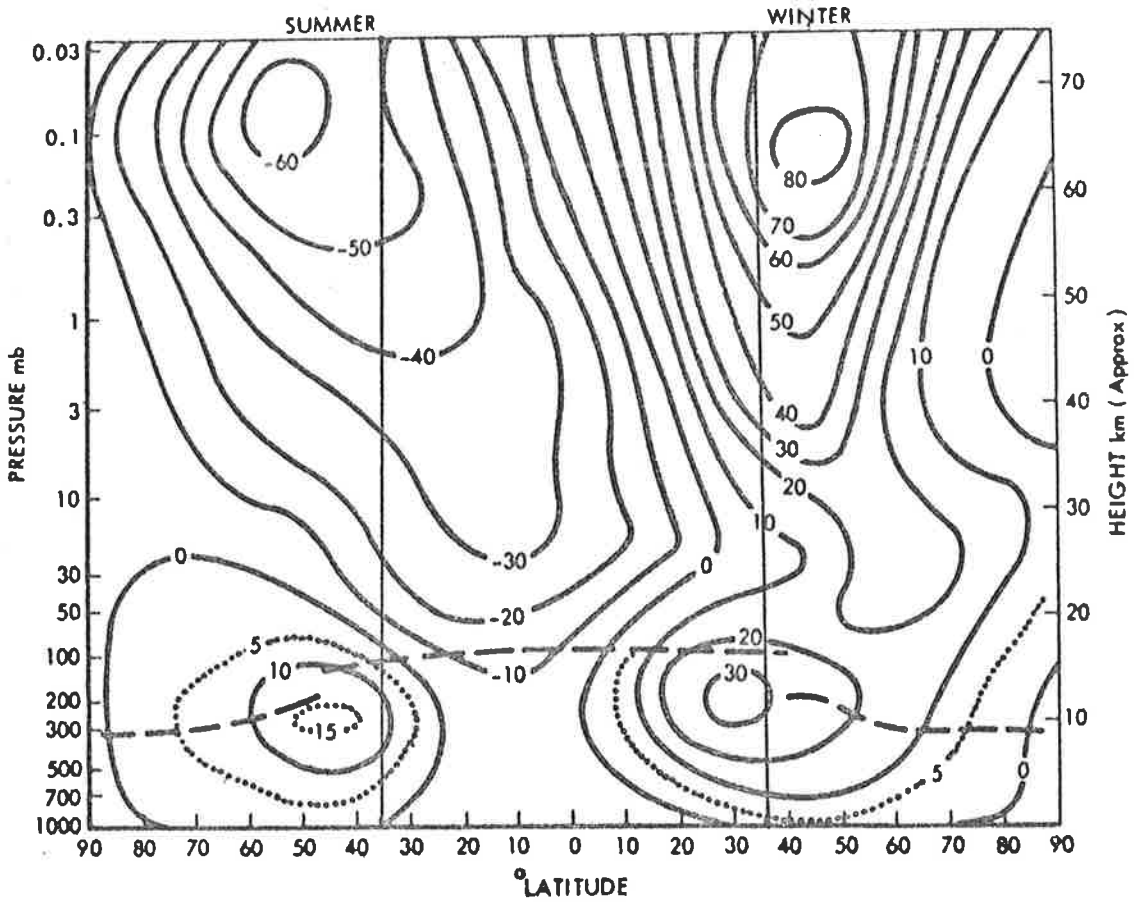
SUMMER
WINTER
PRESSURE mb
HEIGHT km (Approx)
°LATITUDE
0.03
0.1
0.3
1
3
10
30
50
100
200
300
500
700
1000
90 80 70 60 50 40 30 20 10 0 10 20 30 40 50 60 70 80 90
-60
-50
-40
-30
-20
-10
0
5
10
15
20
30
40
50
60
70
80

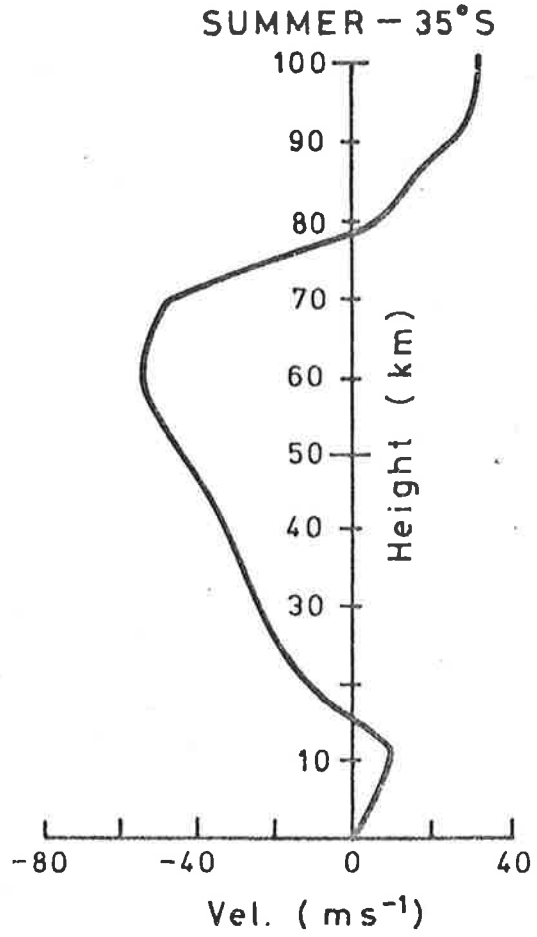
SUMMER – 35°S
Height (km)
100
90
80
70
60
50
40
30
10
-80 -40 0 40
Vel. (ms⁻¹)

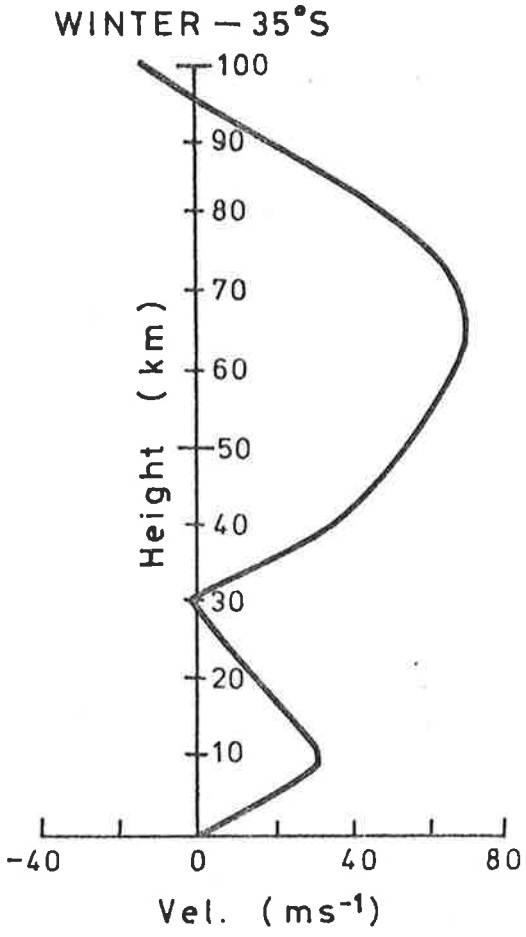
WINTER – 35°S
Height (km)
100
90
80
70
60
50
40
30
20
10
-40 0 40 80
Vel. (ms⁻¹)

program is necessary, and extensive satellite measurements. Houghton (1978) discusses some satellite data in a review of the stratosphere and mesosphere.

Experimental investigation of upper atmospheric tides is a vigorously researched subject. Some good data has been obtained, and a picture of the Earth's atmospheric tides is beginning to emerge. However, a full picture is still some way off. Many papers have been published on individual measurements of tides, but to establish information on the important modes, a grid of stations is necessary over the Earth's surface. An attempt has been made to do this with the CTOP (Cooperative Tidal Observations Program (organized as a joint venture by URSI (International Union of Radio Science) and IAGA (International Association of Geomagnetism and Aeronomy)) but results are only beginning to be compared. The Journal of Atmospheric and Terrestrial Physics, Volume 40, Number 8, 1979, contains a collection of papers on these early coordinated studies. Adelaide University has stations at Adelaide (35°S, 138½°E), Townsville Australia (19°S, 147°E) and is at present cooperating with Christchurch, New Zealand (44°S, 173°E), Broken Hill, Australia (32°S, 141½°E), and Kyoto, Japan (35°N, 136°E), to gain some feel for important modes. Some information on tidal amplitude variations with height, and season, has been gained for Adelaide (e.g. Stubbs, 1973; Stubbs and Vincent, 1973; Stubbs, 1976; Vincent and Ball, 1977; Vincent and Stubbs, 1977). Needless to say, many other stations exist, and are doing similar work (J. Atmos. Terr. Phys., 40, No. 8, 1978). Saskatoon, Canada (e.g. Manson et al., 1979) is another station making tidal observations. The Russians have quite an extensive meteor observatory network.

One point concerning tides is the way diurnal tides often seem to decrease in amplitude as they approach 90km from below (e.g. Elford and

Craig, 1980). One suggestion for this is that energy is being dissipated into turbulence (e.g. Elford and Roper, 1961; Stubbs and Vincent, 1973; also see Fig. 1.9b which shows a possible correlation of diurnal tides and turbulent dissipation). Yet the radio wave partial reflections from 90km seem to be related to turbulence at 90km (see later in this thesis). Then this case serves as a classic example of why, in considering these partial reflections, a wide knowledge of the atmosphere is necessary, and again justifies the rather general approach taken in this chapter. Even if the concept is wrong (standing waves due to reflection of tides have also been invoked to explain the 90km minimum in tidal amplitudes; or mixing of tidal modes with different vertical wavelengths could also explain this minimum (this latter argument is supported by observations of large phase changes across the minimum (e.g. Elford and Craig, 1980))), the necessity for a wide comprehension of the atmosphere can still be seen.

Factors such as day to day variations of tidal strengths (which can be quite dramatic) and seasonal variations, can be found in references such as Stubbs (1976); Manson et al. (1979).

Gravity waves appear to contribute greatly to the dynamics of the mesosphere. In fact, gravity waves, tides and planetary waves (and to some extent acoustic waves; Rind, 1977) are perhaps the major coupling mechanisms between the various levels of the atmosphere. The general view is that these waves are generated in the troposphere and stratosphere, and propagate their energy upwards to the higher regions. This does not discount the possibility that the waves can also be generated higher up (e.g. Ebel, 1978), but present work appears to concentrate significantly on the concept of generation in the lower atmosphere. Not all waves generated in the lower atmosphere reach the upper atmosphere, however. In Appendix C, the concept of critical layers and critical

reflections is discussed, whereby atmospheric waves can be prevented from propagating past certain levels if particular wind and temperature conditions prevail. Hines and Reddy, (1967), for example, discussed filtering of these waves by background winds, and showed that significant portions of the gravity wave spectrum generated below the stratopause may be filtered out on occasions. The prevention of planetary wave propogation by stratospheric winds has already been discussed in Section 1.2.3.

The source of tides in the mesosphere is largely solar heating of atmospheric Ozone and water vapour (e.g. see Appendix C). An understanding of the sources of planetary waves is still some way off although it is known that the latitudinal variation of the Coriolis parameter can drive Rossby waves (Appendix C; also Houghton, 1977, Section 8.4). Baroclinic and Barotropic instability can also generate such waves (Houghton, 1977, Ch. 10). Manson et al. (1979) mentioned the possibility of baroclinic instability in the mesosphere. Gravity waves and acoustic waves may be generated by a wide range of mechanisms. Rind (1977) studied 0.2Hz acoustic waves (microbaroms) generated by large amplitude ocean waves. Such long period acoustic waves, up to the acoustic cut off period (Appendix C) are called infrasound.

With regard to gravity waves, many sources have been proposed - lee waves (these are non-propagating) due to the passage of wind over mountains, thunderstorms, jet streams, cloud convection - in fact almost any effects which cause atmospheric oscillations with periods greater than the Brunt-Vaisala period (which is the period of oscillation for an air parcel oscillating adiabatically in the air). Gravity waves can also be generated in situ - e.g. large amplitude non-linear tidal motions or the interaction of tides and gravity waves can lead to potentially unstable wind shears which may further generate gravity waves

(e.g. Hines, 1960; Sidi and Teitelbaum, 1978). The motion of the moon's shadow over the Earth during an eclipse has also been suggested as a source. However, detailed experimental investigations of these processes is only just beginning.

One technique (called ray tracing) is to take a clearly observed gravity wave in the atmosphere, and effectively "turn it round" on a computer to propagate from whence it came, using a model atmosphere (principle of reversibility). Sometimes the wave can be tracked to sources at ground level (e.g. S.M. Ball of Adelaide has tracked gravity waves seen by E region phase measurements back to tropopause jet streams (private communication); Bertin et al. (1978) also find associations with jet streams, and Hung et al. (1978) claim to be able to track many gravity waves to tornadoes). Sometimes with ray tracing, the tracking stops at some height where the wave could not have penetrated. This means either the wave must have been generated above this level, or the model wind and temperature profiles used were inaccurate. It is clearly important to be able to distinguish between these possibilities, and great care is necessary in the choice of the model atmosphere - otherwise the model may prevent propagation where the real wave may have penetrated on that day. Alternatively, the model may allow propagation whereas in the real case the gravity wave could not have penetrated. Accurate wind measurements at the time of wave propagation are to be preferred for the computer model. Of the authors above, Ball, and Bertin et al. (to some extent), use experimental winds in much of the mesosphere. Hung et al. use a model only.

Other methods of looking at gravity wave sources exist. Clark and Raitt (1976) looked at the possibilities of generation by supersonic motion of the terminator, the equatorial electrojet, and energy deposited in the auroral regions during magnetic activity. (The auroral regions

are regarded as a major source of gravity waves. Manson et al. (1979) by statistical analyses, suggested that the Rocky Mountains of North America are a source for many of the waves they observe in the mesosphere. Rottger (1980) examined gravity waves he felt were generated by jet streams, and by convection in the troposphere. Several observers have looked for solar eclipse induced gravity waves, but results appear to be inconclusive. Some authors claim to see waves, others claim null results (Cornelius and Essex, 1978; Bertin et al., 1977; Butcher et al., 1979; Ball, Stubbs and Vincent, 1980).

The role of the various oscillations in transporting energy from the sources to the mesosphere is another important facet of observation. Rind (1977) has reviewed the major energy dissipation mechanisms in the atmosphere. Rind lists viscosity, heat conductivity, relaxation processes, radiation, bulk viscosity, diffusion, mean free path effect, Joule heating and turbulence as the major mechanisms. Turbulence is perhaps the most important below 100km. Calculations of energy (and momentum) dissipation rates can be made for the mesosphere, using the height variation of RMS wave velocities (e.g. Vincent and Stubbs, 1977; Manson et al., 1979) and results agree with observed turbulent dissipation rates as measured by rockets (e.g. Rees et al., 1972). Energy dissipation in the mesosphere thus appears to be largely due to these waves (typically .01 to 0.5W/Kg). Generally, gravity waves seem to carry more energy to the mesosphere than tides, and tides more than planetary waves, but this may vary from day to day (see Fig. 1.8). Rind (1977) feels that at 110km, acoustic waves can be as important as gravity waves. Elford (1979) has discussed the role of these waves (particularly tides) in the momentum budget of the Earth's atmosphere.

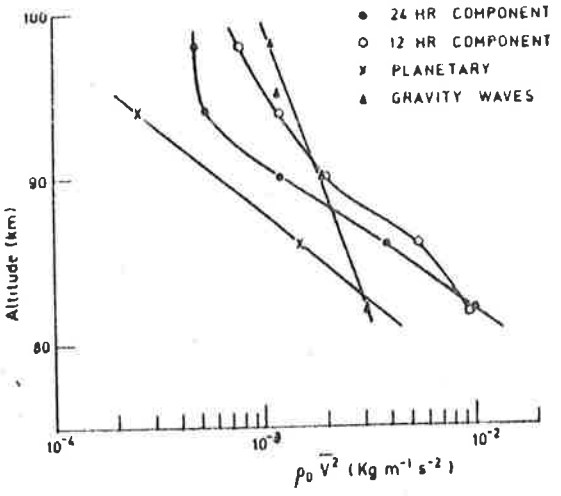

Fig. 1.8 Altitude profiles of ($\rho_0 \overline{V}^2$) (which is proportional to the energy density per unit volume) for the various wave motions of the upper mesosphere at Adelaide, Australia (138½°E, 35°S) for June 15-21, 1973. From Vincent and Stubbs (1977).

The constant of proportionality relating energy and $\rho_0 \overline{V}^2$ depends on the type of energy being considered and the wave type. According to Teitalbaum and Blamont, 1977.,

Total energy = kinetic energy + elastic energy + thermobaric energy.

Generally the elastic energy can be ignored for gravity waves.

For gravity waves, the thermobaric energy is approximately equal to the kinetic energy (and is in phase quadrature), and this is equal to $\frac{1}{2}\rho_0 \overline{V}^2 = \frac{1}{4}\rho_0 V^2_{max}$ (V = velocity of displacement = $\underline{u} + \underline{v}$, $\underline{u}$ and $\underline{v}$ being displacement velocities in orthogonal directions approximately perpendicular to the wave normal).

For the diurnal tide, the kinetic energy is 2 orders of magnitude greater than the elastic energy, and 7 times the thermobaric energy, at 33°N, (and likewise at 35°S), so the total energy is approximately the kinetic energy (Teitelbaum and Barat, 1977).

Notice in all cases the kinetic energy is = $\frac{1}{2}\rho_0 \overline{V}^2$.

Thus the total energy due to tides is $\frac{1}{2}\rho_0 \overline{V}^2$, and that due to gravity waves is $\rho_0 \overline{V}^2$.

1.3.3 Mesospheric Turbulence

Turbulence may play a significant role in the scatter of radio waves from the mesosphere. Some knowledge, then, of mesospheric turbulence structure is essential. A discussion of turbulence, and a collection of important definitions and formulae, can be found in Chapter II. The section below will discuss the height distribution of some important turbulence parameters.

In the mesosphere, the atmosphere is generally potentially turbulent. An appropriate realistic wind shear, or unstable temperature profile, can generate the random irregular motions characteristic of turbulence. However, above a height band, of width about 5km, somewhere in the region 90 to 115km, turbulence of the neutral atmosphere rarely occurs. (Enormous energy inputs would be required to produce turbulence here. However, turbulence can occur in the plasma at greater heights; for example, the Rayleigh-Taylor instability believed to cause spread F (eg. see Chiu and Straus , 1979) is a type of turbulence, and the electrojet irregularities observed by VHF radars may well be a type of plasma turbulence (Sudan et al. 1973).) This height band is known as the turbopause. Its height varies, depending on local conditions. This is not to say, however, that below the turbopause the atmosphere is always turbulent. Some of it may be, but some flow can be laminar, too. (Turbulence often appears in patches, or clouds (eg. Blamont and Barat, 1967; Anandarao et al., 1978). Anandarao et al. claim a correlation between strong wind shears and turbulence, but not all observers have seen this. Blamont and Barat (1967) and Roper (1971) have suggested gravity wave activity may create these patches, perhaps along similar lines to the suggestion of Hodges (1967).) Rather, the turbopause represents the height above which flow, as observed by say a rocket experiment, is always laminar. Most momentum, particle and heat transport takes place by molecular processes rather than turbulent processes at these higher altitudes - in other words, the

molecular diffusion coefficient becomes greater than the eddy diffusion coefficient. (Eddy and molecular diffusion coefficients are defined more precisely in Chapter II. For the present, regard them as parameters indicating how fast momentum, density, temperature and so forth can be transported by turbulent and molecular means respectively.)

If eddy diffusion extends to greater heights on any one day, then greater mixing occurs in the region 90-120km. This can alter the state of the atmosphere, and has been invoked by Koshelev (1979) and others, to explain enhanced 90km NO concentration on anomalous winter days (Section 1.2.3). Blum et al. (1978), and Blum and Schuchardt (1978) have examined the variations of density of He, O, N_2 and Ar in the thermosphere which would be induced by variations of the eddy diffusion coefficient profile (and hence the turbopause height) and temperature. They have then taken the densities of these constituents as measured by satellites and worked backwards to calculate the height of the turbopause as a function of latitude and season. The height varies from 90km to 115km. Their eddy diffusion coefficients agree reasonably well with observed values. The authors do, however, point out that the He, O, N_2 and Ar density variations could also be due to wind transport processes. Their main point is that thermospheric density variations are related, to some degree, to turbopause heights.

Teitelbaum and Blamont (1977) examined the turbopause height using rocket data. They looked at night-time variations. Wind fields were calculated by rocket vapour trail releases, and the height variation of the energy density after removal of tides gave an indication of the turbulence. Two main regimes were found:
around twilight (up to 2200hr in the evening, and after 0400hr in the morning), the mesosphere and lower thermosphere were turbulent up to

heights of the order of 105km; and between 2200 and 0400hr, the turbopause fell to around 95km. The authors explained this behaviour as being due to gravity wave input, which they claim is greater around the twilight hours. This increases turbulence, via processes such as the production of strong wind shears when the gravity waves interact with tides (Teitelbaum and Sidi, 1976). The passage of the terminator over irregularities in Ozone concentration was proposed as a mechanism to explain the increased twilight gravity wave activity. Teitelbaum and Blamont also calculated the eddy diffusion coefficient K as a function of height, and obtained values around 10^6-$10^7 cm^2 s^{-1}$ (10^2-$10^3 m^2 s^{-1}$). These seem typical values (eg. Fig. 1.9c contains a collection of profiles of K). Teitelbaum and Blamont claimed that K increased from around $2 \times 10^2 m^2 s^{-1}$ at 97km to around $10^3 m^2 s^{-1}$ at the turbopause height, with a sharp fall above this height; although the result is very sensitive to the analysis technique. However, other workers have assumed similar profiles (eg. Koshelev, 1979; Blum and Schuchardt, 1978, model KII).

Rees et al. (1972) have also examined the height of the turbopause. They used as their indicator of the turbopause the time t_* ($= (\nu/\varepsilon)^{\frac{1}{2}}$, where ν is the kinematic viscosity and ε is the turbulent energy dissipation rate (this follows by equations 2.2.3.0 and 2.2.3.2c in Chapter II)) taken for the turbulence to become evident in luminescent vapour releases from rockets. (The turbulence is assumed to exist before the rocket release, but it takes time for the vapour to become mixed and hence show evidence of the turbulence.) Observations of turbulence in this case were taken by photographing the development of sodium-based vapour trails, and using visual inspection to determine when flow was laminar, and when turbulent. They found t_* increases dramatically around the turbopause height. Physically, the kinematic viscosity ν becomes just too large to provide a reasonable t_* - enormous energy inputs ε are necessary to produce

turbulence, and so flow is generally laminar. (These large ν at high heights mean that the atmosphere behaves something like honey up there!) Variations in the height of the turbopause are dependent upon the energy dissipation rate ε, since ν is reasonably time independent. Interestingly, Rees et al. found some evidence of turbulence up to heights of 130km, but its effects were very weak relative to molecular diffusion processes. So it is seen, as has been pointed out above, that the turbopause does not represent a clean break between turbulent and molecular diffusion, but rather a transition region (albeit a very sharp transition).

The height of the turbopause is not, of course, the only important parameter measured in the atmosphere. One extremely important parameter is the energy dissipation rate, ε. Rees et al. (1972) calculated this from measurements of t_* (t_* being defined above). That is, $\varepsilon = t_*^{-2}\nu$; and ν, the kinematic viscosity, can be obtained from standard atmospheric profiles. Usually, ε is expressed in units of Watts kg^{-1} ($= m^2 s^{-3}$) (energy deposition rate per unit mass), but often it is useful to express ε in terms of the temperature change such an energy input would make in the atmosphere per day. A useful conversion is

$$(°C/day) = 86.4 \times \varepsilon \text{ (Watts kg}^{-1})$$

at heights of around 90km (eg. Justus, 1967).

Turbulence can be Fourier decomposed as the sum of various sinusoidal spatial oscillations, or "scales". Each scale has a "wavelength" λ, equal to the distance between the maxima of these oscillations. (These oscillations should not be confused with propagating waves; nor do they vary in time. They are simply Fourier scales.) A wavenumber $k = 2\pi/\lambda$ can also be associated with these scales; and sometimes the scale is expressed in length units per radian. A wavelength λ corresponds to a scale $\lambda/2\pi$. This Fourier decomposition results in an energy spectrum of

turbulence E(k). Here, E(k)dk is the energy associated with wavenumbers in the region, k to k + dk. This spectrum falls off with increasing k, until the Kolmogoroff microscale wavenumber

$$k_\eta = \left(\frac{\varepsilon}{\nu^3}\right)^{\frac{1}{4}} \text{ rad. } m^{-1}$$ is reached. (see equation 2.2.3.0)

(The associated scale $\eta = k_\eta^{-1}$ is called the Kolmogoroff microscale.)

Wavenumbers less than $k_\nu \simeq 0.169\ k_\eta$, and greater than a wavenumber k_*, called the "outer scale" wavenumber, lie in the so-called inertial range of turbulence. This is one of the most intensively investigated turbulence regimes. It is discussed in considerable detail in Chapter II. The spectrum follows the form

$$E(k) \propto \varepsilon^{2/3} k^{-5/3} \text{ within this region.}$$

Wavenumbers greater than k_η lie in the "viscous range".

The spectrum falls off extremely fast in this regime, since the shears associated with these small scales are quite strong and are quickly dissipated by viscosity. Rastogi and Bowhill (1976b) quote a spectrum of the form

$$E(k) \sim \left(\frac{\varepsilon}{\nu^2}\right)^2 k^{-7} \exp\left\{\frac{-k}{k_c}\right\},$$

where $k_c = 0.738 k_\eta$, for this viscous region, but there is still some debate as to the actual form of E(k) in this region. The form of the spectrum between k_ν and k_η is a mixture of the two forms discussed above. This is called the Tchen range.

At wavenumbers less than the outer scale wavenumber k_*, buoyancy effects become important. Eddies associated with these large scales also tend to be anisotropic - their horizontal dimensions are larger than their vertical dimensions. This is a gravity-induced effect.

From estimates of ε, the Kolmogoroff microscale can be estimated:

$$\eta = \left(\frac{\nu^3}{\varepsilon}\right)^{\frac{1}{4}} \text{ metres radian}^{-1}.$$

By multiplying by 2π, η can be expressed in metres.

The kinematic viscosity does not vary significantly in time at any one height, although ε can vary considerably. (For example, Fig. 1.9b shows typical seasonal variations of average ε values.) However, variations of ε by 20 times results in variations in η of only about 2 times. Hence η does not vary greatly in time at any one height. Rastogi and Bowhill (1976b) have compiled assorted measurements of ε, and hence η, and have plotted typical profile of k_η as a function of height (their Fig. 5). Some of their data was used to produce Fig. 1.9a in this text.

Fig. 1.9a attempts to delineate the various turbulence regimes as a function of height in the atmosphere. The data has been taken from various references, as explained in the caption. It should be mentioned, however, that the outer scale, as drawn on this graph, and the inner scale of the bouyancy range, L_B $(= \frac{1}{k_B})$, are both very crude estimates. Likewise, the estimates of regions where anisotropy becomes important are only approximate. However, they do at least serve as a reminder that not all the wavenumbers to the left of k_ν are in the inertial range. It may also be worth noting that although the inertial spectrum is not fully valid for wavenumbers between k_ν and k_η, often the inertial spectrum is assumed valid right down to wavenumbers k_η. This assumption is in fact necessary to derive many of the relations between scales, energy deposition rates, times, etc. obtained in Chapter II.

The variations of K, ε, t_*, η and the turbopause height discussed above form the main points of this section. However, it may be worth mentioning that turbulent eddies generally move with random motions, with velocities dependent on the scale size and energy deposition rate. Rind

(1977) gives typical velocities in his Table 3. These vary from around $1ms^{-1}$ at the Kolmogoroff microscale to tens of metres per second at scales of the order of kilometres.

Fig. 1.9a Models of the Kolmogoroff microscale wavenumber, k_η, and other related turbulence parameters. The k_η values above 65km came from Rastogi and Bowhill (1976b, Fig. 5). Estimates of ν were obtained from the United States Standard Atmosphere (USSA, 1962); assorted references were used to estimate ε (see Rastogi and Bowhill, 1976b). The values shown in the two models correspond to ε values around 10^{-2} Wkg^{-1} at 60km altitude (both models), and $\varepsilon \sim 10$ Wkg^{-1} at 100km for model 1, with $\varepsilon \sim 0.1$ Wkg^{-1} at 100km for model 2. It is assumed $\log_{10}\varepsilon$ changes linearly between these limits.

Three axes are shown - the wavenumber in rad m^{-1}, the scale in m rad^{-1}, and the wavelength in metres.

The parameters are plotted for mean ε values, and also using values of ε of 3.0 and 0.3 times the mean. The terms k_ν and k_c delineate the various regions indicated, and are discussed in the text. The Kolmogoroff wavenumber for an energy deposition rate ε closely matches the "k_c, 3ε" line, and the two lines are drawn as one.

A k_η profile based on the data of Rees et al. (1972, Fig. 8) is also shown ($\varepsilon \sim 0.03$ Wkg^{-1} to 0.2 Wkg^{-1} at 90-100km, with a 20m Kolmogoroff scale at 80km, and 40-60m at 90km). It was felt this profile was particularly relevant, because the measurements were made at Woomera, Australia - within a few hundred kilometres of Adelaide, the location of one of the experiments discussed in this thesis. Ground-based experiments at Adelaide, Australia (e.g. Elford and Roper, 1967; Vincent and Stubbs, 1977) have produced results similar to those of Rees et al. Manson et al. (1979) have found similar values at Saskatoon, Canada. Since these values agree with model 2 best, this model is the main one used in this thesis.

The k_η values below 65km were taken from Gage and Balsley (1978, Fig. 21). They all correspond to ε values around .004 to .01 Wkg^{-1}. The diagram of Gage and Balsley also extended above 65km, and closely matched model 1 presented here. However Crane (1980) suggests $\varepsilon \sim 10^{-4} - 10^{-3}$ in the troposphere and stratosphere, so k_η is also plotted for $\varepsilon = 10^{-3}$ and 10^{-4} WKg^{-1}. Caughey et al. (1978) also suggest $\varepsilon \sim 10^{-4} - 10^{-3}$, but at times intense patches of turbulence can occur with $\varepsilon \sim 10^{-2}$. [Note that Crane assumes $(\nu^3/\varepsilon)^{\frac{1}{4}}$ is the Kolmogoroff microscale in metres, rather than m rad^{-1} as has been assumed here. This should be borne in mind when comparing Fig. 1.9a to Crane (1980).]

Times scales can also be associated with these length scales, by virtue of the equation 2.2.3.2c (Chapter II) - namely, $k^{-2}\tau^{-3} = \varepsilon$. τ represents the lifetime of an eddy of size

(---- CAPTION Continued over)

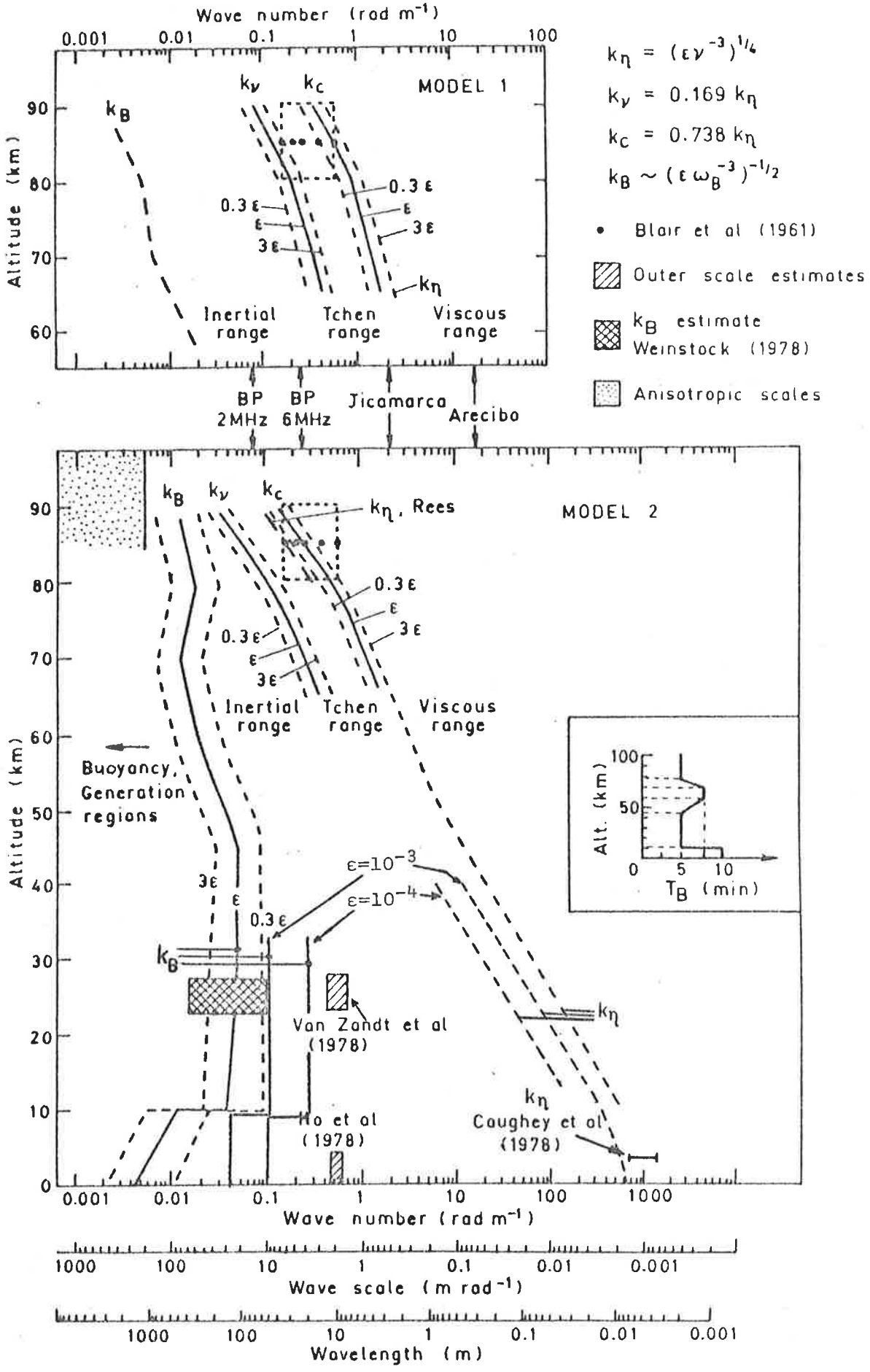
Wave number (rad m⁻¹)
0.001
0.01
0.1
1
10
100
MODEL 1
k_B
k_ν
k_c
k_η
0.3 ε
ε
3ε
Inertial range
Tchen range
Viscous range
Altitude (km)
90
80
70
60
BP 2MHz
BP 6MHz
Jicamarca
Arecibo
$k_\eta = (\varepsilon\nu^{-3})^{1/4}$
$k_\nu = 0.169\, k_\eta$
$k_c = 0.738\, k_\eta$
$k_B \sim (\varepsilon\omega_B^{-3})^{-1/2}$
Blair et al (1961)
Outer scale estimates
k_B estimate Weinstock (1978)
Anisotropic scales
MODEL 2
k_η, Rees
Buoyancy, Generation regions
$\varepsilon=10^{-3}$
$\varepsilon=10^{-4}$
Van Zandt et al (1978)
Ho et al (1978)
Caughey et al (1978)
Alt. (km)
100
50
0
5
10
T_B (min)
Wave number (rad m⁻¹)
1000
100
10
1
0.1
0.01
0.001
Wave scale (m rad⁻¹)
Wavelength (m)

Fig 1.9a ctd.

$\ell \sim \frac{2\pi}{k}$ metres. For example, if $\varepsilon = 5 \times 10^{-2}$ Wkg^{-1}, and $\ell \sim 60$m, $\tau \sim 12$ s rad^{-1} or $\tau \sim 76$s.

Some attempt at describing the outer scale of the inertial range of turbulence is also made in this diagram. The inner scale of buoyancy range, L_B, as estimated by formula 2.2.4.2a", Chapter II, is shown as k_B, where

$$k_B^{-1} = L_B \sim (\varepsilon \omega_B^{-3})^{\frac{1}{2}} = (\nu^3 \eta^{-4} \omega_B^{-3})^{\frac{1}{2}},$$

and ω_B is the Brunt Vaisala frequency. This relation comes about through a formula derived by Weinstock (1978), and is developed in Chapter II. It is difficult to say just how reliable this final form is. Also shown is an estimate of L_B made by Weinstock (1978). Values of ν were obtained from USSA, 1962, and estimates of η from models 1 and 2. The Brunt-Vaisala frequency profile was based on Fig. 5-2 of Gossard and Hooke (1975), and is shown in the inset of Fig. 1.9a. The scale L_B would be expected to be of the order of the outer scale of the inertial range - possibly somewhat larger. Also shown are estimates of the outer scale by Ho et al. (1978) and Van Zandt et al. (1978). Notice further that k_B is more strongly dependent on ε than k_η. Further an increased ε decreases k_B and increases k_η, thus widening the inertial range. Also shown are k_B values for $\varepsilon = 10^{-3}$ Wkg^{-1} and 10^{-4} Wkg^{-1}. These are probably more appropriate in the lower atmosphere (eg. see Lilly et al. (1974); Crane et al. (1980).

Eddies greater than 1km vertical extent tend to be anisotropic at 90km (eg. Rind, 1977) and this is indicated on the diagram. Scales to the left of the k_B line will generally be anisotropic (eg. see Weinstock, 1978), but it is difficult to say exactly at what scales anisotropy becomes important, eg. Bolgiano (1968) has shown that weak turbulence in a strong wind shear can induce anisotropy at small scales.

If these boundaries are estimated at higher heights (not shown in Fig. 1.9a) it is found that the k_B, model 2 and k_η, model 2, lines intercept around 100-120km - the height of the turbopause. This is interesting, and is discussed more in Chapter II. (When $k_B \simeq k_\eta$, no inertial range exists.)

ctd. over.

Fig.1.9a ctd.
Also shown on the graphs are the Bragg scales which give backscatter reflection for various radio wave systems. For example, Jicamarca, using a radio wavelength of 6m, receives reflections from Bragg scale components of wavelength 3m, or $3/(2\pi)\ mr^{-1}$. Buckland Park (near Adelaide) and Townsville, in Australia, were the two major research stations used for the work of this thesis, and operate at frequencies near 2MHz (both stations) and 6 MHz (Buckland Park only). These frequencies correspond to Bragg scales "wavelengths" of 75m and 25m respectively.

As a summary, the best lines to use would be model 2; and below 40km, use the $\varepsilon = 10^{-3}$ and $10^{-4}\ Wkg^{-1}$ lines.

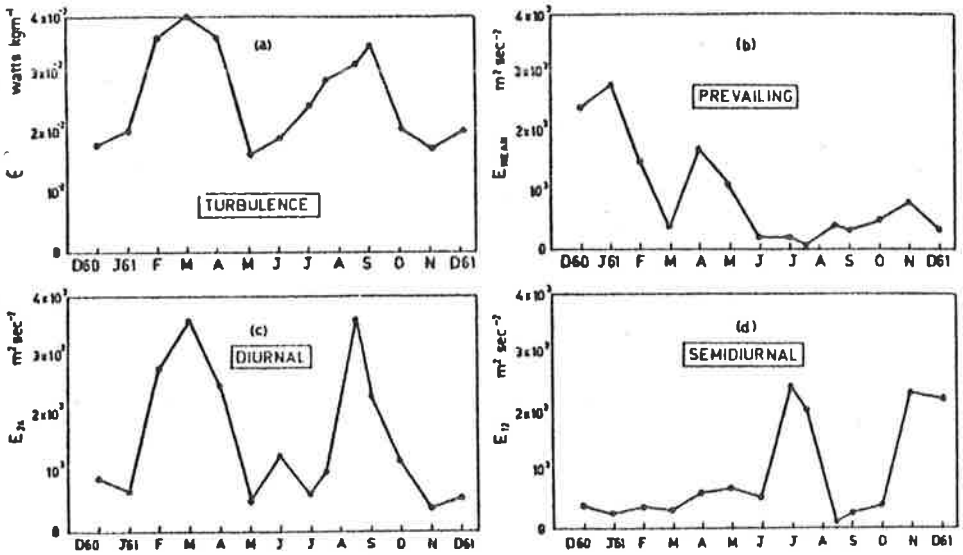

Fig. 1.9b Seasonal variations at Adelaide (35°S) of (a) the rate of dissipation of turbulent energy, (b) the prevailing wind energy, (c) the diurnal wind energy and (d) the semi-diurnal wind energies, at 91km. The mean flow energies are the sums of the squares of the appropriate zonal and meridional wind amplitudes. (From Elford and Roper, 1967).

To convert from Watts kg^{-1} to a heating rate of °C per day, multiply by 86.4 (see text).

Fig. 1.9c Plots of eddy diffusion coefficient K vs altitude. Models 1 and 2 come from the ε values of Fig. 1.9a, and use the formula $K = \varepsilon/\omega_B^2$ (equation 2.2.4.7a'', Chapter II).

Various estimates of K by other authors are also shown. Model 2 seems more agreeable with most other K estimates. When values are estimated at higher heights, model 1 goes to a value of $\log_{10} K = 5.1$ at 110km - considerably larger than accepted values. Models 1 and 2 merge below 60km. Agreement with other authors is worst at about 20km, but the model line assumes $\varepsilon \simeq 10^{-2}$ Wkg^{-1} everywhere below 60km, which may be a little simplistic. Elsewhere, agreement is fair. The formula $K = \varepsilon/\omega_B^2$ may also be a little suspect (see Chapter II).

As discussed in Fig. 1.9a, ε is closer to $10^{-4} - 10^{-3}$ below around 40km. K values have also been plotted for $\varepsilon = 10^{-3}$. Thus realistic K values are $\lesssim 10$ m^{2}s^{-1} below 10km and less again between 10 and 40km. Lilly et al. (1974) estimate K to be around 4 - 10 m^{2}s^{-1} in the stratosphere. The shaded region represents this more realistic range of K values.

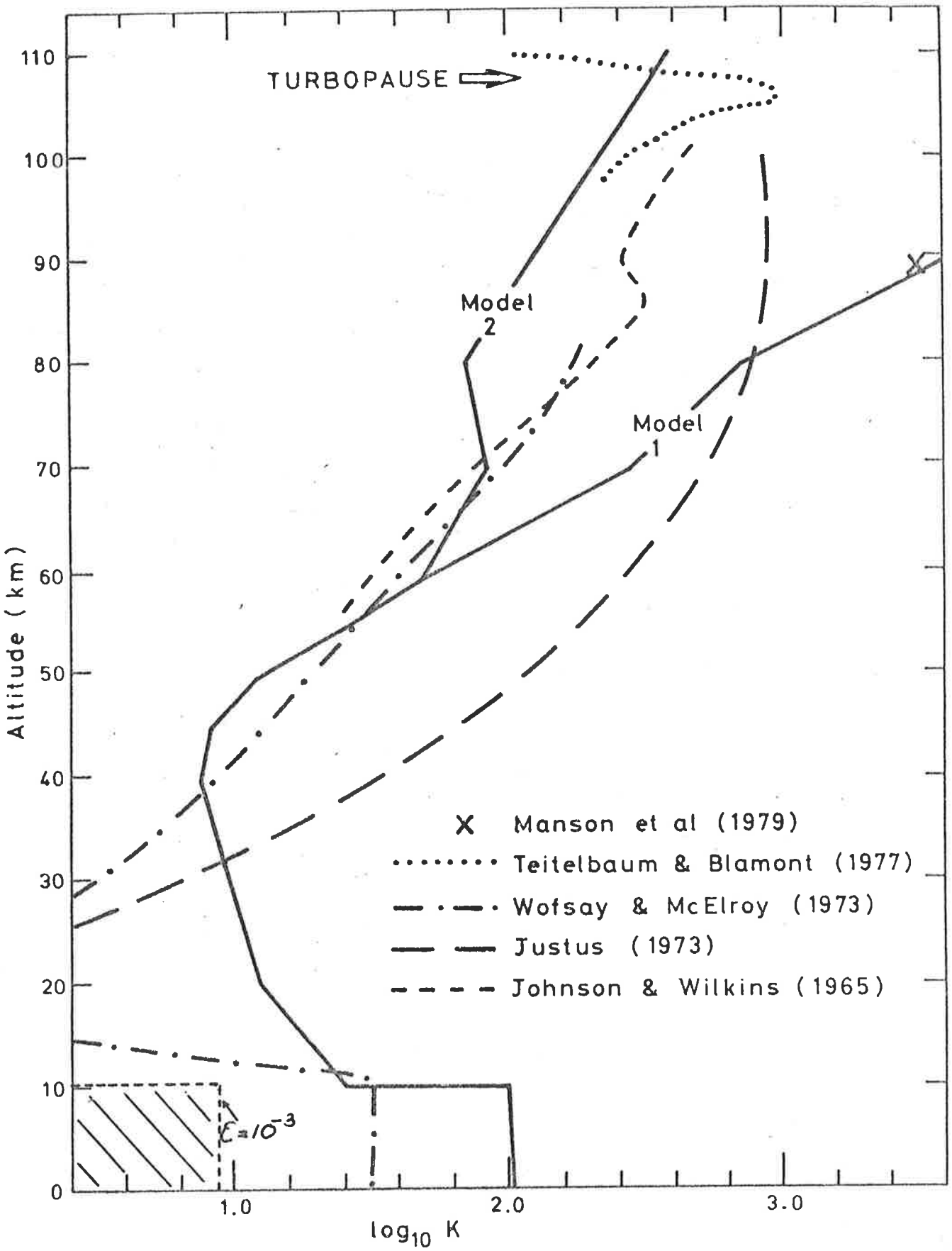
TURBOPAUSE
Model 2
Model 1
Manson et al (1979)
Teitelbaum & Blamont (1977)
Wofsay & McElroy (1973)
Justus (1973)
Johnson & Wilkins (1965)
$\zeta = 10^{-3}$
Altitude (km)
$\log_{10}$ K
0
10
20
30
40
50
60
70
80
90
100
110
1.0
2.0
3.0

1.4 Radio Wave Partial Reflections

The effects of the ionosphere on the propagation of radio waves are extremely varied. Some discussion of this topic has already been presented; for example, Appendix B, and Section 1.2.3. Section 1.3.3 contained a small section on the possibilities of turbulent scatter, but no mention was made of experimental results. Apart from turbulence, the primary effects thus far examined have been critical reflection (to some degree; also see Appendix C), and radio wave absorption.

But one important phenomenon not yet fully discussed is the partial reflection of radio waves. When radio waves enter the ionosphere, they can be partially reflected at heights in the range 50 to 100km. The reflection coefficients corresponding to these reflected signals are in the range 10^{-6} to 10^{-2}, so the process is certainly not strong reflection. These reflections occur over a wide range of frequencies, from less than 2MHz to greater than 50MHz. However, their cause is still largely unknown, and the purpose of this thesis was to gain more insight into the physical mechanism causing the radio scatter. This introductory section will concentrate primarily on the years up to and including 1977; the results of some papers printed after that date will not be included here, particularly if they would pre-empt discoveries discussed later in this dissertation. Rather, these papers will be discussed within the thesis itself, at the appropriate place. All results relating to MF and HF radio scatter up to 1979-1980 will be discussed here, since they pose no challenge to these studies, but most papers relating to VHF investigations after 1977 will be discussed later.

1.4.1 Early Observation at MF and HF

1.4.1a Early Data

Ellyett and Watts (1959) provides a review of the early discoveries of these partial reflections. Some evidence appeared as early as 1930, when Appleton (1930) found indications of these lower echoes. Early hints of such scattering heights also occurred in the period 1930 to 1950, when experiments using VLF, LF and MF radio waves suggested such structures.

Dieminger (1952) presented evidence of these echoes using conventional ionosondes, and appears to have been one of the earliest workers to study the echoes in any real degree of detail. Dieminger found that the echoes could be seen over heights of 75 to 90km, and over a frequency range 1.6 to 4.0MHz (this upper limit is most likely a result of the sensitivity of the system). The heights of the echoes varied diurnally, with a minimum at local noon; and the heights were frequency independent. The low echoes were most frequent in winter, and occurred in groups of days.

Gnanalingam and Weekes (1952) also made some investigations of these echoes.

Gardner and Pawsey (1953) provided perhaps the first detailed study of these echoes, with an experiment specifically designed for investigation of these weak reflections. Their system was quite sensitive, 30 to 40dB more so than Dieminger's ionosondes.

The system used by Gardner and Pawsey was similar in principle to the systems used for the investigations discussed in this thesis. Pulses of radio waves were transmitted regularly, and the returning signal monitored, using a sensitive receiver. Echoes from lower scattering structures return to the receiver first, and the time lag between the transmitted pulse and an echo can be used to calculate the height of

the reflector, by the formula

(1.4.1.1) $h = \frac{1}{2}vt$

h being the reflector height, t the time delay between the transmitted pulse and the receiver echo, and v the speed of the radio waves through the ionosphere to the point of reflection (assumed to be the speed of light in a vacuum, ie. v = c; this assumption results in a so called virtual height h, but this is close to the real height in the D region).

Fig. 1.10 shows a typical profile of echo strength as a function of time delay for Buckland Park, Adelaide, Australia (35°S, 138°E). The horizontal axis gives the time delay, but has been converted to height by formula (1.4.1.1) and assuming v = c (virtual height). The various structures are described in the figure caption. Gardner and Pawsey obtained similar profiles, and presented similar diagrams. In the case shown, there are clearly scatterers at 68, 78 and 92km.

Gardner and Pawsey used a frequency of 2.28MHz, and a pulse length of 30 μsecs. Half wavelength dipoles were used for transmission and reception. Either plane polarized radiation, or circularly polarized [Ordinary (O) or Extraordinary (X)] radiation could be transmitted. The transmitter had a peak power around 1kW. The systems used for the experiments discussed in this thesis were essentially the same as this, except that larger transmitter powers (up to around 40kW peak), large receiving arrays, and other improvements, resulted in much greater sensitivity. Frequencies used were around 2 and 6MHz.

The echo strengths observed by Gardner and Pawsey (near Sydney, Australia) corresponded to reflection coefficients of typically 10^{-5} at heights near 70km and 10^{-3} around 90km. Echoes at 80-100km generally appeared to come down in height until noon, then rise again afterwards. The "60-70km" echoes appeared to rise in height until noon, then decrease

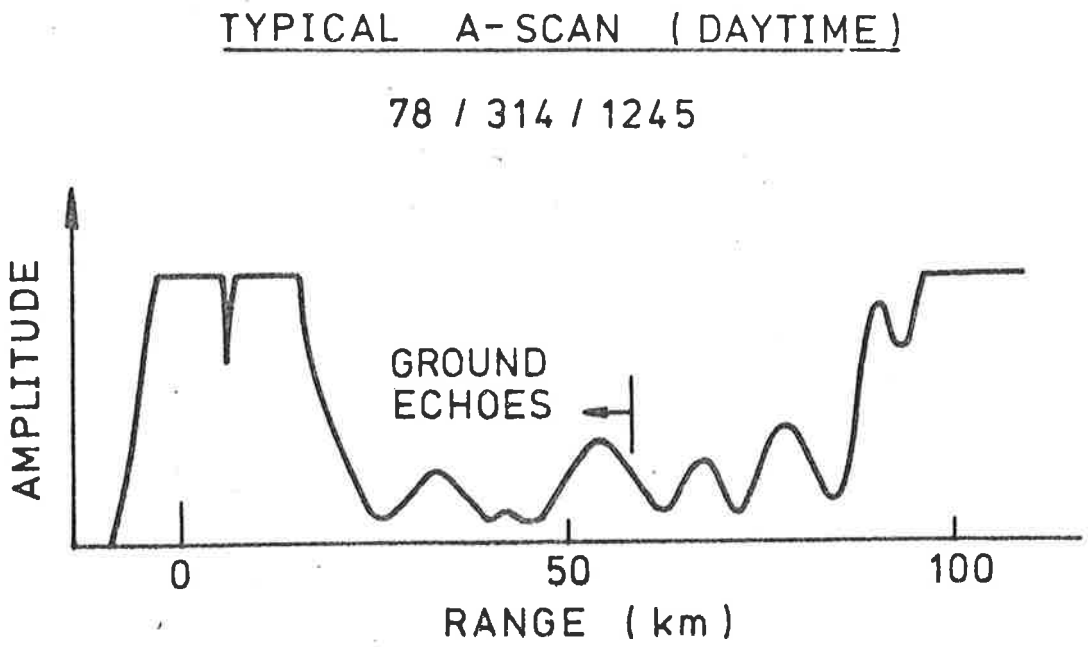

Fig. 1.10 Typical O mode echo structure for a pulse of 2MHz radio waves transmitted into the ionosphere. The system saturates at 10Volts, and this is the reason for the flat tops of the "echoes" at 0 to 100km. The 0km "echo" corresponds to the transmitted echo, and the 100km echo is the totally reflected E region echo. The structures 60 to 90km are genuine D-region ionospheric scatter. The small echo at 55km is not ionospheric, but corresponds to reflections of the pulse off nearby mountains. The "echo" at around 33km may also be a ground echo, or could be ringing of the receiver. The ionospheric echoes change in amplitude and height in a time scale of the order of seconds; the "echoes" less than 60km change very little even from one day to the next, and this is one characteristic which allows them to be interpreted as non-ionospheric.

again. An echo might appear at one height and remain visible (during the day-time) for periods ranging from hours to days. Then it would disappear. Echoes continually came and went. The echoes faded in amplitude with fading times of the order of seconds. However, an echo at any one height would still fluctuate in height around its mean. Echoes below about 80km appeared only during the daylight hours, but above this height, night-time echoes did occur.

The results discussed above provide an accurate assessment of many of the major characteristics of these D-region echoes. One major characteristic can be seen with a comparison of O and X mode echo strengths. (That is, O or X radiation is transmitted and received.) Below about 70km, the X mode echo is often the stronger, but above this height the X mode radiation is strongly absorbed due to the large electron densities, and the corresponding echoes are quite weak. O mode absorption is not so strong, so the O echoes are still quite strong even when coming from heights around 90km. Gardner and Pawsey used these different absorption characteristics to determine the D-region ionospheric electron densities, and thus devised the so-called "Differential Absorption Experiment" (DAE). The DAE is discussed briefly in Appendix B. The technique requires knowledge of the electron collision frequency profile of the atmosphere, and inaccuracies in this parameter can lead to errors in the calculated electron densities. In an extension of this experiment, Belrose and Hewitt (1964) were able to use a theory similar to that for the DAE to calculate this collision frequency near 60km, since at these heights the electron collision frequency is the main reason for absorption of radio waves. However, electron densities are hard to calculate at these low heights, for this very reason. Above 80-85km, X mode strengths become very weak and hard to measure, so electron density estimates above about 85km are also unreliable for the DAE technique

(eg. Lindner, 1972).

However, the Gardner and Pawsey DAE theory relies on the assumption that the echoes are due to rapid changes in electron density of a few per cent with increasing height, which extend over several Fresnel zones horizontally. If, for example, they were due to sudden changes in collision frequency, the theory would have to be modified. (eg. Piggott and Thrane, 1966; Lindner, 1972; Jones and Kopka, 1978). Further, if the scatterers are not planar, extending over several Fresnel zones, but perhaps turbulent eddies, then the returned echoes may come from a wide range of angles, which could also modify the theory (Lindner, 1972, 1975a, b). If, as well, the scatterers cover a thick height region (eg. $\gtrsim$ 1-2km), then other modifications are necessary (Flood, 1968). Clearly, then, it is important to understand the structures causing these echoes much more thoroughly before the DAE can be interpreted correctly.

Gardner and Pawsey did not continue the work reported in their paper. Gregory (1956, 1961), however, did carry on similar observations at Christchurch, New Zealand, using a similar experimental arrangement to that of Gardner and Pawsey, but on a frequency of 1.75MHz. Gregory's work provided the first detailed analysis of seasonal variations, and he also began to look carefully at the problem of preferred heights - that is, do the echoes show preference towards certain heights of scatter, or are the echoes equally likely to come from all heights?

One important point which must be borne in mind with many of these results is the geographical location of these stations. Dieminger's work was in the Northern Hemisphere. Gardner and Pawsey worked near Sydney, Australia (34°S, 151°E). Gregory worked near Christchurch, New Zealand (43° 37'S, 172° 24'E). Thus conclusions drawn by any one author may not be globally true.

Gregory (1956) found scatterers with lower boundaries principally at heights of around 95km and 85km, with occasional occurrences of echoes at heights around 75km, 70km, 65-68km, and in some cases 56-57km. Reflection coefficients generally decreased with decreasing height, from around 5×10^{-4} to 10^{-3} at 95km, to around 4×10^{-4} at 85km, and around 5×10^{-6} to 10^{-4} at the lower heights. At night echoes were observed only from heights above about 80km. The heights of any one echo at the greater heights tended to fluctuate, although at times an echo could be stable to within less than ±1km (especially the 85km echo). The echoes below 80km were primarily a non-summer phenomenon. Their stability would vary - they might last for periods from hours to days. Occasionally echoes would occur in summer, but these were often quite short-lived - some lasting less than a minute. No echoes were observed below 50km. Evidence was also found suggesting that echoes became stronger on days of higher electron density (a similar effect has been observed more recently for the low echoes by Haug et al., 1977 - at least in one specific case). A comparison was made with observations at other locations, and the "85km" echo was found to be a common feature. Insufficient data existed to comment on comparisons of the lower echoes.

In his 1961 paper, Gregory had more data to comment on. Again, preferred heights were found - in particular, around 86km, around 74km, around 66km, around 61km and around 55km. Experiments were also made to determine the thickness of the scattering regions, and these tended to increase from less than about 2km at the lower heights to greater than 5km at 86km. A seasonal variation in the height of the "86km" echo was found, the height of the reflector falling to around 81km in winter, and rising back to 86km in summer. (It should be pointed out that a "preferred height of around 86km" does not mean all echoes come from this height, - there can be quite a spread, eg. see Fig. 1.13a.) Some speculation as

to the nature of the scatterers was also made, and the conclusion was that they are generally due to turbulence. However, echoes had also been seen with very slow fading times, particularly at the lower heights, and rapid changes of electron density (around 10%?) within depths around 10m were suggested as the cause of these echoes. However, the reasons for the stratified turbulence, and the sharp electron density gradients, could not be explained.

1.4.1b Investigations of Echo Structure After 1962

Around the same time as Gregory's papers, some other papers on similar work appeared, but they were not great in number. Gregory's results have been discussed in detail here because he worked at a similar location to the investigations in this thesis. Gregory lists Fejer (1955); Fejer and Vice (1959); and Bjelland, Holt, Landmark and Lied (1959) as the principle other related papers. These will not be discussed here.

After about 1962, until around 1968-9, there appears to have been something of a lull in publication of papers discussing direct investigations of these echoes. The nature of the scatterers was assumed to be sufficiently well known for the partial reflections to be made use of in experiments such as the DAE (eg. Titheridge, 1962a;Belrose and Burke, 1964; Gregory, 1965; Gregory and Manson, 1967; Belrose, 1970 (review)). Some debate and even controversy did continue regarding the nature of the scatterers (Belrose and Burke, 1964; Manson, 1966; Piggott and Thrane, 1966; Flood, 1968), but little experimental data was produced to clarify the situation. Generally the arguments revolved around either Fresnel reflector models (a Fresnel reflector is a planar (mirror-like) reflector extending over several Fresnel zones (see any optics book)) or volume scattering models. The use of the DAE was, however, assumed

valid, provided care was taken. The effect of the scale of the scattering irregularities was felt to be unimportant (eg. Holt, 1969; Flood, 1969). The possibility of off-vertical signals arriving at the receiver (which degrades the range resolution, and makes discrimination of O and X modes more difficult) was eliminated to some degree by using narrow beams (large receiving and/or transmitting arrays). The effects of a finite length radio pulse was also considered by Coyne and Belrose (1973). Belrose et al. (1967) and Belrose (1970) discussed some of the problems associated with the DAE, and gave some typical results obtained. These papers also gave summaries of the main stations doing the DAE at the time. Even quite recently, the DAE has been improved further (eg. Von Biel, 1977); but a really complete interpretation of the DAE still requires a fuller understanding of the radio scattering mechanism.

Other experiments using these partial reflections also began to appear, such as the measurement of drifts in the D-region (eg. Fraser, 1965; Fraser, 1968); but again, the lack of knowledge of the mechanism of scatter restricted interpretation of the results. The measurement of drifts at HF was generally done by the method of similar fades, first used by Mitra (see Mitra, 1949). The earlier work was done using E region total reflection, but during the period from 1965 onwards, the technique was extended to the D region by utilizing partial reflections. The method involved correlating signals received at three (or more) spaced receivers, and using the time delays between the signals received to determine drift velocities. It was subsequently improved (Briggs, Phillips and Shinn, 1950; Briggs and Spencer, 1954; Phillips and Spencer, 1955; Fooks, 1965), to arrive at "Full Correlation Analysis" (FCA). This has become a reasonably widely used method of measurement of ionospheric drifts. Briggs (1977b) has given a review of FCA, and Briggs (1977a) reviewed some of the results and limitations of FCA.

The interpretation of ionospheric drift measurements was debated for some time, however. Did the results give neutral atmospheric motions, or something else? For example Hines (1972) suggested drift measurements could in fact be tracking gravity wave motions, rather than neutral winds, if the ionized irregularities were produced by the waves. On the other hand, if the irregularities were produced by turbulence and then transported by the wind, the method would give the wind velocity. Thus once again uncertainties as to the nature of the partial reflection mechanism resulted in ambiguities in interpretation of results of experiments using these scatterers. A clearer understanding of these D region scatterers was needed. [It may be worth noting here, however, that FCA results have since been compared with other methods of neutral atmospheric wind measurement, such as meteor winds and rocket data (for example, Kent and Wright, 1968; Sprenger and Schminder, 1968; Muller, 1968; Wright, 1968; Stubbs, 1973; Stubbs and Vincent, 1973; Balsley, 1973; Crochet et al., 1977; Vincent et al., 1977; Vincent and Asenstorfer (comparisons with Dóppler measurements - private communication)). The method has been found to be acceptable as an indicator of neutral air motion, at least for the experimental arrangements used in this thesis for D-region measurements (see in particular those papers in which Stubbs and Vincent were involved). Further, as pointed out by Briggs (1980/81), many criticisms of spaced receiver measurements of winds can also be made of Dóppler measurements. In many cases the spaced receiver method has definite advantages. In this thesis, the FCA method of ionospheric drift measurement will be used a great deal, and results will be interpreted as neutral atmospheric winds.]

After about 1968, papers again began appearing which discussed the nature of the scattering irregularities. Vincent, in his thesis (1967), discussed the nature of these echoes to quite a degree, but none of the

data was published till some time later, when he was a joint author in two papers (Gregory and Vincent, 1970; Fraser and Vincent, 1970). Around the same time, Austin and Manson (1969), Manson, Merry and Vincent (1969), and Austin, Bennett and Thorpe (1969) also produced papers investigating the nature of the D-region reflectors, and a clearer picture of the scatterers began to emerge.

Vincent (1963) used phase information of the returned signals to gain a much better feel for height fluctuations and echo "coherence". Results suggested that echoes from above 85km were often quite incoherent (frequent random phase jumps and variations), whereas those from around 70km often showed very smooth phase variations over intervals of several minutes at times, and frequently showed quite slow fading rates. Thus it seemed that echoes from around 70km could well be due to one or two Fresnel reflectors drifting across the beam, producing specular scatter (in some cases, Vincent measured the speed of drift of these reflectors via phase measurements; results appeared to compare favourably with measurements of wind speeds made by the spaced receiver technique). Above about 85km, volume scatter appeared to dominate. The night-time 90km echoes showed similar incoherence to the day time ones. The lower echoes were, at times, found to be extremely stable in height, showing very small fluctuations over quite long periods, particularly during the equinoxes. At times, height fluctuations were less than a few wavelengths over several minutes. However, even these lower echoes became somewhat incoherent during the solstices. Fraser and Vincent (1970) also showed that for these lower echoes, fading times and pattern size (the latter is a measure of the distance required between two aerials for the signals received on the two aerials to become uncorrelated to a significant degree) correlated well with the degree of phase coherence. Figure 1.11, from Fraser and Vincent (1970) shows these

features well. This would not be surprising if the reflections were from Fresnel reflectors - since as the reflectors became more "mirror-like", it might be expected fading would become slower, the phase would show less erratic variation, and the angular spectrum of the scatterers would become narrower, thus giving a larger pattern scale (the last statement follows because the angular spectrum and spatial autocorrelation are Fourier transforms; eg. see Briggs and Vincent, 1973). The suggestion was also made by Vincent (1967) that these scatterers may well be closely related to gravity waves. Vincent speculated that the reason for the seasonal variations of some of the layer characteristics may be related to tropospheric-generated gravity waves. The possibility that the increased electron densities in winter (winter anomaly - see Section 1.2.3) were related to the increase in observed lower echoes in winter was also mentioned.

Austin and Manson (1969) suggested that the D-region scatter in the region 70 to 90km may come from several scatterers, too close together to be resolved with the pulse lengths used (resolutions were typically 4km). They suggested these multiple scatterers may be the result of gravity waves perturbing the neutral atmosphere. If the scatter were to be explained by a single scatterer, perturbations in electron density of the order of 5% to 40% were necessary, according to these authors; but multiple scatterers would require smaller perturbations to explain the observed powers. Other observations (eg. Fraser and Vincent, 1970) have shown at times the existence of single scatterers. Austin and Manson concluded that both situations (scatter from a single reflector and scatter from multiple reflectors) can in fact occur. Some attempt was also made by Austin and Manson to discern the thicknesses of the scattering layers by varying the pulse length used. Results suggested that, at least up to about 84km, the scattering regions never filled a

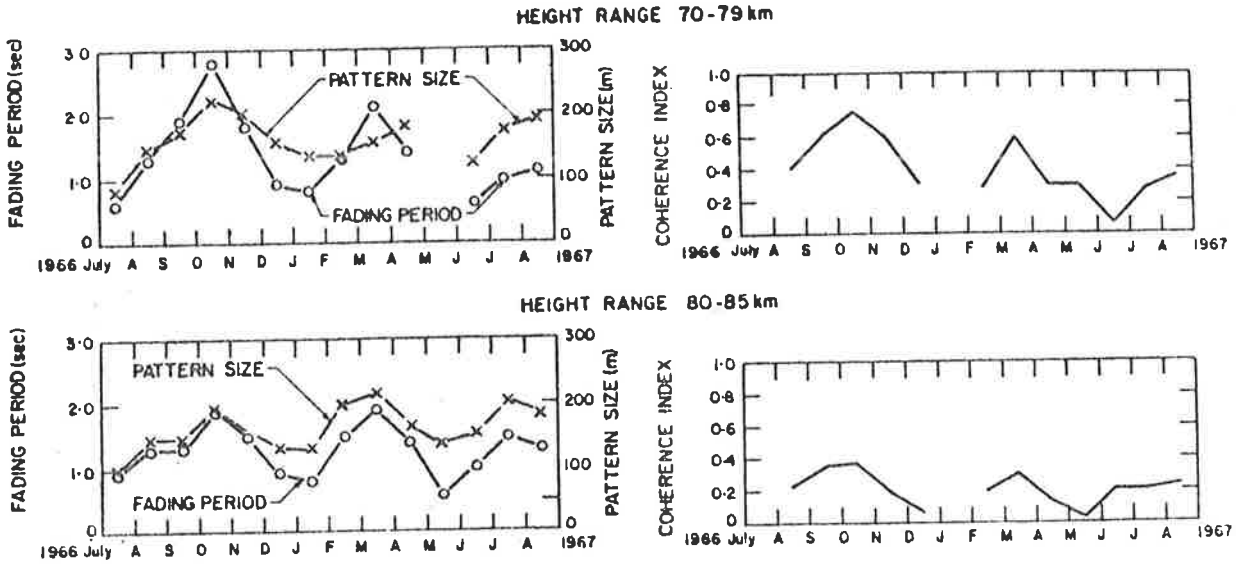

Fig. 1.11 Variation of coherence index, pattern size, and fading time from July 1966 to August 1967, for the height ranges 70-79km and 80-89km. From Fraser and Vincent (1970).

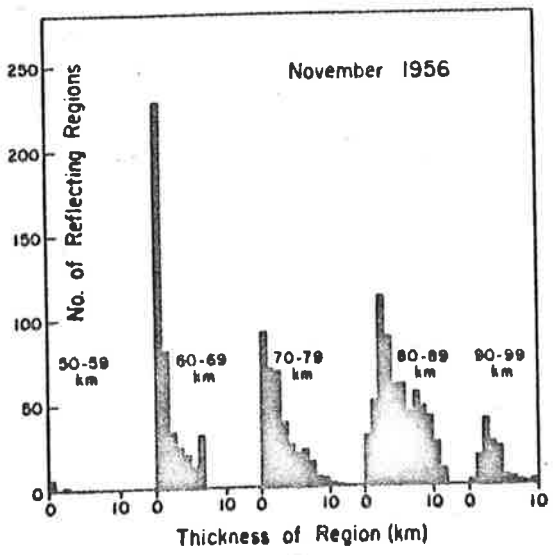

Fig. 1.12 Distribution of thicknesses of reflecting regions, in decile intervals, observed on 1.75MHz vertical incidence backscatter soundings at 44°S. (From Gregory and Vincent, 1970.)

major portion of one pulse length.

1.4.1c Layer Widths

Gregory and Vincent (1970) carried out a more careful analysis of layer widths at Christchurch, New Zealand (44°S, 173°E; L = 2.6). Their system was capable of detecting two reflecting regions, less than 1km thick, if they were separated by more than 4km. The results of their analysis are summarized in Fig. 1.12. Below about 80km, the scatterers appeared in general to be less than 1km in extent, (and possibly less than a few wavelengths thick (λ ~ 170m; f = 1.75MHz)). Rapid changes in electron density with height (steps) were offered as the explanation of these echoes below about 80km. Above 80km, the scattering regions tended to have a mode thickness of 2-3km, and sometimes were as large as 10km. It was not possible to say, however, whether these were continuous scattering regions covering the full estimated thickness, or whether there were several discrete scatterers (or even regions of scatter) with separation too close to resolve.

For a station at a much higher geomagnetic latitude (in the case discussed the station was Saskatoon, Canada; (52°N, 197°W); L = 4.4), indications were that scatter tended to be similar in some ways to that at Christchurch, but tended to be more "diffuse" - that is to say, the layers were not quite so well defined, and appeared "thicker". However, no detailed analysis was carried out at Saskatoon. Belrose (1970) suggested that at Ottowa, Canada (45°N, 76°W), scatter was not uniquely quasi-stratified or turbulent, but rather a combination of the two. Belrose et al. (1967) (also see Austin and Manson, 1969) felt that there were no preferred layers like those seen by Gregory (1956 and 1961 at Christchurch) in the nearer-auroral regions of Canada. Some stratification did exist at Ottowa, however (Belrose and Burke, 1964).

Thus there appeared to be a geomagnetic dependence upon the nature of these scatterers, although at the time no explanation was offered. Conceivably, the increased incidence of precipitating electrons in the auroral regions could partly explain the effect.

It became clear that higher resolution was necessary to deduce any more about the thickness of these layers, and with this in mind, Austin et al. published a paper in 1969 regarding the possibilities of deconvolving the received echoes. Unfortunately, very little in the way of results were presented, and there appears to have been no follow-up paper. The uses and limitations of deconvolution will be discussed later in this thesis in more detail. The technique has potential, but must be done carefully. Chandra and Vincent (1979) have also shown the usefulness of deconvolution, and find several cases where the echoes from two layers have merged to appear as one echo; the layers could be seen separately when deconvolution was applied. Deconvolution is a useful technique, but it has not been used extensively to date.

1.4.1d Rocket Comparisons

Perhaps one of the most obvious things to do in investigating these echoes would be to compare directly the detailed electron density profile, as measured by rocket experiments, with reflections observed by HF radar. This appears never to have been done, however; the first results of such an experiment will be presented later in this thesis.

Manson, Merry and Vincent did, however, present a paper in 1969 which presented statistical comparisons of echoes and high resolution electron density profiles obtained by rockets. Small scale fluctuations in electron density, of the order of 1% to 20%, were observed in the rocket data, with a mode at about 3%. The fluctuations seemed largest at 60-70km, and 80km, which crudely agrees with preferred heights of radio scatter. The winter and autumn rocket firings showed more marked

small scale electron density irregularities, agreeing with the observation that partial reflections appear to be greatest in those months. On two days of anomalous absorption, these density irregularities were found to be enhanced; and this agreed with observations suggesting HF radio scatter is strongest on such days (Gregory, 1956). Calculations using the Sen-Wyller equations suggested that each electron density fluctuation was capable of giving rise to scattered radio pulses with powers of the order of one third to one quarter of those observed by radio techniques. The combined effects of several of these perturbations was quite capable of causing the observed echo strengths. The paper thus concluded that the observed echoes, at least up to around 80km, were due to fine scale (less than 100m) irregular variations of the electron density with height.

1.4.1e Angular Spectrum

In 1973, Briggs and Vincent presented a paper in which they theoretically examined the form of the signal received when radio waves are scattered from "blobs" of electron density. Vincent (1973) followed this up with some experimental results, in which the spatial autocorrelation function of the received signal was found; this could then be used to deduce information about the scatterers. (The Fourier transform of the spatial autocorrelation function gives the angular spectrum of the scatterers (Briggs and Vincent, 1973).) Interpretation of the results suggested that at around 95km the scatterers could be quasi-isotropic blobs; perhaps about three times wider than they were high. At lower heights (say 75km), the scatterers appeared to be sharply bounded, possibly with edges as small as 10m in depth. These lower scatterers appeared to extend several kilometres to tens of kilometres in horizontal dimension.

Vincent found the concept of such sharp edges hard to accept, and with good reason. A step of thickness h would diffuse away with a time scale t around h^2/K, K being the relevant diffusion coefficient (see Chapter II). If turbulence were operative, K ~ $10\text{-}10^2 m^2 s^{-1}$ at 60-80km (eg. Cunnold, 1975, Fig. 3), so if h ~ 10m, t ~ 1-10 seconds. (If flow is entirely laminar, K is the molecular diffusion coefficient, which is roughly equal to the kinematic viscosity, and the value is around $0.3 m^2 s^{-1}$ at 75km (U.S. Standard Atmosphere, 1962). In this case t ~ 1000 seconds ~ 16 minutes). Thus if turbulence were at all operative, as it generally appears to be, a step of thickness around 10m would quickly diffuse out in a few seconds. However, as will be seen later, the conclusion regarding these narrow edges does appear to be quite valid. The conclusion for the 95km echoes may not be entirely valid, since only one type of scatterer was considered. Possibly several scattering mechanisms operate. This will be discussed in more detail later.

Lindner (1972, 1975a) showed how statistical properties of amplitude and phase variations received on neighbouring dipoles can be used to deduce information about the angular spectrum of the scatterers. Then Lindner (1972, 1975b) used these concepts to carry out an extensive series of measurements on ionospheric irregularities at Adelaide, Australia (35°S, 138°E). If the power received in the range of zenith angles θ to $\theta + d\theta$ is $P(\theta)d\theta$, and $P(\theta)$ is assumed proportional to

$$\exp\{-[\sin^2\theta/\sin^2\theta_0]\},$$

then θ_0 serves as a useful parameter for describing the type of scatter. Large θ_0 values suggest more isotropic scatter, and small θ_0 values suggest most scatter is from the vertical. Lindner presented evidence that θ_0 is quite small (around 2°-3°) up to about 80km, and then rises

sharply to 10°-14° at 90-95km. This is essentially consistent with the observations reported by Vincent (1973).

In a later series of measurements at Ottowa, Canada (45°N, 76°W), Vincent and Belrose (1978) obtained further estimates of θ_0, and the results agreed well with those of Lindner for Adelaide. In these experiments, θ_0 was calculated by comparing powers received on two calibrated antenna arrays - one with a wide polar diagram, and one with a narrow polar diagram.

1.4.1f Preferred Heights

It has already been mentioned how Gregory (1956, 1961) observed preferred heights of scatter, but Belrose et al. (1967) found this was not so in the auroral regions. Lindner (1972) obtained an extensive series of observations of echo heights at Adelaide, Australia (35°S, 138°E), and the results are presented in Fig. 1.13a. Similar results have been found for Townsville, Australia (19°S, 147°E), and are presented in Fig. 1.13b. (These latter results were obtained as part of the work for this thesis, but are presented here for ease of reference.) Schlegel et al. (1978) also presented such histograms for their station at Tromso, Norway, and again preferred heights could be seen. These results imply that, certainly in non-auroral regions, scatterers do have preferred heights; and even some quite high latitude stations (eg. Tromso) can exhibit this feature. These heights appear reasonably consistent globally. Particularly common heights are around 65km, 70-74km, (sometimes 76-80km), around 82-86km, and around 90-95km, although there are marked seasonal variations, both in preferred heights, and echo strengths. Schlegel et al. (1978) found echoes weakest in summer, as most other authors have. The heights of peaks of occurrence can also change significantly seasonally. Gregory (1961) found the "around 85-86" km echo became as low as 81km in winter. Similarly,

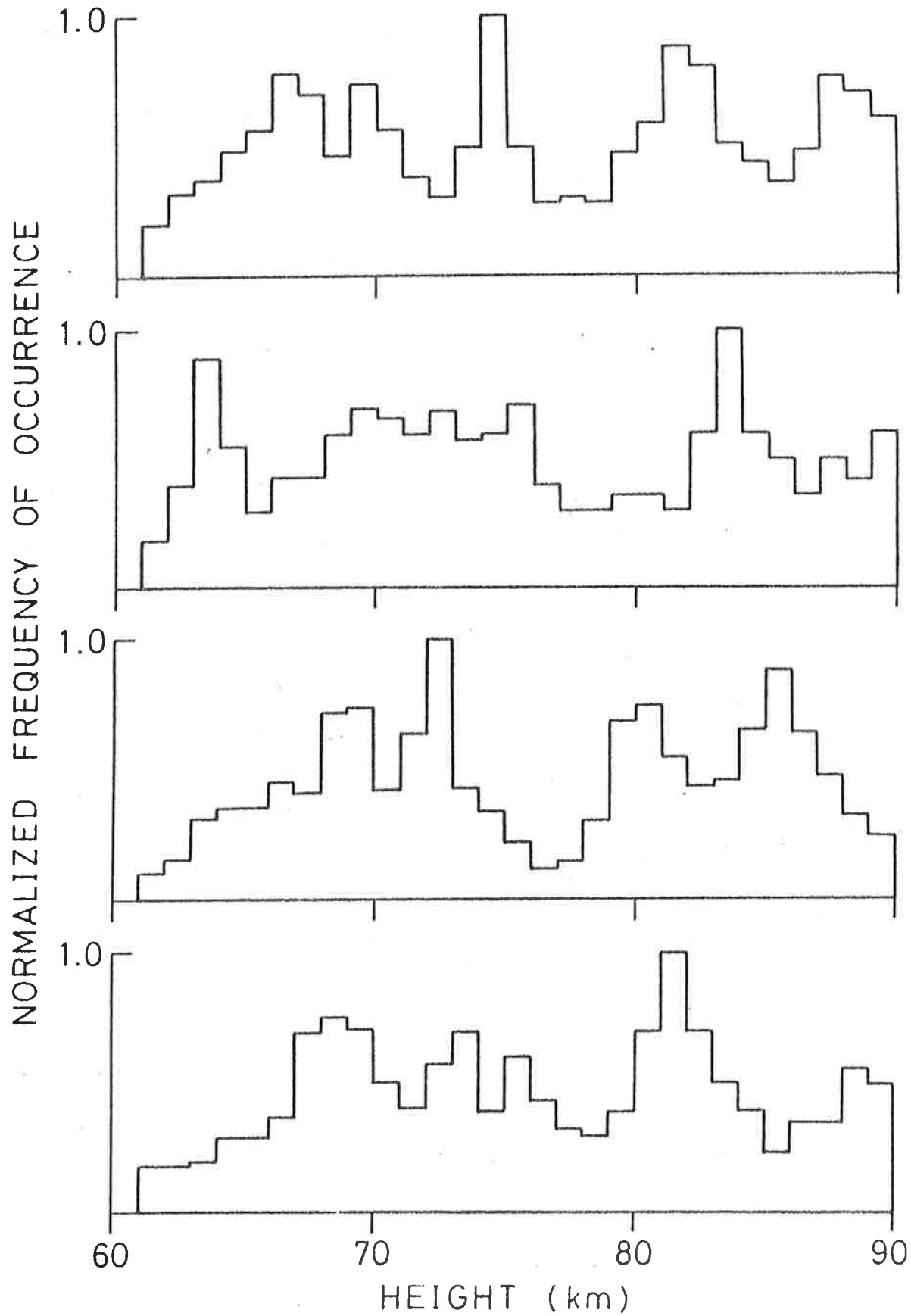

Fig. 1.13a Preferred heights of D region scatterers for summer (Dec-Feb), autumn (March-May), winter (June-Aug) and spring (Sept-Nov) for 1971 at Adelaide, Australia. (Results are from Lindner, 1972)..

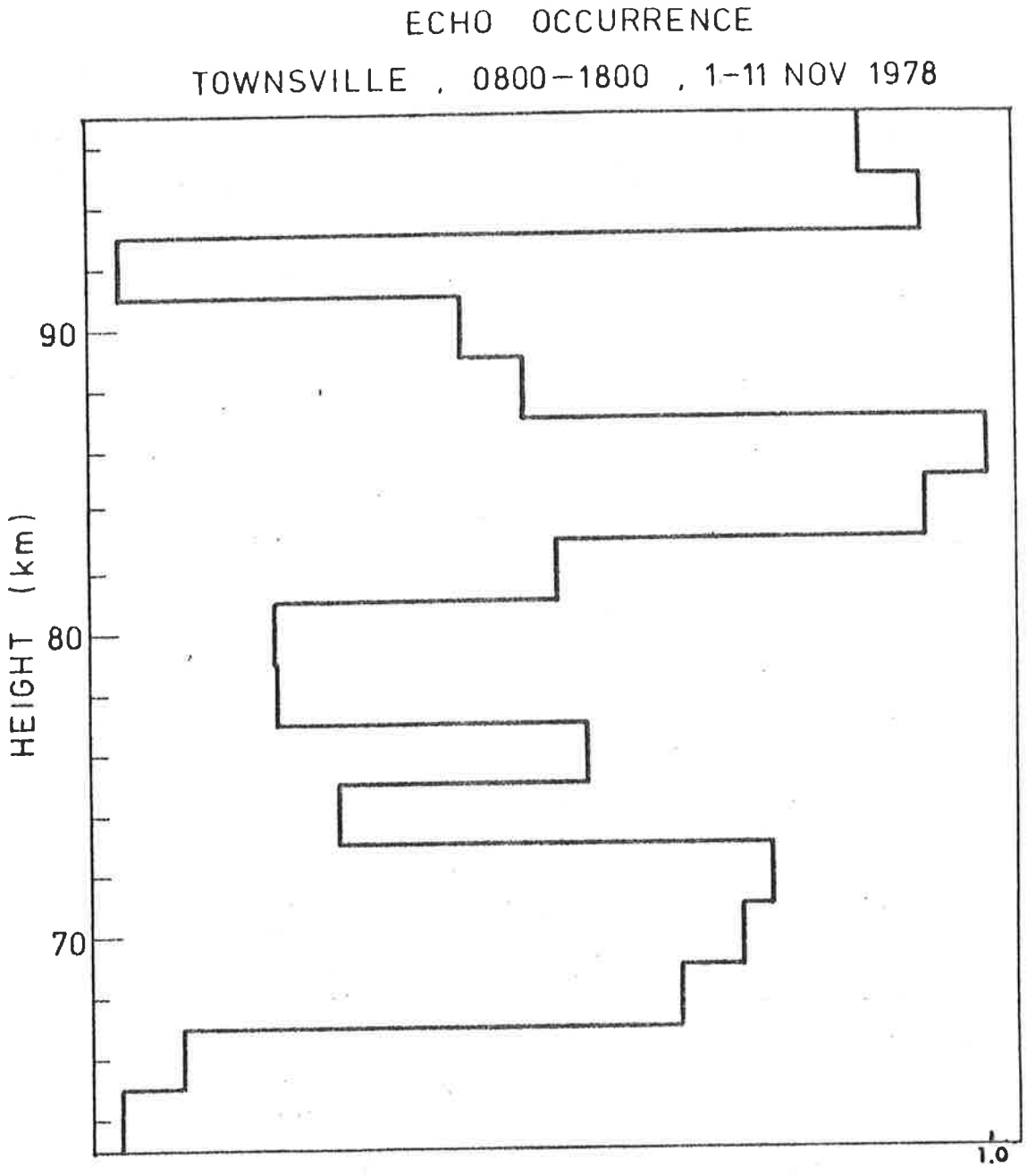

Fig. 1.13b Preferred heights of D region scatterers for Nov (late spring) 1978, at Townsville, Australia (19°S). The echo occurrence has been normalized.

seasonal variations can be seen in Fig. 1.13a. For example, the 83km echo in autumn gives way to two echoes at 80 and 86km in winter. Whether either of these can be regarded as a continuation of the autumn 83km echo is difficult to say. Probably the 86km winter echo shows similar characteristics to the 83km autumn echo (from personal observation).

1.4.1g Amplitude Distribution

If radio waves are scattered from a random distribution of moving scatterers, such as in turbulence, the amplitude distribution follows a characteristic form called a Rayleigh distribution (Rayleigh, 1894). If, however, one scatterer dominates, the situation is akin to finding the probability distribution of a constant vector with many other small random vectors added on. The result is the so-called Rice distribution (Rice, 1944, 1954; Van der Ziel, 1954; Norton et al., 1955; both the Rayleigh and Rice distributions will be derived later in this thesis). Then plotting amplitude distributions can indicate the type of scatterer being examined. Specular scatter, from a simple step in the electron density profile, with a certain degree of horizontal "roughness" superimposed, should be Rice-distributed with a large Rice parameter α (α being a measure of the specular component amplitude to the standard deviation of the random contribution). Turbulence would be expected to produce Rayleigh distributed ($\alpha = 0$) fading.

Unfortunately, things are not so simple in practice. The case of 2 or 3 specular components, of differing amplitudes, is not covered by either case (the distributions in such cases will be derived later). Greater than five roughly equal specular scatterers would also give a close approximation to a Rayleigh-type distribution (Goldstein, 1951; Vincent and Belrose, 1978). Further, if the components do not exhibit all possible phase differences with equal probability, the theory is not valid. Nevertheless, amplitude distributions do offer a possible tool

for D-region investigations.

Von Biel (1971), at Christchurch, New Zealand, appears to have been the first author to attempt this procedure. Mathews et al. (1973) at Ottowa, Canada, followed this attempt, and Newman and Ferraro (40°N, 77°W) produced further results in 1976. All three groups of authors concluded that scatter appeared to be Rayleigh-like below about 80km, but may have some specular contribution above this height. P.K. Rastogi (1979, private communication) working at Tromso, Norway, in some preliminary work, also found Rayleigh-like distributions below 80km, but some indication of specularity above.

These results, then, would appear to contradict the conclusions drawn earlier in this section that, below 80km, scatter appears quite specular, whilst above is more random in nature. Von Biel (1971) in particular offers his results as a direct contradiction of the work of Gregory and Vincent (1970).

Can this apparent contradiction be explained? The answer will be discussed more in later chapters of this thesis, but appears to lie, at least in part, in the assumption that the scatter should indeed be Rice-distributed. Much of the scatter from below about 80km is from a few specular scatterers, but the time intervals used to perform the amplitude distributions are often too short to allow all possible relative phases of the vectors of the scattered radiation. If, however, long data sets (about 10 minutes) are used, it is quite possible that such a time interval is much longer than the lifetime of an echo. A distribution formed from say 10 minutes of data may in fact contain contributions from one scatterer during say the first three or four minutes, then nothing, and then a second scatterer, possibly of different scattering strength to the first, in the last couple of minutes. Consequently, many distributions may be non-Rician. Von Biel (1971) accepted data at the

15% chi-square level. But at the low heights, as will be seen in this thesis, a large percentage of distributions, although indicating specular scatter, should be rejected as non-Rician. (At least, this is true for Adelaide and Townsville, Australia; it is presumably true elsewhere). Interestingly, Chandra and Vincent (1979) have produced Rice parameters which do indeed show strong specularity at the lower heights (below 80km); and it may be significant that they used 3 minute data lengths, compared to Von Biel's 8 minute data blocks.

As an interesting extension of amplitude distribution analyses, Vincent and Belrose (1978) compared their amplitude distributions to those expected for 2 or 3 specular components, and found that for typically 20% of the data the distributions appeared to indicate 2 or 3 principal specular scatterers.

1.4.1h Fading Times

Another parameter of significance in examination of D-region HF echoes is the fading time. This is generally taken as the time for the temporal autocorrelation of the data to fall to 0.5.

Echoes from turbulent scatterers may be expected to give signals at the ground which become uncorrelated after a shift of 1 or 2 seconds (at around 2MHz probing frequency); specular echoes, perhaps due to steps in electron density of the order of kilometres in horizontal extent, may well give rise to much better correlated signals, and thus longer fading times. Some fading time data can be seen in Fig. 1.11, which comes from Fraser and Vincent (1970) for Christchurch, New Zealand. Quite clearly, the lower echoes (70-79km) exhibit longer fading times than the higher ones during the equinoxes. Lindner (1972, 1975b) also presented fading time data for Adelaide, Australia. He found that above about 80km, fading times are typically less than 2-3 seconds, whilst

below, fading times as large as 20 seconds can be attained. Schlegel et al. (1978) found a similar trend for Tromso, Norway, with fading times less than about 4 seconds at 90km but quite large at the lower heights. Unfortunately, Schlegel et al. also tried to relate their fading times to turbulent dissipation rates, but this is not valid unless a very narrow beam is used, or unless the fading time which would be observed by an observer moving with the background wind can be obtained (see Chapter II, equations 2.2.3.11 and 2.2.3.12). Even then, the results are only valid if it can be proved that the scatter is indeed from turbulence. The same paper also reports a seasonal variation in the fading time, but as pointed out by Vincent (private communication), this may in part be due to the seasonal variation of the horizontal wind. After all, with a wide beam (17° beam width for the Tromso case) there would be a wide range of Dóppler shifted frequencies received due to scatter from scatterers at different zenith angles in the beam, and this would contribute in part to the fading (beam broadening). Larger mean wind velocities result in a wider spectrum and hence smaller fading times.

1.4.1i Conclusions of HF Results to Around 1977

Emerging from the above discussions, then, appears the following picture of D-region scatterers.

Scatterers exist from 50 to 95km, with reflection coefficients increasing roughly exponentially with height from around 10^{-5} to 10^{-4} at the low heights (60-75km) to around 10^{-3} at 90-95km. (An upper limit for the scatterers is hard to define at HF. Frequencies at 2-4MHz are often critically reflected by the E region, and this hides any scatter from heights near 100km. It also prevents any signal penetrating above the E region). Echoes from below 80km are primarily a day time

phenomenon; above they may exist at night as well. A distinct height preference seems to exist, at least at low and middle magnetic latitudes; scatterers at around 66, 70-74, 76-80 (at times), around 85 and 90-95km appear to be most common, although the preferred heights do vary somewhat seasonally. The preferred heights seem to be a global phenomenon. The echoes often fluctuate in height by several kilometres - although on occasion the stratifications can be very stable in height. A seasonal variation is evident, particularly for the lower echoes, which almost disappear in summer. Greater coherence is evident in the echoes around the equinoxes, with slower fading. Extremely height-stable echoes sometimes occur during the equinoxes, with variations in echo height of less than 1km, and at times less than 1 wavelength (λ ~ 70-100m). This is particularly true at around 85km, but sometimes lower echoes can also show this effect. The scattering layers can last for periods from a few minutes to several hours and even to days. There are some indications that the lower echoes may be stronger during days of high absorption. Fading times appear to decrease with increasing height. The scatterers at lower heights ($\lesssim$ 80km) appear to be less than 1km in vertical extent, although possibly tens of kilometres in horizontal extent at times. At these lower heights, the angular spectrum of scatter appears quite narrow, suggesting mirror-like scatter. Above about 80km and up to around 92km, the scattering regions tend to be thick (from 0 to 10km in vertical extent), and scatter is more isotropic. (However, it should be noted that layer thickness measurements to date have had a resolution around 4km, so conceivably a 10km deep scattering region could be several scattering layers with less than 2-3km vertical separation).

It also appears that scatter from below about 80km may be from changes in refractive index about 2%-20%, which are less than a few tens

of metres in vertical extent. Often several reflectors may contribute to an echo at any one time, but on occasions a single reflector can be the sole cause of an echo.

However, some of these conclusions are based upon scanty evidence, and much more extensive observations are needed. For example, Lindner, and Vincent and Belrose, appear to have been the only authors to have examined the angular spectrum in any detail, and even then, only by indirect means. Further, it seemed possible that the echoes from above 80km may be due partly to turbulence, but this was not certain. Certainly the reasons for the preferred heights was totally unknown. An explanation of the existence of small steps in electron density, of only a few tens of metres extent, was not forthcoming. The purpose of this thesis, then, was to obtain greater insight into the nature of these phenomena. The complete answer as to their nature is still unknown.

1.4.2 VHF Observations to 1977

Some scatter from the ionosphere at VHF was observed in the 1950s, and Ellyett and Watts (1959) mention that Bailey, Bateman and Kirby, and Pineo, did observe some VHF scatter from 75-90km. Booker (1959) also discussed VHF scatter from around 90km. Villars and Weisskopf (1955) also observed VHF scatter.

However, all these examples were cases of oblique scatter, with transmitter and receiver well separated, so that the scatter came from Bragg scales many times the wavelength of the radiation. In fact, the scatter was most likely due to irregularities of electron density with scales similar in order of magnitude to those causing the previously discussed HF backscatter. (Villars and Weisskopf suggested vertical scales of about 14m, with scatter being from heights below 90km).

However, a significant step forward in the understanding of D-region echoes came about with the detection of backscattered echoes at 40-50MHz from the D-region. Flock and Balsley (1967) reported on such echoes from 75 to 80km at Jicamarca near Lima, Peru (12°S, 77°W), although they mention that Bowles had detected such echoes as early as 1958 in Illinois, U.S.A.. Flock and Balsley then concluded that the echoes they observed must be due to turbulence, and that the scattering regions were less than a few hundred metres thick vertically. If a step in ionization caused the scatter, as had been suggested for HF work below 80km, the step would have to be less than on quarter of a wavelength thick; or less than 2 or 3 metres! (This arises because the refractive index step would, upon Fourier decomposition, have to contain a significant contribution from Bragg scales around $\frac{\lambda}{2}$ metre, λ being the probing wavelength in metres; eg. Atlas, 1965; also see later in this thesis). Admittedly, turbulence would also have to contain such scales, but it is easier to envisage a random arrangement of scatterers of around 2-3m scale produced as part

of a turbulent process, than a well defined step less than 2-3m thick maintaining itself for a few minutes (also see Section 1.4.1e; $t \sim h^2/K$).

However, investigations using VHF were rare up to about 1974-1976. In 1974, Woodman and Guillan published a paper concerning VHF observations of mesospheric (and stratospheric) scatterers (also using the Jicamarca array) and this preceded a great increase in VHF observations of the Mesosphere, Stratosphere and Troposphere. Perhaps the main reason for this increase was the widespread introduction of both amplitude and phase (ie. the complex signal) measurements. This allowed coherent integration of the signal, and hence produced significant improvements in the signal to noise ratio. However, useful coherent integration requires that the integration length be less than one quarter of the smallest fading cycle, and hence higher pulse repetition frequencies and data acquisition rates were necessary. The advent of on-line mini-computers made this high data acquisition rate possible. By recording amplitude and phase, Doppler measurements of wind speeds also became possible.

Woodman and Guillen (1974) interpreted the scatter they saw as due to turbulence, just as Flock and Balsley before them. Under this assumption, they estimated the scattering regions to be less than about 100m thick. They also observed the passage of short period gravity waves with their wind measurements. Again, 75km emerged as a height from which strong mesospheric scatter was obtained.

Rastogi and Woodman (1974), also presented a paper on these VHF echoes. Of significance was the fact that the paper showed detail regarding the temporal variation of echo structure; interestingly, at times strong bursts of power occurred, lasting a few minutes only, and

having powers 10 to 20dB above the "normal" level. Such bursts also seemed to be associated with slower fading.

Cunnold (1975) followed up the above papers with a further discussion of estimation of turbulence parameters from VHF data. A few more parameters apart from those obtained by Woodman and Guillen were estimated. Again, however, the paper made the assumption that the scatter was indeed due to turbulence.

Rastogi and Bowhill (1976a, 1976b) appear to have been the next authors to discuss VHF observations of the mesosphere - again with the Jicamarca radar. They, too, assumed the scatter was due to turbulence. Fading times were found to be typically less than one or two seconds; and evidence existed that strong bursts of power often exhibited slow fading (a similar result had been noted qualitatively by Flock and Balsley, 1967). This result was interpreted to mean that during times of increased power, the thicknesses of the scattering layers decreased. Rastogi and Bowhill also found evidence for at least two scatterers contributing to their echoes, each moving at different velocities. Similar results will be seen later in this thesis.

However, it should perhaps be restated here that the case for turbulent scatter from the mesosphere at VHF was far from established - it was a hypothesis which had been adopted more because nothing else seemed reasonable than for any other reason. The possibility of steps in refractive index less than one or two metres in vertical extent seemed quite unrealistic; such a step may be expected to be destroyed by turbulent diffusion in a time $t \sim L^2/K$; $L \sim 2m$, $K \sim 10^2 m^2 s^{-1}$, so $t \sim .04$ seconds!

In 1977, Harper and Woodman presented more VHF results of mesospheric scatter - again with the Jicamarca array. Again, scatter came particularly from around 75km. Detailed temporal analyses of the echoes were presented, similar to those of Rastogi and Woodman (1974). Results showed that frequent power bursts occurred, often 10-20dB above the

"normal" level, lasting around 2-5 minutes, and with a quasi-periodicity of around 5 minutes. This periodicity, they claimed, correlated with a 10 minute gravity wave observed in the Doppler measured winds at the same height. Thus emerged some of the earliest direct evidence of the possible effects of gravity waves on these D region scatterers. The authors also found a correlation between strong echo power and slow fading - but this did not always exist. At times, there was even an inverse correlation, with strong powers showing quite rapid fading. These results generally supported the findings of Rastogi and Woodman (1974).

VHF radars such as that at Jicamarca are also capable of detecting scatter from clear air in the stratosphere and troposphere, and in recent years a great deal of effort has gone into examination of these echoes, particularly since about 1976. These echoes show many similar characteristics to the mesospheric echoes observed from around 75km; and since temperature measurements are much easier in the lower atmosphere than in the mesosphere, the opportunity existed for extremely detailed investigations of the relationship of winds and temperatures to these structures (assuming, of course, that the lower scatterers were similar in origin and nature to the mesospheric scatterers). The results of these investigations will not be discussed here, since detailed work was only attempted after around 1977-1978. Gage and Balsley (1978) gave a review of the historical development of these VHF radars with regards to clear air scatter. This will not be discussed yet. For the present, it is sufficient to say that further developments in VHF studies have questioned the interpretation that these echoes are always due to turbulence, and have suggested the possibility of specular scatter. These things will be commented upon further at their relevant place in the ensuing discussions.

Just as examinations of lower atmospheric echoes may be helpful in interpreting mesospheric structures, so too may examinations of structures in the ocean be useful. Some interesting structures have been noticed in certain bodies of water, which may help give clues as to the nature of mesospheric echoes. These things, too, will be left till later for a fuller discussion.

Of course, the scatterers causing VHF reflections in the mesosphere may not even be the same ones as those causing HF scatter - that possibility exists, too. But the similarity in heights of VHF and HF echoes (particularly the common occurrence of the 75km echo) would suggest the scatterers are related in some way - even if they might not be one and the same. Thus it is important to follow advances in VHF studies during the course of this thesis.

CHAPTER II

TURBULENCE - A GENERAL DISCUSSION

2.1 Warning

2.2 Description of Turbulence

- 2.2.1 The energy budget
- 2.2.2 Generation of Turbulence
- 2.2.3 The Spectrum, and important Turbulence parameters
  - a. The Spectrum
  - b. Eddy Transport
  - c. Equations involving important turbulence parameters
- 2.2.4 More careful treatment of ε, K

2.3 Correlation formulae, Structure functions, and some more rigorous theory

- 2.3.1 Theory
- 2.3.2 Estimation of C_n^2

2.4 Radar scatter

- 2.4.1 Radar equations

Chapter II Turbulence - A General Discussion

2.1 Warning

No pretence is made in this chapter that turbulence is a well understood phenomenon; there would not be a reference anywhere that would make such a claim. Scorer (1978), in his first two sections of Chapter 7, points this out quite well. Turbulent motions are extremely complex, and to even attempt to explain them in useful terms so that results can be applied generally, requires a statistical description.

What is turbulence? Many definitions have been given. In this thesis, it will be taken simply as any set of zero-mean motions which are too random to describe by concepts such as waves, or any ordered phenomena. In time, it may come about that some of the motions ascribed to turbulence can be explained more simply. As an example, many of the atmospheric motions now known to be due to gravity waves were treated as turbulence before Hines' 1960 paper.

As Scorer points out, there are many different types of turbulence, and descriptions appropriate to one type may not be appropriate to another type. This chapter will concentrate largely on atmospheric turbulence for which no significant boundaries exist (although at very large scales, of the order of thousands of kilometres, the Earth's surface must be regarded as a boundary). Typical parameters used to characterize turbulence will be discussed, and results which can be regarded as generally applicable given. This is not to say the results are always applicable, and on occasion exceptions will be mentioned.

One more point may be worth comment. Two of the most important functions of turbulence are the eventual deposition of mechanical energy into the atmosphere as heat, and increased rates of diffusion . Processes which do not do these things are not turbulence. For example, a random

arrangement of gravity waves passing through a region may look like turbulence - but particles moving under these forces will simply oscillate. They will not diffuse apart. This then, is not turbulence.

2.2 Description of Turbulence

2.2.1 The Energy Budget

A complete discussion of turbulence is beyond the scope of this thesis. However, turbulence probably makes an important contribution to radio wave scattering in the ionosphere. It is thus important that some insight into turbulence be gained. In this chapter, a brief review of some of the important concepts of turbulence will be given, and also a collection of relevant formulae relating eddy sizes, lifetimes, velocities and so forth is given. For a more detailed discussion on the theory of turbulence see, for example, Batchelor (1953); Tatarski (1961); Lumley and Panofsky (1964); Bolgiano (1968); and Tennekes and Lumley (1973). Villars and Weisskopf (1955) also gives a useful introduction to some of the simpler turbulence formulae.

Turbulence is, by definition, a random set of motions. However, its origins still lie in the Navier-Stokes equations (equations C.6a, C.6b). Batchelor (1953), develops his discussion from these equations, as does Bolgiano (1968). The full development will not be given here, but some of the results will be quoted.

The Navier-Stokes equations are often re-arranged to give an equation in terms of energies (eg, Bolgiano, 1968; Villars and Weiskopf, 1955). Dutton and Panofsky (1970) give a particularly simple form of this energy-budget equation, which is quite good for descriptive purposes. The equation

$$\frac{dE}{dt} = M + B - \varepsilon + T \qquad (2.2.1.1a)$$

represents this energy budget.

E represents the turbulent kinetic energy, and t is time.

M represents the mechanical generation of turbulence, and is always

positive (ie, an energy source).

B represents the buoyancy term. It may be either positive (energy source) or negative (energy sink), depending on the atmospheric conditions. B is positive if the rate of fall of temperature, $\frac{-dT}{dz}$, is more rapid than the adiabatic lapse rate. Otherwise, B tends to damp out the turbulence.

ϵ is the rate of loss of turbulent energy through viscous dissipation, and is always positive. Hence $(-\epsilon)$ represents an energy sink.

The term T represents transport of energy (advection) into or out of the region.

The fluctuations in density, velocity, or whatever, induced by the turbulence, can be regarded as the sum of a great variety of plane sinusoidal variations of varying orientations and "wavelengths" (scales) (Wavelength here refers simply to the distance between successive peaks in the sinusoidal fluctuations. These sinusoidal fluctuations should not be confused with propagating waves however; they are simply spatial oscillations). The turbulence can then be expressed as a power spectrum in these wavelengths or scales. (That is, the turbulence can be Fourier analysed.)

Let us assign each scale a wavenumber $\underline{k}$, parallel to the wave normal and of magnitude $\frac{2\pi}{\lambda}$, λ being the "wavelength". Then with regards to these wave numbers k, a more sophisticated form of the energy balance equation (2.2.1.1a) can be derived. Such an equation can be found in Weinstock (1978), and takes the form

$$(2.2.1.1b) \qquad \frac{\partial E(k)}{\partial t} + \frac{\partial Q(k)}{\partial z} = S(k)\frac{\partial U_0}{\partial z} - \frac{\partial \epsilon(k)}{\partial k} + B(k) - 6\nu k^2 E(k),$$

where

(i) E(k) is the spectral kinetic energy density,

(ii) $\frac{\partial Q(k)}{\partial z}$ represents the vertical transfer of energy in physical space caused by the turbulence itself (z is the vertical coordinate),

(iii) $S(k)$ is the spectrum of the Reynold's stress, $= -\langle uw \rangle$, where u is the horizontal velocity fluctuation in the direction of the mean flow U_0, w is the vertical velocity fluctuation, and $\langle\ \rangle$ denotes averaging, so that $S(k)\frac{\partial U_0}{\partial z}$ represents the energy transferred from the mean flow to the turbulence by the Reynold's stress,

(iv) $\varepsilon(k)$ represents the nett rate of spectral energy transfer from wavenumbers smaller than k to wavenumbers larger than k,

(v) $B(k)$ is the spectrum of the buoyancy flux, $\frac{-g}{\rho_0}\langle w\rho' \rangle$, where ρ' is the density fluctuation, ρ_0 is the average density at height z, and g is the acceleration due to gravity, and

(vi) $2\nu k^2 E(k)$ is the rate of energy dissipation by the molecular viscosity ν.

For a feeling for the derivation of this energy budget equation from the Navier-Stokes equation see, for example, Bolgiano (1968).

Weinstock then proceeds to calculate the form of $B(k)$, but the purpose of presenting this equation here is rather to give a further idea of the important processes involved in turbulence.

It is worth commenting here that, over some of the spectral range (and in fact an important range), $\varepsilon(k)$ is approximately a constant, ε, and is generally regarded as the rate at which energy is dissipated to the atmosphere. Why does this follow?

Energy is generally generated in large "eddies" (associated with small k values) - perhaps by rotation started by wind shear or temperature processes - and then these large scale motions generate smaller scale motions inside; and so on. The larger eddies, being affected significantly by gravity, are anisotropic - longish and flattish. At large k values, the eddies become more isotropic. (Some idea of the transition scale between isotropic and anisotropic eddies has been given in Section 1.3.3, Chapter I; generally it corresponds to values of the order of tens and

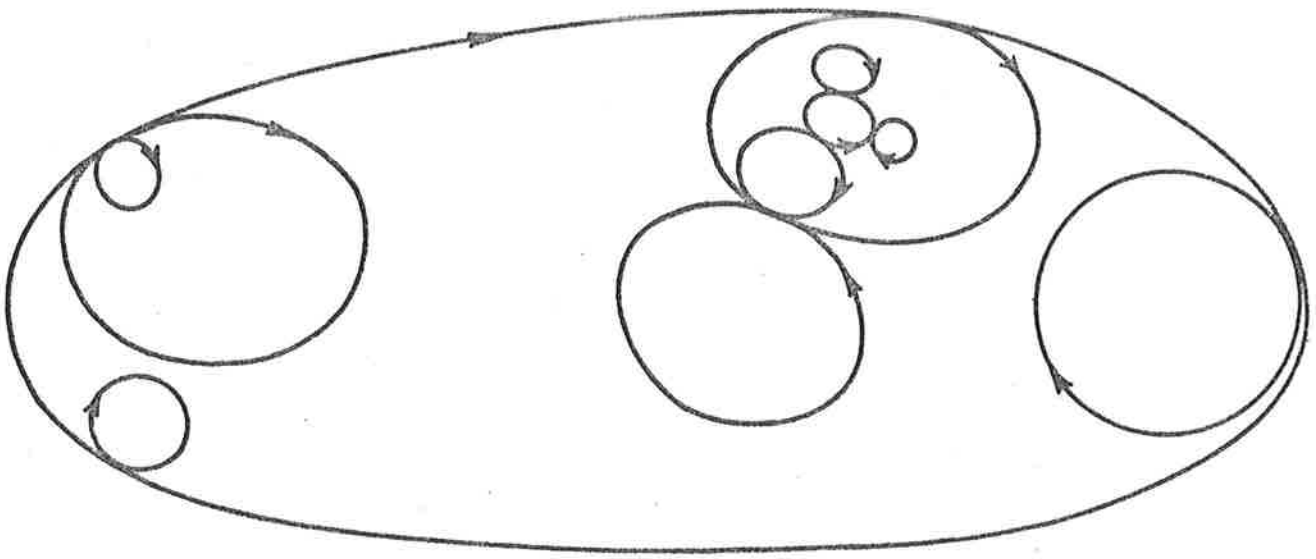

Fig. 2.1a Crude illustration of the development of turbulent eddies.

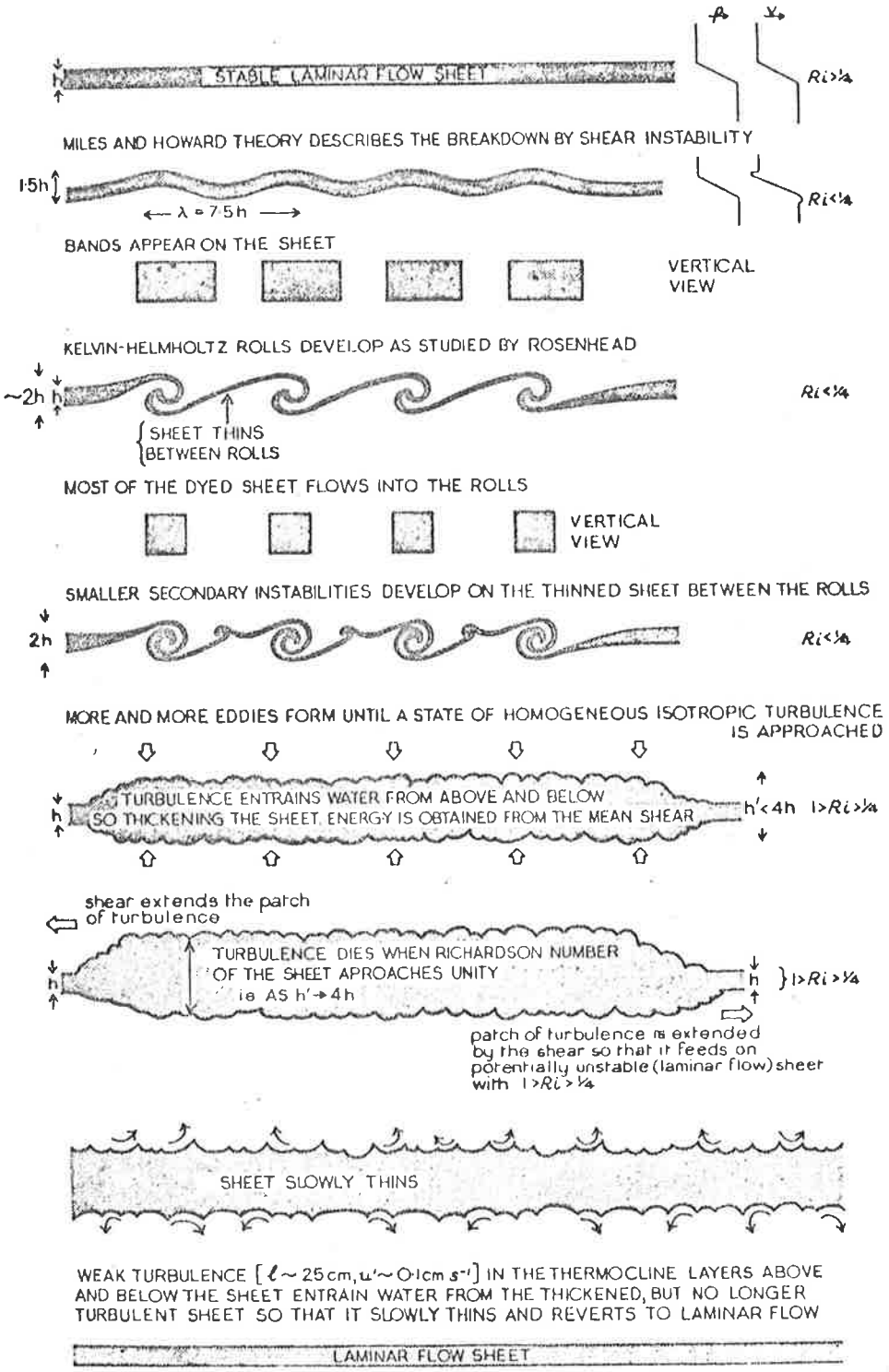

Fig. 2.1b Illustration of the development of turbulence in stratified flow, via the Kelvin-Helmholtz process. From Woods, 1969.

hundreds of metres to a few kilometres vertical extent.) The process is illustrated crudely in Fig. 2.1a, with a more accurate example in Fig. 2.1b. (The R_i parameter is a parameter describing when turbulence is likely. Turbulence may occur if $R_i \lesssim 0.25$. R_i, and Fig. 2.1b, will be discussed in more detail shortly.) Eventually very small scales are reached, and these cannot be maintained since the shears associated with them become so large that viscosity damps them out. Thus the energy of these smaller eddies is eventually dissipated into heat by viscous processes. Then since turbulent energy is generated at large scales, and moves down to smaller scales, it would seem reasonable that the rate of energy transfer between the scales is roughly the same at all scales. The final energy transfer from the smallest scales to heat is also roughly equal to this value. Thus the parameter $\varepsilon(k)$ is approximately independent of k, and is called the energy dissipation rate.

The above description is not exact. At largish scales, some of the energy can be dissipated by buoyancy forces (eg, radiation of energy as gravity waves). The term (vi) in (2.2.1.1b) also acts; although this term is quite small for all but the smallest scales (smallest eddies). However, there is quite a range of the turbulent spectrum where the above description is valid, and energy just propagates down the scales. This region is called the "inertial range" of turbulence. Considerations of such a picture lead to the formula describing the energy spectrum; viz -

$$E(k) = \alpha\varepsilon^{2/3}k^{-5/3} \qquad (2.2.1.2)$$

where $E(k)dk$ is the kinetic energy present in scales of wavenumber k to k + dk. This result was originally due to Kolmogoroff (eg, Batchelor, 1953). It applies mainly to steady-state turbulence, where the sources and sinks are all operative. It does not effectively cover decaying

turbulence, where the sources are no longer active; although it might seem reasonable that it will apply for some time after removal of the source at the larger wavenumbers (smaller scales). Nor does it cover "fossil" turbulence (irregularities which exist in the absence of a generating source (Van Zandt et al., 1978)). In fact, many of the formulae in this thesis refer primarily to steady-state turbulence.

Different authors use different values of the parameter α. Rastogi and Bowhill (1976a, b), give $\alpha = 1.586$. Weinstock (1978) uses $\alpha = 1.4$. Gage and Balsley (1978) give 2.2.1.2 in component form

$$E_i(k) = \alpha_i \varepsilon^{2/3} k^{-5/3},$$

i referring to orthogonal directions. ($E_i(k)dk_i$ is the energy associated with scales aligned in the direction corresponding to i, with wavenumber k_i to $k_i + dk_i$). For wavenumbers parallel to the mean flow (longitudinal component), Gage and Balsley give $\alpha_i \sim 0.5$; and for the transverse components, $\alpha_i \sim 0.65$. Caughey et al. (1978), also give $\alpha_i \sim 0.5 \pm .02$ for the longitudinal component.

2.2.2 Generation of Turbulence

Before discussing further the form of the energy spectrum of turbulence, it might be fruitful to examine just when turbulence is most likely to occur. Refer again to equation (2.2.1.1a). (The following discussion follows Dutton and Panofsky, 1970). Turbulence is likely to occur if the energy sources can overcome the bouyancy effects trying to prevent turbulence. Then the flux Richardson parameter,

$$R_f = \frac{-B}{M} \tag{2.2.2.1}$$

is introduced. R_f measures the ratio of the rate of withdrawal of energy by the stable temperature stratification to the rate of production of energy by a wind shear. Equation (2.2.1.1a) becomes

$$\frac{dE}{dt} = M(1 - R_f) - \varepsilon \tag{2.2.2.2}$$

If B is positive (source), R_f is negative, and both the wind shear and temperature structure favour turbulence. Turbulence is then very intense. If R_f is large and positive, energy is withdrawn so rapidly by the bouyancy term B that turbulence does not develop. But if R_f is small, and positive, the mechanical source may be able to overcome B, and maintain turbulence. There is a constant R_c, such that if

$R_f < R_c$, turbulence can develop,

and if $R_f > R_c$, turbulence is unlikely to develop.

Then if R_c can be determined, and R_f measured, any atmosphere can be classified as turbulent or non turbulent. Unfortunately, R_c cannot be determined and nor can R_f be measured. However, there is a parameter called the gradient Richardson number,

$$R_i = \frac{\omega_B^2}{\left(\frac{\partial \bar{U}}{\partial z}\right)^2} \tag{2.2.2.3}$$

where ω_B is the Brunt-Vaisala frequency of the atmosphere, given by

$$\omega_B^2 = g\frac{\partial \ln\theta}{\partial z}, \quad \theta \text{ being the potential temperature,}$$

$$= -g\left(\frac{1}{\rho}\frac{\partial \rho}{\partial z} - \frac{1}{\gamma p}\frac{\partial p}{\partial z}\right), \quad \text{where } \gamma = \frac{C_p}{C_v},$$

$$= \frac{g}{T}\left(\frac{\partial T}{\partial z} + \Gamma_g\right).$$

Here, Γ_g is the dry adiabatic lapse rate, $= \frac{-\partial T}{\partial z}$ for a dry adiabatic atmosphere, $= \frac{g}{C_p}$ ($\simeq$ 1K/100m at ground level (see Houghton, 1977, section 3.2 for the adiabatic lapse rate for a wet atmosphere, although this is only really relevant in the troposphere)). In the above formulae, ρ is the atmospheric density, p the pressure, C_p and C_v are the specific heats at constant pressure and volume respectively, and T is the temperature. Note ω_B^2 can be negative. This corresponds to a temperature gradient $\frac{-\partial T}{\partial z} > \Gamma_g$, which is a very unstable atmosphere.

$$\left(\frac{\partial \underline{U}}{\partial z}\right)^2 = \left(\frac{\partial u}{\partial z}\right)^2 + \left(\frac{\partial v}{\partial z}\right)^2, \quad \text{where } \underline{U} = (u, v, 0) \text{ is the horizontal velocity}$$

as a function of height, z. The formula (2.2.2.3) assumes a horizonatally stratified atmosphere.

Although R_i is not the same as R_f, it is at least a parameter which can be measured. R_i and R_f are proportional if the ability of the turbulence to transport heat vertically is proportional to its ability to transport momentum. This is often assumed to be the case, although need not be (Dutton and Panofsky, 1970). Experiments suggest turbulence may form whenever

(2.2.2.4) $$R_i \lesssim 0.25$$

(eg., Woods, 1969). Theoretical results (eg., the Miles-Howard theorem (see Miles, 1961; Howard, 1961; Hines, 1971)) also suggest turbulence

occurs when R_i is less than about 0.25.

This is the most commonly used criterion for turbulence in the atmosphere. However, it is not general. For example, for flow in a pipe, the Richardson's number is not applicable - turbulence is, rather, likely to develop when a parameter known as Reynold's number gets larger than some critical value. Reynold's number is given by (eg., Haltiner and Martin, 1957, equation 14.7)

$$R_e = \frac{Ud}{\nu}$$

d being the pipe diameter, U the fluid velocity, and ν the kinematic viscosity. At times, a similar formula has been used as a criterion for turbulence in the atmosphere, with d being a "typical scale", eg., Blamont and Barat (1967). This is not to say both views are applicable - different authors give different reasons for using each. Generally, the R_i approach is used. (It is interesting that Villars and Weisokopf (1955), use an R_e type approach to derive some of the basic equations of turbulence.)

What does R_i actually represent? If $\left(\frac{\partial U}{\partial z}\right)^2$ is large, R_i becomes small. Physically, this simply says large wind shears cause turbulence - just as has already been seen. The term ω_B^2 can be negative or positive. When it is positive, ω_B is the angular frequency of oscillation of an adiabatic parcel of air in the atmosphere. The term ω_B^2 is negative if $\frac{-\partial T}{\partial z} > \Gamma_g$; that is, the atmospheric temperature falls faster than the adiabatic lapse rate, and a parcel of air rising adiabatically would continue to rise - the atmosphere is said to be (hydro-) statically unstable, and in this case the temperature profile also promotes turbulence. Then $R_i < 0$, and turbulence is always possible. The condition

$0 < R_i < 0.25$ is called dynamic instability,

and $R_i < 0$ is called hydrostatic instability.

Turbulence can occur even without wind shear if $R_i < 0$.

However, Dutton and Panofsky point out an interesting fact with regards to atmospheric fronts in the troposphere. Near these fronts, theory suggests that the wind shear is proportional to ω_B^2, so (2.2.2.3) implies

$$R_i \propto \frac{1}{\omega_B^2}$$

in these cases. That is to say, turbulence is most likely in regions of hydrostatic stability, at least when related to boundary layer (first km of the atmosphere) fronts; only hydrostatic stability produces large wind shears in this case.

So hopefully the above survey has given an idea of the situations in which atmospheric turbulence occurs. Fig. 2.1b shows the development of one type of turbulence - the Kelvin-Helmholtz process. This is applicable at the boundary of two fluids, where waves develop and then break down into turbulence (also see Dutton and Panofsky, 1970; Thorpe, 1979).

It may also be worth mentioning that these formulae, such as that for R_i, are only valid for a horizontally stratified atmosphere. (Hines (1971), shows how R_i can be generalized).

When determining R_i experimentally, resolution can be an important factor. For example, Van Zandt et al. (1978), use a probabilistic type of approach in the case where their resolution of temperature and wind height profiles is worse than the true fine scale fluctuations which exist. Coarse resolution can give the mean wind shear, but may miss fine scale fluctuations and hence give estimates of R_i which are too large.

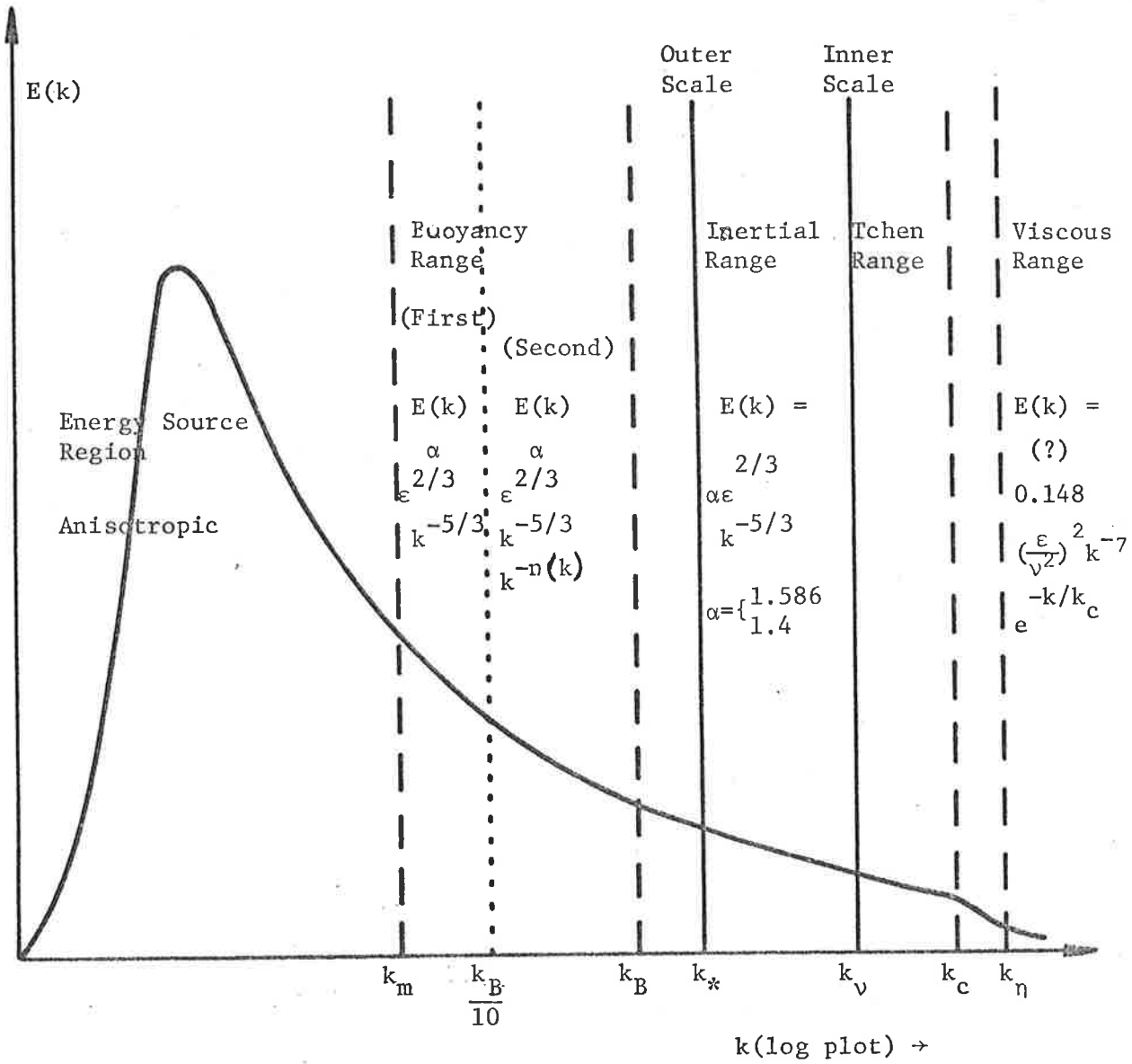

Fig. 2.2 Typical energy spectrum of Atmospheric Turbulence. (Also see, for example, Batchelor (1953), Figs. 7.6 and 7.9.) Here, $E(k)dk$ is the energy contained in scales with wavenumbers between k and $k + dk$. The various ranges are discussed in the text. Here, $k_\nu = 0.169k_\eta$, $k_c = 0.738k_\eta$. The term ε represents the rate of transfer of energy between scales.
Lifetimes can also be associated with these scales (eg., Hines, 1977b). Since $k^{-2}\tau^{-3} = \varepsilon_d$ (equation 2.2.3.2b) for a given energy dissipation rate ε_d, time scales can be assigned to k_B, k_ν. For example, Hines claims that the inertial range in the atmosphere corresponds to lifetimes between about 10s and 150s. However, see section 2.2.3 for more on this.

2.2.3 The Spectrum and Important Turbulence Parameters

2.2.3a The Spectrum

Thus far, it has been seen how wavenumbers are used to represent the turbulence scales, and some discussion of the conditions for which turbulence occurs has been presented. Now, let us take a more detailed look at the energy spectrum of turbulence. Fig. 2.2 shows the approximate form of the spectrum. The derivations of the various regions will not be discussed. Rastogi and Bowhill (1976a, b) can be examined for references regarding the inertial and viscous ranges. Batchelor (1953), also discusses the regimes. Weinstock (1978) discusses the buoyancy range, although several theories have evolved for this range (eg., see Bolgiano, 1968).

As we have seen, energy is generated at small k values. It then passes down through to the smaller scales, until eventually the energy is dissipated at k values too high to be maintained against the effects of viscosity. This final region is known as the viscous region. Above k_c (see Fig. 2.2) the energy density falls rapidly as a function of k, with a spectrum something like that shown in Fig. 2.2. The form of this spectrum has been discussed by Rastogi and Bowhill (1976b) - there has been some debate as to its form. The term k_η is known as the wavenumber corresponding to the Kolmogoroff microscale, and it can be shown that

$$k_\eta = (\varepsilon/\nu^3)^{1/4} \text{ radians per metre.} \qquad (2.2.3.0)$$

This will be derived later. For the present, we may regard it simply as a "cutoff" wavenumber; wavenumbers of higher k do not exist strongly.

It is worth pointing out here that sometimes the reciprocal wavenumber k^{-1} is called the scale. It is easy to confuse this with the "wavelength" associated with this scale, $2\pi/k$, since sometimes "scale" is used to refer to this "wavelength". When referring to scale, it is

often useful to express the units (eg., metres, or metres rad^{-1}, whichever is relevant). Workers in the field of turbulence tend to ignore factors of the order of 2π, and freely mix these different forms of scale. This can complicate matters for experimentalists. For example, some authors call

$$\eta = k_\eta^{-1} \text{ the Kolmogoroff microscale,}$$

and others call $\eta = 2\pi k_\eta^{-1}$ the microscale! It is therefore best to express the units whenever dealing with scales, eg., $\eta = k_\eta^{-1}$ m rad^{-1}, or $2\pi k_\eta^{-1} m/(2\pi^c)$. (Sometimes just called metres). Theoreticians (eg., Batchelor, 1953) tend to use scale in m rad^{-1}.

At k values much greater than k_c, the exponential in the viscous spectrum dominates. At k values between the outer scale of the inertial range, k_*, and the inner scale ($\sim k_\nu$) the energy spectrum is inertial, with the form

$$E(k) = \alpha \varepsilon^{2/3} k^{-5/3}, \text{ as already has been briefly discussed.}$$

In the region between k_ν and k_c, called the Tchen range, the spectrum is represented by a transition between the viscous and inertial formulae.

The region where buoyancy effects are most dominant is still far from understood. Bolgiano (1968) discussed some of the possible theories (eg., Bolgiano, Lumley and Shur, Phillips) relevant to this range. Because it is later, and seems to have been developed in some detail, the theory of Weinstock (1978) is adopted in this discussion. This is not to say it is the final solution.

According to Weinstock, an upper limit to this buoyancy range is given by k_B, where

(2.2.3.½) $$k_B = \sqrt{0.8}\,\frac{\omega_B}{v_m},$$

and v_m is the RMS fluctuating velocity in the combined buoyancy and inertial ranges along a given direction. For $v_m \sim 0.2 ms^{-1}$ (weak turbulence) to $1.5 ms^{-1}$, and $\omega_B^2 \sim 4.6 \times 10^{-4} s^{-2}$ rad^2 (typical stratospheric value), k_B corresponds to scales $L_B \sim 67$ to 500 metres.

In this buoyancy range, energy does not only propagate down the scales. Some energy is lost by the generation of incoherent gravity waves, and is thus propagated away. In the inertial range, such waves could also be generated, but are heavily damped. This loss of energy by gravity wave production in the buoyancy part of the spectrum is partly why Weinstock's buoyancy spectrum for the buoyancy range, B(k) (see equation 2.2.1.1b), differs from that of Lumley and Shur, who found an $\varepsilon^{1/3} k^{-7/3}$ dependence for the buoyancy spectrum (see Weinstock's 1978 paper). Weinstock found a more complex relation. He also derived a form for the energy spectrum E(k) in the buoyancy range. Two main ranges appeared to exist in the general case, although both need not always be present in any particular case of turbulence. The expression for E(k) in the so-called "first buoyancy range" is a little complicated, but is expressed in the form

$$E(k) \propto \varepsilon^{2/3} k^{-5/3} k^{-n(k)}$$

so it "looks like" other spectral turbulence forms. In fact

$$\left(\frac{k}{k_B}\right)^{-n(k)} = 1 + \frac{5}{12} \cdot \alpha^{3/2} \cdot a \cdot \frac{v_m}{v_0} \cdot C\left(\frac{k}{k_B}\right)\left(1 - \frac{1}{R_f}\right)$$

Here, $\alpha \sim 1.4$ according to Weinstock, and ~ 1.586 according to Rastogi and Bowhill (1976b). The parameter a is the ratio of vertical energy density compared to the horizontal energy density at any wavenumber k. In the inertial range, $a \sim 1$; in the buoyancy range, the turbulence becomes anisotropic, and $a \sim 0.5$. The velocity v_m, as discussed, is the RMS velocity in the buoyancy and inertial ranges combined ($k \gtrsim k_m$); v_0

is the RMS velocity in the bouyancy range only. Generally,

$$1 \lesssim \frac{v_m}{v_0} \lesssim 3 \qquad \text{(see Weinstock).}$$

R_f is the flux Richardson number. $C(\frac{k}{k_B})$ is a fairly complex form, and will not be given.

However, for all its complexity, Weinstock considers only 4 cases to be important, depending on

$$\delta = \frac{v_m}{v_0}(1 - \frac{1}{R_f}).$$

These are:

(a) $0 < \delta < 1.4$

Then $E(k) \approx \alpha\varepsilon^{2/3}k^{-5/3}(\frac{k}{k_B})^{-\Delta}, \qquad 0 < \Delta < 0.4.$

Thus E(k) varies only a little faster than $k^{-5/3}$.

(b) $-0.7 \lesssim \delta \lesssim 0.$

Then $E(k) \approx \alpha\varepsilon^{2/3}k^{-5/3}(\frac{k}{k_B})^{+\Delta} \qquad 0 < \Delta < 0.4.$

Thus E(k) varies a little more slowly than $k^{-5/3}$.

(c) $\frac{v_m}{v_0} \approx 3$, $R_f >> 1$. ($\frac{v_m}{v_0} \approx 3$ implies strong turbulence; $R_f >> 1$ implies static stability).

Then $E(k) \approx \alpha\varepsilon^{2/3}k^{-5/3}(\frac{k}{k_B})^{-0.8}$.

This means a rapid variation of E(k), and corresponds to a sink of turbulence, or decaying turbulence.

(d) $\delta < -1.0$ (large $\frac{v_m}{v_0}$ (strong turbulence) and $R_f < 1$ (hydrostatic instability)).

Then $E(k) \approx \alpha\varepsilon^{2/3}k^{-5/3}(\frac{k}{k_B})^{1.0}$.

This is a very slow variation of E(k), and corresponds to a strong source of turbulence.

The "second buoyancy range" may not exist - it depends on whether $\frac{k_B}{10}$ is greater or less than k_m, k_m being the minimum wavenumber for which Weinstock's theory holds. If $\frac{k_B}{10} > k_m$, the second range exists. In this second range, the dissipation rate is not ε; it is greater than ε if $R_f > 1$ (some energy is also lost by buoyancy effects, as the atmosphere is statically stable and thus damps some of the motion; thus the rate at which energy is propagated down the scales gradually decreases as it moves down, until the inertial range is reached, where the dissipation rate is ε), and less than ε if $R_f < 1$.

The transition between inertial and buoyancy ranges is rather ill-defined, but Weinstock feels wavelengths greater than a hundred or so metres must be affected by gravity.

Interestingly, this theory still envisages a $k^{-5/3}$ law at large wavelengths (eg., second buoyancy range), and does not contradict results that even at very large scales, where eddies are decidedly anisotropic - and even nearly two-dimensional (horizontal scales of tens of kilometres and more) - a $k^{-5/3}$ law has been observed (eg., Elford and Roper, 1967; Gage, 1979). Of course, this is not to say that the conditions assumed in deriving the inertial range spectrum are still valid at these scales. Perhaps they are. But just because the law fits the theory does not always imply that the theory is relevant.

With regards to the very large scales (small k), it has already been mentioned that the eddies tend to be anisotropic. Some idea of the scales at which anisotropy becomes significant is given in Section 1.3.3, Chapter I. Generally, in the upper atmosphere eddies with vertical scales greater than 1 to 2km are anisotropic. But the anisotropic region

covers a large range - from mesoscale (horizontal scales of 10's to 100's of km) to synoptic scales (around 1000 km) to macroscales (2-3000 km horizontal extent). The laws governing these regions form a new problem again.

According to Gage (1979) there are two main source scales for turbulence - (This is for the troposphere - but it is mentioned here since similar ideas (e.g. reverse-cascading) may be relevant elsewhere)

(i) small scale - perhaps a few km at most in vertical extent; for example wind shears, thunderstorms, breaking waves; and

(ii) large scale sources, generating eddies of macroscale size - for example, baroclinic instability represents one such source.

Associated with each source is a spectrum like Fig. 2.2. But when both sets of sources occur in the same atmosphere, as they do, a mixing of the spectra occurs. In fact, Gage also mentioned the concept of reverse-cascading, whereby eddies act somewhat coherently to generate larger eddies (in contrast with the earlier scheme whereby large eddies generated smaller ones). Gage then proposed laws for the various regimes, with a scheme something like that described in Fig. 2.3. Both cascading and reverse cascading occur. Gage also claimed that the k^{-3} spectrum A, and the $k^{-5/3}$ spectrum B (Fig. 2.3) are incompatible, implying a sink between the two. Phenomena associated with the decaying stages of cyclone life (cyclones are, after all, just large eddies) were offered as this sink.

It is also worth noting that exceptions occur to the laws in this scheme. Justus (1969) has presented a theory for the spectrum of shear dependent turbulence. The buoyancy range, which does not always have a $k^{-5/3}$ law, has been mentioned. Bolgiano (1968) has also suggested a k_3^{-3} law for weak turbulence in strong wind shears (k_3 being the vertical wavenumber). In such cases, the cut off wavenumber is not k_η, but is given by a form depending on the wind shear strength. Experiment and

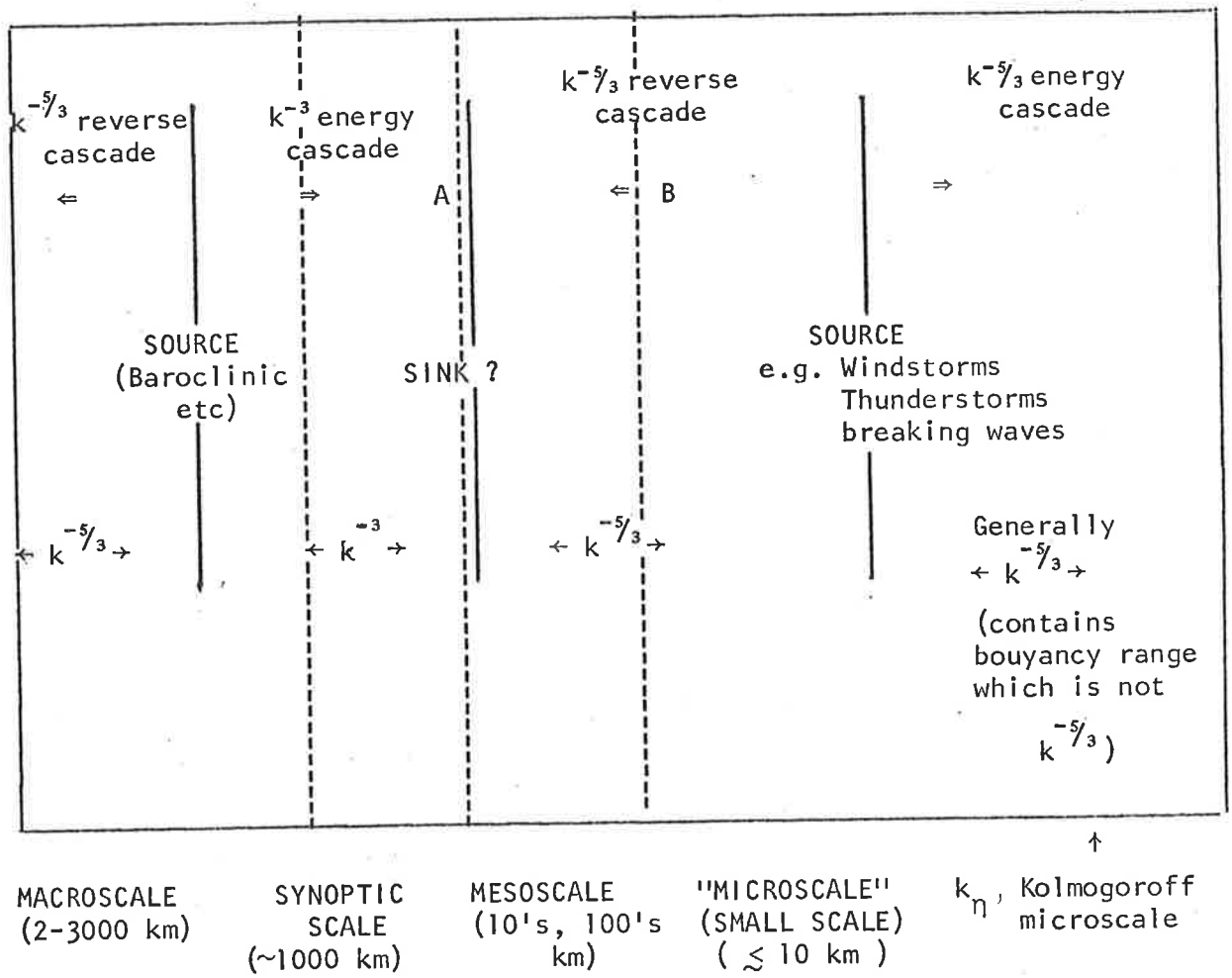

FIG. 2.3 Interaction of eddy scales in the troposphere. The region called "microscale" here is the main region studied in this thesis; and "microscale" will generally refer to scales in the inertial range and close to k_η, rather than the range indicated here.

theory do not always agree in investigations of turbulence, either (eg., Stewart, 1979).

However, it is primarily the region called "microscale" in Fig. 2.3 which will be dealt with in this thesis; and the nomenclature "microscale" will generally refer to scales of the order of the Kolmogoroff microscale. Scales in the inertial and buoyancy ranges will not be considered as "microscale". The largest scales dealt with will be of the order of the scale of the generating mechanisms - for example, a wind shear across a 2km vertical extent can generate eddies no larger than 2km in depth.

2.2.3b Eddy Transport

In this section, we want to discuss the effective viscosity, thermal conduction and diffusion coefficient for a turbulent fluid. These quantities depend upon the transport of momentum, thermal energy, and gas molecules respectively.

As a starting point, however, consider firstly a non-turbulent viscous fluid. Consider the conduction of heat through such a fluid. The rate of flow of heat H through a cross-section A of the fluid is given by (eg., Tabor, 1970, section 4.5.2)

$$\frac{dH}{dt} = -\kappa_m A \frac{dT}{dz},$$

κ_m being a constant called the thermal conductivity.
Likewise, the rate of flow of momentum transverse to the mean motion (Tabor, 1970, section 4.5.1)

$$\underline{F} = \frac{dp}{dt} = \mu A \frac{du}{dz}, \qquad u \text{ being the horizontal velocity.}$$

($\underline{F}$ is in fact also the drag force which would be exerted on a plate parallel to the fluid, and bounding the fluid eg., see Appendix C.)

Here μ is called the dynamic viscosity (also see Appendix C).

In a similar way, the rate of diffusion of density (molecules) is given by

$$\frac{dn}{dt} = -DA\frac{dn}{dz},$$

n being the number density, and D the self-diffusion coefficient (Tabor, 1970, section 4.5.3). (The case of one gas diffusing into another is a slightly more complicated situation eg., Tabor, 1970)

Then Tabor's book shows that

$$\kappa_m = \frac{1}{3} n\bar{c}\lambda c_v,$$

$$\mu = \frac{1}{3} mn\lambda\bar{c}$$

$$D = \frac{1}{3} \lambda\bar{c}$$

where n is the number density of molecules, $\bar{c}$ the rms molecular speed, λ the mean free path of the molecules, c_v the specific heat at constant volume per molecule, and m the mass of a molecule. Using $nm = \rho$, the mass density, these can be rewritten as

$$\kappa_m = \frac{1}{3} \rho\lambda\bar{c}C, \qquad C = \frac{c_v}{m} = \text{specific heat per unit mass at constant volume}$$

$$\mu = \frac{1}{3} \rho\lambda\bar{c}$$

$$D = \frac{1}{3} \lambda\bar{c} = \frac{\mu}{\rho}$$ (The term $\frac{\mu}{\rho}$ is often denoted ν, and is called the kinematic viscosity eg., see Appendix C).

Interestingly, μ can also be written

$$= (2/3\sigma^2) \cdot (mkT/\pi^3)^{\frac{1}{2}},$$

σ being the molecular radius (eg., Starling and Woodall, 1950, p. 215).

Thus μ also depends on the temperature, and the molecular species (through σ).

These rate of transport equations for heat, momentum and molecular number density can also be used to obtain nett diffusion equations. In the following formulae, horizontal flow and horizontal stratification are assumed, for simplicity.

For example,

$$\frac{dT}{dt} = \frac{\kappa_m}{\rho C}\frac{\partial^2 T}{\partial z^2} = \kappa_{tm}\frac{\partial^2 T}{\partial z^2}, \quad \text{(in general, } \frac{dT}{dt} = \kappa_{tm}\nabla^2 T\text{)}$$

(C being the specific heat per unit mass at constant volume.)

describes temperature transport (Tabor, 1970, section 10.3.3).

In the real atmosphere, T would probably be replaced by potential temperature. Notice $\frac{d}{dt}$ is differentiation following the motion

ie. $= \frac{D}{Dt} = \frac{\partial}{\partial t} + \underline{v}.\underline{\nabla}$.

κ_{tm} is called the thermal diffusivity (or temperature conductivity), as distinct from κ_m, the thermal conductivity.

Likewise,

$$\underline{f} = \frac{d\underline{U}}{dt} = \nu\frac{\partial^2 u}{\partial z^2}$$

is the body force per unit mass acting in a fluid when no horizontal pressure gradients or external forces such as gravity act.

This can also be written

$$\frac{dp}{dt} = \nu\frac{\partial^2 p}{\partial z^2}$$ (z being the vertical coordinate; remember horizontal stratification is being assumed)

which describes the transfer of momentum. Here ν is the kinematic viscosity.

This equation is also used to obtain a more complete equation of horizontal motion, eg., see Haltiner and Martin, 1957, pp. 214-216.

$$\frac{Du}{Dt} = -\frac{1}{\rho}\frac{\partial p}{\partial x} + fv + \nu\frac{\partial^2 u}{\partial z^2}$$ (In this case, ρ is allowed to vary with x)

where ρ is the density, p = pressure, u is the velocity in the x direction, v is the velocity in the y direction, and f is the Coriolis parameter = $2\Omega\sin\psi$, ψ being the latitude and Ω the rotation rate of the Earth (radian $\sec^{-1}$). (It should be pointed out the equation of motion is discussed in its general form in Appendix C.)

The full vector equation of motion is (omitting in this case the Coriolis force),

$$\rho\frac{D\underset{\sim}{v}}{Dt}\underset{\sim}{v} = -\mu\underset{\sim}{\nabla} \times (\underset{\sim}{\nabla} \times \underset{\sim}{v}) - \underset{\sim}{\nabla}p$$

eg., Villars and Weisskopf (1955),

$\underset{\sim}{v}$ being the velocity vector. It is interesting to examine this equation for $\varepsilon = \frac{1}{2}\rho\underset{\sim}{v}^2$. Then

$$\frac{\partial\varepsilon}{\partial t} + \nabla.(\underset{\sim}{v}\varepsilon) = -\mu(\underset{\sim}{\nabla} \times \underset{\sim}{v})^2 - (\underset{\sim}{v}.\underset{\sim}{\nabla}p) + \mu\underset{\sim}{\nabla}.(\underset{\sim}{v} \times (\underset{\sim}{\nabla} \times \underset{\sim}{v}))$$

(eg., Villars and Weisskopf, 1955).

If transport of ε is ignored ($\underset{\sim}{\nabla}.v\varepsilon$), only changes in time of ε are examined, and pressure fluctuations ($\underset{\sim}{\nabla}p$) and gradients of velocity are ignored, then

$$\frac{\partial\varepsilon}{\partial t} = -\mu(\underset{\sim}{\nabla} \times \underset{\sim}{v})^2$$

or $$\frac{\partial\langle v^2\rangle}{\partial t} = -\nu(\underset{\sim}{\nabla} \times \underset{\sim}{v})^2 \quad ((\underset{\sim}{\nabla} \times \underset{\sim}{v})^2 \text{ is by definition } (\underset{\sim}{\nabla} \times \underset{\sim}{v}).(\underset{\sim}{\nabla} \times \underset{\sim}{v})).$$

For "order of magnitude" calculations of the time rate of change of a scalar θ due to diffusion, the equation

$$(2.2.3.\tfrac{3}{4}) \qquad \frac{\partial\langle\theta^2\rangle}{\partial t} = -\nu|\underline{\nabla}\theta|^2$$

can be extremely useful. An equation like this will be used in the next section .

Let us now return to the nett diffusion equations. The nett diffusion of particles is governed by

$$\frac{dn}{dt} = D \frac{\partial^2 n}{\partial z^2} \quad .$$

(If chemical effects are also considered, and n refers to one particular gas species,

$$\frac{dn}{dt} = D \frac{\partial^2 n}{\partial z^2} - kn, \qquad k \text{ being a constant,}$$

eg., Rees et al. (1972); but generally kn can be ignored, especially when n is the total number density.)

Thus for diffusion of temperature, momentum and density, the relevant constants relating the rate of diffusion to the temperature/momentum/density height profile are

$$(2.2.3.\tfrac{7}{8}) \quad \begin{cases} \kappa_{tm} = \frac{1}{3} \lambda \bar{c} & \text{thermal diffusivity,} \\ \nu = \frac{1}{3} \lambda \bar{c} & \text{kinematic viscosity,} \\ \text{and } D = \frac{1}{3} \lambda \bar{c} & \text{self-diffusion coefficient.} \end{cases}$$

λ is the mean free path, and $\bar{c}$ the mean molecular speed.
Thus in principle all these diffusion rates are equivalent. Tabor (1970) has also pointed this out in equation 4.61;

$$(\frac{\kappa_m}{\mu}).C = 1 \qquad (C \text{ here} = \frac{c_v}{M} \text{ in Tabor})$$

$$\text{or} \qquad \frac{\kappa_{tm}}{\nu} = 1 \quad .$$

Notice also that because of these equalities, $(2.2.3.\frac{3}{4})$ is also good for order of magnitude estimates when θ is any of RMS velocity, density, temperature, or momentum. However, in reality, κ_{tm}, ν and D are not exactly equal. κ_{tm} and ν are in a constant ratio for any one gas or

liquid, but the ratio varies between 1.4 and 2.5 (Tabor, 1970, p. 57). The ratio $\frac{\kappa_{tm}}{\nu}$ is 1.73 for air, 2.31 for Helium, and 1.45 for Carbon Dioxide (eg., Starling and Woodall, 1950, p. 216). These actual ratios can be derived theoretically if a more careful treatment than that of Tabor is applied. The constant is not 1.0 because of inter-molecular forces and other secondary effects.

Now consider turbulent transport of these properties. No longer are the properties carried by molecules, but rather by turbulent eddies. Thus in the equations $(2.2.3.\frac{7}{8})$, λ should be replaced by a typical outer scale (or "mixing length") of the turbulence, and $\bar{c}$ by typical eddy velocities.

Equations like $\frac{dT}{dt} = \kappa_{tm} \frac{\partial^2 T}{\partial x^2}$ still apply, but κ_{tm} now becomes an eddy thermal diffusivity.

Thus three new turbulence parameters arise.

(i) K_t = eddy coefficient of heat conduction ~ $\ell_t' v_t'$

(ii) K_m = eddy viscosity coefficient ~ $\ell_m' v_m'$

(iii) K = eddy diffusion coefficient ~ $\ell_\ell' v_\ell'$

K_t replaces κ_{tm}, K_m replaces ν, and K replaces D.

Here, the ℓ_i' are mixing lengths of the order of the eddy outer scales, and v_i' are the turbulent velocities associated with these scales.

Notice also

$$\frac{dT}{dt} = K_t \frac{\partial^2 T}{\partial z^2} \text{ can be crudely approximated by}$$

$$\frac{\Delta T}{\Delta t} = K_t \frac{\Delta T}{(\ell)^2}$$

or $$\Delta t = \ell^2 / K.$$

This is the time for turbulence to transport heat through a distance ℓ. Similar dimensional analyses are possible for density and momentum, and

can be quite useful for gaining a physical feel for any situation.

What should be used for ℓ_t' etc.? Haltiner and Martin (1957), p. 245, say that for a given scalar S, with mean <S> and fluctuating component S', ℓ' should be chosen as the scale over which fluctuations in S are comparable to the change in <S>.

ie. $$S' \sim \ell' \frac{\partial <S>}{\partial z}$$

This type of definition is often used to define outer scales (eg., equation 2.2.3.5a - see shortly). However, often in experimental situations, the largest observable eddy is used for ℓ' (eg., see Section 2.2.4).

The work above has all assumed vertical diffusion. Other components of the various K's can be found, although the coefficients are generally assumed to be isotropic. As in the molecular case, the various K's are not all equal in practice; they are, however, generally of the same order of magnitude. Curnow (1966), has suggested that the constant relating any two lies in the range 0.8 to 1.2.

Notice that if a scalar S is considered, then the vertical diffusion coefficient for S is $K_{VS} = \ell_S' v_\ell'$; and $\ell_S' = S' (\frac{\partial <S>}{\partial z})^{-1}$ (see above)

so $$K_{VS} = S' (\frac{\partial <S>}{\partial z})^{-1} v_\ell'$$

or $$<S' v_\ell'> = -K_{VS} \frac{\partial <S>}{\partial z}$$

This is the same result as that achieved by Haltiner and Martin (1957) in their Chapter 15, and gives an exact formula for the determination of K_{VS}, (the minus sign expresses the fact that if $\frac{\partial <S>}{\partial z}$ is positive, then transport is downward).

Diffusion coefficients can be considered more deeply (eg., Curnow, 1966; Booker and Cohen, 1956), but the above discussion is adequate for most purposes.

Many references refer to just a single K. This usually means the eddy diffusivity, but at times it will be taken to represent all of K_m, K_t and K, since the parameters are fairly similar. At other times, distinctions will be made between the various K's. According to Stewart (1969), thermal and density diffusivities are closely related, and $K \equiv K_t$. Teitelbaum and Blamont (1977) also treat K and K_t as equal.

2.2.3c Equations Involving Important Turbulence Parameters

An introduction to some important equations of turbulence is now necessary. Simple dimensional-type derivations will be discussed first; some insight into a more detailed theory will be given later.

Various references exist for this purpose, but one introductory paper which gives some physical insight into these equations is Villars and Weisskopf (1955), particularly Sections III and IV. The paper derives many of the formulae discussed below in a very simple manner. The discussion below is, however, based on that of Cunnold (1975, section 3), who followed Tatarski (1961).

Some mention has already been made of the possible confusion of scales when dealing with turbulence. Length scales are sometimes taken to have units of length per radian, (eg., metres per radian), $\ell = \frac{1}{k}$; and sometimes taken as length per 2π radians, (simply called length) $\ell = \frac{2\pi}{k}$. Likewise, time scales have an associated ambiguity; sometimes a time scale of time per radian is used, and sometimes time per $2\pi^c$ (simply denoted time). For the present, we will simply regard ℓ as a length scale, and τ as a time scale. The confusion as to the factors of 2π will be discussed as the derivations progress.

Consider a tracer of turbulence, θ. This may be perhaps RMS velocity, or refractive index, or one of many other possible parameters. (Some care is necessary before deciding if a parameter is an effective tracer.

Temperature is not a good tracer, but potential temperature is a good one, for example. Refractive index is not a good tracer. The description of a tracer will be discussed more in the "Radar section" of this chapter (Section 2.4).) Then for all scales ℓ the rate of generation of mean square tracer fluctuations is

$$\frac{\partial <|\theta_\ell|^2>}{\partial t} \sim \frac{<|\theta_\ell|^2>}{\tau_\ell}$$

τ_ℓ being a typical lifetime associated with these scales. In the inertial range of turbulence, the rate of generation of fluctuations is equal to the rate at which the smallest scale foluctuations of size around η (η = Kolmogoroff microscale) are lost due to viscous effects, = ε_θ, say. That is, it is assumed large scale eddies generate smaller ones until those smaller ones are damped out by turbulence - and the rate of generation of all scales is assumed the same. For example, if $\theta_\ell = (v_\ell^2/2)^{\frac{1}{2}}$ (α the RMS velocity), $<|\theta_\ell|^2>/\tau = \frac{1}{2}(v_\ell^2/\tau_\ell)$ is the time rate of generation of kinetic energy per unit mass, and $\varepsilon_0 = \varepsilon_d$ is the energy loss rate. The energy is generated at larger scales and propagates down through the smaller scales until the scales become so small, and associated shears so large, that viscous forces damp out the motions. Thus within the inertial range kinetic energy is not created or destroyed - it simply propagates down the scales.

So, $$<|\theta_\ell|^2>/\tau_\ell = \varepsilon_\theta.$$

But the loss rate at the Kolmogoroff microscale is $\varepsilon_\theta \sim \nu|\nabla\theta_\eta|^2$. (This type of equation was discussed in the previous section, eg., equation (2.2.3.3/4); ν is the kinematic viscosity.) Hence

$$<|\theta_\ell|^2>\ \tau_\ell = \varepsilon_\theta = \nu|\nabla\theta_\eta|^2$$

But at the outer scale of the inertial region, L,

$$\frac{\partial <\theta^2>}{\partial t} \left(\approx \frac{<|\theta_L|^2>}{\tau_L}\right) = -K_\theta|\nabla\bar{\theta}|^2$$

(equation 2.2.3.$\frac{3}{4}$ again, but this time looking at large scales, so ν is replaced by K_θ, K_θ being the turbulent diffusion coefficient appropriate to θ. Henceforth, this will simply be denoted K). $\bar{\theta}$ is the mean (time averaged)

value of θ at height z. But $\frac{<|\theta_\ell|^2>}{\tau_\ell}$ is constant, $= \varepsilon_\theta$, for all ℓ, and therefore this is valid for the outer scales L, so

$$\frac{<|\theta_L|^2>}{\tau_L} \approx \varepsilon_\theta$$

and hence $K_\theta|\nabla\overline{\theta}|^2 \sim \varepsilon_\theta$. Assume only a vertical gradient of $\overline{\theta}$. Thus we have

(2.2.3.1) $$<|\theta_\ell|^2>/\tau \sim \varepsilon_\theta \sim \nu|\nabla\theta_\eta|^2 \sim K(\frac{d\overline{\theta}}{dz}) \cdot$$

A velocity

(2.2.3.2a) $$v_\ell \sim \ell/\tau_\ell$$

can also be associated with scales ℓ, where v_ℓ is the typical velocity associated with these scales. For example, an eddy of dimension ℓ (eg., its half-density width may be ℓ) would have a velocity around v_ℓ, and a lifetime around τ_ℓ. To be correct so far as units are concerned, if ℓ is the "width" of the eddy in metres, and τ the lifetime in seconds, v_ℓ should be in m sec^{-1}. However, often ℓ may be taken to be in m rad^{-1}, τ in seconds, and v_ℓ in ms^{-1}, which is incorrect in so far as units are concerned - v_ℓ should be in $ms^{-1}r^{-1}$. For example, the equation

(2.2.3.0) $$\eta = (\frac{\nu^3}{\varepsilon})^{\frac{1}{4}} \qquad (= \text{Kolmogoroff microscale})$$

is incorrect with regard to units; for ν in m^2s^{-1}, ε in m^2s^{-3}, η should have units of metres. But η, as evaluated by this formula, is always taken to be in metres per radian (Batchelor, 1953; Tatarski, 1961; Rees et al., 1972; for example). It is probably best to bear in mind that most of the equations in here are proportionalities at best. Unfortunately, when they are used in interpreting experiments, they are often taken as equalities.

In the viscous range of turbulence, 2.2.3.2a is not valid; rather,

(2.2.3.2b) $$\tau_\ell \sim (\nu\, \ell^{-2})^{-1} = \nu^{-1}\ell^2 .$$

This result is quoted without proof - eg., see Cunnold (1975, Section 4), or Rastogi and Bowhill (1976b). However, as mentioned by Rastogi and Bowhill, this equation comes from the Heisenberg form of the viscous part of the energy spectrum, and this form has been questioned. (The form of the viscous spectrum in Fig. 2.2 is not the Heisenberg form).

Now consider $\theta_\ell = \sqrt{v_\ell^2/2}$ in 2.2.3.1, and set $\tau = \ell/v_\ell$.

Then

(2.2.3.1') $$\frac{\langle v_\ell^2\rangle}{2}/\tau_\ell = \frac{\langle v_\ell^2\rangle}{2} \cdot \frac{v_\ell}{\ell} \sim \varepsilon_d \sim \nu\left|\nabla\sqrt{v_\eta^2/2}\right|^2$$

ie. Energy generated per unit mass per unit time = Energy loss rate = Energy lost to viscosity .

Since this is a dimensional result, the factors of 2 are dropped.

Thus

(2.2.3.3a) $$\varepsilon_d \sim \frac{v_\ell^3}{\ell} \quad \text{or} \quad v_\ell \sim (\varepsilon_d \ell)^{1/3}.$$

Further, using 2.2.3.2a

(2.2.3.2c) $$\tau \simeq \varepsilon_d^{-1/3}\ell^{2/3} .$$

Notice also if we write

$$\nu\left|\nabla\sqrt{v_\eta^2}\right|^2 \sim \nu\left(\frac{\sqrt{v_\eta^2}}{\eta}\right)^2 \sim \frac{\nu v_\eta^2}{\eta^2}$$

then by (2.2.3.1'),

we have $$\varepsilon_d \sim \frac{\nu v_\eta^2}{\eta^2} .$$

But by 2.2.3.3a, $v_\eta \sim (\varepsilon_d \eta)^{1/3}$, giving

$$\varepsilon_d \sim \frac{\nu(\varepsilon_d \eta)^{2/3}}{\eta^2}$$

or $$\varepsilon_d^{1/3} \sim \nu \eta^{-4/3}$$

or

(2.2.3.0) $$\eta \sim \left(\frac{\nu^3}{\varepsilon_d}\right)^{1/4}$$ - the Kolmogoroff microscale.

This formula is taken as an equality in most discussions of turbulence, (equation 2.2.3.0, section 2.2.3a), so

$\eta = \left(\frac{\nu^3}{\varepsilon_d}\right)^{1/4}$; if ν is in $m^2 s^{-1}$, ε_d in $m^2 s^{-3}$, η is generally taken to be in units of metres per radian. (Crane (1980), however, takes η to be in units of metres, resulting in a factor of 2π difference compared to taking η in m rad^{-1}. This should be borne in mind when comparing Figs. 1.9a and c to Crane's diagrams)

Equation (2.2.3.3a) offers the possibility of estimating eddy dissipation rates from measurements of v_ℓ, and ℓ - or for that matter, to decide just what "~" means in (2.2.3.3a).

Lloyd et al. (1972) have derived a more exact form of 2.2.3.3a - namely

(2.2.3.3b) $$v_\ell = (T\varepsilon_d \ell)^{1/3}$$, (see Lloyd et al., page 780)

where v_ℓ is in m/s, ℓ in metres and $T = (4.8\alpha)^{3/2}$ ($\approx 10.$), α being the same constant as occurs in equation 2.2.1.2. Here ℓ is the size of an eddy, and v_ℓ its velocity. The derivation uses more sophisticated formulae than the simple dimensional analysis above. It does rely on the assumption that

$\langle[\underline{v}(\underline{x}) - \underline{u}(\underline{x} + \underline{\ell})]^2\rangle^{\frac{1}{2}}$ is the velocity v_ℓ associated with scale ℓ,

but this is reasonable. A similar assumption was made by Villars and Weisskopf (1955), equation 14.

Briggs and Vincent (1973) have shown that for radio waves of wavelength λ, scatter at vertical incidence from irregularities with a Gaussian density variation

$$\propto_e -\left(\frac{x^2}{a^2} + \frac{y^2}{a^2} + \frac{z^2}{b^2}\right)$$

is a maximum when $b \approx 0.2\lambda$; or $2b$ (the $\frac{1}{e}$ thickness) $\sim 0.4\lambda$. Thus if the velocities v_ℓ due to turbulence can be measured by Doppler techniques, ε_d can be estimated by equation 2.2.3.3b;

(2.2.3.3b') $$\varepsilon_d = \frac{v_\ell^3}{T(0.4\lambda)} \approx \frac{v_\ell^3}{4\lambda} \quad .$$

There are several weaknesses in this derivation.

Firstly, turbulence may not produce Gaussian density variations. An eddy acting on a background electron density gradient may produce a profile of refractive index as illustrated below (though still with an $\exp\{-(x^2 + y^2)/a^2\}$ variation in the x - y plane).

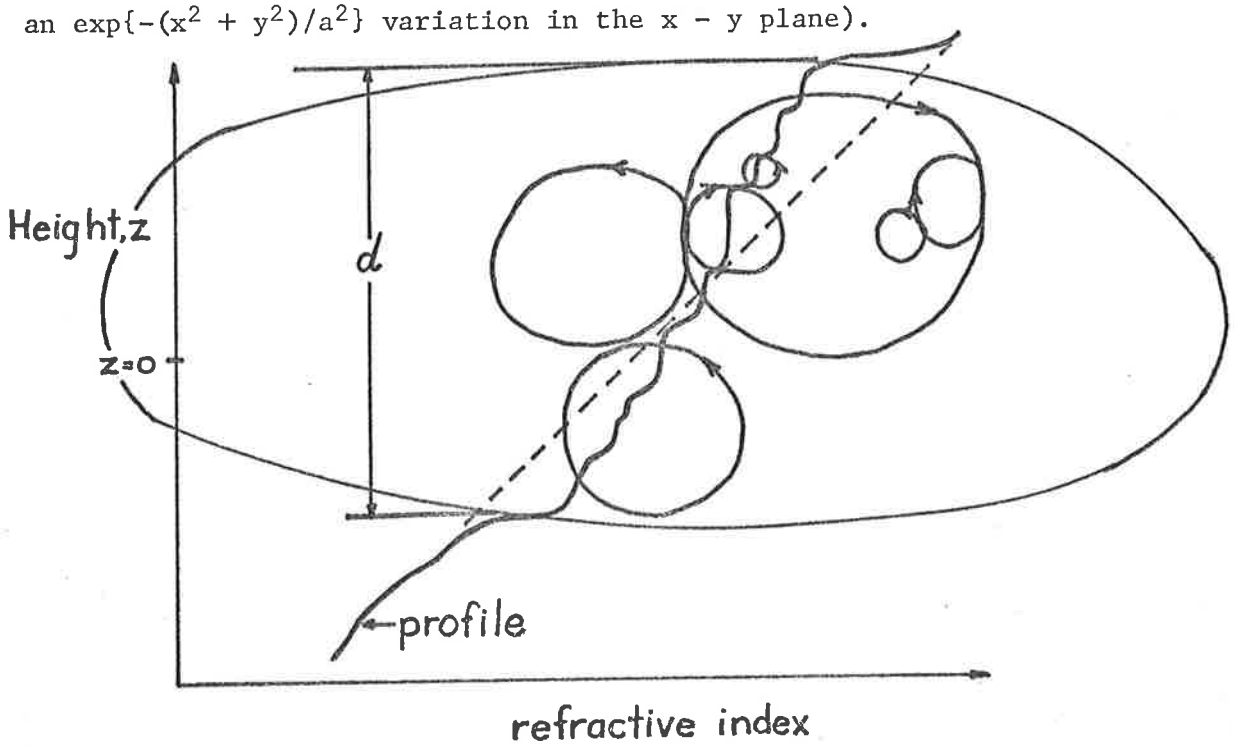

That is, the turbulence due to smaller eddies within the eddy of interest tend to mix up the electrons within the turbulent eddy to produce a more constant electron density. This concept follows a suggestion by Bolgiano (1968) to explain sharp steps in refractive index profiles. In the case discussed here, the same mechanism is assumed operative, but not necessarily to the same degree. The edges do not have to be step functions. The general profile (ignoring small fluctuations can be represented by a function proportional to

$$k_1 z + \exp\{-(x^2 + y^2)/a^2\}.\ z\ \exp\{-z^2/b^2\},$$

or $$k_1 z + \exp\{-(x^2 + y^2)/a^2\}\left(\frac{-b^2}{2}\right)\frac{d}{dz}\left(\exp\{-z^2/b^2\}\right)$$

The $k_1 z$ term produces little significant radio wave scatter, since it extends over a large vertical height range, much greater than one wavelength (eg., see Atlas, 1964). Thus it is only necessary to consider the scatter due to the second part of the function. An approach similar to that of Briggs and Vincent (1973) will be adopted. Then the backscattered amplitude can be found by Fourier transforming the refractive index function, and taking the value at a distance $2(\lambda^{-1})$ from the origin in reciprocal space (ν_1, ν_2, ν_3).

The Fourier transform desired is

$$\pi^{3/2} a^2 b\ \exp\{-4\pi^2\lambda^{-2}(a^2\sin^2\theta)\}.\ (-b^2/2).[2\pi i\nu_3 \exp\{-4\pi^2\lambda^{-2}\nu_3{}^2\}],$$

with $\nu_3 = 2\lambda^{-1}\cos\theta$.

(This uses the fact that if $f(z) \leftrightarrow F(\nu_3)$ where $\leftrightarrow$ means Fourier transform,

then $$\frac{df}{dz} \leftrightarrow 2\pi i\nu_3 F(\nu_3).)$$

For vertical backscatter ($\theta = 0$), the amplitude is

$$\alpha(2.\lambda^{-1})\pi^{5/2}.a^2b^3\exp\{-4\pi^2\lambda^{-2}b^2\}.$$

If a constant value a/b is assumed (= K, say), then the backscattered

amplitude is

$$\alpha\ K^2 b^5 \exp\{-4\pi^2\lambda^{-2}b^2\}.$$

This has a maximum at the point where its derivative with respect to b vanishes; viz.

$$b = \sqrt{5/8}\ .\ \pi^{-1}\lambda$$

or $$b \approx 0.25\lambda.$$

A measure of the eddy thickness is now necessary, and an appropriate one would be d, where d is the distance between the points where the function $z\exp\{-z^2/b^2\}$ is e^{-1} of the maximum value it attains. The function is a maximum at

$$(1 - 2z^2/b^2)\exp\{-z^2/b^2\} = 0, \text{ or } z = b/\sqrt{2}.$$

The value at this point is $(b/\sqrt{2})e^{-\frac{1}{2}}$.

Solving $z_0\exp\{-z^2/b^2\} = ((b/\sqrt{2})e^{-\frac{1}{2}})e^{-1}$

gives $z_0 = 1.500873b,$

or $d = 2z_0 \approx 3b.$

Then $b \approx 0.25\lambda$ means

$$d \approx 0.75\lambda.$$

Thus this profile produces maximum scatter when its width d is about 0.75λ. Then using $\ell \sim .75\lambda$ in 2.2.3.3b gives

(2.2.3.3b") $$\varepsilon_d \approx v_\ell^3/(7.5\lambda).$$

(It is interesting that if the sharp-edged vertical profile illustrated below is assumed (but still with an $\exp\{-(x^2 + y^2)/a^2\}$ variation in x and y) then the back-scattered amplitude at $\theta = 0$ is

$$\alpha\ a^2\sin(2\pi d/\lambda).$$

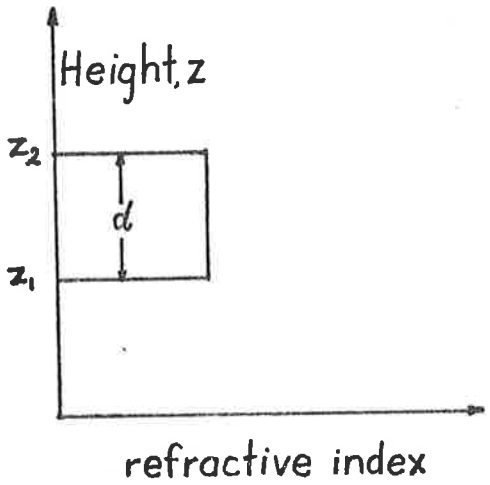

As might be expected, this result can also be obtained by assuming two plane reflectors at z_1 and z_2 and adding the two reflected waves (and assuming the area of scattering is $\propto a^2$)

$$(\text{amplitude} \propto a^2[\{1 + \cos(2d/\lambda.2\pi + \pi)\}^2 + \sin^2(2d/\lambda.2\pi + \pi)]^{\frac{1}{2}}$$

$$\propto a^2(1 - \cos(4\pi d/\lambda))^{\frac{1}{2}}$$

$$\propto a^2\sin(2\pi d/\lambda)).$$

Strongest interference occurs at $d = \lambda/4, 3\lambda/4, 5\lambda/4$ etc.
However, if it is assumed (a/d) is a constant, = K, maximum backscatter occurs at the maxima of

$$K^2d^2\sin(2\pi d/\lambda).$$

The first maximum occurs at $d = .364\lambda$, which is quite close to the result obtained for a Gaussian density variation ($2b = 0.4\lambda$). The maxima are not $\lambda/4$, $3\lambda/4$ etc., because a/d was assumed constant, so by increasing d, the scattering area ($\propto a^2$) is also increased.

Likewise, a double stepped vertical profile, as illustrated below, gives scattered amplitude

$$\propto a^2(1 + \cos(4\pi d/\lambda))^{\frac{1}{2}}$$

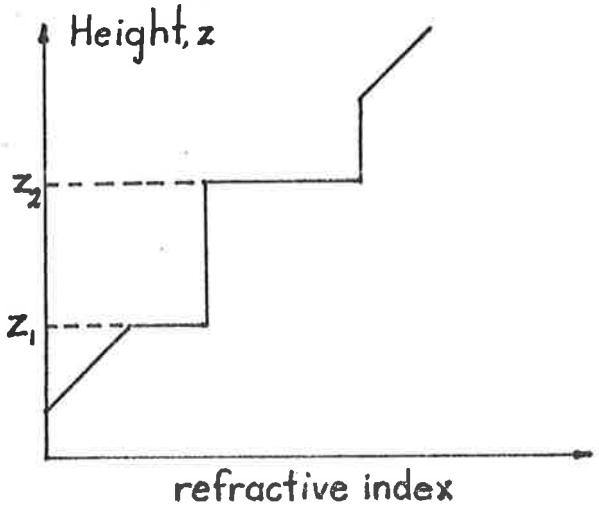

(using the concept of adding reflected rays from z_1 and z_2 in this case), and this has its first important maximum (for (a/d) = K) at d = 0.58λ (there is a small maximum at d = .171λ, but it is not important). This can be compared to d = 0.75λ for the z $\exp\{-z^2/b^2\}$ variation. So Gaussian and stepped variations in z produce similar results - although in the sharp edged cases, there are also other possible d).

A weakness with this whole approach is the concept of considering "eddies" - strictly, one should consider only the power spectrum and look at the power associated with scale ℓ = 1/k m rad^{-1}. The Bragg scale of scatter for an incident wave of wavelength λ metres corresponds to a turbulent scale of λ/2 metres (per $2\pi^c$) or λ/4π metres per radian. Thus the intensity of scatter at radio wavelength λ is proportional to the turbulence spectral density at a scale λ/4π m rad^{-1}. This is all perfectly valid; but many authors extend the concept to equation 2.2.3.3a; they take v_ℓ as the velocity measured (by Doppler techniques) due to the turbulence and then assume 2.2.3.3a is an equality. This is not necessarily valid. Thus they substitute ℓ = λ/4π directly in that equation (or in some cases, ℓ = λ/2 or λ), eg. Rottger et al. (1979) used $\ell = 1/k_{turb} = \lambda/4\pi$, as did Cunnold (1975). Batchelor (1953, equation 6.4.1) also used $\varepsilon = v^3/\ell$, ℓ in m rad^{-1}. Manson and Meek (1980) have considered using ℓ = λ.

The major questions are

(i) Can 2.2.3.3a be assumed to be an equality?

(ii) Or is 2.2.3.3b more appropriate? In this case, ℓ need not be the Bragg backscatter scale.

(iii) In the cases where it is physically possible to observe turbulent eddies, ℓ is taken as either the eddy "size" in metres, or the eddy size divided by 2π. Which is relevant? Is either relevant? Probably 2.2.3.3b is more relevant in this case.

(iv) In cases where v_ℓ is measured by Doppler radar methods, is it appropriate to take $\ell = \lambda/2$ or $\lambda/4\pi$? If 2.2.3.3a <u>is</u> an equality for either $\ell = \lambda/2$ or $\lambda/4\pi$, then it is valid for that choice of ℓ. But if 2.2.3.3a is not an equality, then this is not valid. The constant relating ε and v^3/ℓ is unknown, and in this case, it may be better to believe 2.2.3.3b as a means of deriving this constant and in this case, ℓ represents a typical <u>eddy</u> size. Then the previous discussion showing maximum backscatter for eddy sizes $\sim .4\lambda$ or $\sim .75\lambda$ may be more valid.

Thus two sets of possibilities exist

(2.2.3.3c') (i) $\varepsilon_d = v_\ell^3/\ell, \quad \ell = \lambda/4\pi$, or $\lambda/2$.

This is an unproven equality.

Alternatively,

(2.2.3.3c') (ii) $\varepsilon = v^3/T\ell, \ \ell \approx 0.75\lambda$ (or may be 0.4λ)

or perhaps the half widths of the eddies should be used ($\ell \approx 0.375\lambda$, (or $\sim 0.2\lambda$)).

I shall wirte this as

(2.2.3.3c") $$\varepsilon_d = (T_*)^{-1} v_\ell^3/\ell,$$

where ℓ is either in length units or length rad^{-1} units.

For example, if 2.2.3.3c' (ii) is valid, and T = 10, and the eddy

"half width" is ~ 0.375λ, then

$T_* = (3.75)(4\pi) = 15\pi$ when $\ell = 1/k_{turb} = 4\lambda/4\pi$ is in units of m rad^{-1}, v in m s^{-1}. This would be my personal choice. Alternatively, T_* could be = 1.0.

There are clearly large differences in the estimated magnitudes of ε_d. Suppose λ = 150m, v_ℓ = 5 m s^{-1}.

Then

$\varepsilon_d = v_\ell^3/\ell$, $\ell = \lambda/4\pi$, gives ε_d = 10.5W Kg^{-1} ≈ 905 K day^{-1} at 90km.

$\varepsilon_d = v_\ell^3/\ell$, $\ell = \lambda/2$, gives ε_d = 1.7 W Kg^{-1} ≈ 147 K day^{-1} at 90km.

$\varepsilon_d = v_\ell^3/(10.(0.2\lambda))$ gives ε_d = 0.4 W Kg^{-1} ≈ 35 K day^{-1} at 90km.

$\varepsilon_d = v_\ell^3/(10.(.375\lambda))$ [$= v_\ell^3/(T_*\ell)$, $T_* = 15\pi$] gives ε_d = 0.2 W Kg^{-1} ≈ 17 K day^{-1} at 90km.

$\varepsilon_d = v_\ell^3/(10.(.75\lambda))$ [$= v_\ell^3/(T_*\ell)$, $T_* = 30\pi$] gives ε_d = 0.1 W Kg^{-1} ≈ 8.6 K day^{-1} at 90km.

(The conversion to heating rate per day at 90km is calculated by a relation in Section 1.3.3, Chapter I).

Thus the extreme estimates differ by a factor of 100. A heating rate of 905K/day is far too large, but then perhaps so is v_ℓ ~ 5m s^{-1}.

Because it is not just a dimensional derivation my personal preference is for an equation like (2.2.3.3c") but it may also be that some incorrect assumptions were made in this derivation. But at least this discussion has, I hope, elucidated the fact that 2.2.3.3a <u>is</u> only a dimensionally derived equation, and should not be taken directly as an equality without some more justification. Perhaps that justification exists, but I have not seen it. Authors have even used the ℓ and τ values most likely to give the final results they favour! This was

also pointed out by Hines (1974, page 73) who further illustrated the ambiguities in ℓ and τ.

Unfortunately, similar problems existed in the derivation of ε estimates used in Fig. 1.9a. Rees et al. (1972) used equation (2.2.3.2c) with $\ell = \eta$, so

$$\tau \sim \varepsilon_d^{-1/3}[(\nu^3/\varepsilon_d)^{1/4}]^{2/3}$$

or

$$\varepsilon_d \sim \tau^{-2}\nu \ .$$

τ was taken as the time for turbulence to begin to show in rocket releases of luminescent vapour; which again, was a bit of a guess for τ. However, the resulting ε values corresponded to a heating rate of ~ 8.6 K day^{-1} at 90-100km, which is not unreasonable. If τ had been taken as this time divided by 2π, ε_d would have been ~ 340 K day^{-1}, which is perhaps unrealistically large. Most estimates of ε_d using turbulence parameters strike problems like this. A more sophisticated set of equations is necessary, or at least an evaluation of the constants relating ε and v^3/ℓ. This could perhaps be done experimentally. For example, ε could be estimated from height-rate-of-change of gravity wave amplitudes, and v_ℓ in the region could be measured using a radio wavelength λ. It may then be possible to estimate β, assuming $\varepsilon = \beta\, v^3/\ell$. However, there would be problems. This assumes gravity waves are the only source of the turbulence, and that all the energy lost by these waves goes into turbulence. Measurements of v_ℓ could perhaps be over-estimates, too, if radio scatter came preferentially from regions of intense turbulence.

Thus far, it has been assumed the energy dissipation rate ε_d, which represents the energy loss by viscous heating, is also the rate of transfer of energy between scales. But as seen in previous discussions, some energy can be lost to buoyancy forces, particularly in the buoyancy

range. Thus the rate of supply of energy ε, may be greater than ε_d. Cunnold (1975) quoted a relation

$$(2.2.3.4a) \qquad \varepsilon = 0.75K\left(\frac{\partial \underline{U}}{\partial z}\right)^2 = 0.75\ K\left[\left(\frac{\partial U_x}{\partial z}\right)^2 + \left(\frac{\partial U_y}{\partial z}\right)^2\right],$$

where $\underline{U}$ is the wind vector = $(U_x, U_y, 0)$, and where K represents the diffusion coefficient. However, whether the constant is 0.75, or some other number, depends on whether K represents momentum, heat or density transfer. This will be discussed later (see 2.2.4.9c). But the equation does show that the (mechanical) energy supply is a function of wind shear. It should also be borne in mind that $\varepsilon > \varepsilon_d$, although often in turbulence analyses, it is assumed $\varepsilon \sim \varepsilon_d$.

It is now necessary to look in more detail at the concept of an outer scale. Following the lead of Section 2.2.3b, an appropriate outer scale is the scale at which turbulent fluctuations of the tracer θ become comparable with the ambient changes due to the existence of a vertical gradient of θ, so that the outer scale L is defined by

$$(2.2.3.5a) \qquad L^2\left(\frac{d\bar{\theta}}{dz}\right)^2 = \langle|\theta_2|^2\rangle \ .$$

Again, confusion of scales can arise. Some authors like to regard L as a length unit, and the associated outer scale is then $L/2\pi$ metres per radian. I shall rewrite this equation as

$$(2.2.3.5b) \qquad L^2(m)\left(\frac{d\bar{\theta}}{dz}\right)^2 = \langle|\theta_2|^2\rangle,$$

to distinguish the L(m) defined in this equation from the outer scale L. For example, it may be desirable that all previous ℓ's are expressed in metres radian^{-1}, but L(m) in metres; so the outer scale L m rad^{-1} = L(m)/2π. (L is assumed to have the same units as ℓ in equation (2.2.3.1).) Or it may be both L(m) and ℓ are in m rad^{-1}, so L(m) = L; and so forth.

Tatarski (1961) defined a parameter L_0, which we will see is identical to L(m), and appears to have regarded L_0 as length per radian (see 2.2.3.8a); and he usually regarded scales ℓ to be length per unit radian.

Now by 2.2.3.1, and (2.2.3.2a)

(2.2.3.1") $$<|\theta_L|^2> \sim \varepsilon_\theta \, L(\bar{v}_\ell)^{-1}$$

(2.2.3.1 was valid for all ℓ in the inertial range, and hence is valid for the outer scale L).

Then using 2.2.3.3c", with L used for ℓ, and also using (2.2.3.1') gives

$$<|\theta_L|^2> \sim \varepsilon_\theta L^{2/3} \varepsilon_d^{-1/3} T_*^{-1/3}.$$

However, again this is not an equality, so we may as well drop the T_*.

So

(2.2.3.6a) $$<|\theta_L|^2> \sim \varepsilon_\theta L^{2/3} \varepsilon_d^{-1/3}$$

Combining this with 2.2.3.5b gives

(2.2.3.6b) $$L^2(m) \left(\frac{d\bar{\theta}}{dz}\right)^2 \sim <|\theta_L|^2> \sim \varepsilon_\theta L^{2/3} \varepsilon_d^{-1/3}$$

Notice by comparison with Cunnold's (1975) equation (11), Cunnold uses $L(m) \equiv L$. Yet in equation (18) of that reference, L is taken to be in metres; but Cunnold uses scales ℓ as metres rad^{-1}. There is clearly an inconsistency here - it would again appear to be a case of choosing the dimensions to fit a pre-desired objective. A factor of 2π is quite significant to an experimentalist. Perhaps the crude dimensional analyses used to derive these equations do not warrant an accuracy better than a factor of 2π, but experimentalists have taken the equations more precisely than this; and having done so, they must at least establish a consistent set of formulae to make comparisons of data possible.

More equations may now be derived. By (2.2.3.1) and (2.2.3.3c")

(2.2.3.7a) $$<|\theta_\ell|^2> \sim \varepsilon_\theta \ell^{2/3} \varepsilon_d^{-1/3}$$

(similarly to 2.2.3.6a, and again dropping the T_*).

Then

(2.2.3.7a') $$<|\theta_\ell|^2> \sim L^2(m)/L^{2/3} . \ell^{2/3} (\frac{d\bar{\theta}}{dz})^2$$

since $\varepsilon_\theta \varepsilon_d^{-2/3} \sim L^2(m)/L^{2/3} . (\frac{d\bar{\theta}}{dz})^2$ by (2.2.3.6b).

Notice if L(m) was defined equal to $2\pi L$

(2.2.3.7b) $$<|\theta_\ell|^2> \sim 4\pi^2 L^{4/3} \ell^{2/3} (\frac{d\bar{\theta}}{dz})^2$$

and if L(m) = L,

(2.2.3.7c) $$<|\theta_\ell|^2> \sim L^{4/3} \ell^{2/3} (\frac{d\bar{\theta}}{dz})^2 .$$

Now, some equations relating the diffusion coefficient K to ε_d, ℓ, v_ℓ, and L may be useful.

By (2.2.3.1)

$$<|\theta_L|^2> \sim K(\frac{d\bar{\theta}}{dz})^2 . \frac{\ell}{v_\ell}$$

and by 2.2.3.7a',

$$<|\theta_L|^2> \sim (L^2(m)/L^{2/3}) . \ell^{2/3} (\frac{d\bar{\theta}}{dz})^2 ,$$

so that

$$L^2(m) L^{-2/3} \ell^{2/3} \sim K(\ell/v_\ell) .$$

Substituting for v_ℓ by 2.2.3.3c" gives (again dropping T_*, as these are only dimensional analyses)

(2.2.3.8a) $$K \sim \varepsilon_d^{+1/3} L^2(m) L^{-2/3} .$$

If $L(m) = 2\pi L$,

(2.2.3.8b) $$K \sim \varepsilon_d^{1/3} 4\pi^2 L^{4/3},$$

and if $L(m) = L$ is assumed,

(2.2.3.8c) $$K \sim \varepsilon_d^{1/3} L^{4/3}.$$

(This relation can also be seen in Tatarski (1961) by equations 3.31 and 3.28, where Tatarski's L_0 is $\equiv$ L here. The relation can also be seen in Cunnold (1975), equation 14, except that there are numerous misprints in his equation (eg., small k should be K etc.).)

The equation (2.2.3.8c) also gives

(2.2.3.9) $$L \sim (K^3/\varepsilon_d)^{1/4},$$

and it is interesting to compare this to 2.2.3.0,

$$\eta = (\nu^3/\varepsilon_d)^{1/4}.$$

We thus see that (2.2.3.8c) is not a surprising result; η refers to the largest scales at which viscous processes are important; L refers to the largest scales at which turbulent processes act (inertially). Thus it would seem reasonable that the molecular diffusion coefficient could simply be replaced by the turbulent diffusion coefficient in (2.2.3.0) to get the outer scale of turbulence.

Direct substitution of (2.2.3.2c) into (2.2.3.8a) gives

(2.2.3.10a) $$K \sim L^2(m) L^{-2/3} k^{-2/3} \tau^{-1}.$$

If $L(m) = 2\pi L$,

(2.2.3.10b) $$K \sim 4\pi^2 L^{4/3} k^{-2/3} \tau^{-1},$$

and if $L(m) = L$,

(2.2.3.10c) $\quad K \sim L^{4/3}{}_k{}^{-2/3}{}_\tau{}^{-1}$

where L is the outer scale in length per unit radian units.

If we use $K \sim 10^2 m^2 s^{-1}$, $\varepsilon_d \sim .04$ W Kg^{-1} (typical of about 80-90km), then by (2.2.3.8b), $L \sim 4.5\ mr^{-1}$, or ~ 28 metres. If (2.2.3.8c) is used, $L \sim 70\ mr^{-1}$, or ~ 400m. Eddies as large as ½ a km high have been seen in the mesosphere, so this suggests 2.2.3.8c may be more appropriate (and hence 2.2.3.10c) for experimental work. This still does not mean the equation is exact.

These formulae, then, give relations between ε_d, L, $(\frac{dU}{dz})^2$, K and η. These are perhaps the most important turbulence parameters. ε_d is often found from knowledge of two of the parameters ℓ, v_ℓ and τ_ℓ. However, it is necessary to bear in mind that the statements are only dimensional in some cases. The formulae are summarised in Table 2.1.

Thus a radio experiment working at a wavenumber k_i, which can measure the RMS velocity of the turbulence at this radio wavelength, and the mean wind vectors (by the width and Doppler shift of the power spectrum, say), can be used to estimate all the parameters ε_d, L, $(\frac{dU}{dz})^2$, K, and η (assuming ν is known, ν being the kinematic viscosity). The turbulent scale ℓ corresponds to $(2k_i)^{-1}$ metres per radian; that is, Bragg scatter occurs from scales $\ell = (2k_i)^{-1}$.

How is v_ℓ measured? For a radar with a very narrow beam (narrow enough that Doppler broadening due to the mean wind and the finite beam width (beam broadening) is unimportant relative to turbulence effects), v_ℓ is related to the width of the power spectrum, and thus also to the half-correlation-half-width $\tau_{0.5}$ of the autocorrelation function of the signal (that is, the time lag from zero along the time axis at which

the autocorrelation falls to 0.5).

If amplitude only is recorded (in this case, Doppler information is not available), denote the half width by $\tau_{R0.5}$. Then

(2.2.3.11) $$v_{RMS} = (\tau_{R0.5})^{-1}(\lambda/4\pi)\sqrt{\ln 2}$$ (Briggs, 1980/81).

If, on the other hand, amplitude and phase are recorded, the magnitude of the complex autocorrelation can be found; in this case, denote $\tau_{0.5}$ as $\tau_{c0.5}$.

Then

(2.2.3.12) $$v_{RMS} = (\tau_{c0.5})^{-1}(\lambda/4\pi)\sqrt{2 \ln 2}$$ (Briggs, 1980/81).

If a wide beam is used, then more care is necessary to obtain $\tau_{0.5}$. The effect of beam broadening must be removed; that is, the fading time must be the same as that which would be obtained if the observer was moving with the mean wind (Briggs (1980/81). This parameter can be readily evaluated from full correlation analysis (at least in principle), or by appropriate removal of beam broadening effects. These matters will be discussed more in a later chapter (Chapter VII). It is imperative to see that chapter before using "v_{RMS}" to deduce turbulence data.

2.2.4 More Careful Treatment of ε, K

In the previous sections, a brief mention of the various types of energy dissipation machanisms was made, but only the viscous dissipation rate ε_d was discussed in much detail.

In a more careful discussion at least three energy deposition rates should be considered (Justus, 1967):

(i) ε_d, the rate per unit mass at which energy is dissipated by viscous forces at the Kolmogoroff microscale;

(ii) ε_g, the rate per unit mass at which energy is dissipated by buoyancy forces;

and

(iii) ε, the total rate per unit mass at which energy is deposited into the atmosphere due to the turbulence.

If the temperature gradient is stable, the development of turbulence is restricted, and ε_g is positive - turbulent energy is lost to the background. In such cases, ε, the total energy loss rate, is also equal to the rate of supply of energy by mechanical processes (wind shear).

Recall that energy is lost to buoyancy forces most effectively in the buoyancy range (eg., by the generation of gravity waves). Viscous dissipation is most effective near the Kolmogoroff microscale. A crude illustration of energy deposition is given below.

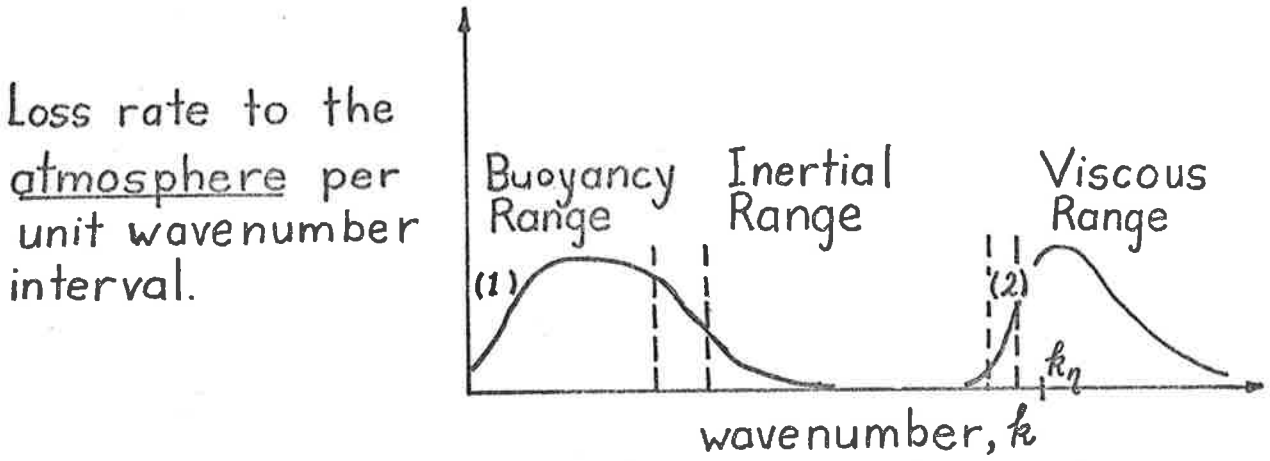

ε_g represents the integrated effect of curve (1), and ε_d the integrated effect of curve (2). Recall, too, that ε_d is the rate of transfer of energy from wavenumbers less than k to wavenumbers greater than k.

If the temperature gradient is unstable, ε_g will be negative, and the temperature gradient will also help to generate turbulence.

According to Justus (1967), the total energy supply (and therefore deposition) rate is

$$(2.2.4.1) \qquad \varepsilon = -\langle v_i v_j \rangle \frac{\partial U_i}{\partial x_j}$$

$$\left(\approx -\langle v_1 v_3 \rangle \frac{\partial U_1}{\partial x_3} - \langle v_2 v_3 \rangle \frac{\partial U_2}{\partial x_3} \quad \text{for } U_3 \text{ small}\right),$$

where $\underline{U} = (U_1, U_2, U_3)$ is the background wind,

$\underline{v} = (v_1, v_2, v_3)$ are the turbulent velocities,

$\langle\ \rangle$ implies average over time (and possibly space),

and $\underline{x} = (x_1, x_2, x_3)$ describes any point in a cartesian co-ordinate system with x_3 vertical. Repeated indices imply summation.

Justus gives the buoyancy dissipation rate to be

$$(2.2.4.2a) \qquad \varepsilon_g = -\omega_B{}^2 \langle \zeta v_3 \rangle,$$

ζ being the vertical displacement of an eddy of scale ~ L, (taken as the inertial range outer scale defined similarly to equation 2.2.3.5b; also see 2.2.4.4 shortly) from its mean during oscillation, and ω_B is the Brunt Vaisala frequency.

It is fruitful to campare this to equation (2.2.3.½); viz

$$L_B \sim v_m/\omega_B, \qquad (\sqrt{0.8} \sim 1.0).$$

L_B being the "inner scale" of the buoyancy range, and v_m the RMS turbulent velocity in the combined buoyancy and inertial ranges. The energy associated with a scale L_B is

$$\varepsilon_B \sim \frac{v_B^3}{L_B} \qquad \text{(equation 2.2.3.3c")}.$$

If we assume $v_B \sim v_m$ (possibly not unreasonable as L_B lies between the inertial and bouyancy ranges), then

$$\varepsilon_B \sim \left(\frac{v_m}{L_B}\right).v_m^2 \sim \left(\frac{v_m}{L_B}\right) L_B^2 \omega_B^2$$

so

$$\varepsilon_B \sim \omega_B^2 L_B v_m,$$

which is rather similar to (2.2.4.2a) (if it is assumed a typical eddy displacement δ is about the eddy size, L). However, L_B is of the order of the outer scale of the inertial range, so

$$\frac{v_B^3}{L_B} \simeq \varepsilon_d. \quad \text{Hence } \varepsilon_B \sim \varepsilon_d .$$

But comparison with (2.2.4.2a) suggests $\varepsilon_B \sim \varepsilon_g$.
Frequently in discussions on turbulence, it is assumed $\varepsilon \sim \varepsilon_g \sim \varepsilon_d$, and the above gives a somewhat crude "justification".

However, closer inspection of Justus's (1967) paper shows this approximation is not exactly valid. Justus's figure 3 shows that the terms differ at most (in that case) by a factor 10 times below 110km, and generally only by 2 to 3 times below 105km. For most order of magnitude calculations, a factor of 2 or 3 is not important.

Then if we take (2.2.4.2a) with $\zeta \to L$, and uses $v \sim \varepsilon^{1/3} L^{1/3}$ (2.2.3.3c"), we obtain

$$(2.2.4.2a') \quad \begin{cases} \varepsilon_d \sim \omega_B^3 L^2 \\ \text{or} \quad L \sim \varepsilon_d^{\frac{1}{2}} \omega_B^{-3/2} \end{cases} .$$

If $\varepsilon_d = \nu^3 \eta^{-4}$ is used, (2.2.3.0),

(2.2.4.2a") $L \sim (\nu^3 \eta^{-4} \omega_B^{-3})^{\frac{1}{2}}$.

Then these equations give a crude estimate of the outer scale of the inertial range of turbulence. They were used to plot L on graph 1.9a. L should be taken to be only a rough estimate from these formulae, but at least these equations illustrate some points regarding L. For example, intense turbulence (large ε_d) has a large L and small η - that is, increased turbulence widens the inertial range of turbulence. It is also worth noting that no inertial range exists when $\eta \sim L$. Thus

$$(\nu^3 \varepsilon_d^{-1})^{\frac{1}{4}} \sim \varepsilon_d^{\frac{1}{2}} \omega_B^{-3/2}$$

or $$\nu^{3/4} \varepsilon_d^{-3/4} \sim \omega_B^{-3/2}$$

or $$(\nu/\varepsilon_d)^{\frac{1}{2}} \sim \omega_B^{-1}$$

or $$\tau_\eta \sim \omega_B^{-1}$$

where τ_η is the timescale associated with the Kolmogoroff microscale (equations 2.2.3.0 and 2.2.3.2c, with $\eta = \ell$, gives $\tau_\eta \sim (\nu/\varepsilon_d)^{\frac{1}{2}}$).

Thus it may be expected that the turbulence is unlikely to develop strongly if $\eta \sim L$, or, equivalently $\tau_\eta \sim \omega_B^{-1}$. (In this case, it might be reasonable for τ_η to be in seconds per radian, since this is the units of ω_B^{-1}.) This point was mentioned briefly in Chapter I in association with Fig. 1.9a, and it was interesting that with model 2, Fig. 1.9a shows L and η roughly intersect around the turbopause. This may give more physical insight into why little turbulence exists above the turbopause - there is no inertial range of turbulence, and viscous

forces act at scales in the buoyancy range. Certainly the fact that $\tau_\eta \sim \omega_B^{-1}$ when this occurs is not inconsistent with the definition of the turbopause adopted by Rees et al. (1972) - namely that it is the level where the time scale associated with the Kolmogoroff microscale becomes large. (It is also worth noting that by 2.2.3.0 and 2.2.3.9, when $\eta = L$, $(\varepsilon_d/\nu^3)^{\frac{1}{4}} = (\varepsilon_d/K^3)^{\frac{1}{4}}$, so $\nu = K$ - ie. molecular diffusion is comparable to eddy diffusion. This is also consistent with the concept of the turbopause. For example Blum and Schurchardt (1978) used such a concept to define the turbopause.) It seems somehow reasonable that turbulence cannot develop when the time scale associated with the Kolmogoroff microscale becomes comparable to the period of oscillation of a parcel of air in the atmosphere ($= 2\pi\omega_B^{-1}$). This is also not inconsistent with Fig. 3 of Justus (1967) where it can be seen that the viscous dissipation rate falls quite markedly above 115km, whilst the buoyancy dissipation rate shows no such fall.

The viscous dissipation rate can be written as

(2.2.4.3a) $$\varepsilon_d = \nu\left\langle \frac{\partial v_i}{\partial x_j} \frac{\partial v_i}{\partial x_j} \right\rangle$$ (compared with 2.2.3.1') .

Then

(2.2.4.3b) $$\varepsilon_d = 15\nu\left\langle \left(\frac{\partial v_1}{\partial x_1}\right)^2 \right\rangle$$ for isotropic turbulence (Rastogi and Bowhill, 1976a)

(2.2.4.3c) or $$\varepsilon_d = (15/2)\nu\left\langle \left(\frac{\partial v_1}{\partial x_2}\right)^2 \right\rangle$$ (Justus, 1967)

ν being the kinematic viscosity.

A characteristic length (outer scale) can be defined for the turbulence by

(2.2.4.4) $$L(m) = v_1\left(\frac{\partial U_1}{\partial x_3}\right)^{-1} = v_2\left(\frac{\partial U_2}{\partial x_3}\right)^{-1}$$

(eg. as seen in equation 2.2.3.5b). Justus (1967) takes L(m) as a length unit.

Then by 2.2.4.1 and 2.2.4.4,

(2.2.4.5) $$\varepsilon = - \langle L_m v_3 \rangle \omega_s^2$$

where $$\omega_s = \left[\left[\left(\frac{\partial U_1}{\partial x_3}\right)^2 + \left(\frac{\partial U_2}{\partial x_3}\right)^2\right]\right]^{\frac{1}{2}}$$

is the vertical wind shear.

Justus (1967) defined the momentum eddy diffusivity as

(2.2.4.6a) $$K_m = - \langle L(m) v_3 \rangle \quad .$$

Thus

(2.2.4.6a') $$\varepsilon = K_m \omega_s^2 \qquad \text{by 2.2.4.5} \quad .$$

This is a reasonable definition, by comparison with section 2.2.3b, where diffusion coefficients were shown to be of the order of the typical outer scale multiplied by the associated velocity. L(m) would seem to be the relevant outer scale since by 2.2.4.4 it is related to the shear in velocity and therefore momentum .

In a similar fashion the thermal eddy diffusivity was defined by Justus as

(2.2.4.7a) $$K_t = - \langle \zeta v_3 \rangle$$

ζ being the eddy displacement associated with scale L.

(The true values of K_t should be defined by the relation

$$\frac{\partial T}{\partial t} = K_t \frac{\partial^2 T}{\partial x^2} \qquad (T = \text{temperature})$$ - see section 2.2.3b.

Likewise K_m really has a more precise definition.)

This also means, by 2.2.4.2a, that

(2.2.4.7a') $\qquad \varepsilon_g = K_t \omega_B^2$.

(Thermal diffusivity is also closely related to density (molecular) diffusivity eg., see Stewart (1969) - viz. $K \approx K_t$, K being the eddy diffusion coefficient. This would seem reasonable in view of 2.2.4.7a. The eddy carries both its particles and heat; and it seems reasonable then that K and K_t are related to the actual eddy displacement.)

It will be recalled that in deriving 2.2.4.2a', we assumed $L(m) \sim \zeta$, so $K_t \sim K_m$ by 2.2.4.6a and 2.2.4.7a. However, Justus (1967) devotes the bulk of his paper to a discussion of this assumption, and claims L(m) and ζ are not exactly equal. This will be discussed more fully below.

Note that both 2.2.4.6a and 2.2.4.7a give the diffusion coefficients $K \sim \langle L(m) v_3 \rangle$, and as seen in 2.2.4.7a, and assuming $\varepsilon_g \sim \varepsilon_d$, all K are roughly given by

(2.2.4.7a'') $\qquad K \sim \dfrac{\varepsilon_d}{\omega_B^2}$.

This relation was used to form Fig. 1.9c. Some doubts as to its validity will be discussed shortly.

(Alternatively $K \sim L(m) v \sim L(m)(L^{1/3} \varepsilon^{1/3})$ (using 2.2.3.3c'')

so $\qquad K \sim L^{4/3} \varepsilon_d^{1/3} \sim (L^4 \nu^3 \eta^{-4})^{1/3})$.

However, let us consider 2.2.4.6a and 2.2.4.7a in more detail. What exactly is the relation between ζ and L?

The Prandtl number is defined as

(2.2.4.8) $\qquad P_r = K_m / K_t$

According to Justus, this is proportional to L/ζ, the ratio of outer

scale eddy size to eddy displacement. Justus found that P_r lies between 2.2 and 5.1. However, Teitelbaum and Blamont (1977) assumed $P_r \sim 0.7$. Thus there appears to be some doubt as to this number, although it appears to be generally assumed to be around 0.7 - 1.2. For order of magnitude estimates, $K_m \approx K_t \approx K$ is roughly valid, but for more exact analysis the K value must be chosen carefully. (It may be reasonable to take the eddy diffusion coefficient K equal to K_t however (eg. see section 2.2.3b; also Stewart, 1969).) For example, (2.2.4.6a) implies

$$\varepsilon = K_m\left(\frac{\partial U}{\partial z}\right)^2 \qquad (z \equiv x_3), \tag{2.2.4.6b}$$

and if $P_r \sim 0.7$, this means

$$\varepsilon = 0.7K_t\left(\frac{\partial U}{\partial z}\right)^2, \tag{2.2.4.9a}$$

which closely agrees with (2.2.3.4a) if $K \equiv K_t$.
But if, as Justus claimed, P_r lies between 2 and 5, then

$$\varepsilon = (2 \rightarrow 5).K_t\left(\frac{\partial U}{\partial z}\right)^2 . \tag{2.2.4.9b}$$

Thus it appears that P_r needs more accurate measurement. It may perhaps even be wrong to assume P_r is a constant - it could, for example depend on the type of turbulence. Recall that for the Richardson gradient and flux numbers (R_i and R_f) to be interchangeable as a criterion for the onset of turbulence required that the heat and momentum transport rates to be proportional (ie. $K_t \propto K_m$). This is generally assumed to be valid, and this amounts to assuming P_r is constant.

Then the real form of equation 2.2.3.4a should be

$$\varepsilon = K_m\left(\frac{\partial U}{\partial z}\right)^2 = P_r K_t\left(\frac{\partial U}{\partial z}\right)^2, \tag{2.2.4.9c}$$

ε being the total energy deposition rate.

It is now instructive to compare these equations to some deduced by Lloyd et al. (1972). In that paper (p. 786) a relation

$$K_e = \frac{T\varepsilon_d}{\omega_B^2} \qquad (2.2.4.9d)$$

is derived, where $T = (4.8\alpha)^{3/2}$ ie., the same T as in (2.2.3.3b). So $T \approx 10$. Lloyd et al. used a slightly different outer scale to that of Justus (1967). (Lloyd et al. used L as the thickness throughout which the given rate of dissipation of turbulent energy would be able to render the temperature profile adiabatic.) So perhaps 2.2.4.9c and 2.2.4.9d are not directly comparable (the different scales used can lead to the "dropping" of different terms in a quasi-dimensional analysis). Certainly the ε in 2.2.4.9d is the viscous dissipation rate ε_d, since the equation comes about through their equation (2), which comes directly from Batchelor (1953); and Batchelor only considered ε_d. It should be pointed out most formulae for K use a form Lv_i; the definition of this outer L must be chosen carefully. Any differences in this choice (eg. Justus compared with Lloyd et al.) will be reflected in the final K estimates. Choices like that of Justus have been used in this chapter and appear to be used more commonly. The equation $K = Lv_i$, which is generally assumed, might also be questioned. Is it fair to assume an equality?

As a further alternative, Gage and Balsley (1978) assumed the relation

$$K_t = \frac{1}{3}\varepsilon_d/\omega_B^2 \quad . \qquad (2.2.4.9e)$$

Crane (1980) also derives a relation similar to this, although his definitions of ε differ marginally from those adopted here.

There appears to be some degree of discrepancy in these formulae (2.2.4.9).

I should like to emphasize again the assumption that many authors make in assuming $\varepsilon \sim \varepsilon_g \sim \varepsilon_d$. The various forms of energy dissipation are freely mixed at times, and this can lead to grave errors. As has also been discussed, it is not infrequent to see a dimensionally derived result taken as an equality. Any worker must be clear on which relations are being used to derive various quantities, and whether the relations are exact, or only dimensional.

Some last points of interest can be seen by comparing equations 2.2.4.9 ($\varepsilon_d \propto K_e \omega_B^2$, or $\varepsilon_d = CK_t\omega_B^2$ say (assuming $K_e = K_t$)), equation 2.2.4.6b ($\varepsilon = P_r K_t (\frac{\partial U}{\partial z})^2$), and equation 2.2.4.7a' ($\varepsilon_g = K_t \omega_B^2$). We have the following interesting results

(2.2.4.10) (a) $\varepsilon_d/\varepsilon_g = C$ (b) $\varepsilon_d/\varepsilon = C/P_r.\omega_B^2/(\frac{\partial U}{\partial z})^2 = C/P_r.R_i$

and (c) $\varepsilon_g/\varepsilon = 1/P_r.R_i$.

Notice also that $\omega_B^2 \propto (\frac{\partial U}{\partial z})^2$ in cases where turbulence acts. This is not surprising - when turbulence acts, R_i is approximately 0.25, and $\omega_B^2 = R_i(\frac{\partial U}{\partial z})^2$. It is also interesting that if we add (b) and (c), and take $\varepsilon_g + \varepsilon_d = \varepsilon$, then

(2.2.4.10d) $R_i = P_r/(1 + C)$.

R_i depends on atmospheric conditions, which suggests either P_r or C does also (although bear in mind that this equation is only applicable when turbulence exists). It would not be surprising if C were dependent on atmospheric conditions. That is, atmospheric conditions might affect the way in which the total energy input was shared between ε_g and ε_d, and thus affect C. But for shear-induced turbulence, it is not un-

reasonable to assume $R_i = 0.25$. Larger values will not produce turbulence; and once turbulence develops ($R_i = 0.25$), it will mix the wind shear to some extent, thus preventing R_i dropping significantly below 0.25. If R_i is assumed equal to 0.25, and P_r taken as about 0.7, then C = 1.8.

However, the possibility also exists that we are assuming too much in assuming all the equations (2.2.4.10a-c) are exact - perhaps we are trying to get more out of these equations than their original crude formulation allows. For example, recall K was calculated from equations of the form <Lv>, and there was some debate as to the exact form of L. In fact, it can even be questioned as to whether K = <Lv> should be an equality. The equation (2.2.4.10d), however, is possibly quite valid - K_t does not enter into it.

If, however, we can assume the equations (2.2.4.10), then determination of ε_d and $(\partial \underline{U}/\partial z)^2$ allows determination of ω_B^2, ε_g and ε (assuming $R_i = 0.25$, $P_r = 0.7$, and hence C = 1.8). K_t may also be calculated by any of the relations $\varepsilon_d = CK_t\omega_B^2$, $\varepsilon = P_r K_t(\partial \underline{U}/\partial z)^2$ or $\varepsilon_g = K_t\omega_B^2$. If ω_B^2 could actually be measured, as well as ε_d and $(\partial \underline{U}/\partial z)^2$, this would allow determination of R_i, and hence C, assuming $P_r = 0.7$. One important point should be mentioned here, however. It may be that $(\partial \underline{U}/\partial z)^2$ is only determined to a poor resolution. In this case, $\omega_B^2 = 0.25(\partial \underline{U}/\partial z)_{expt}^2$ is not a valid assumption - there may be larger fine scale wind shears not observed. This is discussed more in section 2.3.2.

Lloyd *et al.* (1972, equation 6) assumed the eddy diffusion coefficient K_e could be written $K_e = L_0 w_0$, L_0 being an outer scale which they defined (see above) and w_0 the associated vertical velocity. They then derived the relation $K_e = T\varepsilon_d\omega_B^{-2}$, T ≈ 10 (as discussed above). However, if $K = C^{-1}\varepsilon_d\omega_B^{-2}$, C ≈ 2, as derived above, then this suggests that if Lloyd *et al.* had used $K \approx 0.05 L_0 w_0$, they would have arrived at

$K = 0.5\varepsilon_d \omega_B^2$ also. There was no justification for taking $K = L_0 w_0$. After all, K_t is actually defined by the relation

$$\frac{dT}{dt} = K_t \frac{\partial^2 T}{\partial z^2} \qquad \text{(section 2.2.3b).}$$

However, in a similar way, the equation $\varepsilon_g = K_t \omega_B^2$, which was assumed to derive (2.2.4.10d), may not be an equality. This then puts the relation (2.2.4.10d) in doubt.

It would be better to write

(2.2.4.11) $$\varepsilon_d = C_1 K_t \omega_B^2, \quad \varepsilon = C_2 P_r K_t \left(\frac{\partial U}{\partial z}\right)^2, \text{ and } \varepsilon_g = C_3 K_t \omega_B^2 .$$

These would be exact, with C_1, C_2, and C_3 yet to be determined. Then

(2.2.4.12) $$\varepsilon_d/\varepsilon_g = C_1/C_3, \quad \varepsilon_d/\varepsilon = C_1/(C_2 P_r), \quad \varepsilon_g/\varepsilon = (C_3/(C_2 P_r))R_i,$$

and finally

(2.2.4.13) $$R_i = C_2 P_r/(C_1 + C_3) .$$

These would be exact. In the equation (2.2.4.10), we have assumed $C_1 = C$, $C_2 = C_3 = 1.0$. Accurate determination of C_1, C_2 and C_3 would be a great help for better use of turbulence relations. In fact, only two of these need be found - the third could be found by (2.2.4.13), using $R_i = 0.25$, $P_r = 0.7$.

Formulae for K, K_t and K_m can also be derived in other fields. For example Teitelbaum and Blamont (1977) have shown one method by which K_t ($\approx$ K) may be estimated from gravity wave parameters. Vincent and Stubbs (1977) have also estimated K from gravity wave scale heights, as have Manson et al. (1979) (eg. see Fig. 1.9c). These formulae will not be discussed here in detail. However, it is worth commenting that these K values only apply when the atmosphere is turbulent. If there is no

turbulence, molecular transport coefficients must be used. Crane (1980) emphasises this point, and also emphasizes that in cases where turbulence occurs in stratified layers, K estimates may perhaps not be the best estimators of large scale transport rates, since turbulence does not exist between the layers.

Hopefully, however, these last few pages have given some feel for the treatment of turbulence parameters, and the uncertainties involved.

2.3 Correlation Formulae, Structure Functions, and Some More Rigorous Theory

In the preceding sections, the concept of analysing turbulence as a spectrum of scales has been developed. However, many of the formulae have been given without proof, and the specification of an energy spectrum E(k) implicitly assumes a directional independence of $\underline{k}$ - that is, E(k) was assumed a function of magnitude only - or, in other words, the turbulence was assumed isotropic whenever E(k) was applied. Hence no spectrum was given for anisotropic turbulence.

This section (based to some extent on Rastogi and Bowhill, 1976a, Appendix 2) will not prove many of its statements, but will attempt to give a feel for the methods used in a theoretical approach to turbulence, and briefly explain how such concepts as E(k) come about. More thorough approaches can be found in Batchelor (1953) and Tatarski (1961) for example.

It may seem a strange approach to give the theory last, but to an experimentalist a feel for measurable parameters often takes priority over a feel for the theory.

2.3.1 Theory

One of the first functions encountered in turbulent theory is the 2 point velocity correlation function

$$(2.3.1.1) \qquad R_{ij}(\underline{r}) = \langle v_i(\underline{x}) v_j(\underline{x} + \underline{r}) \rangle$$

where $\underline{v}(\underline{x}) = (v_1, v_2, v_3)$ represents the turbulent velocity at $\underline{x} = (x_1, x_2, x_3)$. The vector $\underline{r}$ [$= (r_1, r_2, r_3)$] represents the vector joining the two points $\underline{x}$ and $\underline{x} + \underline{r}$. $\langle\ \rangle$ denotes time and space average. (More general correlation functions can be defined, as in Batchelor (1953) but R_{ij} is perhaps the most common.)

Likewise correlations can be defined for scalars θ like density, temperature and so forth; namely,

$$(2.3.1.2) \qquad R_\theta(\underline{r}) = \langle \theta(\underline{x}) \theta(\underline{x} + \underline{r}) \rangle .$$

(2.3.1.1) and (2.3.1.2) actually are only valid for homogeneous turbulence. In the more general case, R_θ is also a function of position $\underline{x}$. For example, Bolgiano (1968, equation 11) expresses $\langle v_i(\underline{x}) v_j(\underline{x} + \underline{r}) \rangle = R_{ij}(\underline{r}) a(\underline{x})$ where $a(\underline{x})$ expresses positional dependence. However, such complications will be ignored in this simple discussion.

For isotropic, homogeneous turbulence,

$$(2.3.1.3a) \qquad R_{ij}(\underline{r}) = F(\underline{r}) r_i r_j + G(\underline{r}) \delta_{ij} \qquad \text{(Batchelor, 1953, §3.4)}$$

or

alternatively,

$$(2.3.1.3b) \qquad R_{ij}(\underline{r}) = U^2 \left(\frac{f - g}{|\underline{r}|^2} r_i r_j + g \delta_{ij} \right)$$

where $g = f + \frac{1}{2} r \frac{\partial p}{\partial r}$, and $U^2 = \overline{U_p^2} = \overline{U_n^2}$.

Here, $\overline{U_p^2}$ is the mean square turbulent velocity parallel to the fluid velocity and $\overline{U_n^2}$ is the mean square turbulent velocity normal to the

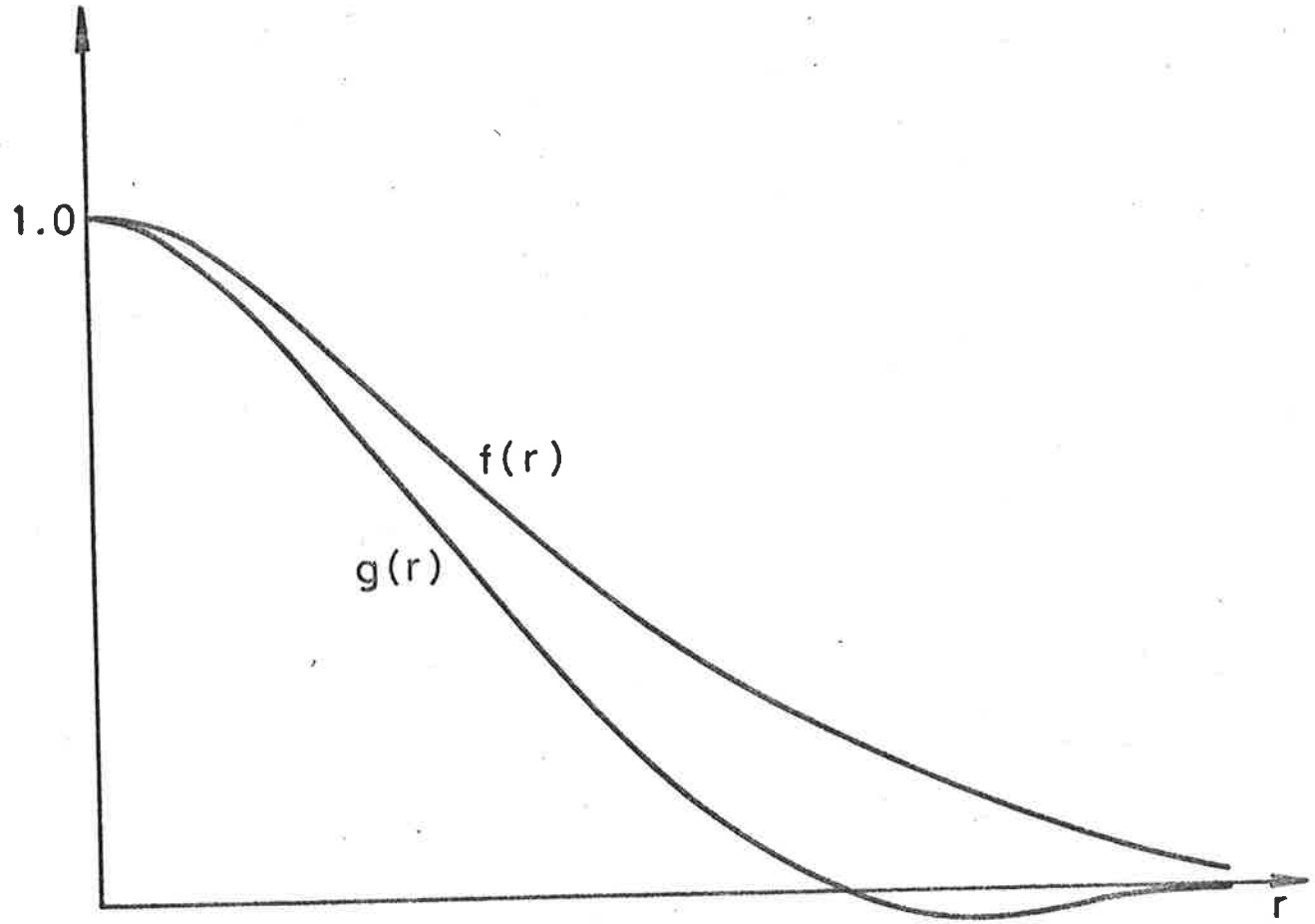

Fig. 2.4 Forms of the functions f(r), g(r) (From Batchelor, 1953, Fig. 3.2)

mean fluid motion. The general form of f(r) and g(r) are illustrated in Fig. 2.4.

Then, having viewed the form of this correlation, let us now Fourier transform back into $\underline{k}$ space. A spectrum tensor $\Phi_{ij}(\underline{k})$ can be defined,

$$(2.3.1.4) \qquad \Phi_{ij}(\underline{k}) = (2\pi)^{-3} \int_{\infty}^{\infty} R_{ij}(\underline{r}) \exp\{-i\underline{k}.\underline{r}\} d^3r$$

For isotropic (and homogeneous) turbulence,

$$(2.3.1.5) \qquad \Phi_{ij}(\underline{k}) = (\delta_{ij} - \frac{k_i k_j}{k^2}) \frac{E(k)}{4\pi k^2}$$

where $\int_{\infty}^{\infty} E(k)dk = \frac{1}{2}\langle u^2 \rangle$,

u being the turbulent velocities.

Hence the relation between the previous E(k) approach, and this correlation approach, can be seen through this formula. E(k) is really only valid for isotropic turbulence - this is why no form was given for it in Fig. 2.2.

Likewise, a 3 dimensional Fourier transform can be formed for $R_\theta(\underline{r})$;

$$(2.3.1.6) \qquad \Phi_\theta(\underline{k}) = (2\pi)^{-3} \int_{\infty}^{\infty} R_\theta(r) \exp\{-i\underline{k}.\underline{r}\} d^3r \quad .$$

A three dimensional spectrum $E_\theta(k)$, depending only on the scalar wave number $k = |\underline{k}|$, is obtained by integrating $\Phi_\theta(\underline{k})$ on a spherical shell of radius k;

$$(2.3.1.7) \qquad E_\theta(k) = \tfrac{1}{2}\oint \Phi_\theta(\underline{k}) k^2 ds,$$

ds being an element of solid angle. $E_\theta(k)$ is then the spectrum of the variance of θ, since

(2.3.1.8) $$\int_{-\infty}^{\infty} E_\theta(k)dk = \tfrac{1}{2}\langle\theta\rangle^2 \ .$$

In the isotropic case, Φ_θ depends on k, and hence

(2.3.1.9) $$E_\theta(k) = 2\pi k^2 \Phi_\theta(k) \ .$$

The "density" of fluctuations in θ at wavenumber k can also be written, for the inertial range, as

(2.3.1.10a) $$\Phi_\theta(k) = 0.033 C_\theta{}^2 k^{-11/3}$$ (Tatarski, equation 3.24)

where $C_\theta{}^2$ is a constant.

(2.3.1.10b)

(i) $C_\theta{}^2 = a^2 L^{4/3} (\frac{d\bar{\theta}}{dz})^2$ (From Tatarski, equation 3.29", after it has been corrected (there is a mistake in 3.29"; it should be $C_\nu{}^2 = a^2 L_0{}^{4/3} (\text{grad } \bar{\nu})^2$, as can be seen by using Tatarski's 3.31 in 3.29'. (The correct form of the equation is used later in the book e.g. 3.51))

Recall also that Tatarski's L_0 is = L in our case - see equation (2.2.3.8c).

Other formulae for $C_\theta{}^2$ can then be derived; eg.

(ii) $C_\theta{}^2 = a^2 \varepsilon_\theta \varepsilon_d{}^{-1/3}$ by 2.2.3.6b, using $L(m) \equiv L$, as decided;

or

(iii) $C_\theta{}^2 = a^2 K (\frac{d\bar{\theta}}{dz})^2 \varepsilon_d{}^{-1/3}$

[$a^2 \sim 2.8$, eg. Van Zandt et al., 1978, equation 4; also see shortly].

It can be seen from 2.3.1.10a and 2.3.1.9 that E(k) is indeed $\propto k^{-5/3}$ in the inertial range, as previously mentioned.

It is also worth pointing out that 2.3.1.10a and b imply that to get significant fluctuations of θ, $\frac{d\bar{\theta}}{dz} \neq 0$. That is to say, the turbulence must have a background gradient of $\bar{\theta}$ to mix. In particular, if θ is taken as the refractive index, this says no significant radio wave scatter will occur from the atmosphere unless there is a background gradient of the potential refractive index. (Note the use of the words "potential refractive index". One must be a little careful in the choice of parameters which can be used as passive tracers of turbulence. This will be discussed again below.)

This last statement is not exactly correct. For example, Villars and Weisskopf (1955) have derived a relation for the turbulent density fluctuations produced in a situation where the potential density is unchanging with height viz. -

$$(\Delta\rho)^2 \approx \rho^2 \left(\frac{S_0}{\rho}\right)^{4/3} . \ell^{4/3} v_M^{-4} \quad \text{(their equation 25).}$$

Here v_M is the RMS velocity of the molecules, ℓ is the scale of fluctuation, S_0 the energy supply, and ρ the "potential density". This can then be related to electron density and hence refractive index fluctuations. However, the radio scatter produced by this effect is considerably less than that produced by the turbulent mixing of a background gradient. For example, in the case discussed by Villars and Weisskopf, a background electron density gradient of less than about $2cm^{-3}$ per km (which is extremely small) would be sufficient to make the backscatter produced by turbulent mixing of the background gradient comparable with the above effect.

With steeper electron density gradients, the scatter due to mixing of the gradient dominates. Thus for most purposes, a background gradient in θ is necessary to achieve significant radio backscatter.

Another common parameter used in turbulence theory is the structure function,

(2.3.1.11) $$D_\theta(r) = \langle\{\theta(\underline{x} + \underline{r}) - \theta(\underline{x})\}^2\rangle,$$

θ being a scalar, and $\langle\ \rangle$ denoting spatial averaging.

In the inertial range D_θ takes the form

(2.3.1.12a) $$D_\theta(r) = C_\theta^2 r^{2/3}$$

where C_θ^2 is the same parameter which appeared in (2.3.1.10a). In fact, equation (2.3.1.12a) is usually used to define C_θ^2, and 2.3.1.10a is derived from this definition. The derivation will not be given here, but can be found in Tatarski, section 3.2. The formula (2.3.1.10b) can then be derived, but this is not done here.

In the viscous range of turbulence, $D_\theta(r)$ takes an r^2 form;

(2.3.1.12b) $$D_\theta(r) = C_\theta^2 \ell_0^{2/3} . (r/\ell_0)^2,$$

where $\ell_0 = (27a^6\nu^3\varepsilon^{-1})^{1/4}$ (a is the same constant which has appeared elsewhere).

ie. $\ell_0 = 3^{3/4}a^{3/2}\eta$, η being the Kolmogoroff microscale.

However, discussion will largely concentrate on the inertial range. Tatarski (1961) gives more on the viscous range.

In some cases, such as θ equivalent to velocity, C_θ^2 can be directly related to the energy dissipation rate, eg., for velocity, (in this case the vector velocity $\underline{v}$ is used, and averaging is over all directions)

$$D_{\underline{v}}(r) = \langle\{\underline{v}(\underline{x} + \underline{r}) - \underline{v}(\underline{x})\}^2\rangle = C_v^2 r^{2/3} = 4.8\alpha\varepsilon^{2/3}v^{2/3} \quad ;$$

$\alpha \sim 1$ to 1.5, as seen in equation 2.2.1.2.

Thus

$$C_v^2 = 4.8\alpha\varepsilon^{2/3}$$ (eg. see Elford and Roper, 1967; Batchelor, 1953, equations 6.5.5 and 6.5.7).

Caughey et al. (1978) looked at only one component parallel to the mean flow (longitudinal) and derived the formula

$$C_{v_1}^2 = 2\varepsilon^{2/3}$$

$$(\langle\{v_1(\underline{x}) - v_1(\underline{x} + \underline{r})\}^2\rangle = C_{v_1}^2 r^{2/3}).$$

Gage and Balsley (1978) gave a component form

$$(C_v^2)_i = (a_v^2)_i \varepsilon^{2/3}, \text{ where}$$

$(a_v^2)_i \approx 1.75$ for the longitudinal component (ie. parallel to the mean flow), and

$(a_v^2)_i \approx 2.35$ for the transverse components.

(The appropriate structure functions are of course $\langle\{v_i(\underline{x}) - v_i(\underline{x} + \underline{r})\}^2\rangle$.) Formulae like these can be used to obtain ε estimates from a single observing station, provided it can be assumed that $\underline{v}(\underline{x} + \underline{r})$ is equal to $\underline{v}(x)$ at a time $t = (r/\bar{u})$, $\bar{u}$ being the mean wind velocity (Taylor's hypothesis eg. see Caughey et al., 1978; Gage, 1979). This is not, however, always valid; it assumes the turbulence is "frozen" in the background wind, and does not change in form greatly as it moves.

Thus the above statements all say

$$C_v^2 = \gamma\varepsilon^{2/3}, \quad \gamma \text{ being a constant.}$$

Notice also that by 2.3.1.10b, (iii)

$$a^2 K (\frac{dv_i}{dz}) \varepsilon_d^{-1/3} = \gamma \varepsilon_d^{2/3},$$

so

$$a^2 K_t (\frac{dv_i}{dz})^2 = \gamma\varepsilon_d: \text{ but this} \approx \gamma P_r K_t (\frac{\partial U}{\partial z})^2 \text{ by (2.2.4.9c),}$$

so $a^2 (\frac{dv_i}{dz})^2 = \gamma P_r (\frac{\partial U}{\partial z})^2$ - or, in other words, the shear in turbulent velocities is proportional to the shear in the mean velocities.

2.3.2 Estimation of C_n^2

In this section we will obtain some estimates of C_n^2. But the problem of what serves as a passive tracer must firstly be discussed. Such a quantity should be one for which positional variations have no effect on the tracer. For example, if density is used, an eddy would change density as it moved vertically and the density would not be independent of height. Similarly, temperature is not a good tracer. However, potential temperature makes a good passive tracer. (Potential quantities are values an air parcel at some position $\underline{x}$ would have if moved adiabatically to a standard pressure p_0; p_0 is usually 1000 millibars.)

One important quantity for the work reported in this thesis is the refractive index, since the strength of radio wave scattering depends on this parameter. As it stands, refractive index is not a good passive tracer. For example, Tatarski discusses the refractive index of air, and finds

$$n = n(z, p, \theta, q)$$

where z = height, p = pressure, θ = potential temperature, and q = specific humidity(q is also a potential quantity).

Suppose an eddy moves from height z_1 at pressure p_1, and has $\theta = \theta_1$, $q = q_1$, to a height z_2. At z_2, the pressure is p_2, and the environmental θ and q are θ_2 and q_2. However, the parcel itself has $\theta = \theta_1$, and $q = q_1$, still, as it moved adiabatically. Hence the difference in refractive index between the parcel and its environment at z_2 is

$$\underbrace{n(z_2, p_2, \theta_1, q_1)}_{\text{parcel}} - \underbrace{n(z_2, p_2, \theta_2, q_2)}_{\text{environment}}$$

$$\Rightarrow \quad \Delta n = \left(\frac{\partial n}{\partial \theta}\frac{\partial \theta}{\partial z} + \frac{\partial n}{\partial q}\frac{\partial q}{\partial z}\right)\Delta z \quad .$$

Thus the effective refractive index gradient to be used in equations like (2.3.1.10b) for $\frac{d\bar{\theta}}{dz}$ is

$$(2.3.2.1) \qquad M = \left(\frac{\partial n}{\partial \theta} \cdot \frac{\partial \theta}{\partial z} + \frac{\partial n}{\partial q} \cdot \frac{\partial q}{\partial z}\right)$$

ie. $C_n^2 = a^2 L^{4/3} M^2$. Van Zandt et al (1978) write this as $C_n^2 = a^2 \alpha' L^{4/3} M^2$, $\alpha' \sim 1$, and $a^2 \sim 2.8$.

Notice this is not the full refractive index gradient, which would be

$$\frac{dn}{dz} = \frac{\partial n}{\partial z} + \frac{\partial n}{\partial p}\frac{\partial p}{\partial z} + \left(\frac{\partial n}{\partial \theta}\frac{\partial \theta}{\partial z} + \frac{\partial n}{\partial q}\frac{\partial q}{\partial z}\right)$$

($\frac{\partial n}{\partial z} = 0$; n has no explicit height dependence except through p, q.)
The quantity M can also be regarded as the gradient of a "generalized potential refractive index", provided care is taken (Ottersten, 1969a) - namely, that the reference pressure p_0 for this generalized potential refractive index is the mean pressure at the level of turbulence, rather than 1000mb.

What, then, of the problem of ionospheric radio wave scatter? (It should be noted that the following work up to equation 2.3.2.11, is largely original, so may be in error.)

In this case, the refractive index is given by

$$(2.3.2.2a) \qquad n = n(N, \nu_m, \underline{B})$$

where N is the electron density, ν_m the electron collision frequency, $\underline{B}$ the magnitude and direction of the magnetic field, and z the height. (There is actually not an explicit dependence on z; that comes through N, ν_m and $\underline{B}$ variations with height; hence $\frac{\partial n}{\partial z} = 0$.)

However, N is not a passive tracer - the electron density changes as the eddy oscillates in height. $\underline{B}$ can be regarded as constant over the

vertical scale of turbulence, so we may regard n as

(2.3.2.2b) $\quad n = n(N, \nu_m) \qquad (\frac{\partial B}{\partial z} \approx 0).$

The desired passive parameter for electron density is,rather, the difference between the parcel density and that of its environment. To discuss this, a clearer understanding of potential temperature is necessary.

So let us consider the concept of potential temperature in more detail. This is defined, at height z, with a temperature T,

as $\quad \Theta = T(p_0/p)^{\frac{\gamma-1}{\gamma}} \qquad$ (eg. Houghton, 1977)

where p is the pressure at height z, $\gamma = C_p/C_v$ is the ratio of specific heats, and p_0 is the pressure at a reference height z = 0. (Θ is in fact the temperature a parcel of air at z would have if moved adiabatically to z = 0.) Consider firstly an isothermal atmosphere. The pressure $p = p_0\exp(-z/H)$, H = scale height $= RT/M_r g = (C_p - C_v)T/g$ (Houghton, 1977, equations 1.4 and 1.6) $= (1 - \frac{1}{\gamma})(C_p/g)T$.

Thus

$$\Theta = (\gamma - 1)/\gamma . \Gamma_a^{-1} T \qquad (\Gamma_a = g/C_p = (9.8 ms^{-2})/(1005 m^2 s^{-2}) = .98°C\ km^{-1})$$

Then

$$\Theta = T(p_0/p)^{\frac{\gamma-1}{\gamma}}, \text{ and } p = p_0\exp\{-z.(\tfrac{\gamma}{\gamma-1}).\Gamma_a T^{-1}\}$$

means $\quad \Theta = T\exp\{z.\Gamma_a/T\}$ (if T is a constant).

For small Θ ($z \lesssim 5km$), this gives

$\Theta \approx T + \Gamma_a z$. But it must be emphasized that the reference level z = 0 must be chosen close to the region of interest. A similar situation occurs for the concept of potential density (Ottersten, 1969a).

The usual definition of potential temperature is to take p_0 = 1000mb, so z = 0 roughly corresponds to ground level. It is important to note

in all these formulae that we are using a generalized potential temperature; p_0 must be chosen close to the level of interest; and it is implicitly assumed that all displacements associated with turbulence are less than about 5km, so $\Theta = T + \Gamma_a z$ is valid. It is worth commenting here that Tatarski (1961) "derived" a relation which implied $\Theta = T + \Gamma_a z$ exactly. This is not so. It was assumed that for the parcel, moving adiabatically,

$$\frac{dT}{T} = \left(\frac{\gamma - 1}{\gamma}\right)\frac{dp}{p}$$, and this is of course correct.

Then the hydrostatic equation,

$dp = -gpdz$ was used, and this is also valid.

Finally, $p = \rho RT$ (R = gas constant per unit mass in this case)

$= \rho(C_p - C_v)T$ was used.

But it is important that the pressure p is that of the background atmosphere, (which is also that of the parcel), and so

$$p = \rho(C_p - C_v)T_{atmos.}$$

Then the relation

$$\frac{dT}{T} = \left(\frac{\gamma - 1}{\gamma}\right)\frac{dp}{p} = -\left(\frac{\gamma - 1}{\gamma}\right).\frac{\rho dz}{\rho(C_p - C_v)T_{atmos.}}$$

was used. If the parcel has moved over a large distance, T and $T_{atmos.}$ cannot be assumed equal. (In the troposphere, the atmosphere is often nearly adiabatic, so $T \approx T_{atmos.}$ is nearly valid.) Tatarski assumed they were equal and cancelled them, resulting in the relation

$\left(\frac{dT}{dz}\right)_{parcel} = \Gamma_a$, so $T = \Gamma_a z - H$; H is a constant, which Tatarski took to be the potential temperature.

But it must be pointed out this is not general; nor, for that matter, is the relation $\Theta = T\exp\{z\Gamma_a/T\}$ - that is only valid for an isothermal atmosphere. The only true definition of Θ is $T(p_0/p)^{\frac{1-\gamma}{\gamma}}$. However, the approximation $\Theta = T + \Gamma_a z$ will be used in the following discussion - provided it is borne in mind that $z = 0$ must be taken at a level close to region of interest. If this is done, the relation is sufficiently accurate for the analysis of problems in which it is used.

The desired parameter for electron density fluctuations is, then, the difference between the parcel and its environment.

Consider an air parcel at height z_1, temperature T_1 (potential temperature Θ_1) and suppose it moves to height z_2, where the background temperature is T_2 and pressure p_2.

Then the parcel density is (using $p = \rho R_* T$)

$$\rho_{parcel} = \frac{p_2}{R_*} \cdot \frac{1}{\Theta_1 - \Gamma_a z_2} \qquad (T \text{ of parcel at } z_2 = \Theta_1 - \Gamma_a z_2).$$

But $\Theta_1 = T_1 + \Gamma_a z_1$,

(2.3.2.3)

so $$\rho_{parcel} = \frac{p_2}{R_*} \cdot \frac{1}{T_1 - \Gamma_a dz} \qquad dz = z_2 - z_1.$$

(2.3.2.4) The environment density at z is $\rho_{environ} = \frac{p_2}{R_*} \cdot \frac{1}{T_1}$.

Then the difference in (ρ_{parcel}) and $(\rho_{environ})$

(2.3.2.5) $$= \frac{p_2}{R_*}\left(\frac{1}{T_1 - \Gamma_a dz} - \frac{1}{T_2}\right).$$

However, it is the electron density difference we desire.

If $\chi(z)$ is the ratio of electron density to total density of the parcel, then by (2.3.2.3)

(2.3.2.6) $$N_{parcel} = \chi(z_1)\frac{p_2}{R_*} \cdot \frac{1}{T_1 - \Gamma_a dz} \qquad \text{at } z_2.$$

An important assumption has been made here - it has been assumed that the electron density to total density ratio $\chi(z)$ is unchanged as the parcel moves. If this is not valid, the derivation here fails. This assumption means, for example, that the electron partial pressure of the parcel differs from that of the environment at z_2. (If it were felt that the electron pressure should equal that of the environment at z_2, the analysis would be done by saying

$$N_{environ} = \frac{p_{2e}}{R_*} \cdot \frac{1}{T_2}, \quad N_{parcel} = \frac{p_{2e}}{R_*} \cdot \frac{1}{T_1 - \Gamma_a dz}, \quad p_{2e} = \text{electron partial pressure.}$$

However, the assumption seems reasonable. Equilibrium of total pressure at all heights is a reasonable concept (ie. p_2 is used in 2.3.2.3 and 2.3.2.4, but surely if the parcel can be regarded as a unit, then it can be regarded as maintaining all its particles, including its electrons?). Equilibrium of partial pressures is not such a valid concept. Gallet (1955), in dealing with a similar problem, assumed $(d\rho/\rho) = (dN/N)$ for the parcel, which is similar to the assumption made here ($\rho \propto N$). Villars and Weisskopf (1955) made a similar assumption. The problem will be discussed again later.

The electron density of the background is

$$N_{environ} = \chi(z_2) \frac{p_2}{R_* T_2} \quad \text{by (2.3.2.4).}$$

Then $d\hat{N} = N_{parcel} - N_{environ}$

$$= \frac{p_2}{R_*} \left(\frac{1}{\frac{T_1}{\chi(z_1)} - \frac{\Gamma_a dz}{\chi(z_1)}} - \frac{1}{\frac{T_2}{\chi(z_2)}} \right)$$

$$= \frac{p_2}{R_*} \frac{\frac{T}{\chi}(z_2) - \frac{T}{\chi}(z_1) + \frac{\Gamma_a dz}{\chi(z_1)}}{\left(\left[\frac{T}{\chi}(z_1) - \frac{\Gamma_a dz}{\chi(z_1)}\right] \cdot \frac{T}{\chi}(z_2)\right)}$$

$$= \frac{p_2}{R_*} \frac{d(\frac{T}{\chi}) + \frac{\Gamma_a}{\chi(z_1)} dz}{\left(\frac{T}{\chi}(z_1) \frac{T}{\chi}(z_2) - \frac{T}{\chi}(z_2) \cdot \frac{\Gamma_a dz}{\chi(z_1)}\right)} .$$

Using the expansion $\frac{1}{1+x} = 1 - x$ for small x, and dropping second order terms like $d(\frac{T}{\chi})dz$,

$$\Rightarrow \quad d\hat{N} = \frac{\chi^2 p_2}{R_* T^2} \left(d(\frac{T}{\chi}) + \frac{\Gamma_a dz}{\chi(z)}\right) .$$

Then $\frac{\chi p_2}{R_* T} = N(z_2)$

so

$$(2.3.2.8) \qquad d\hat{N} = \frac{\chi N}{T}\left(d(\frac{T}{\chi}) + \frac{\Gamma_a dz}{\chi}\right)$$

Expanding further gives

$$d\hat{N} = \frac{\chi N}{T}\left(\frac{1}{\chi} dT - \frac{T}{\chi^2} d\chi + \frac{\Gamma_a}{\chi} dz\right)$$

$$= \frac{\chi N}{T}\left(\frac{1}{\chi} d\theta - \frac{T}{\chi^2} d\chi\right)$$

$$= \frac{N}{T}\left(d\theta - \frac{T}{\chi} d\chi\right) .$$

Thus

$$(2.3.2.9) \qquad \frac{d\hat{N}}{dz} = \frac{N}{T}\frac{d\theta}{dz} - \frac{N}{\chi}\frac{d\chi}{dz} \qquad \left(= \frac{N}{T}\frac{d\theta}{dz} - \frac{dN}{dz} + \frac{N}{\rho}\frac{d\rho}{dz}\right), \quad \rho = \text{air density}$$

expresses the rate of change of density difference between the parcel and background with height. The result seems reasonable, as

(i) in an adiabatic atmosphere, Θ = const, so the only change in $\hat{N}$ occurs due to the gradient of the mixing ratio, χ.

(ii) If the mixing ratio $\chi = \frac{N}{\rho}$ is independent of height, the only fluctuations which occur are due to the adiabatic expansion of the parcel.

Notice also the $-\frac{dN}{dz}$ in the second form of 2.3.2.9. This arrives purely by definition of $d\hat{N} = N_{parcel} - N(z_1)$, where as

$$dN = N(z_2) - N(z_1).$$

Now by 2.3.2.2b,

$$n = n(N, \nu_m), \text{ so } \frac{dn}{dz} = \frac{\partial n}{\partial N}\frac{\partial N}{\partial z} + \frac{\partial n}{\partial \nu_m}\frac{\partial \nu_m}{\partial z}$$

(Recall n has no explicit dependence on z).

But the more useful parameter is

$$\hat{n} = \hat{n}(\hat{N}, \nu_m)$$

where the relation between $\hat{n}$ and $\hat{N}$ is the same as that between n and N. That is to say

$$\frac{d\hat{n}}{dz} = \frac{\partial \hat{n}}{\partial \hat{N}}\frac{\partial \hat{N}}{\partial z} + \frac{\partial n}{\partial \nu_m}\frac{\partial \nu_m}{\partial z}$$

(the change in refractive index of the parcel due to collision frequency changes is assumed to be the same as the change in background value in going from z_1 to z_2),

and $\frac{\partial \hat{n}}{\partial \hat{N}}$ simply expresses the change in refractive index for a given change in electron density, so

$$\frac{\partial \hat{n}}{\partial \hat{N}} = \frac{\partial n}{\partial N} \quad .$$

$\frac{\partial \hat{N}}{\partial z}$ expresses the variation in $\hat{N}$ due to a given change in z, but no change in ν_m, and this is given by 2.3.2.9 ($\hat{N}$ is independent of ν_m).

Thus

(2.3.2.10a) $\frac{\partial \hat{n}}{\partial z} = \frac{\partial n}{\partial N}(\frac{N}{T}\frac{d\theta}{dz} - \frac{N}{\chi}\frac{d\chi}{dz}) + \frac{\partial n}{\partial \nu_m}\frac{\partial \nu_m}{\partial z} = M_e$, say, is the parameter which should be used for $(\frac{d\bar{\theta}}{dz})$ in equations like 2.3.1.10b. (Here $\theta = T + \Gamma_a z$, z being the displacement from a reference height close to the region of interest (as discussed), $\chi = N/\rho$, N is the electron number density, and ρ is the neutral air density.)

Can (2.3.2.10a) be simplified? Consider the region 85 - 95km - in particular, two heights; 85 and 90km. Firstly, rewrite (2.3.2.10a) as

(2.3.2.10a') $M_e = \frac{\partial n}{\partial N}(\frac{N}{T}\frac{d\theta}{dz} - \frac{dN}{dz} + \frac{N}{\rho}\frac{d\rho}{dz}) + \frac{\partial n}{\partial \nu_m}\frac{\partial \nu_m}{\partial z}$.

Firstly, consider $\frac{N}{\rho}\frac{d\rho}{dz} = N\frac{d\ln\rho}{dz}$.

By Fig. I.2.11, US Standard Atmosphere (1962),

$$\frac{d\ln\rho}{dz}(\approx \ln 10.\frac{d}{dz}\log_{10}\rho) = -1.4 \times 10^{-4}m^{-1}.$$

This is true over the entire region 0 to 120km, so

(2.3.2.10a'') $M_e = \frac{\partial n}{\partial N}(\frac{N}{T}\frac{d\theta}{dz} - \frac{dN}{dz} - (1.4 \times 10^{-4}m^{-1})N) + \frac{\partial n}{\partial \nu_m}\frac{\partial \nu_m}{\partial z}$.

From Mechtley et al. (1972) Table 5, $\frac{dN}{dz} \sim 2 \times 10^{6}m^{-4}$ at 85km (where a strong ledge of increasing electron density existed for this data), and $\sim 3 \times 10^{6}m^{-4}$ at 90km. $N \sim 2.5 \times 10^{9}m^{-3}$ at 85km, and $\sim 10^{10}m^{-3}$ at 90km. Thus $(1.4 \times 10^{-4}N)m^{-4}$ is comparable with $\frac{dN}{dz}$ at 85 - 90km (eg. at 90km, $1.4 \times 10^{-4}N = 1.4 \times 10^{6}$, which is $\sim \frac{1}{2}\frac{dN}{dz}$). Thus neither of these two terms should be dropped.

What about $\frac{N}{T}\frac{\partial\Theta}{\partial z}$? This = $\frac{dT}{dz} + \Gamma_a$. Examination of Fig. 5-1 of Gossard and Hooke (1975) shows $\frac{dT}{dz}$ ~ 3K/km at 90km, and ~ 0 at 85km. Thus $\frac{\partial\Theta}{\partial z}$ ~ $.013 Km^{-1}$ at 90km, and ~ $.01 Km^{-1}$ at 85km. T is ~ 200K at these heights. Thus at 90km, $\frac{N}{T}\frac{d\Theta}{dz} \approx 6.5 \times 10^5 m^{-4}$ (which is about ¼ of $\frac{dN}{dz}$). At 85km, $\frac{N}{T}\frac{d\Theta}{dz} \approx 1.25 \times 10^5$ ($\frac{1}{16}$th of $\frac{dN}{dz}$).

Thus neither can this temperature term be ignored. So (2.3.2.10a") should be the appropriate form of M_e - or, alternatively,

(2.3.2.10a")
$$M_e = \frac{\partial n}{\partial N}\left\{\frac{N}{T}\left(\frac{dT}{dz} + \Gamma_a\right) - \frac{dN}{dz} - (1.4 \times 10^{-4} m^{-1})N\right\} + \frac{\partial n}{\partial \nu_m}\frac{\partial \nu_m}{\partial z} .$$

Notice M_e is a complex number, since $\frac{\partial n}{\partial N}$ may be complex. However, the important term is $|M_e|^2$, as we will see shortly.

In the HF limit, $\frac{\partial n}{\partial N} \approx -(2\pi)^{-1} r_e \lambda^2$ (r_e being the classical electron radius (= $2.8 \times 10^{-15} m$) and λ the wavelength of the probing radiation) but this is not true at 2MHz (eg. Vincent, 1973), and the more accurate Sen-Wyller formulae must be used to estimate $\frac{\partial n}{\partial N}$.

If $\frac{N}{T}\frac{d\Theta}{dz}$ and $\frac{N}{\rho}\frac{d\rho}{dz}$ were both negligible, then (2.3.2.10a) gives

(2.3.2.10b) $$M_e = \frac{\partial n}{\partial N}\frac{dN}{dz} + \frac{\partial n}{\partial \nu_m}\frac{\partial \nu_m}{\partial z} = \frac{\partial n}{\partial z} .$$

We have see, however, that this approximation is not often valid. However, it is often (erroneously?) assumed.

So (2.3.1.10b) implies

(2.3.2.11)
$$\begin{cases} \text{(i)} & C_n^2 = a^2 L^{4/3} |M_e|^2 \\ \text{or (ii)} & C_n^2 = a^2 K |M_e|^2 \varepsilon_d^{-1/3} \\ \text{or (iii)} & C_n^2 = a^2/P_r \cdot \varepsilon\varepsilon_d^{-1/3} |M_e|^2 \left(\frac{\partial U}{\partial z}\right)^{-2} \text{ (by 2.2.4.9c,} \\ & K = (\varepsilon/P_r)\left(\frac{\partial U}{\partial z}\right)^{-2}), \end{cases}$$

where M_e is given by the equations (2.3.2.10).

(I have denoted these as C_n^2 - they should perhaps be written $C_{\hat{n}}^2$. In future, C_n^2 and $C_{\hat{n}}^2$ will mean the same thing.)

The third version of 2.3.2.11 can, by assuming $\varepsilon \sim \varepsilon_d$, be written as

2.3.2.11 (iv) $C_n^2 = a^2 P_r^{-1} R_i \omega_B^{-2} \varepsilon_d^{2/3} |M_e|^2$

where $\omega_B = (g \frac{\partial \ln\theta}{\partial z})^{\frac{1}{2}}$ is the Brunt Vaisala frequency (θ = potential temperature) and R_i is as defined by (2.2.2.3). For wind shear induced turbulence, R_i is unlikely to get below R_i(critical) $\simeq$ 0.25; since as soon as R_i reaches 0.25, turbulence develops, and this smooths out the wind shear, increasing R_i (similar to Fig. 2.1b). Gage et al. (1980) have used this final form for C_n^2, with R_i replaced by R_i(critical) (= 0.25).

Thus these equations provide another useful set for the interpretation of radio wave scattering experiments. For example, (2.3.2.10a) and (2.3.2.11(iii)) offer the opportunity for estimating $\frac{dT}{dz}$ from measurements of C_n^2, the mean wind shear, energy deposition rates, and the electron density gradient. However, if the $\frac{N}{\chi}\frac{d\chi}{dz}$ term swamps the $\frac{N}{T}\frac{d\theta}{dz}$ term, (eg. 2.3.2.10b), this is not possible in practice. But the possibility certainly exists for determination of temperature gradients from ground based measurements using these formulae.

It is worth commenting here that C_n^2 can only be estimated (for radar work) if the turbulence fills the radar volume (volume defined by the radar pulse and polar diagram). This is often not the case, and the true C_n^2 for turbulence (C_n^2(turb) say) is given by C_n^2 (as estimated by the radar, assuming turbulence fills the radar volume), [= C_n^2(radar), say] divided by F, F being the fraction of the radar volume filled by turbulence. Thus

$$C_n^2(\text{turb}) = C_n^2(\text{radar})/F \quad .$$

For example Van Zandt et al. (1978) discussed the determination of F for the troposphere and stratosphere. They felt that turbulence occurred in narrow layers, with many such layers occurring in one pulse length. They suggest F was generally about .01 to 0.1 in the troposphere and stratosphere. Individual estimates of F were based on the mean wind shear, and upon the assumption that any mean wind shear has fine structure associated with it (which could not be seen by the radar), some of which is able to create turbulence. It was assumed that the spread of fine wind shear gradients about the mean shear was a function of the mean wind shear. Thus strong wind shears have a larger spread of fine scale wind shears. Turbulence would develop when the fine scale wind shear $\frac{\partial U}{\partial z}$ obeyed the relation $(\frac{\partial U}{\partial z})^2 \gtrsim \omega_B{}^2/0.25$ (by equation 2.2.2.3). The term $\omega_B{}^2$ could be estimated by temperature soundings of the atmosphere. Then the probability that

$$(\frac{\partial U}{\partial z})^2 > \omega_B{}^2/0.25$$

gave the fraction of the radar volume filled by the turbulence. The theory assumed a Gaussian distribution of fine scale wind shears about the mean.

However, the assumptions made in deriving 2.3.2.10 must be borne in mind; namely

(i) that the mixing ratio (electron to total densities) at the parcel is constant as the parcel oscillates, and

(ii) that the collision frequency for an electron in the parcel, being proportional to the total pressure, adjusts continuously to the background value.

Assumption (i) deserves perhaps a little more comment. The assumption amounts to assuming that the parcel carries all its neutral particles and electrons and ions with it at all times, and that the chemical reaction rate within the parcel do not change. However, there is the possibility of electron diffusion into the background, particularly as the electron partial pressures in the parcel, and outside, differ. Assumption (i) is invalid if this diffusion time is less than the oscillation time of the eddy. Electrons have larger mean free paths, and move faster, than the neutrals, so could diffuse quite rapidly. However, the rate of electron diffusion is controlled to some extent by the ions. But it is still possible for the electrons to diffuse faster than the ions and neutrals, at least at low heights, of the order of 65km (for example, Hill and Bowhill, 1979, p. 623, mention this possibility). Generally, however, the lifetime of a parcel of scale ℓ(m) (length scale) is given by

$$\tau_L = \frac{\ell^2(m)}{D}$$

where D is the maximum diffusion coefficient of the possible diffusive mechanisms (for example, mechanisms include turbulent diffusion (D = K), ambipolar diffusion ($D = D_\alpha$, the ambipolar diffusion coefficient) or even molecular diffusion). The equation follows, at least for turbulence, by 2.2.3.9b, where τ becomes the lifetime associated with scales of the order of the eddy size, so $k = \frac{1}{\ell}$, and $\ell(m) = 2\pi\ell$. It is only valid, for turbulence, however, for scales within the inertial range - 2.2.3.2b is more appropriate, for example, in the viscous range.

If, then, the appropriate D is in fact the eddy diffusion coefficient (that is, turbulent diffusion acts much faster than any other process), then assumption (i) is crudely valid. At 90km, $D_\alpha \sim 3.6 m^2 s^{-1}$ (see Hill

and Bowhill, 1979; $\tau \sim 2.5$s for $\ell \sim 3$m for ambipolar diffusion means $D_\alpha = 3.6$) so ambipolar diffusion is not significant in the inertial range ($\ell > 60$m) - lifetimes for ambipolar diffusion are $\sim 1.5 \times 10^4$s at ℓ(m) ~ 75m, compared to times ~ 5-50s ($K \sim 10^2 - 10^3 m^2 s^{-1}$) for turbulent diffusion. Thus, at least around 85 - 90km, and up to around 105km, ambipolar diffusion is not important at scales around 70m.

However, processes other than diffusion can also occur in displaced turbulent eddies, which can affect assumption (i). Hill and Bowhill (1979) give an excellent discussion of the processes which can occur in a displaced air parcel. The temperature of the parcel changes upon displacement, as do of course the number densities of the various constituents. The photo dissociation rate also changes. Consequently, reaction rates within the parcel change upon displacement, and the electron production and loss rates also change accordingly. Hence it is quite possible that the electron density to neutral density ratio of the parcel does change as a function of displacement. The lifetimes involved in these processes can be quite short - of the order of the lifetime of an ~ 75m eddy ($\tau \sim \varepsilon^{-1/3}\ell^{2/3}$ by 2.2.3.2c (or ℓ^2(m)/K as seen previously)), so for $\varepsilon \simeq 0.01 \rightarrow 0.1$ W/kg, $\tau \sim 30 - 80$s at ℓ(m) ~ 75m and some of the processes depicted by Hill and Bowhill produce significant effects within this time scale - particularly below 80km. At 85km (Fig. 1, Hill and Bowhill), the processes are not quite so rapid - only small changes in the electron to neutral density ratio of the parcel occur over 100 to 200s for a 200m displacement (eddies of scale ℓ(m) typically are displaced around ℓ(m) over a lifetime).

Thus the results of Hill and Bowhill suggest that above around 80 - 85km, equation (2.3.2.1c) may be roughly relevant, but at lower heights assumption (i) is far from valid, and the problem of estimation

of C_n^2 is very complex indeed. In fact the spectrum of scattered radiation as a function of frequency might no longer be a simple $k^{-11/3}$ law, even though the neutral turbulent spectrum may be. No refinements upon C_n^2, as calculated in (2.3.2.10) will be attempted in this thesis.

2.4 Radar Scatter

2.4.1 Radar Equations

Having discussed turbulence, we must now examine the scattering of radio waves from the turbulence. The turbulence produces variations in refractive index which are especially important when it acts upon a pre-existing gradient of refractive index (equation 2.3.2.10). These in turn produce radar scatter. But is it possible, from measurements of the radiation scattered, to deduce C_n^2?

Consider firstly the case of an atmosphere with random variations of refractive index n, and hence of permittivity ε. Let the "normalized" (see shortly) $\underline{k}$ spectrum of these fluctuations be given by $P(\underline{k})$. Consider a radio wave of wave number $k_{\lambda i}$, and wavelength λ, incident on these fluctuations, and suppose we examine the component scattered in the direction $\underline{k}_{\lambda s}$.

Then according to Booker (1956) (also Rastogi and Bowhill, 1976a, and Ottersten, 1969b), the scattered power, per unit volume of scattering medium, radiated into a unit solid angle in the direction $\underline{k}_{\lambda i}$, for unit incident power in the direction $\underline{k}_{\lambda i}$, is

$$\sigma = \left\langle \left| \frac{\Delta\varepsilon}{\varepsilon} \right|^2 \right\rangle \frac{\pi^2}{\lambda^4} \; P(\underline{k}_{\lambda s} - \underline{k}_{\lambda i}) \sin^2\chi \quad . \tag{2.4.1.1a}$$

Here, χ is the angle between $\underline{k}_{\lambda s}$ and the $\underline{E}$ field vector of the incident wave, and $\left\langle \left| \frac{\Delta\varepsilon}{\varepsilon} \right|^2 \right\rangle$ is the mean square fluctuation of permittivity averaged over all wave numbers k. (It is interesting that this formula, although generally attributed to Booker (1956) was also derived earlier by (or at least a similar form was) by Villars and Weisskopf (1955).)

For most cases in this thesis, the transmitter and receiver have the same location (monostatic case), so the case of interest is $\underline{k}_{\lambda s} = -\underline{k}_{\lambda i}$ ($\chi = \frac{\pi}{2}$), and (2.4.1.1a) becomes

(2.4.1.1b) $$\sigma_{backscatter} = \langle\left|\frac{\Delta\varepsilon}{\varepsilon_0}\right|^2\rangle \frac{\pi^2}{\lambda^4} P(2\underline{k}_{\lambda i}) ,$$

This says that the power scattered back for incident wavelength λ comes from scales in the fluctuations of n of wavelength $\lambda/2$, which is to be expected, by analogy with Bragg reflection from crystal planes (Bragg Scales).

Flood (1968) also discusses derivations of this scatter cross-section, but considers the effects of the loss of energy by absorption as the incident wave passes through the medium, which is an effect not considered by Booker. Consequently, he derives a more sophisticated form of "cross-section". He assumes radio pulses are used, and the "cross section" emerges as a function of the pulse lengths (assuming the region of refractive index fluctuations "fills" the pulse);

(2.4.1.1c) $$\eta_{Flood} = \beta\ 4\pi \langle\left|\frac{\Delta\varepsilon}{\varepsilon_0}\right|^2\rangle \frac{\pi^2}{\lambda^4} P(2\underline{k}_{\lambda i})$$

where

$$\beta = (1 - e^{-4\pi n^i c\frac{\tau}{\lambda}})/(4\pi n^i c\frac{\tau}{\lambda})$$

Here, n^i is the imaginary part of the refractive index, (and therefore related to absorption - see Appendix B), τ is the pulse length, and c the speed of light in a vacuum.

In this case, the cross section η_{Flood} is the scattered power radiated into a full sphere (assuming the radiated power to be the same in all directions as in the particular direction being examined) for unit incident power. Flood shows it is not strictly possible to define a cross section per unit volume, but in the case $\beta \sim 1$, it is valid. Then a cross section η equal to the scattered power per unit volume radiated into a full sphere (assuming the radiated power to be the same in all

directions as in the particular direction being examined) for unit incident power can be defined. Then $\eta = \eta_{Flood}/v_{nom}$, v_{nom} being the volume of scatterer. This is similar to the definition for σ, ie.

(2.4.1.2) $\eta = 4\pi\sigma$.

For most cases in this thesis, β is assumed $\simeq 1$, so the Flood and Booker formulae agree. (This amounts to assuming weak absorption across one pulse length; $n^i \frac{\tau}{\lambda}$ must be small.)

What of $P(\underline{k})$?

Firstly, compare the 2.4.1.1 equations to Ottersten (1969a);

(2.4.1.1d) $\sigma = 4(2\pi)^3 \frac{\pi^2}{\lambda^4} \cdot \Phi_n(2k_{\lambda i})$ (Ottersten, equation 2)

where $\int_{\text{all } k} \Phi_n(\underline{k})d\underline{k} = <|\Delta\hat{n}|^2>$.

Then $\Phi_n(k)$ can be written

(2.4.1.3a) $= <|\Delta\hat{n}|^2> P_0(\underline{k})$

(2.4.1.3b) where $\int_{\text{all } k} P_0(k)dk = 1$.

Further, for an isotropic medium,

$$n^2 = \frac{\varepsilon}{\varepsilon_0}$$

so $$2ndn = \frac{d\varepsilon}{\varepsilon_0}$$

and so

(2.4.1.4) $$<|\Delta\hat{n}|^2> = \tfrac{1}{4}<\left|\frac{\Delta\hat{\varepsilon}}{\hat{\varepsilon}}\right|^2> .$$

The $\hat{}$ symbol again denotes difference between value for a parcel, and that for the background environment (eg., equations 2.3.2.8 - 2.3.2.10).

Then (2.4.1.1d), (2.4.1.3a), and (2.4.1.4) give

(2.4.1.1e) $$\sigma = (2\pi)^3\{<|\frac{\Delta\varepsilon}{\varepsilon_0}|^2> \frac{\pi^2}{\lambda^4} P_0(2\underline{k}_{\lambda i})\}$$

and by comparing this to 2.4.1.1b, $(2\pi)^3 P_0(2\underline{k}_{\lambda i}) = P(2\underline{k}_{\lambda i})$ - clearly different normalizations are used in the two equations.

(2.4.1.1f) By (2.4.1.3b), P_0 is normalized as $\int P_0(k)dk = 1$, so P must be normalized as $\int P(k)dk = (2\pi)^3$.

So all the equations are consistent provided these normalizations are kept in mind.

$\Phi_{\hat{n}}(k)$ is also given by $0.033C_{\hat{n}}^2 k^{-11/3}$ (equation 2.3.1.10a, bearing in mind that monostatic radar backscatter experiment only sees 1 dimensional spectrum - that is it only sees scales perpendicular to the radar beam).

Here the normalization is

$$\int\Phi_{\hat{n}}(k)dk = <|\hat{n}|^2> \qquad (2.3.1.8,\ 2.3.1.9).$$

Thus by 2.4.1.1d, where that Φ_n has a similar normalization,

$$\sigma = 4(2\pi)^3 \frac{\pi^2}{\lambda^4} 0.033C_{\hat{n}}^2 (\frac{4\pi}{\lambda})^{-11/3}$$

giving $\sigma = .030C_{\hat{n}}^2\lambda^{-1/3}$, or

(2.4.1.5) $$\eta = 0.38C_{\hat{n}}^2\lambda^{-1/3}$$ (but note the warning below!)

as also obtained by Ottersten (1969b).

However, notice that (2.4.1.5) assumed equation 2.4.1.4. In the ionosphere which is an anisotropic medium, the permittivity is a tensor, not a scalar (see Appendix B, and the susceptibility matrix). The refractive index depends on the angle of the radio wave normal to the

magnetic field; 2.4.1.4 may be valid if ϵ is taken as a "component" in the direction of the radio wave (I am not sure). In this thesis, (2.4.1.5) will be assumed quite valid, and in equations 2.4.1.1, at times $4<|\frac{\Delta n}{n}|^2>$ may be used in place of $<|\frac{\Delta\epsilon}{\epsilon}|^2>$, to "remove" ambiguity in the ϵ.

One point must be mentioned with regards 2.4.1.5. Although this equation (which appears in many texts) appears to treat $C_{\hat{n}}^2$ as a constant, this is not the case - for a given patch of turbulence, $C_{\hat{n}}^2$ is strongly wavelength dependent! - and equation 2.4.1.5 is very misleading. The $\lambda^{-1/3}$ dependence expresses the wavelength dependence of the spectrum. But the $C_{\hat{n}}^2$ term depends on the reflection mechanism - and this mechanism has a wavelength dependence of its own.

Proof: The refractive index structure function is (equations 2.3.1.11, 2.3.1.12)

$$(2.4.1.6) \qquad D_{\hat{n}}(\underline{r}) = <\hat{n}(\underline{x}+\underline{r}) - \hat{n}(\underline{x}))^2> = C_{\hat{n}}^2\, r^{2/3}$$

$$= <\{\Delta\hat{n}(\underline{x},\underline{r})\}^2> \qquad \text{where}$$

$$\hat{n}(\underline{x}+\underline{r}) - \hat{n}(\underline{x}) = \Delta\hat{n}(\underline{x},\underline{r})$$

and the refractive index $\hat{n}$ is related to the electron density fluctuations $\hat{N}$;

$$\Delta\hat{n} = \frac{\partial n}{\partial N}\,\Delta\hat{N} \qquad \text{(also see between equations (2.3.2.9) and (2.3.2.10))}$$

(Fluctuations in $\Delta\hat{n}$ due to collision frequency changes are assumed negligible for simplicity).

Hence $$<\{\Delta\hat{n}(\underline{x},\underline{r})\}^2> = (\frac{\partial n}{\partial N})^2\, <\{\Delta\hat{N}(\underline{x},\underline{r})\}^2>$$

so

$$(2.4.1.7) \qquad C_{\hat{n}}^2 = (\frac{\partial n}{\partial N})^2 C_{\hat{N}}^2 .$$

But for a given patch of turbulence, $C_{\hat{N}}^2$ is a constant. Thus $C_{\hat{n}}^2 \propto (\frac{\partial n}{\partial N})^2$, which is extremely wavelength dependent. For example ,

for the VHF case (e.g. Vincent, 1973)

(2.4.1.8) $\varepsilon/\varepsilon_0 = 1 - \frac{\lambda^2 r_e}{\pi} N$, where $r_e = \frac{e^2}{4\pi\varepsilon_0 m_e c^2}$ is the classical electron radius.

Here, N = electron density, λ is the radio wavelength, e is the charge of an electron, m_e the electron rest mass, and c the speed of light in a vacuum.

Then

$$d\varepsilon = \frac{-\lambda^2 r_e (dN)}{\pi} . \varepsilon_0$$

$$\Rightarrow \quad 2dn = \frac{-\lambda^2 r_e (dN)}{\pi} \qquad \text{by 2.4.1.4.}$$

so

$$\left| \frac{dn}{dN} \right|^2 = \lambda^4 r_e^{\,2} / (4\pi^2)$$

and $C_n^{\wedge 2}$ clearly has a λ^4 dependence.

For the more general case, the Sen-Wyller equations must be used to obtain $\frac{\partial n}{\partial N}$ (for example, Vincent (1973), Fig. 8, shows the ratio of the backscatter cross section evaluated by the VHF formula to the true Sen-Wyller cross section, at 2.4 MHz. This in fact is the ratio of $\left(\frac{\partial n}{\partial N}\right)$ by the VHF approximation to the true $\frac{\partial n}{\partial N}$, as a function of height).

This wavelength dependence of $C_n^{\wedge 2}$ should be borne in mind when comparing values at different wavelength - it may be better to evaluate $C_N^{\wedge 2}$ and compare these. (Often $C_n^{\wedge 2}$ is used as an indicator of backscattered signal, as distinct from σ).

One final point should also be made concerning radio backscatter measurements of turbulent spectra. The radar spectrum gives the 1D spectrum of scales normal to the beam. This is not the same spectrum

as would be measured by a probe moving through the atmosphere, since such a detector measures the spectrum on a line moving through the full 3D turbulence spectrum - it detects effects of all scales with all orientations. Ottersten (1969b) gives an excellent discussion of the difference between these two situations.

Table 2.1

Some Important Turbulence Formulae

(See text for any qualifications related to these formulae)

The following symbols are used in this table.

ε = Total energy dissipation rate (per unit mass)

ε_g = buoyancy energy dissipation rate (per unit mass)

ε_d = viscous energy dissipation rate (per unit mass), and also equals the rate of transfer of energy between scales in the inertial range

k refers to turbulence wave numbers

ℓ ($\propto k^{-1}$) refers to turbulence scales

v_ℓ refers to turbulent velocities associated with scale ℓ

τ_ℓ refers to lifetime associated with scale

θ is a tracer of turbulence

L = outer scale of turbulence

K_m = momentum diffusivity (eddy viscosity)

K_t = heat diffusivity

K = eddy diffusivity ($K \approx K_t$)

ω_B = Brunt-Vaisala angular frequency

ν = kinematic viscosity

ζ is the typical displacement of an eddy of size ~ L

n = refractive index

N = electron number density

T = temperature

Γ_a = (dry) adiabatic lapse rate

ν_m = electron collision frequency with neutral molecules

(i) Energy Spectrum

Buoyancy Range: $E(k) \sim \varepsilon_d^{2/3} k^{-5/3} [k^{-n(k)}] \quad k = |\underset{\sim}{k}|$

$n(k)$ takes a variety of complex forms - see text

Inertial Range: $E(k) \sim \alpha \varepsilon_d^{2/3} k^{-5/3} \quad k = |\underset{\sim}{k}|$

$\alpha = 1.4$ (Weinstock, 1978)

1.586 (Rastogi and Bowhill, 1976a, b)

Inertial Range, component form:

$$E_i(k_i) = \alpha_i \varepsilon_d^{2/3} k_i^{-5/3} ;$$

i refers to 3 orthogonal directions

$\alpha_i = 0.5$ for the direction parallel to mean flow

(Caughey et al., 1978; Gage and Balsley, 1978)

$\alpha_i = 0.65$ for the directions transverse to mean flow

(Gage and Balsley, 1978). In these component cases, a normalization $\int E_i(k_i) dk_i = \overline{u_i^2}$ is used e.g. Kaimal *et al*, (1972).

Viscous Range: $E(k) \sim 0.148(\varepsilon_d/\nu^2)^2 k^{-7} \exp\{-k/k_c\}$?

$k_c = .738 k_\eta$

(Rastogi and Bowhill, 1976a, b)

(ii) Other Formulae (Inertial Turbulence)

Kolmogoroff Microscale: $\eta \overset{\text{dfn}}{=} (\nu^3/\varepsilon_d)^{1/4}$ (units of length per radian)

Outer scale $\begin{cases} L \sim (K^3/\varepsilon_d)^{1/4} \quad [\text{or } L \sim (K^3/\varepsilon_d)^{1/4}(4\pi^2)^{-3/4} \text{ ??}] \\ - \text{former more appropriate} \end{cases}$

$$\langle |\theta_\ell|^2 \rangle \tau \sim \varepsilon_\theta \sim \nu |\nabla \theta_\eta|^2 \sim K \left(\frac{d\bar{\theta}}{dz}\right)^2$$

$$v_\ell \sim \ell/\tau_\ell$$

$$\varepsilon_d \sim v_\ell^3/\ell$$

often assumed;

$$\varepsilon_d = (T_*)^{-1} v_\ell^3/\ell$$

for radar work, $\ell = 4\pi/\lambda_i$, λ_i = radar wavelength. What of T_*?

Choices include 1.0, 2π, 15π (see text).

T_* = 1.0 frequently assumed. Personal choice, 15π or 30π.

If ℓ is actually measured, use

$$\varepsilon_d = 1/10 \quad v^3/\ell(m), \quad \ell(m) = \text{scale in metres} \qquad \text{(equation 2.2.3.3b)}$$

Definition of outer scale: $L^2(m)\left(\frac{d\bar{\theta}}{dz}\right)^2 = \langle|\theta_L|^2\rangle$

$$K \sim L^{4/3}k^{-2/3}\tau^{-1}: \quad \text{constant relating equation uncertain.}$$

Use $L \sim (K^3/\varepsilon_d)^{1/4}$ and ε_d as above - a better method.

$$\varepsilon = \varepsilon_d + \varepsilon_g$$

$$\varepsilon \sim \varepsilon_d \sim \varepsilon_g \quad \text{often assumed.}$$

$$\varepsilon = -\langle v_i v_j\rangle \frac{\partial U_i}{\partial x_j} = -\langle Lv_3\rangle \left(\frac{\partial U}{\partial z}\right)^2$$

(v_i are turbulent velocities)

$$\varepsilon_g = -\omega_B^2 \langle \zeta v_3\rangle$$

$$\varepsilon_d = \nu\left\langle \frac{\partial v_i}{\partial x_j} \frac{\partial v_i}{\partial x_j}\right\rangle$$

Isotropic turbulence: $= 15\nu \langle (\partial v_1/\partial x_1)^2\rangle$ (Rastogi and Bowhill, 1976a)

$= (15/2)\nu \langle (\partial v_1/\partial x_2)^2\rangle$ (Justus, 1967)

$$K_m = \langle Lv_3\rangle$$

$$K_t = \langle \zeta v_3\rangle$$

$$\varepsilon_d \sim \varepsilon_g \sim \varepsilon \sim K_m \left(\frac{\partial U}{\partial z}\right)^2$$

$$\sim P_r K_t \left(\frac{\partial U}{\partial z}\right)^2$$

where $P_r = K_m/K_t$ = Prandtl number

$P_r = 0.7$ (eg. Teitelbaum and Blamont, 1977); $P_r \sim 2 - 5$ (Justus, 1967)

$P_r = 0.7$ probably best estimate.

Eddy diffusivity and temperature diffusivity roughly equal.

$\varepsilon = K_m \omega_S^2$ $\quad \varepsilon_g = K_t \omega_B^2$ (Justus, 1967); ω_S = wind shear

$K_t \sim (c^{-1})\ \varepsilon_d/\omega_B^2$

Possible c; $\quad$ c = 1.0 (used in Fig. 1.9c)

⟶ $\quad$ c = 1.8 (this chapter, section 2.2.4)

$\quad$ c = 0.10 (Lloyd et al., 1972)

$\quad$ c = 3 (Gage and Balsley, 1978)

$\varepsilon_d/\varepsilon_g = c$; $\quad \varepsilon_d/\varepsilon = c/P_r\ R_i$; $\quad \varepsilon_g/\varepsilon = 1/P_r\ R_i$ $\quad R_i = P_r/(1+c)$

Exact relations

$$\varepsilon_d = c_1 K_t \omega_B^2,\ \varepsilon = c_2 P_r K_t \left(\frac{\partial U}{\partial z}\right)^2,\ \varepsilon_g = c_3 K_t \omega_B^2$$

$$\varepsilon_d/\varepsilon_g = c_1/c_3,\ \varepsilon_d/\varepsilon = c_1/(c_2 P_r) R_i,\ \varepsilon_g/\varepsilon = c_3/(c_2 P_r)\ R_i$$

$$R_i = c_2 Pr/(c_1+c_3)$$

Above, have assumed $c_1 = c$, $c_2 = c_3 = 1$

These are probably fair. Probably c ~ 1-3

Radar Formulae

$$D_\theta(r) = \langle\{\theta(\underline{x} + \underline{r}) - \theta(\underline{x})\}^2\rangle$$

$$= C_\theta{}^2 r^{2/3} \qquad \text{(Inertial)}$$

$$C_{\hat{n}}{}^2 \sim a^2 L^{4/3} |M_e|^2 \qquad (a \sim 1)$$

$$\sim a^2 K |M_e|^2 \varepsilon_d{}^{-1/3}$$

$$\sim (a^2/P_r)\ \varepsilon\ \varepsilon_d{}^{-1/3}\ |M_e|^2\ (\frac{\partial \underline{\underline{U}}}{\partial z})^{-2}$$

+ other forms (see equation (2.3.2.11)

Where

$$M_e = \frac{\partial n}{\partial N}\{\frac{N}{T}(\frac{dT}{dz}) + \Gamma_a) - \frac{dN}{dz} - (1.4 \times 10^{-4} m^{-1})N\} + \frac{\partial n}{\partial \nu_m}\frac{\partial \nu_m}{\partial z}$$

$C_{\hat{n}}{}^2{}_{turb} = C_{\hat{n}}{}^2{}_{(radar)}/F$ F = Fraction of radar volume filled by turbulence

$$\sigma = \langle|\frac{\Delta\varepsilon}{\varepsilon_0}|^2\rangle\ \pi^2/\lambda^4\ \ P(2\underset{\sim}{k}_{\lambda i})\ \ m^2 sr^{-1}$$

ε refers to permittivity here; λ is probing wavelength. $P(k_i)$ is spectrum of turbulence normalized st $\int P(k)d\underset{\sim}{k} = (2\pi)^3$

$$\sigma = (0.38)C_{\hat{n}}{}^2\lambda^{-1/3}$$

But bear in mind $C_{\hat{n}}{}^2$ has strong λ dependence.

For observation of turbulence by radar

$$v_{RMS} = (\tau_{0.5})^{-1}(\lambda/4\pi)\sqrt{\ln 2} \qquad \text{(amplitude data)}$$

$$v_{RMS} = (\tau_{0.5})^{-1}(\lambda/4\pi)\sqrt{2\ln 2} \qquad \text{(complex data)}$$

v_{RMS} is the velocity associated with scattering scales $\ell = \lambda/4\pi$. (However, if long lengths of data are used, and if the polar diagram used has a wide beam, important complications arise. See Chapter VII for correct interpretation of v_{RMS}.)

For turbulent velocity,

$$C_v^2 = (a_v^2)\varepsilon^{2/3} \qquad (D_v(r) = \langle\{\underline{v}(\underline{x} + \underline{r}) - \underline{v}(\underline{x})\}^2\rangle)$$

$a_v^2 = 4.8\alpha$ (Elford and Roper, 1967; Batchelor, 1953).

(α as in Energy spectrum formulae)

Component form

$$C_{v_i}^2 = (a_{v_i}^2)\varepsilon^{2/3} \qquad (Dv_i(r) = \langle\{v_i(\underline{x} + \underline{r}) - v_i(\underline{x})\}^2\rangle)$$

$a_{v_i}^2 = 2$ (Caughey et al., 1978), Longitudinal component (ie. parallel to mean flow)

$a_{v_i}^2 = 1.75$ (Gage and Balsley, 1978), Longitudinal component

$a_{v_i}^2 = 2.35$ (Gage and Balsley, 1978), transverse component

CHAPTER III

INTRODUCTION, CALIBRATION, AND SOME PRELIMINARY OBSERVATIONS

3.1 Introduction

3.2 General Description of Technique

a. The Transmitter

b. Reception

c. Temporal Variations

d. Data Acquisition and Recording

e. Phase Recording

3.3 Calibration

3.3.1 Ground Characteristics

3.3.2 Techniques of Calibration

a. Definition of Units

b. Relating Measurements to Reflection Coefficients

c. Experimental Determination of Calibration Constants

d. Turbulent Scatter

3.4 Some Simple Observations

3.5 The Field Sites

3.5.1 Buckland Park

3.5.2 Townsville and Woomera

Chapter III Introduction, Calibration and some Preliminary Observations

3.1 Introduction

This chapter summarises the experimental techniques used in this thesis. However, only the basic principles will be discussed; the actual equipment used will be considered largely as "black boxes" which receive an input and produce an output. For example, details concerning the electronics of the transmitter and receivers will not be considered, unless it is felt necessary for a clearer interpretation of some of the results obtained.

The discussion will also show how the systems may be calibrated, and the types of errors involved. To do this the reflection coefficient of the ground must be known, and some space will be given to consideration of ground dielectric constants and conductivities. Polar diagrams of the aerial arrays used will be presented, and estimates of the efficiencies given.

Finally, some simple information which can be gained by just watching the received signal will be presented.

Two main field stations were used in the work for this thesis. The major one was at Buckland Park (34°38'S, 138°29'E), near Adelaide (34°56'S, 138°36'E) Australia. Observations were made at frequencies of 1.98MHz and 5.995MHz. The second station was near Townsville, Australia (19°15'S, 146°54'E), and operated at a frequency of 1.94MHz. The site itself was at (19°40'S, 146°54'E). A third station at Woomera, Australia (30°45'S, 136°18'E) had also been in use up to 1976. Although this station was closed before the work for this thesis began, some important insights into D-region scatterers were obtained by analysing some data produced at this site. This will be discussed in a later chapter.

3.2 General Description of the Technique

A brief discussion of the technique used to study D-region radio wave scatterers has been given in Chapter I, in connection with the experiments performed by Gardner and Pawsey. Basically, pulses of radio waves are transmitted into the ionosphere, and these are partly reflected by scatterers in that region. The reflected signals (or "echoes") are then picked up by receiving aerials and can thus be analysed. The delay between the transmission of the pulse and the reception of the signal is determined primarily by the altitude of the scatterer in the D-region, at least for frequencies greater than about 2MHz.

Fig. 3.1 shows the simplest arrangement used for the work of this thesis. It is in fact a general view of the system used at Townsville. The description of the technique used will be based on this diagram. More detailed photographs and parameters of the Townsville system will be given towards the end of the chapter (eg. Fig. 3.13, Table 3.3b). The transmitter, receiving and recording equipment were housed in a caravan at the centre of the array, represented by the small dark rectangle in the centre of Fig. 3.1.

3.2a The Transmitter

The transmitter produced a pulse of the appropriate radio frequency, with a Gaussian envelope. The half power width of the envelope was variable, but was generally about 30μs. Such a pulse was transmitted at a constant pulse repetition frequency (PRF) of, typically, 20 to 50Hz. At Townsville, the PRF was intitially 15Hz, but was later changed to 20Hz. This pulse was then carried by transmission lines to two pairs of parallel folded half-wave dipoles.

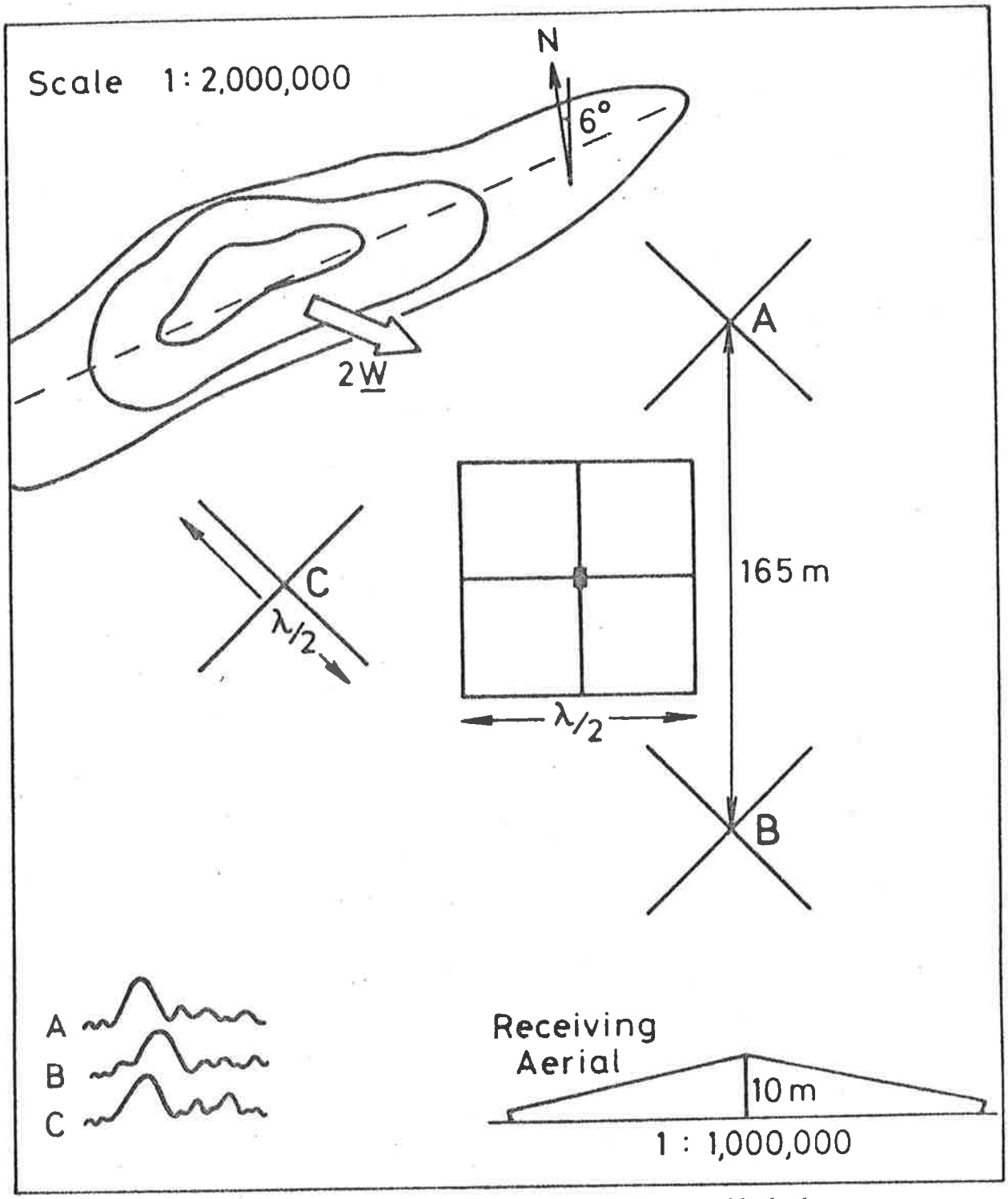

Fig. 3.1 Plan view of the Townsville aerials. The small dark central rectangle represents the caravan which houses the equipment, and the large square the transmitting array. The lines leading from the large square to the caravan represent the transmission lines which carry the signal to the transmitter dipoles. The contours represent lines of constant amplitude of the diffraction pattern produced by the scatterers at height h. The vector $2\underline{W}$ represents the drift direction of this diffraction pattern, and $\underline{W}$ is the drift vector of the scatterers at height h. In the bottom left hand corner are typical amplitude signals which might be received on aerials A, B and C as the diffraction pattern drifts across.

See the text for a more detailed description. Figs. 3.13 also show photographs of the Townsville array.

The peak power of the pulse was monitored by measuring the peak voltage on one side of one of these transmission lines. Generally, this was about 600 Volts. In Fig. 3.1, the top and bottom lines of the large square represent one dipole pair, and the two lines perpendicular to these represent the other pair. Considerable care was taken in matching the transmitter impedance to that of the dipoles. The two pairs of dipoles were phased separately. In this way, various types of radiation could be transmitted. For example, circularly polarized radiation with either a clockwise or anticlockwise sense of rotation could be transmitted if one pair of dipoles led the other by $\pi/2$ radians. These types of radiation produced were approximately O (ordinary) or X (extraordinary - also denoted E) radiation for the latitudes used. Linearly polarized radiation would have been transmitted had the two pairs of dipoles been phased equally. The normal mode of operation in the work for this thesis was to use either O or X modes. The transmitting dipoles were generally about one quarter of a wavelength above the ground at all sites.

3.2b Reception

The radiation scattered from the ionosphere was received on three sets of aerials, denoted A, B and C in Fig. 3.1. In the arrangement used at Townsville, these were in fact two crossed orthogonal inverted-V-dipoles, with peak heights about 10m above the ground. One inverted-V-dipole is shown in the bottom right hand corner of Fig. 3.1. The dipole impedances were transformed to 50Ω purely resistive, and 50Ω coaxial cables carried the signal received back to the caravan, where the receiving and recording equipment was stored. Here, the separate signals from the orthogonal dipole pairs were added, with an appropriate phase change ($\pm \pi/2$ radians) to allow for reception of O or X

polarized radiation. This phasing was arranged to match the transmitter polarization. By only allowing one polarization to be received the atmospheric noise was reduced and polarization fading (interference between O and X modes) was also dampened. However, this was not always done. At Buckland Park (Adelaide), for example, such phasing for reception was not always done. Simple linear half-wave dipoles were used for reception in that case, although frequently the signals on several of these dipoles were added (before entering the receiver) to produce a stronger signal and narrower polar diagram.

The received signal entering a receiver was then amplified, beaten down to an intermediate frequency (IF) of generally 400-500kHz, amplified again, and finally the amplitude envelope obtained. This could then be monitored on a Cathode Ray Oscilloscope (CRO). At a later stage in the thesis work, facilities were added to allow measurement of phase and amplitude. This will be discussed in more detail later.

Every time a pulse was transmitted, a form something like that shown in Fig. 1.10 appeared on the CRO. As discussed in Chapter I, the time lag from the transmission of the peak of the pulse to any later time was expressed as a "virtual range", by multiplying the time lag by c/2, c being the speed of light in a vacuum. Thus a peak at a lag of 600μs corresponded to a virtual range of 90km. If a peak in the received signal occurred at a virtual height of 90km, it could usually be assumed that this was in fact due to a scatterer 90km away, since the speed of light in the D-region at frequencies of 2MHz and greater is close to c. Above about 95 to 100km, however, the virtual height may be somewhat greater than the true height of scatter at 2MHz. This is because the electron density becomes

sufficiently large that the group velocity of pulses at frequencies near and below 2MHz becomes somewhat less than the speed of light in a vacuum. Finally, the pulse is critically reflected at around 100 to 110km when operating at frequencies near 2MHz during the day. At 6MHz no such effects generally occur until F-region heights are reached (250-300 km). (At times however a strong sporadic E layer can occur at around 110km which can reflect 6MHz radiation). These 2MHz effects are illustrated adequately by Fig. 1.10. The possibility of ground echoes was also discussed in Fig. 1.10. At night times, the electron densities are reduced considerably. and the observed structure differs from that seen in the daytime. Night-time echoes will be discussed later.

3.2c Temporal Variations

On each transmission of a pulse the signal received on the CRO changes form, as the scatterers vary in reflection strength, shape, orientation, distance and so forth. If the signal at any one virtual height is monitored, time series such as those shown in Fig. 3.1 are produced. If the scatterers are moving overhead, the aerials A, B and C receive similar signals, but with displacements in time. By determining the shifts of these signals necessary to make them best match up, the apparent velocity of drift of the scatteres can be determined under the assumption that motion is purely horizontal. For example, suppose the contours drawn in Fig. 3.1 represent contours of equal amplitude of the diffraction pattern produced by scatterers at a particular height in the ionosphere, and suppose initially that they do not change in form as they drift. These will move over the ground in the direction of the scatterers' movement at speed $2\underline{W}$, $\underline{W}$ being the scatterer drift velocity (eg., Ratcliffe, 1956 - point source effect). Let the shift between signals received on aerials

A and B be τ_{AB} and let d_{AB} be the distance between A and B. If the broken line (which specifies the contour orientation) in Fig. 3.1 were perpendicular to the drift direction, the value d_{AB}/τ_{AB} would give $2\underline{W}/\cos\alpha$, the velocity of drift of the pattern along the line $\overline{AB}$. Here α is the angle between the wind vector $\underline{W}$ and the line $\overline{AB}$. By using the other pairs of aerial (AC and BC), $\underline{W}$ and α can be determined. However, the contour orientation may not be perpendicular to $\underline{W}$, as illustrated in Fig. 3.1. To properly consider such cases, Full Correlation Analysis (FCA) was developed, by means of which the true velocity $\underline{W}$ could be determined even in these anisotropic cases (eg., Briggs, Phillips and Shinn, 1950; Briggs and Spencer, 1954; Phillips and Spencer, 1955; Fooks, 1965). The possibility of the contours of constant amplitude varying in time was also considered by FCA.

There has been some debate as to what D-region drift measurements actually do measure, but experiments have shown that it is generally valid to take the measurements to be the neutral wind velocity (see Chapter I). These wind measurements determined by the Full Correlation Analysis technique will be used extensively in this thesis. A fuller discussion of FCA can be found in Briggs (1977b).

3.2d Data Acquisition and Recording

The final stages of instrumentation used in these experiments were the data acquisition and recording systems. The pulses scattered from the D-region can be observed on a CRO, as discussed, and their temporal variations inspected visually. But to analyse the echoes properly requires recording the signals. Generally, the signal was monitored at several virtual ranges, and the voltage at each range stored on 7 track magnetic tape as a number between 0 and 63 (ie.,

digitized to 6 levels). Such numbers were stored at regular intervals for each height - typically at intervals of 0.1 to 0.8 seconds. For example, initially the Townsville system could record data at 10 ranges, in steps of 2 km (for example 60, 62, 64, ..., 78 km) every 0.2 seconds. The starting height could be set at any multiple of 10. Alternatively, the system could cover 20 ranges, again in steps of 2km, and again every 0.2 seconds. The data could then be analysed later on a digital computer. At a later date, the Townsville system was changed, and this will be discussed shortly in the section regarding recording of phase.

Towards the end of the work for this thesis, a mini-computer was installed at the Adelaide (Buckland Park) research station, and in the near future much of the analysis may be able to be done at that site itself, without the need for data storage on tape. The installation of this computer allowed data to be collected more efficiently, and in its initial stages it was used to store data on tape more systematically. This also resulted in a change in the way in which the data was recorded. The PRF was changed to 20Hz, whereas previously it had generally been 50Hz, and sometimes 25Hz. The ranges used to pick data formerly started at multiples of 10, plus 2 km (eg., 62, 72 km etc.) and subsequent ranges increased in (generally) 2km steps. The new system had starting heights at multiples of 10, eg., 60, 70 km, increasing in steps of 2 km. Ten ranges were generally recorded simultaneously on the new system. The former version could record either 10 or 20 heights simultaneously.

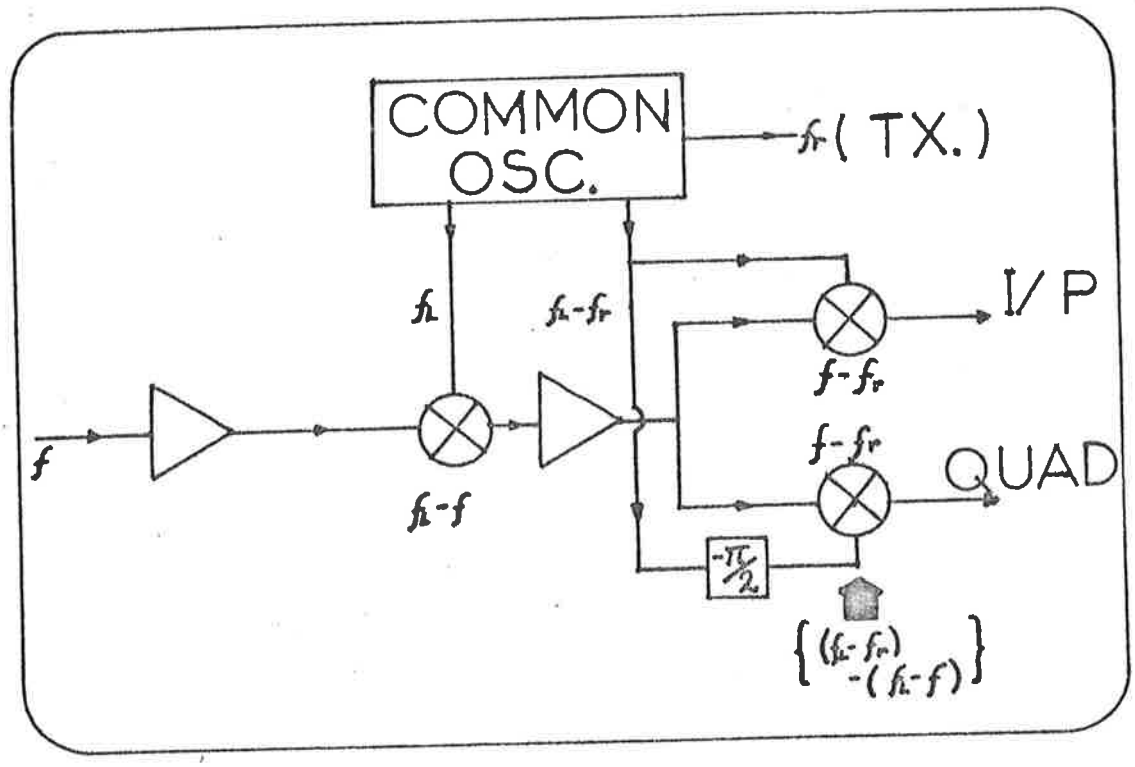

Fig. 3.2 Schematic diagram of the electronics used to record in-phase and quadrature components. Here, f_r is the transmitted central frequency, f_L the local oscillator frequency, and f the received (possibly Doppler shifted) radio frequency.

3.2e Phase Recording

Another major improvement to the receiving and recording systems was the ability to record both amplitude and phase information simultaneously. The early work presented in this thesis was obtained by recording amplitude only, and chapters IV to VI discuss conclusions drawn using amplitudes. The ability to determine the phase of the signal allowed determinations of velocity by Doppler techniques (see later), and also allowed detailed monitoring of height fluctuations of individual scatterers. The amplitude and phase were not directly recorded, but rather the "in-phase" and "quadrature" components. That is to say, the returned signal for a specific virtual range, E(t), could be written as

$$E(t) = E_{IP}(t)\cos \omega_r t + E_Q(t)\sin \omega_r t,$$ ω_r being the angular frequency of the radiation transmitted. The term $E_{IP}(t)$ represents the "in phase" component, and $E_Q(t)$ the "quadrature" component. Since $\cos \omega_r t$ and $\sin \omega_r t$ form an orthonormal set of axes, E(t) can be represented as a complex number,

$$E_{IP}(t) + jE_Q(t), \qquad j = \sqrt{-1}$$

Thus the points $[E_{IP}(t), E_Q(t)]$, which are the values stored by the recording system, are directly amenable to complex Fourier analysis.

Fig. 3.2 illustrates the principle of determination of E_{IP} and E_Q. The signal E(t) is amplified, and then mixed down by beating with a local oscillator, of angular frequency ω_L, to produce an IF (intermediate frequency) signal. This is further amplified, and then mixed with a cw IF signal of angular frequency $(\omega_L - \omega_r)$.

This mixing effectively multiplies the signals of frequencies $(\omega_L - \omega)$ and $(\omega_L - \omega_r)$, and thus produces frequencies $[(\omega_L - \omega) + (\omega_L - \omega_r)]$ and $[(\omega_L - \omega) - (\omega_L - \omega_r)]$. A low pass filter then insures only those frequencies close to zero Hz - namely $(\omega - \omega_r)$ - are allowed through. This filter must be chosen so as to allow a reasonable range of frequencies $(\omega - \omega_r)$ to pass, but so as not to allow any of the other components through.

As an example, consider a purely sinusoidal input. Suppose the received RF is $E(t) = \cos \omega t$, and let the transmitted central angular frequency be ω_r. Then the IF signal will be $\cos(\omega_L - \omega)t$, after mixing with a local oscillator of angular frequency ω_L $(> \omega_r)$ and removing all frequencies except those near $(\omega_L - \omega)$. This signal is then mixed with an IF reference signal, $\cos(\omega_L - \omega_r)t$. (For example, at Townsville the IF was 485kHz). The resultant is

$\cos(\omega - \omega_r)t$, after removal of all frequencies except those near 0Hz. This is the "in phase" component. Mixing $\cos(\omega_L - \omega)t$ with $\sin(\omega_L - \omega_r)t$ produces

$\sin(\omega - \omega_r)t$ after filtering. This is the "quadrature" component.

Thus if E(t) was a purely sinusoidal oscillation with angular frequency ω, then E_{IP} and E_Q are also (slowly varying) sinusoidal oscillations, with angular frequency $(\omega - \omega_r)$. If $\omega > \omega_r$, $(\omega_L - \omega) < (\omega_L - \omega_r)$. That is to say, the IF produced is less than $(\omega_L - \omega_r)$, and the in-phase component leads the quadrature component. If $\omega < \omega_r$, $(\omega - \omega_r)$ is a negative frequency. Physically, this means that the quadrature component leads the in-phase component. It can thus be seen negative frequencies have a real meaning in this case.

This system can be used to determine the component of the velocity of a scatterer towards the transmitter - receiver system. A positive frequency means $\omega > \omega_r$, or the scatterer was approaching the receiver. The radial velocity is given by the relation

$$2v_r = (\Delta f/f).c$$

or

$$v_r = (\lambda/2)\Delta f,$$

λ being the radiation wavelength and Δf $(= (\omega - \omega_r)/2\pi)$ the offset of the frequency from 0Hz. If Δf is negative, movement away from the array is indicated.

A system to record phase and amplitude in this manner was installed in the Townsville equipment in March, 1979. A version was also installed in the Buckland Park equipment during 1977, but it could only operate on one receiver. It was not until May, 1980, that in-phase and quadrature components could be recorded on several receivers simultaneously at Buckland Park.

The installation of the phase equipment at Townsville was also accompanied by a change in the PRF (to 20Hz) and also the method of storing data on tape. The ability to record "in-phase" and "quadrature" components also allows "coherent integration"; that is, several successive points may be averaged together, to reduce the effect of noise. The "integration time" must be less than the smallest realistic fading period of the signals E_{IP} and E_Q, however. If amplitude only is recorded, averaging of n successive points results in a signal to noise increase by roughly $\sqrt{n}$ times in power, whilst averaging n successive points recorded as "in phase" and "quadrature" improves the signal to noise ratio by n times in power. Further, averaging amplitude-only data is strictly speaking an incorrect

procedure - this distorts the time series and can affect such things as the autocorrelation and cross correlations. These points are discussed in more detail in Chapter VI. Such distortions do not occur when averaging in-phase and quadrature data (ie., the complex data). The Townsville equipment made use of this fact by recording data at each height 20 times per second, and then averaging sets of 8 consecutive points using a small microprocessor (SC/MP). These averages were then stored on tape. Thus data was stored every 0.4 seconds on the later version of the Townsville data acquisition system.

3.3 Calibration

When a radio pulse is scattered from the ionosphere, the strength of the signal received on the ground can be used to determine the cross-section of backscatter for the scatterer, or scattering cross-section per unit volume in the case of volume scatter. To do this, however, the system must be correctly calibrated, and the description of how this may be done follows shortly. With the method adopted, however, it is important to have some knowledge of the reflection coefficient of the ground, and the first part of this section is devoted to a discussion of ground characteristics at the sites used.

3.3.1 Ground Characteristics

The reflection coefficient at the ground for radiation incident at an angle i to the ground normal is given by

$$(3.3.1.1) \qquad R_{\perp} = \frac{n\cos i - \sqrt{1 - n^2\sin^2 i}}{n\cos i + \sqrt{1 - n^2\sin^2 i}}$$

when the $\underline{E}$ vector is perpendicular to the plane of incidence, and

$$(3.3.1.2) \qquad R_{\parallel} = \frac{\cos i - n\sqrt{1 - n^2\sin^2 i}}{\cos i + n\sqrt{1 - n^2\sin^2 i}}$$

when the $\underline{E}$ vector is in the plane of incidence (eg., Jackson, 1975, equations 7.39 and 7.41). $R_{\perp}$ and $R_{\parallel}$ are both complex numbers, indicating the possibility of phase change upon reflection. In these equations, it has been assumed the refractive index of air is 1, and that the permeability of the ground, μ, is equal to that for free space. The term n represents the complex refractive index of the ground, and

$$(3.3.1.3) \qquad n^2 = \varepsilon'/\varepsilon_0 = \kappa.(1 - j\sigma/(\varepsilon_0\omega\kappa)) \qquad j = \sqrt{-1} \text{ (MKSA)}$$

[or $n^2 = \mu\kappa(1 + j\ 4\pi\sigma/(\omega\kappa))$ in cgs. (Jackson, 1975, equation 7.68). Notice this has a "+" sign, compared to a "-" in 3.3.1.3. It doesn't matter whether a "+" or "-" is used; $|n|$ is still the same. A "+" is used if wave propagation is written as $\exp\{j(k.x - wt)\}$, and a "-" if $\exp\{j(wt - \underline{k}.\underline{x})\}$ is used (eg., Slater and Frank, Ch. VIII equations 1.4 and 1.5, compared with Jackson (1975) equation 7.68] Here, σ is the conductivity, and κ the real part of the dielectric constant, $\kappa' = \varepsilon'/\varepsilon_0$. ε' is the complex permittivity. ω is the angular frequency of the radiation, and $= 2\pi f$, f being the frequency.

Notice for perpendicular incidence, (i = 0),

(3.3.1.4) $$R_{\perp} = R_{||} = \frac{n - 1}{n + 1} \cdot$$

The above formulae imply

(3.3.1.5) $$n = n_R + jn_i$$

where, in cgs units

(3.3.1.6) $$\begin{cases} n_R = 1/\sqrt{2} \cdot (\sqrt{\kappa^2 + (2\sigma/f)^2} + \kappa)^{\frac{1}{2}} \\ \text{and} \\ n_i = 1/\sqrt{2} \cdot (\sqrt{\kappa^2 + (2\sigma/f)^2} - \kappa)^{\frac{1}{2}} \end{cases}$$ (eg., Jackson, 1975, equation 7.69)

These formulae (3.3.1.6) can be simplified if $(\sigma/f\kappa) << 1$ (good dielectric; poor conductor) and if $(\sigma/f\kappa) >> 1$ (poor dielectric; good conductor), but these simplifications will not be considered here.

McPetrie (1938) has presented graphs by which it is easy to determine $R_{\perp}$ and R_{11} given κ and (σ/f). For the work in this thesis, only perpendicular incidence will be considered. Then what are reasonable estimates of $R_{\perp} = R_{||} = R$ for vertical incidence? Smith-Rose (1934), has measured κ and σ for a great variety of soil types in England. Fig. 3 of that reference suggests κ and σ should be reasonably constant over the range 2 to 6 MHz. Table 2 of Smith-Rose gives values of (κ) at 1.2MHz ranging from 10 to 90, and σ ranging from $.12 \times 10^5$ to $20 \times 10^8 s^{-1}$ (cgs units) in most cases. (cgs units can be converted to σ in mho m^{-1} (MKSA) by multiplying by $4\pi\varepsilon_0 = (1/9) \times 10^{-9}$). For granite, and slate, smaller κ and σ values are possible, and for very salty red clay, κ values greater than 100 were possible. But the sites involved in work for this thesis were not granite or slate,

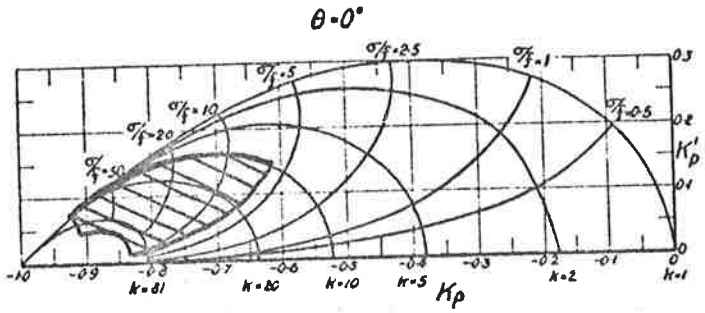

Fig 3.3 Graphical determination of the reflection coefficient for radio waves incident vertically upon the ground. κ_p represents the real part, and κ_p' the imaginary part, of this reflection coefficient. Here, σ must be in cgs units (s^{-1}) and f in Hz. Then, given the ground conductivity σ and real part of the dielectric constant, κ, the reflection coefficient can be determined. Typical ranges at Buckland Park and Townsville for κ and (σ/f), and hence (κ_p, κ_p'), are shaded for frequency of 2MHz.

The graph comes from Fig. 3a of McPetrie (1938).

so the limits of κ will be taken as given. Then (κ, σ/f) at 2MHz range from (10, 6) to (90, 1000). Examination of Fig. 3.3 (which is Fig. 3a from McPetrie) shows Re(R) lies between about -0.6 and -0.9, and Im(R) is less than about 0.15. Thus $|R|$ is greater than about .62, and probably less than about 0.9, at both the Townsville and Buckland Park sites, at 2MHz.

At 6MHz, the limits of (κ, σ/f) are about (10, 2) and (90, 300), so (R) lies between about -.55 and -.9. In both cases, Im(R) is significantly less than $|Re(R)|$, so the phase change upon reflection is close to π^c. Thus at both frequencies, the reflected signal is between 6 to 1 dB down on the incident amplitude.

At Townsville, the soil is a grey clay, generally quite dry and cracked. Smith-Rose (1934), Table 2, samples 144 to 147, might suggest κ to be about 70, and σ about 10^8 (cgs units) at 2MHz, giving (κ, σ/f) = (70, 50), and R $\approx$ (-0.85, 0.1) ($|R|$ = .85, or a 1.3dB loss on reflection). However, there may be some doubt as to whether English conditions are applicable in Australia. Nicol (1974, 1980) suggests $\kappa \sim 10$ is more typical of Australian conditions, in which case $|R|$ may be as low as 0.5.

Buckland Park may be an interesting case. The soil type is very sandy, so samples 166 of Smith-Rose (1934) would suggest $\kappa \sim 8$, $\sigma \sim 0.12 \times 10^8$, (= 1.3 millimho m^{-1}) so that $\sigma/f \sim 6$ at 2MHz, and ~ 2 at 6MHz. Then R $\approx$ (-0.6, 0.1) at 2MHz, and $\sim$ (-0.55, 0.05) at 6MHz. Thus only about 60% of the incident radiation is directly reflected. However the optical depth of this sand is $\delta = (2\varepsilon_0 c\sqrt{\kappa}) = \sqrt{\kappa}/(188\sigma)$, where σ is in MKSA units. For $\kappa = 10$, and $\sigma = 0.12 \times 10^8 \times 4\pi\varepsilon_0 = 1.3 \times 10^{-3}$mho m^{-1}, $\delta \approx 9$ metres. But the site is quite close to the sea, and a very salty water table lies under the surface at

a depth of about 3 to 5 metres. Thus that radiation which does not get reflected directly, but propagates down through the soil, (attenuating in amplitude), is significantly reflected by this water table (κ ~ 80, σ large ?) before decaying completely in amplitude. The total path travelled to the water table and back up is about one optical depth, so up to around 30% of the radiation which was not reflected originally may in fact eventually be reflected. Of course, this description is quite simplistic - the complete solution of the reflection coefficient for a radio wave incident on such a doubly stratified medium would be somewhat more complex. But certainly the water table at Buckland Park would play a significant role in ground reflection at 2 and 6 MHz. In fact, measurements of the impedance of a 2MHz half wave dipole 10m above the ground given values around 20Ω - j20Ω (eg., Trott, 1967) at Buckland Park. Reference to say Proctor (1950) suggests that this means the ground at Buckland Park is very highly conducting (high κ (around 100?) and σ).

Thus at both Buckland Park and Townsville, the reflection coefficient at 2 and 6MHz may be only 1 or 2dB down on a reflection coefficient of 1.0. In this thesis the amplitude reflection coefficients will be taken as about

$$10^{\frac{-4(\pm 2)}{20}}$$

and a π^c phase change upon reflection will be assumed). Perhaps in the future, σ and κ can be measured at the sites. Even quite crude estimates could place much better bounds on the reflection coefficient R.

3.3.2 Techniques of Calibration

A detailed discussion of the techniques of calibration can be found in Piggott et al. (1957). However, the discussion below will proceed somewhat independently of this.

3.3.2a Definition of Units

In these experiments, a small signal scattered from the ionosphere was amplified and recorded. The output of the receivers was a DC voltage, which lay between 0 and 10 volts. Any stronger signals saturated at 10 volts. To examine these stronger signals, the gain of the receiver was reduced until the DC output level fell below 10 volts. Experiments showed that the receivers were quite linear in their response up to an output value of about 9 volts. That is to say, the DC output level was proportional to the input RF amplitude.

It was desirable to know the actual strength of the signal before amplification. Suppose that the peak DC amplitude of an echo recorded at a virtual range R is D_s volts. The input signal strength may be measured by removing the cable carrying the signal and feeding a small RF signal from a signal generator, at a frequency equal to the transmitted central frequency, into the receiver. Then adjust the signal generator level until the DC output of the receiver lies in the range 0 to 10 volts also - say D_{SG} volts. The receiver gain should not be changed during this process. Suppose the signal generator now reads V_{SG} volts. Then the input signal had a strength

$$V_S = (D_S/D_{SG})V_{SG} \qquad (3.3.2.1)$$

Generally, V_S and V_{SG} are of the order of μV for D-region scatter, and mV for strong E region scatter.

For most experiments discussed in this thesis, the receivers were calibrated in this way. The gain was not changed after this calibration. Increases in scattered power were kept below receiver saturation by using an accurately calibrated attenuator between the antenna and the receiver to decrease the signal strength. Since the amount of attenuation (XdB say) used was known, this could be taken into account by multiplying (3.3.2.1) by $10^{X/20}$. Thus the actual voltages produced by the receiving aerials, V_A say, could be monitored.

However, V_A itself is not the most desirable unit in which to express the results. Variations in transmitter power will vary V_A, and it is desirable that the unit used to express amplitudes of scattered radiation be independent of transmitter power. In this way, the unit can be related directly to back-scatter cross-sections of the ionospheric scatterers. The unit chosen was

$$A = (V_A/V_{TX}) \qquad (3.3.2.2)$$

where V_{TX} is a parameter proportional to the peak amplitude of the transmitted pulse. An estimate of V_{TX} was obtained by measuring the voltage of the RF pulse transmitted on one side of a transmission line leading to a transmitting dipole (see Fig. 3.1). Call this V_{TX1}. To be consistent, this measurement was always made on the same side of the same transmission line, at the same point (close to the transmitter), and always when the transmitted radiation was O mode. O and X mode transmitted powers were assumed equal, and this appeared to be valid. It may be expected V_{TX1} could vary as the standing waves on the transmission lines varied with ground conditions, but the

effect was not noticeable. An alternative way of monitoring V_{TX} - namely, monitoring the signal strength on a properly terminated dipole some distance from the transmitting array to give a strength V_{TX2} - did appear to show considerable variation, depending on whether the ground was wet or dry. A plot of V_{TX1} against V_{TX2}, taken over several years, showed a roughly linear trend on any one day, but the slope varied significantly on different days, resulting in quite a large scatter when a composite graph was created. The reason for this is not fully understood, but may be due to changes in the ground conductances and the position of the effective electrical ground plane.

The following units were adopted.

At Buckland Park, the unit chosen was

(3.3.2.3) $$A = V_A/V_{TX},$$

where $V_A = (D_S/D_{SG}).V_{SG}$ (see 3.3.2.1).

V_{TX} was taken as the peak to peak pulse voltage measured on a transmission line divided by 200. This was done for both 2 and 6MHz. The division by 200 was chosen rather arbitrarily. V_{SG} was taken as the peak voltage of the CW signal fed in from the signal generator. Such units were called PRAIRS (Parameter of Reflection for Adelaide Ionospheric Research), and were denoted by Pr. Of course two measurements of this quantity as measured on a single dipole, and on several dipoles coupled together, cannot be compared directly. It is necessary to distinguish between them. Buckland Park is a large array of aerials (see shortly), and two particular configurations were commonly used

(a) 4 dipoles coupled together, to produce a wide polar diagram,

and (b) 89 dipoles coupled together, to produce a narrow polar diagram.

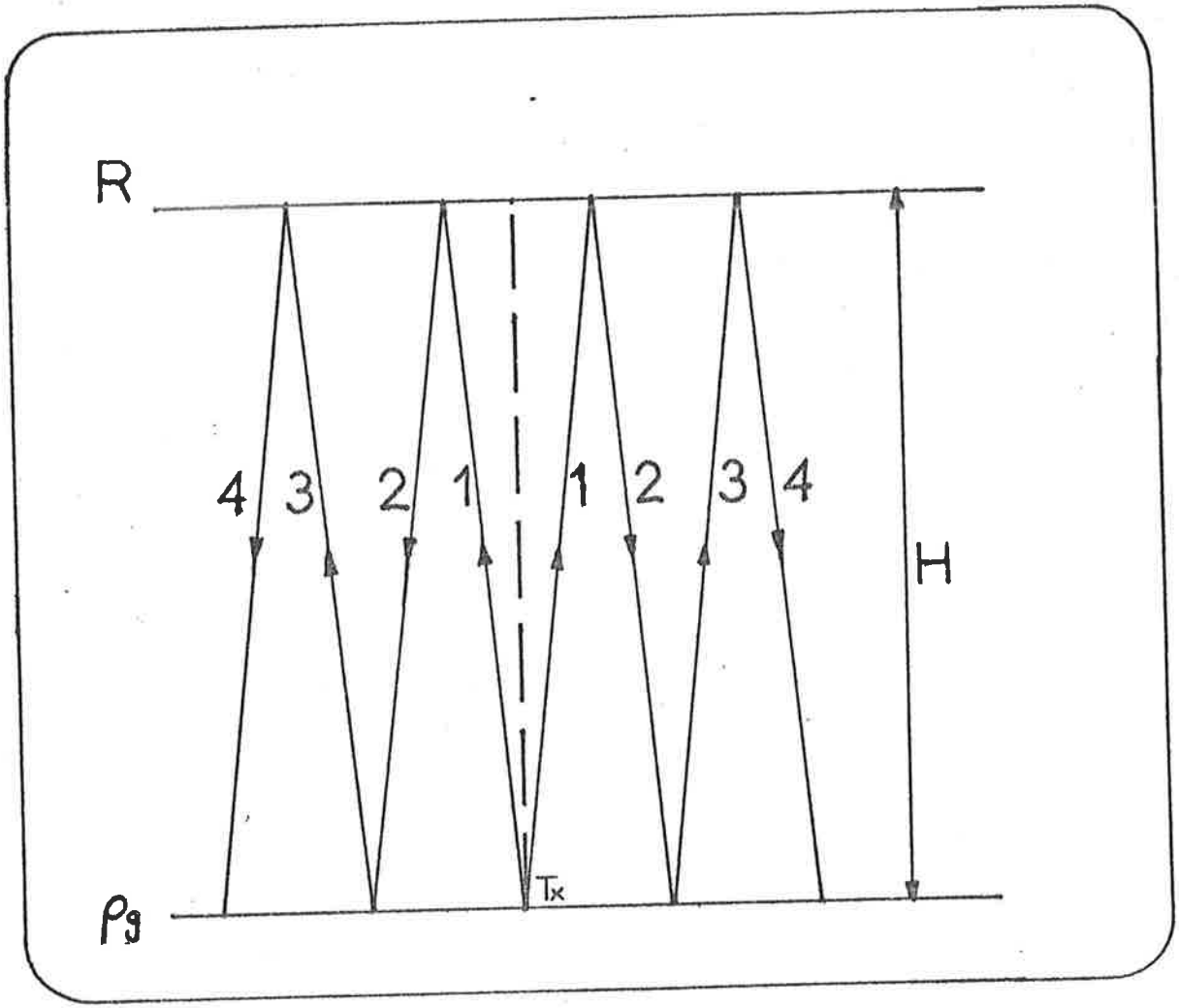

Fig. 3.4 Ray paths for a ray critically reflected from the ionosphere.

Prairs as measured on configuration (a) are denoted by Pr_{2W} (the 2 stands for 2 MHz, W for the "wide beam"). For case (b), Pr_{2M} (the 2 stands for 2MHz, M for "main array") was used. Similar definitions are possible at 6 MHz and Prairs produced by 6 MHz experiments are denoted Pr_{6W} and Pr_{6M}. [Pr_M, Pr_W may also be used. These will mean 2MHz.]

At Townsville,

(3.3.2.4) $$A = V_A/V_{TX}$$

where $V_A = (D_S/D_{SG}).V_{SG}$ (see 3.3.2.1).

V_{TX} was taken as the peak to peak pulse voltage measured on a particular transmission line, divided by 1000. V_{SG} was taken as the RMS voltage of the CW signal fed in from the signal generator. Such units were called TIRPs (Townsville Ionospheric Reflection Parameter), and were denoted by T. At Townsville, only one frequency (1.94MHz) and one aerial type (crossed inverted Vs) were used.

3.3.2b Relating Measurements to Reflection Coefficients

In Fig. 3.4 a transmitter is assumed to be at T_x, and a plane reflector is at height h, with a reflection coefficient R. Then the amplitude received by an array of dipoles is

$$V_A \propto (h)^{-1}.V_{TX}.R$$

(The wavefront emitted by the transmitter is assumed spherical, and falls off in amplitude as 1/r, r = distance travelled. In this case, r = 2h).

This gives

$R \propto (h)A$, A being the normalized amplitude defined previously.

Write this as

(3.3.2.6) $$R = K_*(h)A$$

If it is possible to determine K_*, and measure A, the reflection coefficient R can be determined. (K_* depends, of course, on the exact definition of A.)

Method I

One very simple way to measure K_* is to measure A at night, for scatter from a level which is known to produce total reflection. Such situations often occur when a strong sporadic E layer is present in the ionosphere. These are thin sheets of strong ionization. They produce almost complete reflection of incident radiation below their critical frequency, with very little absorption during this process (as distinct from say daytime critical reflection from the E region, when deviative absorption can be important - see Chapter I). If it is late at night, so there is very little D region ionization to cause non-deviative absorption, it can be assumed R = 1, so

(3.3.2.7) $$K_* = (h)^{-1}A^{-1}$$

Method II

Method I requires very special conditions, and one can never be sure that there is no D region absorption. A better technique can be produced by examination of Fig. 3.4. The pulse produced by the transmitter propagates up to the reflection region and back, suffering absorption along the way. Let R' be an effective reflection coefficient, equal to the field strength received at the ground divided by the field strength which would have been received had R been equal to 1, and had there been no absorption.

(3.3.2.8) Then $$R' = R\, e^{-2\frac{\omega}{c}\int_0^z \mu_I . dz}$$

where μ_I is the imaginary part of the ionospheric refractive index at height z, and the integral is performed up to the height of reflection z. The "2" arises because the pulse must go up and back.

Then the normalized amplitude measured by the Receiver/Transmitter system is

(3.3.2.9) $$A_1 = K_*^{-1}(h)^{-1}R'.$$

Upon striking the ground, much of the radiation will be re-reflected back up to the reflection height and back to the ground (paths 3 and 4 in Fig. 3.4). The result will be another pulse on the CRO, at a virtual height of 2h, and reduced in amplitude. The process repeats itself, and pulses at heights 3h, 4h, etc. will be produced. This second pulse (called a "second hop" echo) will have a strength

(3.3.2.10) $$A_2 = [K_*^{-1}(2h)^{-1}R'].\rho_g R'$$

The (2h) arises because the pulse has now travelled a distance twice that in producing A_1. The term ρ_g represents the ground reflection coefficient. The R' term arises again because the pulse again suffers absorption and reflection, as along paths (1) and (2).

(3.3.2.11) $$A_2 = K_*^{-1}(2h)^{-1}(R')^2\rho_g$$

Generally, this second hop is far too weak to see for D region scatterers (R' less than about 10^{-3}), but for E region reflection, a second hop can often be seen, particularly on days of weak D-region absorption. At night, several "hops" of the night time F region echo can often be seen on 2MHz. If there is a sporadic E, as discussed in

method I, this may hide the F region echo (it reflects all the radiation, preventing any propagation to higher levels), but it will have its own second, third etc. hops.

By (3.3.2.9) and (3.3.2.11),

$$\frac{A_1^2}{A_2} = \frac{K_*^{-2}h^{-2}(R')^2}{K_*^{-1}(2h)^{-1}(R')^2\rho_g}$$

or

(3.3.2.12) $$K_* = \left(\frac{2}{h} \cdot \frac{A_2}{A_1^2}\right)\cdot\frac{1}{\rho_g}$$

The quantity

(3.3.2.13) $$K = \frac{2}{h} \cdot \frac{A_2}{A_1^2}$$

can readily be measured. If ρ_g is also known, K_* can be calculated, and the array will be fully calibrated. Any measurement of A can be directly related to an effective reflection coefficient, R', allowing comparisons between measurements made at different sites, and allowing comparisons of experiment and theory.

The main relation is

(3.3.2.14) $$\boxed{R' = K_* h A,} \quad \text{where} \quad K_* = \rho_g^{-1}K,$$

and K is defined by 3.3.2.13. Alternatively, K_* can be found by (3.3.2.7) at times.

Of course, each type of unit A has its own K and K_*. (See 3.3.2.3 and 3.3.2.4). For example, a 4-dipole array at Buckland Park, working at 2MHz, has a value K_{2W}. Using the full array at Buckland Park, one uses a constant K_{2M} at 2MHz, and K_{6M} at 6MHz. At Townsville,

Fig. 3.5 Illustration of some of the effects which can produce fading. The surfaces represent isopleths of constant electron density with a critical frequency equal to that of the incident radio wave. The arrowed lines represent ray paths.

(a) shows focussing - radiation transmitted is focussed at the receiver, thus producing an increase in power;
(b) represents focussing which occurs after 2 hops
(c) represents de-focussing, which implies only a weak signal is received;
(d) represents beating. The oblique ray, upon reflection, has a Doppler shift, and beats with the vertical ray
(e) represents the effect of a tilt. Vertically propagating radiation does not return to the receiver, but is reflected away. However, there is still a strong signal due to the ray incident normally upon the isopleth - unless the system has a very narrow polar diagram. As time progresses, these isopleths move and change form, thus producing fading.
(f) shows a typical amplitude distribution for E region fading.

In connection with (d), it may be noted that if the oblique scatter is at a large range, the reflected pulse may not significantly overlap that due to the vertical reflection. There will be little beating in this case, but the obliquely reflected pulse will produce its own "echo" at a greater virtual range than the E region echo. In general, there usually are such weaker echoes at greater virtual ranges than the E region. It should be borne in mind that these are generally not due to scatter from above the E region, but oblique scatter. Multiple reflections between the E layer and a strong 90km D region echo can also produce some of these echoes at large virtual range.

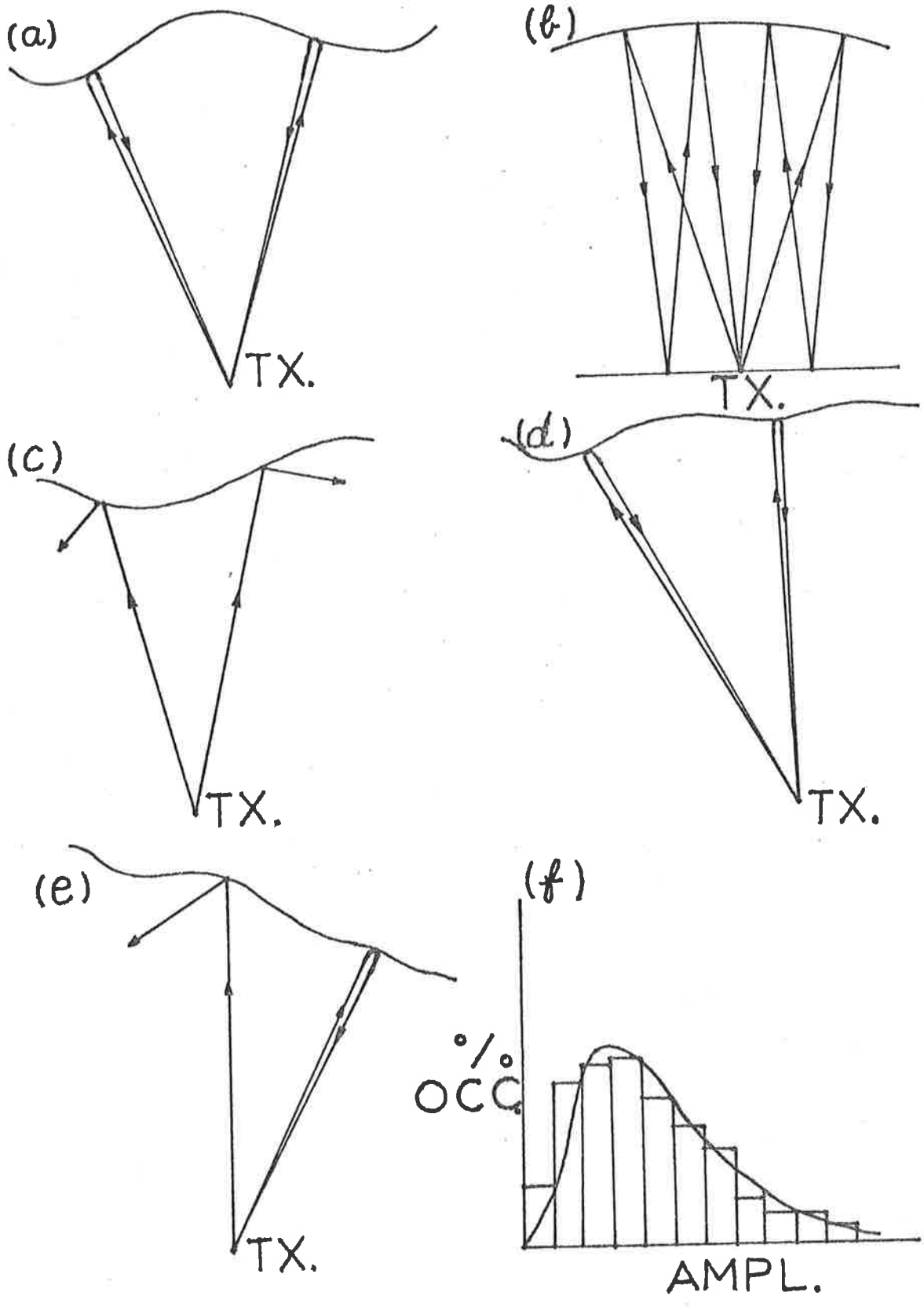
(a)
TX.
(b)
TX.
(c)
TX.
(d)
TX.
(e)
TX.
(f)
% OCC.
AMPL.

the constant is denoted K_{T3} (The "3" indicates that aerial 3 (C in Fig. 3.1) is used at Townsville, as distinct from aerials A and B.) It makes no sense to compare A values produced with the different arrays, but comparisons of R' values is both meaningful and important.

3.3.2c Experimental Determination of Calibration Constants

Before the work for this thesis the Buckland Park array had never been calibrated. By doing such calibrations, a new dimension was added to investigations of D region scatterers. Although in principal estimate of K is quite simple, in practice it can be quite difficult. Piggott et al. (1957) have discussed this to some degree. The power received by a receiving system from a particular height varies considerably as a function of time - the echoes are said to "fade". These variations in time of the signal have already been mentioned, and examples shown in Fig. 3.1. The fading occurs due to a variety of processes. For total reflection from the E region, two of the main reasons are focusing effects, and tilting of the isopleths of constant electron density. Beating of signals scattered from various oblique angles can also play a role. Fig. 3.5 illustrates these processes. In general it is necessary to obtain average A_1 and A_2 values, although a freak occurrence of a large amplitude "burst" can bias this mean, and it is often better to plot amplitude histograms as well. To minimize these effects, days should be chosen when fading is very slow (on these occasions, the constant electron density isopleths should be fairly flat). Further, during the daytime the E_2 (second hop E echo) is often close to the noise level (D region absorption weakens the E_2 echo). There can be a danger that E_2 values are only recorded during focussing as in Fig. 3.5b, giving biased K values.

Table 3.1 Table of estimates of K_* and K. These are estimated for use in the equation (3.3.2.14), $R' = K_* hA$, A being received amplitude of signal in calibrated power units, h the height of the scatterer and R' the effective reflection coefficient. Generally, K_* has been obtained from K. ie. $K_* = \rho_g^{-1} K$, and in all cases here, ρ_g has been assumed to equal $10^{-4/20}$ (ie. a 4dB loss on reflection), except in those mentioned, (in one or two cases direct measurement of K_* was made).

The various estimates of K and K_* have quite large errors, since in general observations were made by eye. This was because the recording equipment could not record echoes at a vertical height of 200km - about the usual E_2 range. However, measurements of (K_W/K_M) could be made quite accurately, by recording the same signal on the 2 arrays (wide beam and narrow (main) beam), and assuming R' was the same in each case. Comparisons of the normalized power estimates allowed accurate determination of (K_{2M}/K_{2W}). For example, on day 77/151, comparison was made using a 73km D-region echo which was known to be from a Fresnel-like, flat reflector. Knowledge of this ratio (K_{2M}/K_{2W}) will be useful later for comparison of signal strength received on the two aerial arrays.

It will be noticed that there is a considerable degree of fluctuation in the K values. This is partly experimental error (see text), and may also be function of season. For example, changes in ground conditions may change the polar diagram, and hence gain, of the array, thus altering the K values. In this thesis, the one K value will be used throughout for each system, but perhaps later workers could obtain K values as a function of season. Ideally, a K value should be obtained each day an experiment is carried out.

It will be noticed that the earlier K_{T3} estimate were around 1.7, but later estimates were around 0.6. This is probably because these were daytime measurements, so the E_2 echo was very weak. As discussed in the text, this can lead to a bias of taking periods when E_2 focussing occurs (see Figure 3.5b), thus leading to over-estimates of K_{T3}. This problem was not quite so severe at Buckland Park, where increased transmitter power, and better receiving aerials meant the E_2 was usually above the noise level.

Table 3.1 : Calibration Constants.

K / Day of Observation	77/118 & 77/151	77/284	77/304-9	78/047	78/076	78/146	78/155-163	78/278	78/306	79/248	79/274	80/020	80/064	80/065	80/071	80/072
K_{2W}	.42±.3	.9±.4			.8±.4			1.2±.3	1.0±.1							
K_{*2W}	.6±.5	1.5±.7			1.3±.6			1.9±.5	1.2							
K_{2M}	.3±.3	.5±.3		.12± ?	.5±.2			.7±.1	0.6	3.6						
K_{*2M}	.4±.4	.8±.4		.19± ?	.8±.3			1.1±.2	.75	5.7						
K_{2W}/K_{2M}	1.6±.3					1.75		2.0±.3								
K_{6M}										1.6			2.8±1.2	1.7±1.0	3.5	1.7±.5
K_{*6M}										2.4			4.5±2.0	2.7±1.6	5.6	2.7±.8
K_{T3}			1.1±.3				.4±.2				.4±.2	.35				
K_{*T3}							.6±.3				.6±.3	.55				
Comments	Day	Day	Day - Bad Estimates	Bad Fading - bad Estimates	Dry - Quite Good		Night Time - Good Estimates	Day - Quite Good	Night - Ex.	Day - Bad fading - Very wet						
X Indicates bad conditions			X	X						X						

Notes

(1) 78/306 Direct measurement of K_* and K in both cases. Sugests $\rho_g \equiv$ 2dB loss on reflection, (and 5dB at worst) for Buckland Park. This is not surprising, as discussed in Section 3.3.1.

(2) 79/248 These measurements may be unreliable, as fading was bad. However, they may also indicate possible changes in K due to changes in ground effects. This possibility should be borne in mind (see caption).

(3) K_{T3} Measurements represent averages over the periods shown. Not all K_{T3} individual measurements are shown.

(4) 78/156 (0400-0600 hrs). Direct measurement of both K_{*T3} and K_{T3}. This suggested $\rho_g \equiv \sim$ 3dB loss on reflection at Townsville.

(5) 78/274 (0300 hrs) suggested $\rho_g \sim$ 4dB at Townsville.

Conclusion

$K_{2W} = 1.0 \pm .4$; $K_{*2W} = 1.5 \pm .6$; $K_{2M} = 0.5 \pm .3$; $K_{*2M} = .8 \pm .4$;

$K_{2W}/K_{2M} = (K_{*2W}/K_{*2M}) = 1.8 \pm .4$; $K_{6M} = 2.4 \pm 1.0$;

$K_{*6M} = 3.8 \pm 1.6$; $K_{T3} = 0.4 \pm .2$; $K_{*T3} = 0.6 \pm .3$

In these final estimates I assume $\rho_g = 0.67$ ($\equiv$ 3.5dB) for 2MHz, and $\rho_g \equiv$ 4dB for 6MHz.

To obtain the best K values, night time observations, using a strong, slowly fading sporadic E echo (or even the F layer) should be used at 2MHz. At 6MHz, critical reflection occurs from the F layer, not the E. However, absorption at 6MHz is considerably weaker than at 2MHz, and F_2 echoes can usually be seen in the daytime. The K_6 estimates are possible in the daytime.

At times, it is possible to use both method I (to calculate K_*) and method II (to calculate K) if a good early morning E_s can be found. This allows estimates of ρ_g. This has been done on two occasions at Townsville, and it was found ρ_g corresponded to about 3 to 4dB loss on reflection (i.e. reflection coefficient of about $10^{-3/20}$). This is in line with suggestions made in Section 3.3.1. However, the accuracy involved in these measurements is uncertain, and may be as large as ± 3dB.

Table 3.1 summarizes all useful measurements of the various K and K_* values, with comments as to their accuracy.

3.3.2d Turbulent Scatter

The previous discussions have been based on Fresnel type reflection, but the possibility of turbulent scatter also exists. These calibration constants can also be used to determine backscatter cross-sections. Imagine a wavefield incident on a volume of scatterers. Then define η as the scattered power per unit volume of scatterer which would be radiated into a full $4\pi^c$ if all the scattered power was the same as the backscattered power, for unit incident power. Alternatively, define σ as the back-scattered power per unit steradian per unit volume of scatterer, for unit incident power. Both these terms are called "cross-sections of backscatter". (Also see section 2.4, chapter II). It is clear

(3.3.2.15) $\eta = 4\pi\sigma$.

Now recall

(3.3.2.14) $R' = K_* hA$

is the strength received at the ground divided by the field strength which would have been received had there been total reflection and no absorption. If we have non-Fresnel reflection, the quantity

(3.3.2.17) $(R')^2 = K_*^2 h^2 A^2$

may be more useful. It represents the power received at the ground divided by the power which would have been received had there been Fresnel total reflection and no absorption.

But now consider a wave field emitted from a transmitter with Poynting vector of magnitude P_t at unit range. At a range h, the Poynting vector magnitude is P_t/h^2. Suppose the wave is now scattered by a region with backscatter cross section σ. The backscattered power per unit steradian is

$$(P_t/h^2).e^{-\frac{2\omega}{c}\int_0^h \mu_I ds} . V_{eff} ,$$

V_{eff} being the volume of space producing the scatter (this is defined by the beam of the polar diagram and the pulse length). Each scatterer in the region scatters independently, so no longer does the energy travel as a single wave front. Rather, the power again falls off as $1/h^2$. Thus the power per unit area received at the ground is

(3.3.2.17) $$e^{-4\int_0^h \frac{\omega}{c} \mu_I ds} (\sigma P_t/h^2)\frac{V_{eff}}{h^2} = \sigma P_t/h^4 . e^{-4\int_0^h \frac{\omega}{c} \mu_I ds} . V_{eff}$$

Suppose there had been total Fresnel reflection at height h and no absorption. The power per unit area received at the ground would have been

(3.3.2.18) $\quad P_t/(2h)^2 = P_t/(4h^2)$

But the ratio of 3.3.2.17 to 3.3.2.18 is just R'^2, as defined above, so these two equations imply

$$R'^2 = \sigma P_t/h^4/P_t/(4h^2).e^{-4\int_0^h \frac{\omega}{c}\mu_I ds}.V_{eff} = (R^2).e^{-4\int_0^h \frac{\omega}{c}\mu_I ds} \quad \text{say,}$$

so

(3.3.2.19) $\quad R^2 = (\frac{4\sigma}{h})^{V_{eff}} = (\eta/(\pi h^2)).V_{eff} = \eta\theta_0^2 L$

[as $\frac{V_{eff}}{h^2} = \pi\theta_0^2 L$, where L = pulse length, θ_0 = ½ power ½ width of the beam]

(This formula may also be seen by equation 13c of Flood (1968), since R^2 as defined above = $|E_s|^2/|E_0/2|^2$ in Flood's notation, and Flood's "σ" is equivalent to our η times the effective volume).

So if the received power is averaged over some time, and

(3.3.2.20) $\quad \overline{R'^2} = K_*^2 h^2 \overline{A^2}$

and thence $\overline{R^2} = \overline{R'^2}.e^{4\int_0^h \frac{\omega}{c}\mu_I ds}$

found, the crossection of backscatter can be found by means of equation (3.3.2.19). Having thus obtained σ, it is now possible to estimate terms such as C_n^2 (see Chapter II, section 2.4).

However, as discussed in Chapter II, it should be noted that these estimates of σ and η are average values for the radar volume (that is, that region of the ionosphere covered by the width of the polar diagram and the depth defined by width of the pulse for a range r_0). If the scatter comes from a few isolated scatterers within this volume, the σ and η values for these scatterers will in fact be much larger than these average values.

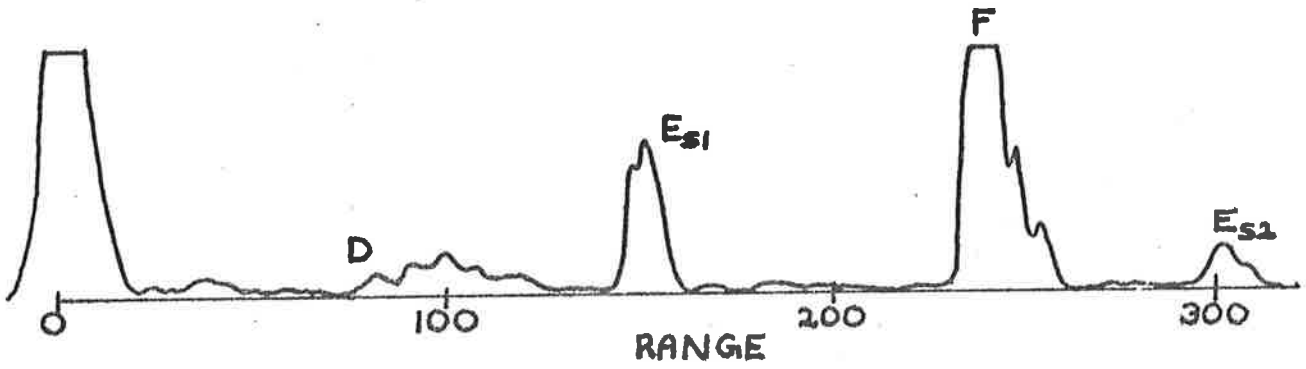

Fig. 3.6 One form of night-time echo structure as seen at a frequency of around 2MHz. The diagram is only crudely to scale vertically; D region echoes correspond to reflection coefficients of around 10^{-4} to 10^{-2}, whilst the E_{S1} echo, and F echo, correspond to effective reflection coefficients R' of greater than 10^{-1}.

3.4 Some Simple Observations

Although most of the results discussed in this thesis were obtained by recording the data on digital magnetic tape and later analysing the results on a computer, a surprising amount of information can be gained by just watching the received signal on the CRO.

As discussed, Fig. 1.10 illustrates typical day time conditions. But it is instructive to consider the changes which occur at other times in the day. I shall describe the situation seen on 2MHz during one day. As the sun sets, D region absorption decreases, as the electron density decreases. The totally reflected E region echo eventually disappears (and this disappearance can be quite rapid, as the electron density critical frequency falls below 2MHz). This allows propagation of the radiation to higher heights, and total reflection now does not occur until about 250-300km. By this time it is perhaps 2100 hours. The partial reflections below 80km have disappeared, but some still exist between 80 and 110km. These can show quite strongly, as the D region absorption is reduced. However, the noise is now at its worst for the 24 hours, presumably because the decreased D region absorption allows propagation of noise signals over larger distances (a plot of the noise as a function of time of day will be given in a later chapter). The situation may then stay like this all night - total reflection from about 250-300km, and weak scatter from 80-110km. However, often a "sporadic E" can form in the region 110 to 200km, and this is a very interesting scatterer. It may reflect all incident radiation (a "blanketing" layer) but at times it can be only partially reflecting, so the higher F region reflection can still be seen. Fig. 3.6 presents an example of such a case. Notice also the presence of the second hop E_{S2}. There would also be second, third and fourth etc. F hops (F_2, F_3, F_4, at multiples of 240km (the F_1 echo height).

This "E_S" generally moves down during the night. Many sporadic E layers are generally thought to be due to convergence of metallic ions produced by East-West vertical wind shears. (e.g. Whitehead (1961); Whitehead (1976); Miller and Smith (1978, Fig. 14), Smith and Miller (1980)). North-South wind shears can at times also produce an effect. Usually E_S layers are thought to occur around 100-120km, but these weaker, higher "E_S type" layers do occur (e.g. see MacDougall (1974); Rowe (1974); MacDougall (1978)). These are also called "sequential E_S" layers. MacDougall (1974, 1978) has explained them as being due to the wind shear mechanism acting at the nodes of tides in the ionosphere. Thus their downward propagation actually indicates the phase progression of these tides. This can be used to determine whether the diurnal or semidiurnal component dominates, and also allows determination of the phase (e.g. MacDougall (1974, 1978)). Briggs and Vincent (private communication) have shown that the phase determined by these E_S echoes matches well that determined by PRD measurements.

At other times, particularly during January at Adelaide, and regularly at Townsville, another E_S layer can form at about 90 to 100km. This can often last all night - and at times, can even exist during the day, partly masking the "usual" E echo, and also hiding some of the higher D region echoes. This E_S layer at Townsville can be interesting to watch at night. Sometimes it totally reflects X mode polarized 1.94MHz radiation, but allows propagation of O mode to greater heights. (The X mode critical frequency for a given electron density is greater than that for O mode). This fact will be utilized later (section 4.2.4a, Chapter IV).

Around midnight, the radio noise decreases somewhat. Absorption also continues to decrease. (This can be seen by examining the strength of X mode F reflections). By early morning, absorption is at its lowest. Then, at sunrise, the region becomes quite active. The electron densities begin to build up rapidly, and absorption increases. The noise drops

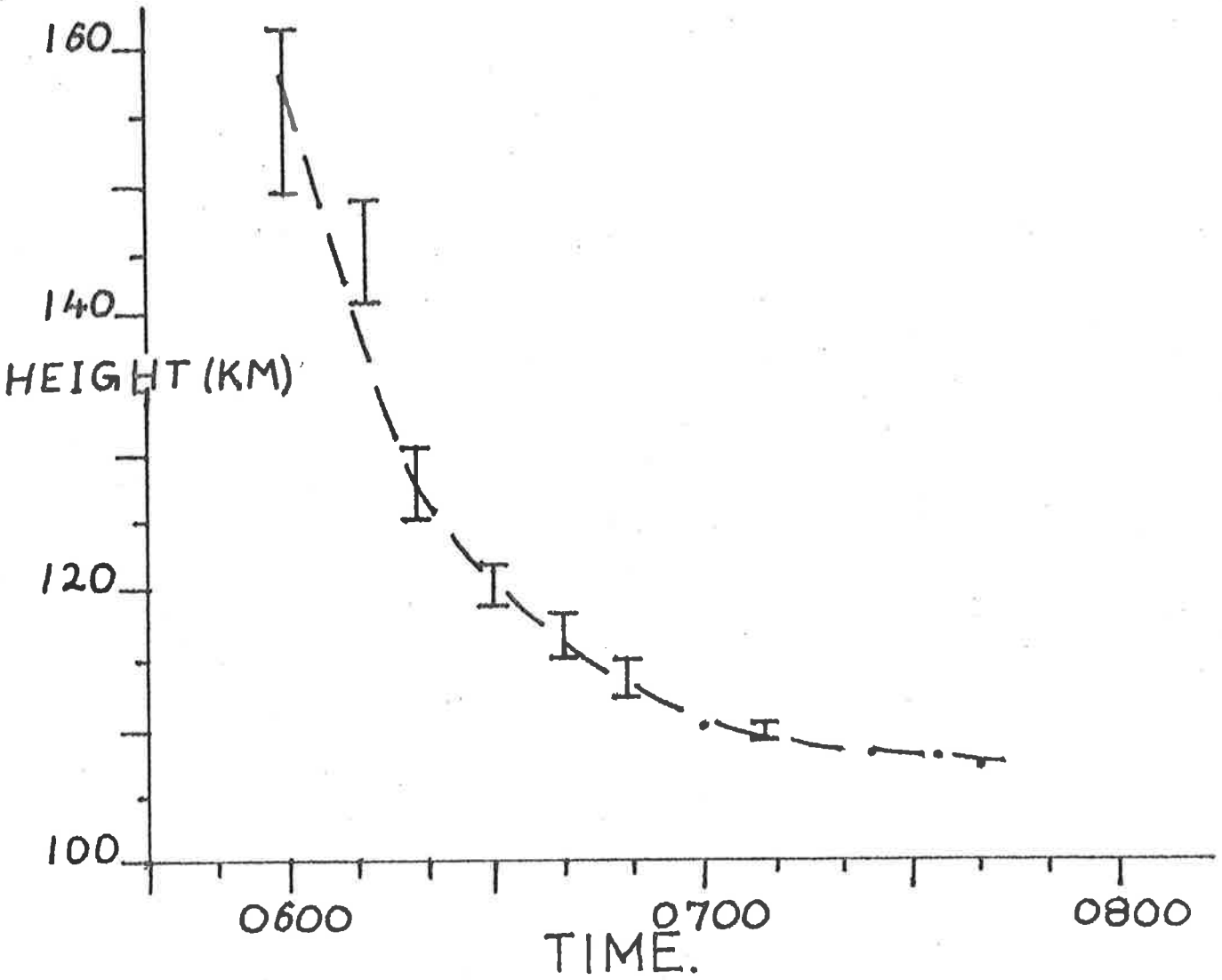

Fig. 3.7 Early morning development of the E layer. This graph shows the height of critical reflection at 1.94MHz, O mode, as a function of time, for January 19, 1980 at Townsville. The error bars give an idea of the variability of height of the critical level of reflection over a 5 to 10 minute period. By 0700, the critical reflection level is nearly stable, and the E layer has formed.

Fig. 3.8 (a) & (b)

Absorption L vs. time of day (Eastern Standard Time) for Townsville, Australia, during January 1980.

Graph (a) shows "normal" conditions, with a smooth daily variation of absorption. After about 2100 at night, and before about 0600, absorption is generally less than about 10 to 20dB.

The graphs in (b) show behaviour after a major flare on the sun on day 25. The smoother curve is typical of the days before day 26. It can be seen day 26 is a little abnormal with quite a sharp fall to high absorption by 0900. Day 28 is particularly "abnormal". Two periods can be seen when absorption increased dramatically (0930 and 1300) (these are termed Short Wave fadeouts). The general character of these days is a rapid increase in absorption around sunrise, an approximately constant value to sunset, and then a rapid rise.

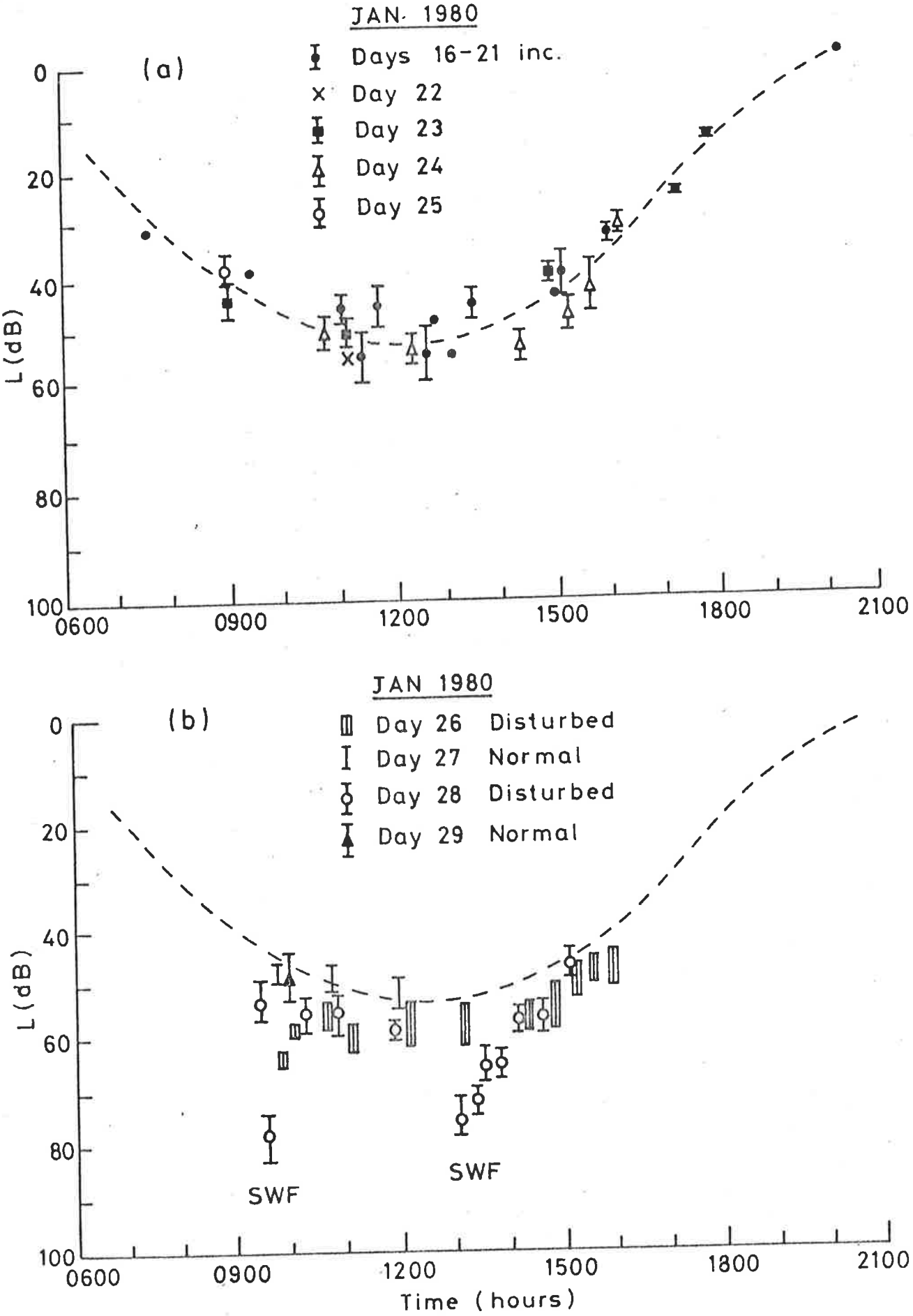
JAN. 1980
(a)
Days 16-21 inc.
Day 22
Day 23
Day 24
Day 25
L(dB)
0
20
40
60
80
100
0600
0900
1200
1500
1800
2100
JAN 1980
(b)
Day 26 Disturbed
Day 27 Normal
Day 28 Disturbed
Day 29 Normal
SWF
SWF
Time (hours)

considerably. Finally, a totally reflected echo appears quite high up (around 150km), and as the electron density builds up, this echo moves down. Fig. 3.7 shows the typical movement of such an echo. It can be seen that it falls about 20 to 30km in 20 minutes initially - a very rapid fall. Also, the lower D region echoes begin to show (although D region echoes are not always observed), and by perhaps 0900, a picture like Fig. 1.10 again emerges (although the actual heights of the D region echoes may vary).

The build-up of D region total electron density is illustrated best by Figs. 3.8 (a and b). In these graphs, the E region strength is used to estimate the parameter L (see equation 1.2.3.1) at Townsville. Larger L values crudely mean greater D region total electron densities. The graphs illustrate how the total absorption changes. They show some of the diurnal changes discussed in section 1.2.3 of Chapter I - graph (a) shows a typical $\cos^{n}(\chi)$ variation (χ = solar zenith angle), and (b) shows cases where the absorption increases rapidly at sunrise, remains high all day, and then decreases at sunset. Case (b) also shows some typical short wave fadeouts. The case (b) occurred after a major solar flare on Jan. 25, 1980, and magnetic disturbances were reported after this event. Such effects are due to increase X ray activity, (e.g. Taubenheim, 1962), and delayed effects are thought to be due to precipitating electrons (e.g. see Chapter I, Section 1.2.3 e.g. Montbriand and Belrose, 1976 etc.).

3.5 The Field Sites

The previous sections of this chapter have basically been devoted to general discussions of observational technique. It will now be fruitful to discuss some of the more specific aspects of the various systems used in the work for this thesis.

3.5.1 Buckland Park

Buckland Park was the largest and most powerful installation used for this thesis. The transmitter arrays (2 and 6MHz) are similar in form to the general form already discussed - namely, four half wave folded dipoles arranged in the form of a square, about one quarter of a wavelength above the ground (actually, about 30 metres above the ground at 2MHz and 10m at 6MHz). The dipoles are fed by 600Ω transmission lines (each 47m long). (This length was chosen so that the impedance at the transmitter was purely real.) The impedance seen at the transmitter end of these lines is roughly 350-400Ω (almost purely resistive), and so when all four are coupled together in parallel, this gives an impedance of about 80Ω. As discussed, opposite dipoles transmit in phase, and may be given a phase shift with respect to the other pair to produce O or X mode polarization. The aerials are matched to the transmitter output impedance. The 600Ω transmission line does not match to the aerial perfectly, but the Standing Wave Ratio is less than 1.7.

The transmitter power could be monitored by measuring the voltage of the pulse on one side of a transmission line near the transmitter. This gives a value of typically 1000 volts peak, suggesting the voltage difference across the transmission line would be 2000V. The peak output power is thus typically $E_0^2/R = (2000)^2/(80\Omega)$, or about 50kW.

The receiving array comprises a square grid of 89 pairs of crossed orthogonal half-wave dipoles (for 1.98MHz) with a circular perimeter,

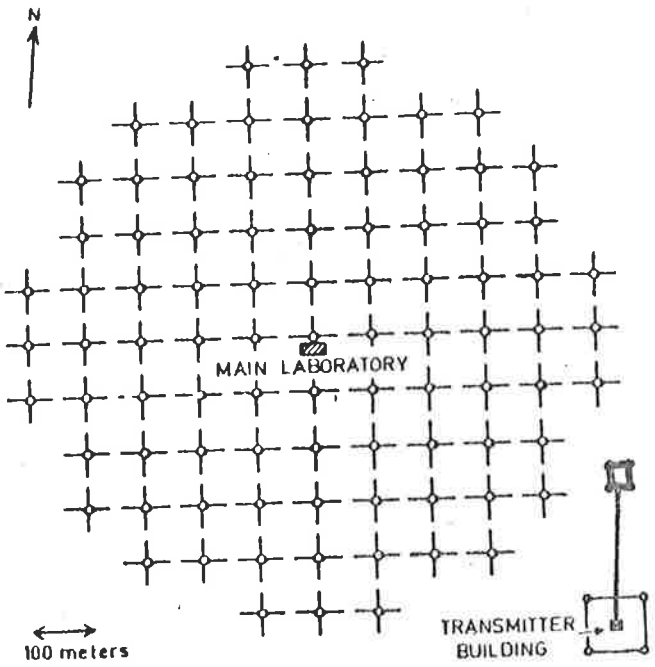

Fig. 3.9 Plan of the Buckland Park Array. There are 89 pairs of crossed orthogonal dipoles. Each of the 178 dipoles is connected to the main laboratory by a separate underground coaxial cable. The 2MHz transmitting aerial consists of four folded dipoles arranged to form a square, with the transmitter in the centre. The 6MHz transmitting aerial is represented by the small square north of the 2MHz array. The 6MHz transmitter is housed in the transmitter building, and its signal carried to the aerials by a transmission line. The diagram comes from Briggs et al. (1969).

Fig. 3.10

(a) A long view of the Buckland Park Aerial Array. The extremely tall towers in the middle are 1.98MHz transmitter towers, about 30m high. There are four of these in the form of a square, with horizontal folded dipoles between them. The building in the foreground is the technician's workshop. The small building to the right of the sign in the very background is the central receiving hut. The 6MHz transmitter array was to the right of this photo. Both transmitters were located in the transmitter hut, which is hidden behind the sign. The faint vertical poles behind the transmitter towers are the posts used to support the receiver aerials. They cover the full width of this photo and more.

(b) The central receiver hut at Buckland Park. The vertical pole is one of the supports for the 178 receiving dipoles. On the top, a small box exists (just out of the photo), and this transforms the impedance of the dipole to 70Ω, so it can be matched to the cable which carries the signal back to the central hut. All cables are buried underground, and are a multiple of half wavelengths long, so all signals arrive back at the hut in phase.

The instrumentation in the receiver hut is not shown. It is similar to that in the Townsville photos shown later except that a mini-computer is also attached. Likewise the actual transmitters resemble the Townsville one.

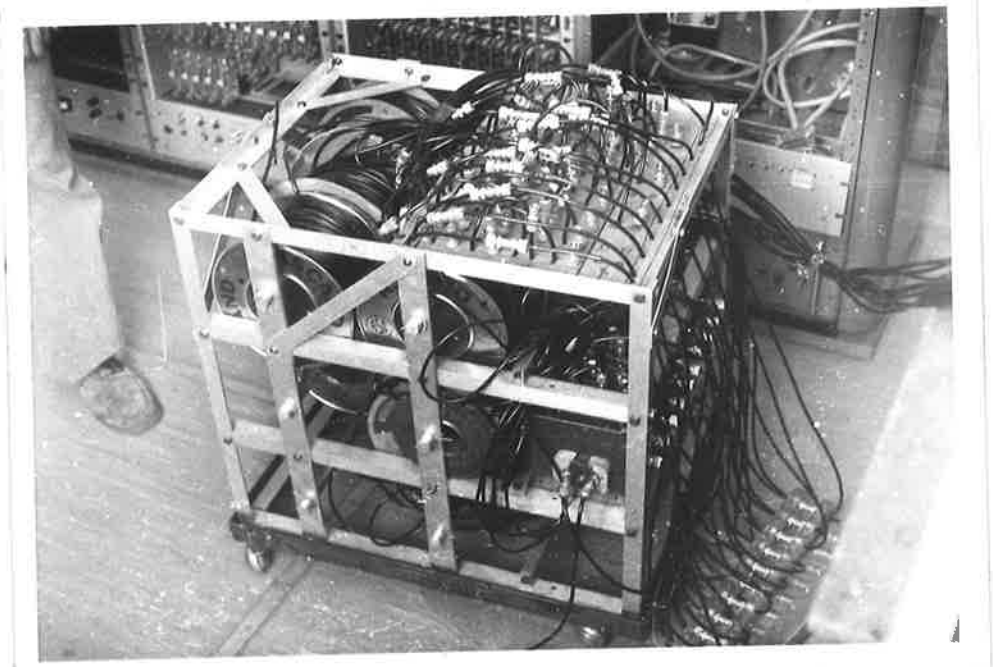

Fig. 3.10c Photograph of the instrument used to tilt the beam of the array.

the dipoles being separated by 0.6 wavelengths and the array diameter being about 900 metres. The dipoles are close to resonant at the transmitted frequencies of 1.98MHz (when they are half-wave dipoles) and 5.995MHz (when they are three half-wavelength dipoles). Each dipole is connected independently to a central receiving hut.

A more complete description of the array can be found in Briggs et al. (1969). Fig. 3.9 shows a plan of the array, and Figs. 3.10a and b some photographs of the array.

In the early work for this thesis, only 2MHz was used. The 6MHz transmitter was not finished until late 1979. When used at 2MHz, the array was generally used in the following manner. A full set of 89 parallel dipoles (generally those aligned East-West) were coupled together to form a large array with a narrow polar diagram. This polar diagram had half-power points at ± 4.5°, and the first minimum was at 11.6° from the zenith when phased for reception from the vertical. This beam will be referred to as the "narrow" or main beam. Twelve of the North-South aligned dipoles of the array were used to simultaneously measure winds by the partial reflection drift technique. These twelve dipoles were used to form an approximately equilateral triangle, each corner of the triangle comprising a set of four adjacent dipoles in the form of a square coupled together. The half power width of the polar diagram of such a square was approximately 20°. This beam will be called a "wide" beam. For more information concerning measurement of winds see Stubbs (1973).

One of the earliest projects for the work of this thesis was the construction of a phasing system to tilt the narrow beam of the array when operating at 2MHz. The dipoles were coupled into eleven rows, and the impedances transformed to 50Ω. Phase shifts were introduced for each row by passing the signals through 50Ω cables of appropriate length. These phase shifted signals were then coupled together, transformed up to 50Ω

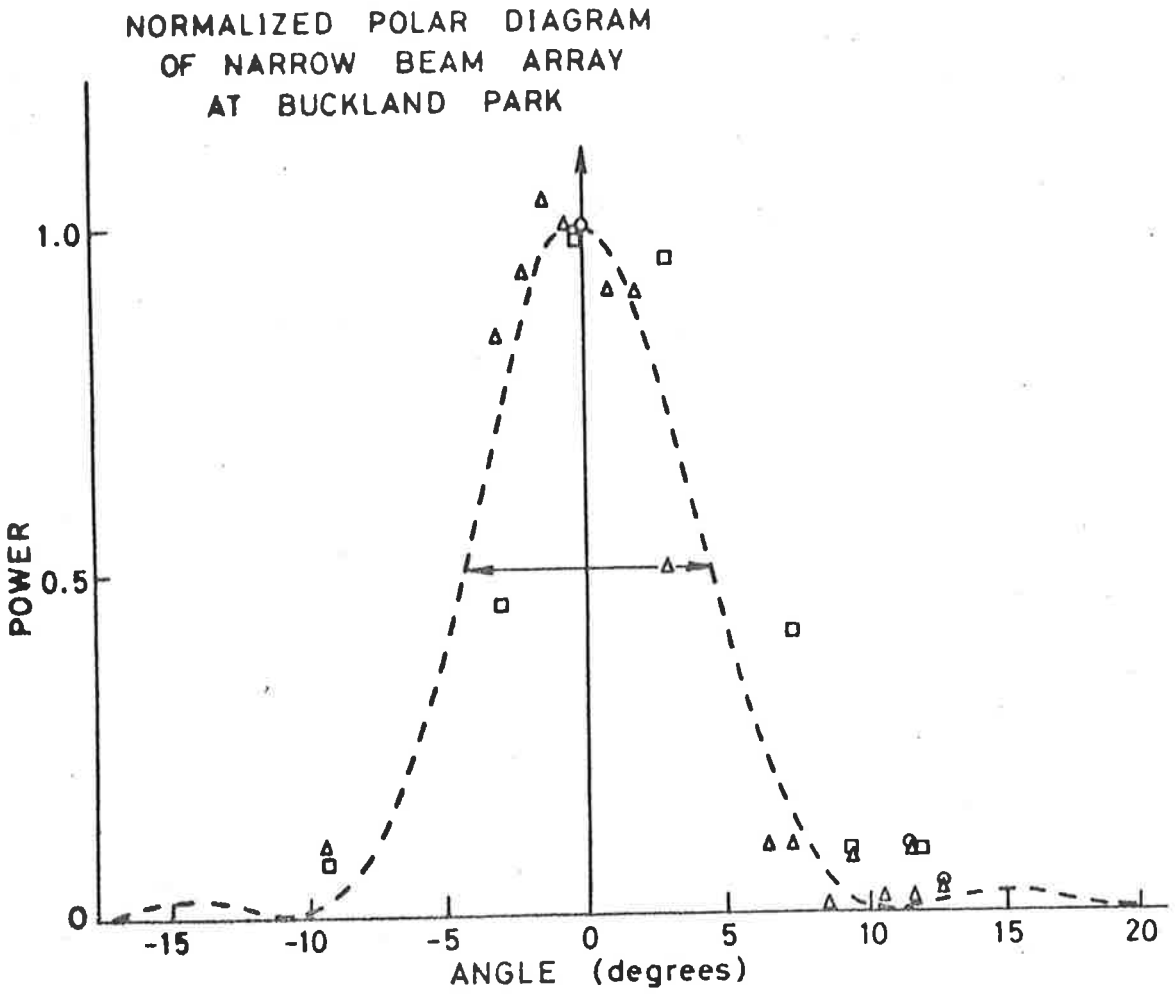

Fig. 3.11 Measurements of E region scattered signal strengths as a function of tilt angles from the vertical for the full array at Buckland Park. The measurements have been normalized to 1.0 at a tilt angle of 0°. The broken line represents the theoretically predicted polar diagram (see text). Agreement is quite reasonable. Notice on day 76/202, the E region appears to have a small tilt. (The various symbols refer to

Δ 76/202 (202nd day of 1976)
O 76/209
□ 76/259

again, and then fed into the receiver. By means of a series of switches, the phase shifts between successive rows could be altered, thus altering the tilt angle of the beam. If the phase shift between successive rows was ϕ radians, the angle of tilt from the vertical was

3.5.1.1 $\theta = \sin^{-1}((\phi/2\pi).(1/0.6))$,

since adjacent rows of the array were 0.6 wavelengths apart. The phase could be adjusted in steps of cable lengths of .01λ, λ being the wavelength. This corresponds to steps of ϕ of $\Delta\phi = 2\pi/100^c$, although there were some multiples of $\Delta\phi$ which could not be attained. Generally, however, it was possible to tilt the beam in small steps ($\Delta\theta \sim 1°$ in the range $\theta = 0°$ to $20°$, and increasingly coarser steps at larger θ) from $\theta = 0°$ to $\theta = 90°$. A more complete discussion of this beam swinging apparatus will not be given here. One can be found in Hocking (1976). Fig. 3.10c shows a photograph of the beam swinging apparatus.

The phasing system was tested initially by measuring E-region reflected powers at a variety of angles, on those occasions when the E-region appeared to be behaving as a smooth horizontal mirror. The received signal strength varied as a function of angle in the manner expected from the theoretically predicted polar diagram. Fig. 3.11 shows some typical results.

The polar diagram of the full array was calculated numerically on a computer. The subroutine used for this calculation is called "BPRES" and can be found in program "VOLSCAT", which appears in the appendices. The effects of the dipoles were summed, incorporating the dipole polar diagrams. The ground was considered by including a ground reflection coefficient. The major weakness of the program was that this reflection coefficient was assumed to be real, with a phase change of π^c upon

Figs. 3.12 Slices through the polar diagrams of the Buckland Park Aerial array. These diagrams are the combined polar diagrams of the transmitter and receiver aerials. All assume a reflection coefficient at the ground of 1.0, with a π^c phase change. Changing the ground reflection coefficient does not greatly affect the shape of the polar diagram-at least, not near 0°. The 2MHz array uses $\lambda/2$ dipoles for transmission and reception, and the 6MHz system uses $\lambda/2$ dipoles for transmission and $3\lambda/2$ dipoles for reception. The receiving dipoles are 10m above the ground. The 2MHz T_X dipoles are 30m above ground, and the 6MHz T_X dipoles 10m above ground. Graphs (b) and (c) show the grating lobes at 6MHz. Grating lobes only appear at these ϕ values; at all other orientations, there are no such lobes.

3.12 (a)

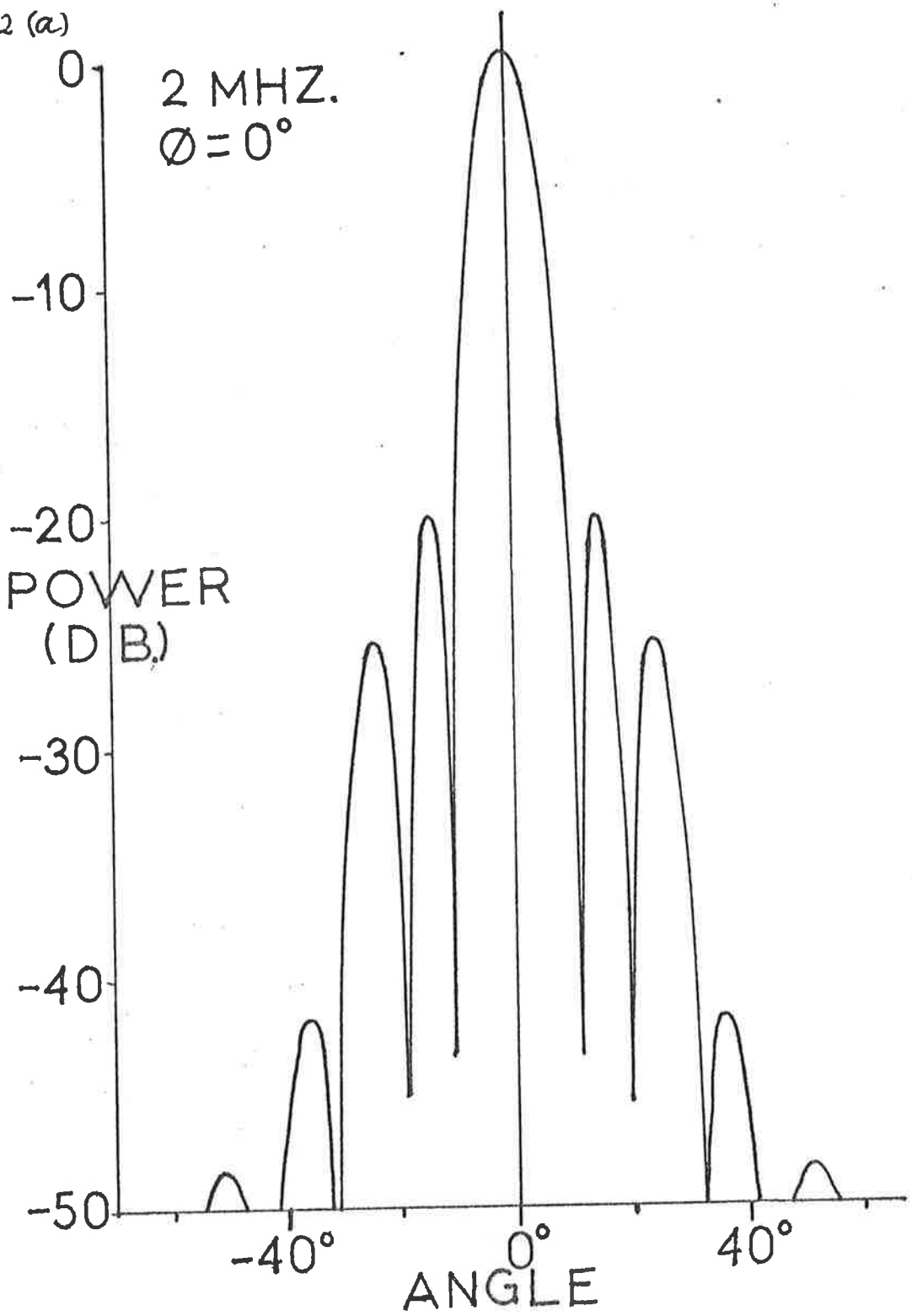

3.12 (b)

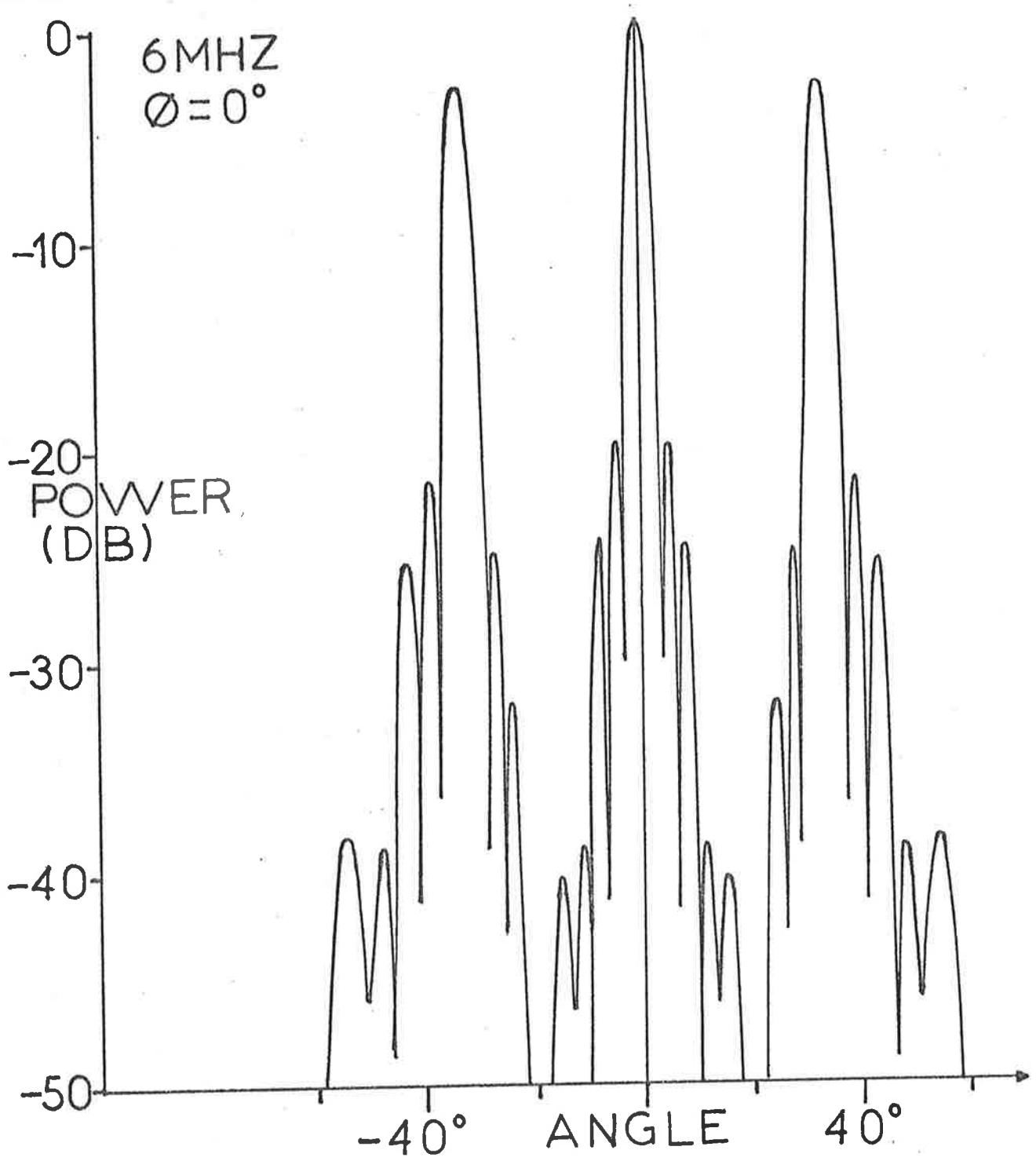

3.12(c)

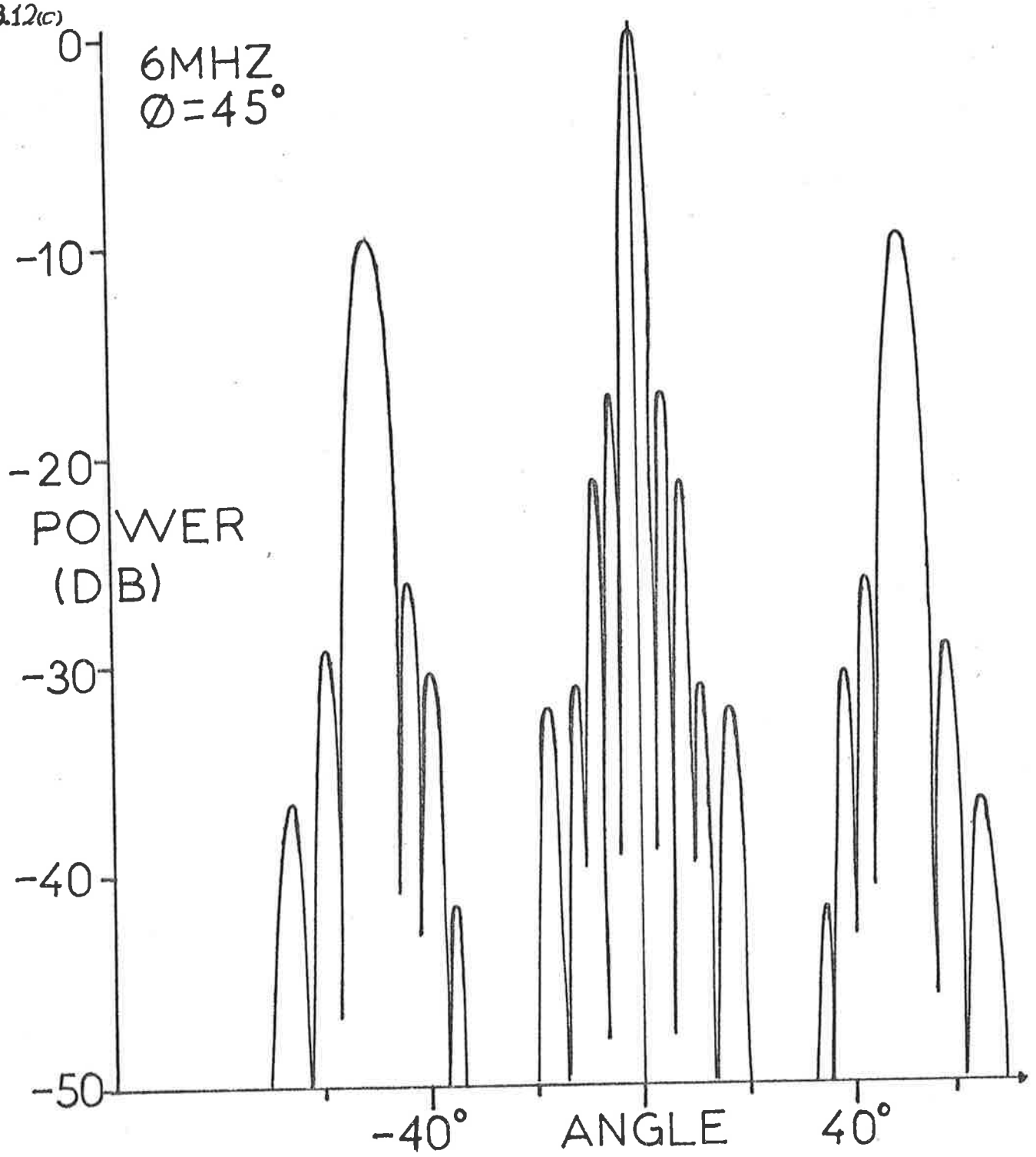

reflection, and was assumed independent of the zenith angle. These are not major errors, as it was seen in section 3.3.1 that the ground reflection coefficient is largely real and negative, and the graphs of McPetrie (1938) show the reflection coefficient is reasonably independent of angle out to about 30°. Most of the power received was well within ± 30°.

Figs. 3.12a, 3.12b and 3.12c show cross-sections of the polar diagrams of the full Buckland Park array, for operation at 1.98 MHz and 6.0MHz. The transmitter polar diagram has also been considered by regarding it as two parallel dipoles parallel to the receiving dipoles, and ignoring the other two dipoles of the transmitter. This is not exactly valid, but quite a good approximation near the vertical. The half power widths of the arrays are ± 4.5° at 2MHz, and ± 1.5° at 6MHz. Notice also the presence of "grating lobes" on the 6MHz polar diagram. This is because when used for 6MHz, the receiving dipoles (which are 3-half-wavelength dipoles) are greater than one wavelength apart (1.8 wavelengths in fact). There are eight such grating lobes - two at ± 33.8° in the direction parallel to the dipoles, two at ± 33.8° in the direction perpendicular to the dipoles, and four at ± 51.8° in the four directions at ± 45° from the dipole orientation. These grating lobes are shown in Fig. 3.12c. Notice they are down in strength compared to the 0° lobe, partly due to the effect of the transmitting antenna array.

Using this computer subroutine, it was also possible to estimate the directivity, effective areas and radiation resistances of the arrays. The directivity is given by

$$(3.5.1.2) \quad D = 4\pi.P(0,0)/\left(\int_{\theta=0}^{\pi/2}\int_{\phi=0}^{2\pi} P(\theta,\phi)d\Omega\right),$$

where $P(\theta,\phi)d\Omega$ is the power transmitted (or received) into solid angle $d\Omega$ at a zenith angle θ and azimuth angle ϕ.

Ground Refl. Coefficient	1.98 MHz D	$A_{eff}(m^2)$	$R_r(\Omega)$	$r_{eff}(m)$	6.0 MHz D	$A_{eff}(m^2)$	$R_r(\Omega)$	$r_{eff}(m)$
0.0 (absorbing ground)	200	3.6×10^5	0.3	340	146	$.29 \times 10^5$	0.82	96
0.5	320	5.8×10^5	0.25	430	358	$.70 \times 10^5$	0.74	152
1.0	420	7.2×10^5	0.24	475	405	$.83 \times 10^5$	1.16	163

Table 3.2 Estimates of directivity (D), effective area (A_{eff}) and radiation resistance (R_r) for the full Buckland Park array, and for the specified ground reflection coefficients. A π^c phase change was assumed upon reflection. The radius of a circle of area A_{eff} is also given (r_{eff}), and this can be compared to the true array radius of 450m. (although bear in mind that the true effective radius may be larger than this, as the effective area of the outer dipoles extends beyond these dipoles). The transmitter has not been included in these calculations. Notice how at 6MHz, the effective radius is considerably less (by 3 times) than 450m, due to the effect of the grating lobes in (3.5.1.4). The ground reflection coefficient is greater than 0.5, so the directivities may be taken as about 350 to 400 in each case.

When the reflection coefficient at the ground was not 1.0, the power absorbed by the ground must also be included in the integral term above.

The radiation resistance is

(3.5.1.3) $$R_r = \iint P(\theta,\phi)d\Omega/(0.5(N\ I)^2),$$

where I is the current in one dipole, and N is the total number of dipoles.

The effective area is then

(3.5.1.4) $$A_{eff} = D\lambda^2/4\pi$$

These parameters were tabulated for various ground reflection coefficients, and appear in Table 3.2. The program was checked by estimating the radiation resistance of a single dipole in free space, and the correct value of around 73Ω was obtained.

These parameters have not been determined for the 4-dipole array. However, taking the effective diameter as crudely the diagonal distance between 2 corners of the square gives an effective area of 1.3×10^4 m^2, and a directivity of 7. The true directivity may be as large as 10.

These estimated directivities, along with the K_* estimates made previously, can be used to determine the efficiency of the arrays.

Imagine the peak power output of the transmitter is W. The vertically transmitted Poynting vector is $P_t(r) = W/4\pi r^2 . D_T\ \varepsilon_T$ where D_T is the transmitter directivity, and ε_T the efficiency. ($D_T\varepsilon_T$ = gain). Suppose the wave travels to a height h, and is totally reflected. Assume no absorption occurs. Then the Poynting vector magnitude at the ground is

$$P_t(2h) = W/(4\pi(2h)^2).D_T\varepsilon_T$$

The power received by a receiver is thus

$$(W/(4\pi(2h)^2).D_T\varepsilon_T).(A_{eff}\cdot\varepsilon_R)$$

where A_{eff} is the effective area, and ε_R the receiver efficiency.

$A_{eff} = D_R\lambda^2/4\pi$, so

(3.5.1.5) Power received = $W/64\pi^2h^{-2}D_TD_R\lambda^2(\varepsilon_T\varepsilon_R)$

But by (3.3.2.14), the received amplitude (in Prairs) in this case is

(3.5.1.6) $A(P_r) = K_*^{-1}h^{-1}$ $(R' = 1)$

But A = (peak volts received going into the 50Ω receiver)/V_{TX} ,

V_{TX} being a measure of the transmitter volts, (as defined).

So the received peak power is $A^2V_{TX}^2/50\Omega$ (since the receiver impedance is 50Ω).

So the

(3.5.1.7) peak power received = $(K_*^{-1}h^{-1})^2V_{TX}^2/50$ Watts

Equating 3.5.1.5 and 3.5.1.7 gives

(3.5.1.8) $\varepsilon_T\varepsilon_R = (64\pi^2.V_{T_X}^2)/(D_TD_R\lambda^2K_*^2.50.W)$

Typically, when $V_{TX} = 10$, the transmitter volts are 1000 volts peak on 1 side of a transmission line, so the total volts are 2000 volts. However, only the 2 dipoles parallel to the receiving dipoles are important, so the total useful power output is $(2000)^2/80\Omega \times 0.5 = 25$kW. So $V_{TX}^2/W = 4 \times 10^{-3}$. D_T is the directivity for the 2 parallel dipoles, say about 4. Also bear in mind that in Table 3.1, K_* is for h in km, so if h is in metres, divide by 10^3. In this case, for the narrow beam use $K_{62M} = .0008$.

Then

$\varepsilon_T\varepsilon_R \sim 0.2\%$ (Narrow beam)

For a wide beam, $K_{*2W} \sim 0.0015$, $D_T \sim 7$, so

$$\varepsilon_T\varepsilon_R \sim 3\% \qquad \text{(Wide beam)}.$$

These numbers may be in error by perhaps a factor of 2 or 3 if the assumed transmitter and receiver directivities are wrong. But it can be seen the efficiencies are not high, particularly for the narrow beam. In fact it only receives at best about four times the power of the wide beam ($K_{*2W}/K_{*2M} \approx 1.8$). However, the narrow beam does have the advantage of cutting out a lot more noise than the wide beam, since most noise comes in from the off-vertical directions. In building such a large array, the improvement of the signal to noise ratio is perhaps the main requirement. The above efficiencies also include the transmitter efficiency. If we assume a wide beam and the transmitting array have similar efficiencies then

$$\varepsilon_{\text{wide beam}} \sim \varepsilon_T \sim 17\% \quad (\text{ie. } \sqrt{3\%})$$

Thus

$$\varepsilon_{\text{narrow beam}} \sim 1\%.$$

In the 6MHz case, $V_{TX} = 10$ when the transmitter volts are about 1000V peak on 1 side of a transmission line. In this case, however, the transmitter feeds into a single transmission line which carries the signal out to the centre of the transmitting array, and from there four feeder lines go up to the dipoles. In this case, the transmitter sees an impedance of about 400-500Ω. Only half the aerials are important as before, so $W \approx (2000)^2/400 \times 0.5 = 5\text{kW}$. So $(V_{TX})^2/W = .02$. Assume $D_T \sim 4$, $D_R \sim 400$, $K_{*6M} \sim .0038$ (for height in metres). Then

$$\varepsilon_T\varepsilon_R \sim .4\%$$

Assuming $\varepsilon_T \sim 17\%$ again gives $\varepsilon_{R(6\text{MHz})} \sim 2\%$.

3.5.3 Townsville and Woomera

Most of the important features regarding the Townsville site have already been discussed. Figs. 3.13 show photographs and diagrams of the site, and there is little more that need be said. The system began as an amplitude-only system, but graduated to recording in-phase and quadrature components in March 1979.

The Woomera system was simpler than the Townsville system, but its basic design was quite similar. Four receiving aerials were used instead of three, however, and it only recorded amplitude data. None of the data taken was ever calibrated.

This chapter concludes with Table 3.3, which summarizes the main characteristics of the system used in the work for this thesis.

Fig. 3.13 (a) Photograph of the Townsville transmitting array. The caravan which housed the transmitter and receivers can also be seen.

(b) This is an expanded diagram of the photograph in (a). The broken line square indicates approximately the area covered in the photograph (a).

Also shown are magnified views of various parts of the main figure. D shows how the folded dipoles were attached to the main towers. The small dark vertical rectangles on the dipoles are called spacers, and hold the wires of the dipoles apart. All were insulators, except those on each end of the dipole, which were conducting. Some support cables to support the tower are also shown, although in reality there were many more. The dipoles were insulated from the main towers. The dipoles were attached to halyards, so they could be wound up and down without bringing the tower down. These halyards have not been drawn. The dipoles were about 15cm between opposite wires.

E shows the point where the transmission line meets the dipole.

C shows a view of a typical receiving aerial. The 2 orthogonal dipoles did not actually touch; one passed under the other. Each dipole fed into a small box, which transformed the impedance to 50Ω. The signal was then carried back to the central caravan by 50Ω cables, each cable being a three half wavelengths in length. The signal received by each dipole was carried separately back to the caravan.

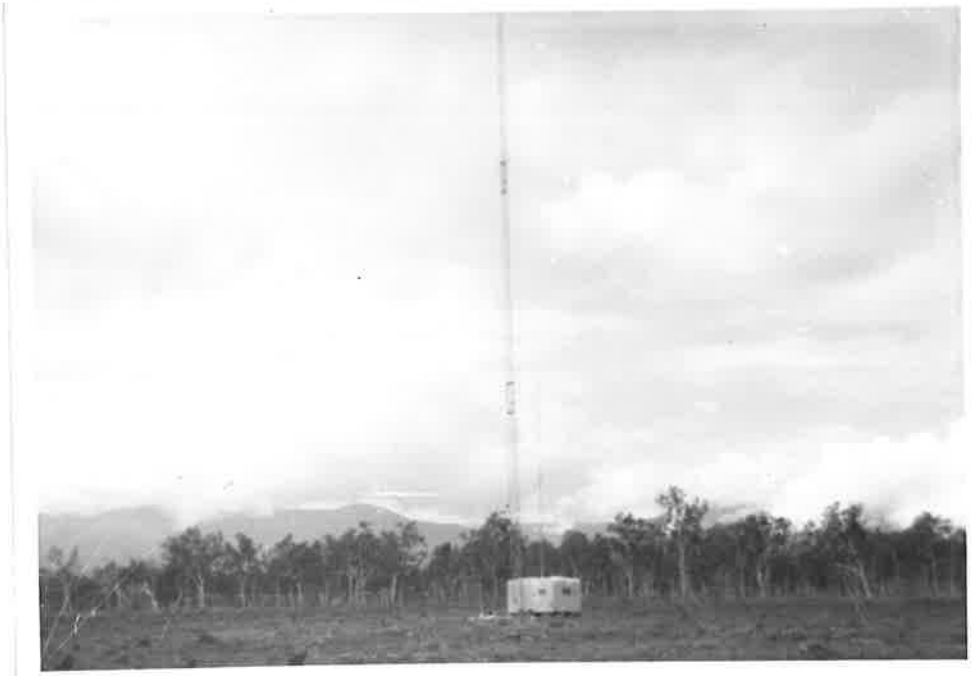

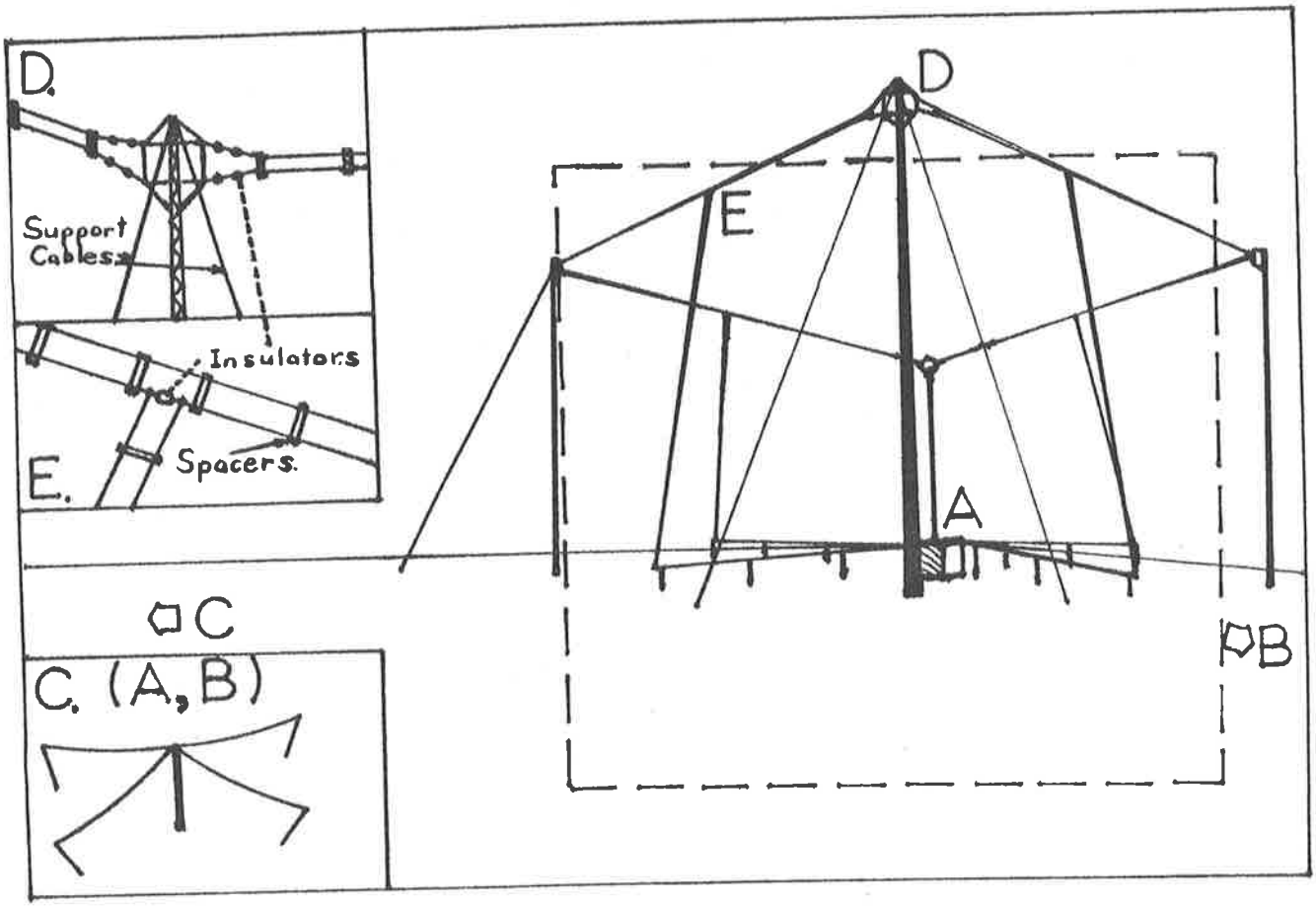
D.
Support Cables
Insulators
E.
Spacers
D
E
A
C
B
C. (A, B)

Fig. 3.13 (c) Photograph of the transmitter inside the caravan at Townsville. (An air conditioner to control the temperature can also be seen in the background. This also doubled as a fridge!). The various levels, starting from the top, are: the Aerial Switching Unit (ASU), Aerial Tuning Unit (ATU), Power Amplifier and Driver (that is the one with the meters), the pre-driver section, the Power Amplifier Modulator, the power supply and the High Tension Power Supply (with meters) and finally a fan at the bottom. The transmitter attached to the transmission lines through the roof of the caravan.

(d) View of the receiving equipment used at Townsville. The tape recorder can be seen at the top. The transmitter can be seen in the foreground, and the CRO used to examine the echoes visually is between the transmitter and receivers. The cables hanging on the sides of the receiving rack were used as phase shifters. The two cables from a pair of orthogonal receiving aerials were each fed into two 70Ω, quarter wavelength cables, which transformed their impedances up to 100Ω. Then one of these was passed through a 100Ω, quarter wavelength cable to give it a $\pi/2$ radian phase lag. This was then added to the signal from the other dipole; in this way, either O or X polarization could be received, depending on which dipole had its signal pass through the 100Ω cable.

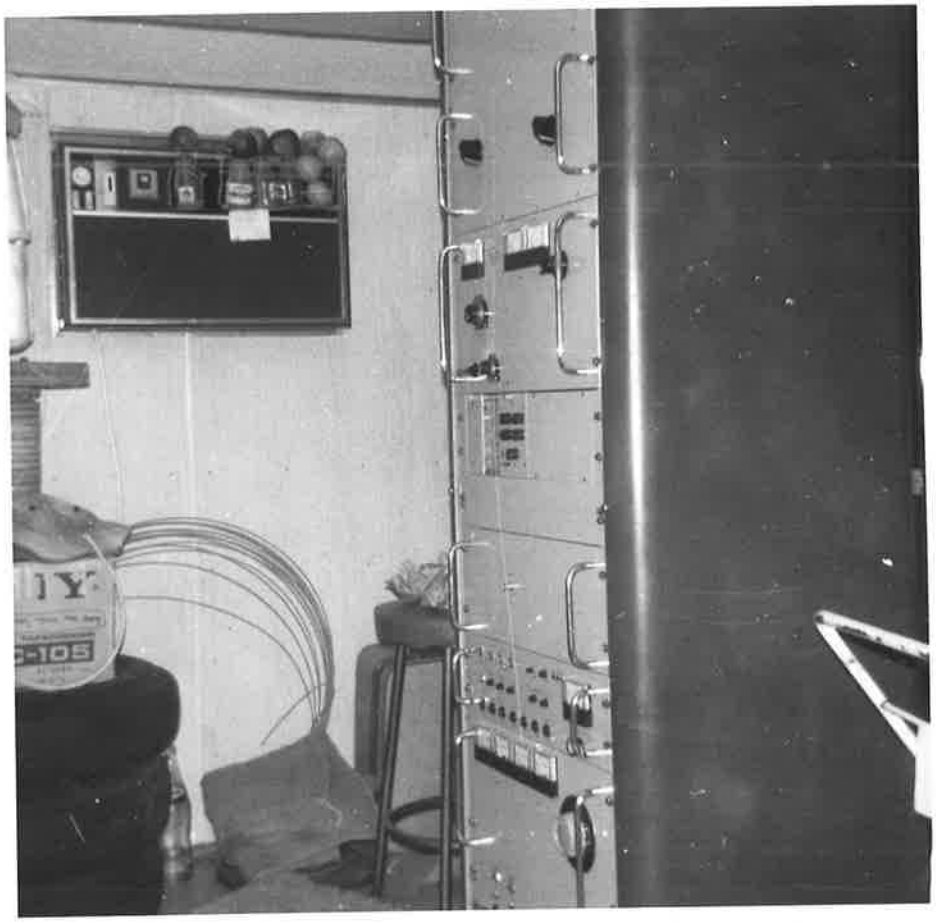

TABLE 3.3a BUCKLAND PARK AERIAL ARRAY ("2MHz" and "6MHz")

(as of January 1980)

A

GENERAL	"2MHz"	"6MHz"
Location	(34° 38'S, 138° 29'E)	(34° 38'S, 138° 29'E)
Magnetic Co-ords	(45° S, 213° E)	(45° S, 213° E)
Beginning of operation	1968	Late 1979
Central frequency (f_0)	1.98MHz	5.995MHz
Central wavelength (λ)	151.4m	50.0m
Modes of Polarization	O, X generally	O, X generally
Ground reflection coefficient ?	0.6-0.9 - probably ~0.8	0.5-0.8 - probably ~0.7

B

Transmitter		
Tx Array	4 half-wave folded dipoles in the form of a square, approx. $\lambda/4$ above ground.	4 half-wave folded dipoles in the form of a square, approx. $\lambda/4$ above ground.
Pulse repetition frequency (PRF)	Usually 50 Hz in 1978 Generally 20 Hz after January 1978	20 Hz
Nominal pulse length	50 μs basewidth, 30 μs half-power width	} → "
Range resolution	4.5 km	4.5 km
Peak volts on one side of Tx feeder lines	~ 1000V	~ 1000V
Tx aerial impedance seen at Tx	80Ω	400-500Ω
Peak Tx pulse power	50 kW	10 kW
Tx effective area Tx radiation resistance	} The calculations have not yet been done	
Tx directivity	~ 4-8 ?	~ 4-8 ?
Half power, half-width of polar diagram	~ 30°	~ 30°
Efficiency	~ 17% ?	~ 17% ?

/continued.....

TABLE 3.3(a) continued.....

C.

Receiver aerials and receivers	"2 MHz"	"6 MHz"
Rx aerial type (2 main aerial types at B.P. designated (i) and (ii). (i) = narrow (main) beam (ii) = wide beam	(i) 89 parallel half-wave dipoles 90 m spacing in a square grid with circular perimeter, ~ 450 m radius (ii) 4 parallel half-wave dipoles 1.8λ space, at the four corners of a square	(ii) As for 2MHz, but dipoles are 3-half-wavelength (only (i) used at present)
Bandwidth of Rxers	~ 30 kHz half power	~ 30 kHz half power
Rx effective area	(i) $(3.6 \rightarrow 7.2) \times 10^5 m^2$ (ii) $10^4 m^2$?	(i) $(.29 \rightarrow .83) \times 10^5 m^2$
Radius of a circle of given effective area	(i) 340 m → 475 m (ii) 60 m ?	(i) 96 m → 163 m
Rx radiation resistance	(i) (.3 → .24)Ω (ii) ?	(i) (.82 → 1.16)Ω
Rx array directivity (Tx polar diagram not included)	(i) 200-420 (ii) ~7 ?	(i) (146 - 405)
Half power half-width of polar diagram	(i) 4.5° (ii) ~ 20°	(i) 1.5° There are grating lobes also: 4 at 32° from vertical, 4 at 52°.
Efficiency	(i) ~1% ? (ii) ~ 17% ?	~ 2%
Recording System		
No. of heights recorded simultaneously	Before 1978: 1, 5, 10 or 20, 1978 →; possible to alternative diff. sets of 10 hts each min	} → "
Steps between successive heights recorded	2 km	2 km
Coherent integration over n pts	1	1
Frequency of data collected per height (after coherent integration)	5 Hz	5 Hz
No. of receivers recorded simultaneously	4	4

NOTES:

(i) The system was modified to run off a mini computer around January 1978.

(ii) Effective areas, radiation resistance, gains, only calculated properly for narrow beams; other estimates not properly calculated (yet). Question marks generally mean calculations have not been done fully. No question mark generally indicates the proper integrals have been performed on a computer.

(iii) Some 6 MHz work had been done before 1979, but with a much less powerful transmitter. The work all involved F-region scatter. No system previous to that made in 1979 has been able to see D-region echoes at 6 MHz at Buckland Park.

TABLE 3.3b TOWNSVILLE AERIAL ARRAY ("2MHz")

(as of January 1980)

(a) General

Location	(19° 40'S ; 146°, 54'E)
Magnetic Co-ords	(29° S, 219° E)
Beginning of Operations	September, 1977
Central frequency (f_0)	1.95 MHz
Central Wavelength (λ)	154.4 m
Modes of polarization	O, X
Ground reflection coefficient	~ 0.6 - 0.9 ?

(b) Transmitter

Tx array	4 half wave folded dipoles in the form of a square, approx. $\lambda/4$ above ground (30 m actually)
Pulse repetition frequency (PRF)	15 Hz up to March 1979; 20 Hz thereafter
Nominal pulse length	50 μs basewidth; 30 μs half power width
Range resolution $\approx c(2t_{\frac{1}{2}})/2$	4.5 km
Peak volts on one side of Tx feeder lines	~ 600V
Tx aerial impedance seen at Tx	~ 80Ω
Peak Tx pulse power	~ 20 kW
Tx effective area	?
Tx radiation resistance	?
Tx directivity	?
Half power half width of polar diagram	~ 30°
Efficiency	?

TABLE 3.3b continued.....

(c) Receiver Aerials and Receivers	
Rx aerial types	3 pairs of orthogonal crossed inverted V, half wave dipoles, 165 m spacing, to form an equilateral triangle
Bandwidth of Rx	~ 30 kHz half power
Rx effective area	?
Radius of a circle for a given effective area	?
Rx radiation resistance	?
Rx array directivity (Tx polar diag. not included)	?
Half power half width of polar diagram	?
Efficiency	?
(d) Recording System	
(No. of heights recorded simultaneously, steps between successive hts recorded)	(10 or 20, 2 km steps)
Coherent integrat^{n} over n points	Before March 1979, no coherent $\int$; after, 8 pts.
Frequency of data collected per height, per receiver (after coherent integration)	Before March 1979, 5 Hz; after, 2.5 Hz
No. of receivers recorded simultaneously	3 ; before March 1979, amplitude only - after, I/P, Quad on each receiver

NOTE:

(i) System originally had PRF 15 Hz, and recorded amplitude only. In March 1979, PRF became 20 Hz, and system recorded amplitude and phase.

CHAPTER IV

ANGULAR AND TEMPORAL CHARACTERISTICS OF D-REGION SCATTERERS USING AMPLITUDE-ONLY DATA

4.1 Introduction

4.2 Investigations using time scales of the order of minutes

4.2.1 Temporal variations

4.2.2 Angular spectra

4.2.3 O and X mode comparisons

4.2.4 Height fluctuations

(a) Upper limits of echoes

(b) Temporal height fluctuations

4.3 Short term temporal changes

4.3.1 Temporal fading

(a) Introduction

(b) Some theory to help interpretation

(c) Experimental

4.3.2 Height fluctuations

4.4 Spatial extent of scatterers

4.5 A review of VHF studies

4.5.1 Introduction

4.5.2 The scattered pulse profile

4.5.3 Experimental VHF observations

4.6 Water body refractive index profiles

Chapter IV Angular and Temporal Characteristics of D-Region Scatterers Using Amplitude-Only Data

4.1 Introduction

In the previous chapters, studies of radio frequency scatterers in the D-region have been reviewed, and some of the techniques used in the work for this thesis have been introduced. It is now appropriate that some early observations be presented.

In some ways, it might have been useful to present some additional theory first, particularly some important techniques for the estimation of noise from the received signal. But in practice, this would have been unwise. After three chapters, with very little in the way of experimental results having been presented, the reader is no doubt ready for some actual data. Hence the chapter regarding estimates of noise will be left until Chapter VI. This also has the advantage of placing this thesis in something of a chronological order, since the theory regarding estimates of mean noise from the signal did not evolve until late 1977, sometime after many of the observations presented in this chapter were taken. Before that date, noise was estimated by simply turning the transmitter off, and monitoring the received signal. This practice was maintained even after the development of the noise estimation theory, since it gives more accurate estimates than the theory. But the noise theory could be used at times when the system was un-manned, and it was for this purpose that it was derived. The actual mean signal power could be found as the mean received power minus the noise power.

In the early stages of the work for this thesis, the systems used could only record amplitudes, and this chapter discusses results obtained using amplitude alone. A considerable amount of information could be obtained with these techniques, and important insights into the structure

of D-region scatterers will be presented.

A review of studies at VHF by other authors will also be presented, and it will be seen that the observations at HF and VHF complement each other to some degree. Valuable information has been gained by pooling the two sets of results.

Fig. 4.1a Contour plot of 1-min means of calibrated power vs. range and time taken using a narrow beam on day 77/151. The means were smoothed by interpolation. X mode polarization was used for transmission. The presence of a distinct minimum at 80-82km is the most obvious feature. Strong bursts of power at 66-70, 74-76 and 90km can be seen. (The power levels can be converted to dBs of $(\mu Pr_M)^2$ by subtracting 9db).

Much of the signal from above 80km was probably actually O mode leakage.

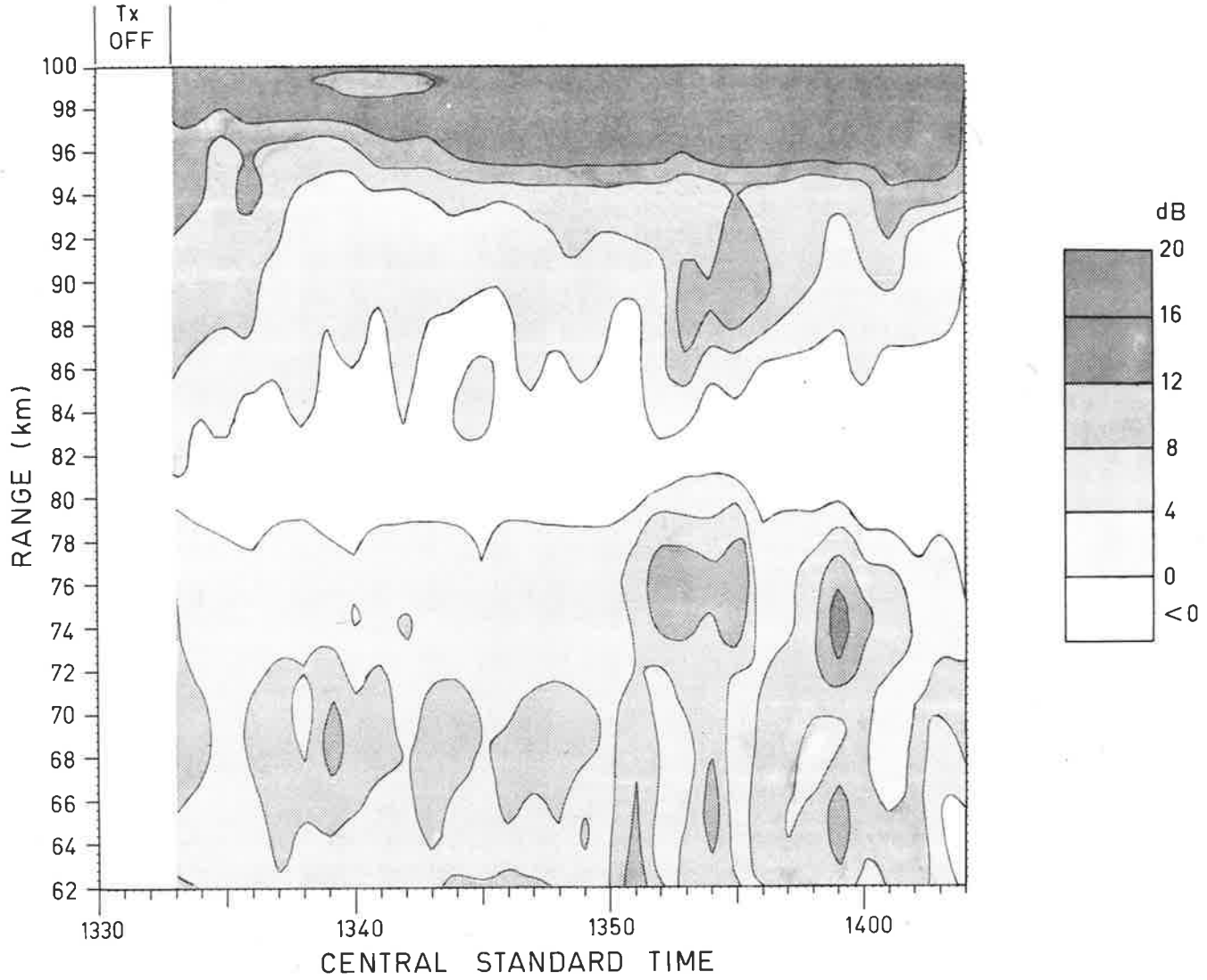
Tx
OFF
100
98
96
94
92
90
88
86
84
82
80
78
76
74
72
70
68
66
64
62
RANGE (km)
1330
1340
1350
1400
CENTRAL STANDARD TIME
dB
20
16
12
8
4
0
<0

Fig. 4.1b Contour diagram of smoothed 1-min power means vs. range and time, taken with (a) a narrow and (b) a wide beam on day 77/151. The power levels are not dBs of $(\mu Pr)^2$. Rather, they have been corrected to allow for the differing gains of the two antennae, and arbitrarily adjusted so that the minimum level is around 0dB. To convert to dBs of $(\mu Pr)^2$, subtract 13dB for the narrow beam and 17dB for the wide beam.

Powers are strongest in a layer centred on 88-90km for the narrow beam, and strongest at 88-92km with the wide beam. The larger powers on the wide beam, the increase in range when the narrow beam was pointed at 11.6° off-zenith, and the strong powers at 11.6° all indicate significant off-vertical scatter for this layer. O mode polarization was used, since this suffers less absorption than X mode. Maximum powers correspond to reflection coefficients of about 1.3×10^{-3}.

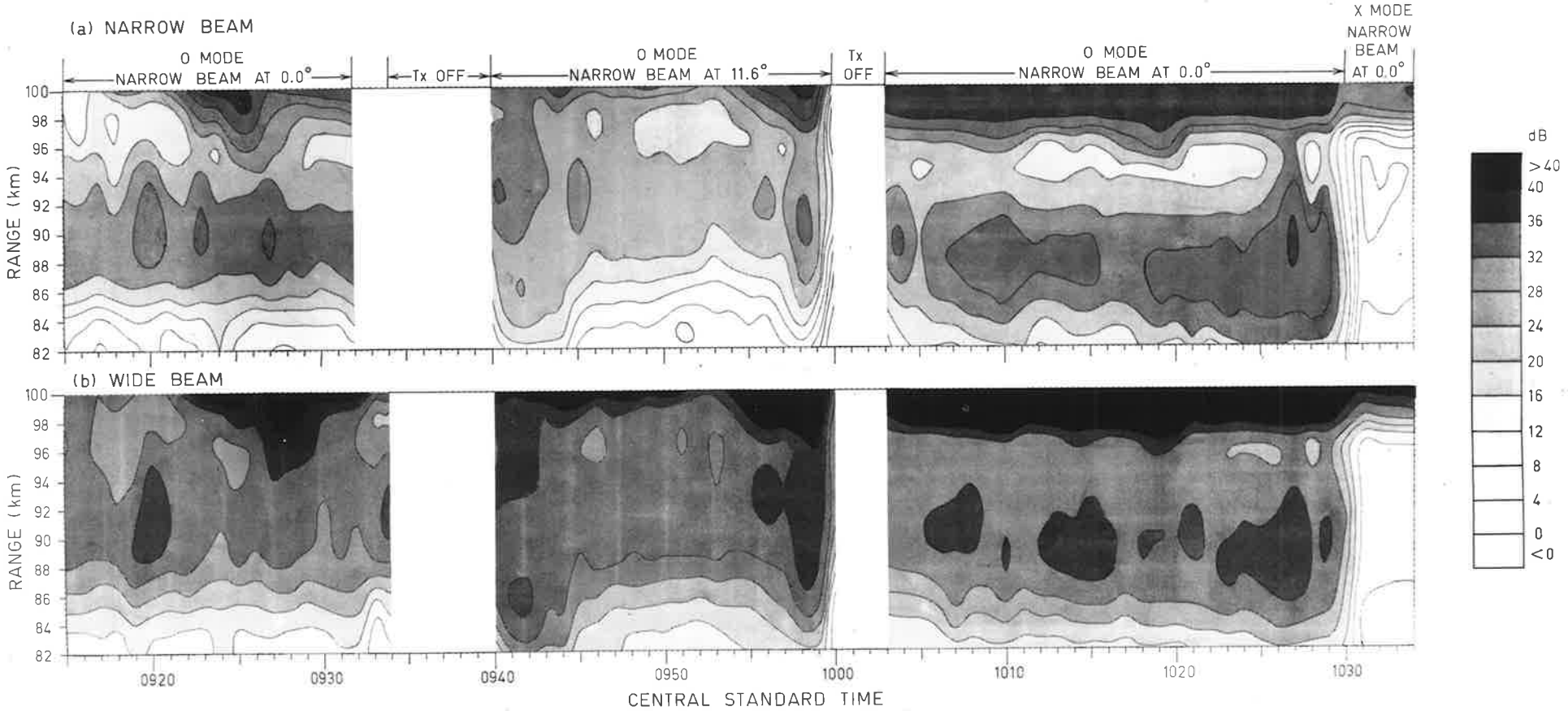
(a) NARROW BEAM
O MODE
NARROW BEAM AT 0.0°
Tx OFF
O MODE
NARROW BEAM AT 11.6°
Tx
OFF
O MODE
NARROW BEAM AT 0.0°
X MODE
NARROW
BEAM
AT 0.0°
(b) WIDE BEAM
RANGE (km)
100
98
96
94
92
90
88
86
84
82
0920
0930
0940
0950
1000
1010
1020
1030
CENTRAL STANDARD TIME
dB
>40
40
36
32
28
24
20
16
12
8
4
0
<0

Fig. 4.1c Contour plot of smoothed 1-min power means vs. range and time, taken with (a) a narrow beam and (b) a wide beam on day 77/151. The power levels are not dBs of $(\mu Pr)^2$. Rather, they have been corrected to allow for the differing gains of the two antennae, and arbitrarily adjusted so that the minimum level is around 0dB. To convert to dBs of the respective $(\mu Pr)^2$, subtract 9dB for the narrow beam and 13dB for the wide beam.

Strong bursts of scatter will be noted in a layer centred on 74km. The lack of significant power recorded whilst the narrow beam was at 11.6°, and the very close similarity between corrected echo powers on the two beams suggests that most scatter came from the vertical. X mode polarization was transmitted, since it is reflected more effectively than O mode, and there is little absorption up to such heights. Maximum powers correspond to reflection coefficients of about $2\text{-}4 \times 10^{-4}$.

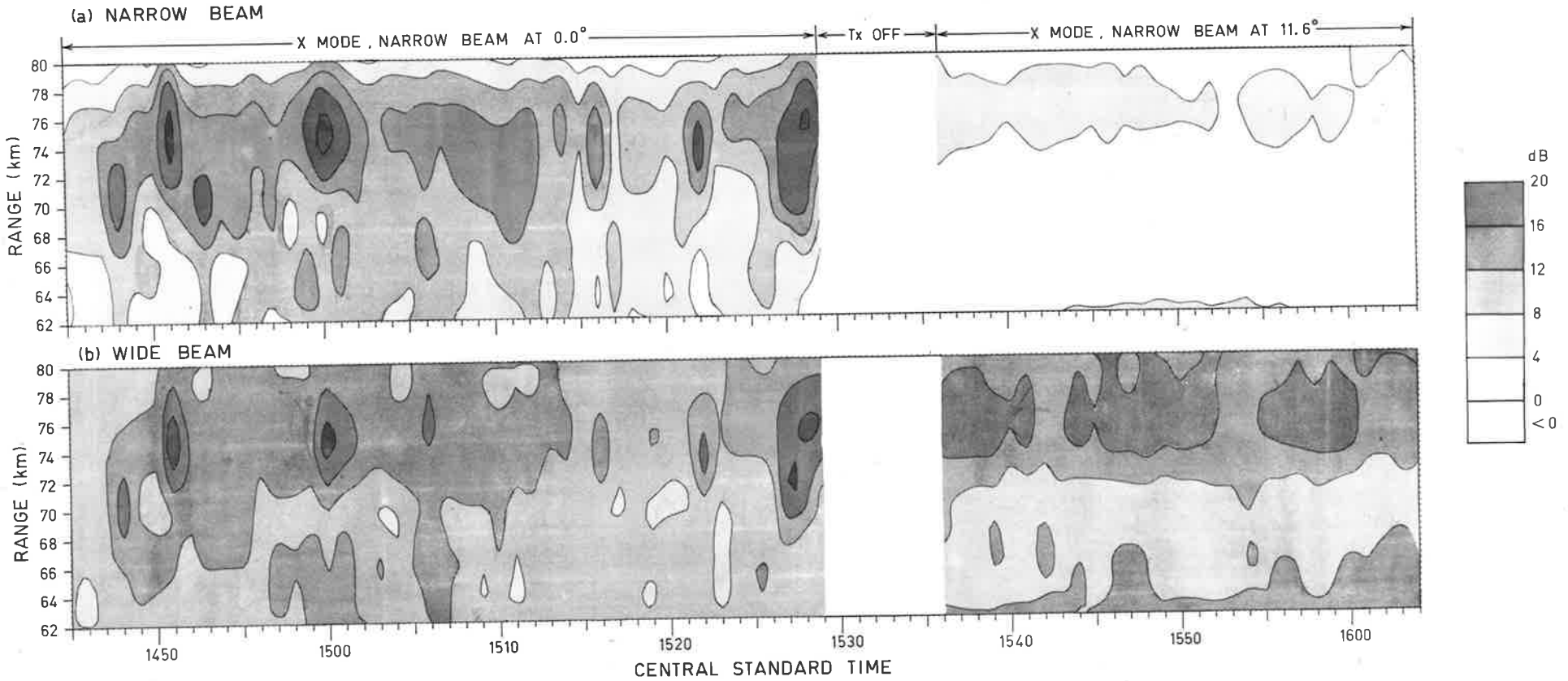
(a) NARROW BEAM
X MODE, NARROW BEAM AT 0.0°
Tx OFF
X MODE, NARROW BEAM AT 11.6°
RANGE (km)
80
78
76
74
72
70
68
66
64
62
(b) WIDE BEAM
RANGE (km)
1450
1500
1510
1520
1530
1540
1550
1600
CENTRAL STANDARD TIME
dB
20
16
12
8
4
0
< 0

4.2 Investigations Using Time Scales of the Order of Minutes

Until about 1970 the bulk of observations of ionospheric D-region echoes had been made with photographic recording, using similar techniques to those of Gardner and Pawsey (1953). This allowed only qualitative examination of echo strength fluctuations. To obtain quantitative values of echo power, it was necessary to record the data on magnetic tape. Furthermore, few investigations of the angular spectrum of these scatterers had been undertaken. Lindner (1975a, b) and Vincent and Belrose (1978) had obtained some indirect results, but little other work had been done. More detailed investigations of temporal variations and angular distributions were necessary.

4.2.1 Temporal Variations

Figs. 4.1a, 4.1b and 4.1c present some of the earliest quantitative results of D-region investigations. The diagrams come from a paper published in "The Journal of Geophysical Research", March, 1979. This paper is reproduced as Appendix D.

The diagrams are contour graphs of the power received at Buckland Park for the 151st day of 1977 (denoted 77/151 (May 31, 1977)), plotted as a function of time and range. The powers were recorded at 2km range intervals, at a rate of 2.5Hz per range, and were then averaged in one minute blocks. These mean powers were then smoothed by computer interpolation (Akima, 1974). Wind measurements were also made using the partial reflection drift technique. As discussed in the captions, the powers were fully calibrated. The powers are not in $(\mu Pr)^2$, but were adjusted for the purposes of the paper. The powers may be readily converted to $(\mu Pr)^2$ as described in the captions.

Fig. 4.1a is a contour diagram of power as a function of range and time using the narrow beam of the Buckland Park array pointing vertically, and using X-mode polarization for transmission. Intermittent increases of signal power will be noted at ranges of approximately 66-70km, 74km and 90km. Thus the D-region irregularities were clearly quite stratified on that day. Stratification of the scatterers has already been discussed in Chapter I. The X mode is strongly absorbed above 80km and so the 90km reflection coefficients are actually much larger than they appear from this diagram. A very definite "valley" can be seen at 80-82km. The strong signal above 96km is due to total reflection from the E-region, which saturates the receivers. Some of this may in fact be O mode leakage of the totally reflected signal. The time interval shown in Fig. 4.1a coincides with the period of most frequent burst of power at 66km on this

particular day. On other days, however, the layer can be more significant.

Figure 4.1b shows contour diagrams of the power returned from 82 to 100km range during the period 0915 to 1034 hr. on both a narrow and a wide beam, and Fig. 4.1c is a similar pair of diagrams for the ranges 62 to 80km from 1445 to 1604 hr.

A layer in the region 85 to 95km is a common feature at Buckland Park, and this layer often persists throughout night and day. The 90km layer on day 77/151 had a minimum O mode reflection coefficient of about 6×10^{-4}, and rose to 1.3×10^{-3} on some occasions. If it is assumed that the scatter was due to turbulence, then the backscatter cross-section is $\overline{\eta} = \overline{R^2}/(\theta_{\frac{1}{2}}{}^2 L)$ (equation 3.3.2.19, Ch. III). For the narrow beam, $\theta_{\frac{1}{2}} \approx 4.5°$, and the pulse half power length on this day was about 6km. Then $\overline{\eta} \approx .027\overline{R^2}$, so for $\overline{R^2} \sim 10^{-6}$,

$\eta \approx 2.7 \times 10^{-8} m^{-1}$, or $\overline{\sigma} \approx 2.15 \times 10^{-9} m^{-1}\ sr^{-1}$. Then

$\overline{C_n^2} \approx (\overline{\eta}/.38) \times (151.5)^{1/3}$ by equation 2.4.1.5, or

(4.2.1.1) $\overline{C_n^2} \approx 14.0\overline{\eta}\ m^{-2/3} \approx .38\overline{R^2} \approx 176\overline{\sigma}$

at 2MHz using the narrow beam at Buckland Park. For $\overline{R^2} \approx 10^{-6}$, $\overline{C_n^2} \approx 3.8 \times 10^{-7}$.

These calculations assume that the turbulence fills the radar volume. If this is not so, $\overline{C_n^2}$ (turbulence) is even larger, as discussed in section 2.3.2, Chapter II. The effects of absorption have not been removed, and this means that $\overline{C_n^2}$ values are understimates. Typically the error is only a matter of 2 or 3dB for heights below 90km on O mode at 2MHz. (This absorption estimate was made using a "typical" D-region electron density profile, and integrating the effects of absorption over the path a ray would take. Refractive indices were calculated with the Sen-Wyller equations).

One feature of both graphs 4.1b and 4.1c is the occurrence of strong

bursts of power, those at 90km rising by around 3dB over the normal level, and those at 74km by around 10dB. The bursts at each height have a quasi-periodicity of between about 5 and 15 minutes. For the 74km layer, bursts often last less than 2-3 minutes. This "burstiness" is very similar to some VHF results obtained using scatter from 70 to 74km altitude (e.g., Rastogi and Woodman (1974); Harper and Woodman, 1977), and suggests that VHF and HF experiments are observing the same structures. This point has already been briefly discussed in Chapter I, and will be discussed in more detail later.

Wind observations made on this day showed a strong, principally eastward, wind jet at 74km, which attained speeds up to $70ms^{-1}$. Discussions of correlations between layers of scatter and wind profiles will be left until a later chapter. However, imagine a scatterer of small horizontal extent moving at a velocity of $70ms^{-1}$, and with a narrow polar diagram. Suppose the angular spectrum of the scatterers is given by $\exp\{-(\sin\theta/\sin\theta_0)^2\}$, and say $\theta_0 \sim 2°-4°$. (It will be seen shortly that indeed θ_0 is around 2°-4° at 70km). Such a scatterer would take between 1 and 2 minutes to pass between the half power points of its angular spectrum. The fact that the "lifetime" of the scatterers at 74km is the same on both the narrow and wide beams must be because the effective half power beam width is defined by the scatterer, and not the array beams. A scatterer of several kilometres dimension horizontally would take correspondingly longer to pass through the half power points of the effective polar diagram, and measurements of the "lifetimes" of the echoes suggest these 74km scatterers have horizontal dimension of the order of 3-10km (see Appendix D). The horizontal scale must be of the order of 1 Fresnel zone to produce such anisotropic scatter, which implies a size of greater than $(\lambda.\text{height of scatterer})^{\frac{1}{2}} \approx 3.2$km at 70km.

Thus it appears that the "lifetimes" of these power bursts are defined by the time it takes a scatterer to pass overhead, rather than the lifetime of the scatterer. If the scatterer did not pass directly overhead, the

observed lifetime of the burst would be even less than that for one that did. However, these observations do not rule out the possibility that the scatterer lifetimes could also be of the order of 1 or 2 minutes. Röttger et al. (1979), using data collected at VHF, suggested that some of the scatterers they observed did have quite short lifetimes, and may have actually been formed in their beam.

Reflection coefficients for the lower echoes typically varied between about 2×10^{-5} to greater than 2×10^{-4} for the 74km echo when observing on X mode, and about 5×10^{-5} for the 66km layer on X mode. These can be converted to backscatter cross-sections if the scatter is due to isotropic turbulence. A reflection coefficient of 2×10^{-4} corresponds to a value for $\overline{C_n^2}$ of about $.38\overline{R}^2 \sim 1.5 \times 10^{-8} m^{-2/3}$ assuming $\overline{R}^2 \sim (\overline{R})^2$. However, as will be seen, the scatter at this height is certainly not isotropic, and so this $\overline{C_n^2}$ estimate is not meaningful.

The results quoted in this section are quite typical of the echoes observed both at Buckland Park and Townsville. Echo strengths below 80km do appear to be stronger at Townsville, and these lower echoes appear to be even more "bursty" in nature than their Buckland Park (Adelaide) counterparts. The Townsville echoes frequently show increases in power of greater than 10dB, and can be quite short-lived, often lasting less than one minute. These are quite likely due to scatterers formed and/or destroyed within the beam. (They could perhaps be meteors, but this seems unlikely at these low heights). Echoes can become very strong at around 70km at Townsville - on one occasion, on 22nd January, 1980, a 70km echo with a reflection coefficient of 10^{-3} was observed. This echo lasted for some hours. However, it was not typical of Townsville echoes.

The echoes from above 80km show comparable reflection coefficients at Buckland Park and Townsville. Those at Buckland Park may be marginally

Fig. 4.2 Typical mean power-range profiles for Townsville. Power averages were formed using 1 to 3 minutes of data. This system had quite a wide reception polar diagram, as discussed in Chapter III. Powers are dBs of $(\mu T \text{ irps})^2$.

-------- = X mode

_____ = O mode

The actual starting times of the various observations were

(1)	X mode:	77/306/1415		
(2)	X mode:	77/306/1315		
(3)	X mode:	77/305/1900	(Night time)	
(4)	X mode:	77/304/2340	(Night time)	77/304 = 31st Oct, 1977
(5)	X mode:	77/304/2200	(Night time)	77/305 = 1st Nov, 1977
(6)	O mode:	77/306/2200	(Night time)	77/306 = 2nd Nov, 1977
(7)	O mode:	77/305/1400		
(8)	O mode:	77/305/1420		
(9)	O mode:	77/305/1600		

Notice all X mode observations above 80km are night time observations. During the day, X mode observations from above 75-80km were very weak (even weaker than any 60-70km echoes) due to the large absorption in the day time.

Preferred heights of scatter can clearly be seen.

Also shown are radio noise estimates for the Townsville data, expressed in $(\mu T)^2$ for typical transmitter powers.

a = day time noise after coherent integration of 8 points (see chapter on phase observations (Ch. VII).
b = day time noise with no coherent integration.
c = night time noise (around midnight) with no coherent integration.

Night time radio noise is generally far more severe then day time noise. This will be shown in more detail in Chapter VI.

These powers are not directly comparable to those in Fig. 4.3, but if converted to effective reflection coefficients, can be compared.
($\overline{R} \approx (\overline{R^2})^{\frac{1}{2}} = K_* H.\sqrt{P}$, P = power $\{(\mu T)^2$ or $(\mu Pr)^2\}$, H = height of echo; see Ch. III).

($K_{*T3} = .6 \pm .3$, and $K_{*2M} = .8 \pm .4$)). However, if volume scatter predominates, $\overline{R^2}$ is proportional to the radar volume and the back-scatter cross-section, so the beam widths of the array beams should be considered before backscatter cross-sections can be compared.

SAMPLE POWER / RANGE PROFILES , TOWNSVILLE , NOVEMBER 1977

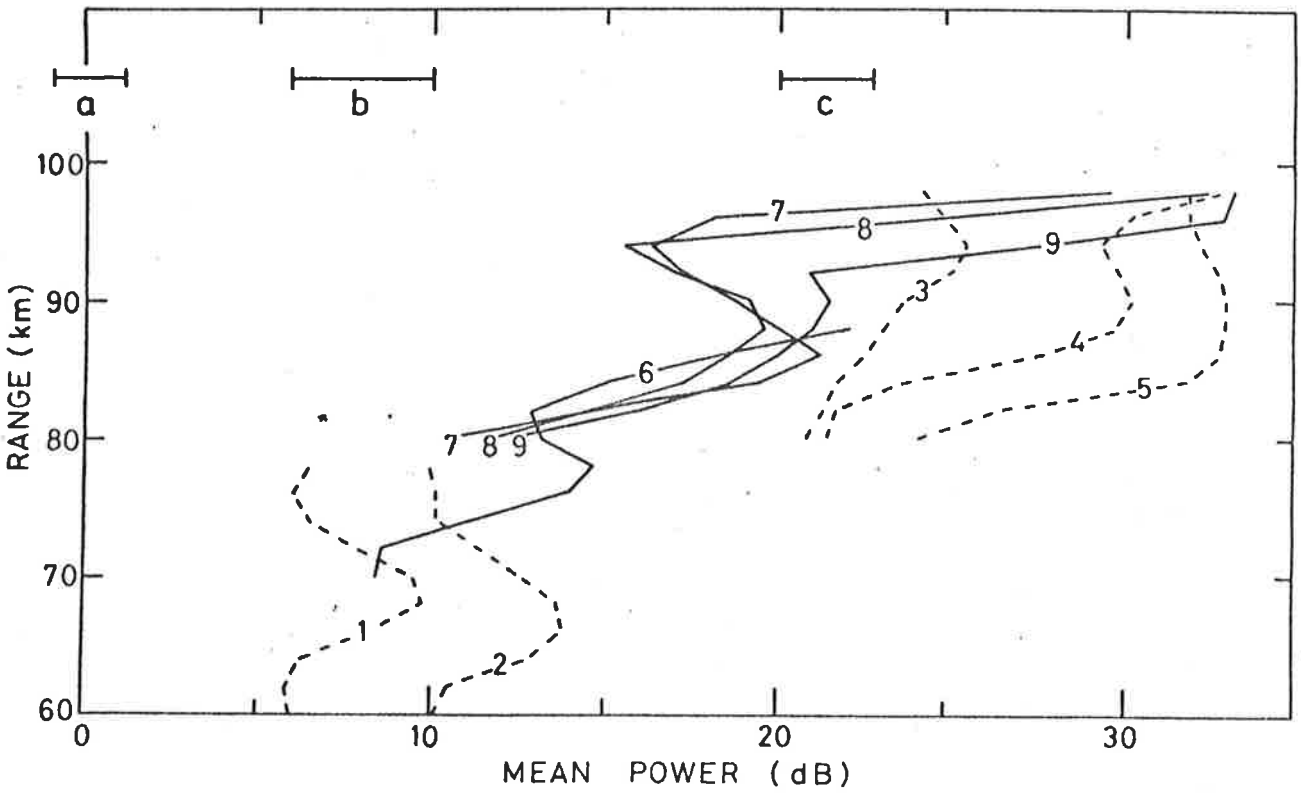

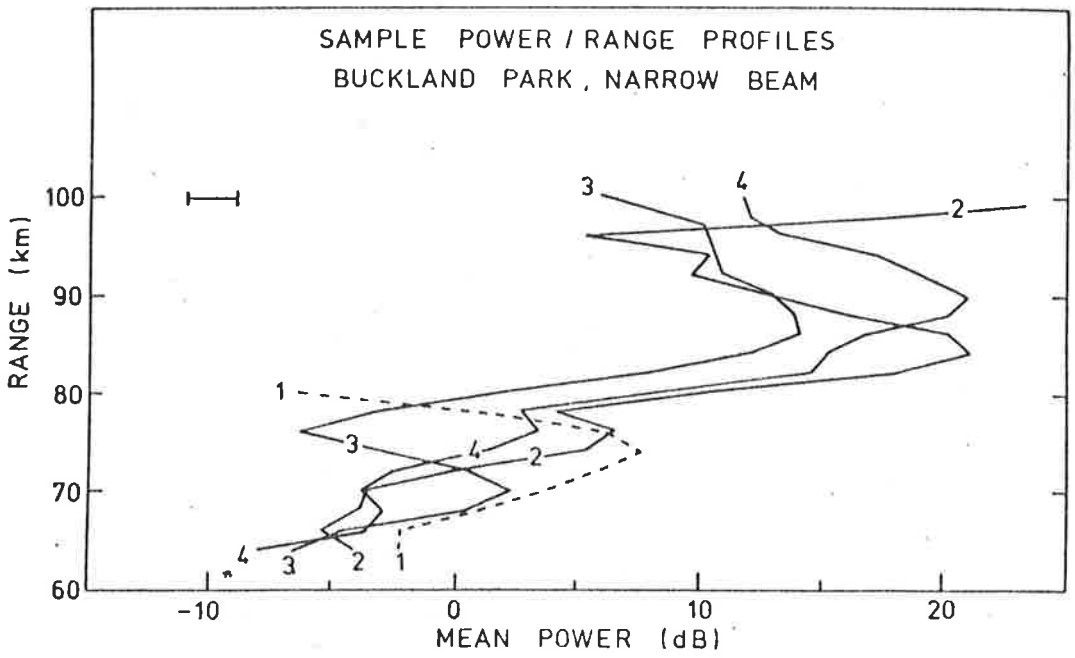

Fig. 4.3 Typical mean power-range profiles for Buckland Park, using the narrow beam(5°). Profiles correspond to means over intervals of between 1 and 3 minutes. Powers are in $(\mu Pr_M)^2$.

-------- = X mode

_____ = O mode

The actual starting times of the various observations were:

(1)	X mode:	77/151/1425	77/151 - 31st May, 1977
(2)	O mode:	77/201/1224	77/201 = 20th July, 1977
(3)	O mode:	77/201/0740	
(4)	O mode:	77/201/0850	

Preferred heights of scatter can clearly be seen.

The small horizontal line indicates typical day time noise at Buckland Park as observed by the narrow beam in $(\mu Pr_M)^2$ for typical transmitter powers.

The powers are not directly comparable to those in Fig. 4.2, but if converted to effective reflection coefficients can be compared. The procedure is described in Fig. 4.2. Bear in mind that the beam-width can be important for isotropic scatter, as also discussed in Fig. 4.2.

stronger on average. As mentioned briefly in Chapter III, the 90km echo at Townsville often becomes an E_s type echo, with near-total reflection. Some radiation usually can penetrate, so the E echo can be seen with a similar strength to this 90km echo. At Buckland Park, E_s type layers may form at 90km during January (summer), but at most times of the year this does not happen. Echoes from 90km at Buckland Park appear to be from isotropic scatterers, and have effective reflection coefficients of about 10^{-3}.

Night time scatterers frequently exist above 80km, and these often have larger reflection coefficients than their day-time counterparts. This is at least partly due to the reduction in ionospheric absorption at night, coupled with the fact that X mode polarization is usually used at night, thus giving larger reflection coefficients (since X mode radiation is scattered more efficiently than O mode). However, the noise is also stronger at night, so the signal to noise ratio can still be much less than during the day. Although echoes at night do generally only occur above about 80km, weak echoes from below can at times be seen. For example, a 76km layer was observed at Buckland Park at 0035 hr on day 78/307. The ionization at these heights is probably maintained by Cosmic Rays (see Ch. I).

Figs. 4.2 and 4.3 show typical power-"height" profiles for Townsville and Buckland Park. The powers are not directly comparable until converted to effective reflection coefficients. The graphs have not been presented as effective reflection coefficients due to the uncertainties of the calibration K_* values (see Ch. III). Recall K_{*T3} for Townsville is about 0.6, and K_{*2M} for Buckland Park is about 0.8. ($\overline{R} = K_*$H.amplitude). Also shown on these graphs are typical noise levels. The techniques used to derive these noise estimates will be discussed in a later chapter.

Echoes from below 80km are principally a daylight hours phenomenon, as has been discussed. They may appear at any time during daylight hours. However, they generally seem to be most common, and strongest, during the afternoon, particularly between about 1300 hr and 1700 hr. Sometimes, however, layers can form quite soon after sunrise. For example, on day 77/201 at Buckland Park, a 70km echo formed around 0700 hr, and echoes from that height occurred intermittently all day, peaking in strength at about 1500 hr.

It is also worth commenting that although many echoes do show a burst-like character, at times quite time-stable echoes can be observed below 80km. Echoes from below 80km do, however, appear "bursty" generally.

These temporal investigations form an important part of this work. Of perhaps greater importance, however, were the results contained in Figs. 4.1a-c regarding the angular spectra of the scatterers.

Fig. 4.4 Profiles of 3 minute means of power vs. range for a layer at about 64km on day 76/259. The vertical scale is a linear scale of uncalibrated power. The gain of the receiver was constant for all measurements, so it is valid to compare powers.

The reduced power at 9.6° and 11.6° from the zenith is the main point to be noticed. This suggests highly aspect-sensitive scatter.

The observations were taken at the following times.

(1) 1240-1243 -------- X mode, (3.0° from zenith)
(2) 1246-1249 -------- X mode, 11.6°
(3) 1255-1258 _____ X mode, 9.6°
(4) 1300-1303 _____ Xmode, 0°

Notice also that there is a slight increase in range at 9.6° and 11.6°, suggesting some off vertical scatter, but certainly not a great deal. The small shift in peak power range may be due to changes in height of the scattering layer, but this is unlikely, as the two near-vertical observations (curves 1 and 4) were made before and after the two off-vertical observations, yet have similar peak ranges.

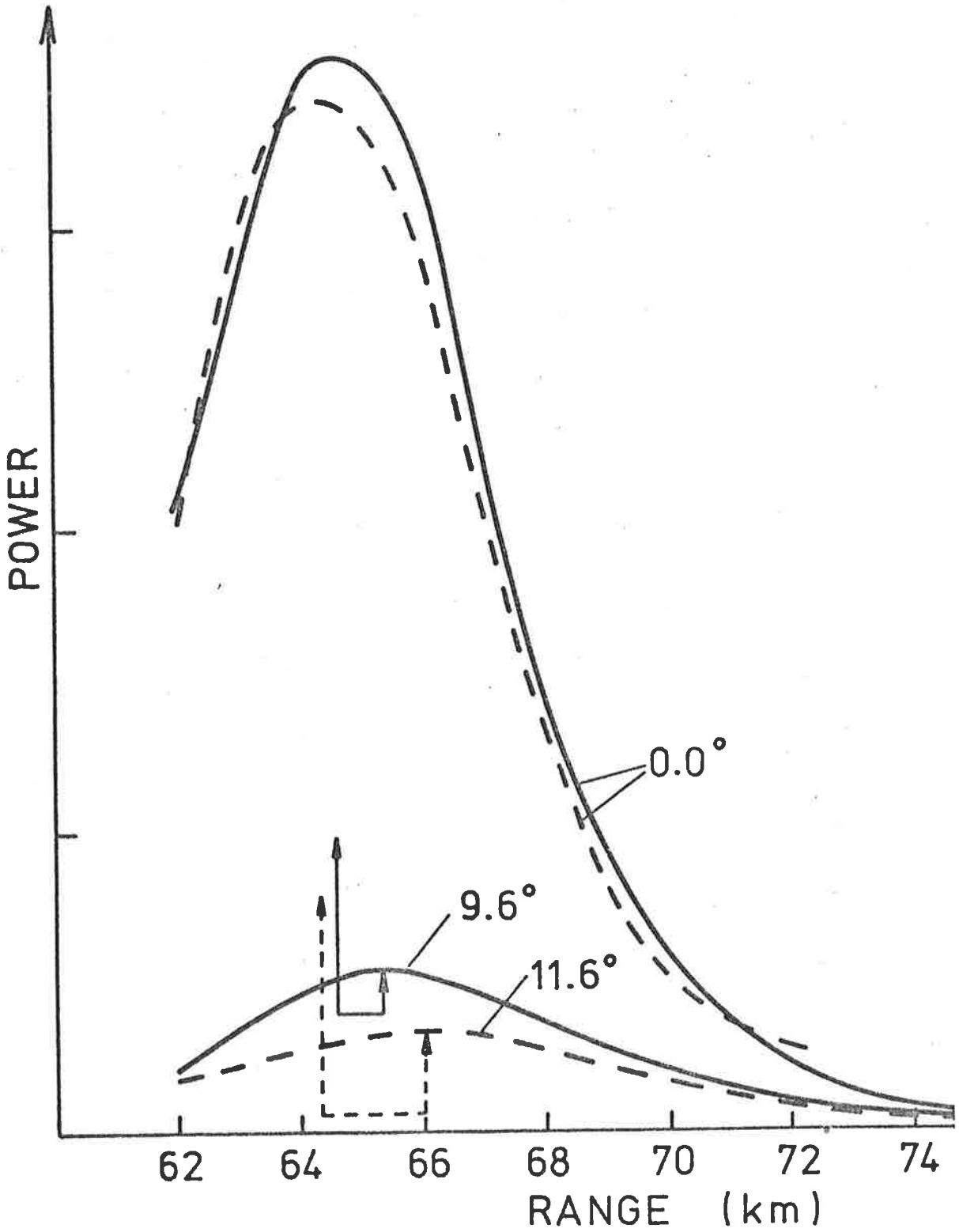
POWER
0.0°
9.6°
11.6°
62
64
66
68
70
72
74
RANGE (km)

4.2.2 Angular Spectra

During the observations made on day 77/151, the narrow beam of the Buckland Park Aerial array was tilted to an angle of 11.6° from the zenith at times. This was done to determine the nature of the angular spectra of the scatterers. A large fall-off in received power compared to the 0° case would suggest a horizontal mirror-like reflector, and only a small change would suggest isotropic scatter (some change might be expected due to changes in antenna gain, beam width etc.). The angle 11.6° was chosen because this places the first minimum of the polar diagram in the vertical direction, thus reducing leakage of scatter from the vertical.

Fig. 4.1c shows that the 74km layer backscatters very little power at 11.6° relative to that at 0.0°. There is a slight increase in range of this layer at 11.6° at this time of measurement. This would be expected if there were some backscatter from 11.6°, since scatter from that angle would have its range increased by a factor sec(11.6°). However, the wide beam shows a similar change in range on this occasion, suggesting that this increase is due to an actual increase of the layer height with time, rather than being a result of tilting the beam. Hence it seems reasonable to assume that the majority of the power recorded at 11.6° is really leaking in from the near vertical, through the edge of the main lobe and through the first side lobe of the polar diagram, in spite of the fact that a null was pointing vertically. Fig. 4.4 shows another similar set of observations for a ~64km layer on day 76/259. Again, scatter was greatly reduced when the beam was tilted off vertical. Interestingly, there was a small increase in height when the beam was tilted, suggesting some off-vertical scatter. Possibly a more detailed investigation of the data for Fig. 4.1c might show a similar increase.

Fig. 4.5 These two diagrams show temporal variations of range-profiles of power. They were formed from 3 minute mean power profiles, with 2-dimensional interpolation being used to smooth the surface. Notice that the largest range is at the front. It can be seen that the temporal variations on the narrow and wide beams are quite similar for the 64-66km echo. As discussed in the text, the scatterers causing this echo scattered quite anisotropically.

Of greater interest is the 76-78km echo observed on the wide beam, which does not show on the narrow beam. The reason for this is discussed in the text.

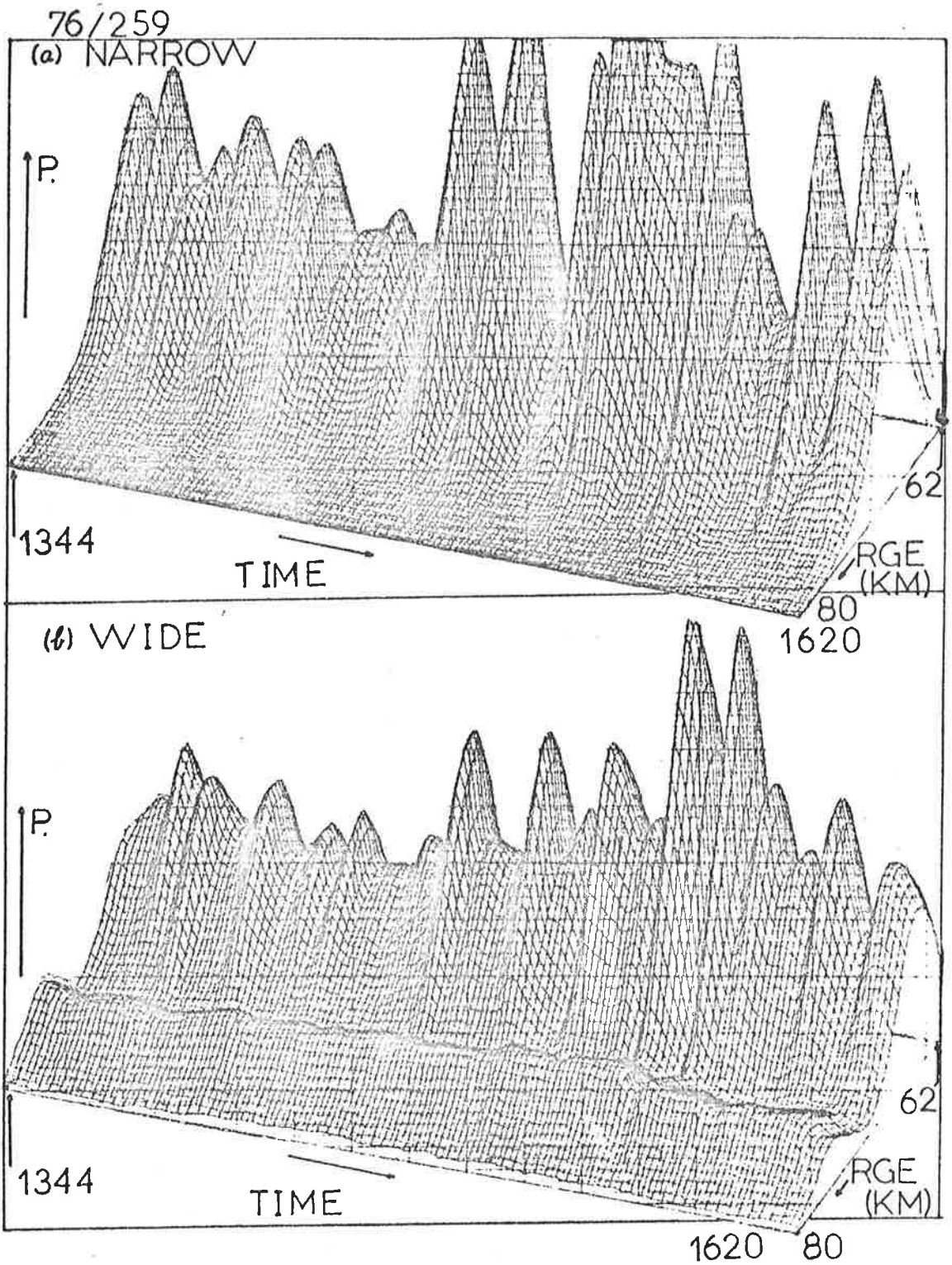
76/259
(a) NARROW
P.
1344
TIME
62
RGE
(KM)
80
1620
(b) WIDE
P.
1344
TIME
62
RGE
(KM)
1620
80

But certainly the behaviour of most echoes from heights below about 74km have generally suggested very anisotropic scatter.

If the power backscattered per unit solid angle is assumed to obey a function proportional to $\exp\{-(\sin\theta/\sin\theta_0)^2\}$, θ being the angle from the vertical, then it can be concluded that $\theta_0 \lesssim 2°\text{-}4°$ for this layer on day 77/151, and indeed for most scattering layers below about 74km. This supports the findings of Lindner (1975a, b). At times, scatter can be seen from the off-vertical, but it is usually weak. For example, the narrow and wide beams give remarkably similar results in Fig. 4.1c, suggesting very little off-vertical scatter. Likewise the 66km layer in Fig. 4.5 (day 76/259) shows very similar behaviour on the narrow and wide beams. At times, the wide beam may show a burst which the narrow beam does not, suggesting it is due to off-vertical scatter, but this requires that no scatterers are overhead to mask the effect. Fraser and Vincent (1970) at Christchurch, New Zealand, have seen 70km scatterers out to around 10°, but amplitudes were quite weak. It is fair to conclude, then, that the scatterers below about 75km are quite anisotropic. For such Fresnel scatter, it is also required that the dimensions of the scatterer cover greater than a Fresnel zone = $(\lambda z)^{\frac{1}{2}}$, z being the height of scatter and λ the wavelength. (This implies a dimension of at least 3km at 70km height.)

In contrast to the 74km layer, the higher 90km layer clearly shows strong scatter at 11.6° from the zenith (Fig. 4.1b). Further, the received power on the wide beam is around 6dB larger than on the main beam, when allowance is made for the different gains, and this also suggests the existence of strong scatter from off-vertical angles. An increase in the range of the layer of about 2km at 11.6° compared to 0.0° can also be seen, further suggesting significant off-vertical scatter. Similarly, the mean range of the layer observed with the wide beam is greater than the range measured using the narrow beam.

Occasionally it is possible to determine the location of individual bursts. One might expect all bursts received on the narrow beam to be received on the wide beam, but the wide beam might, on occasion, pick up a burst at some angle from the zenith which the narrow beam might not receive. For example, at 1007 in Fig. 4.1b, the wide beam receives a strong burst whilst the narrow beam does not show a similar structure, suggesting the bulk of reflections came from the off-vertical on this occasion. On the other hand at 1010, a strong burst shows on the narrow beam, but only weakly on the wide beam. This was probably a small region of scatter directly overhead. Its relative strength on the wide beam would probably be small compared to the normal wide beam strengths because that beam receives much of its signal from the off-vertical. The range of this echo is 88km on both beams, compared with the normal 90km mean height on the wide beam, again suggesting an overhead reflection.

In general, for this particular 88-90km layer, the average power at 11.6° is reduced by a factor of 3 compared with the vertical beam, suggesting $\theta_0 \sim 12°$ in an $\exp\{-(\sin\theta/\sin\theta_0)^2\}$ model. This is again consistent with Lindner (1975a, b).

In fact, all scatterers above about 80km showed quasi-isotropic scatter during the investigations involved in this thesis.

The actual transition region from scatterers of small θ_0 ($\lesssim$ 4-5°) to scatterers of large θ_0 ($\gtrsim$ 11°) is actually quite sharp, and lies between about 76 and 80km (e.g., Lindner, 1975a, b; Vincent and Belrose, 1978). Scatterers appear to be either quite Fresnel like (small θ_0), or fairly isotropic; there do not seem to be many intermediate cases. However, the actual height of the transition region is a little hard to define. It appears it may vary from day to day. Lindner's results suggest the transition is at about 80km. However, at times 76km echoes can appear quite isotropic. At other times 74-76km echoes can appear

quite anisotropic. An example of an isotropic 76-78km scattering layer is illustrated by Fig. 4.5. It can be seen that simultaneous observations on a narrow beam and a wide beam indicate a layer at 76-78km on the wide beam, but nothing on the narrow beam. Observations on the Cathode Ray Osciloscope (see Chapter 3) showed occasional weak bursts of scatter on the narrow beam, but no sustained echo. The wide beam did, however indicate a steady echo. These observations can be explained by a layer at 76 to 78km, consisting of "blob-like" irregularities separated horizontally. The narrow beam would only see a burst when a blob was overhead - but the wide beam would always see some scatter if the irregularities were quasi-isotropic, since there would always be some irregularities in the wide beam. When 3 minute means were taken, an effect would only be seen on the wide beam, the weaker effect on the narrow beam being "swamped" by the tails of the echoes from the 66km reflecting layer.

As a further point, it can now be stated that the backscatter cross-sections (σ and η) estimates made previously are not relevant below about 75km, as the echoes are Fresnel-like. Above 80km, however, the scatter has been seen to be quasi-isotropic. Thus turbulence cannot be ruled out as a possible mechanism of scatter, and the σ estimates may be useful for calculations of turbulence parameters. (It will be seen later that turbulence can still be invoked to explain the lower echoes, at least in one model of the mirror-like scatter, but the σ estimates will still not be useful for determination of relevant turbulence parameters such as ε and K, the energy dissipation rate and eddy diffusion coefficient.)

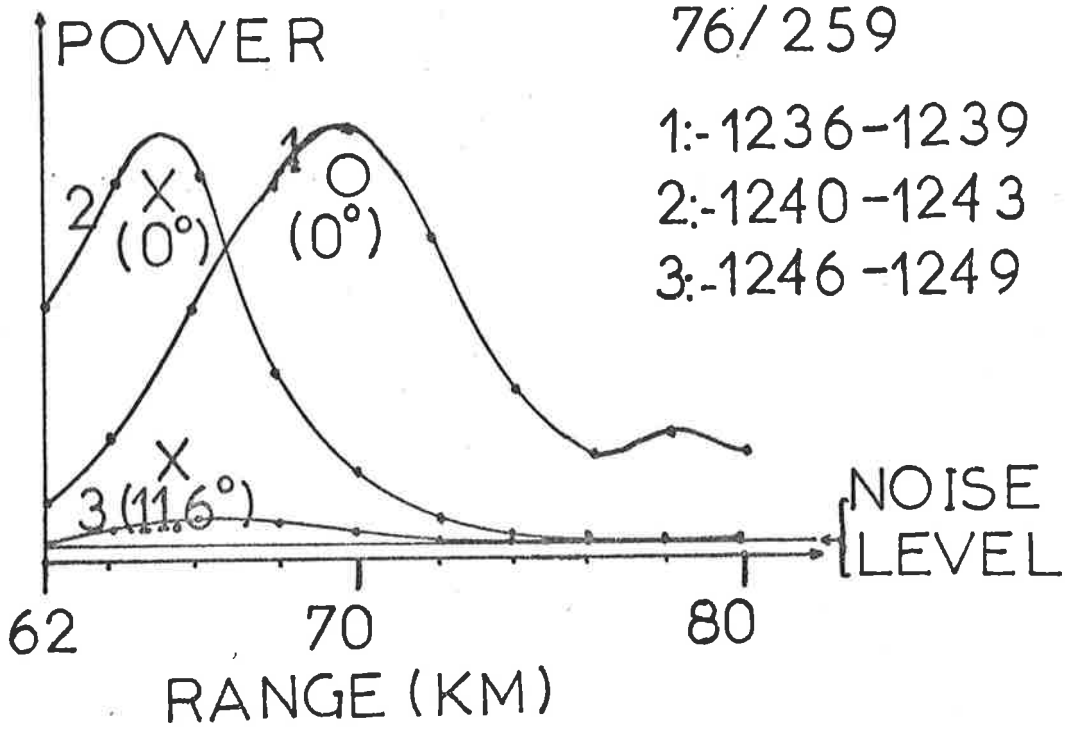

Fig. 4.6a Illustration of the differences O and X mode power profiles can have, using the narrow beam. The angles shown are angle of tilt of the array beam from the zenith. An 11.6° observation (number 3) clearly shows the scatter was quite anisotropic. Most of the scatter received was thus from the vertical. For this reason, curve 2 has been written as a 0° observation, although in reality the beam was tilted at 3.0°.

Fig. 4.6b Profiles of 1 minute mean powers due to a layer at about 86-88km on day 77/201, using the narrow beam. All powers are in $(\mu Pr_M)^2$. The times given are the start time of the minute for which the mean was calculated. The observations were made in the early morning, when absorption was fairly low, but increasing rapidly with time. The layer was only beginning to form, as can be witnessed by comparing O mode powers at 0740 (curve 1) and 0843 (curve 5). The layer was also monitored on a wide beam, and its mean range on any one mode did not fluctuate more than a kilometre or so. This can be seen by comparing curves 1 and 5 - the difference in range is less than 2 km. Absorption can be seen to be low up to 85km, because curve 2, which used X mode, has greater powers than curve 1. The region was monitored continuously during this period, and these curves are typical of the time periods they represent.

Of major interest are ;

(i) the reduced height of X mode echoes compared to O mode echoes when looking vertically (curves 2 and 3 compared to curves 1 and 5);

(ii) the increased range on O mode at 11.6° compared to the 0° echoes, and the fact that 11.6° powers are only 3dB down on 0° powers (curve 5 compared to curve 4);

and

(iii) the fact that the 11.6° X mode observations do not show a great increase in range compared to the 0° observations, and are down in power by 6dB compared to 0° (curve 3 compared to curve 2).

These points are discussed in the text.

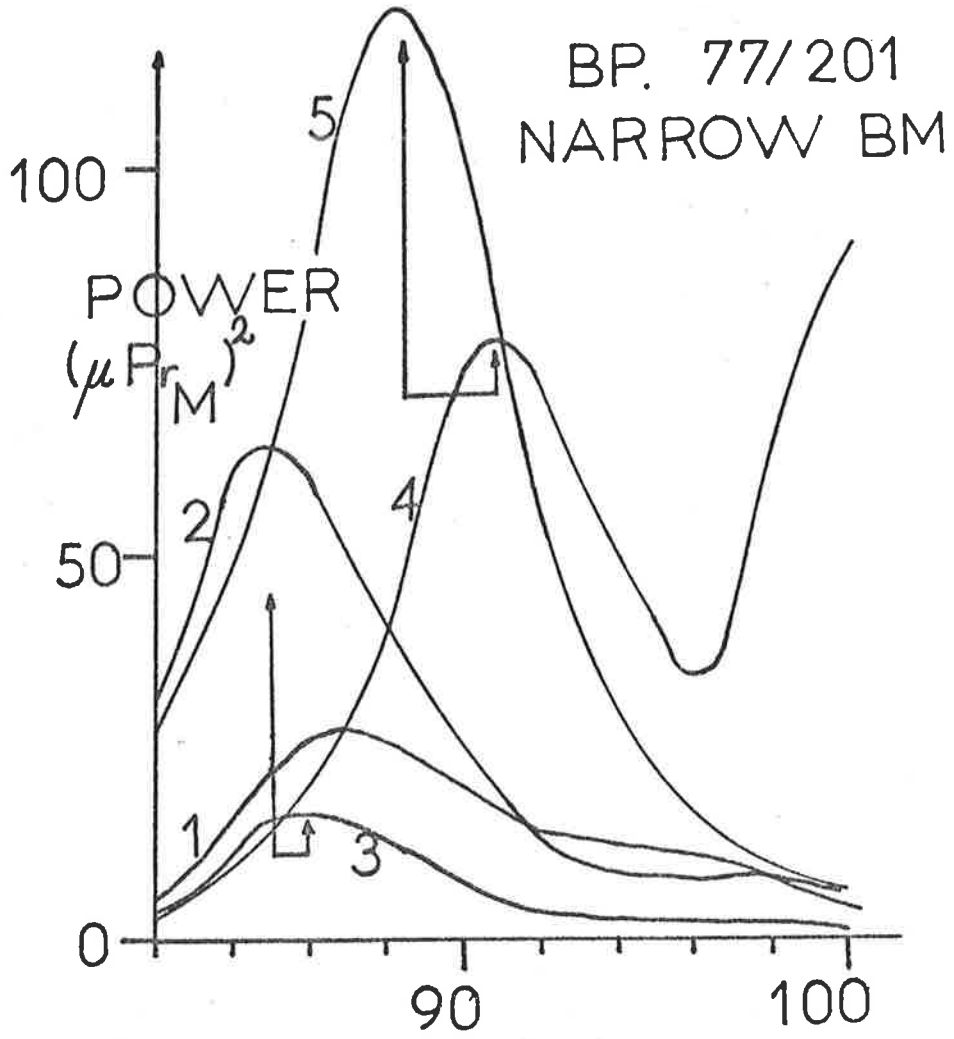

1. 0740 - O MODE, 0°
2. 0745 - X MODE, 0°
3. 0802 - X MODE, 11.6°
4. 0822 - O MODE, 11.6°
5. 0843 - O MODE, 0°

4.2.3 O and X Mode Comparisons

Fig. 4.6a shows some examples of near-simultaneous observations of the D region echoes on O and X modes. It can be seen the structures differ considerably. It is worth considering why this is so.

As radio waves enter the ionosphere, they are absorbed, as we have seen, and suffer some partial reflection. X mode is reflected most strongly from these partial reflections, but also suffers strong absorption as the electron density increases. Thus X mode scatter returned from higher regions of the ionosphere is highly absorbed and hence quite weak compared to O mode. The height region in which X mode scatter strengths change from strong to weak can be of the order of a few km. Echoes on O and X mode are often significantly different around this transition region.

The case presented in Fig. 4.6a probably corresponds to an ionosphere with two principal scattering layers - one at about 64km, and one at 70-72km. The stronger X mode reflection coefficient at 64km, and increased absorption above 70km, results in the 64-66km layer showing most strongly on X mode. On O mode, the absorption is not significant up to 74km, so this shows the more strongly reflecting 70-72km scatterer. The effect of the 64-66km echo is still present, but is hidden by the larger 70-72km echo - the result is a "widening" of the leading edge of the 70-72km echo. (Bear in mind that these profiles are 3 min. means). Once gain, the effect of tilting the beam of the array to 11.6° can be seen by means of the 1246 echo, and again the scatterers were clearly highly anisotropic.

The case presented in Fig. 4.6b is even more interesting. On this day (77/201), a very stable layer at about 86 to 88km altitude occurred. Again, it would be reasonable to speculate that the reduced X mode height

was due to the effect of a rapid increase in absorption at this height, with strong reception from below this transition region, and weak reception from above. The scatter could either be due to a continuum of scatterers near this region, several kilometres in vertical extent, or due to perhaps a few close layers, some just below the region of high absorption, and some above. Whichever is correct, the scattering region had to be several kilometres from the bottom to the top. The O mode 11.6° observations suggest quasi-isotropic scatter, since the range is increased by about 2km and the power only down by 3dB compared to the 0° observations. Conversely, X mode observations on 11.6° suggest scatter to be more anisotropic, with an increase in range of only 1km, and a power reduction of 6dB, compared to the 0° observations. This may suggest that the X mode scatter came from a different type of scatterer to that from which the O mode came. Hence it could be speculated that the region consisted of anisotropic scatterers at the lower heights, and more isotropic ones higher up. However, the possibility also exists that by tilting the beam of the array, thus making the radiation enter the highly absorbing region obliquely, the X mode radiation might have been absorbed even more quickly than at 0°. This would also result in a reduction in the range of the peak of returned power compared to an assumed sec(11.6°) increase in range. This problem has not been quantitatively examined.

Whatever the reason, however, the data certainly suggests a scattering region several kilometres in vertical extent, and also suggests an extremely rapid increase in absorption at this height. Such a rapid increase in absorption suggests in turn a large increase in electron density at this height. Such "ledges" have often been observed in the region 80 to 90km altitude (e.g., section 1.2.1, Chapter I). (This could perhaps have been investigated more thoroughly with a differential

absorption analysis of the O and X mode profiles. However, the fact that the observations were taken at separated times, and during a period when electron density was building up rapidly, would make the results only qualitative at best).

Ledges of this type may be very important. One will be discussed in much greater detail in a later chapter, using simultaneous rocket measurements and partial reflection observations. It will be seen that ledges of this type, and echoes from heights of about 86km, may well be related. By doing a 1-dimensional computer simulation (using Sen-Wyller formulae) of the passage of an HF wave of frequency 1.98MHz through the electron density profile deduced by rocket experiments, and assuming all Fresnel scatter, it was possible to simulate this difference of O and X mode heights. The details of this particular analysis will not be presented, however, due to lack of space. It will also be seen later that scatter from 86km is not entirely Fresnel-like (indeed this is obvious from the quasi-isotropic O mode scatter already noted) so this one dimensional simulation is not entirely valid. However, it does at least illustrate the absorption on X mode can change sufficiently rapidly to produce the desired effect. It is also interesting that often a small dip in electron density below the large ledge occurs - perhaps the X mode scatter observed on day 77/201 was related more to this dip than the ledge itself, explaining the different nature of the X mode scatter?

It will be noticed that this observation was made during the early morning. As the day progressed, the electron density built up more, and X mode radiation was significantly absorbed at lower heights before reaching this ledge. Thus later during the day, the effect was less pronounced.

The layer also showed a height variation during the day, falling to an altitude of around 80 to 82km around noon and then once again rising back to about 86km by late afternoon.

4.2.4 Height Fluctuations

Observations of height fluctuations and distributions of echoes can show some interesting effects, and provide some useful data. Stratification of echoes has already been dealt with in Chapter I, and needs no more comment. There is no doubt that the D region is generally quite stratified, with echoes coming from particular heights on any one day.

4.2.4a Upper Limits of Echoes

Before discussing temporal variations of echo heights, one particularly relevant observation bears discussion. It has been seen how echoes are produced at heights above 50 to 60km, and it has been mentioned that echoes can be seen up to 95 to 100km. At greater heights, total reflection from the E region hides any other echoes in the day time. The question arises, then, as to how high partial reflections would extend if there were no total reflection? The best time to examine this is at night, when there is no total E region reflection. We saw in Chapter III that E_s echoes can occur above 100km at night. Partial reflection echoes can occur up to 150km in range, but the strongest echoes fall off in strength around 110-120km. In fact, the echoes from above about 110km range are generally obliques. This was made quite clear on one night in June 1978, at Townsville (day 78/183 at 2045 hr). On this occasion there was a sporadic E (E_s) echo at about 110km, which totally reflected on X mode (no F layer could be seen), but partially transmitted on O mode (an F layer was visible). Thus all scatter from ranges greater than 110km on X mode had to be by obliques, or possibly multiple scatter processes below 110km. Yet O and X mode range profiles above 110km were quite similar, suggesting that all O mode scatter occurred by the same processes as X mode scatter. This, then, suggested that there was very

little scatter from altitudes of greater than 110km. The reason for this fall off is not immediately obvious. However, if we were to speculate (as others have done - see Chapter I) that these partial reflections were due to turbulence, then the fact that the echoes die out above 110-120km could be explained by the fact that this is of the order of the turbopause height, so no significant turbulence exists at greater heights. (See section 1.3.3, Chapter I;- the night time turbopause height before about 2200 hr is at 105-110km according to Teitelbaum and Blamont (1977). Other estimates vary, but are around this value.) Recall, however, that Rees et al. (1972) have found evidence of weak turbulence up to heights of 130km, so some weak, unseen turbulence could exist up to 130km. Such turbulence would produce weak scatter, as radio wavelengths of 150m would generally be in the viscous region of turbulence above 95-100km, according to model 2 in Fig. 1.9a. Particularly strong patches of turbulence (with large energy deposition rates) could perhaps be seen in the inertial range on occasions.

It is fair to say, however, that this fall off in echo strengths above 110km is quite compatible with a turbulence mechanism. (This does not mean, however, that no echoes ever occur above 110-120km. Sequential sporadic E layers have been discussed in Chapter III, and meteors can also occur.)

4.2.4b Temporal Height Fluctuations

In keeping with the rest of this section, only height fluctuations on time scales of the order of minutes will be discussed here. Fluctuations on the scale of seconds will be considered later.

Although the vertical resolution of the pulses used in the work for this thesis was about 4km, some information can be gained at better resolution. The peak of an echo can be located quite accurately by

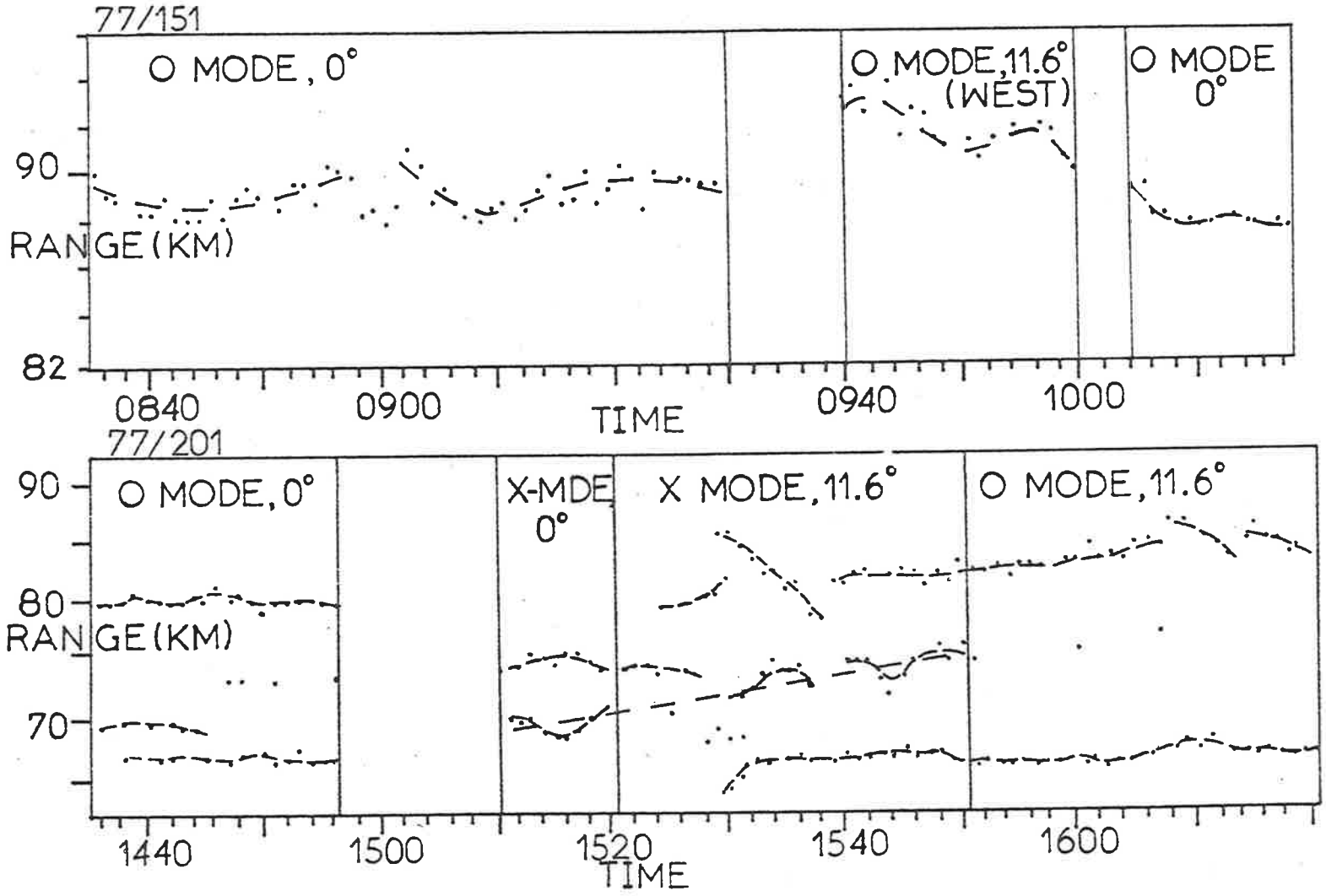

Fig. 4.7a Ranges of the peaks of one minute mean echo profiles plotted as a function of time, for

(i) day 77/151
and (ii) 77/201.

spline interpolation. If these peaks are located for 1 minute mean power profiles, and plotted as a function of height and time, graphs like Fig. 4.7a result. These can give potentially important information, although the data cannot always be interpreted unambiguously. However, with reasonable assumptions, they can be quite useful. For example, the scatter of points in Fig. 4.7a(i) indicates either that a thin region of scatterers are moving in height significantly, or that the layer producing the scatter is several kilometres thick, and the variations of the heights of the peaks results from differing interference of scattered pulses during each minute. The second suggestion seems more likely. The curve from 0840 hr to 0900 hr in Fig. 4.7a(i) either suggests that this layer is oscillating vertically, or that we are seeing the effects of a large cloud which drifts across the beam, thus decreasing in range until overhead, and then increasing as it moves away. The second case seems more likely, so this data suggests a spatial variation in scattering strengths, and the existence of "clouds" of scatterers.

The period between 0940 hr and 1000 hr shows two cycles of a rather regular oscillation. The beam was tilted at 11.6° from the zenith to the West. It would seem reasonable to assume that this was due to a gravity wave perturbing a cloud of scatterers - possibly oscillating it. The general downward slope suggests the cloud was moving towards the region immediately above the array. At 1004, the beam was pointed vertically, and it seems we may (fortuitously) be seeing the same scatterer as that at 11.6°. (It is also possible that the effect is due to a layer moving down vertically, and also oscillating vertically, but the fact that the oscillations are greatest at 11.6° suggests much of the oscillatory movement is in the horizontal plane. Thus this alternative seems unlikely.) Thus it appears that we have tracked a cloud. The period of oscillation

was about 10 to 14 minutes. This is not the period of the gravity wave, but rather a Doppler shifted period, as the cloud was (probably) passing through the gravity wave at the speed of the background wind. The cloud, when observed at 0940, was at a range of about 93km, whilst at 1010, when overhead, it was at 88km. This suggests that at 0940, the cloud was at an angle of about 15° to 18° from the zenith. This information should be useful to determine the velocity of this cloud.

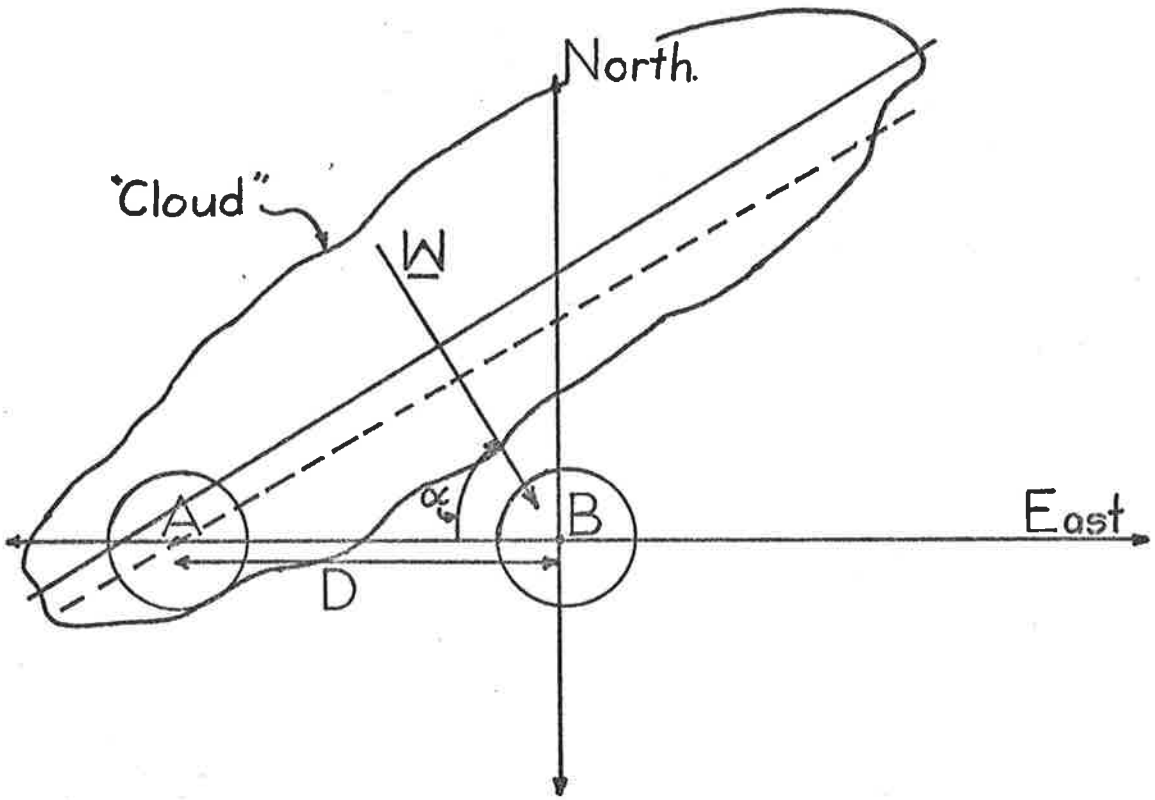

However, this is not as simple as it at first appears, as indicated by the above diagram. Circle A represents the area of the ionosphere at 88km covered by the array beam at 11.6°, and B that for a vertical beam. $\underline{W}$ is the wind vector. Let $W = |\underline{W}|$. The distance D is given by 88km x sin(15° → 18°), i.e. about 25km. The time to travel this distance is about 1010-0940 = 30 minutes. This suggests $W/\cos\alpha = 25/30\text{km m}^{-1} \approx 13\text{m s}^{-1}$. There is insufficient information to

determine W and α, although clearly $W \lesssim 13 m\ s^{-1}$.

However, this calculation also assumes the scatter at 0940 comes from a point at the same distance from the axis of the cloud as that at 1010, and also that the cloud is aligned perpendicular to the direction of drift. Neither of these need be valid. (Also see the discussion of full correlation analysis in Chapter III.) Partial reflection drift measurements suggested that the wind vector was about $28 m\ s^{-1}$ towards the south-east at this time. These calculations thus show the difficulties in making crude estimates of velocities. It may be more meaningful to compare this W estimate to apparent velocities determined by PRD.

Fig. 4.7a(ii) shows more interesting cases. It can be seen, for example, that the 80km echo is very stable in height. (This layer has already been discussed to some degree in relation to Fig. 4.6b, when it was at 86km height.) This suggests either that it was very thin and stable in height, or that its basic profile remained quite constant throughout the day. The second case seems more likely, as it was shown in connection with Fig. 4.6b that the scatter region was a few km thick. A very stable layer at about 65-68km can also be seen. Another layer (or set of layers) lay between 70 and 75km. The long broken line drawn between 1510 and 1550 shows an ascending layer, with possible gravity wave oscillations present with periods of the order of 10 min. These dips in range could also be due to scatterers moving overhead, but the dips are around 2km deep, suggesting the scatterers would be up to 12° off-zenith. If this were so they should be weak in strength at that stage, being quite anisotropic. This was not so, and the gravity wave hypothesis is preferred. Either the scatterers were oscillating in height, or the region of scatter was changing, induced by the gravity wave. (It will be seen again and again in this thesis that these

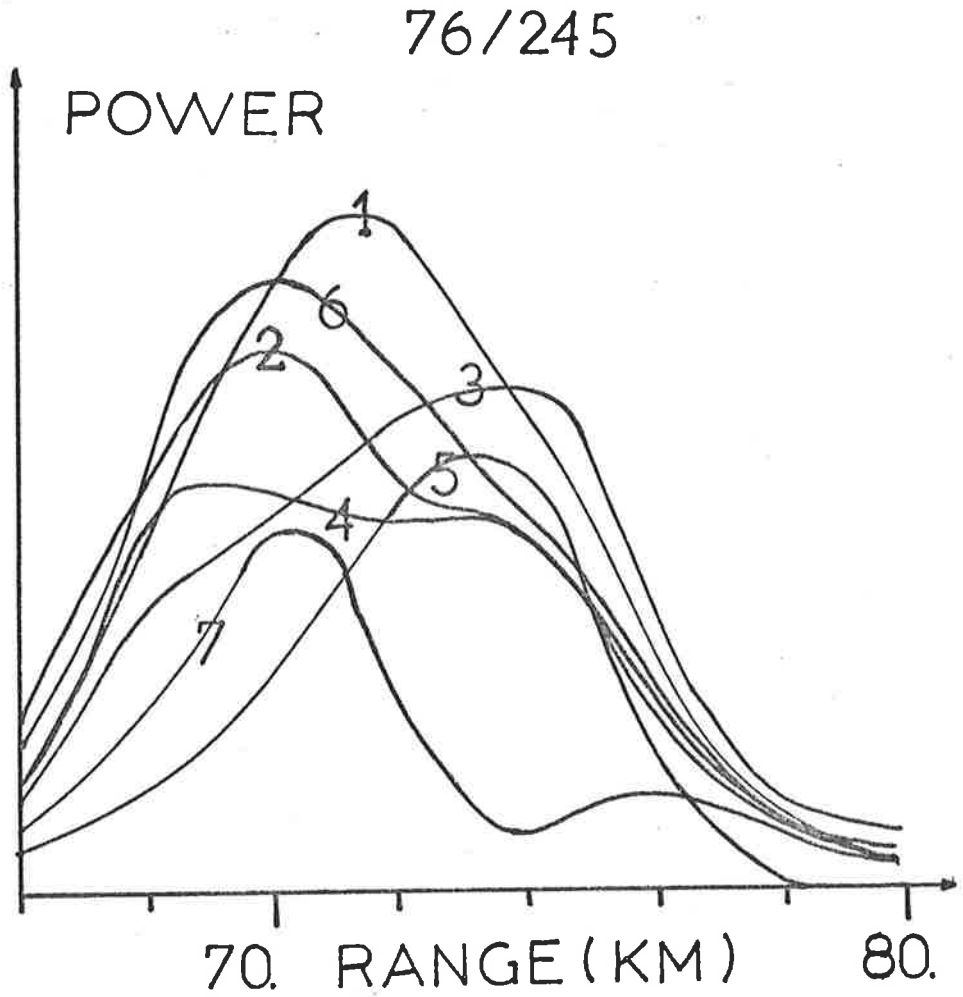

Fig. 4.7b Half minute mean power profiles for day 76/245, showing the variations in form of the profiles due to the interference of several scatterers between 70 and 74km. The profiles correspond to the following time periods:

1 = 1418-1418.5
2 = 1418.5-1419
3 = 1419-1419.5
4 = 1419.5-1420
5 = 1420-1420.5
6 = 1420.5-1421
7 = 1421-1421.5

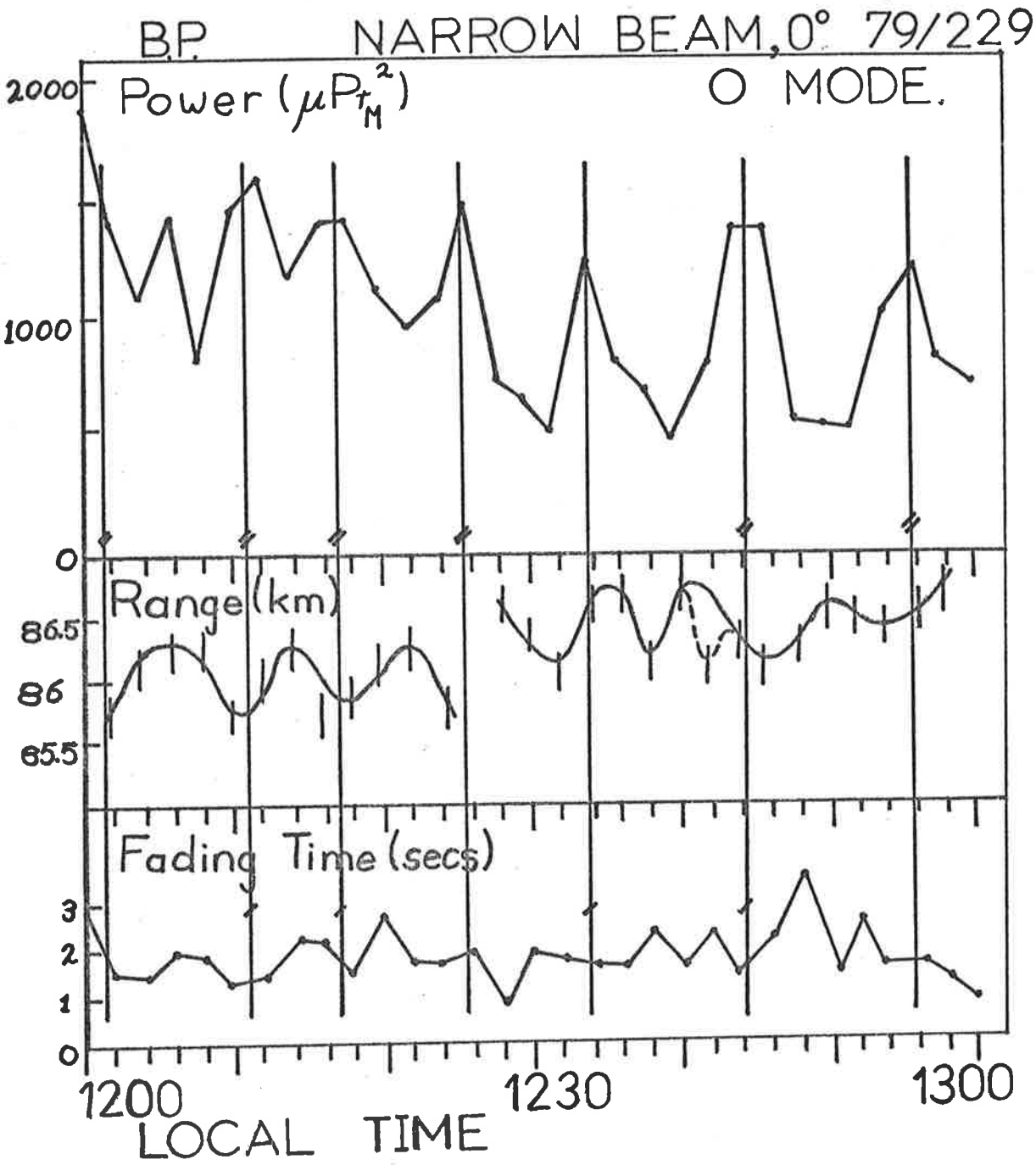

Fig. 4.8 Graphs of 2 min. mean powers, the range of the peak of the profile, and mean one minute fading times, for day 79/229 for the "86km" layer. The vertical lines correspond to maxima of power. Double dashes on these lines indicate anticorrelation of power and range. Single dashes (bottom graphs) indicate an anticorrelation of power and fading times. Powers and range seem to be anticorrelated. Powers and fading times appear to be weakly anticorrelated, and range and fading times weakly correlated.

The jump in range at 1229 appears to be real, although the reason for it is uncertain.

scattering layers often appear related to quasi-regular oscillations of periods of 5 to 15 minutes.) The curves linked by the broken line as shown on Fig. 4.7a(ii) were chosen because the wide beam, which was being used simultaneously, suggested this was all the one scattering layer. This does not rule out the possibility that the oscillations at 75km between 1530 and 1550 could, rather, be related to the 75km echoes at 1510-1520 hr. Often it is hard to decide which echoes belong to which layers, particularly for these lower echoes. This is illustrated in Fig. 4.7b, where it can be seen the peaks of the echoes move around quite a lot. This is probably due to interference between layers located between 70km and 74km or even a continuum of scatterers in this region (or perhaps even just two layers of scatterers near 70 and 74km). This type of fluctuation in height is quite common. At times, quite height-stable echoes can be seen (for example the 65-68km echo in Fig. 4.7a(ii)), but often too, this type of large height fluctuation occurs, even on scales of the order of seconds, as will be seen later.

Fig. 4.8 is a particularly striking example. It shows temporal variations of the range of 2 minute mean power profile peaks, and of the actual power. (Fading times are also shown - these will be discussed shortly.) There would appear to be a significant degree of anti-correlation, with strong power bursts during minima in range. Both sets of fluctuations appear to be associated with an oscillation of period around 8 min. The reasons for this correlation are unclear, but could be along similar lines to the suggestion of Hodges (1967), whereby unstable temperature gradients are created at one particular point in a gravity wave cycle, thus possibly generating turbulence. It is significant that power bursts occur only once per gravity wave cycle, as distinct from observations at VHF by Harper and Woodman (1977 - also see Chapter I, section 1.4.2) which suggested power bursts twice per gravity

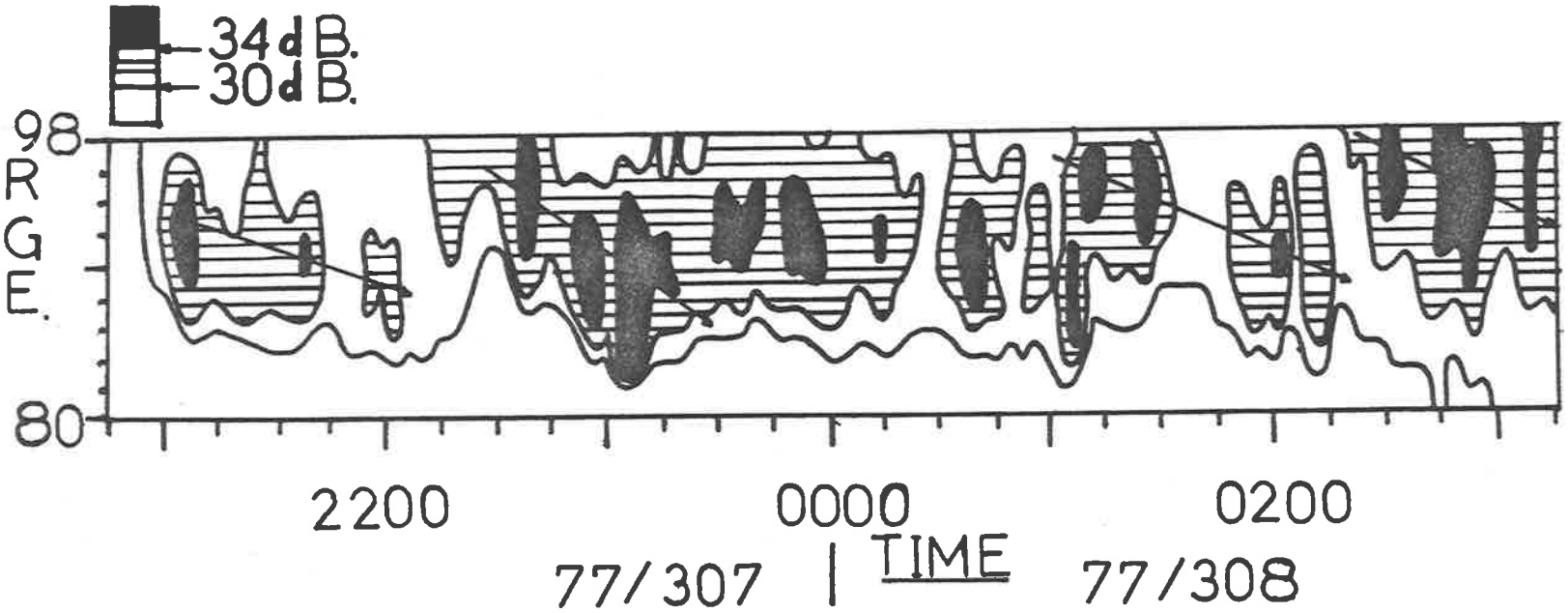

Fig. 4.9 A particularly interesting night-time contour plot of power against range and time. One minute mean powers were used, and smoothed by computer interpolation. The wide beam was used for reception. Note how power bursts appear at 98km and appear to propagate down to lower levels sequentially. Powers are in dBs of $(\mu Pr_W)^2$. Bursts of 38dB correspond to reflection coefficients of 10^{-2}. Thus these echoes are stronger than normal day-time echoes, partly due to the reduced absorption at night time, and also due to the fact that X mode polarization was used. (X mode reflects more efficiently than O mode.)

wave cycle. Van Zandt et al. (1979) have also observed gravity wave-power correlations, with one power burst per gravity wave cycle, in the troposphere.

One other interesting occurrence which may suggest a gravity wave induced effect is illustrated in Fig. 4.9, which shows some night-time observations. Bursts of scatter appear at the upper heights, (around 98km) and then appear to move down to heights of about 90km in about 1 hour. The bursts then disappear, and a new set appear at the upper heights. Notice also that these echoes correspond to effective reflection coefficients of about 10^{-2}. This is quite strong when compared to day-time 90km echoes, which usually have reflection coefficients of about 10^{-3}. No doubt the reduced absorption at this time of night is part of the cause for the stronger echoes.

This behaviour suggests that the region 86-98km may be close to being unstable; a gravity wave propagating through may then render the region unstable, producing scatterers. At lower heights, the atmosphere may be sufficiently stable that the gravity wave cannot induce instability. Alternatively, the wave may have been generated at 86km, propagating energy upwards, and so giving the usual downward phase propagation. Another possibility is that the gravity wave could generate turbulence in all regions, but only in regions of large electron density gradient would significant scatter occur ($C_n^2 \propto |M_e|^2$: Chapter II, equation 2.3.2.11). Electron density gradients are often quite large at 90-100km at night (e.g., Mechtly and Smith, 1968). This latter possibility will be discussed more in Chapter IX.

4.3 Short Term Temporal Changes

In examining changes of echo structure on time scales of the order of seconds, it is most desirable to record both amplitude and phase information. Interpretation of amplitude - only data can be difficult and ambiguous. However, some useful information can be gained from amplitude only, and some preliminary effects will be discussed in this section.

Fig. 4.10a Raw fading at Buckland Park. Amplitudes of the received signal have been plotted as a function of time at various ranges. Successive ranges have 2km steps between them. O mode polarization was used.

A significant power burst can be seen at 68km, with applitudes maximizing at 1144-1145. Fading became very slow and shallow (specular?) during this period.

Data was only recorded every second minute up to 70km, but continuously above. The data was recorded using a wide beam for reception.

This graph also shows the vertical resolution of the pulses used. For example, 70km and 76km echo oscillations show a reasonable degree of independence. Even 70km and 74km show significant differences. But 70 and 72km fluctuations are quite similar. The resolution is thus 4-6km.

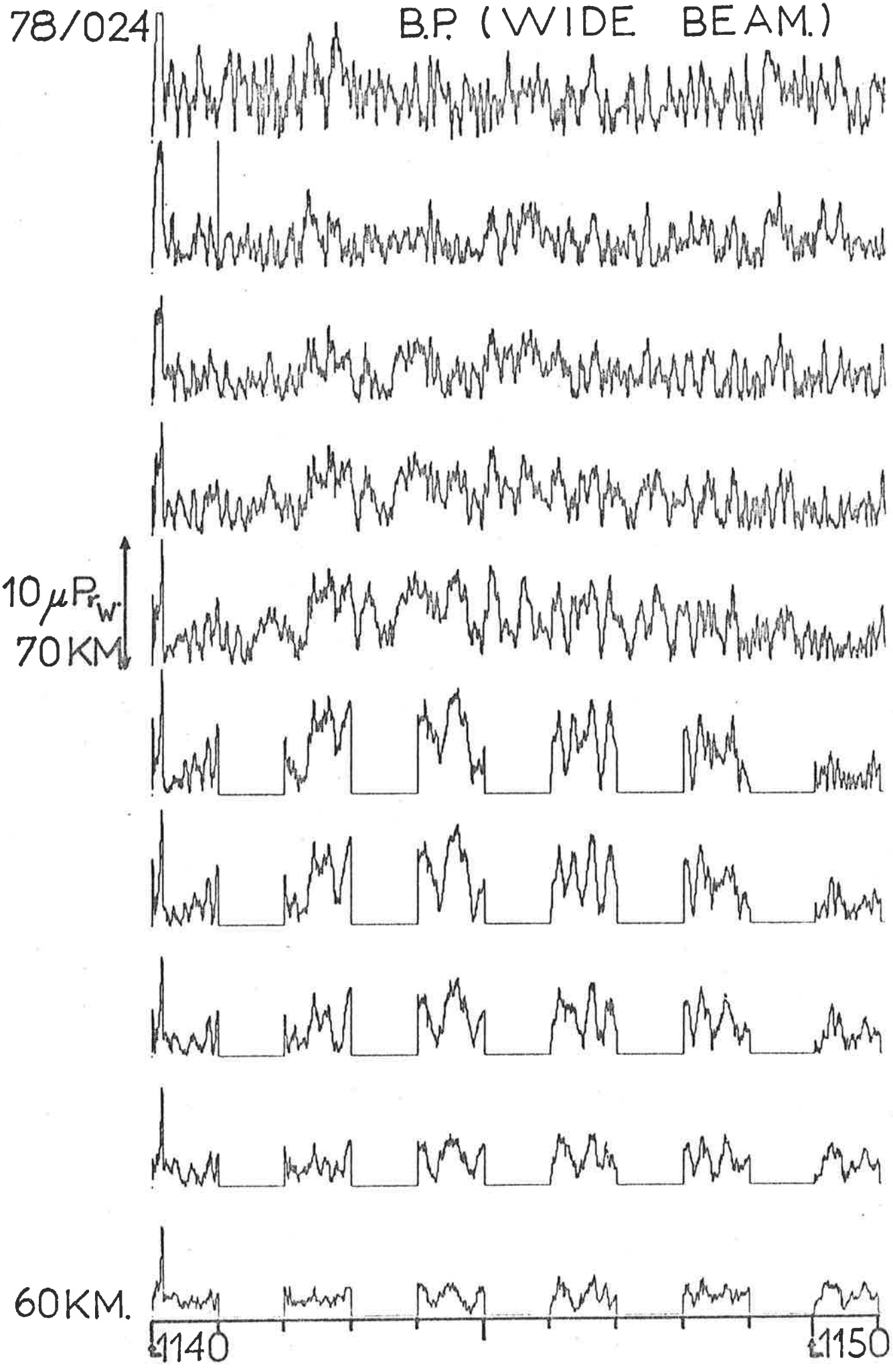
78/024
B.P. (WIDE BEAM.)
10 μPr.w.
70 KM
60 KM.
1140
1150

Fig. 4.10b Another example of detailed fading. This data was recorded using a wide beam at Buckland Park, near midnight on day 77/307. X mode polarization was transmitted. Notice how the height of maximum power decreases from 92(±1)km to 90(±1)km and then rises again to 92(±1)km. [94km amplitudes have not been shown, but were always less than those at 92km.] This sequence is not uncommon, and suggests a cloud of scatterers drifting overhead.

If it were assumed that the cloud had small horizontal dimensions (less than 1km say), then the velocity of the cloud was about $((2 \times 90\text{km} \times \cos^{-1}(90/(92\pm1)))/5 \text{ min})\text{km min}^{-1}$ - i.e. about 90-150 m s^{-1}. If the cloud was extended horizontally, so the effective scatter point moved back along the cloud as the cloud drifted through, then the velocity would be somewhat more. Partial reflection drift measurements showed apparent velocities reached greater than 100 m s^{-1} at 86-90km in the period 2329-2347 hr at times. The apparent velocity may be better to compare the above estimates with, as the above calculations do estimate a form of apparent velocity rather than a true velocity. True velocities were about 50 m s^{-1} in this period, as estimated by full correlation analysis.

Thus, although agreement is not perfect, the estimated velocity of the scatter is of a similar order to the PRD velocities. Considering the crude velocity estimation technique used, this result may support the concept of this being a cloud moving overhead. Notice also how the fading becomes slower as the cloud moves overhead. Before and after being overhead, the Doppler shifted scattered radiation from the cloud beats with the radiation from weaker scatterers overhead, producing fast fading. But whilst overhead the Doppler-shifted frequency of the scattering cloud is quite small (little vertical motion) so beating effects are slower.

77/307 (B.P.)

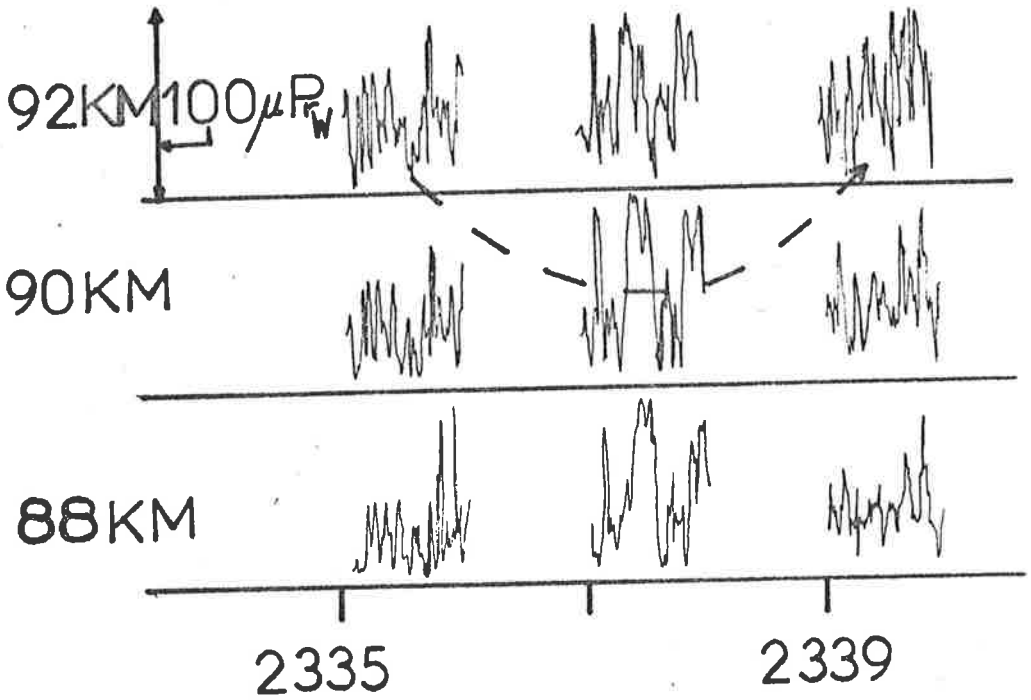

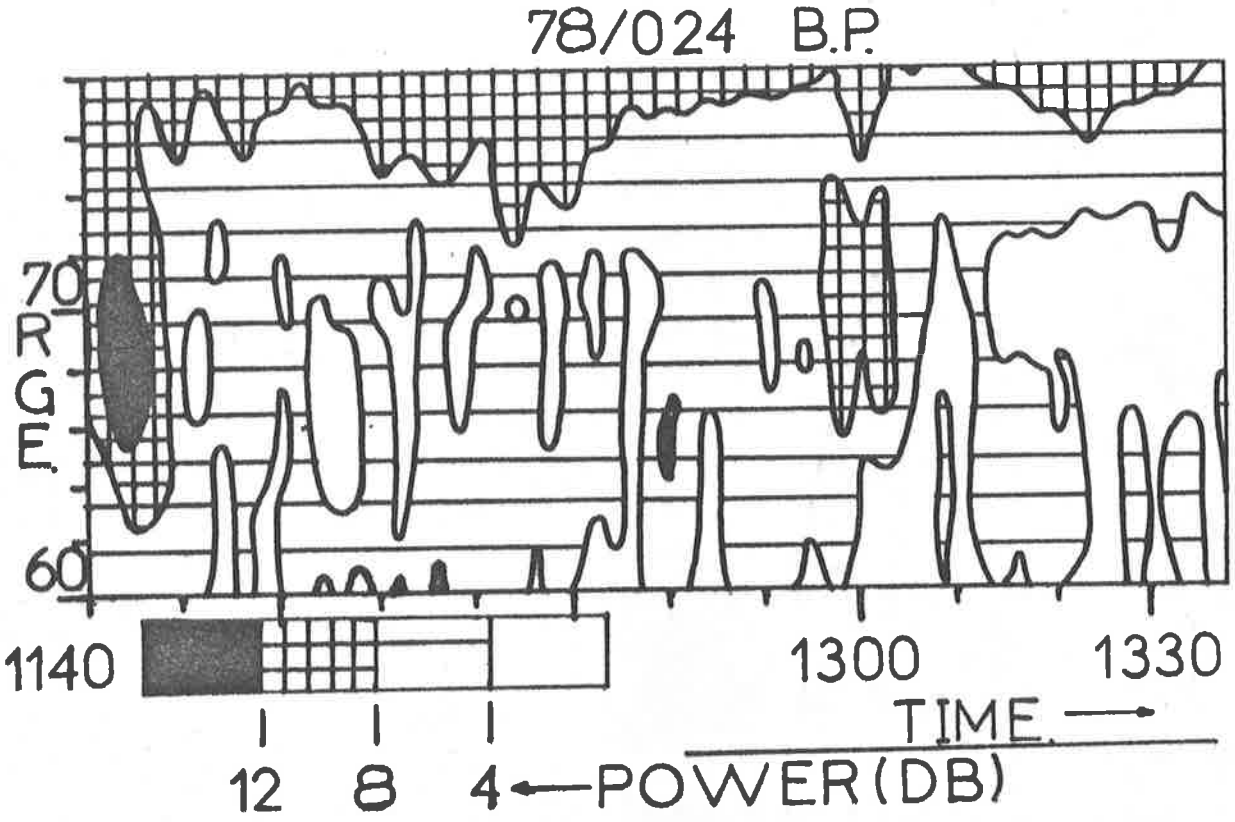

Fig. 4.11 Smoothed contour diagram of 2-minute mean powers as a function of time and range for 24th January, 1978, at Buckland Park. The wide beam was used for reception. Powers are dBs of $(\mu Pr_W)^2$. The diagram illustrates well the temporal variability of the lower echoes. A strong burst at 1145, 68km can be seen, and then the 68km height region shows very weak scattered power. Another strong burst occurred at 1300, 70km. The detailed fading associated with the 1145 burst was shown in Fig. 4.10a.

4.3.1 Temporal Fading

4.3.1a Introduction

Figs. 4.10a and b show typical examples of the type of amplitude fluctuations which are generally seen at a frequency of 1.98MHz at Buckland Park. Consider firstly Fig. 4.10a. Below 70km, data was only recorded every second minute. Clearly fading is quite slow (that is, the amplitude changes slowly) below 76km, particularly in the period 1144-1145. The 1 minute mean powers were calculated below 70km, and 2 minute mean powers above. These were then smoothed and plotted on a time-height contour diagram, and the result can be seen in Fig. 4.11. There was clearly a strong power burst at 1145 hr at 68km. Above 76km, fading is much more rapid, and this is quite common.

Fig. 4.10b shows some typical night time fading. As discussed in the caption, this scatter may well be a cloud drifting overhead.

Rather than saying fading is "slow", or "fast", however, it would be better to be more quantitative. This can be achieved by calculating the autocorrelation function of the amplitude time series $a(t_i)$. This is given by

$$\rho(\tau_j) = \frac{\sum_{i=1}^{n} a(t_i).a(t_i + \tau_j)}{\left[\sum_{i=1}^{n} (a(t_i))^2\right]} \qquad (4.3.1.1a)$$

where $a(t_i)$ has had the mean subtracted.

Such a calculation generally gives a function of the form shown in Fig. 4.12a. Notice $\rho(0) = 1$. The narrow spike on Fig. 4.12a at $\tau = 0$ arises due to noise, which becomes uncorrelated after one shift. This spike is usually interpolated across, and the autocorrelation "renormalized" so that the value ρ_I is assigned a value 1.0; all other $\rho(\tau)$ values are also

Fig. 4.12 (a) Typical autocorrelation of a data sample (typically one to three minutes of data was used) up to about a 15s lag. The narrow spike at $\tau = 0$ arises due to the effects of random noise.

(b) Autocorrelation of 3 minutes of data from Townsville, with a lag out to 120s. Although the regular oscillations look meaningful, they must be treated with great care. If a strong specular signal, and a weaker one of different Doppler shifted frequency added to cause the signal, a fairly regular oscillation results. i.e;

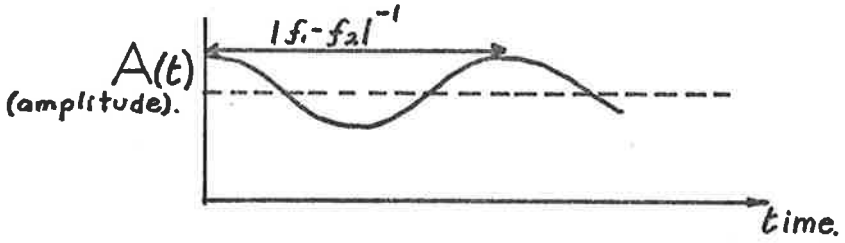

This would produce a smoothly oscillating autocorrelation like that shown. (This oscillation is similar to that of the in phase component of the weaker signal, at a frequency modified by the frequency of the stronger signal - see later in text.) (If the 2 specular signals had equal amplitudes, the minima would be deeper and more sharply dipped, and the autocorrelation could not be so regular.) The raw data for this autocorrelation did in fact look like the above diagram.

Before computing this autocorrelation, the data was multiplied by a Hanning window, which has the effect of placing greater emphasis on the middle data of the sample. This was not the usual practice, however.

Even though these oscillations look very regular, extreme care is necessary. Quasi-regular oscillations in the autocorrelation function can also be produced by semi-random data, as will be seen in Chapter VII. It is unlikely that the oscillations in this figure were due to random data, as the raw data showed 4 oscillations over at least 4 periods. The possibility of it being random exists, however, and great care is necessary in interpretation. Complex data is easier to interpret.

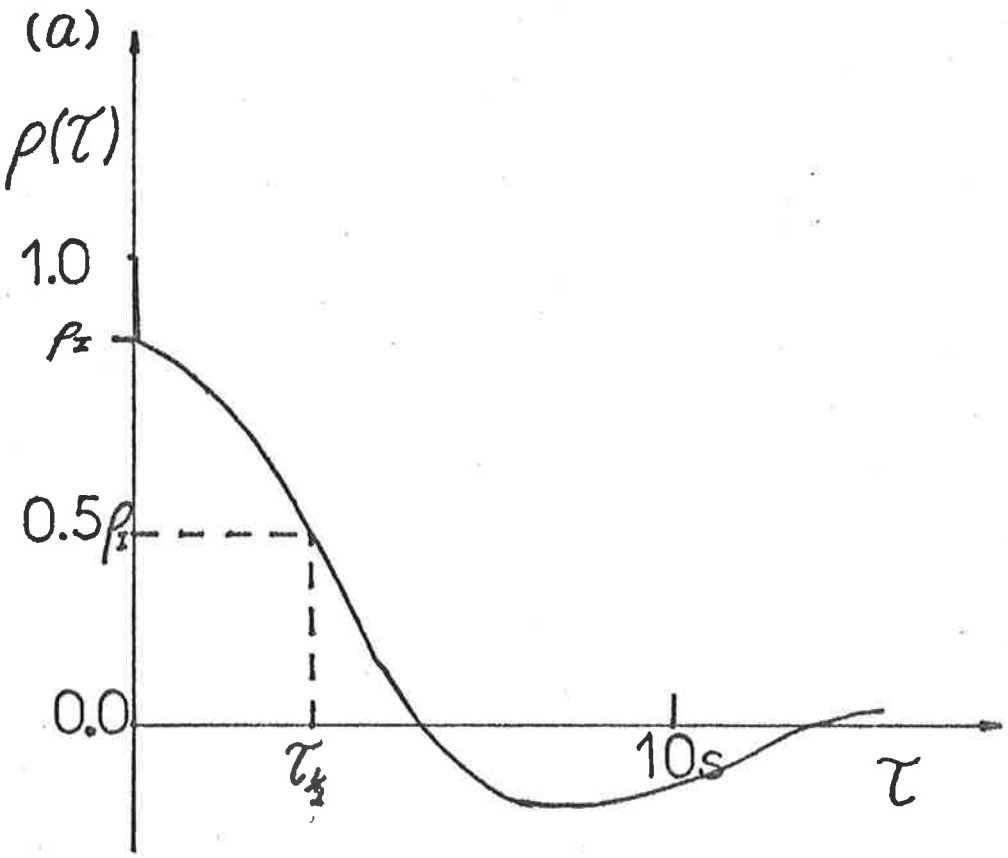

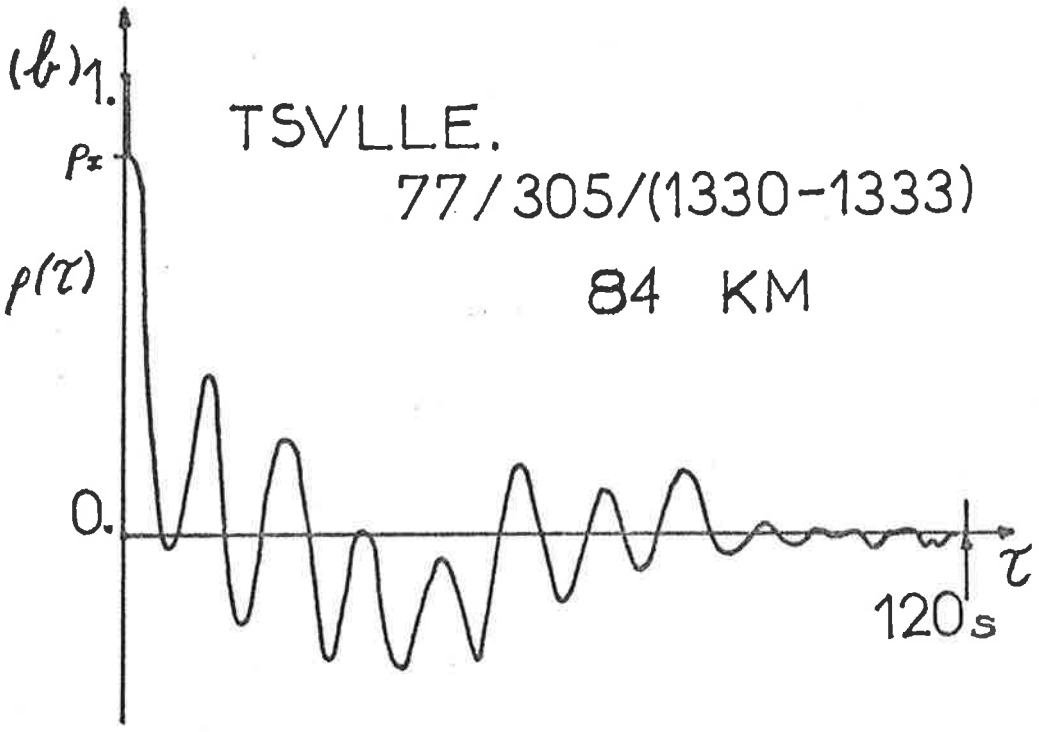

TSVLLE.
77/305/(1330-1333)
84 KM

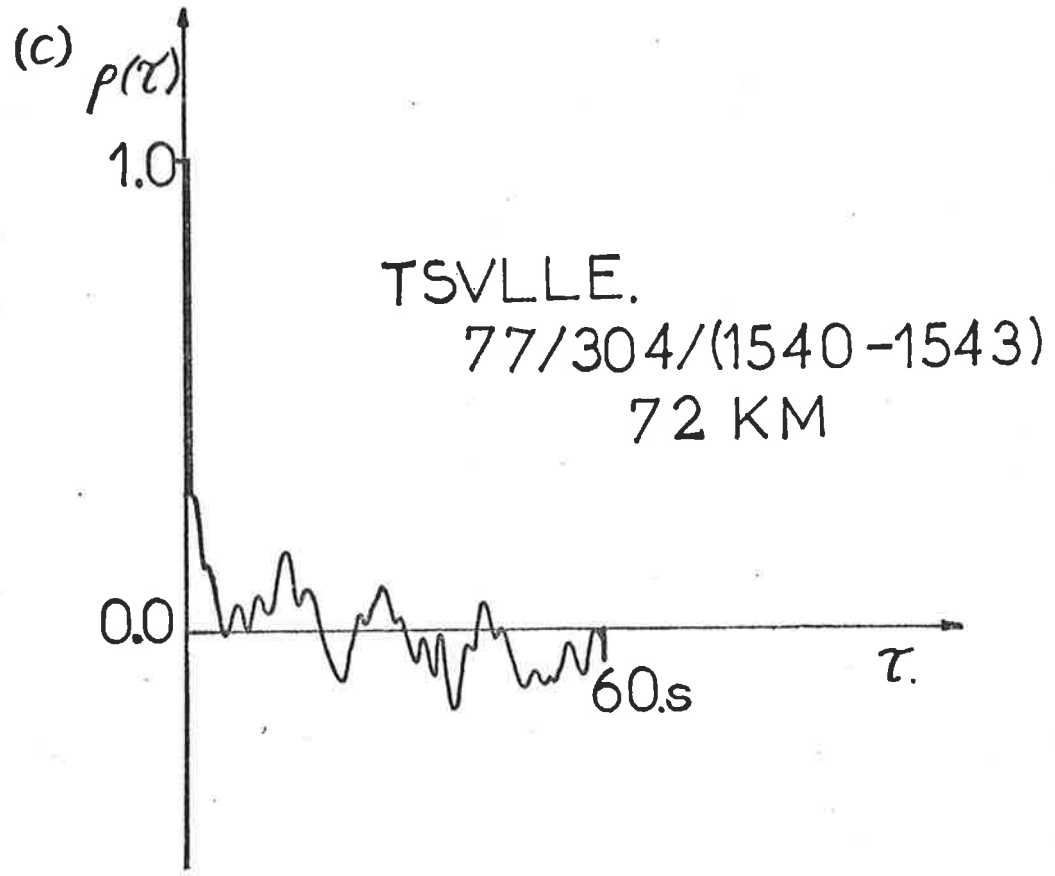

Fig. 4.12c A more typical autocorrelation than (b). Some oscillation exists, but not as obviously as in (b). The sample was quite noisy, as can be seen by the large spike at 0 lag.

All the autocorrelations presented here have been taken from noisy data, but this is not always the case. It is often possible to obtain signals which are so strong that the noise spike does not show - particularly for the echoes from 90km.

multiplied by $(\rho_I)^{-1}$. The rapidity with which this function falls to zero is then a measure of the speed of fading. The value of τ at which $\rho(\tau) = 0.5$ is denoted $\tau_{\frac{1}{2}}$, or $\tau_{0.5}$, and is called the fading time. Usually, in the work for this thesis, $\tau_{\frac{1}{2}}$ was calculated for blocks of data one or two minutes in length.

4.3.1b Some Theory to Help Interpretation

Before discussing the results of these fading time estimates, however, some comments are necessary. Firstly, the spike at $\tau = 0$ in Fig. 4.12a is not completely useless. It can be used to estimate the mean noise. This will be seen in Chapter VI. Secondly, the existence of noise distorts the autocorrelation. The autocorrelation with the spike removed is not the same as that which would have been obtained had there been no noise. (This means the $\tau_{\frac{1}{2}}$ estimate, even after removal of the noise spike, may be in error.) If, on the other hand, both amplitude and phase (i.e., the complex data) had been recorded, and its complex autocorrelation calculated, removal of the spike at 0 does produce the autocorrelation which would have been achieved had there been no noise. If, also, powers (or intensity) were used to obtain the autocorrelation, then removal of the spike does produce the same autocorrelation as that which would have been achieved if there were no noise. For this reason, all fading times presented in this chapter will be for autocorrelations of the powers. The proofs of the above statements will be given in Chapter VI.

It is also worth considering the effects of recording amplitude-only in some simple situations. Consider two radio scatterers at similar heights, moving with slightly different radial velocity components (the radial velocity is the velocity component along the line from the transmitter-receiver system to the scatterer). These will each produce

a Doppler shift, and the frequencies received from each will be different; f_1 and f_2 say. Assume that the received frequencies f_1 and f_2 have equal amplitudes. Then, the received signal will be a radio frequency of $(f_1 + f_2)/2$ with a beating envelope, as illustrated below.

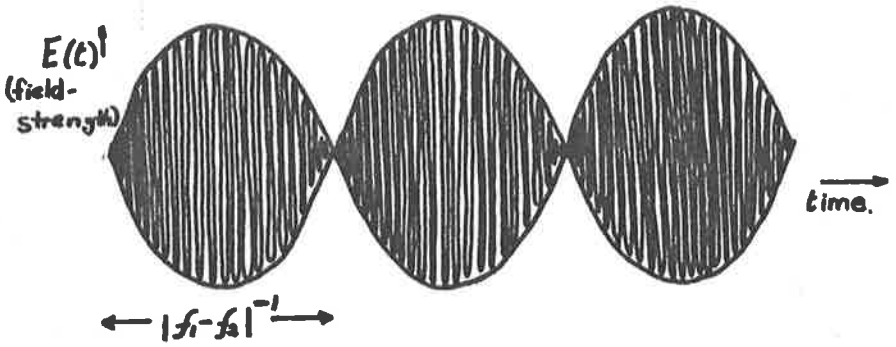

If this information were recorded as inphase and quadrature data, as discussed in Chapter III, then the result would be as illustrated below. (——)

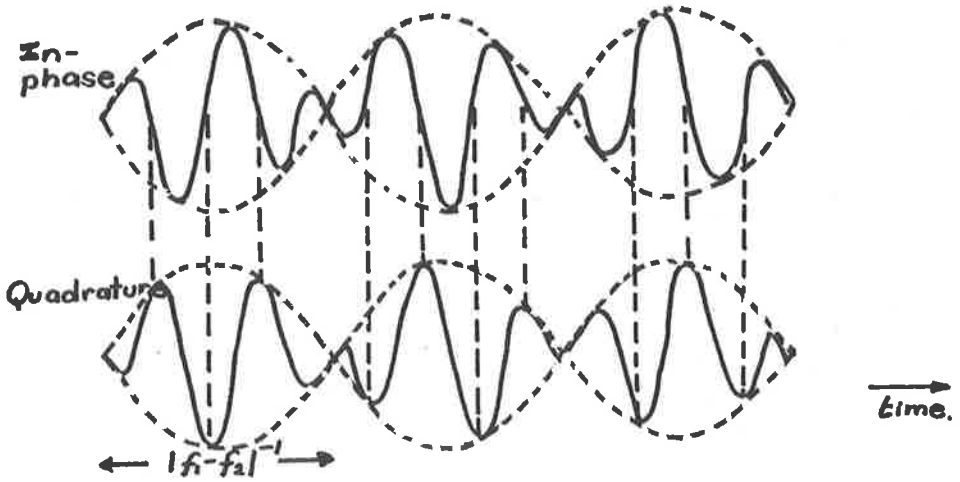

In this case, the beat period is still $(f_1 - f_2)^{-1}$, but the oscillation inside has frequency $(\frac{f_1 + f_2}{2} - f_t)$, f_t being the transmitted frequency.

If plotted as amplitude and phase, this signal would appear as follows. It is assumed that there are just over 2 cycles of the internal oscillation per beat in the above diagram.

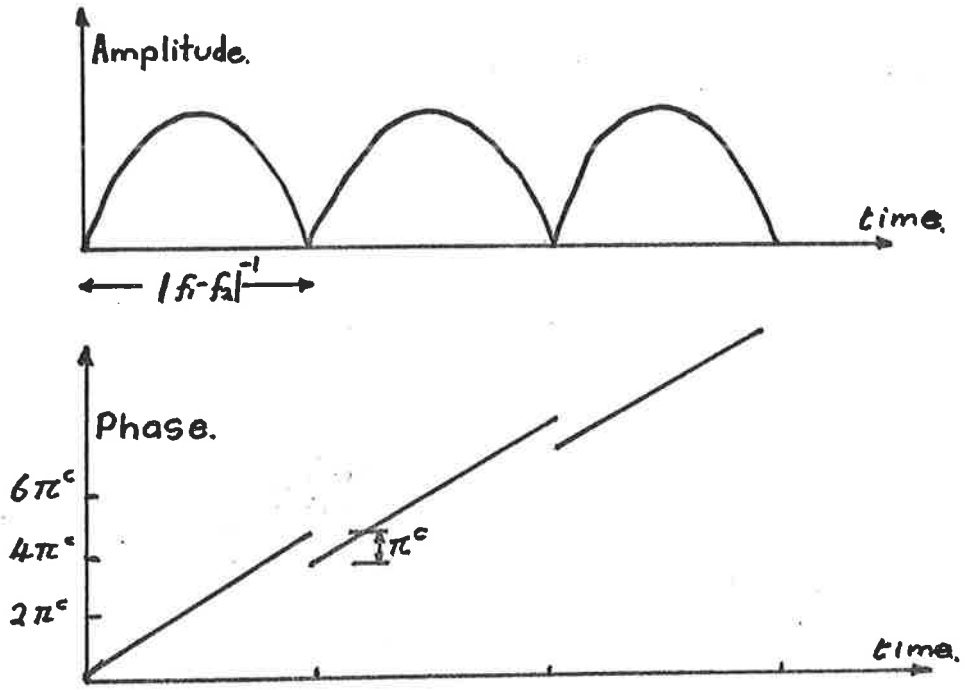

If the amplitudes of the two signals differ, the phase variation becomes more complicated, and this will be discussed more in Chapter VII. The amplitude fluctuations still look like those presented above, but the amplitude minima do not reach zero.

If the in phase (a_i) and quadrature (a_q) components are recorded (see Ch. III ; i.e., the complex signal $\underline{a}(t) = a_i(t) + ja_q(t) = A(t)e^{j\phi(t)}$), then a complex autocorrelation can be defined as

$$(4.3.1.1b) \quad \rho(\tau) = \frac{\int_{-\infty}^{\infty} \underline{a}^*(t).\underline{a}(t+\tau)dt}{\{\int \underline{a}^*(t).\underline{a}(t)dt\}^2}$$

(Champeney, 1973, equation 5.6)
(* denotes complex conjugate)

which is just a generalization of 4.3.1.1a.

Then if the complex signal were Fourier analysed, and the power spectrum computed, it would show two quite pronounced spikes at frequencies

$(f_1 - f_t)$ and $(f_2 - f_t)$, i.e., the Doppler shifts. The complex auto-correlation (which is the Fourier transform of the power spectrum) would appear as follows. (——)

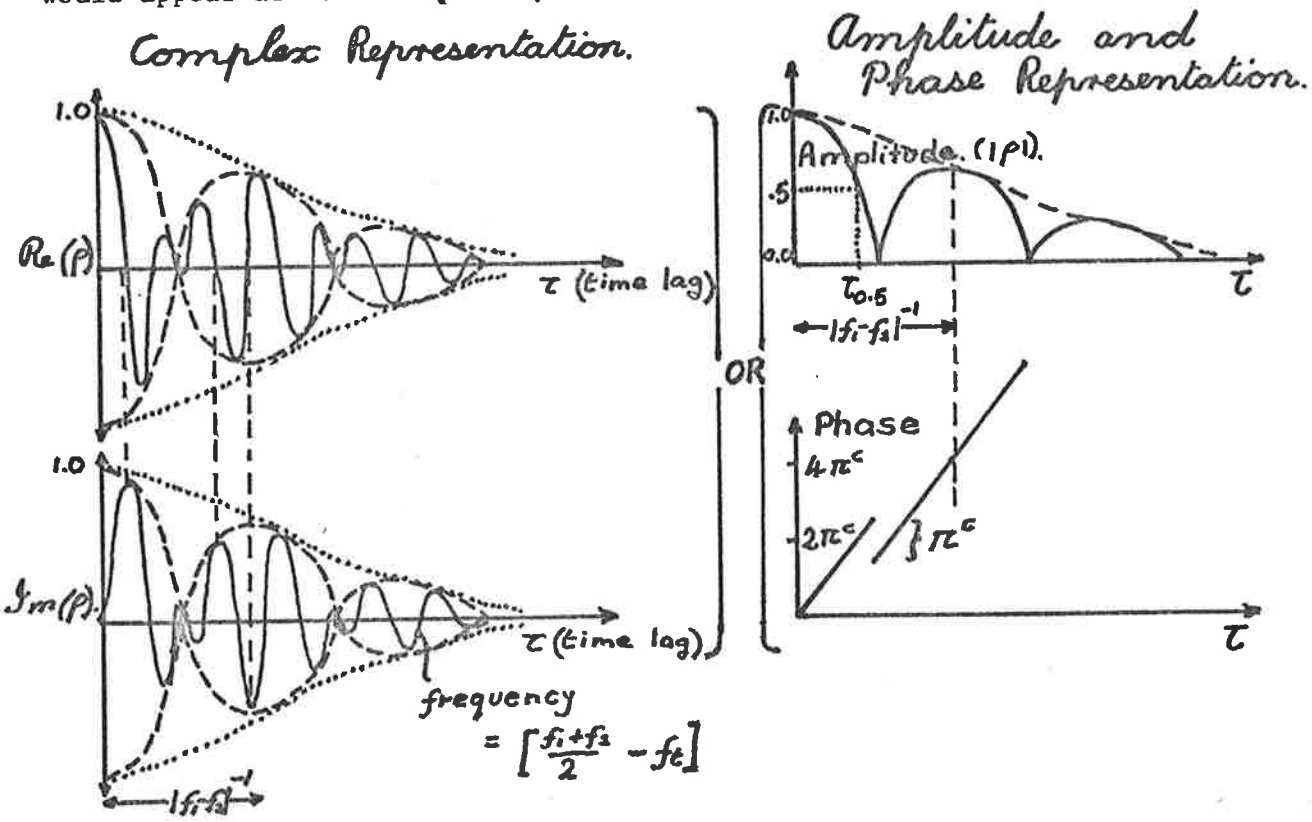

(If the Doppler shifted frequencies were delta functions, the dotted (.....) envelopes would in fact have a constant value of 1.0. I have assumed the frequencies have finite bandwidth so this envelope decays with time lag. The wider the spectral peaks, the faster this overall envelope falls away.)

Thus interpretation is easy in this case if the complex data is recorded. If, however, only amplitude is recorded, interpretation is harder. The Fourier transform will be that of the function illustrated here.

(a)

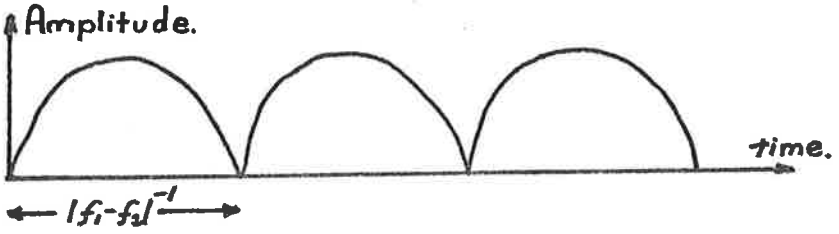

This is the Fourier transform of

(b)

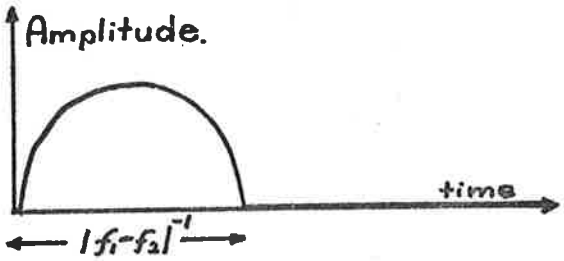

but multiplied by F(f), where F(f) is a delta function at frequency 0, $\pm(f_1 - f_2)$, $\pm 2(f_1 - f_2)$ etc., since the initial function (a) is simply this second one (b) repeated over and over. This Fourier transform should then be convolved with the Fourier transform of a box function of length equal to the data length, to obtain the full Fourier transform.

The Fourier transform of the function (b) is the Fourier transform of the product of the functions (c) and (d) below,

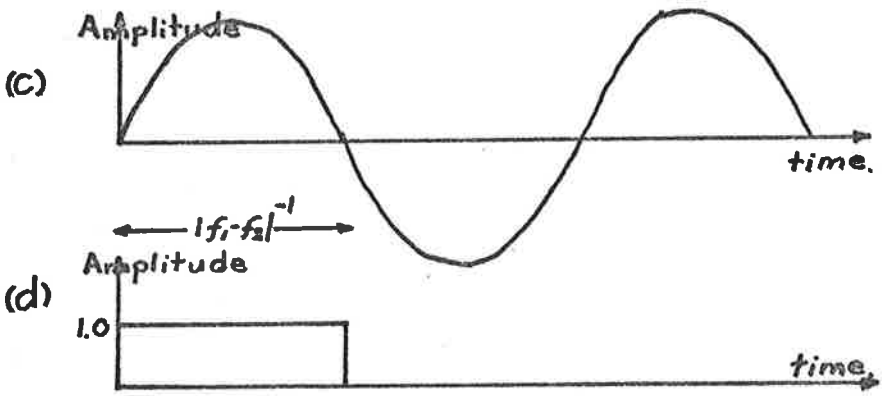

which is of course the convolution of the individual Fourier transforms of c and d.

Then combining all these procedures gives the power spectrum of the amplitude series. It looks a bit like a $(\sin f/f)^2$ function, but the analytic function is more complicated. It is very hard to interpret, although this can be done; the positions of the minima, and secondary peaks, are related to $(f_1 - f_2)$.

The autocorrelation is a little easier to deal with. It basically oscillates with a period $(f_1 - f_2)^{-1}$, and the negative minima do not reach values as large in magnitude as the positive maxima. An example is shown below. Also shown (-·-) is the magnitude of the complex autocorrelation which would have been obtained with the same data.

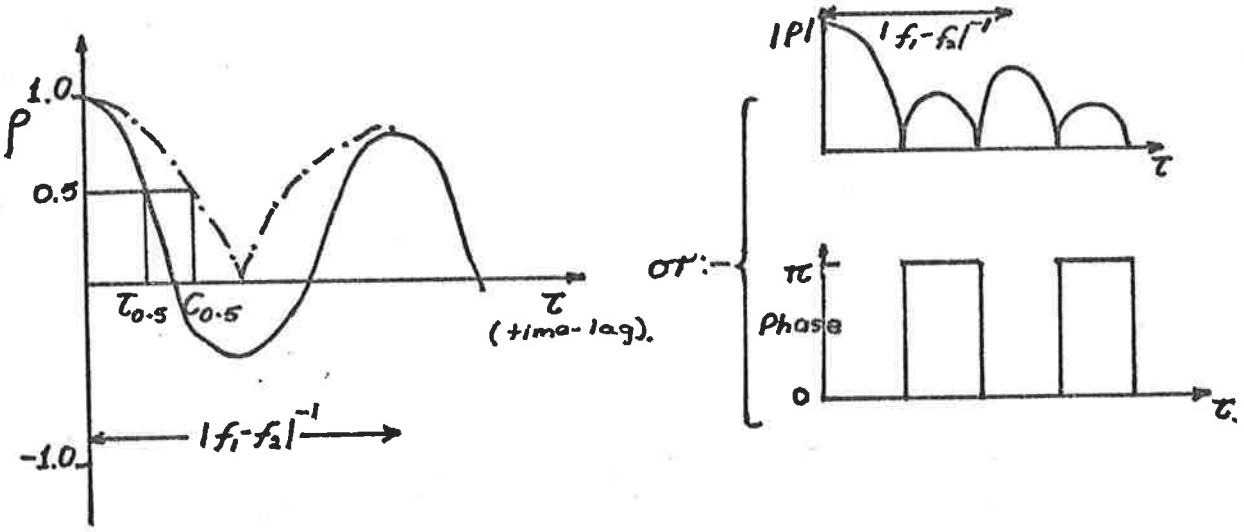

Notice $\tau_{0.5}$ will be less in this case than the value which would be obtained for the fading time from the complex autocorrelation, $C_{0.5}$. $(C_{0.5} \approx 2\tau_{0.5})$.

It is interesting to note that if a strong, constant specular RF signal, frequency f_1, is received, as well as weaker ones, then the amplitude of the resultant is closely equivalent to that of the in-phase component of the weaker signals (beaten down in frequency by f_1) plus the specular amplitude. For example, consider a weak signal of frequency f_1 and a strong one of frequency f_2.

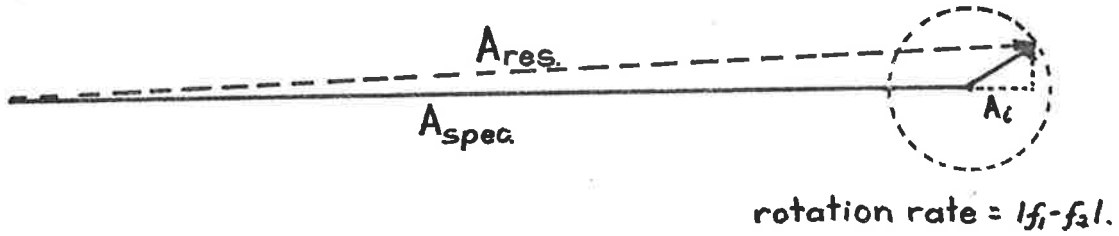

Then $A_{res} \approx A_{spec} + A_i$, and the amplitude A_{res} oscillates with a frequency $(f_1 - f_2)$.

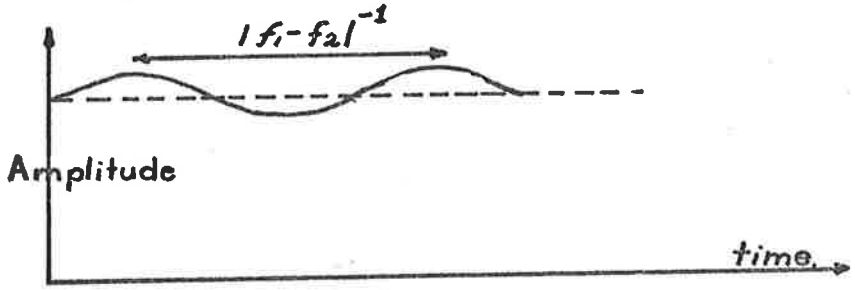

The autocorrelation is thus the in-phase component of the weaker components' complex autocorrelation, beaten down by a frequency f_1; in this case, simply the in-phase component of a sinusoidal oscillation of period $(f_1 - f_2)^{-1}$.

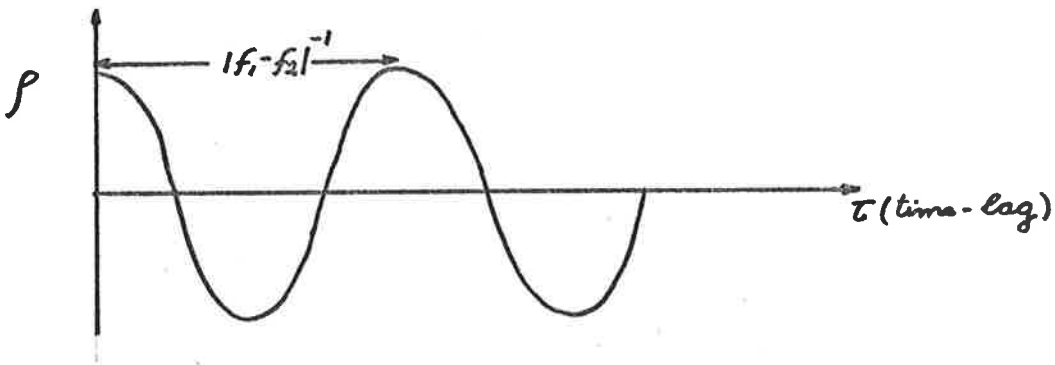

Likewise if two equal, weak signals, frequency f_2 and f_3, occur with a strong specular signal f_1, the resultant autocorrelation is

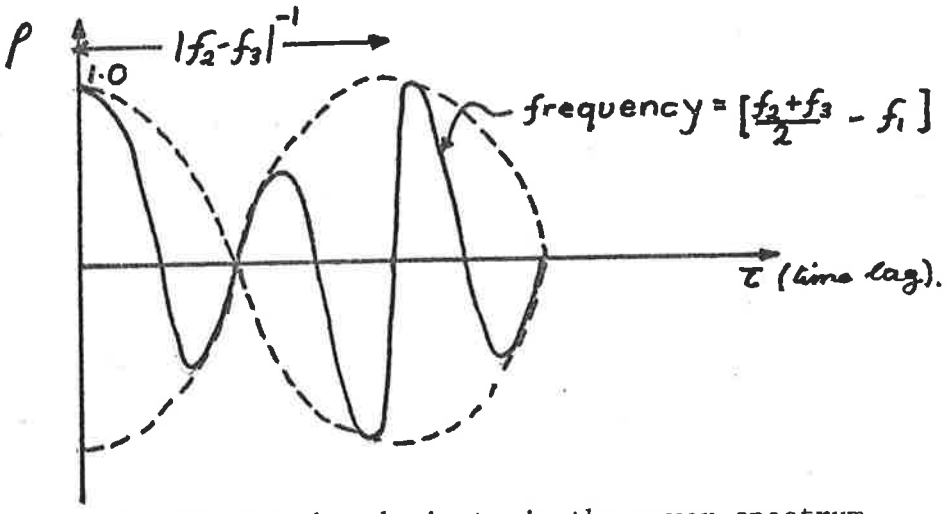

Thus if only a few frequencies dominate in the power spectrum, oscillations may be expected in both the complex, and amplitude (or power) - only correlations. Notice, however, that in these cases $\tau_{0.5}$ is a function of this beat frequency, and it will be seen shortly that this can be important for interpretation. Fukao et al. (1980) have also mentioned that fading times can be determined by "beat frequencies" if the spectrum has more than one peak.

Now consider another extreme case. Suppose we have entirely isotropic turbulent scatter. Assume a Gaussian distribution of radial velocity components., i.e., the probability of a radial velocity in the range v to v + dv is proportional to $e^{-v^2/2v^2_{RMS}}$ dv. Then the power spectrum associated with this can easily be found. This can then be Fourier transformed to give the autocorrelation, and hence the fading time in terms of v_{RMS}. Measurement of $\tau_{0.5}$ thus gives v_{RMS} if there is no mean horizontal wind. The results of such an analysis were given in Chapter II (equations 2.2.3.11 and 2.2.3.12). (In reality, a mean wind generally also exists, which produces beam broadening, and so $\tau_{0.5}$ and v_{RMS} are no longer simply related. The effect of beam broadening can be removed by using Full Correlation analysis, as discussed in

Chapter II, and in Briggs (1980/81). However, v_{RMS} estimates calculated in this way for a wide beam cannot be directly interpreted as the RMS velocity associated with the Bragg scales of the radiation used. The reasons for this will be seen in Chapter VII).

In principle, the autocorrelations associated with such turbulence-produced scatter should fall smoothly to zero, and stay close to zero for larger τ. Thus one may naively expect that if oscillations appear in an autocorrelation such as in Fig. 4.12b and c, they indicate a few specular scatterers are causing the signal fading. In fact, this is not necessarily so. It will be shown in Chapter VII that a signal with a simple Gaussian power spectrum, and random phase (as may be expected from turbulent scatter, and beam broadened scatter) can in fact have oscillations in the autocorrelation. It will be seen that if only one or two minutes of data is taken using the full Buckland Park aerial array, the (complex) power spectrum of turbulence and beam-broadening induced fading can often consist of just one or two surprisingly narrow spectral peaks. Thus the autocorrelation will have oscillations. Awe (1964) has also shown this effect using computer simulations. To obtain meaningful autocorrelations, at least 4 or 5 minutes of data should be used when recording with the narrow beam at Buckland Park - but in this time, the dominant scatterers may have changed, or disappeared (e.g., we have already seen that bursts of power of less than 2 or 3 minutes duration often occur). In this chapter, one or two minutes of data are generally used for autocorrelations, since the power can change so rapidly. But it should be borne in mind that data obtained from these correlations must be interpreted with extreme caution.

If, however, the raw data is examined, and the beating can be seen, and there are at least 4 or 5 cycles, this probably does imply genuine

beating between two scatterers. For example, Fig. 4.10a, at 70km, shows a beating type of fading. The period 1145 to 1148 shows quite regular beating, and this could possibly indicate one or two specular scatterers. Also, as discussed in Fig. 4.12b, the oscillations in that figure also probably imply several discrete scattering regions. Criteria for the acceptance or rejection of "specular scatterers" will be discussed more in Chapter VII.

It is interesting to note that Gardner and Pawsey (1953) also observed such beating effects by recording on photographic film. They were able to see the signal strongly for a few seconds, then it died, then rose again, and so forth (e.g., see their Fig. 4c and their section 4.2). However, at the time those authors were not able to interpret their results.

The main points to come out of this section are given below.

(i) Oscillations in the autocorrelation produced from one or two minutes of data with the narrow beam at Buckland Park do not necessarily imply a few discrete scatterers, but may do.

(ii) The fading times deduced from such autocorrelations are similarly unreliable. If the fading were due to say two specular scatterers, the fading time would be related to the beat period of these scatterers. This is an important point. If the fading were related to turbulence, however, the calculated fading time may still not be that expected from the root mean square radial velocity of the scatterers, particularly if the observation time is too short and the beam width too narrow. Peaks with no physical significance can occur in the power spectrum, and the fading time may be related to the beat periods associated with these peaks (also see Chapter VII). (This is not saying the power spectrum is not that of the data sample. It is. But what it does say

is that the peaks cannot, for example, be interpreted as spectral peaks due to a few separate eddies within the turbulence. The peaks have no meaning in this regard.)

(iii) Amplitude and phase data is much easier to analyse than amplitude-only data.

4.3.1c Experimental

With the points from the previous section in mind, consider now some experimental observations of fading times. Fig. 4.13 shows a smoothed contour diagram of fading times, and also a power contour plot, for Buckland Park. Fig. 4.14 shows a similar pair of graphs for the region 80-98km at Townsville, and Fig. 4.15 a similar pair for the lower heights at Townsville. Fig. 4.16 shows 1 minute fading times recorded for over an hour, averaged together, and presented as a height profile. The associated power profile is also shown. Several points are immediately clear. Firstly, fading is generally slower (larger $\tau_{1/2}$) at the lower heights. Secondly, maxima of powers and $\tau_{1/2}$ occur at similar heights. Thirdly, it will be seen that at times strong bursts of power are associated with slow fading, but this is not always so. Fourthly, fading is slower on the narrow beam than on the wide beam (Fig. 4.16). At heights above 80km, the narrow beam fading times are at least 50% greater than those for the wide beam. Below 70km, the narrow beam fading times are only 30% greater than those for the wide beam. The region of 70-80km will be discussed later.

Let us consider these points. The first (slower fading at lower heights) is consistent with previous observations. The beam broadening of the spectrum increases as $\theta_* . v_{horiz}$ increases. Here, θ_* is the angular half-width of the angular spectrum of the observing beam convolved with that of the scatterer, and v_{horiz} is the horizontal drift

Fig. 4.13 Contour plots of (a) Power and (b) fading time as a function of range and time for observations made at Buckland Park on day 79/229 using the narrow beam. Powers are in $(\mu Pr_M)^2$. The powers were computed as 2-min means; fading times were calculated in one-minute data blocks, and then averaged in 2 min sets. Also plotted are the positions of the peaks in the power profile (black line near 86km). The height of this peak clearly shows a regular oscillation. This data has already been presented in Fig. 4.8. However, the fact that such a smooth oscillation occurs does not necessarily imply that the height of the scatterer is changing - perhaps the layer is a km or so thick, and the dominant reflecting region may be changing. It can also be seen that the heights of the lower echoes vary considerably.

Three lower echoes appear to exist - at 70, 75 and 80km - but clearly they are not stable in height. This point has also been mentioned in the text. At times it can also be seen that strong power bursts accompany slow fading, but this is not always so. This point is illustrated more in Fig. 4.18, and discussed in the text.

Apologies are also offered for the bad smudging which has occurred - this seems to have been produced by the photocopying procedure. Likewise for Fig. 4.14.

BUCKLAND PARK 79 / 229

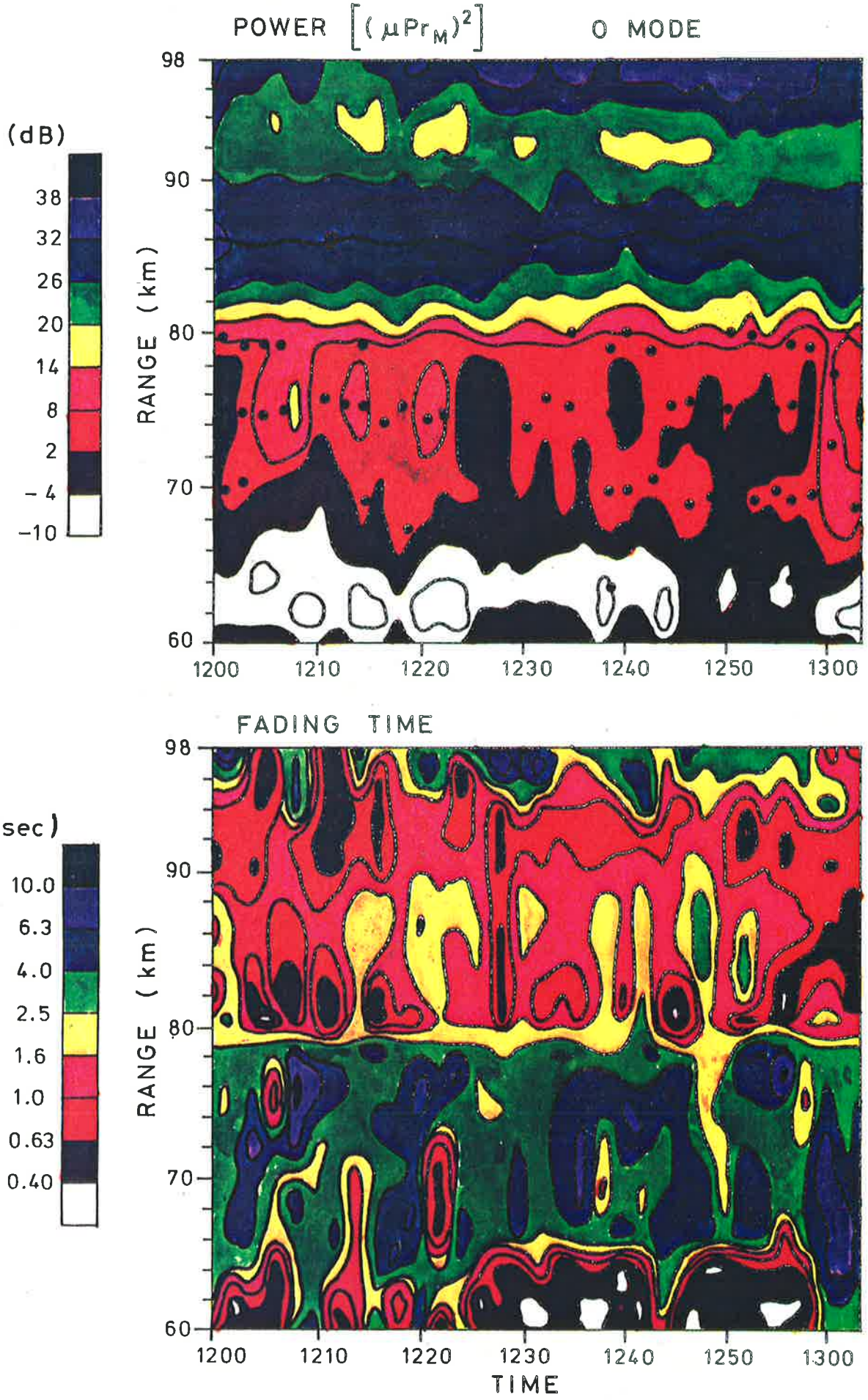

Fig. 4.14 Contour diagrams of (a) power and (b) fading times as a function of time and range, recorded at Townsville on day 77/305. The powers are 3 minute means, recorded every 5 mins in the periods 1200-1305 and 1850-1915, and recorded every 10 mins in the period 1310-1850. The fading times are 1 minute fading times using the first minute of each 3 min data block. A strong echo at around 90km occurred, although at times it does not show as an actual peak, but rather a point of inflexion imposed upon the stronger E region totally reflected echo. Bursts of power can be seen rising at times by as much as 5-10dB over the "normal" level. Fading times are generally greater than 2 seconds, and at times reach greater than 4 seconds. Occasionally slow fading (large $\tau_{1/2}$) can be seen to be associated with strong power bursts (e.g., 1700-1730), but in general this is not necessarily so. At other times strong power occurs with rapid fading (small $\tau_{1/2}$) (e.g., 1400-1430).

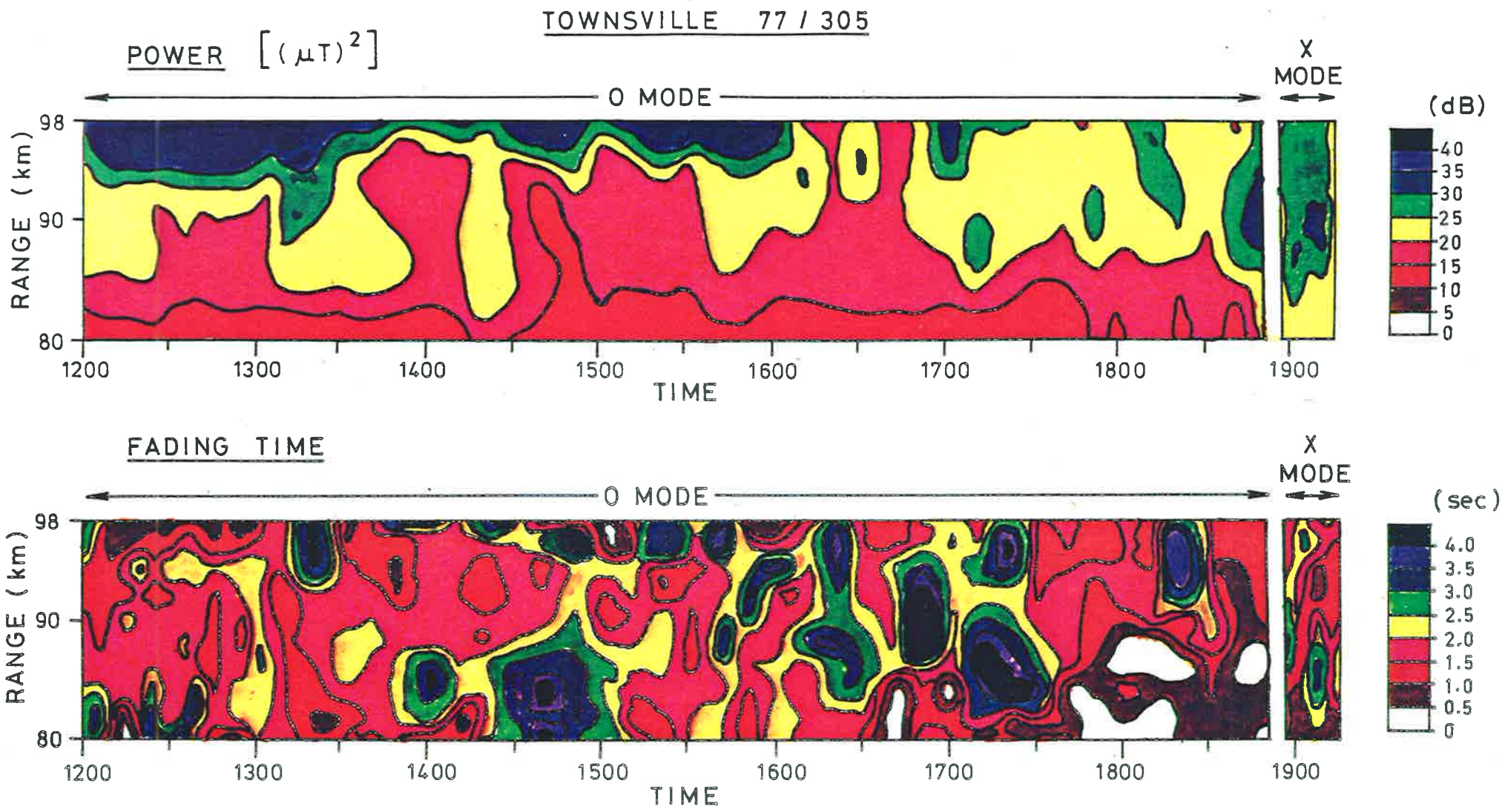
TOWNSVILLE 77 / 305
POWER [(μT)²]
O MODE
X MODE
(dB)
40
35
30
25
20
15
10
5
0
RANGE (km)
98
90
80
1200
1300
1400
1500
1600
1700
1800
1900
TIME
FADING TIME
O MODE
X MODE
(sec)
4.0
3.5
3.0
2.5
2.0
1.5
1.0
0.5
0
RANGE (km)
98
90
80
1200
1300
1400
1500
1600
1700
1800
1900
TIME

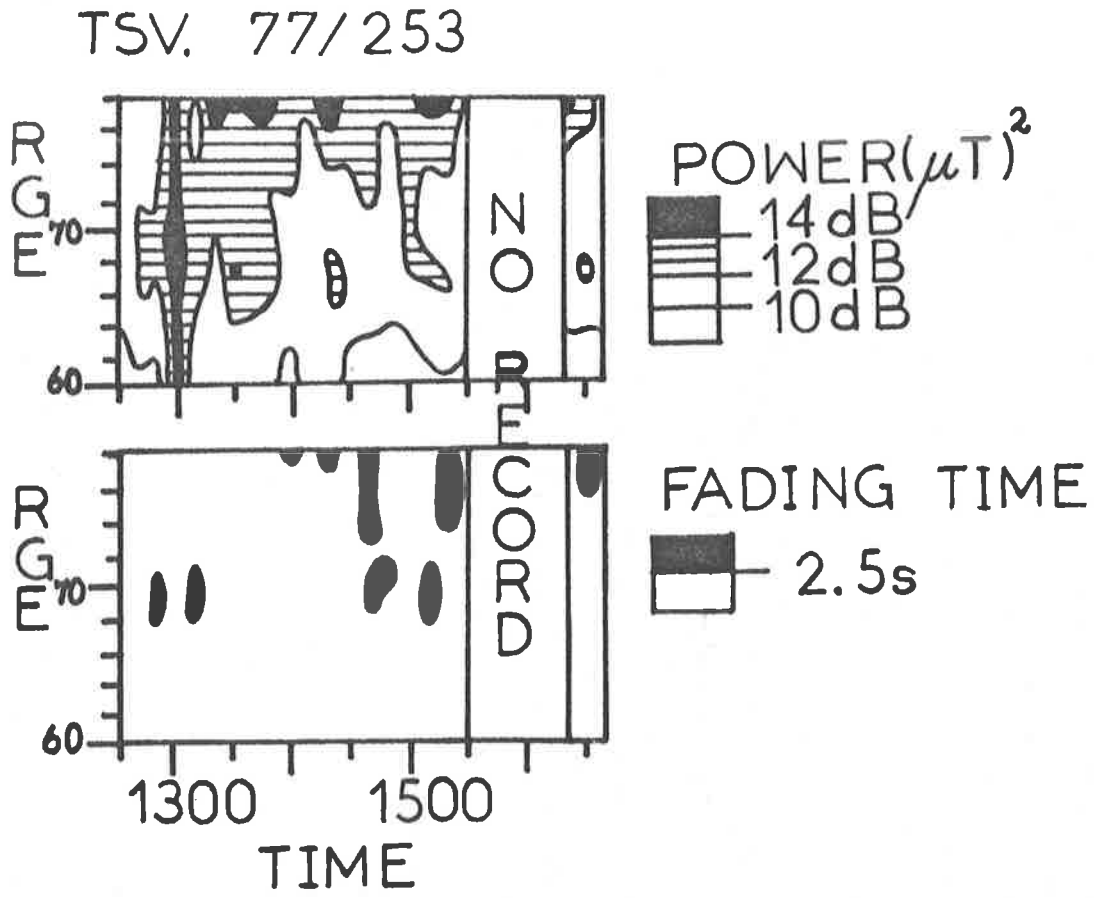

Fig. 4.15 Three minute mean power contours, and 1-min fading time contour diagrams for Townsville, day 77/253, 60-78km. Data was recorded in 3 minute blocks every 10 minutes. Fading times greater and less than 2.5s are shown. These graphs are typical of many of the lower echoes at Townsville - short burst of scatter, followed by a lull. At times, steady lower echoes can be seen, but in general the Townsville echoes appear to be even more "bursty" than those at Buckland Park. At times strong bursts of power are associated with slower fading (e.g., 1500), but this is not always so. The power burst at 1300 is interesting in that fading is lowest before and after the burst.

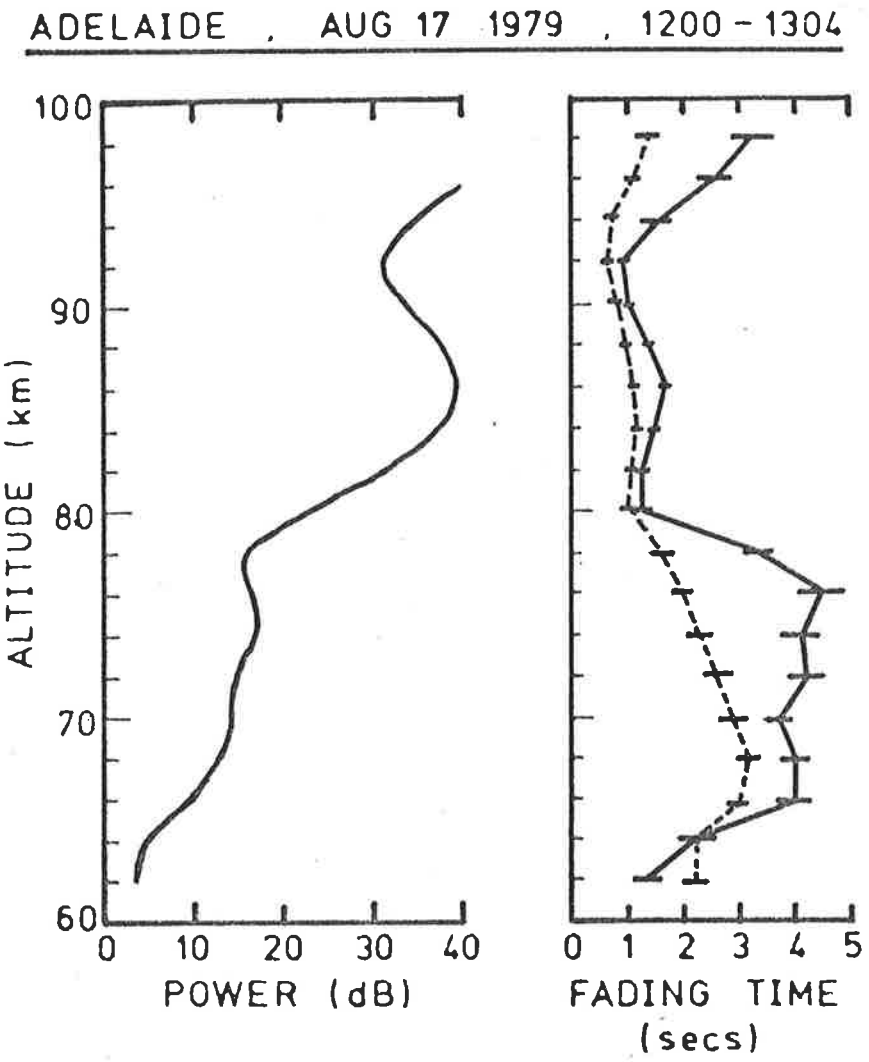

Fig. 4.16 Plots of power $\{(\mu Pr_M)^2\}$ vs range for the narrow beam at Buckland Park on day 79/229, and of one-minute fading times for both the narrow and wide beams. These graphs are averages over the period 1200-1304 hr.

_____ narrow beam

---------- wide beam

Error bars are standard deviations for the mean, and each mean comes from approximately 33 points.

Wind speeds were about 90m s^{-1} on this day at 86-90km (principally eastward), so fading times were quite small due to beam broadening at 86km.

velocity of the scatterer. As usual, vertical motions are assumed to be negligible. The lower scatterers (below 75-80km) have narrow angular spectra, and hence small θ_* values, so that the fading produced by them is quite slow. Fading times of up to 20s have been observed for these lower echoes.

The fact that fading times and power profiles peak at the same height is also not surprising. Much of the signal received at the minima is due to the tails of pulses reflected from the more strongly scattering layers, and the tails from pulses above and below beat to produce rapid fading.

The third point is quite significant. Should we expect a correlation between power bursts and fading times? If the scatter were due to turbulence, an inverse correlation may be expected. The fading time is proportional to $(v_{RMS})^{-1}$, and $v_{RMS} \propto \varepsilon^{1/3}$ (Chapter II, equations 2.2.3.3c"), so $\tau_{0.5} \propto \varepsilon^{-1/3}$. The scattered power is proportional to C_n^2, if turbulence fills the radar volume, and

$$C_n^2 = a^2 P_r^{-1} R_i \omega_B^{-2} \varepsilon_d^{2/3} |M_e|^2 \qquad \text{(Chapter II, equations 2.3.2.11)}$$

Thus power and fading time would be reciprocally related - $C_n^2 \propto \varepsilon_d^{2/3} \propto \tau_{0.5}^{-2}$, all else being constant. A rise in ε_d would increase the scattered power and decrease $\tau_{0.5}$ (also see Liu and Yeh, 1980). The first 20 minutes of Fig. 4.8 do show an inverse correlation of fading time and power. But this assumes that the turbulence fills the radar volume. If this were not so, a change in the volume of turbulence would also affect C_n^2(radar), and the relation between received power and $\tau_{0.5}$ may not be so simple (see section 2.3.2: C_n^2(radar) = C_n^2(turb)$\cdot$F, F = fraction of radar volume filled by turbulence).

What if, on the other hand, some type of specular mechanism produced the scatter? Let us assume that somehow the scattering layer consists

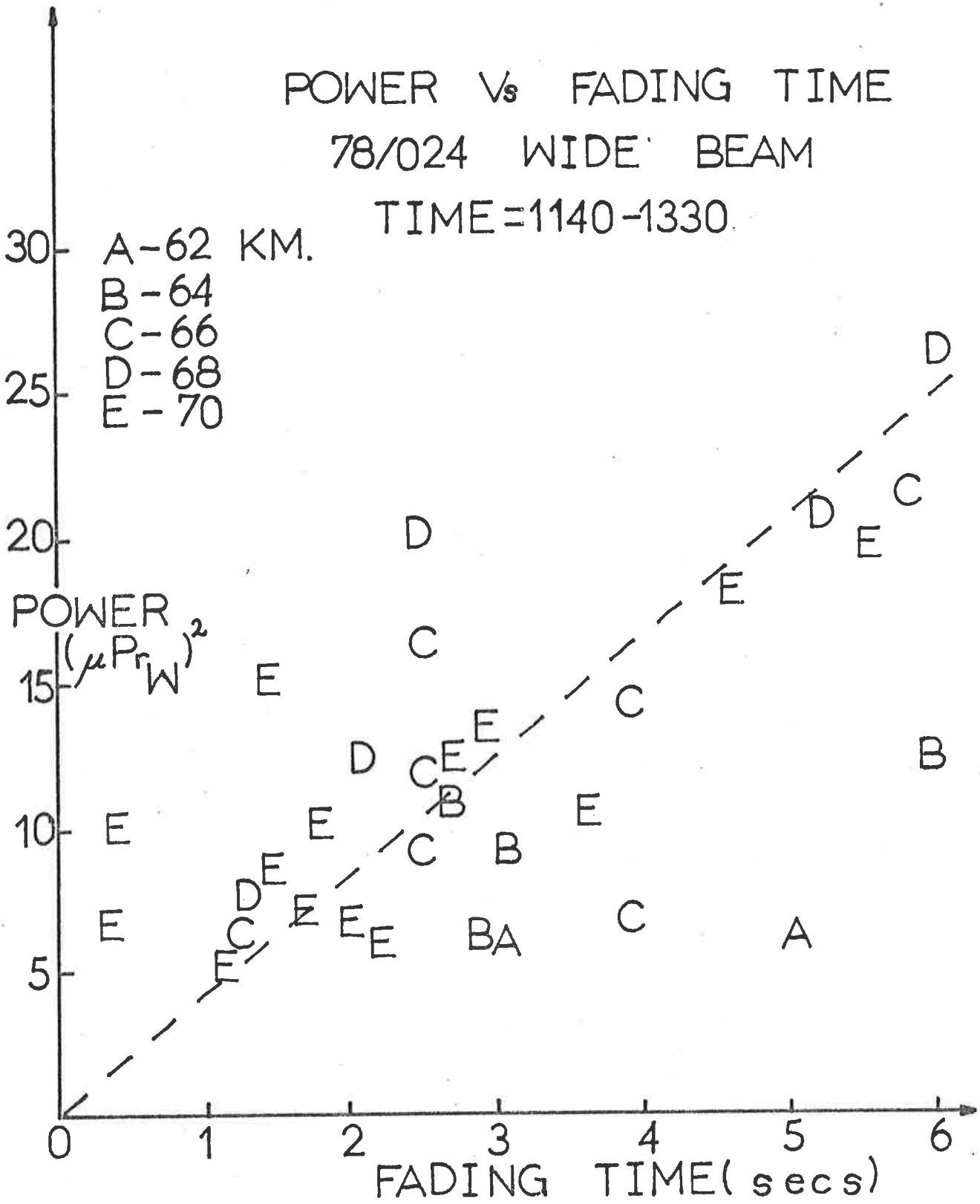

Fig. 4.17 One minute mean powers plotted against one-minute fading time for the same one-minute period, for ranges from 62 to 70km on day 78/024 at Buckland Park. The wide beam was used for reception. There is a weak linear trend (particularly for the D and E points). Large bursts of power do often seem to be associated with slow fading.

Not all points in the period 1140-1330 were plotted. There were more on the low power, short fading-time portion of the graph, but these have not all been plotted to prevent over-crowding.

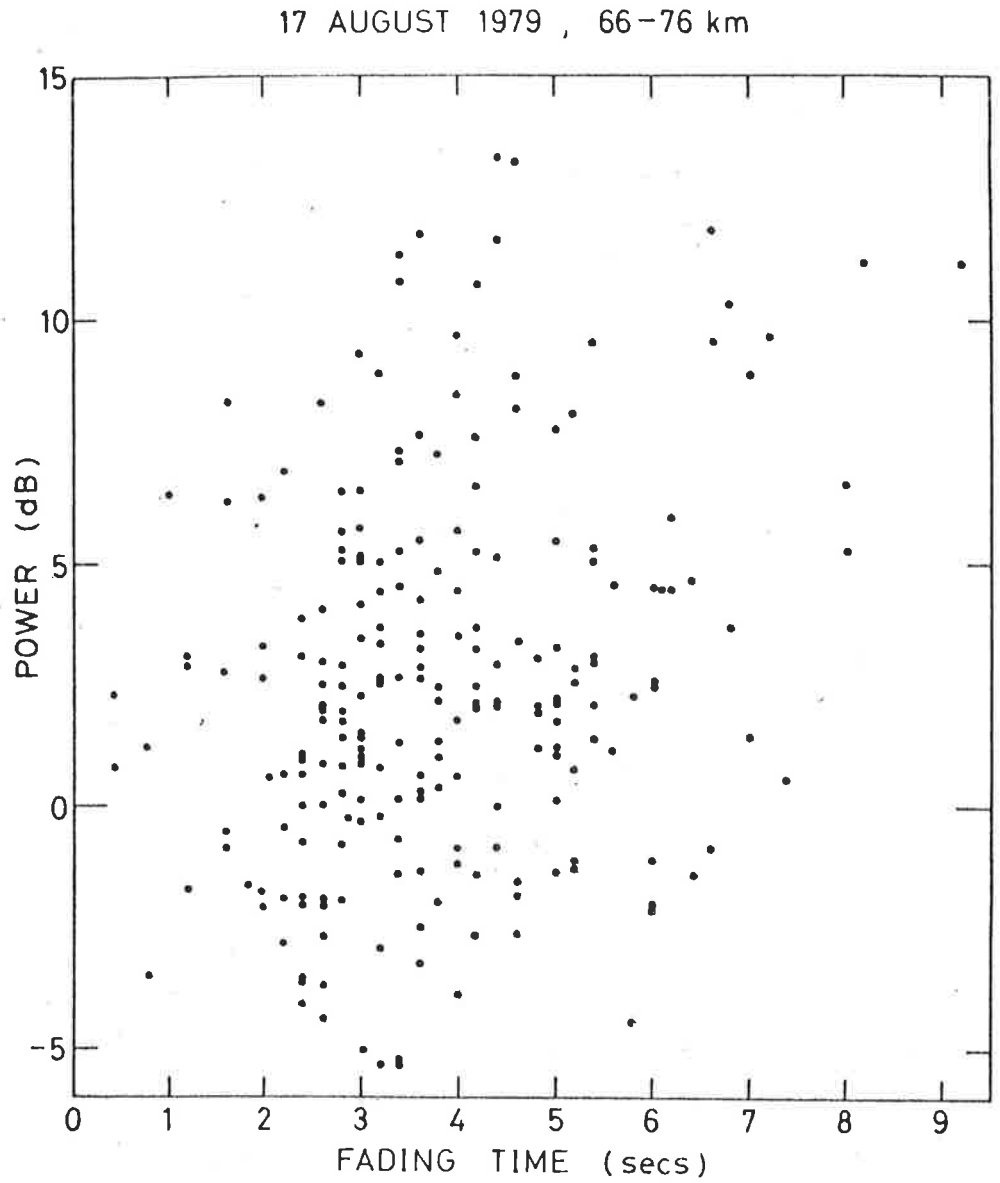

Fig. 4.18 Another plot of power fading-time correlations, similar to Fig. 4.17, but for day 79/229. Powers are in dBs of $(\mu Pr_M)^2$. All points from the height range 66-76km have been included. A weak linear trend may exist, but it is not strong.

Notice however that all powers greater than 10dB have fading times greater than 3s.

of small horizontal stratifications, several kilometres in extent, forming and decaying - or even just drifting across the observing beam. If a particularly strong scatterer comes into view, it may be expected to dominate the scatter. The power would increase, and fading would become quite slow. In this case, we may expect the fading time to increase as the power increases. The fading would be due more to processes such as those illustrated for the E region in Chapter III (Fig. 3.5). But now carry this further. Suppose 2 such scatterers formed. The power would no doubt increase - but the fading time would now be related to the beat frequency of the Doppler shifted frequencies produced by these scatterers. This would depend on the scatterers' radial velocities. In this case, no obvious relation between fading times and power need occur. However, if both scatterers were overhead, their radial velocity would be least (assuming primarily horizontal movement), so we may still expect fading to be fairly slow. If one were at the edge of the beam, and one overhead, fading would be faster. We may expect $\tau_{1/2}$ to generally increase as power does, but the relation need not be one to one. Fig. 4.17 and 4.18 show quite typical plots of power against fading time for the heights below 76km. There may be a weak relation between the parameters, but it is far from well-defined. The heights 68-70km on day 78/024 (Fig.4.17) do show quite a well defined trend. This can also be seen by examining Fig. 4.10a, also for that day. During the strong burst at 1143-1145, fading was clearly quite slow. Fig. 4.18 also shows a plot of power against fading time. Again, there may be a weak positive trend, but it is again not definite. These results are quite typical.

Finally, a brief discussion of the comparison of fading times on the wide and narrow beams is warranted. As seen in Fig. 4.16, the wide beam produces much faster fading than the narrow beam. This is probably

due to the increased beam broadening suffered by the wide beam. At very low heights ($\lesssim$ 70km), the wide and narrow beam fading times are quite similar, suggesting that in this case the "beam width" is not defined so much by the array beams as by the scatterers themselves. This again supports the previous statements that the angular spectrum of the scatterers is quite narrow at these heights. The region from 70 to 78km is quite interesting. The reduced wide beam fading times suggest some degree of isotropy of scatter. However, it should be borne in mind that bursts of power occur intermittently at these heights (see Fig. 4.13). During periods when no scatterers were overhead, a scatterer formed at a position several degrees off zenith may show, even if its angular spectrum is quite narrow, simply because nothing else exists to produce strong scatter. If perhaps 2 or 3 of these scatterers formed at oblique positions, and their weak signals were received, quite rapid fading may result. With the narrow beam, the effects of these oblique scatterers would be cut out. Thus the difference between the narrow and wide beams in this case is probably not so much due to isotropic scatter as due to the temporal and spatial intermittency of strong bursts.

Above 80km, fading times are 50% greater on the narrow beam than on the wide beam, showing the beam broadening effect.

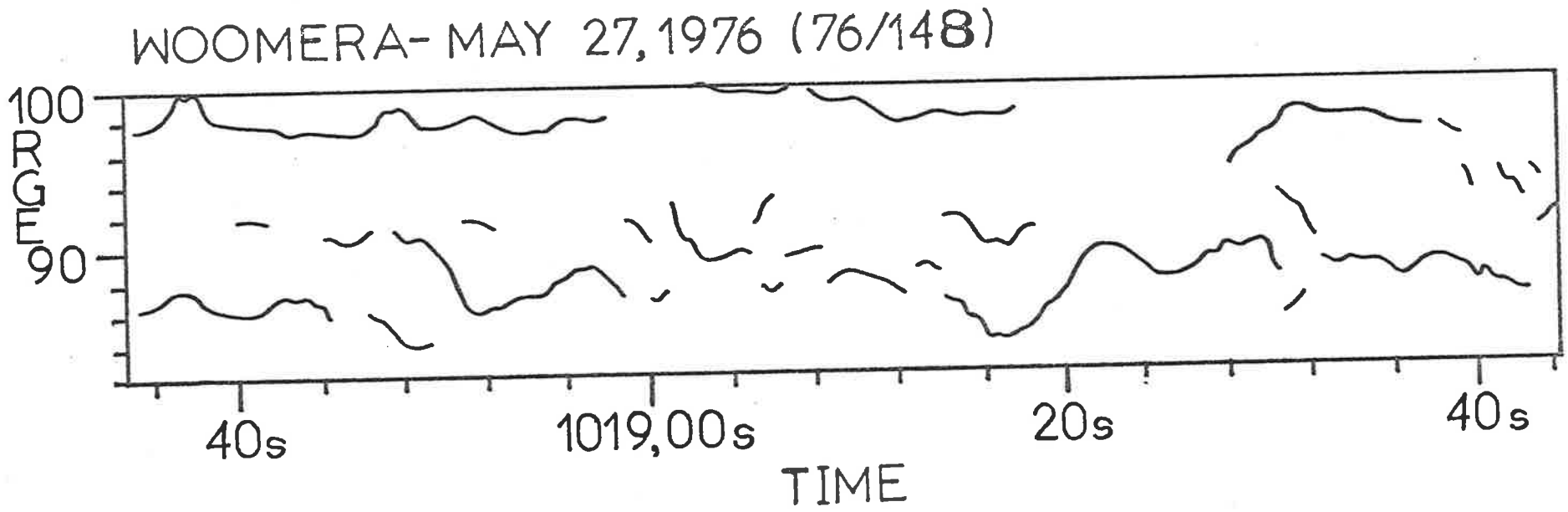

Fig. 4.19 Example of short-term height fluctuations of peaks of echoes. The positions of the peaks were calculated from profiles obtained every 0.4 seconds, and interpolated, to produce the above lines. The pulse width used corresponded to 4km resolution. The upper echoes (98-100km) may be related to E region total scatter and will be ignored. It can be seen that the peaks of the profiles vary between 84 and 94km for the lower echoes. This data was recorded using a wide receiving beam, so some of the larger range echoes may be obliques. However, it can be seen echoes come from a wide range of heights on this day. It is not clear whether the scatter was due to several scattering layers at closer resolution than one pulse width, or a continuum of scatterers. However, a histogram analysis (using a longer sequence of data) showed that scatter came from 2 main ranges - one at about 84km (± 2km) and one at 88-92km. The peaks at around 86km are often due to interference between the 84km and 88-92km echoes.

It can be seen that the position of the peaks varies substantially in a short time (e.g., around 6km in 8s at 1019, 20s). This is not due to large scale movements of scatterers, but simply changes in interference effects of the pulses from the various contributing scatterers. It was not clear whether the 88-92km scatter was due to a continuum of scatterers, or several discrete scatterers within this region. This type of wide height variation is quite typical of ~ 86-94km scatter. However, at some times, quite height-stable echoes do also occur. For example, the 86km echo on day 79/229 (Fig. 4.13) showed much less height fluctuation.

4.3.2 Height Fluctuations

Even on time scales of the order of seconds, the heights of peaks of echoes tend to vary. In fact, Fig. 4.7b would often be similar even if say 5 or 10 second mean profiles had been taken. This is particularly true of the 88-94km echoes. At times, an echo at around 86km can be quite stable in height, (e.g., Figs. 4.7b, 4.8, 4.13) but generally these show significant height variation, at least of 1 or 2km. On some occasions, too, the lower echoes (70-74km) can exhibit little variation of height, but, again, this is the exception rather than the rule. Fig. 4.19 shows the short-term variation of the height of the peaks of power profiles. The results were actually recorded at Woomera, using a wide beam, but are fairly typical. Use of a narrow beam does cut down the variation in range observed somewhat, but does not eliminate it entirely.

The fact that these height oscillations occur on such short time scales shows quite definitely that scatter generally comes from a range of heights within any height regime, whether it be a continuum of scatterers or just a few discrete scatterers. The variations in heights of the echoes within any one layer is an interference effect. It is difficult to conceive a single scatterer moving about this much on such a short time scale.

Thus monitoring of the fluctuations of these peaks is a useful means of determining estimates (under-estimates) of layer thicknesses (within the resolution of the radar pulse).

4.4 Spatial Extent of Scatterers

The investigation of the spatial extent of individual scatterers, and also the horizontal dimensions over which similar ionospheric conditions exist, are both important problems. Neither is dealt with particularly extensively in this thesis.

Some elementary work was done to determine the horizontal scale of scatterers, and values of the order of kilometres were obtained. For example, Appendix D shows calculations giving typical sizes of 3 to 10km at 74km. Such calculations are, however, quite crude. The calculation in Appendix D relied heavily on the assumption that the 1/e power half width of the angular spectrum of the scatterer was $\theta_0 \sim 2\text{-}3°$.

With regards to the horizontal extent of D region radio wave scattering structures, it can be said that the ionospheres at Adelaide and Townsville certainly did not appear to be the same. The presence of a scattering layer at say 86km at Townsville certainly did not imply one would also exist at Adelaide at the same time.

On day 79/229, a very simple receiver was taken to Willunga, 70km south of Buckland Park, and the ionospheric scatter from the transmitter at Buckland Park was monitored using a simple half wave dipole attached to this receiver. Scatterers were present at 86km, 76km (at times) and 70km altitude, according to observations made at Buckland Park (1200-1300). Indications were that during the period 1230 hr - 1300 hr, echoes due to scatterers at around 85-90km, and possibly some at a lower height (70-75km altitude) were received at Willunga. This may suggest that similar ionospheric conditions extend at least over about 35-40km. The equipment used was perhaps a little too inaccurate to state this unambiguously, however.

But certainly, the question of the spatial extent of these scatterers, and their physical dimension, is an important problem. It should be

simple to investigate, using simple half-wave antennas placed at varying distances from the main Buckland Park Array, and recording the transmitter pulses scattered by the ionosphere to those dipoles.

4.5 A Review of VHF Studies

4.5.1 Introduction

Some discussion of early VHF studies has already been given in Chapter I. The period up to 1976-7 was covered. Having now seen many of the features of HF echoes produced by mesospheric scatterers, it is fitting that observations at other frequencies be compared here. The review will concentrate on VHF studies. This is primarily because only at frequencies below about 100MHz have significant echoes (apart from Thomson (incoherent) scatter) been observed from the mesosphere (e.g., see Gage and Balsley, 1980, Fig. 6). Observations at VLF and LF will not be considered any more than the discussions already presented in Chapter I.

Before discussing experimental observations however, it is worthwhile considering the form of a pulse after scatter from a horizontally stratified atmosphere. The results of this analysis will be useful for interpretation of experiments at all frequencies. A more generalized, three-dimensional treatment will be given in a later chapter.

4.5.2 The Scattered Pulse Profile

The following section attempts to illustrate some important points regarding a pulse scattered from Fresnel scatterers. The discussion will be largely pictorial, rather than involving a great degree of mathematics.

Assume a horizontally stratified atmosphere, and imagine a pulse of radio waves which propagates vertically (z direction) through this atmosphere. Let the refractive index profile be n(z). (n is complex). Then the Fresnel reflection coefficient at any height is given by $(\frac{dn}{dz})dz$ at that height. Let

$$r(z) = \frac{dn}{dz} \qquad (4.5.2.1)$$

This will be at times referred to as a reflection coefficient, although of course the real reflection coefficient between z and z + dz is r(z)dz.

Let the transmitted pulse at position z and time t be

$$\frac{1}{z}\, g(t - \int\frac{dz}{v}).e^{j\omega(t - \int\frac{dz}{v})} \qquad (4.5.2.2)$$ (Appendix B, equation B.17)

In this approximate analysis, let us assume that the speed of the radiation, v, is equal to the speed of light in a vacuum, c. Also, we shall ignore the z^{-1} dependence. Let the pulse at z = 0 be given by

$$g_t(t)e^{j\omega t} = g_z(\xi)e^{\frac{j2\omega\xi}{c}} = g_p(\xi), \text{ say,} \qquad (4.5.2.3)$$

where $\xi = \frac{ct}{2}$ is a length coordinate.

Then the pulse received at time τ_0, corresponding to a virtual range $z_0 = c\tau_0/2$, is given by

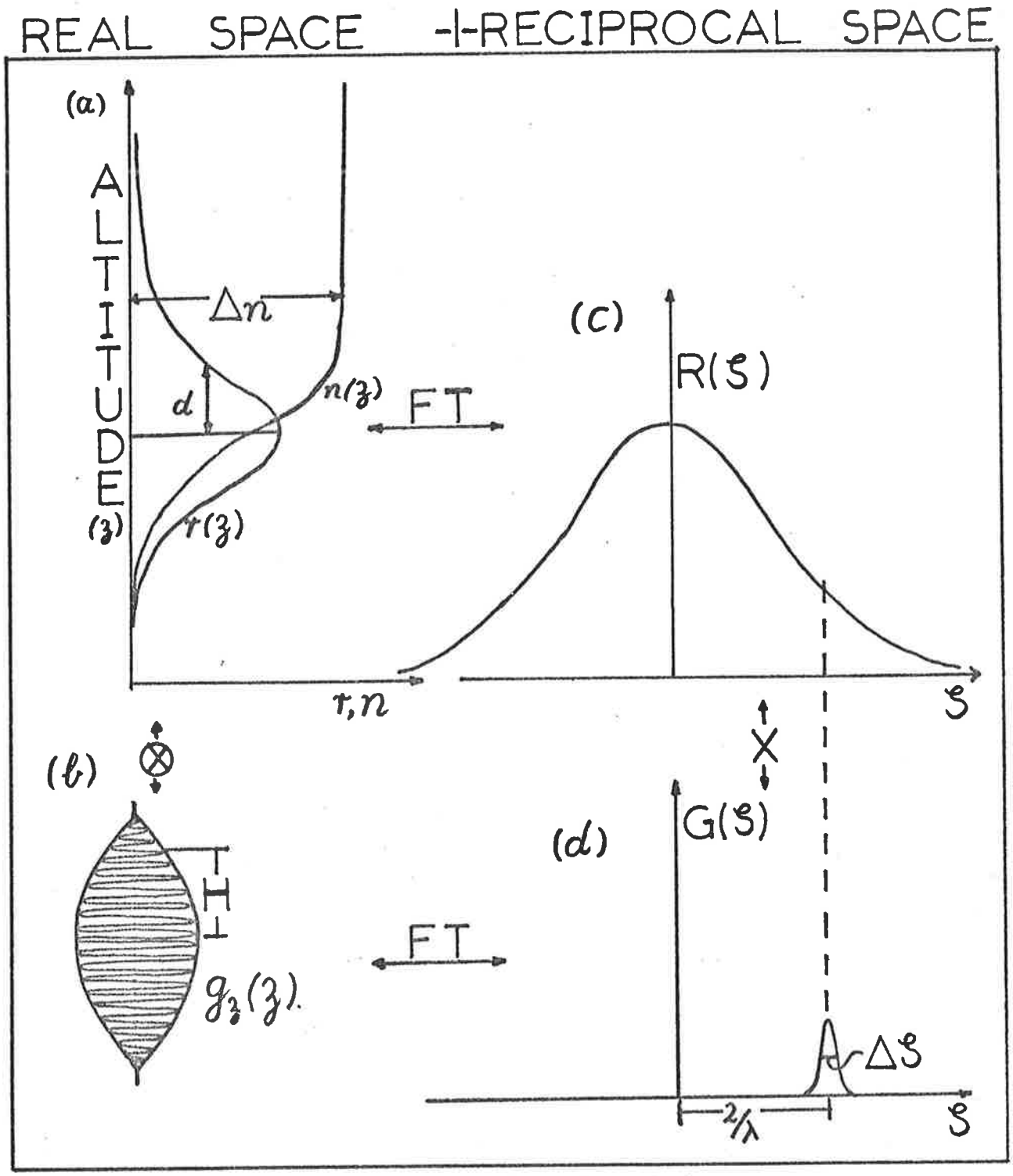

Fig. 4.20 Figure illustrating

(a) an assumed refractive index profile n(z), with the associated reflection coefficient profile r(z)

and

(b) a pulse of radiation transmitted into the ionosphere.

The graphs (c) and (d) show the corresponding Fourier transforms of r(z) and $g_z(z)$.

If the transmitted pulse were actually a simple cosine oscillation inside the envelope (as is usually the case), G(S) also contains a Gaussian peak at $-2/\lambda$. However, for the discussion in the text relating to this diagram, this is an unnecessary complication and has been ignored.

(4.5.2.4) $$g_R(z_0) = r(z) \otimes g_p(z)$$

$$= \int_{-\infty}^{\infty} r(z)g(z_0 - z)dz$$

(e.g., see Austin et al., 1969, and Appendix B, equation B.2b)

Now examine Fig. 4.20. Let n(z) in (a) be the refractive index profile (a smooth step), and let r(z) be also as shown. For simplicity, assume

(4.5.2.5a) $$r(z) \propto e^{-(\frac{z^2}{d^2})}$$

Let the transmitted pulse be

(4.5.2.5b) $$g_z(z) = e^{-\frac{z^2}{H^2}} \cdot e^{j(2\pi.(\frac{2z}{\lambda}))}$$

Let us now examine the peak amplitude of this convolution. It is easier to do the convolution in reciprocal space, so obtain the Fourier transforms; i.e.

$R(\zeta)$ for $r(z)$ and $G(\zeta)$ for $g_z(z)$, where $\zeta = z^{-1}$. These are drawn schematically as (c) and (d) in Fig. 4.20. (R and G are generally complex, but in this case r and g are symmetric so R and G are real.) The peak amplitude of the convolution mentioned above is proportional to the area under the product of R and G. It is assumed $\Delta\zeta$ in Fig. 4.20d is small. Then the area under the product of R and G is approximately proportional to $R(2/\lambda)$ (assuming the pulse width H, and therefore $\Delta\zeta$, are constant). A narrow step in n(z) means d is quite small, so $R(\zeta)$ becomes a wide function, thus increasing this area, and so resulting in greater scattered peak amplitude. A thick step means $R(2/\lambda)$ is quite small, thus suggesting reduced scattered amplitude.

In conclusion, the scattered amplitude in this Gaussian-stepped case is approximately proportional to

$$(4.5.2.6) \qquad R(2/\lambda) \propto e^{-\pi^2(2/\lambda)^2 d^2} \ ,$$

assuming the step size Δn is constant, the pulse length H is constant, and ignoring effects of the fall off in peak power for increasing range.

Thus it can be seen if $d = \lambda/4$, the scattered power has fallen off by 0.08 times compared to $d \sim 0$. For larger d, the scattered amplitude falls off very rapidly. This is why, when Fresnel scatter is observed from the atmosphere, it is usually assumed (e.g., see Ch. I, section 1.4.2) that the scatter had to come from steps in refractive index less than about $\lambda/4$ in extent - unless the step in refractive index Δn is quite large.

Many other cases for r(z) can be examined quite simply with the above pictorial approach. Some discussion of double-sided scatterers has already been undertaken in Chapter II, section 2.2.3,with regards to scattering eddies. However, it should be borne in mind that in that case horizontal stratification was not assumed, and a fuller 3-dimensional treatment was undertaken. But examinations of several horizontally stratified "δ-function" reflection coefficients (sharp steps in n(z)) is also a useful case to consider. The possibilities of perhaps 2 or 3 of these producing scatter which beats together has already been considered.

One extremely important case which will be considered is the case where r(z) is a random function and covers a height range greater than the pulse length. Such a case has been considered by Gage and Balsley (1980), and Green and Gage (1980). Intuitively, it may be expected that

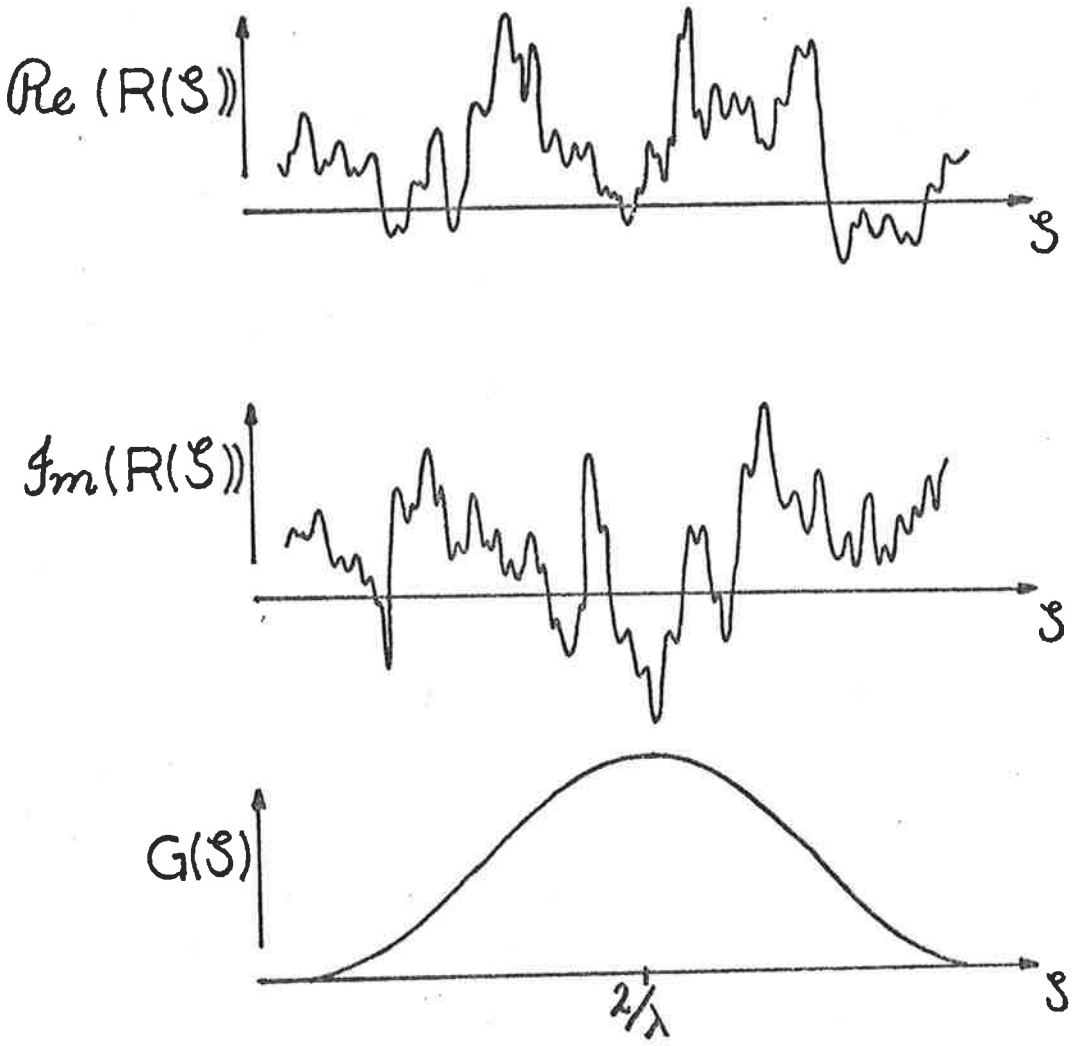

Fig. 4.21 Fourier transform G of the transmitted pulse g_z, and the Fourier transform R(ζ) of the reflection coefficient r(z) for a random variation of r(z).

the peak power received would be proportional to the pulse width. These authors, however, achieved the result that the peak power is proportional to the pulse width squared. This is an erroneous result. Their argument goes briefly as follows. Scatter is produced from Bragg scales in the vertical of scale $\lambda/2$. By doubling the pulse length, the number of oscillations of this scale in one pulse length doubles. Thus the scattered amplitude doubles, and the power becomes $(2)^2$ times as much as that for the original pulse length. The argument is presented most fully in Gage and Balsley (1980).

The error is, of course, in considering only one Bragg scale. The transmitted pulse has a finite length, and so its Fourier spectrum has a finite width. If reciprocal space is considered, as in Fig. 4.20, the resulting $R(\mathcal{S})$ and $G(\mathcal{S})$ are as illustrated in Fig. 4.21.

The peak power of the scattered pulse in this case is equal to

$$(4.5.2.7) \qquad \left|\int R(\mathcal{S})G(\mathcal{S})d\mathcal{S}\right|^2$$

If the pulse width is increased by x times, the area under the pulse envelope of $g_z(z)$ increases x times, and so the peak value of $G(\mathcal{S})$ increases x times. The width of $G(\mathcal{S})$ becomes x^{-1} of its former width. So what happens to 4.5.2.7? This integral is equivalent to adding m randomly phased phasors. The power is proportional to m (e.g., see Chapter V). By decreasing the width of $G(\mathcal{S})$ by x times, this effectively reduces the number of phasors m, by x times, so the power reduces by x times. However, $G(\mathcal{S})$ is x times larger at its peak, so this increases the power by x^2 times, resulting in an overall increase in power by x times. The result can be proved more precisely, but this is not warranted here.

Under this analysis, however, the argument presented by Gage, Green and Balsley is quite clearly wrong. By assuming a single Bragg scale, it effectively assumed $R(\mathfrak{S})$ was a delta functioning at $\mathfrak{S} = 2/\lambda$. If indeed the scatter was due to a single Bragg scale, then the result of 4.5.2.7 would be proportional to the amplitude of $G(2/\lambda)$ squared - the changes in width of $G(\mathfrak{S})$ is not important. We saw $G(2/\lambda)$ increased by x^2 times, so the result is that the returned peak power is proportional to the pulse width squared. But such a case certainly cannot be used to approximate a random r(z), which is what was assumed.

One more point does arise. $R(\mathfrak{S})$ will not be completely uncorrelated between successive points. Thus $R(\mathfrak{S})$ may vary more slowly with $\mathfrak{S}$ than that shown in Fig. 4.21 - it is possible that $R(\mathfrak{S})$ may not show a great deal of fluctuation across $\Delta\mathfrak{S}$. In such cases, the scattered peak power would be proportional to the area under $G(\mathfrak{S})$, which is simply proportional to the transmitter peak power. Thus in this case the scattered power would be independent of the pulse width. But the "degree of fluctuation" is inversely proportional to the total layer width - if in fact $R(\mathfrak{S})$ does not show much fluctuation across $\Delta\mathfrak{S}$, then this will mean that the scattering layer is in fact much narrower than one pulse width.

Thus, for a scattering layer much narrower than the pulse width, the scattered peak power is independent of the pulse length. For a layer much thicker than the pulse length, with random fluctuations in r(z), the scattered peak power is proportional to the pulse length. (Gage and Balsley (1980), have called this Fresnel scatter, as distinct from Fresnel reflection: they use this latter term to refer to reflection off single steps of n(z)).

It should also be noted that these results apply at both VHF and HF. With these points in mind, it is now possible to proceed to a review of VHF studies.

4.5.3 Experimental VHF Observations

A considerable number of reviews of VHF observations of the atmosphere exist - for example, Gage and Balsley (1978); James (1980); Crane (1980); Harper and Gordon (1980); Gage and Balsley (1980). The Journal "Radio Science", volume 15, number 2 (March-April, 1980) contains some extensive reviews. The short summary presented here will have mesospheric echoes as the main point of emphasis.

Early results of VHF atmospheric studies in the mesosphere have been presented in Chapter I. As discussed, turbulence was generally regarded to be the cause of the scatter observed. Tropospheric investigations of VHF have been going on since about 1940, generally using oblique ray paths, with the transmitter and receiving being well separated (forward scatter). The review by Gage and Balsley (1978) discusses these early years.

The advent of systems which could record phase allowed much better signal to noise ratios to be obtained and also led to measurements of winds by Doppler techniques. This procedure also allowed measurement up to much greater heights than had been previously possible, through the facility of coherent integration. (Mean scattered powers fall off exponentially with increasing height, at least up to about 20km, e.g., see Balsley et al., 1980, Fig. 10). With these improvements, several VHF stations for lower atmosphere (troposphere and stratosphere) studies were made. The establishments near Boulder (Colorado, USA (the Sunset radar)) and Northern Germany (SOUSY Radar) were two of these. An extremely powerful VHF radar near Jicamarca, Peru, has already been in service for some time. This was used initially for VHF Thomson (incoherent) studies of the E and F regions of the ionsophere. Several other radars are also being built. Only the most powerful radars can observe in the stratosphere and mesosphere. These are called MST (mesosphere, stratosphere and

troposphere) radars.

In 1978, two papers were published which presented evidence for specular reflections in the first 20km of the atmosphere. These were due to Röttger and Liu (1978), and Gage and Green (1978). As both papers pointed out, the existence of specular scatter had been proposed as early as 1949 (e.g., Friend, 1949; Saxton et al. 1964). These later (1978) papers presented very strong evidence of specular scatter using backscattered radiation. Strong scatter occurred from the vertical, and much weaker scatter from off-zenith angles. The authors were also able to make rough measurements of the ratio of specular to isotropic scatter. Röttger and Vincent (1978) also showed that significant Fresnel scatter occurs in the troposphere and stratosphere, as has Röttger (1980).

The existence of this form of scatter suggested that quite sharp vertical steps in refractive index occur in the lower atmsophere, which extend some distance horizontally, to produce this highly aspect-sensitive scatter. These steps must be less than one or two metres in vertical extent, for significant scatter only occurs for steps of width less than about ¼ of the probing wavelength, as we have seen. Furthermore, they must be highly stable, since these echoes can exist for tens of minutes (e.g., Röttger and Liu, 1978). Quite sharp refractive index gradients of thickness 10 metres and less have also been observed by in-situ measurements (e.g., Crain, 1955).

With the realization that some of these lower atmospheric echoes were caused by horizontally stratified scatterers, it became clear that some mesospheric VHF echoes might also be due to similar scatterers, no matter how intuitively unlikely it seemed. The assumption that all mesospheric scatter of VHF was due to turbulence would have to be re-examined. However, results of investigations of specularity at VHF in the mesosphere had to wait until 1979-80 before they were published.

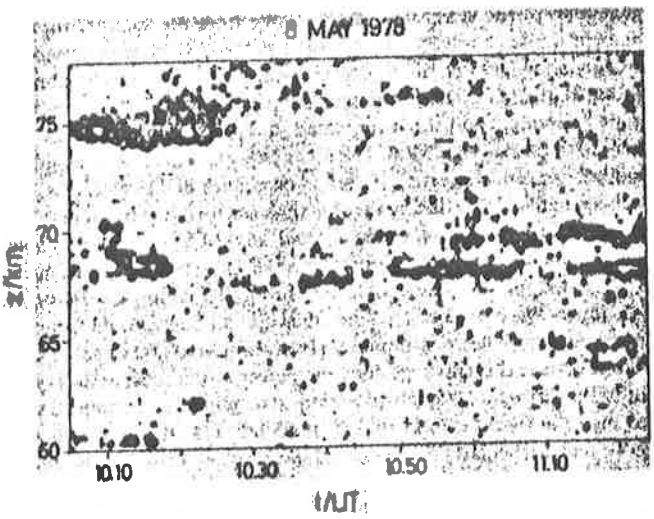

Fig. 4.22a Contour plot of the received echo power from mesospheric structures as a function of height and time for a period of 80 mins, using the SOUSY VHF radar in Germany (from Czechowsky et al., 1979).

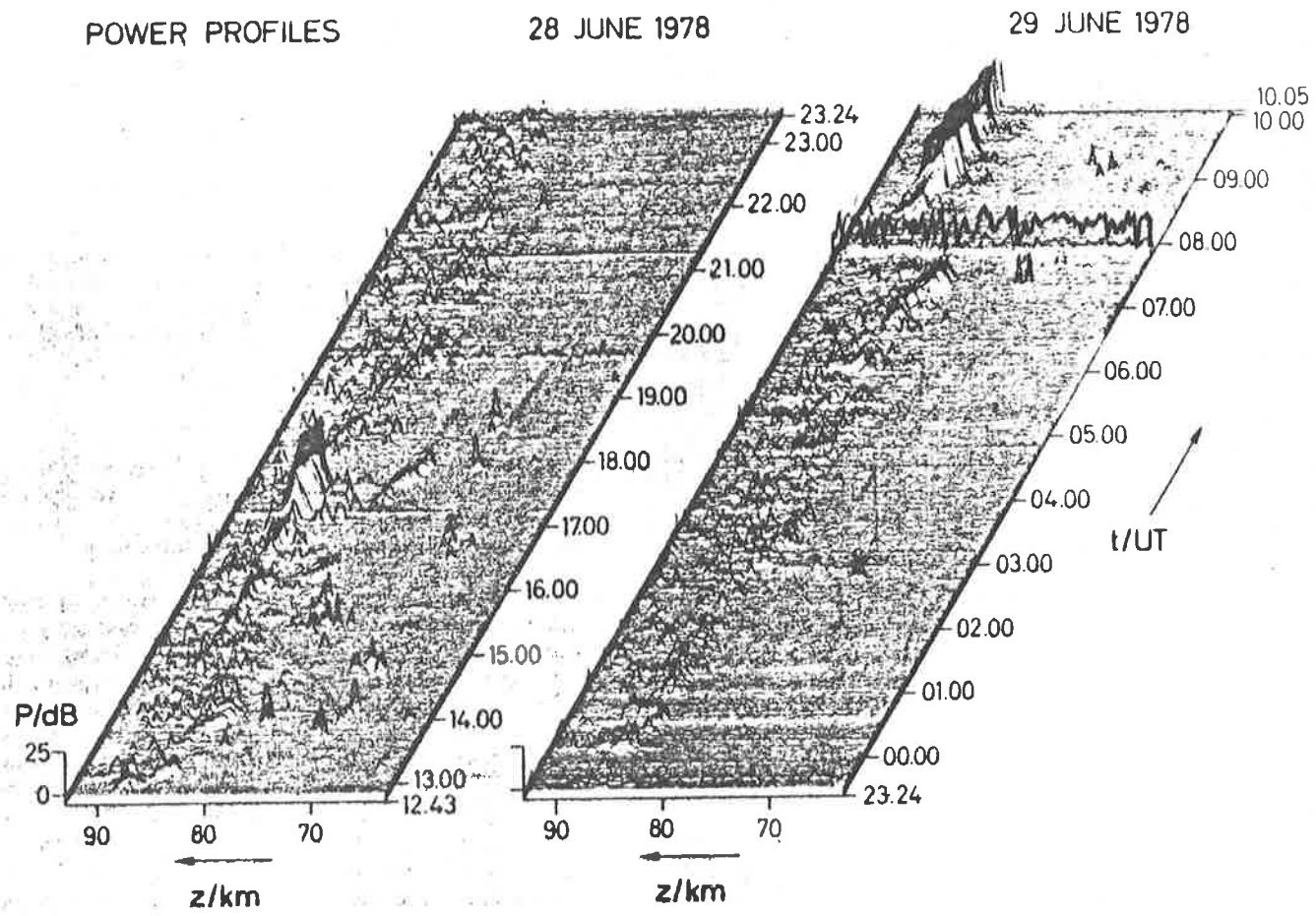

Fig. 4.22b Three-dimensional graph of the mesospheric echo power as a function of height and time at VHF for the German Summer (from Czechowsky et al., 1979).

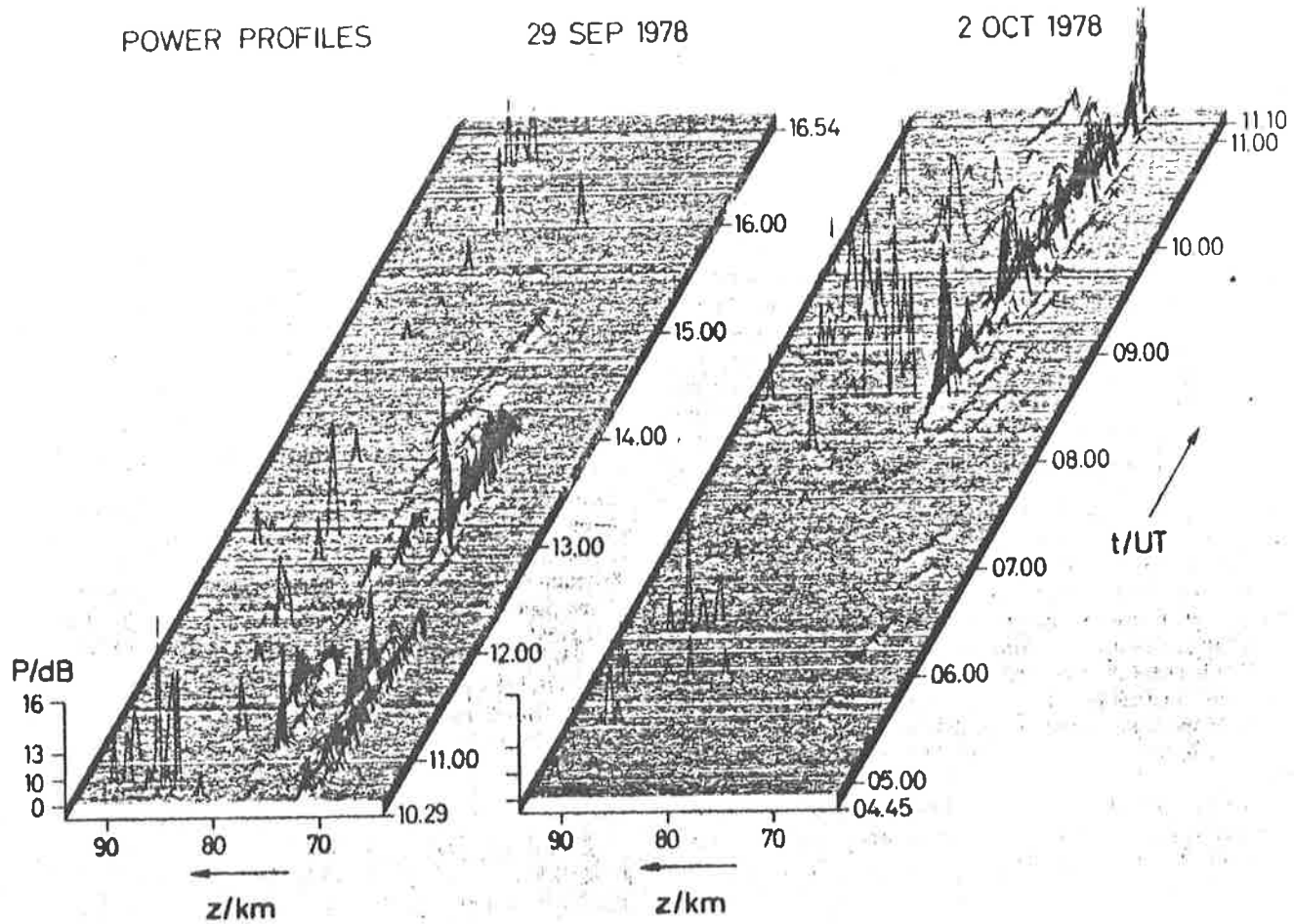

Fig. 4.22c Three-dimensional graph of the mesospheric echo power as a function of height and time for the German autumn at VHF. (From Czechowsky et al., 1979). Note that the single spikes are due to meteors; all others are genuinely mesospheric.

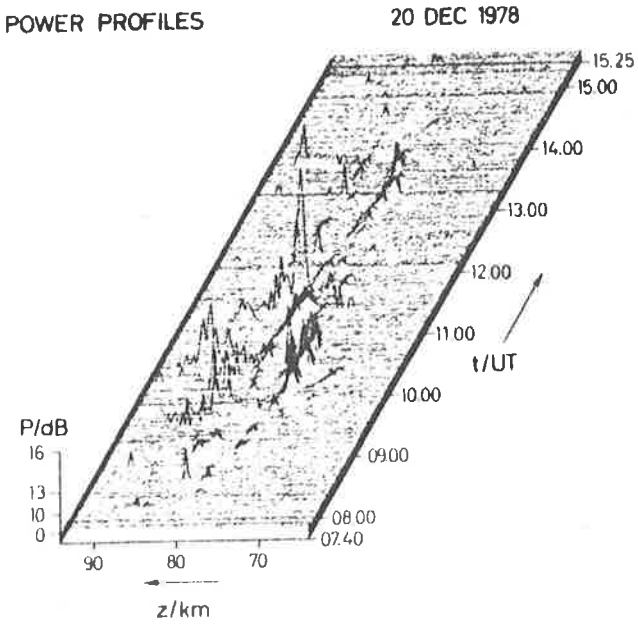

Fig. 4.22d Three-dimensional graph of the mesospheric echo power as a function of height and time at VHF for the German winter. (From Czechowsky et al., 1979).

Other interesting VHF observations were made in the meantime. Two of the most important papers concerning mesospheric echoes were those of Czechowsky et al. (1979) and Röttger et al. (1979). Both sets of observations were made at 53.5MHz, and both achieved height resolutions which had never previously been achieved for mesospheric observations. These papers contributed greatly to the understanding of these scatterers. The improved resolution was achieved by using pulse-coding techniques. The techniques will not be discussed here (see, for example, Schmidt et al. (1979), and Woodman (1980a)). Czechowsky et al. achieved a resolution of 300m, and Rastogi et al. 150m.

The diagrams of Figs. 4.22 show typical results from Czechowsky et al. (1979). It should be borne in mind that none of this scatter is due to incoherent (Thomson) scatter, since the SOUSY radar is not sensitive enough to detect such scatter (Harper and Gordon, 1980). The data were prepared from 40s means of power for Fig. 4.22a, and 95s means of power for the other figures. Quite clearly stratification of echo structure occurs, just as it does at HF (e.g. compare with Figs. 4.1a-c). The rapid increases in power by around 10-20dB which last a few minutes, referred to by earlier VHF workers (e.g., Rastogi and Woodman, 1974; Harper and Woodman , 1977) also appear in these diagrams. Miller et al. (1978) also reported temporal intermittency of VHF signals observed with the Urbana, USA, facility.

Various types of structure can be seen in Figs 4.22, which would not be resolved at the 4km resolution of HF studies. Czechowsky et al. (1979) classified the echoes into four categories - blobs, sheets, and thin and thick layers. The short duration (1-2min) bursts in Fig. 4.22a were denoted blobs. Longer duration (tens of minutes and more) thin structures (less than about 1km thick) were called sheets. The scatter at 68km in Fig. 4.22a was such a sheet. The notation "layers" referred

to long duration bursts (tens of minutes and greater - some persisted for hours) of thickness greater than 1km. "Thin layers" referred to structures up to 5km thick, and thicker layers were denoted as "thick". Thicker layers generally had longer lifetimes (Fig. 5 of Czechowsky et al., 1979), which may mean they were larger horizontally, since the lifetime is defined in part by the time taken for the scattering region to pass through the array beam. Alternatively, the lifetime may actually be the lifetime of the scattering region. Very thick layers generally occurred at greater heights. Below about 70km, layer thicknesses were generally less than 2km, and in summer were always less than 0.5km. These findings are quite similar to HF results (e.g., Chapter I, section 1.4.1c), where it was found that echoes from below 75-80km appeared to be quite thin, but scatter from above could come from regions upt to 10km in vertical extent. The difference in transition height (70km at VHF in Germany compared with 75-80km at HF in New Zealand, Australia, and Canada) may reflect latitudinal differences, or may indicate something about the scattering mechanisms. For example, suppose at all heights scatter was produced by turbulence and also by Fresnel scatter from steps in refractive index of depth equal to a Kolmogoroff microscale. At heights where this microscale was less than one quarter of the incident wavelength, the thin steps may dominate - at greater heights where the microscale was larger, the turbulent scatter may dominate. The turbulent scatter would be less affected by the change in Kolmogoroff microscale, as reflection from a step falls of very rapidly once thicknesses greater than $\sim\lambda/4$ are reached (§4.5.2). Such effects will be discussed more in Chapter IX. The transition region would be lower at VHF (see Fig. 1.9a). Röttger et al. (1979) also supported this statement that thin sheets occur mainly below 70km.

Echoes at VHF in Germany were strongest in summer, and were strongest from the region above 80km. However, they did occur over the full range

60-90km. The echoes from above 80km persisted throughout day and night. This is consistent with HF observations, which show echoes throughout day and night above 80km. However, HF echoes are weakest in summer, particularly those from below 80km. VHF echoes occurred only between 70 and 80km in autumn. This is not the case at HF, for at those frequencies echoes occur over the full height range 60 to 100km in autumn, winter and spring. Just as at HF, however, the lower echoes were a day-time phenomenon only. In winter, VHF scatterers occurred predominantly in the regime 60 to 80km. The summer 80 to 90km echoes were 6-10dB stronger than the autumn and winter echoes (which were from below 80km). This is also true at HF, where the lower echoes have effective reflection coefficients of the order of 10^{-5} to 10^{-4}, and the higher ones have effective reflection coefficients around 10^{-3}.

Thus the most striking difference between VHF and HF observations concerns the 80 to 90km echoes. We have seen that HF scatterers in this region are quasi-isotropic, and may be turbulence generated. Examination of Fig. 1.9a, model 2, suggests that the upper limit of turbulence scales which can be observed in the inertial range of turbulence with the frequency used by Czechowsky et al. (1979) is about 75-80km. Scatter from greater heights should be from scales in the viscous subrange, and thus significantly reduced in intensity. Fukao et al. (1980b), however, have suggested that they observed scatter at 75-85km with the Jicamarca VHF radar, and that the scatter was from turbulence scales in the viscous subrange. It should be borne in mind that the intensity of radio wave scatter from turbulence depends on the gradient in electron density, and scattered power is proportional to the potential refractive index gradient squared, (e.g., Chapter II, equation 2.3.2.11). This is true in both the inertial and viscous ranges (e.g., Harper and Gordon, 1980). The existence of a steep electron density ledge may thus help to produce significant scatter from turbulence, even if the scatter is from scales in the viscous

range. A very steep ledge often exists at 80-90 km (e.g. see Chapter I; also Trost, (1979)). In fact this ledge is also capable of producing scatter at HF, even though it is much thicker than one quarter of a wavelength, due to the large electron density change across the ledge (this will be seen in Chapter VIII). Perhaps it can also produce significant specular scatter at VHF, although the results of Fukao et al. (1980b) do suggest that VHF scatter is isotropic at these heights. The summer appearance of VHF echoes at 80-90km may be a commentary on the appearance of this electron density ledge (with either associated specular or (more likely) turbulent scatter) or some other feature which produces a large potential refractive index gradient (e.g., see Ch. II, equations 2.3.2.10 - the potential refractive index gradient also depends on the temperature gradient, and the total electron density). During summer, it is possible for sporadic-E type echoes to appear at heights as low as 90km at HF (e.g., such a structure occurred during January, 1978,at Buckland Park) and these summer VHF echoes could perhaps (alternatively) be related to these structures.

Röttger et al. (1979), also using the SOUSY radar, found very similar results to Czechowksy et al.. Scattering regions were quite narrow in height ($\lesssim$ 1km) below 70km, but could be thicker at greater heights. These authors also found, by spectral analysis, that spectral widths generally seemed wider for thicker layers. This would be expected for turbulence, since larger energy dissipation rates imply larger outer scales and larger rms velocities. Fading times at low heights (70km and below) were quite large - of the order of 4s - and these values are larger than those observed at Jicamarca (1-2s, e.g., Harper and Gordon, 1980). This might suggest non-turbulent scatter (Harper and Gordon, 1980).

Röttger et al. also discussed the possibility of Fresnel scatter. They felt that there could perhaps be some such scatter from steps in refractive index caused by intense turbulence, presumably along similar lines to a model proposed by Bolgiano (1968). This model will be

discussed more in Chapter IX, but basically it proposes that intense turbulence can mix up an electron density gradient so much that sharp steps, of large horizontal extent, can occur between turbulent and non-turbulent regions. Röttger et al. (1979) felt that actual Fresnel reflection was unlikely: any such turbulence - produced steps should have fluctuations in depth of the order of the Kolmogoroff microscale. The Kolmogoroff microscale at such heights is similar in value to the probing wavelength used with the SOUSY radar, so this would mean genuine Fresnel reflection (i.e., reflection from a flat "mirror-like" step) could not occur. But the scatter from such "rough mirrors" might still produce scatter which is somewhat aspect sensitive (the authors called this "diffuse reflection" (also see Röttger, 1980)). The authors also claimed to have done, and to know of some experiments due to Countryman at Jicamarca, which suggested that there was some aspect sensitivity of VHF scatter at mesospheric heights, but no actual data were presented.

The authors felt that the blob-like irregularities arose from scatterers which were formed, and/or died out, within the beam. The observed lifetime of sheets and layers could sometimes be determined by the time it takes a scatterer to drift through the beam, however, so in such cases the lifetime would not be the actual scatterer's lifetime. The possibility of a new scatterer entering the beam as another leaves could also produce artificially long "lifetimes".

Röttger et al. (1979) then attempted to make estimates of turbulence parameters in a similar manner to Cunnold (1975).

But it is felt that one point must be mentioned here. The above arguments against Fresnel scatter assume that turbulence is in fact active. If the region were dynamically stable, turbulence may not act, and perhaps quite sharp steps in refractive index could form by some non-turbulent mechanism. The molecular diffusion coefficient at 75km is around $.3 m^2 s^{-1}$

(see Ch. I, section 1.4.1e) so a step of thickness 2m would last around $(2)^2/0.3 \approx 13$s. Larger steps would last correspondingly longer. Although it has been assumed that step sizes are less than about $\lambda/4$, it is not possible to determine the step size until estimates of effective reflection coefficients are made. A step of size around λ would produce only weak reflection (e.g., see section 4.5.2), but it would produce some reflection.

Thus it can be seen that these VHF papers have improved our understanding of mesospheric scatterers - although many of the results such as scatterer sizes had been estimated earlier from HF studies (e.g., see Ch. I; also, for example, Vincent, 1973). Röttger et al. (1979) discussed briefly the possibility of specular reflection, but showed little evidence, however. This was still a major experiment to be performed and reported.

One particularly important point is to determine the nature of the atmosphere in the region of the scatterers - is it turbulent, or stable? Are the scatterers associated with wind shears? Some results of such investigations will be presented in a later chapter (Ch. IX) but it is worth considering the state of the tropospheric and stratospheric atmosphere at scattering heights, where much more data is available for comparison.

Gage and Green (1978) found, by using near simultaneous measurements of winds and temperature with their observations of VHF scatter, that highly aspect-sensitive scatter (i.e., significant vertical backscatter, but little off-zenith backscatter) was associated with regions of great hydrostatic stability. Vincent and Röttger (1980), found their Fresnel-like scatter came from regions of high Richardson number (i.e., great hydrostatic and dynamic stability). Thus specular reflection does appear to be related to stable regions. Since the stratosphere is

generally hydrostatically stable, it is generally true that this region contains aspect-sensitive stable layers. The troposphere generally shows more isotropic scatter, and scatter is generally due to turbulence (although specular scatter can, and often does, occur (e.g., Vincent and Röttger, 1980)). These differences can be used to determine the height of the tropopause (Green and Gage, 1980). An increase in power when looking vertically, as well as a decrease in the ratio of power when looking at an off-zenith angle to that when looking vertical, signify the tropopause. Green and Gage (1980) have had good success in estimating tropopause heights by this technique.

Van Zandt et al. (1978) assumed that tropospheric VHF scatter is generally due to turbulence which occurs in thin strata (also see Crane, 1980), and developed a model by means of which measurements of winds and temperature with relatively poor resolution (1-2km) can be used to estimate scattered strengths. This has been discussed briefly in Chapter II. The idea assumes that any mean wind shear has fine scale fluctuations, and Van Zandt et al. (1978) used probabalistic arguments to determine the percentage of radar volume which would have wind shears of sufficient intensity to produce turbulence. Such fine scale fluctuations do exist, as can be seen, for example, in Crane (1980), Fig. 2.

Some observations at UHF, and even higher frequencies, are also worth noting. Aso et al. (1977) have presented early investigations in the stratosphere using the Arecibo dish at UHF (430MHz), and found no non-Thomson scatter exists from above the stratosphere. This is consistent with a turbulence mechanism, since above those heights the probing wavelength will correspond to scales in the viscous range of turbulence, so little scatter should be expected (although some may if the background potential refractive index gradient is large). Fig. 4.23 shows the Kolmogoroff microscale as a function of height in the

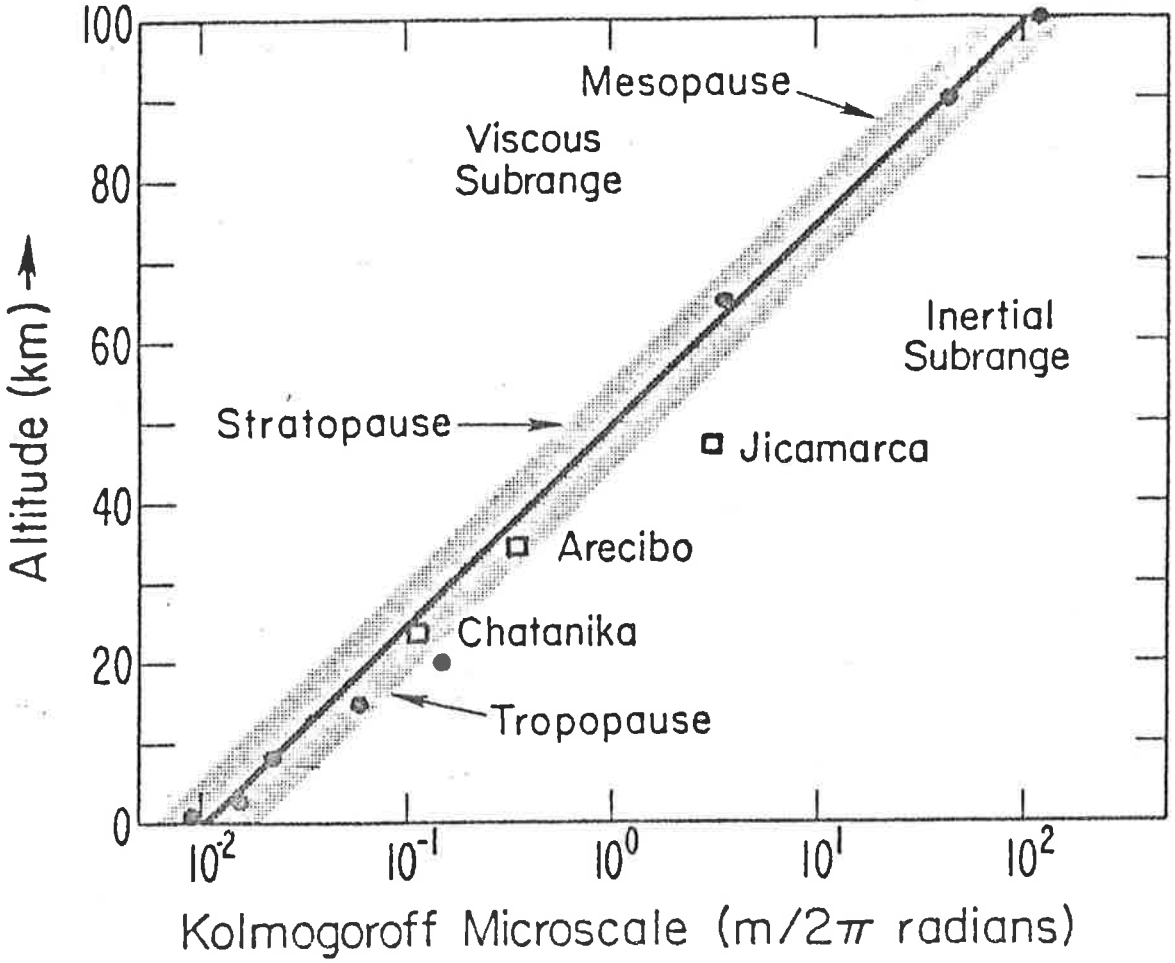

Fig. 4.23 Height distribution of Kolmogoroff microscale, as given by Gage and Balsley (1980). The solid dots represent experimental estimates by various authors, and the solid line a "best fit" line. The shading shows the effect of an order of magnitude change in ε. The open squares represent the upper height limits of echoes observed at the various sites, and are plotted at a scale corresponding to the Bragg scale of scatter for the wavelength used at the site. It is to be expected that the upper limit should be approximately the height where the Bragg scale reaches the Kolmogoroff microscale (although bear in mind that scatter from within the viscous subrange of turbulence can still occur).

Notice that this curve agrees well above 60 km with that shown as model 2 in fig. 1.9a, Chapter I. Below 60 km, the above curve is consistent with $\varepsilon_d \sim 10^{-4} \rightarrow 10^{-3}$ W kg^{-1} in Fig. 1.9a.

atmosphere, and also the upper limit of echoes obtained at various frequencies. The two sets of data are generally in agreement, suggesting that the smallest scales causing backscatter are indeed related to the Kolmogoroff microscale.

Relevant observations regarding the existence of narrow turbulent layers can be found in Woodman (1980a, b). In these papers, results of experiments are presented which were carried out at frequencies of 430MHz (UHF) and 2380MHz (S band). A resolution of 150m was obtained at 430MHz, and of 30m at 2380MHz. Results for the stratosphere showed that extremely narrow turbulent layers exist - often less than 30m thick. Crane (1980) has also shown the existence of thin turbulent layers, and Fig. 1 of that reference shows a histogram of layer thicknesses. These vary from 10 to 1000m. The mode for light and moderate turbulence is at about 20 to 50m. The mode for all turbulence measured was 100-200m. These thicknesses would be greater than the outer scale of turbulence relevant for each observation. Woodman described his echoes as being due to turbulence, which is interesting. VHF observations from the stratosphere are often specular (e.g., Green and Gage, 1980), so perhaps this indicates that VHF echoes may be from different structures to those of Woodman. Simultaneous VHF, UHF and S band measurements should be made to ascertain if indeed this is the case, or whether the different radars are observing different characteristics of the same layer (e.g., VHF may be observing a sharply stepped edge of the turbulence (e.g., Bolgiano, 1968)). The fact that Gage and Green (1978) suggest that specular scatter is associated with stable regions, whilst turbulence requires instability, might suggest that the radars are looking at different layers.

The question arises as to whether such thin layers exist in the mesosphere. The outer scale of turbulence is around $(K^3/\varepsilon_d)^{\frac{1}{4}}$ m rad^{-1}

(e.g., Chapter II, equation 2.2.3.9). At 80-90 km, $K \gtrsim 100 m^2 s^{-1}$, $\varepsilon_d \sim .1 W/kg$ (Figs. 1.9, Ch. I), so $L_o \gtrsim 400$ metres. It would seem reasonable that the mean wind gradient does not change significantly within a distance L_o, so any turbulent layers at 80-90 km should be greater than about 0.5 km thick. At heights of 60 - 80 km, $\varepsilon_d \lesssim .01 \text{ W kg}^{-1}$, $K \sim 30 - 100 \text{ m}^2 \text{ s}^{-1}$ (fig. 1.9c), so $L_o \gtrsim 100m$ (on average). Thus, even at mesospheric heights, the possibility of wind shear fluctuations of less than the pulse resolution exists.

Other radar investigations of the lower atmosphere have been undertaken at other frequences. Richter (1969), used a frequency range centred on 3GHz ($\lambda \sim$ 10cms) with up to 200MHz fluctuation either side, and resolutions of the order of a metre have been obtained. A striking amount of detail can be seen in results obtained with such equipment, although only measurements within the lower troposphere can be made. The system can also be used to measure winds (Gossard et al., 1978). No doubt some of the observations made with this equipment may also be relevant to the mesosphere. For example Merrill (1977) has shown how sharp gradients in temperature and pressure (and thus refractive index) only a few metres in vertical extent can form due to propagation of shear - generated gravity waves into a critical layer. Perhaps a similar mechanism may be relevant for the mesosphere. However, the effect of the ground is important in the boundary layer, and the results obtained by Merrill may result from the ground and the critical level acting as a waveguide. Care must thus be taken before applying tropospheric results to the mesosphere.

Results have recently been published which suggest scatter from the mesosphere can be quite aspect-sensitive at VHF. It appears that scatter is predominantly from the vertical below 70km, and fairly isotropic above, at VHF. Wakasugi et al. (1980) reached this conclusion by examining the depolarization of radio waves, although the interpretation of such an experiment can take other forms. Fukao et al. (1979) and Fukao et al.

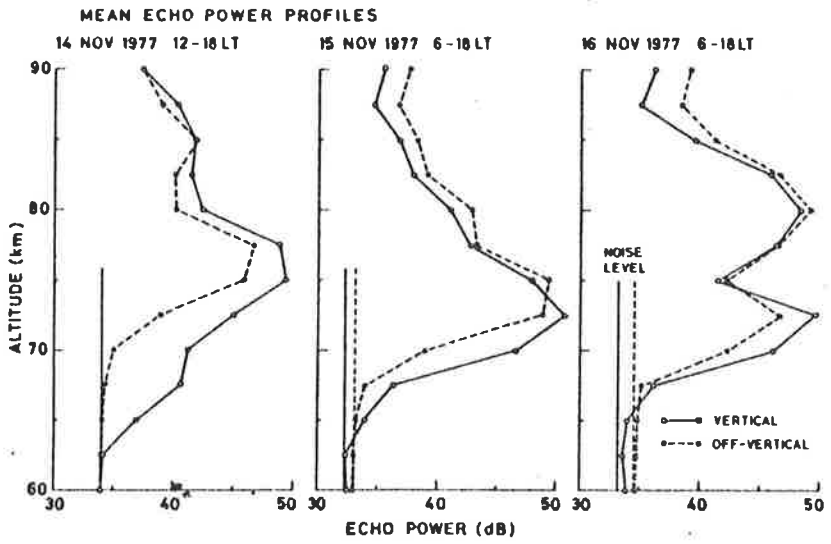

Fig. 4.24a Mean echo power vs. altitude plots for vertical and off-vertical beam directions at VHF, using the large Jicamarca array. The off-vertical beam was tilted at 3.45° from the zenith, so a shift in range (compared to 0°) of only about .13km at 70km height should be expected due to tilting the beam. (From Fukao et al., 1980).

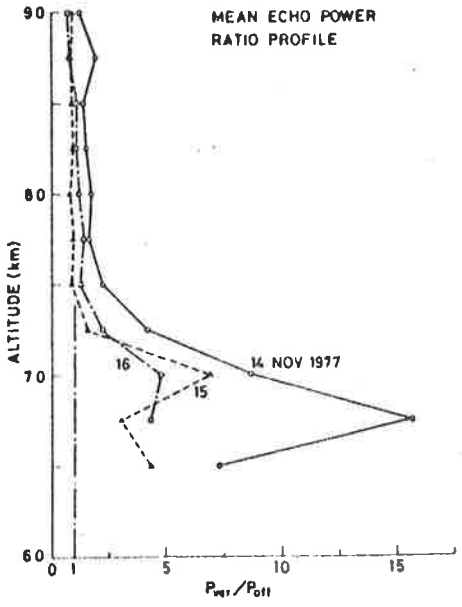

Fig. 4.24b Ratio of off-vertical to vertical powers for Fig. 4.24a. The scatterers at 65-70km on Nov. 14, 70km on Nov. 15, and 72km on Nov. 16, appear to be quite aspect-sensitive. (From Fukaeo et al., 1980).

(1980) appear to have presented the first published papers in which the aspect sensitivity of VHF signals from the mesosphere has been investigated by beam-swinging. They used the powerful Jicamarca radar. (Röttger et al. (1979) did mention some similar results breifly, but no data was presented.) Fukao et al. found that below 70-75km, scatter was quite anisotropic, with strong vertical scatter, and little at off-zenith angles. Fading times appeared to increase with increased power. Above 75km, however, scatter appeared to be fairly isotropic, and fading times decreased with increased power. This suggests turbulent scatter. Thus the region at 70-75km appears to mark a transition region, with Fresnel-like reflection below, and turbulence-produced scatter above. Figs. 4.24 shows typical results from Fukao et al. (1980). Fig. 4.24a also shows that the echo power falls off at around 80km, and the large bursts observed by Czechowsky et al. (1979) at 80-90km do not occur in this data. In fact, much of the scatter received from above 80km may well be incoherent (Thomson) scatter - Harper and Gordon (1980) have stated that non-Thomson scatter strengths approach the Thomson scatter levels at 85-90km for Jicamarca. Thus it is not possible with this data to comment on whether the 80-90km echoes observed by Czechowsky et al. (1979) show any aspect sensitivity.

A comment here may be worthwhile. In these notes, anisotropic (aspect-sensitive) scatter has been taken to imply Fresnel-like scatter. However, highly anisotropic turbulence could also cause this, as mentioned by Gage and Balsley (1980). The possibility seems intuitively unlikely, since turbulence seems hardly likely to be severely anisotropic at scales of a few metres, (and the aspect sensitive scatter is highly aspect-sensitive). But this is no concrete reason to dismiss the idea. Shear generated turbulence can be quite anisotropic (e.g., Bolgiano, 1968), although not usually to the extent of rendering 2-3m vertical scale eddies

severely anisotropic.

Another interesting point regarding VHF echoes is that the Poker Flat radar in Alaska has recently given results suggesting that the strengths of 60-70km echoes increases with increased ionospheric absorption (e.g., Balsley et al., 1980). This is consistent with HF observations by Gregory (1961) and also by Haug et al. (1977) (also see Chapter I, section 1.4.1a).

Thus investigations at VHF have clearly helped to resolve the nature of D-region ionospheric scatterers. But many questions remain. Important experiments remaining include investigations of the mesospheric atmospheric stability associated with these scatterers. Are the echoes associated with stable regions, as stratospheric and tropospheric echoes are? The role of gravity waves is also important to ascertain. Some evidence has been presented that gravity waves may be important, e.g., Figs. 4.8, 4.9; also Harper and Woodman, 1976; Van Zandt et al. (1979); and more will be given in Chapter IX. Improved height resolution to determine the exact dimensions of these echoes would be a great help. Simultaneous observations on a variety of frequencies from HF to VHF would also be useful.

Investigations into azimuthal asymmetries of the echoes may also prove fruitful. For example, Harper and Gordon (1980, Fig. 5) have discussed tropospheric evidence due to Balsley and Gage, obtained with the Chatanika radar, which shows an azimuthal dependence of aspect sensitivity. The possibility that scatter was due to parallel rolls was discussed (i.e., an asymmetry in the horizontal plane). This is something which should be investigated for mesospheric scattering, both at VHF and HF. Both isotropic turbulence, and Fresnel scatter, would produce no asymmetry.

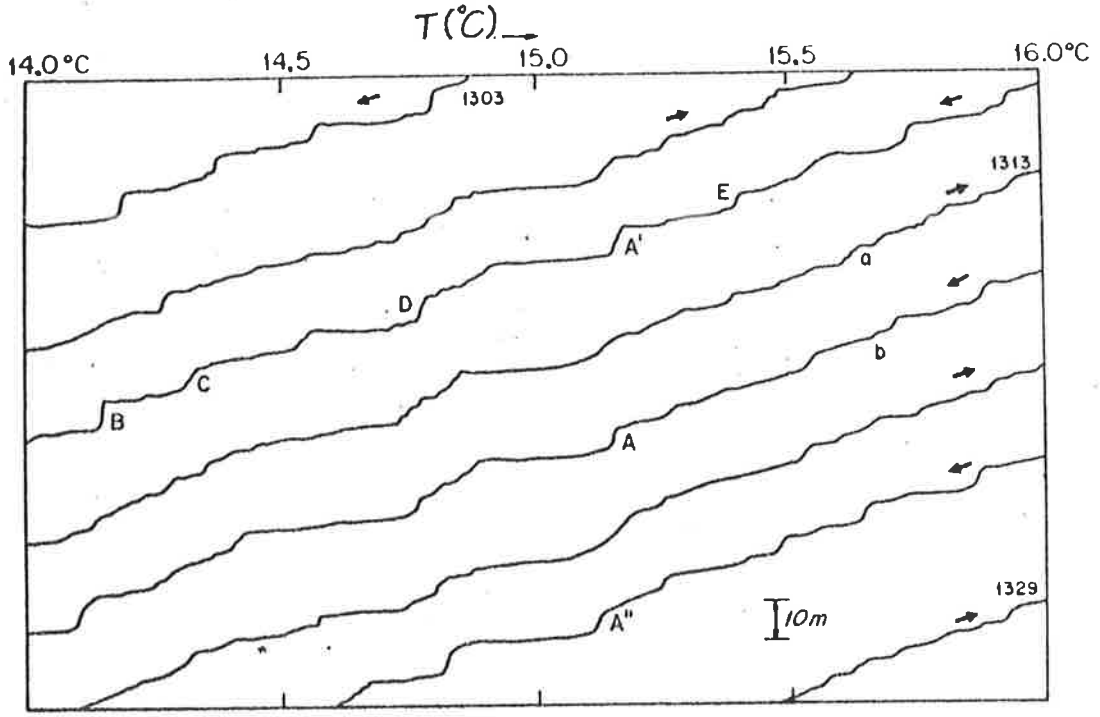

Fig. 4.25a

Several successive temperature soundings within the upper part of the main oceanic thermocline. (From Cooper and Stommel, 1968).

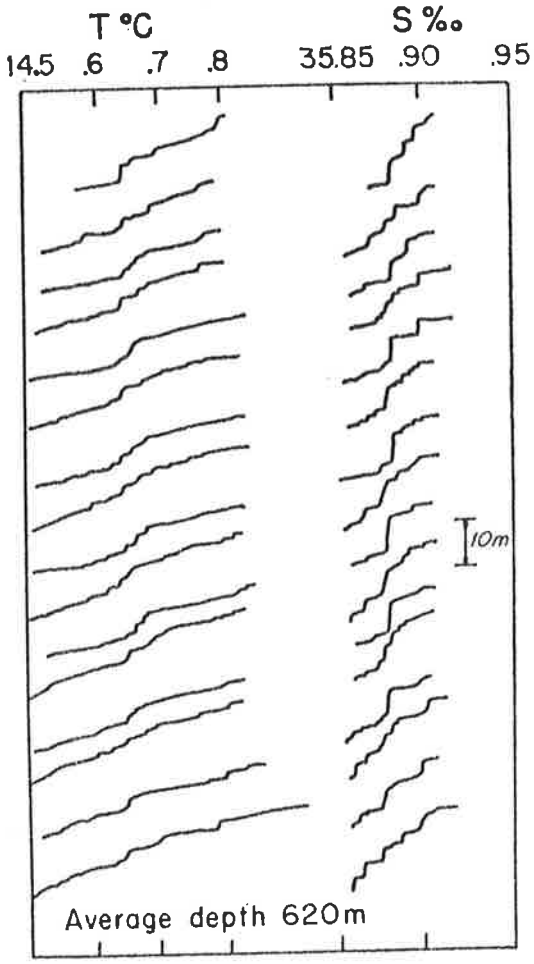

Fig. 4.25b →

Several soundings of temperature and salinity in the ocean, made in rapid succession across a single homogeneous step. (From Cooper and Stommel, 1968).

4.6 Water Body Refractive Index Profiles

Investigations of temperature and salinity height profiles in oceans and lakes over recent years have shown some highly interesting microstructure. Fig. 4.25 shows some profiles taken from a paper by Cooper and Stommel (1968). Stable steps in temperature and salinity can be seen. Later, measurements in fresh water were also made by Simpson and Woods (1970), and similar steps in temperature were found - with even finer structure than that observed by Cooper and Stommel.

The reason for these steps was unknown. Simpson and Woods gave a small review of ideas which were postulated at the time. Some authors believed the steps to be due to layers originating at separate locations meeting and interweaving. Others believed the layers would inevitably develop due to different vertical diffusion rates of heat, salt and momentum. For example, a "salt-finger" mechanism developed by Turner, Stommel and Stern relied on the difference between molecular diffusivities of salt and heat. The mechanism required a stable temperature gradient and an unstable salinity gradient, or the reverse situation. The detection of steps in temperature in a fresh water lake by Simpson and Woods (1970) implied that a mechanism other than the salt finger mechanism acted. The possibility of steps arising due to differences in turbulent diffusivities of buoyancy (density) and momentum was mentioned.

Whatever the reason for the steps, however, they do have remarkable similarities to the proposed Fresnel scatterers in the atmosphere. For example, they are narrow in vertical extent, yet extend over kilometres horizontally and can remain stable for hours (e.g., Simpson and Woods, 1970). Other observations of this microstructure have also been noted by Wunsch (1972). Of particular interest is the fact that some of this microstructure appeared associated with highly stable regions (Richardson number around 23 in one case). This, too, is consistent with observations

of "Fresnel scatterers" in the atmosphere.

If the atmospheric and oceanic structures are the same, clearer understanding of the atmospheric structures would be possible. This is because the water body structures can be simulated in laboratories, and thus are amenable to controlled experiments. For example Baker (1971) and Calman (1977) have simulated such stepped structures in laboratory experiments. Calman also discussed models for production of the steps, and feels the steps are due to a "viscous diffusive instability of geostrophic shear". This is not to say other mechanisms cannot produce steps - for example Calman mentioned (p. 278) that internal waves, breaking when they encounter a slope, give rise to steps in the density field. However, such turbulence related steps require small Richardson numbers, not large ones. Baker proposed a theory developed by McIntyre (1970a, b; also see McIntyre, 1968, for some experimental details) to explain the steps observed in his experiments. McIntyre's proposal involved a "viscous overturning instability".

Although I have not been able to fully follow all these theories, it does appear that many of the analyses involving instability analysis. (In this procedure, it is assumed a whole spectrum of wavenumbers may develop. These all grow in time, and the fastest growing scale is assumed to describe the final situation (e.g., see Verlarde and Normand (1980); also Merrill (1977) adopts a similar technique for investigations of shear-generated gravity waves.)). Almost all the theories for these steps appear to rely on differences in various diffusivities. Certainly density, heat and momentum turbulent diffusivities in the mesosphere are different, so perhaps these mechanisms could operate in the atmosphere.

CHAPTER V

AMPLITUDE DISTRIBUTIONS

5.1 Introduction

5.2 Theory

5.2.1 Rice Distributions

5.2.2 The Rice Parameter

5.2.3 Removal of Noise from the Rice Parameter

5.2.4 Fitting the Data to the Distribution

5.3 Interpretation of Experimental Amplitude Distributions

5.3.1 Non-Rician Characteristics

5.3.2 Statistical Fluctuations of the Rice Parameter

5.3.3 Procedure for Determination of Specularity

5.4 Experimental Estimates of Specular to Random Scatter Ratios

5.4.1 The Distributions

5.4.2 Rejection Criteria

5.4.3 Results

Chapter V Amplitude Distributions

5.1 Introduction

The study of amplitude distributions can make an important contribution to the understanding of scattering processes in the D-region. Unfortunately, their interpretation can be ambiguous, and there are many pitfalls to be avoided. Some brief mention of these distributions, and discussions of various papers using them, have already been presented in Chapter I, Section 1.4.1g. The topic will be discussed in three sections in this chapter - firstly, the theory, then the interpretation, and finally the results of experimental work. The first section presents no difficulty. The other two, however, are more problematical, and at times interpretations may be presented which conflict with the few papers already published on the topic (see Section 1.4.1g, Ch. I).

The following notation will also be adopted in this chapter; $\underline{x}$ will indicate a complex vector, and x will be used to represent its magnitude ($x = |\underline{x}|$).

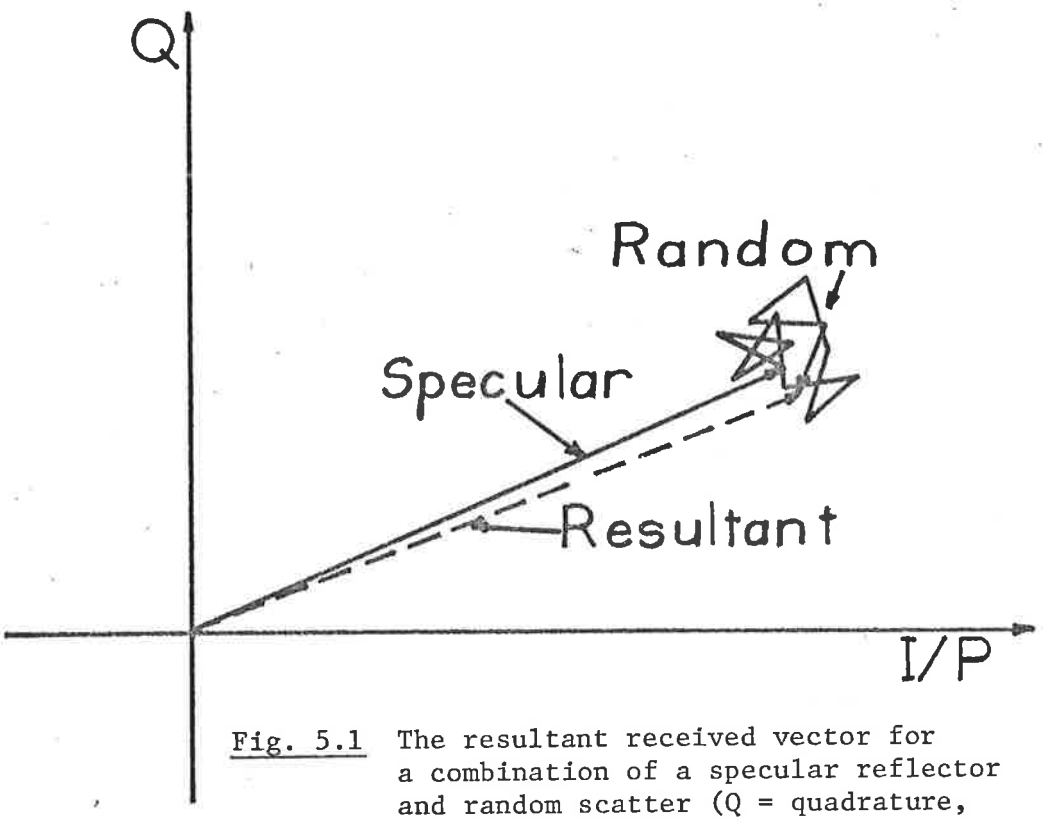

Fig. 5.1 The resultant received vector for a combination of a specular reflector and random scatter (Q = quadrature, I/P = in phase).

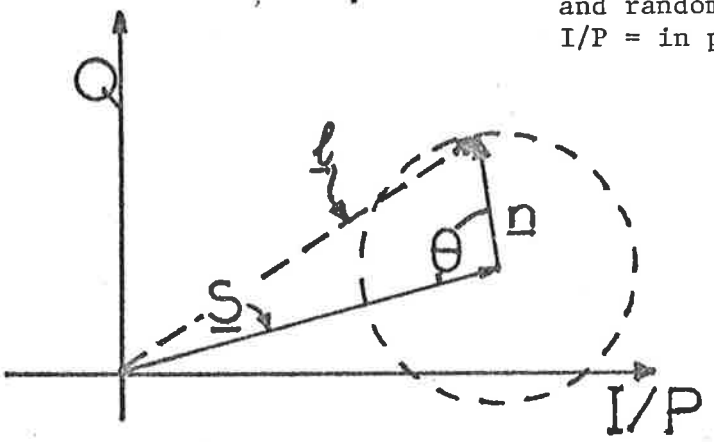

Fig. 5.2 Resultant vector $\underline{\ell}$ for vectors $\underline{S}$ and $\underline{n}$ of random phase θ.

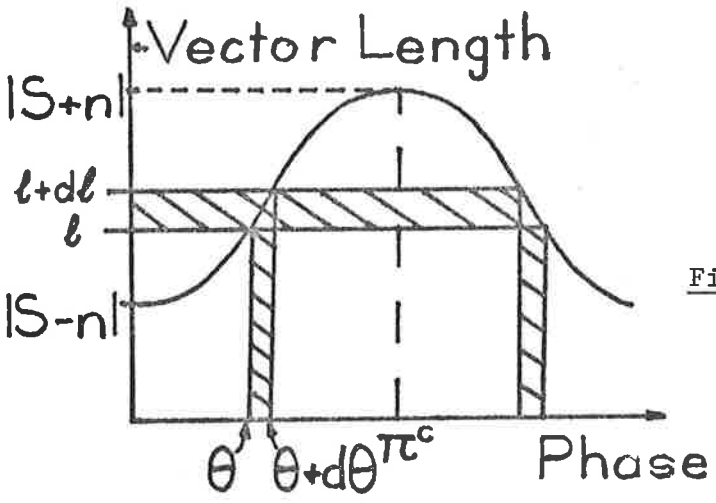

Fig. 5.3 Distribution of ℓ for Fig. 5.2. "Phase" refers to the angle θ between $\underline{S}$ and $\underline{n}$.

5.2 Theory

5.2.1 Rice Distributions

In the previous chapters, two primary mechanisms of scatter have been discussed - Fresnel scatter, and turbulent scatter. It might be expected that Fresnel scatter would give a strong, steady (specular) signal, and turbulent scatter would produce many scattered signals which would add up to a final fluctuating received signal. Fig. 5.1 represents a combination of the two processes, and shows the resultant complex vector.

This diagram represents the easiest situation to discuss and analyse, and the amplitude distribution resulting from such a combination is known as a Rice distribution (eg., Rice, 1944, 1954; Van der Ziel, 1954; Norton et al., 1955). The case in which the specular component is zero is termed a Rayleigh distribution, after Lord Rayleigh (1894). (This is the so called two dimensional random walk problem.) In the simplest case, the specular component is taken as a constant magnitude vector $\underline{S}$ (which may change phase freely), and all the random vectors (of which there must be a large number) are taken to have a constant length n say, and completely random phases distributed uniformly over the range 0^c to $2\pi^c$. In fact, a similar distribution results if this condition is relaxed somewhat, and the random vectors are allowed to have a random amplitude distribution (Norton et al., 1955), provided their RMS sum is constant.

The distributions mentioned have been derived by Rayleigh (1894) and Rice (1944, 1954), but it is instructive to re-derive them in this chapter. However, the distributions will not be derived by the approaches of the above authors, but by a different, and hopefully more unifying and instructive, approach.

We begin by considering Fig. 5.2. Two vectors $\underline{S}$ and $\underline{n}$, of randomly varying phase, add to produce a vector $\underline{\ell}$, with length $|\underline{\ell}|$. What is the probability distribution of $|\underline{\ell}|$? The assumption of random phase θ can be replaced by the assumption that all values of θ are equally likely. Thus a smoothly varying relation for the phase of $\underline{\ell}$ and $\underline{n}$ will give the same distribution.

The clearly, if $\ell = |\underline{\ell}|$, $S = |\underline{S}|$ and $n = |\underline{n}|$,

(5.2.1.1) $\ell^2 = S^2 + n^2 - 2Sn\cos\theta$,

and thus

(5.2.1.2) $\theta = \cos^{-1}\{(S^2 + n^2 - \ell^2)/2Sn\}$.

also note that

(5.2.1.3) $\overline{\ell^2} = S^2 + n^2$, as cos θ averaged over all θ is zero.

Examination of Fig. 5.3 shows that each increment $d\theta$ is associated with an increment of resultant length , $d\ell$. The probability of the phase lying in the region θ to $\theta + d\theta$ is $d\theta/2\pi$, so the probability $P_2(\ell)d\ell$ of the vector length lying in the corresponding region ℓ to $\ell + d\ell$ is $2d\theta/2\pi$ (the extra 2 arises due to symmetry implicit in Fig. 5.3 - each $d\ell$ is associated with 2 phase ranges).

Thus

$$P_2(\ell)d\ell = 2\left(\frac{d\theta}{2\pi}\right) = \frac{1}{\pi}\frac{d\cos^{-1}}{d\ell}\left(\frac{S^2+n^2-\ell^2}{2Sn}\right)d\ell$$

or

(5.2.1.4) $P_2(\ell)d\ell = \left(\frac{-\ell}{\pi Sn}\right)\{1 - \left(\frac{S^2+n^2-\ell^2}{2Sn}\right)^2\}^{-\frac{1}{2}}\, d\ell$

(Note that the probability of an ℓ value greater than ℓ_0 is equal to

$$\int_{\ell_0}^{S+n} \pi^{-1} \frac{d}{d\ell} \cos^{-1}\{(S^2+n^2-\ell^2)/2Sn\}d\ell$$

$$= \pi^{-1} \cos^{-1}\{\frac{\ell_0^2-(S^2+n^2)}{2Sn}\}$$

For S = n this gives the same result as Norton et al. (1955, equation 5).

The next step is to consider the resultant for the sum of three randomly phased vectors. For simplicity, assume each has an equal length, n. The diagram below illustrates the situation.

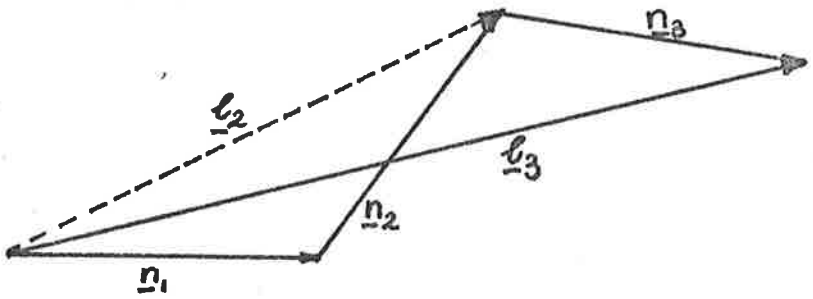

The probability distribution for ℓ_3 can be determined by means of equation 5.2.1.4. We know the distribution of ℓ_2 by 5.2.1.4.

Then the probability of a length for the resultant between ℓ_3 and $\ell_2 + d\ell_3$ is;

(5.2.1.5): $P_3(\ell_3)d\ell_3$ = probability of a length ℓ_2 to $\ell_2 + d\ell_2$ when 2 vectors of length n are added, multiplied by the probability of a length ℓ_3 to $\ell_3 + d\ell_3$ when a vector $\underline{n}$ is added to a vector $\underline{\ell}_2$, this being summed over all possible ℓ_2, (ie., from $\ell_2 = |\ell_3 - n|$ to $|\ell_3 + n|$,

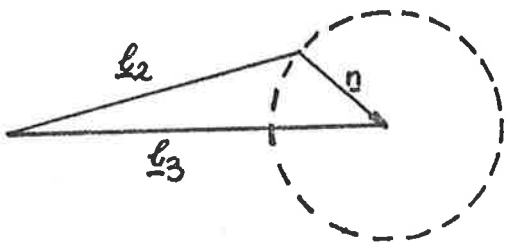

),

for any given length ℓ_3.

Thus

(5.2.1.6)

$$P_3(\ell_3)d\ell_3 = \left\{ \int_{\ell_2=|\ell_3-n|}^{\ell_2=\ell_3+n} \left[\frac{\frac{1}{n\pi}\cdot\frac{\ell_2}{n}}{\sqrt{1-\left\{\frac{2-(\frac{\ell_2}{n})^2}{2}\right\}^2}} \right] \cdot \frac{1}{\ell_2\pi} \frac{(-\frac{\ell_3}{n})}{\sqrt{1-\left(\frac{\ell_2^2+n^2-\ell_3^2}{2\ell_2 n}\right)^2}}\, d\ell_2 \right\} d\ell_3$$

by 5.2.1.5 utilizing 5.2.1.4 (firstly for the case S = n, and then S = ℓ_2). If the square root is imaginary, set it to 0. This means an impossible configuration has been assumed, eg., if ℓ_3 = 3n (3 vectors added with no phase diff.), ℓ > 2n is impossible. This comes out in the equation as an imaginary square root, and thus any imaginary square root should be set to 0, there being no probability of it occurring.

It is thus quite simple to calculate the distribution for the sum of three equal length vectors, by either analytically or numerically integrating 5.2.1.6.

In fact, the procedure may be generalized. If $P_N(\ell_N)d\ell_N$ is the probability distribution for the amplitude ℓ_N of the sum of N vectors of length n, and 5.2.1.4 is written as $P_*(S,n,\ell)d\ell$, then

(5.2.1.7)

$$P_N(\ell_N)d\ell_N = \left\{ \int_{\ell_{N-1}=|\ell_N-n|}^{\ell_{N-1}=\ell_N+n} P_{N-1}(\ell_{N-1}) \cdot P_*(\ell_{N-1},n,\ell_N)d\ell_{N-1} \right\} d\ell_N$$

where

$$(5.2.1.8)\quad P_*(S,n,\ell) = \frac{\ell}{\pi S n}\left\{1 - \left(\frac{S^2+n^2-\ell^2}{2Sn}\right)^2\right\}^{\frac{1}{2}}$$

and P_* is taken = 0 if the square root is imaginary.

Thus it is a simple matter (in principle), by successive integrations,

to build up P_3, P_4, ... etc., given $P_* \ (= P_2)$.

5.2.1.7 can be further simplified. It can be shown that

$$\{1 - (\frac{S^2+n^2-\ell^2}{2Sn})^2\} = \frac{\ell^2}{S^2}\{1 - (\frac{S^2-(\ell^2+n^2)}{2n\ell})^2\}$$

Using this in 5.2.1.8, and inserting in 5.2.1.7, and then using the change of variables

$$\cos\phi = \frac{S^2-(\ell^2+n^2)}{2n\ell} \qquad \text{changes 5.2.1.7 to}$$

$$(5.2.1.9) \quad P_N(\ell_N)d\ell_N = \frac{2\ell_N}{\pi} \int_{\phi=-\pi}^{0} \frac{P_{N-1}(\ell_{N-1})}{2\ell_{N-1}} \cdot d\phi$$

where $\ell_{N-1}^2 = 2n\ell_N\cos\phi - (\ell_N^2 + n^2)$

This is a useful formula. For example, consider the case $N \to \infty$. The P_N and P_{N-1} may be expected to have similar forms.

Try $$\frac{P_{N-1}(\ell_{N-1})}{2\ell_{N-1}} = Ke^{\frac{-\ell_{N-1}^2}{(N-1)\alpha^2}}$$

i.e. $$P_N(\ell_N) = 2\ell_N Ke^{\frac{-\ell_N^2}{N\alpha^2}}$$

The N has been placed in the exponent, as it may be expected that the width of the distribution widens as more vectors come into play. Also,

$$\int_0^N P_N(\ell_N)d\ell_N = 1.0 \text{ as } N \to \infty$$

so $$\int_0^\infty 2\ell_N Ke^{\frac{-\ell_N^2}{N\alpha^2}} d\ell_N \quad (= 2KN\alpha^2 \text{(Dwight, equation 860.12, 1961)}) = 1$$

and thus $K \to (N\alpha^2)^{-1}$ as $N \to \infty$.

Substitution of $P_N(\ell_N) = (N\alpha^2)^{-1} 2\ell_N e^{\frac{-\ell_N^2}{N\alpha^2}}$ into 3.2.1.9 (and likewise P_{N-1}) gives

$$\frac{2\ell}{N\alpha^2} e^{\frac{-\ell^2+n^2}{N\alpha^2}} = \frac{2\ell}{(N-1)\alpha^2} \cdot \frac{1}{\pi} \left[\int_{-\pi}^{0} e^{\frac{-2n\ell\cos\phi}{N\alpha^2}} d\phi \right] e^{\frac{-\ell^2+n^2}{(N-1)\alpha^2}}$$

As $N \to \infty$, this equation is consistent, showing this P_N is a solution of 5.2.1.9. In fact, $\alpha = n$, although this procedure does not show this (see Rayleigh, 1894, pp. 34-42 for the original derivation of the Rayleigh distribution, which involved differential calculus).

Thus the amplitude distribution for the resultant vector ℓ due to the sum of N vectors of length n (N being a large number) with random phases is

(5.2.1.10) $$P_R(\ell)d\ell = \frac{2\ell}{Nn^2} e^{\frac{-\ell^2}{Nn^2}}$$ (the Rayleigh distribution).

In a similar way to 5.2.1.3, it can be shown that the mean square value for ℓ is $\overline{\ell^2} = Nn^2$, so 5.2.1.10 can also be written

(5.2.1.11) $$\boxed{P_R(\ell)d\ell = \frac{2\ell}{k^2} e^{\frac{-\ell^2}{k^2}}, \quad \text{where } k^2 = \overline{\ell^2}}$$

Equation 5.2.1.7 can also be used quite simply to derive the Rice distribution for a specular vector of length S plus a set of N random vectors n, N being large. 5.2.1.7 becomes

(5.2.1.12) $$P_S(\ell)d\ell = \left\{ \int_{\ell_N=|\ell-n|}^{\ell+n} P_R(\ell_N) . P_*(\ell_N, S, \ell) d\ell_N \right\} d\ell$$

where ℓ is the total resultant vector, and ℓ_N is the resultant for the random vectors. By identical manipulations to those used in producing 5.2.1.9, the result

$$(5.2.1.13)\quad P_S(\ell)d\ell = \frac{2\ell_N}{\pi}\int_{\phi=-\pi}^{0}\frac{P_R(\ell_N)}{2\ell_N}\,d\phi \quad , \quad \ell_N^2 = 2S\ell_N\cos\phi-(\ell_N^2+S^2)$$

can readily be achieved, so that, using 5.2.1.11,

$$(5.2.1.14)\quad P_S(\ell)d\ell = \left\{\frac{2\ell}{k^2}\cdot e^{\frac{-\ell^2+S^2}{k^2}}\cdot\frac{1}{\pi}\int_0^{\pi} e^{\frac{2S\ell}{k^2}\cos\phi}\,d\phi\right\}d\ell$$

Hence

$$(5.2.1.15)\quad \boxed{P_S(\ell)d\ell = \frac{2\ell}{k}\,e^{\frac{-\ell^2+S^2}{k^2}}\cdot I_0\left(\frac{2S\ell}{k^2}\right)d\ell}$$ is the amplitude

distribution (called the Rice distribution) for Rayleigh distributed noise of mean square resultant k^2 added to a specular signal S. Here, $I_0(\xi) = \frac{1}{\pi}\int_0^{\pi} e^{\xi\cos\phi}d\phi$ is the zeroth order modified Bessel function (Abramowitz and Stegun, 1970, equation 9.6.16).

Equations 5.2.1.11 and 5.2.1.15 represent the two most common distributions dealt with in this thesis. Clearly others are possible, and many alternative assumptions can be made. For example see Beckmann (1962), for a far more generalized set of distributions. If the distribution of the in-phase and quadrature components of the contributing random vectors are Gaussian, but with different variances, a so called "Hoyt distribution" results. The case of two or more specular components of random phase added to a set of smaller random vectors with a Rayleigh

distributed resultant could also be considered. It is worth noting, however, that the addition of more than about 5 equal length vectors produces very nearly a Rayleigh distribution (eg., Vincent and Belrose, 1978).

Another important distribution is the log-normal distribution. This will be discussed later.

However, this thesis deals mainly with Rice distributions, since only two parameters, S (= $|\underline{S}|$) and k (= $|\underline{k}|$) are then necessary, and the assumptions behind their derivation are probably fairly well satisfied by D-region scatter. As will be discussed in section 5.3, a really detailed description of D-region fading may well be more complex than any of these theories can provide. It thus seemed reasonable to adopt the simple Rice distribution as a working tool, since it is simple to use, rather than opt for extra complexity without gaining very much information.

Some other statements are useful. Firstly, if two Rayleigh distributed sets of vectors are added, with mean square resultants k_1^2 and k_2^2, then the final distribution is also Rayleigh, with mean square resultant $k_1^2 + k_2^2$ (Rayleigh, 1894). Secondly, the mean square resultant of the sum of a specular component $\underline{S}$ and a set of random vectors of mean square resultant k^2 is

$$\overline{\ell^2} = S^2 + k^2 \qquad (5.2.1.16)$$

This may readily be derived in a similar manner to 5.2.1.3.

It also follows that the sum of a Rice distributed series of specular component S and RMS noise k_1, and a Rayleigh series (RMS noise = k_2) (summed <u>before</u> detection) is also Rice distributed with specular component S and RMS noise $(k_1^2 + k_2^2)^{\frac{1}{2}}$.

5.2.2 The Rice Parameter

If the same conditions as those discussed for the Rice distribution are considered, then the distribution of the in phase and quadrature components of the resultant $\underline{\ell}$ can be derived.

Let the probability of a resultant $\underline{\ell}$ lying in the area ΔA in Fig. 5.4 be $P(x,y)\Delta A$.

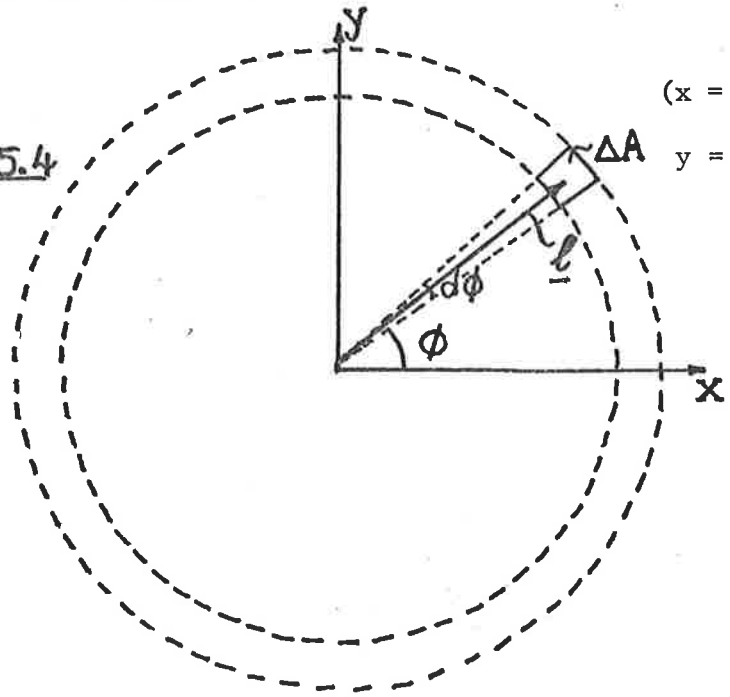

Fig 5.4

(x = in phase component
y = quadrature component)

Then

$$(5.2.2.1)\quad P(x,y)\Delta A = P_R(\ell).d\ell.\frac{d\phi}{2\pi\ell} = \frac{1}{2\pi\ell}\frac{2\ell}{k^2}e^{\frac{-\ell^2}{k^2}}d\ell d\phi = \frac{1}{\pi k^2}e^{\frac{-\ell^2}{k^2}}d\ell d\phi$$

Then the probability of the in-phase component lying between x and x + dx is

$$(5.2.2.2)\quad P_x(x)dx = \left\{\int_{y=-\infty}^{\infty}\frac{1}{\pi k^2}e^{\frac{-e^2}{k^2}}dy\right\}dx = \frac{1}{\sqrt{\pi}k}e^{\frac{-x^2}{k^2}}dx \quad (\text{using } \ell^2 = x^2 + y^2).$$

Likewise for the y component. Thus the in-phase and quadrature distributions are both Gaussian distributions with variance

$$(5.2.2.3)\qquad \sigma^2 = \left(\frac{k^2}{2}\right) .$$

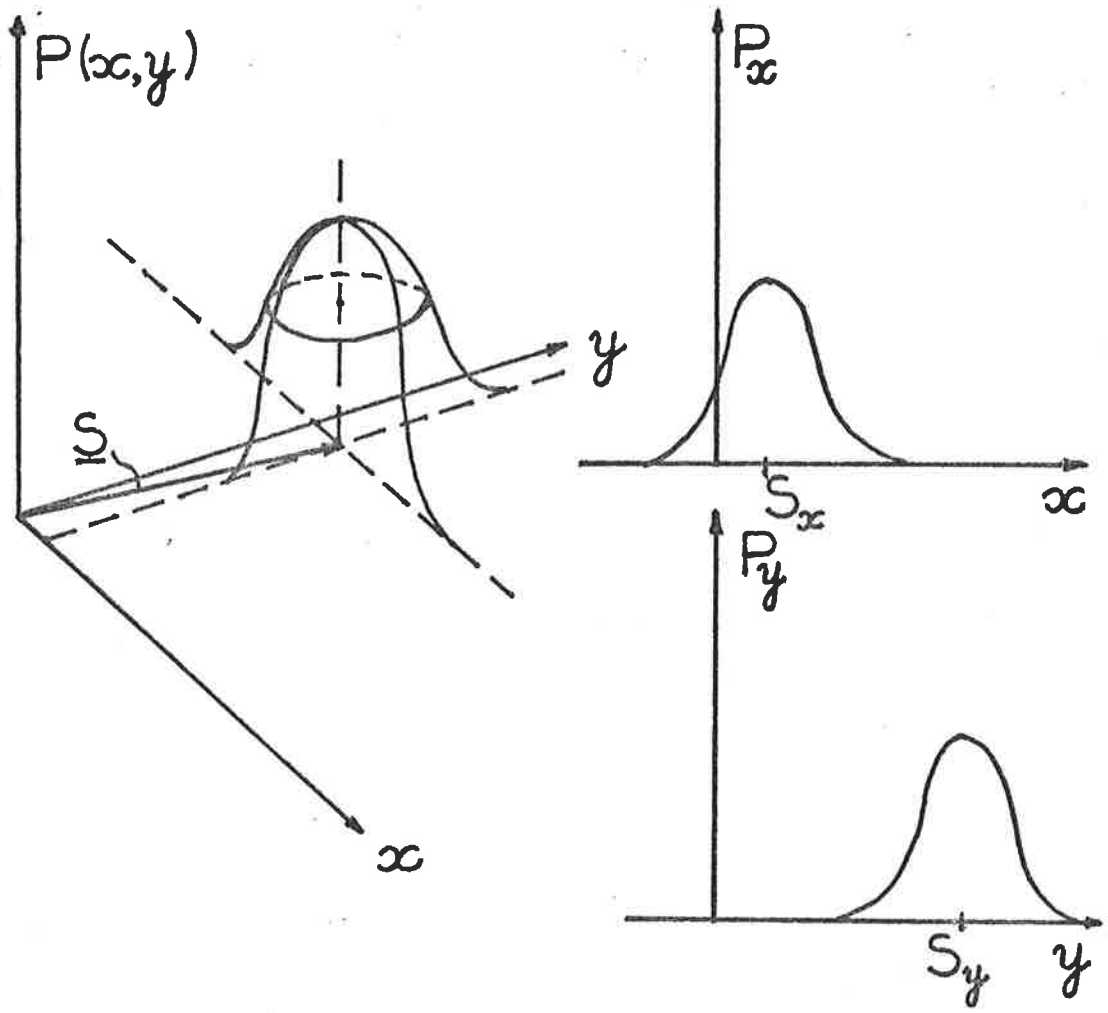

Fig. 5.5: Probability distributions P(x, y), $P_x(x)$ and $P_y(y)$ for the in-phase and quadrature distributions of a Rice-distributed signal. The vector $\underline{S} = (S_x, S_y)$ represents the specular component.

Such a distribution added to a specular component gives a probability distribution P(x, y) as illustrated in Fig. 5.5. Also shown in Fig. 5.5 are the distribution $P_x(x)dx$ = probablity that the x component lies between x and x + dx, regardless of y value, and also $P_y(y)$.

The Rice parameter is generally defined as

(5.2.2.4) $\alpha = \frac{S}{\sigma}$ $(= \frac{\sqrt{2}S}{k})$ (or sometimes as $\frac{S^2}{\sigma^2}$; in this thesis, the definition given here is used). Here, $S = |\underline{S}|$.

It is the determination of this parameter which is the basic reason for using Rice distributions in this thesis. Large values of this parameter (greater than 1.0) imply a large specular contribution to the scatter; small values imply random (possibly turbulent) scatter. If in-phase and quadrature components are available, the determination of α is simple, provided phase fluctuations of the specular component can be removed (see shortly).

If the signal is $\underline{z}(t)$, (complex), and the specular component has constant phase,

(5.2.2.5) then $\underline{S} = \langle \underline{z}(t) \rangle$, and σ is the standard deviation of each of the in-phase and quadrature components. (<> indicates mean value).

For much of the work for this thesis, only amplitude data was available, and determination of α was more difficult in that case. Towards the end of the work for the thesis, some work using complex data was done, but none will be presented. The assumption that the in phase and quadrature components have equal variances (an important result of Rayleigh theory) is not necessary when dealing with in-phase and quadrature data. (Relaxation of this assumption produces the Hoyt distribution (eg., Beckmann, 1962; Röttger, 1980a)). However, if the specular component changes phase as time progresses, the resultant mean in phase and

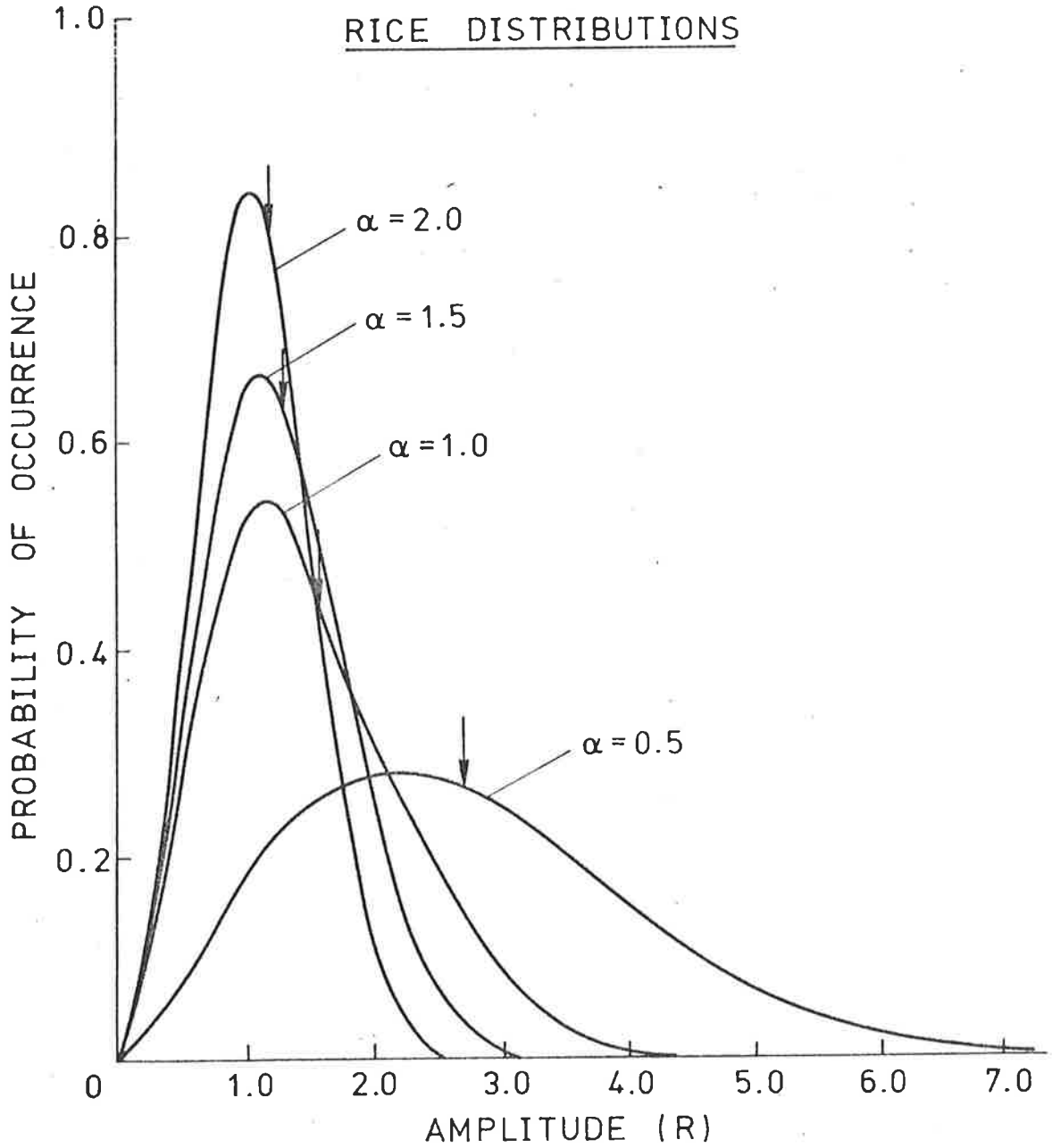

Fig. 5.6a: Rice distributions in steps of $\alpha = 0.5$ as a function of $R = \ell/S$, where S = specular amplitude, ℓ = received amplitude. These may also be regarded as the distributions for a constant specular component of 1.0, and varying degrees of scattered power ($k = \sqrt{2}/\alpha$). The arrows show the means of each distribution.

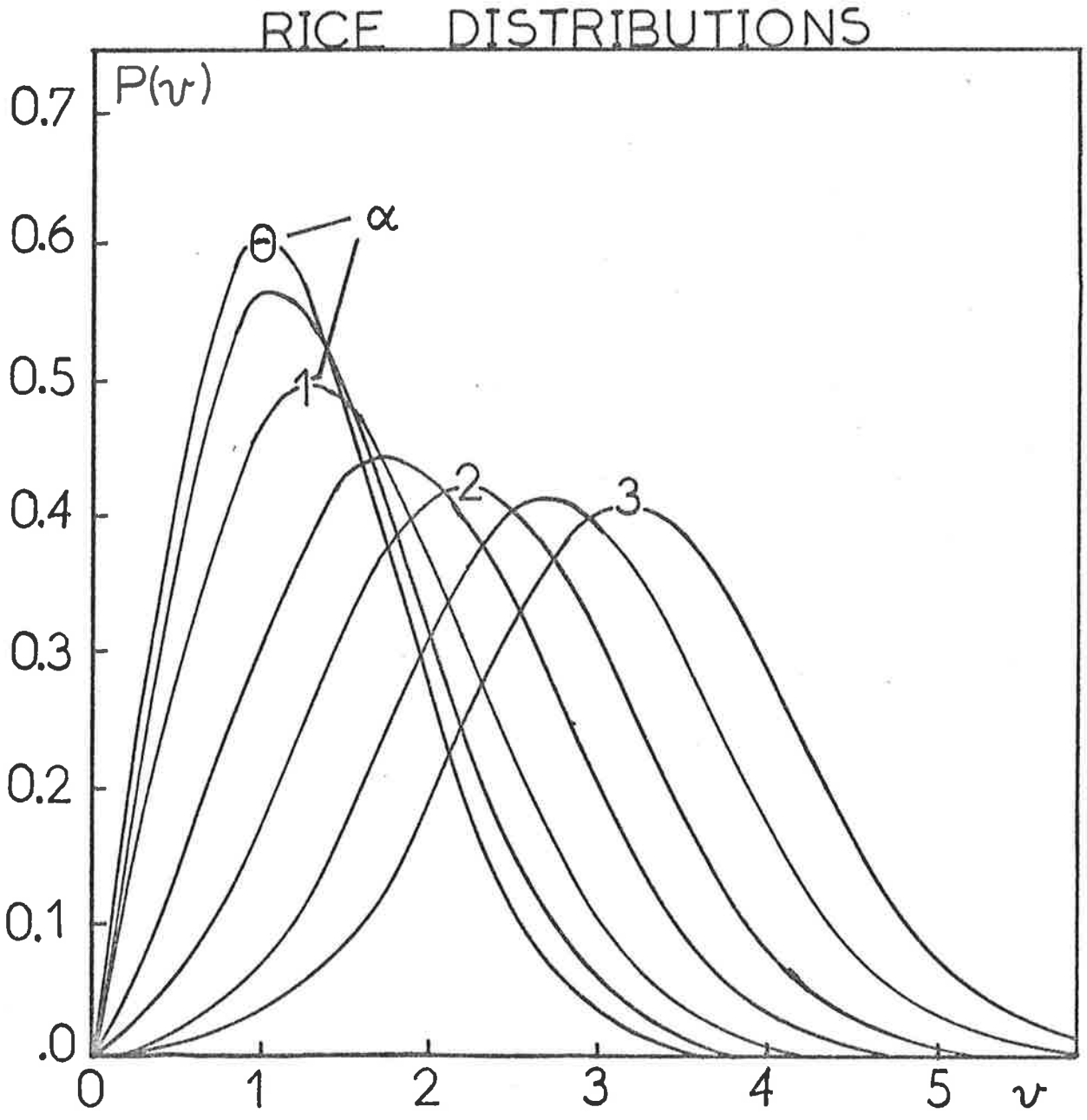

Fig. 5.6b: Rice distributions in steps of $\alpha = 0.5$ as a function of $v = \ell/\sigma = \sqrt{2}\ell/k$, where ℓ = received amplitude, k = RMS scattered power and σ = the standard deviation of both the in phase and quadrature components of the scattered signal. These may also be regarded as the distribution for a constant RMS scatter k = 1.0, and varying specular components ($S = \alpha/\sqrt{2}$).

quadrature components will NOT give the true specular component. If, however, amplitude only data is used, phase changes of the specular component will not be important provided all phases of the random components are equally likely, and estimates of the specular to random ratio will be accurate. This is perhaps the main reason why the emphasis in this thesis is on amplitude distributions.

The estimation of α by amplitude - only data can be done by fitting the data to curves like those illustrated in Fig. 5.6a, which are curves of the form

$$(5.2.2.6a) \quad P_s(r)dr = 2r\alpha^2 e^{-\frac{1}{2}\alpha^2(1+r^2)} I_o(r\alpha^2)dr,$$

where $r = \frac{z}{S}$, and $\alpha = \frac{\sqrt{2}S}{k}$ is the Rice Parameter. Here S is the specular component, and z the resultant vector. (In future, $\underline{z}(t)$ will be used to represent the received signal as a function of time; previously, $\underline{\ell}$ has been used as the resultant vector, but now we are looking at time sequences of data $\underline{z}(t)$ will be used.)

Adjusting α adjusts the shape of the curve. (For a more complete description of fitting the curves, see section 5.2.4.)

However, other methods exist to determine α, generally be utilizing the expression

$$(5.2.2.7) \quad E(z^n) = (2\sigma^2)^{n/2} \Gamma(\tfrac{n}{2} + 1) \; {}_1F_1(\tfrac{-n}{2}; 1; \tfrac{-\alpha^2}{2}).$$

where z represents the received (Rician) amplitude signal, σ^2 is the variance as defined in 5.2.2.4, Γ is the gamma function and ${}_1F_1$ is the confluent hypergeometric function (Abramowitz and Stegun, 1970, p. 556). E represents the expectation. This formula can be found in Marcum, 1960; Whalen, 1971). Then, as pointed out by P.K. Rastogi (private communication), if one calculates

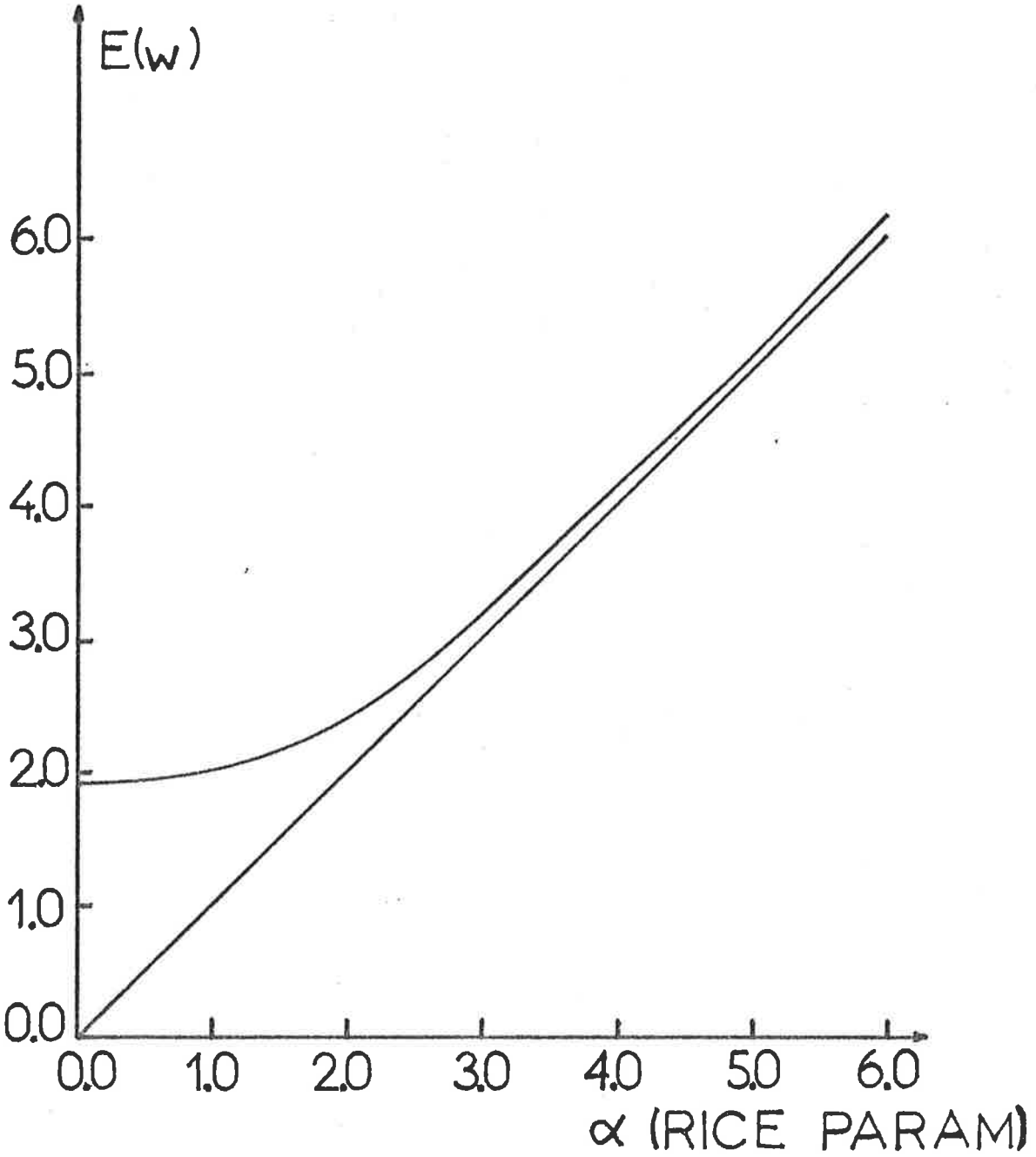

Fig. 5.7: Plot of the expected value E(w) (= $(\bar{z}/\sigma_z)$, z being the received amplitude, $\bar{z}$ the mean, and σ_z the standard deviation, $(w = z/\sigma_z)$), as a function of the Rice Parameter α, for a Rice distributed series, z(t). The line $E(w) = \alpha$ is also shown. Note E(w) is a monotonic function of α, so if nothing more, α does serve as a measure of the depth of fading (σ_z) to the mean $(\bar{z})$.

(5.2.2.8) $w = \frac{z}{\delta_z}$, δ_z being the standard deviation, then

(5.2.2.9)

$$E(w) = \frac{\sqrt{\frac{\pi}{2}}\ {}_1F_1(-\tfrac{1}{2};\ 1;\ \frac{-\alpha^2}{2})}{\sqrt{(1+\frac{\alpha^2}{2}) - \tfrac{1}{4}\pi\,[{}_1F_1(-\tfrac{1}{2};\ 1;\ \frac{-\alpha^2}{2})]^2}}$$

since $\sigma_z = \sqrt{E(z^2) - (E(z))^2}$, and $E(z^2) = 2\sigma^2(1 + \frac{\alpha^2}{2})$ (or $= S^2+2\sigma^2 = S^2+k^2$).

Then 5.2.2.9 can be readily solved by numerical means for α, if $E(w)$ has been estimated from the raw data. Fig. 5.7 shows a plot of $E(w)$ as a function of α. Notice that for $\alpha \leq 1$, very small fluctuations in the estimate for $E(w)$ can drastically affect the estimated α. Thus α values ≤ 1.0 are generally taken to imply random type scatter. I shall denote α values calculated in this way as α_{12}, as they are calculated using the first and second moments of z. (As a point of interest, $E(w)$ in the case of 2 equal vectors (see equation 5.3.1.4) = 2.068.)

However, alternative methods of estimating α exist, again using 5.2.2.7. We know

$${}_1F_1(-\tfrac{1}{2};\ 1;\ \frac{-\alpha^2}{2}) = \sum_{n=0}^{\infty} \frac{(-\tfrac{1}{2})_n (\frac{-\alpha^2}{2})^2}{(+1)_n\, n!}$$

where $(a)_n = a(a + 1) \ldots$

Then if $\alpha = \frac{\sqrt{2}S}{k}$,

(5.2.2.10) $E(z^2) = S^2 + k^2$, (also see 5.2.1.16)

(5.2.2.11) and $E(z^4) = S^4 + 4S^2k^2 + 2k^4$.

Solving gives

(5.2.2.12a) $k^2 = E(z^2) - \sqrt{2(E(z^2))^2 - E(z^4)}$

so

(5.2.2.12b) $\alpha = \frac{\sqrt{2}S}{k} = \frac{\sqrt{2}\sqrt{E(z^2) - k^2}}{k}$, where k is calculated by 5.2.2.12a.

Rice parameters calculated in this way (ie., using the second and fourth moments) will be denoted α_{24}.

There are an infinite number of ways to estimate α - all that are necessary are 2 moments $E(z^n)$ and $E(z^m)$, and equations can be solved to get α from these moments. If the distribution is genuinely Rician, all estimates of α should be identical.

Generally in the work for this thesis, α was calculated by both of the above methods, (α_{12} and α_{24}) although α_{12} was used more commonly. However, a χ^2 goodness-of-fit test was also used to ensure that the distribution was reasonably Rician (see later). If the fit was good, α_{12} and α_{24} agreed moderately well.

5.2.3 Removal of Noise from the Rice Parameter

In any ionospheric experiment, there are usually two types of random signal apart from any specular signal S - a scattered random component, and an external noise component. If the mean square scattered signal is k^2_{scat}, and the external noise k^2_{ext}, then the total received scattered component is Rice distributed but the random contribution to the mean power is $k^2 = k^2_{scat} + k^2_{ext}$ (see previously) (assuming the external noise is Rayleigh distributed). The parameter we seek is

$$\alpha_{true} = \frac{\sqrt{2}S}{k_{scat}}\ ;\ \text{we in fact calculate } \alpha_{tot} = \frac{\sqrt{2}S}{\sqrt{k^2_{scat}+k^2_{ext}}} = \frac{\sqrt{2}S}{k}$$

Assume k^2_{ext} can be measured (eg., by switching the transmitter off). Then

(5.2.3.1) $$\alpha_{tot}/\alpha_{true} = k_{scat}/k = \sqrt{k^2 - k^2_{ext}}/k.$$

But $k = \sqrt{2}S/\alpha_{tot} = \sqrt{2}(\sqrt{E(z^2) - k^2})/\alpha_{tot}$, since $E(z^2) = S^2 + k^2$ by 5.2.2.10.

Solving this gives

$$k^2 = 2E(z^2)/(\alpha^2_{tot} + 2), \text{ so}$$

$$\alpha_{true} = \alpha_{tot}\, k/k_{scat} \text{ (by 5.2.2.13)} = \alpha_{tot}\sqrt{1 - k^2_{ext}/k^2}$$

(since $k^2_{scat} = k^2 - k^2_{ext}$).

Thus α_{true} can be estimated from α_{tot}, given k_{ext} and $E(z^2)$, as

(5.2.3.2) $$\alpha_{true} = \alpha_{tot}/\sqrt{1 - \frac{k^2_{ext}}{k^2}}$$

(5.2.3.3) where $k^2 = 2E(z^2)/(\alpha^2_{tot} + 2)$

This formula allows the Rice parameter to be estimated from a noisy signal. In this thesis, this quantity was at times estimated, but generally only signals with a good signal to noise ratio were used, thus eliminating the need for this expression.

It is believed that the work in this section 5.2.3 is original.

5.2.4 Fitting the Data to the Distributions

It was mentioned previously that given an amplitude distribution, various α values can be tried to achieve a good fit. However, before this can be done, either S (the specular component) or k^2 (random component mean square value) must also be known. (This is to effectively "normalize" the amplitude axis. If the standard deviation of the random component alone could be obtained, this would be sufficient, since graphs like 5.6b could be fitted. This is not usually possible however.) In this thesis, the formula

(5.2.4.1) $$S^2 = E(z^2)/(1 + 2\alpha^{-2})$$

was used. ($E(z^2)$ and α are for either the signal plus external noise, or for just the signal - provided the same data is used for each. Generally the total signal plus external noise must be used.)

This formula follows because

(5.2.4.2) $E(z^2) = S^2 + k^2$, so that $S^2 = E(z^2) - k^2$.

But $\alpha = \sqrt{2}\ S/k$, so $k = \sqrt{2}\ S/\alpha$.

Substitution in 5.2.4.2 shows

$$S^2 = E(z^2) - 2S^2/\alpha^2,$$

so that $$S^2 = E(z^2)/(1 - 2/\alpha^2).$$

Then, given α and S, k could be calculated as $k = \sqrt{2}\ S/\alpha$.

Thus, given a set of data, $E(z^2)$ could be found, α could be estimated (α_{12} or α_{24}), and the number of data points could be noted. Then S and k could be obtained, as described above, and thus the expected distribution derived by substitution in equation 5.2.1.15. A χ^2 test could then be applied. If better accuracy were required for α, then this parameter could be varied, S and k re-calculated, the distribution of equation 5.2.1.15 reformed, and a new χ^2 test performed.

Then α could be adjusted to minimize χ^2. This was not usually done in practice, since α_{12} and α_{24} usually provided sufficient accuracy.

Fig. 5.8 shows the computer program used to calculate the theoretical distribution expected for the calculated $E(z^2)$ and α values. This theoretical distribution could then be compared with the experimental one, and a χ^2 goodness of fit applied. Examples will be seen shortly.

```
      FUNCTION FCR(RICET,KOUNT,SPEC,XMID,XINT,SUMSQ)
    CALCULATES NO OF PTS IN XMID  S INTERVAL FOR TRUE RICE DISTRIBUTOON
   IF  SPEC SMALL(OR APPROX EQUIV,RICET LT 0.1,SAY),CANT DIVIDE BY SPEC
      IF(RICET.GT.0.1)GO TO 47
   RICET=0 MEANS MEAN SQUARE NOISE=POWER=SUMSQ
      F1=2.0*XMID/SUMSQ
      F2=EXP(-1.0*(XMID*XMID/SUMSQ))
      F3=1.0
      FCR=F1*F2*F3*FLOAT(KOUNT)*XINT
      RETURN
 7    CONTINUE
      FC1=XMID*(RICET*RICET)/(SPEC*SPEC)
      FC2=EXP(-0.5*(RICET*RICET)*(1.0+XMID*XMID/(SPEC*SPEC)))
   IO(X)--SEE ABRAMOWITZ AND SEGUN SECTION 9.8.1
      T=(XMID*RICET*RICET/SPEC)/3.75
   DIFF EXPANSIONS FOR T.GT.1 AND T.LT.1 (9.8.2 IN ABRAMOWITZ AND STEGUN)
      IF(T.GT.1.0)GO TO 48
      FC3=1.0+3.5156229*T*T+3.0899424*T**4.0+1.2067492*T**6.0+
     $ .2659732*T**8.0+.0360768*T**10.0+0.0045813*T**12.0
      GO TO 49
 8    X=T*3.75
      FC3=1.0/ SQRT(X)*EXP(X)*(.39894228+.01328592/T+.00225319/(T**2.0)
     $-.00157565/(T**3.0)+.00916281/(T**4.0)-.02057706/(T**5.0)
     $+.02635537/(T**6.0)-.01647633/(T**7.0)+.00392377/(T**8.0)   )
 9    CONTINUE
      FCR=FC1*FC2*FC3*FLOAT(KOUNT)*XINT
      RETURN $ END
```

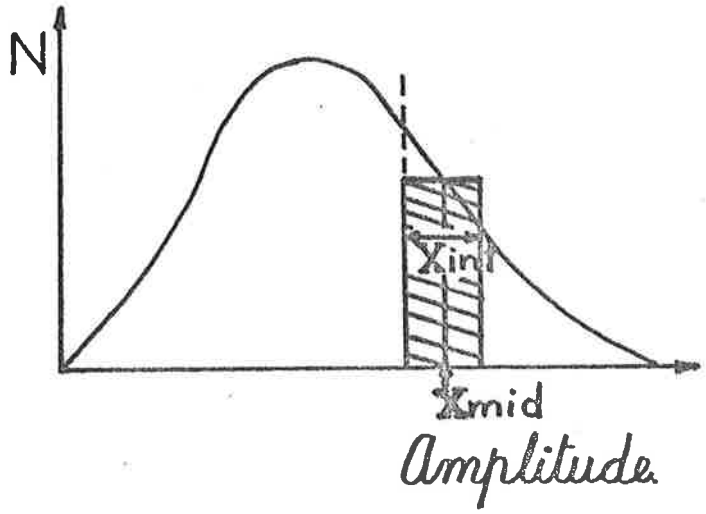

Fig. 5.8: Fortram computer function used to estimate number of points expected for a Rice distribution in the interval of width XINT centred on XMID, given the total number of points KOUNT, the Rice parameter RICET, the specular component SPEC (calculated by equation 5.2.4.1), and the mean square value of the data, $E(z^2)$ = SUMSQ.

In this function, the random component of the signal is referred to as "noise", although bear in mind that it is not really unwanted noise in the true sense. The program calculates the formula 5.2.1.15 with $k = \sqrt{2}\ S/\alpha$. A very simple rectangular form of integration is used - the shaded area is assigned to the point X_{mid}. A more accurate integration was felt not to be warranted for the simple purposes for which the function was written.

5.3 Interpretation of Experimental Amplitude Distributions

5.3.1 Non Rician Characteristics

A review of experimental results from Rice-fitting was given in Chapter I, Section 1.4.1g.

One of the major problems in studying amplitude distributions is to determine how often the data should be sampled, and what data lengths are necessary. Von Biel (1971) used 10 points per minute to ensure that each point was statistically independent, and data lengths of the order of 10 minutes, to ensure a reasonable number of points. This immediately presents a problem. It has already been seen that strong bursts of power can grow and die within 2 or 3 minutes, particularly at heights below 80km. Clearly, as mentioned in section 1.4.1g, a 10 minute sample of data will not have the temporal statistical stationarity necessary for Rice theory to be applied in such a case. A 10 minute sample could even contain two or three independent bursts, interspersed with long periods of weak signal. In such a case, a non-Rician form of distribution could conceivably occur, with a sharp rise to a maximum (due to the presence of a lot of weak signal between bursts), and then a long tail. In such a case, the distribution may be expected to be perhaps more like a log-normal distribution (the log-normal distribution is defined shortly). (If a distribution is formed from observations of a process which is a function of many independent variables, it seems that a log-normal distribution can be expected (eg., Foldes, 1960). A distribution of amplitudes formed from several short (independent) bursts imposed on a weaker signal could perhaps be regarded as such a process. Certainly a distribution with a large probability of small amplitudes could be expected, and this would look more log-normal than Rayleigh.)

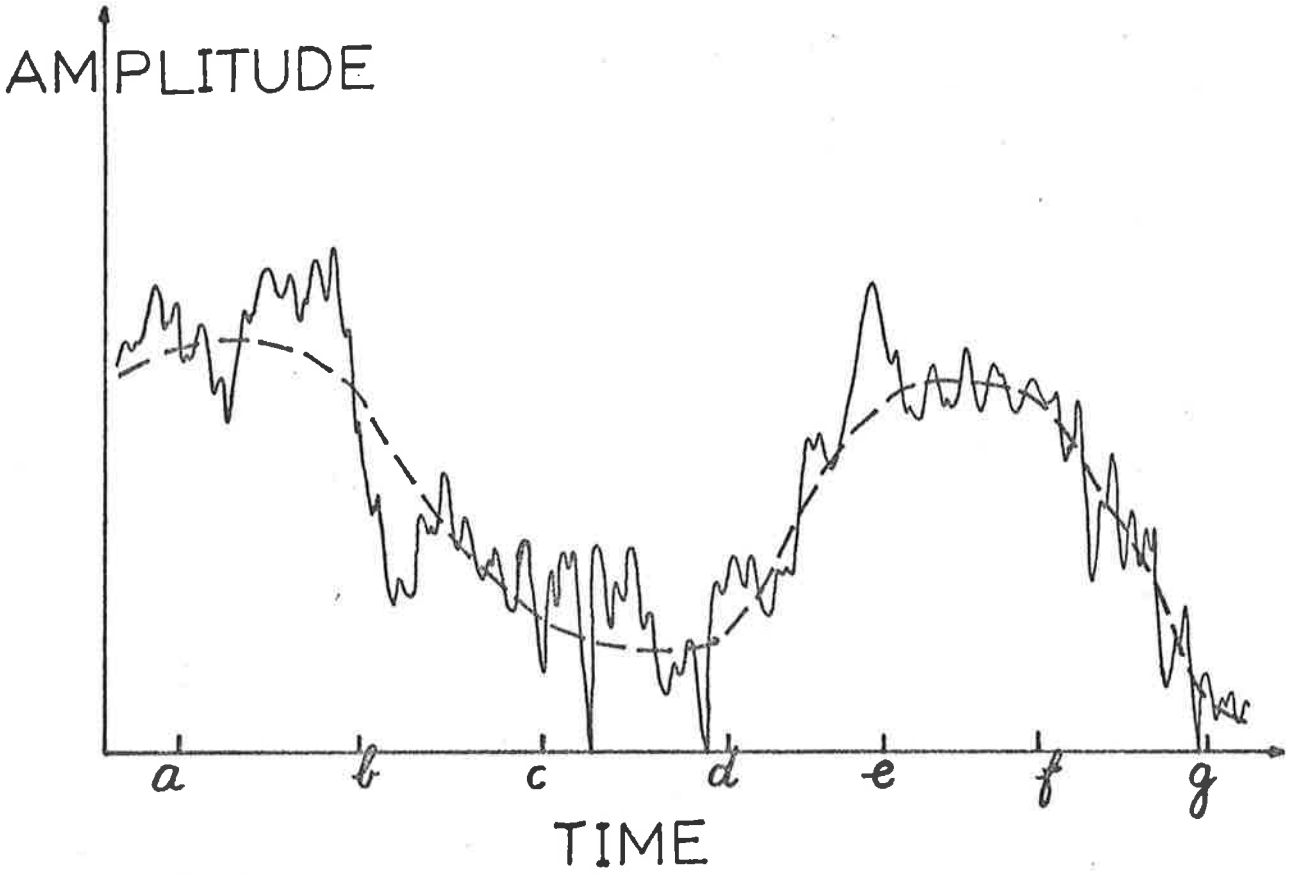

Fig. 5.9: Typical amplitude fluctuations due to random scatter superimposed on a slowly vary specular component.

However, the basic form may look crudely Rician, and may be accepted into a Rice analysis. If each burst was sufficiently different in scattered power, a multiple peak distribution may result, but such distributions should be rejected before any analysis is applied. Even at heights greater than 80km, statistical stationarity in time is doubtful.

Another problem exists, too. The definition of "specular" signal depends somewhat on the length of data used. It could be imagined that if scatter were caused in part by Fresnel scatter from a gently undulating surface, scatter as shown in Figs. 3.5, Chapter III, may occur (focussing etc.). Clearly the "specular component" of the signal may also vary in time, complicating the matter further. The amplitude fluctuations may appear like those in Fig. 5.9. Clearly if the interval $\overline{ab}$ were used for analysis, a high specular to random ratio would result, yet in the period $\overline{cd}$, a low ratio would occur. If the full period a to g were used, a quite low ratio may result. The definition of what is meant by "specular" scatter depends to some extent on the length of data used!

The distribution in this case would be non-Rician but would generally be sufficiently similar in form to be accepted by most Rice tests (eg., χ^2_7 test at the 5% level).

It is thus clear that many non-Rician processes will contribute to the amplitude distributions. In the case described in Fig. 5.9, it is possible to derive the true distribution. Let the "specular component" as a function of time be $S(t)$, and assume its amplitude distribution is $G_1(S)$. Let the random component have RMS value k, a constant. Let the in phase and quadrature standard deviation of this random component be $\sigma = k/\sqrt{2}$. Then at any time the Rice parameter is

$$(5.3.1.1) \qquad \alpha(t) = \frac{S(t)}{\sigma}$$

Let the distribution of α values be $G_2(\alpha)$.

Then $G_2(\alpha)d\alpha = G_1(S)dS$

$$(5.3.1.2) \qquad G_2(\alpha) = G_1(S)\frac{dS}{d\alpha} = \sigma G_1(S) = \sigma G_1(\alpha\sigma).$$

Then if we class the received amplitude z(t) into groups of constant S, (and therefore constant α), we get a Rice distribution for each one, something like the illustration below.

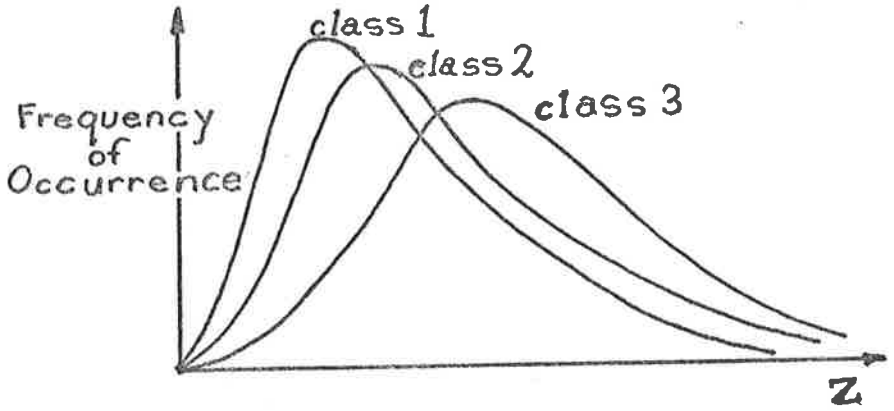

The final distribution is the sum of all these curves, ie., F(z) say.

Thus

$$(5.3.1.3) \qquad F(z)dz = \left\{\int_{\alpha=0}^{\infty} G_2(\alpha)R_\alpha(z)d\alpha\right\}dz = \left\{\sigma\int_{\alpha=0}^{\infty} G_1(\alpha\sigma)R_\alpha(z)d\alpha\right\}dz$$

where

$R_\alpha(z)$ is the Rice distribution for parameter α.

Other interesting non-Rician cases should be considered, too. For example, imagine the case of two equal strength specular scatterers, and no random scatter. Imagine the specular scatterers vary in phase, either regularly (to produce a beating envelope) or randomly. In either case, the amplitude distribution $P(\ell)$ will be given by equation 5.2.1.4,

(a)

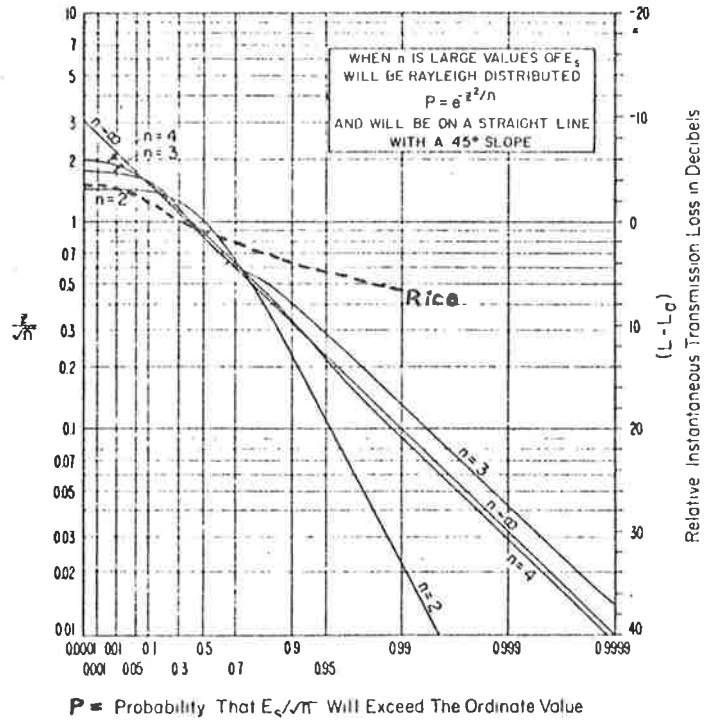

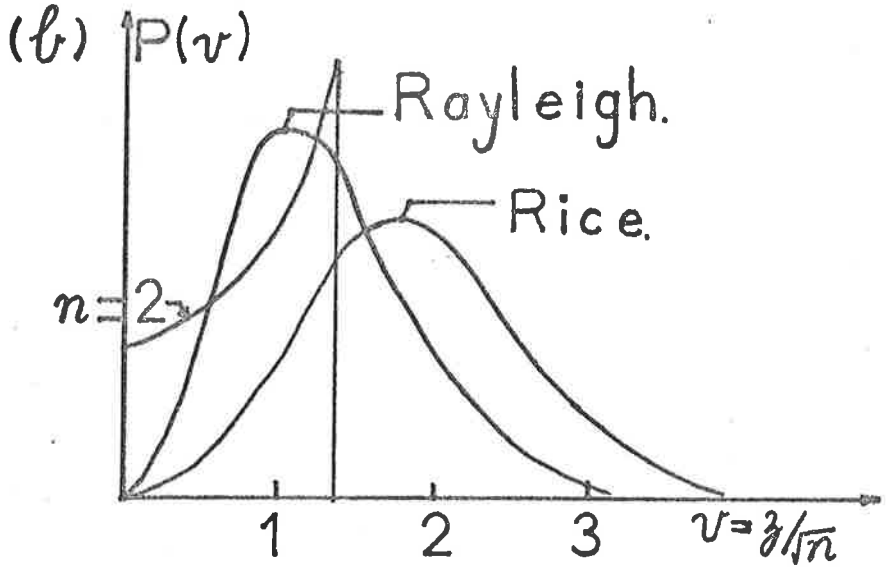

Fig. 5.10: (a) Cumulative probability distributions for a Rayleigh distribution, a typical Rice distribution, and the distributions for the sum of n equal length (unit length) vectors, for n = 2, 3, 4, plotted on Rayleigh paper. (from Norton et al., 1955). In the Rayleigh and Rice cases, $n = \sigma^2$, the variance of the in phase and quadrature components of the random contribution to the signal.

(b) Illustrative diagram of the probability distribution functions of some of the situations in (a). For $n \to \infty$, $\sqrt{n} = \sigma$ for the Rayleigh case. Note that the function P in (b) is not the same as that in (a), since P in (a) is a cumulative distribution.

(a)

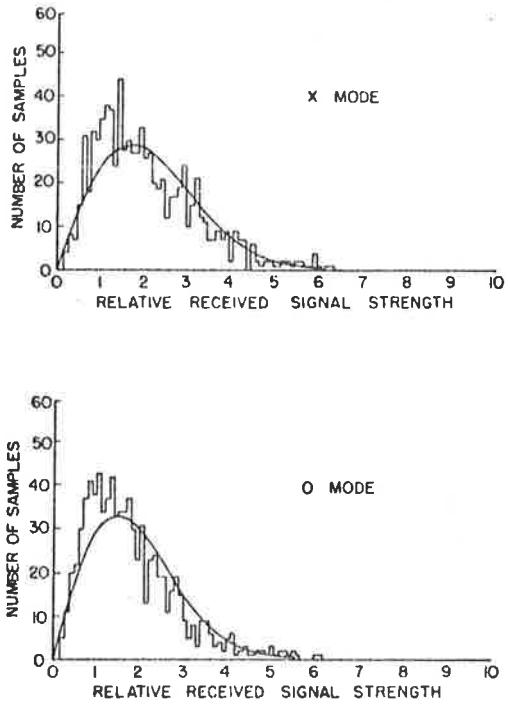

(b)

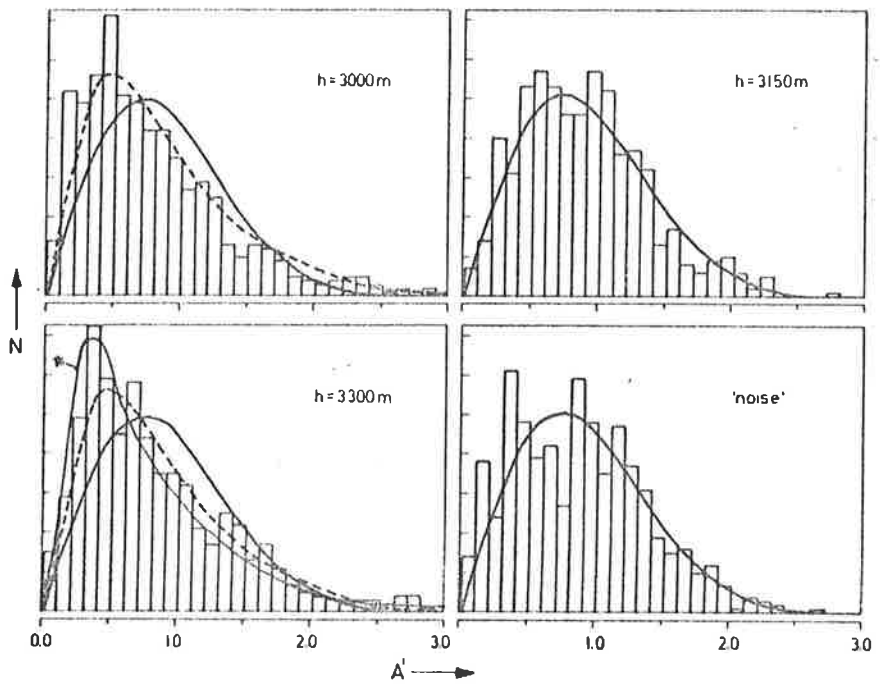

Fig. 5.11: (a) Amplitude histograms of data taken at 1055-1125 EST, January 26, 1974, at State College, Pennsylvania, for a height of 85km at 4.5MHz. (From Newman and Ferraro, (1976)). The solid lines are Rayleigh distributions.

(b) Normalized amplitude distributions ($A' = A/\langle A^2 \rangle^{\frac{1}{2}}$) for VHF scattered radiation from the troposphere. The dark solid lines are Rayleigh distributions, and the broken lines are Hoyt distributions for a ratio of standard deviations of in-phase and quadrature components of about 5-10 (From Rottger, 1980a). The faint solid line in the bottom left hand corner is a log-normal distribution fitted to the data.

with S = n; ie

$$(5.3.1.4) \qquad P(\ell)d\ell = \frac{-\ell}{\pi n^2}\left(1 - \frac{2n^2-\ell^2}{2n^2}\right)^2)^{-\frac{1}{2}}d\ell \ ,$$

where ℓ is the resultant length, and n the scattered amplitude due to one scatterer. This distribution has a mean value of $\frac{4}{\pi}n = 1.27n$, a mean square of $2n^2$, and a variance $\sigma^2 = (2-\frac{16}{\pi^2})n^2 = .3789n^2$. (If the scatterers had different amplitudes, the distribution is even more complex (see 5.2.1.4).) What does the distribution look like in this case? Figs. 5.10a and b give an indication of this. The value on the lower axis for a given ordinate value in Fig. 5.10a is equal to the area to the right of this value in 5.10b. It can be seen the n = 2 case gives a clearly non-Rician distribution. This should be rejected in any Rice tests. Vincent and Belrose (1978) examine amplitude distributions and compared them to the expected distributions for 2 and 3 equal strength scatterers. They found that a significant number of distributions had these forms (about 15-20%).

Fig. 5.11a shows a distribution from Newman and Ferraro (1976). It seems fair to say that the second diagram in this figure - and possibly both - are not really Rayleigh, but rise somewhat more steeply. Newman and Ferraro accepted these as Rayleigh.

Another interesting distribution is the Hoyt distribution. If the scattering points in the ionosphere are distributed in such a way that the rms deviation of the path lengths to these points is less than one wavelength, the Hoyt distribution results. Such a case exists when scatter from a rough Fresnel reflector occurs, with undulations less than a wavelength in height (Röttger, 1980a). The variances of the in-phase and quadrature components need no longer be equal (Beckmann, 1962; Röttger, 1980a). (In this case, not all phase distributions of all the vectors occur. The assumption that all phase distributions do occur

was an important criterion assumed in deriving the Rice distributions.)

Fig. 5.11b shows an interesting example of an amplitude distribution formed from 26 minutes of data (from Röttger, 1980a). The data was actually taken using a VHF radar, and is for clear air scatter in the troposphere. However, it is quite relevant for illustrative purposes. A Hoyt distribution has been plotted, and it is clear it peaks before the Rayleigh case. (Also see Beckmann, (1962, Fig. 5)). Also shown on the same figure is a log-normal fit (this curve does not appear in the figure presented in Rottger's original paper (1980a)). This, too, is a much better fit than a Rayleigh distribution. Whether the log-normal or the Hoyt distribution is the better fit is debatable. The log-normal distribution has not been optimized to produce the least χ^2 value, either. Rather,

$\mu = \langle \ln(A') \rangle$, $\sigma^2 = \langle \ln(A')^2 \rangle - \langle \ln(A') \rangle^2$ has been used.

[The log-normal probability distribution function is given by

$$g(x) = (\sigma\sqrt{2\pi})^{-1} x^{-1} \exp\{-(\ln x - \mu)^2 / 2\sigma^2\}$$

(eg., see Hogg and Tanis, 1977, p. 345)]

However, the important point is that the data is clearly non-Rician - yet the best fit Rice curve would have a Rice parameter of zero, and hence would suggest a random type of scatter. Yet the process described by Röttger (1980) (diffuse scatter) to explain his proposed Hoyt distribution is certainly not random scatter. Nor does the assumption of a log-normal distribution necessarily imply random scatter. Yet both of these distributions would provide better fits to the data of Fig. 5.11a than a Rayleigh distribution.

(5.3.1.5) Clearly, then, if Rice parameters are the only values calculated, highly specular reflection mechanisms exist which in fact would result in a Rice parameter of zero, thus leading to erroneous conclusions.

5.3.2 Statistical Fluctuation of the Rice Parameters

Even with a purely Rayleigh data sample, estimations of the Rice parameter will not always give a zero value. Statistical fluctuations will occur and it is important to know what effect these will have.

To examine this the following numerical simulation of a Rayleigh distributed signal of the sort which might be received in a D-region scatter experiment was undertaken. A Gaussian power spectrum centered on 0Hz, of half power half width $n_{\frac{1}{2}}$ was generated. Random phases were associated with each frequency, and the square root of the power at each frequency was found. Then this function was Fourier transformed to produce a complex time series. This thus simulated the in phase and quadrature components received in a scatter experiment. Frequencies of the power spectrum were chosen so that the data series had points every 0.8 seconds, and the total data length varied between 50 and 100 minutes. These time series were then broken up into blocks of length T, and Rice parameters estimated for each block, by formulae 5.2.2.9 (α_{12}) and 5.2.2.12 (α_{24}). Results were quite similar in each case, so only α_{12} will be discussed.

Although it is usual to use statistically independent points in forming these parameters (ie., points separated by greater than about $4\tau_{\frac{1}{2}}$, where $\tau_{\frac{1}{2}}$ is the time lag for the autocorrelation to fall to 0.5 ($\tau_{\frac{1}{2}} = \frac{\ln 2}{\pi}.n_{\frac{1}{2}}^{-1} = \frac{.22}{n_{\frac{1}{2}}}$), this was not done in this case. This is because using all the points does not appear to drastically alter the amplitude distribution (see later). Knowledge of the number of statistically independent points is necessary to determine the error of the Rice parameter, however. The approach adopted in this section will use the ratio $T/\tau_{\frac{1}{2}}$ to determine the range of α values expected (and hence the error implicit in any single measurement), so direct knowledge of the

Fig. 5.12a: Probability distributions of Rice parameters α (calculated by equation 5.2.2.9 ie α_{12}) for various data lengths (T) expressed as a multiple of $\tau_{\frac{1}{2}}$ (see the top right hand corner) for a Rayleigh distributed data series. Each data block contained at least 20 points, and up to 750 points in some cases. Data was effectively collected at 2.5Hz. N refers to the number of data blocks used in each distribution. The error bars were calculated as $\sqrt{n}$, n being the number of points in each column. Notice that the columns to the right of $\alpha = 3$ refer to all α values > 3.0.

The mean α values have been estimated assuming each column has the midpoint value, except for the (0-0.5) column, where a value 0.0 has been assumed. This is because most values in this column are generally 0.0. If a value 0.25 is assumed, about 0.1 must be added to α.

The minima at α = 0.5-1.0 arise because α is clearly very sensitive to $\bar{z}/\sigma_z$ (= E(w)) in this range (see Fig. 5.7), and small statistical fluctuations result in an α outside this range. All values of E(w) less than 1.913 are assigned a value $\alpha = 0.0$, so there are many $\alpha = 0$ values. Notice as the data length increases, the distribution has more low α values. However, even for quite large data lengths (eg., if $\tau_{\frac{1}{2}} = 3s$, the data length is 10 mins. for $T = 200\tau_{\frac{1}{2}}$), a significant number of α values up to 1.5 occur, even though the distribution is Rayleigh-distributed. Even for $T = 600\tau_{\frac{1}{2}}$, α values as large as 1.5 can occur (see 5.12b).

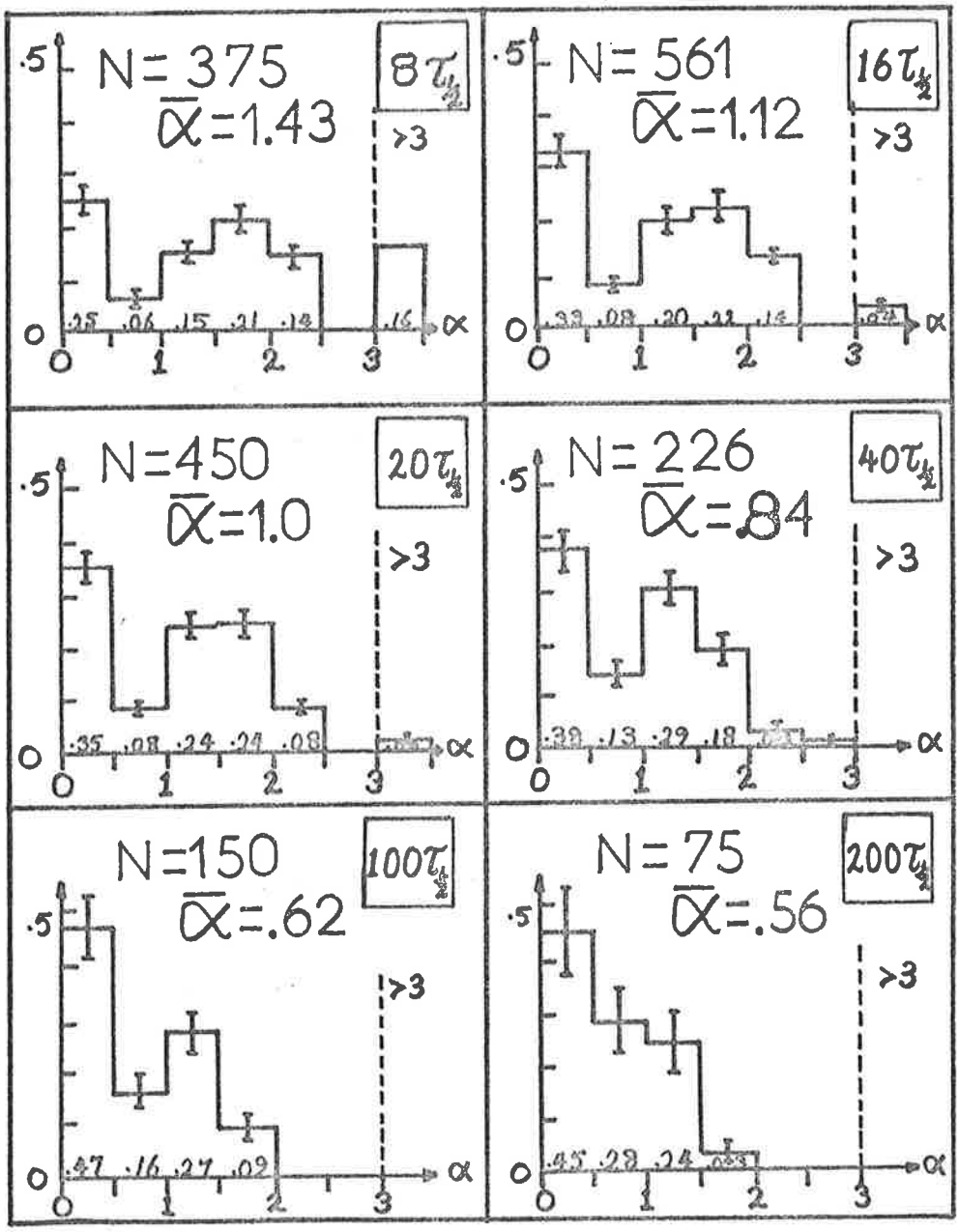
N= 375
$\bar{\alpha}$=1.43
8$\tau_{\frac{1}{2}}$
>3
.5
0
.25 .06 .15 .21 .14 .16
0 1 2 3 α
N= 561
$\bar{\alpha}$=1.12
16$\tau_{\frac{1}{2}}$
>3
.5
0
.33 .08 .20 .22 .14 .03
0 1 2 3 α
N=450
$\bar{\alpha}$=1.0
20$\tau_{\frac{1}{2}}$
>3
.5
0
.35 .08 .24 .24 .08
0 1 2 3 α
N= 226
$\bar{\alpha}$=.84
40$\tau_{\frac{1}{2}}$
>3
.5
0
.39 .13 .29 .18
0 1 2 3 α
N=150
$\bar{\alpha}$=.62
100$\tau_{\frac{1}{2}}$
>3
.5
0
.47 .16 .27 .09
0 1 2 3 α
N= 75
$\bar{\alpha}$=.56
200$\tau_{\frac{1}{2}}$
>3
.5
0
.45 .28 .24 .03
0 1 2 3 α

Fig. 5.12b: The small upper graph is a continuation of the series in Fig. 5.12a, for a data length of $600\tau_{\frac{1}{2}}$. There were only 20 data blocks used, so there is a large uncertainty in the distribution - but certainly cases with α up to 1.5 exist.

The largest graph is a collection of smoother versions of the graphs in Fig. 5.12a. The numbers on each graph are $T/\tau_{\frac{1}{2}}$. Bear in mind, however, that these graphs are only relevant if data is grouped in classes of 0.5 - ie., the resolution is quite poor. The height in each α interval has been assigned to the midpoint of each interval. Notice that as the data length increases, the height of the $\alpha = 0.25$ column rises, and the tail shrinks to the left. Also bear in mind that there are errors associated with the height of each point (see Figs. 5.12a). The $200\tau_{\frac{1}{2}}$ case has only been dotted on due to the rather large errors associated with it.

Clearly, a data length of $T \lesssim 8\tau_{\frac{1}{2}}$ is not advisable, since a large number of large α values occur. However, provided $T \gtrsim (16\text{-}20)\tau_{\frac{1}{2}}$, any data length can be used and interpreted.

The small inset graph shows a plot of $\bar{\alpha}$ vs $T/\tau_{\frac{1}{2}}$. Notice $T/\tau_{\frac{1}{2}}$ is on a log scale.

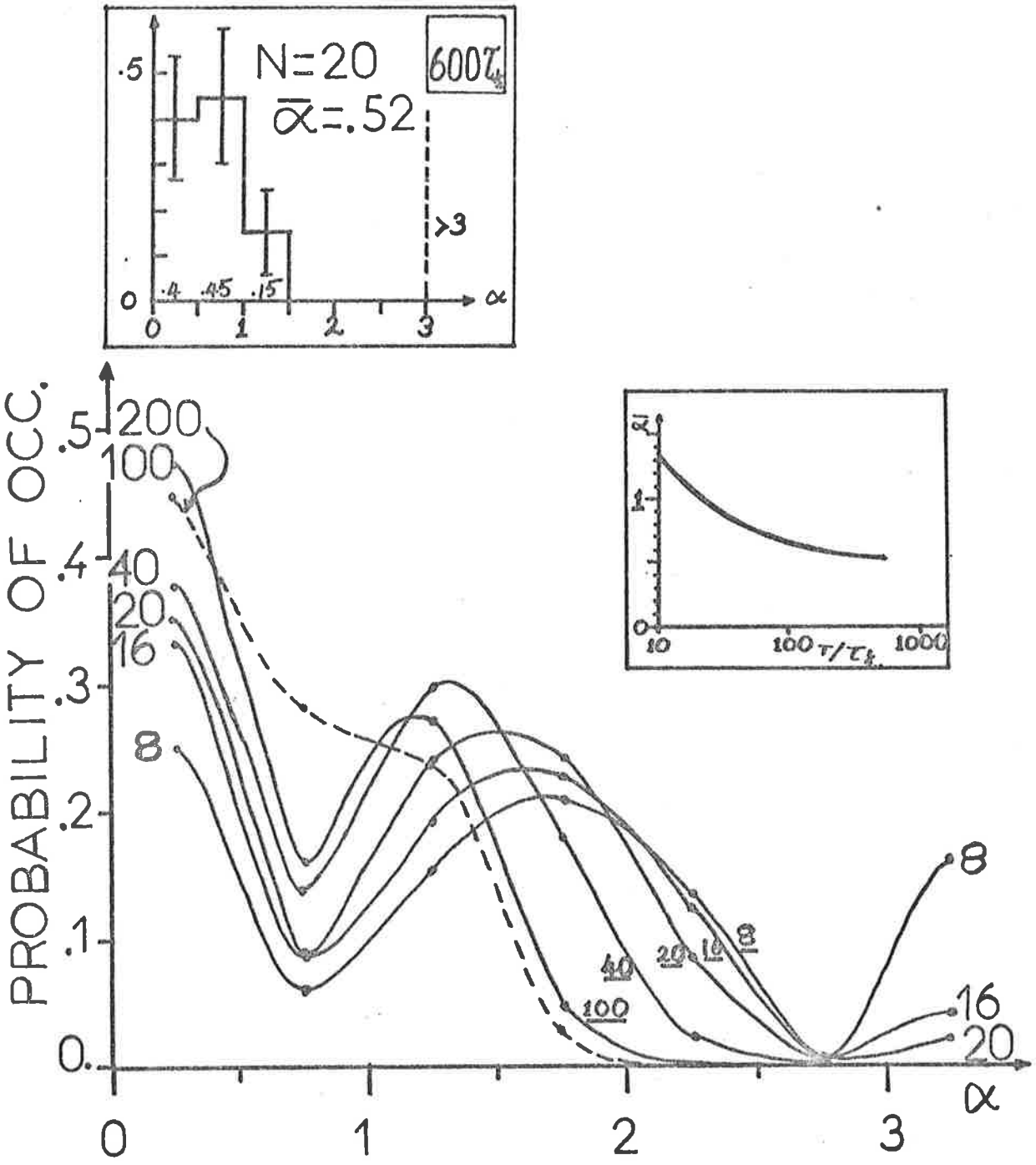
N=20
$\bar{\alpha}$=.52
600τ_s
.5
0
.4
.45
.15
>3
α
0
1
2
3
PROBABILITY OF OCC.
.5
.4
.3
.2
.1
0.
200
100
40
20
16
8
α
0
1
2
3
α_1
1
0
10
100 τ/τ_s
1000

number of statistically independent points is not necessary.

Having obtained these α estimates, histograms of the probability distributions of α, for various values of $T/\tau_{\frac{1}{2}}$, were evaluated. These are shown in Figs. 5.12. As discussed in the caption, even for very long data samples, quite large Rice values can result. Error bars were obtained by assuming the height of each column had a Poisson distribution, so that the variance equals the number of points in the column. This speculation was checked by breaking the data blocks into smaller subsets and replotting the distributions, with associated error bars. All column heights agreed to within these error bars, supporting the assumed errors. In fact about 60% of the column heights agreed to within an accuracy less than half the assigned errors. Also shown are mean α values for each distribution (α_E).

It is worth mentioning here that these distributions are indeed dependent only on $T/\tau_{\frac{1}{2}}$, and not on the value of T, or $\tau_{\frac{1}{2}}$. Imagine a data series which is compressed down to half its original length. $\tau_{\frac{1}{2}}$ must become $\frac{1}{2}$ of its original value, so $T/\tau_{\frac{1}{2}}$ is unchanged, and of course the points are still the same ones, so the Rice parameter will be unchanged. This hypothesis was checked by varying T and $\tau_{\frac{1}{2}}$, and it was indeed found that the distributions of α were dependent only on $T/\tau_{\frac{1}{2}}$.

It is thus quite clear that even for quite long data series (if $\tau_{\frac{1}{2}}$ = 3s, T = 18 minutes for $\tau/\tau_{\frac{1}{2}}$ = 600), Rice parameters as large as 1.5 can still result, and for shorter time series Rice parameters up to 2.5 and 3 can occur, due simply to statistical fluctuations. Yet the original data series was Rayleigh distributed! Thus even with data blocks as long as 30 minutes, a Rice parameter of 1.0 to 1.5 does not necessarily imply a non-Rayleigh distribution, unless there are more of such values than Figs. 5.12 would suggest.

The statistical non-stationarity of scattered power has already been discussed, and some of the results presented in previous papers have been seen to be possibly erroneous. Given these curves in Figs. 5.12, however, we are now in a position to discuss a better procedure for determination of whether a signal is specular or random. The following procedure has been used in this thesis.

5.3.3 Procedure for Determination of Specularity

(1) Decide on a data length T over which the received signal will be statistically stationary (typically 1-5 mins. - preferably less than 3 minutes-see Chapter IV). T should be greater than about $16\tau_{\frac{1}{2}}$, since Figs. 51.2a and 5.12b show that some very large but spurious Rice values can occur with shorter time series. Non stationarity on time scale $\geq$ T will consequently not distort the results in this approach; unless of course the form of scatter also changes.

(2) Obtain the Rice parameters for each data interval. (This procedure should also involve a χ^2 test to ensure rejection of double-peaked distributions, saturating data, etc.)

(3) Plot the distribution of these parameters in groups of 0.5, with errors equal to $\sqrt{n}$, n being the number of points in each interval.

(4) Compare these curves with the corresponding "theoretical" distribution (Figs. 5.12) and see if the curves are significantly different.

(i) An abnormally large number of large Rice values may suggest a specular contribution to the signal (although I have not done it, it would be a worthwhile project to plot similar α distributions for a genuinely Rician signal, to make estimation of the true specular to random ratio possible. However, temporal variability of the "specular component" would also complicate the matter, as discussed).

(ii) An abnormally large number of Rice values in the region 0 to 0.5 may suggest a non-Rayleigh type of scatter - perhaps log-normal, or Hoyt.

(iii) Agreement of the curves suggests Rayleigh scatter could be acting - it does not say it is (ie., the test is a rejection test, rather than an acceptance test).

(5) It is also useful to compare the mean Rice parameter $\bar{\alpha}$ (and variance σ_α^2) of the sample with the expected means α_E presented in Figs. 5.12.

(i) If $\bar{\alpha} \gtrsim \alpha_E + \sigma_\alpha$, this may suggest some specular scatter.

(ii) If $\bar{\alpha} \lesssim \alpha_E - \sigma_\alpha$, this suggests non-Rayleigh scatter (log normal, or Hoyt, etc.).

(iii) If $\alpha_E - \sigma_\alpha \lesssim \bar{\alpha} \lesssim \alpha_E + \sigma_\alpha$, the data series may be Rayleigh distributed.

(6) The interpretation of a specular component is also important, as discussed earlier. With the procedure described here, the detection of "specular scatter" means there exists a greater contribution from frequencies with periods greater than 2T than would be expected from purely Rayleigh scatter.

This is really the only way to do amplitude distribution analysis. Thus the results in previous papers must be interpreted with caution. Von Biel (1971), Mathews et al. (1973) and Newman and Ferraro (1976) all used data lengths greater than 10 mins, so that their statements regarding Rayleigh scatter at 60-80km may be in error. Rather, their distributions would probably have been log-normal or Hoyt, or at least some sharply rising function at small amplitudes, so the best Rice fit would have been $\alpha = 0.0$. This distribution is a result of the non-stationarity of the signal, although exactly why this form should arise is unclear.

As for the higher heights ($\gtrsim$ 80km), it is not possible to say correctly whether their data was Rician without more analysis. We have seen that a purely Rayleigh distributed series can produce α values up to 1.5 - the important issue is the percentage of records with these large values. Chandra and Vincent (1977, 1979) used 3-5 minute data blocks, and thus overcame the problem of non-stationarity. However, they

did not correctly analyse their results, which would have involved comparing their means to α_E values as calculated in Figs. 5.12. Rather, they assumed that Rice values greater than 1.0 meant significant specular scatter, and values less meant random scatter. However, their results are certainly closer to the truth than those of most other authors.

Another problem which should be mentioned concerns grouping of data. Von Biel, Mathews et al., and Newman and Ferraro, all group their data into height intervals without paying any regard to the heights of peaks of power. This is a dangerous practice. It will be seen shortly that Rice parameters tend to maximize at the heights of maximum power. At intermediate heights, and in the minima of scattered power, Rice parameters are often zero, simply because the signal being observed is due to a mixture of the tails of the pulses of scatterers above and below the region. The signal is not zero in strength, so signal to noise rejection tests will not always reject this data.

The problem of non-Rician scatter has also been discussed to some extent by Von Biel (1979), who proposed fitting another form of distribution to the amplitude histograms. However, because the parameters of the distribution do not have a readily recognizable physical significance, this approach has not been pursued.

As a summary then, it can be stated that the statistical non-stationarity of ionospheric echoes, and the statistical fluctuations inherent in estimates of the Rice parameter, have not been adequately dealt with in most previous studies of specularity of ionospheric scatter.

Figs. 5.13a, b, c (following):

Typical amplitude-time series, and the associated distributions. All recorded points were used to plot the histograms. Data was generally collected at either 5Hz or 2.5Hz per height. Fig. 5.13(a) shows a signal with a significant specular component. Fig. 5.13(b) shows an essentially Rayleigh-distributed signal. Fig. 5.13(c) shows a case where clearly the fading is too slow to record a useful histogram. Such cases must be rejected in any Rice-analysis, and the procedure for doing this is discussed in the text. In Fig. 5.13(c), the letters A, B and C on the first graph show the points where the peaks in the histogram come from. The Rice parameter α_{12} has been calculated, although clearly it is not relevant in case c.

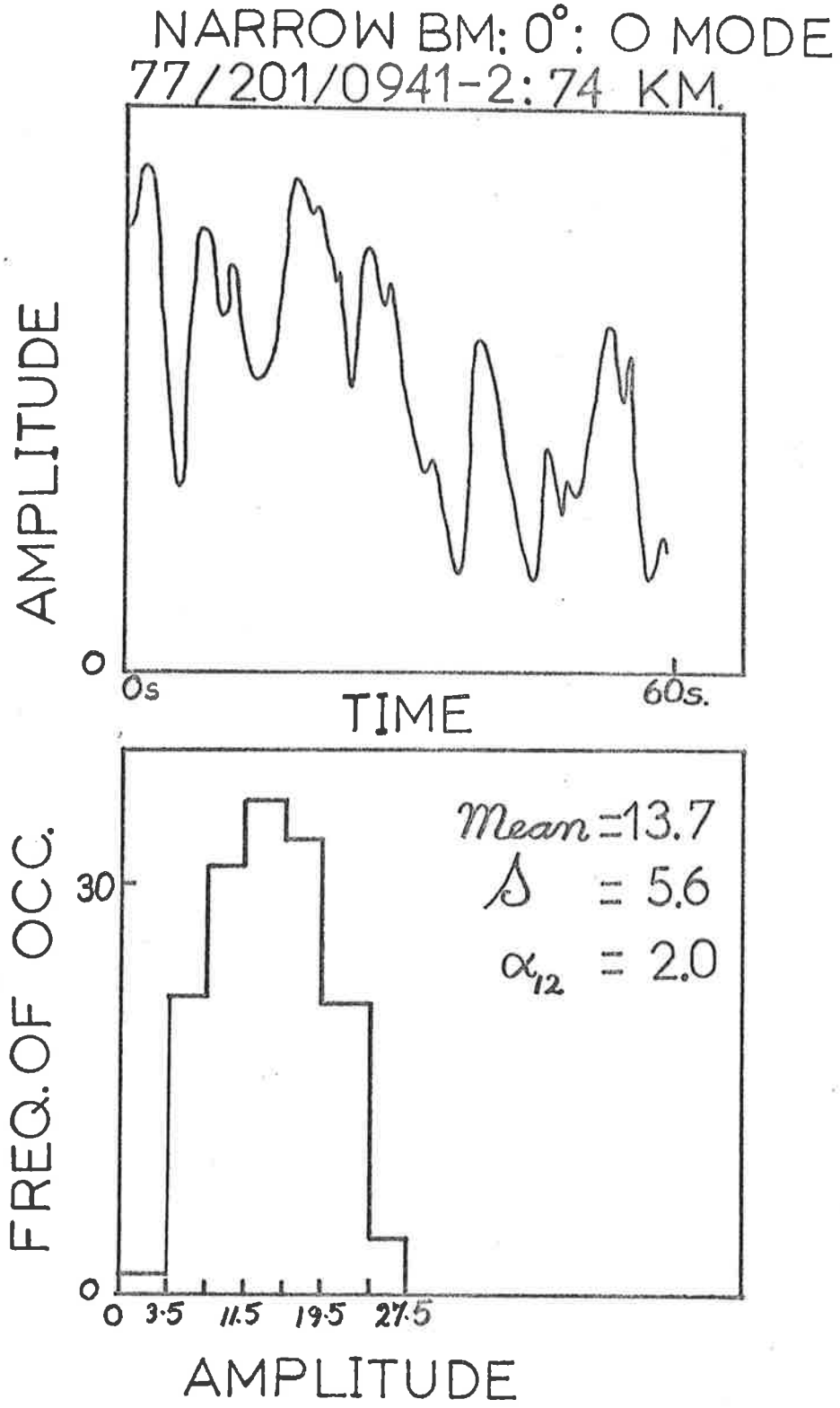
NARROW BM: 0°: O MODE
77/201/0941-2: 74 KM.
AMPLITUDE
0
0s
60s.
TIME
FREQ. OF OCC.
30
0
Mean = 13.7
S = 5.6
α12 = 2.0
0 3·5 11.5 19·5 27·5
AMPLITUDE

Fig 5.13a

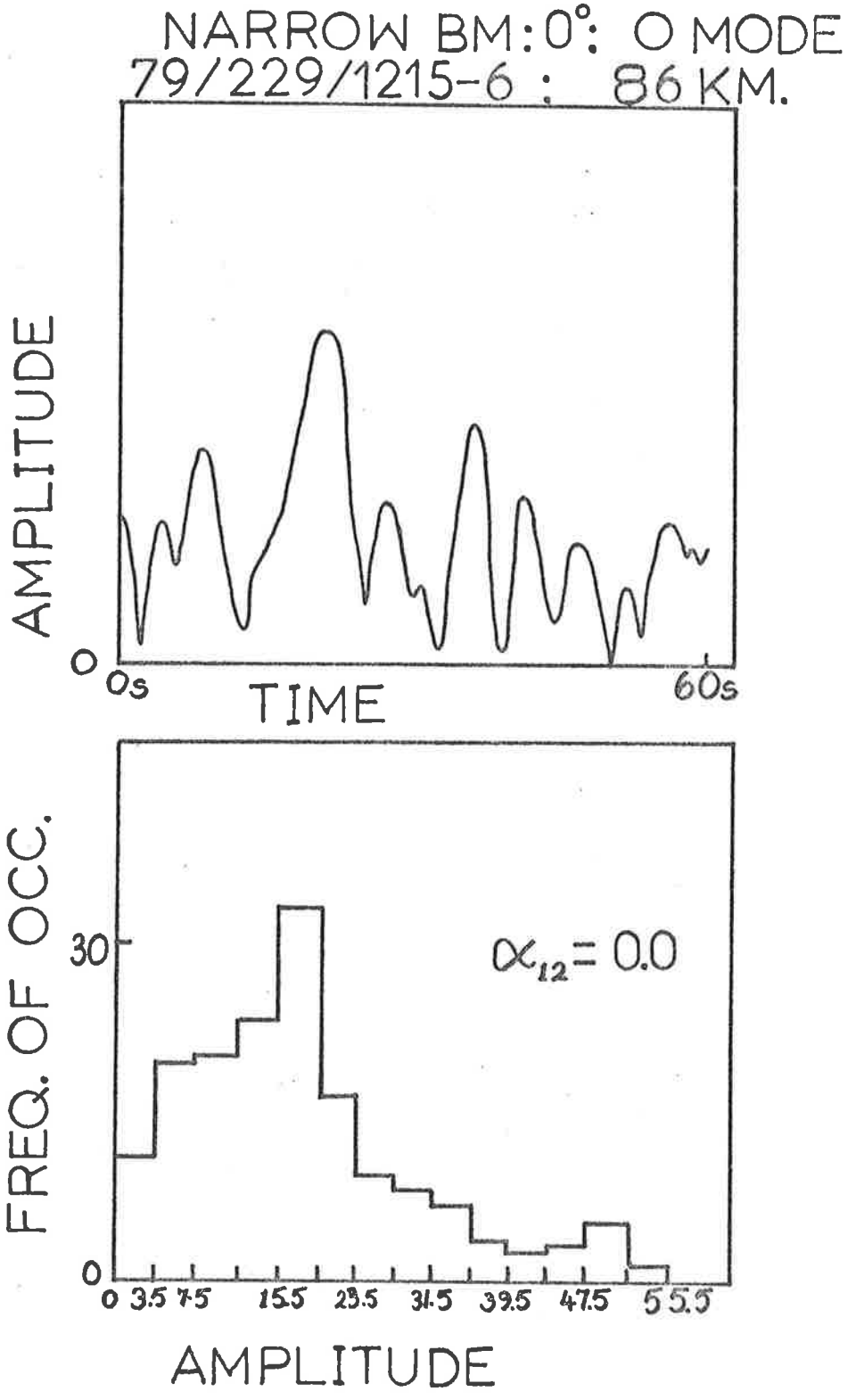
NARROW BM: 0°: O MODE
79/229/1215-6 : 86 KM.
AMPLITUDE
0
0s
TIME
60s
FREQ. OF OCC.
30
0
α_{12} = 0.0
0 3.5 7.5 15.5 23.5 31.5 39.5 47.5 55.5
AMPLITUDE

Fig 5.13 b.

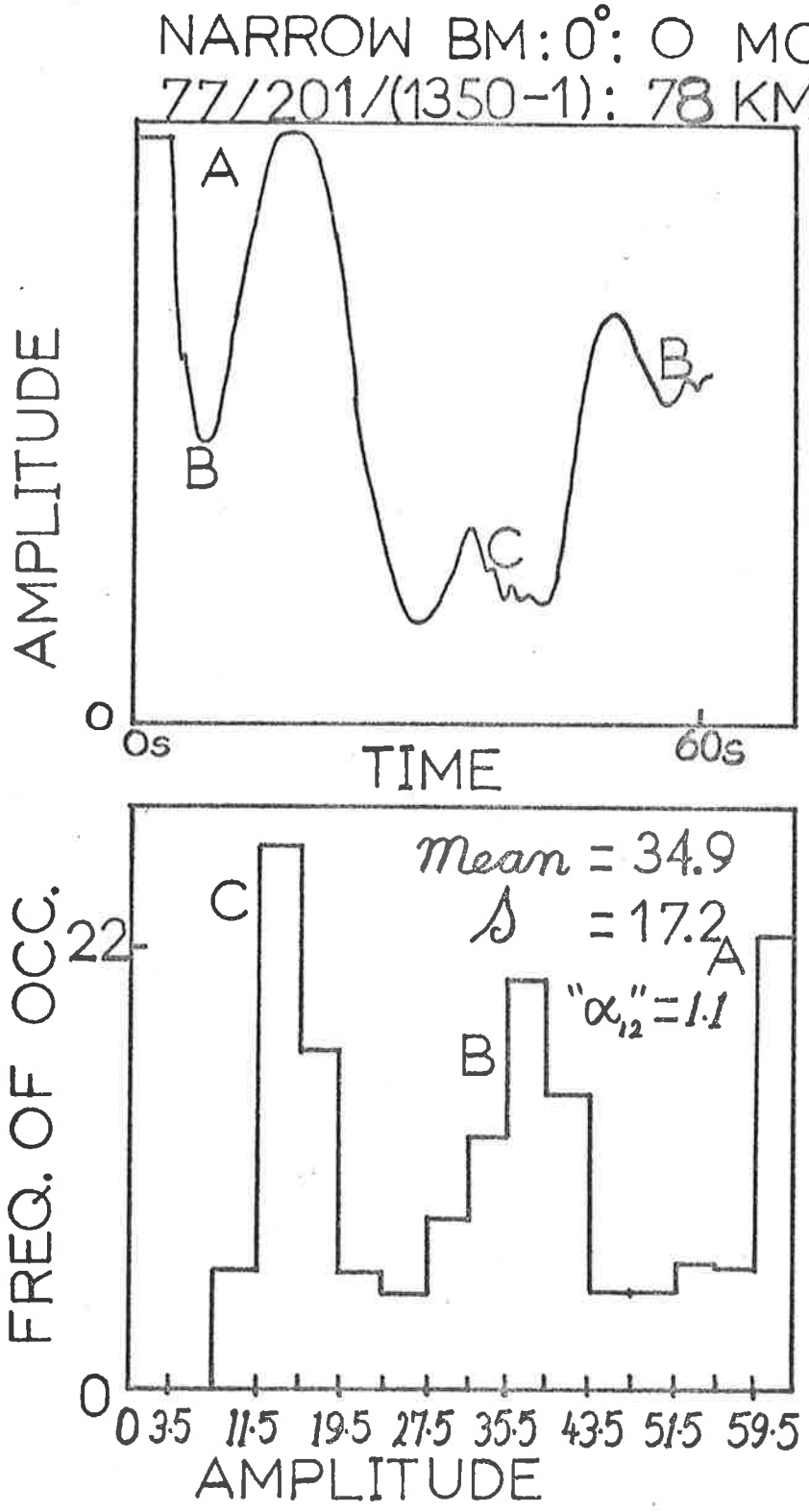
NARROW BM: 0°: O MODE.
77/201/(1350-1): 78 KM.
AMPLITUDE
A
B
C
B
0
0s
TIME
60s
FREQ. OF OCC.
Mean = 34.9
S = 17.2
"α12" = 1.1
C
A
B
22
0
0 3·5 11·5 19·5 27·5 35·5 43·5 51·5 59·5
AMPLITUDE

Fig. 5.13c.

5.4 Experimental Estimates of Specular to Random Scatter Ratios

5.4.1 The Distributions

Data for the amplitude distributions presented in this thesis were recorded in the same way as all other data - namely, on digital tape, with 64 levels of digitization. Great care was taken to remove any DC offset present in the receivers, since this could bias the results. Data was then generally grouped into classes of 4 levels (0-3 inclusive, 4-7 inclusive, 8-11 inclusive, etc.), or classes of 3 levels (0-2 inclusive, 3-5 inclusive, etc.).

Figs. 5.13a, b and c show some 1 minute sets of amplitude-time series, with the corresponding amplitude distributions and the Rice parameter α_{12}. The case 5.13c is not typical, but care must be taken to eliminate such distributions from any analysis.

To eliminate cases like 5.13c, a χ^2 test was used (eg., see Croxton, 1959; Bevington, 1969). Classes with less than 5 points were grouped with adjacent classes, as is usual in such tests. Then the value

$$\chi^2 = \sum_{\text{all classes}} \frac{(E_i - O_i)^2}{E_i} \qquad (5.4.1.1)$$

was calculated, O_i being the observed number of points in class i, and E_i the expected number (for some assumed distribution - in this case, the Rice distribution). This value is then compared to a standard set of tables (the chi-square distribution tables). A particular acceptance level is chosen, and if the calculated χ^2 is less than the χ^2 associated with the acceptance level, the data is accepted. The acceptance level represents the probability that a data sample derived from a sample with the assumed (expected) distribution would produce a χ^2 value greater than the χ^2 value associated with this level. Generally acceptance at about

a 5% level means the data is reasonably acceptable.

Figs. 5.14a, b show typical distributions, with the Rice distributions for the given Rice parameters shown. However, the χ^2 values shown are not χ^2 values in the true sense, as discussed below.

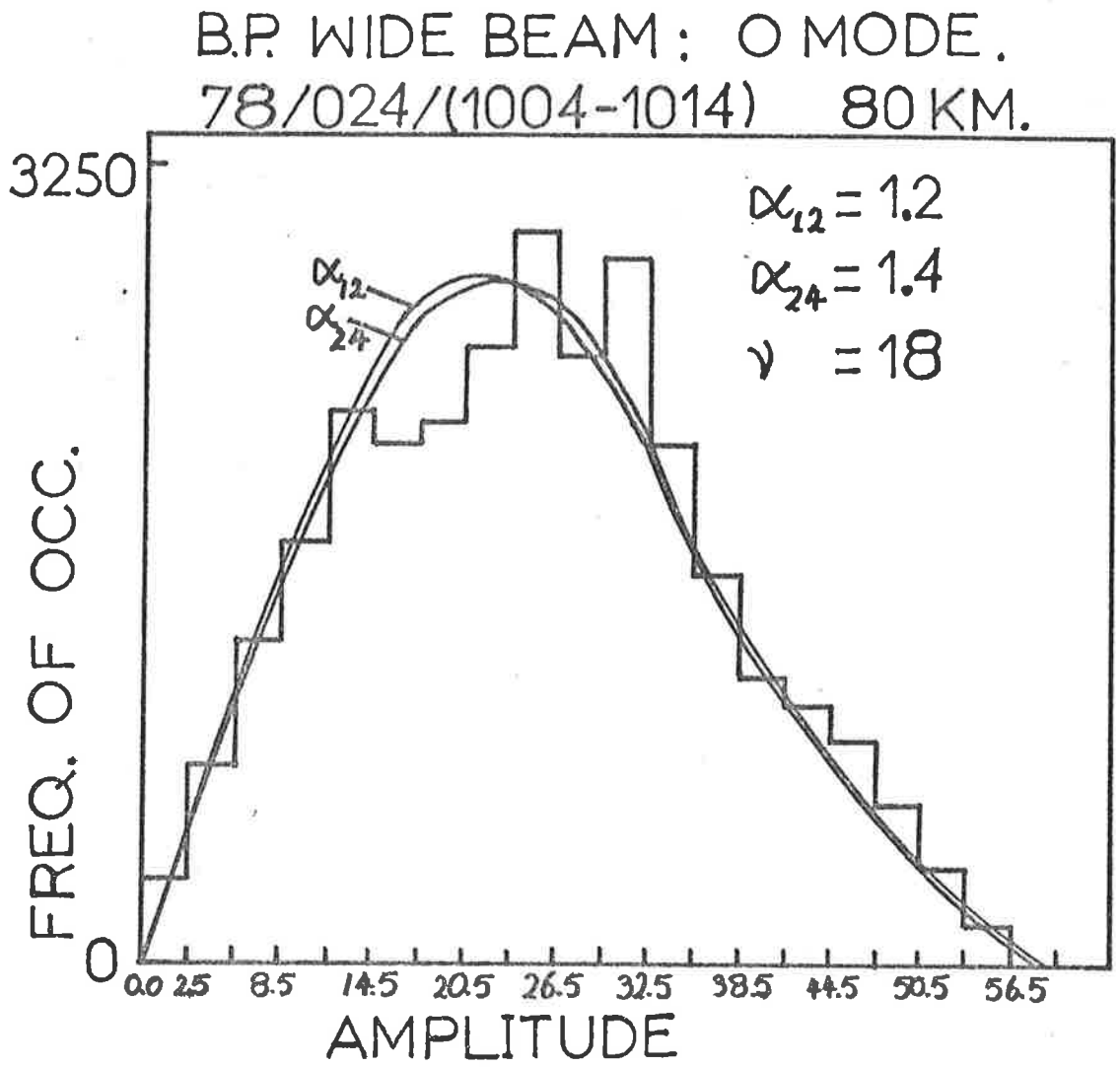

Fig. 5.14a: Histogram of 10 minutes of data from 80km using a wide beam at Buckland Park. Both α_{12} and α_{24} are shown, and their corresponding probability distributions. The number of degrees of freedom is $\nu = 18$. A χ^2 value was calculated assuming α_{12} was the expected Rice parameter. It was found that $\chi^2 = 81.6$, but this was using all points, with a sampling rate of 5Hz. Only points at least 2s apart would be statistically independent (ie., $\geq \tau_{\frac{1}{2}}$), so a more realistic χ^2 value would be around 81.6/10 ~ 8.16 (see text). This corresponds to a high level of acceptance.

Notice this histogram was formed using 10 minutes of data. This was possible on this day at this height because the scattered powers were reasonably constant in time. This is not always so, and certainly 10 minutes of data would produce a less than useful histogram at heights below 80km, as has been discussed in the text.

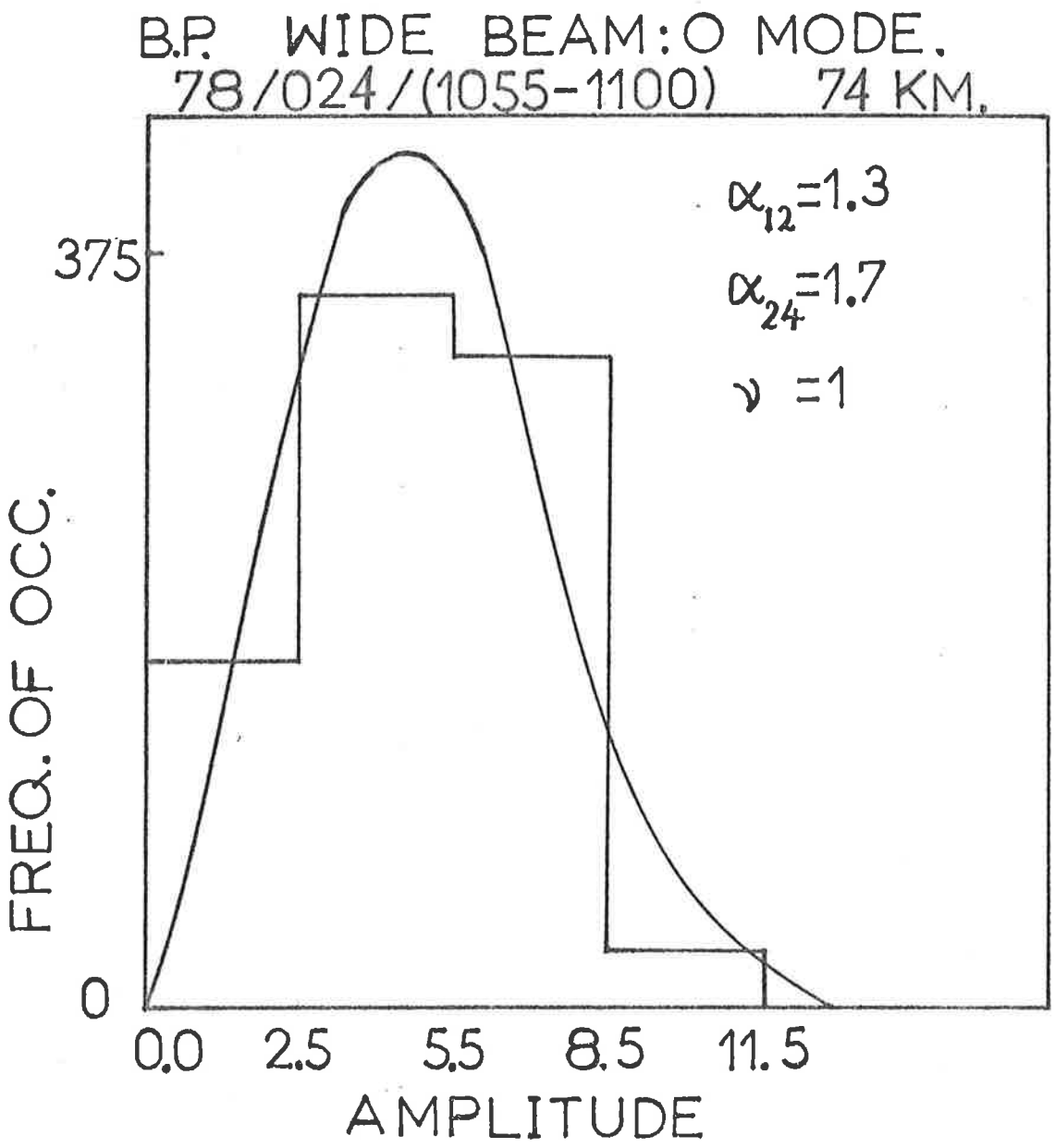

Fig. 5.14b: Another histogram of amplitudes, for a height of 74km. In this case, only 5 minutes of data were used (and data were recorded on the 1st, 3rd and 5th minutes only, for instrumental reasons). Notice the maximum amplitude is about 11. Normally, gains were sufficiently high that most of the 64 levels of digitization were covered, but not so high that significant saturation occurred. However, this was not always possible. Even for amplitudes of the low levels given here, quite reasonable Rice parameter estimates could be achieved (ν = number of degrees of freedom).

5.4.2 Rejection Criteria

As a first criterion, distributions were rejected if they had means less than 3 or within 3 of saturation (60). Then a χ^2 criterion was used. The fits in Figs. 5.14a, b are reasonably typical. If a χ^2 value is calculated, quite large values result (eg., Fig. 5.14a gives $\chi^2 \sim 80$). However, bear in mind that all data points have been used to form this distribution, and hence each point is not statistically independent. Now

$$(5.4.2.1) \qquad \chi^2 = \sum_{\text{all classes}} \frac{(NP_i - O_i)^2}{NP_i}$$

N being the total number of points, O_i the observed number in class i and P_i the expected probability of a point in class i. N should be the number of statistically independent points. However, suppose it is not, but is rather the total number of recorded points. Suppose it can be assumed the distribution of statistically independent points is the same as for all the points, and let the total number of statistically independent points be N_{stat}. Thus the observed number of statistically independent points in class i is $\approx (N_{stat}/N).\ O_i$

Then using all points, we calculate

$$\chi^2_{\text{all points}} = \sum \frac{(NP_i - O_i)^2}{NP_i} \approx \frac{N}{N_{stat}} \sum \frac{(N_{stat} - \frac{N_{stat}}{N} O_i)^2}{N_{stat} P_i} \approx \frac{N}{N_{stat}} \chi^2_{\text{true}}$$

or

$$(5.4.2.2) \qquad \chi^2_{\text{true}} \approx \frac{N_{stat}}{N} \left[\chi^2_{\text{all points}}\right]$$

Thus, if, for example, data is recorded at 5Hz, but only points 2s apart are statistically independent, $\chi^2_{\text{true}} \approx \frac{1}{10} \chi^2_{\text{all points}}$.

However, the problems involved with obtaining sufficient statistically independent points have already been discussed, given the non-stationarity

of ionospheric scatter. The approach in this thesis has been to simply calculate χ^2 using all points. Visual inspection of many graphs suggested χ^2 values of several hundred were generally unacceptable, but values of χ^2 of less than about 200 were generally reasonable. Thus χ^2 values were rejected or accepted around such values. Data was often accepted at a "10^{-10}%" acceptance level, using $\chi^2_{\text{all points}}$. Bear in mind, then, that this is not a true χ^2 test, but for the purposes of these experiments, the procedure proved more than adequate. It is not surprising that the accepted "χ^2" values are less than 100→200. If N/N_{stat} ~ 10→20, then we may expect the limiting $\chi^2_{\text{all points}}$ to be around 10→20 times the χ^2_{true} acceptance value. But χ^2_{true}/ν is around 3→1.5 for around 4→20 degrees of freedom (ν) at the 5% level, and in the histograms presented here, ν is around 4→20. Then the limiting $\chi^2_{\text{all points}}$ is $\geq$ (10→20) x ν x (1.5→3).

As a point of interest, it was noted that data obtained using a wide beam often produced smaller "χ^2" values than those recorded with the narrow beam, particularly above 80km. This may be partly because the fading times were less, so that (N_{stat}/N) was greater, reducing "$\chi^2_{\text{all points}}$" for a given χ^2_{true}. It may also be because of the presence of more oblique scatter, thus increasing the "random scatter" component, and so hiding fluctuations in the "specular component" to some extent.

There was also some doubt as to the number of degrees of freedom ν relevant for a histogram. Since the number of points, the mean, and the standard deviation are known, Croxton (1959) takes ν = number of intervals, N, minus 3. Bevington (1969) takes ν = N-2, as he feels the number of points, N, is not really a statistic. The former approach was adopted in this thesis.

Fig. 5.15: (a) Contour diagram of 1 minute mean power and (b) a "table" of 1 minute Rice parameters, as a function of range and time. Measurements were only taken every second minute. The powers have been smoothed by computer interpolation.

In (b), the numbers refer to α parameters. 0 means 0 to 0.5, 1 means 0.5 to 1.5, 2 means 1.5 to 2.5 etc. Values of 1.5 to 2.5 have also been shaded. A black square is used for values > 2.5. Blanks mean the data was rejected by a χ^2 test. Notice more are rejected at the lower levels. In particular, notice during the power burst at 76km, 1206-1210 hr., few amplitude histograms are accepted as Rician. Likewise at the 70km, 1300 hr power burst .

The large Rice values at 60km are due to the presence of a ground echo at 58km. The arrows on the right of (b) show approximately the heights of important echoes on this day.

BP : NARROW BM : 0° : O MODE.

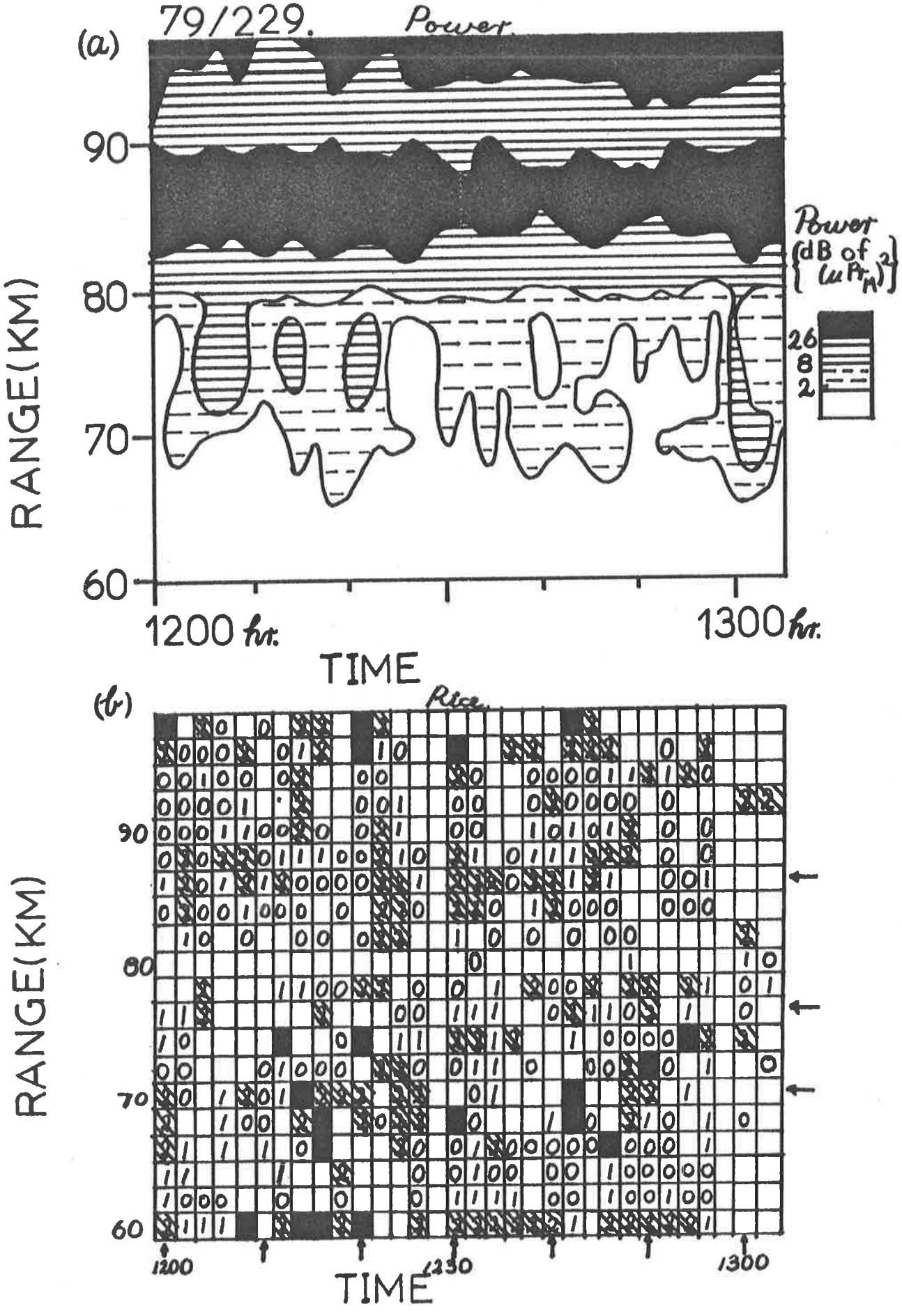

Fig. 5.16: Contour diagrams of (a) 3 minute mean power in $(\mu T_{irps})^2$ and (b) 3 minute Rice values, for Townsville (80-98km) during November, 1977. A contour diagram of (a) can also be found in Fig. 4.14, Chapter IV. Data was recorded in 3 minute blocks, either every 5 or every 10 minutes (see Fig. 4.14). At times, correlations between power bursts and Rice parameters can be see at around 90km. The echo above about 95km is due to the E region total reflection - hence the large Rice parameters.

For this data, no χ^2 test was applied. However, even if the distributions are not Rician (and most probably are Rician), the Rice parameters do serve as a measure of depth of fading to the mean fading (see Fig. 5.7). Note that some degree of correlation between mean power and Rice parameter is not surprising - if fading is deeper, the mean power would be less, even if the range of amplitudes covered were unchanged.

In (b) dark patches below 95km generally correspond to α values between 1.5 and 2.0. Above this height (E region reflections), α values are generally $\gtrsim 4$.

TOWNSVILLE: 77/305. O MODE

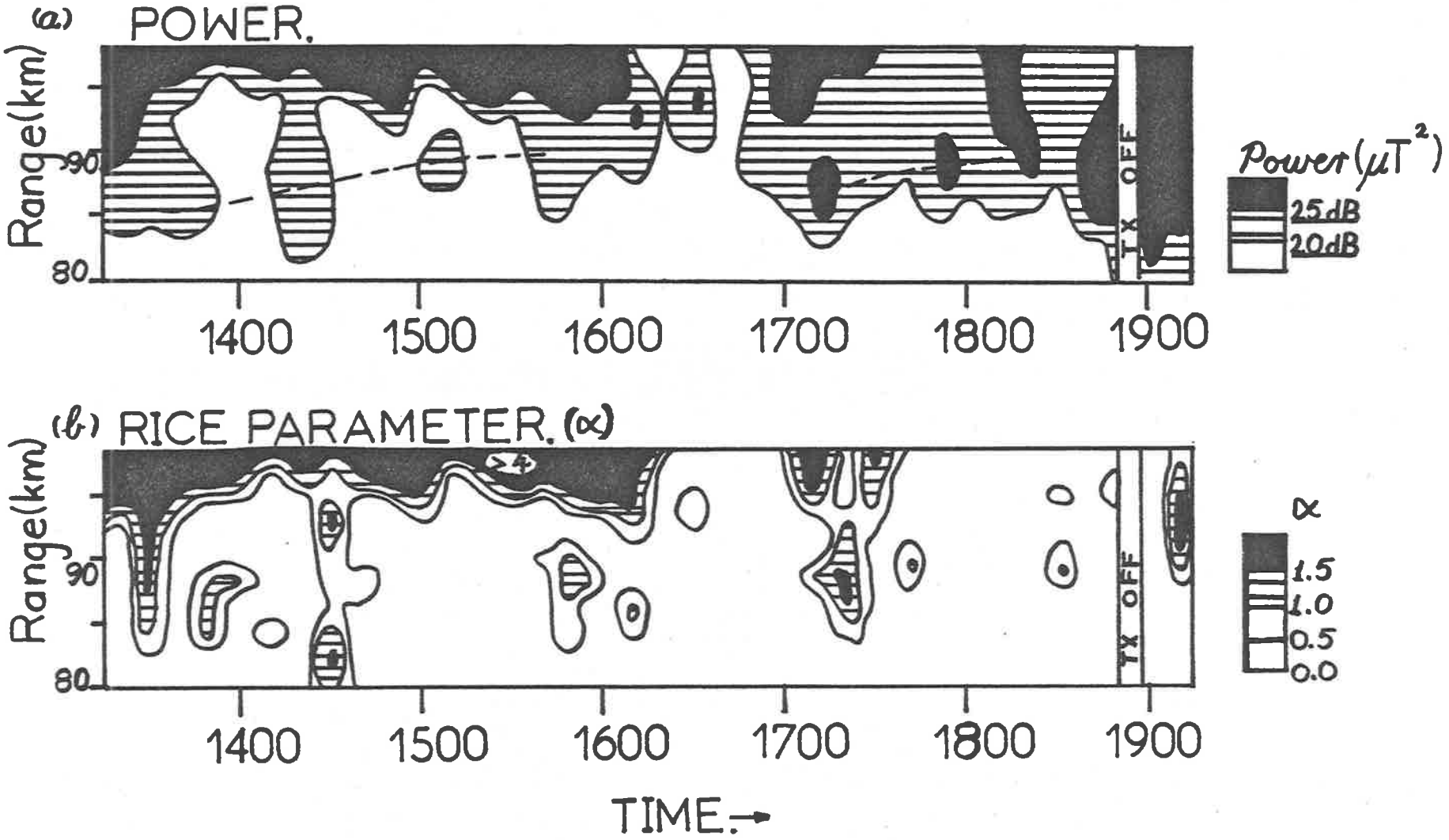

5.4.3 Results

Fig. 5.15 shows a typical contour diagram of the Rice parameter as a function of time; one and two minutes of data were used, as described in the caption. Also shown is a contour plot of the mean power as a function of time and range. A better diagram of the same data was presented in Fig. 4.13, Chapter IV. Fig. 5.16 shows a similar pair of diagrams for Townsville, 80-98km.

These graphs make some points immediately clear. Rice parameters appear to be minimum at the heights of minimum power. This is most likely because the echoes received at these (virtual) heights are due to the superposition of the tails of echoes from above and below. At times, too, there appears to be a positive correlation between power bursts and large Rice parameters. For example, Fig. 5.16 shows a few such correlations. However, not all large power bursts are necessarily associated with large Rice parameters, nor vice versa. Fig. 5.16 also is also typical of some night-time echoes at 80-98km; for example, during November 1977 on the night 307-8 at Buckland Park, similar correlations were noted. However, before reading too much into these correlations, it must be borne in mind that there is considerable statistical fluctuation in any Rice parameter estimate, as seen in section 5.3. To properly investigate Rice parameters, the data sets must be treated as groups. It is interesting to notice, however, that at the lower heights ($\lesssim$ 70km), amplitude histograms are often rejected as non-Rician during large power bursts. This will have important consequences in estimates of specularity of scatter at these lower heights, as these large power bursts (often extremely specular and slow fading) are not included in such analyses. However, it is not surprising that at low heights, strong power bursts associated with slow fading would produce large Rice parameters (eg., see Fig. 4.10a; a Rice parameter estimation at 70km, 1142-1145, would clearly

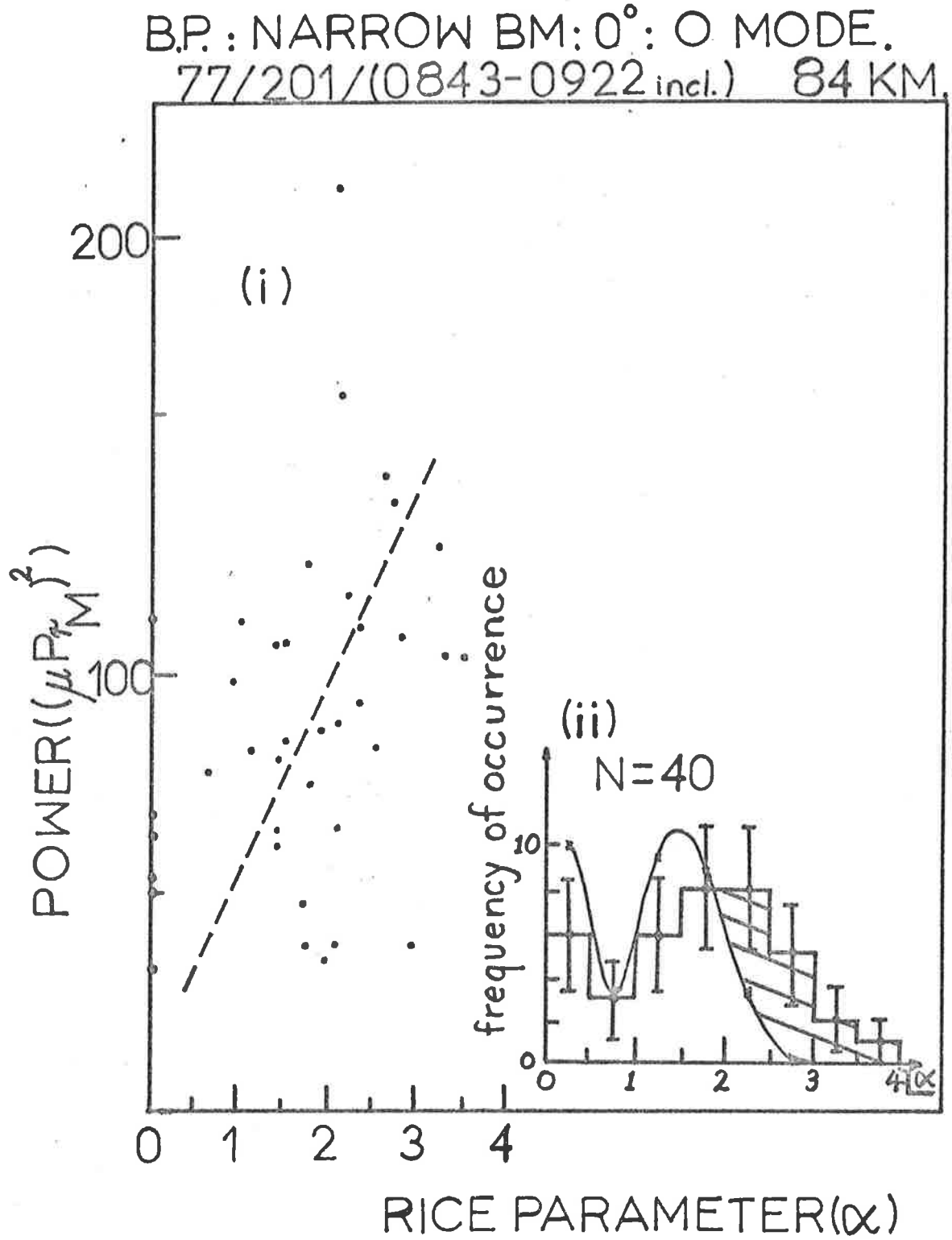

Fig. 5.17a: (i) Correlation of 1 minute mean powers and 1 minute Rice parameters (α_{12}) at 84km for day 77/201 at Buckland Park using the vertical narrow beam. There appears to be a positive correlation.
(ii) Distribution of the 1 min. Rice parameters, with error bars equal to $\sqrt{n}$. The solid line represents the expected distribution of Rice parameters for a Rayleigh distributed signal with $T/\tau_{\frac{1}{2}} = 20$ (see section 5.3).

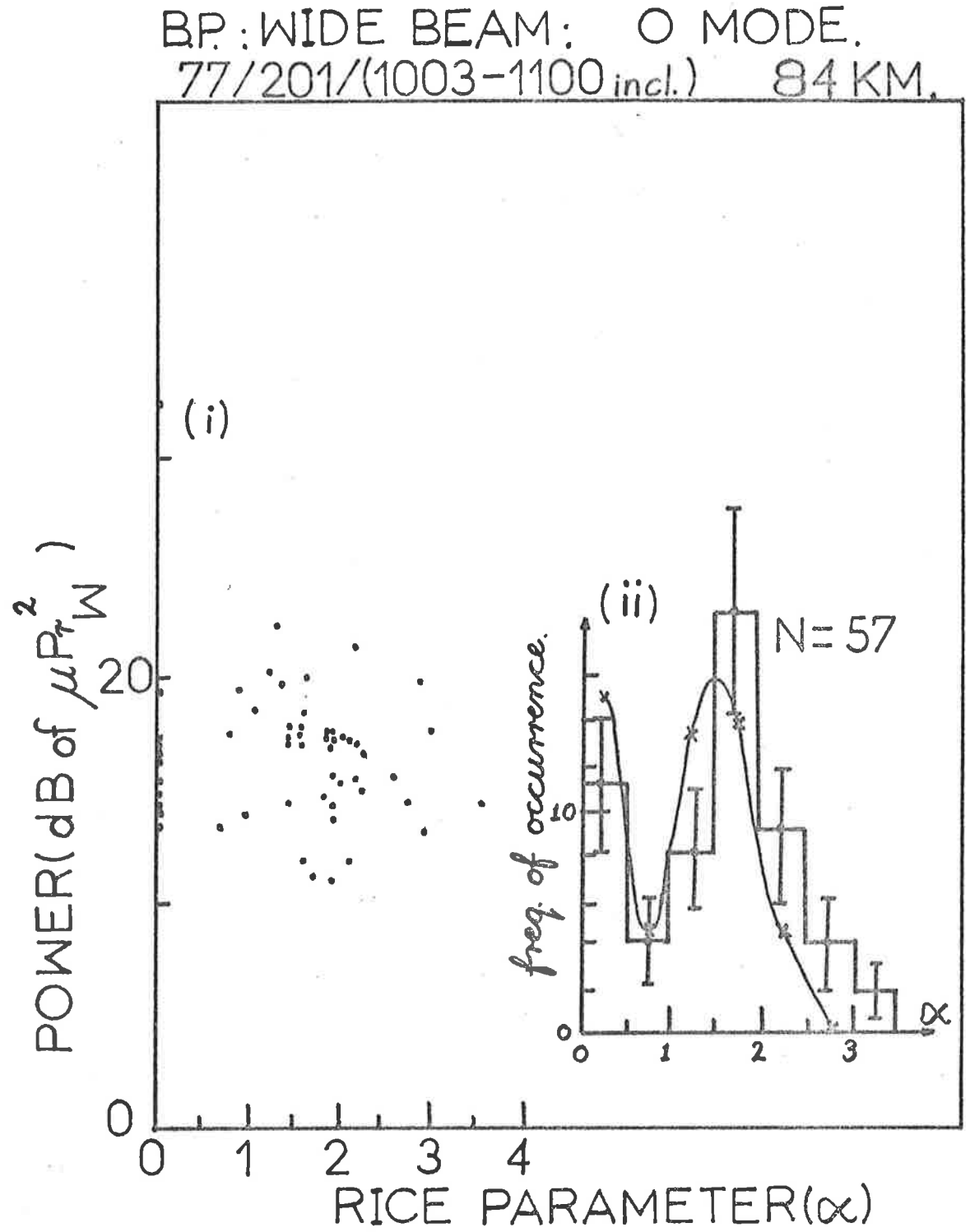

Fig. 5.17b: (i) Correlation of 1 min. mean powers and 1 min. Rice parameter (α_{12}) for day 77/201 at Buckland Park using a wide beam, for a height of 84km.
(ii) Distribution of the 1 minute Rice parameters, with error bars equal to $\sqrt{n}$. The solid line represents the expected distribution of Rice parameters for a Rayleigh distributed signal with $T/\tau_{\frac{1}{2}}$ ~ 20 to 30 (see section 5.3).

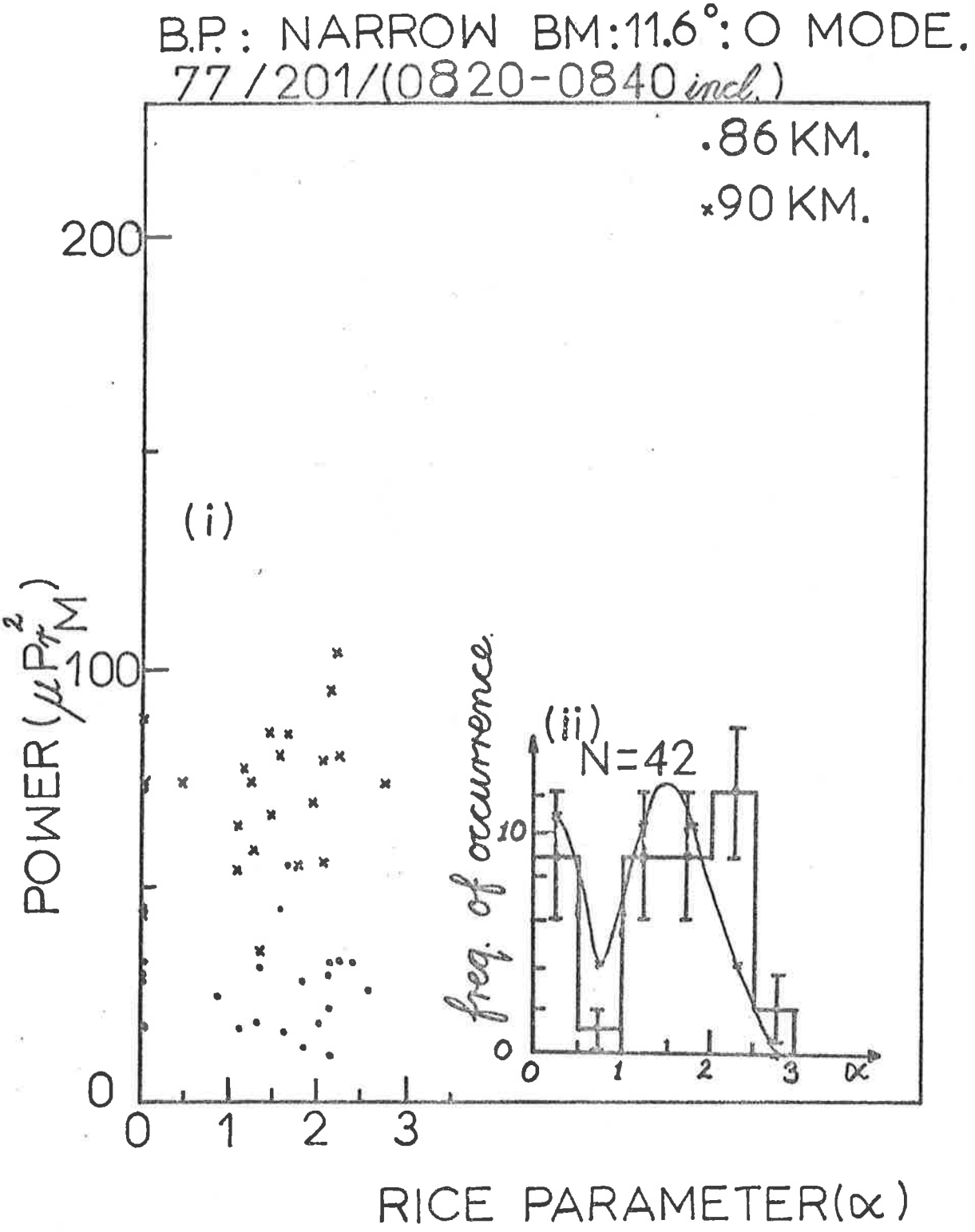

Fig. 5.17c: (i) Correlation of 1 min. mean powers and 1 min. Rice parameters at 86km (.) and 90km (x) for day 77/201 at Buckland Park using the narrow beam tilted to 11.6° off-zenith.
(ii) Distribution of the 1 min. Rice parameters, with error bars equal to $\sqrt{n}$. The solid line represents the expected distribution of Rice parameters for a Rayleigh distributed signal, for $T/\tau_{\frac{1}{2}} \sim 20$ (see section 5.3).

give a large Rice parameter, and indeed did). Many of the rejected cases are also interesting. These have multiple humps, or distributions more appropriate to the cases of 2 or 3 specular scatterers. However, they will not be discussed here.

Figs. 5.17a, b and c show much more detailed assessments of the Rice parameters. The data is for a scattering structure situated at around 84-86km on the morning of day 77/201. The layer descended to about 80-82km by 1200, and then rose again.

Fig. 5.17a is typical of the conditions observed with the narrow beam. It can be seen that there appears to be something of a linear trend on the power/Rice correlation graph. This may suggest that increases in power are in part due to more Fresnel-type scatter. Certainly the distribution of Rice parameters suggests there is a contribution from specular scatter, since there are more Rice parameters greater than 2.0 than a Rayleigh-distributed signal would be expected to give.

Fig. 5.17b shows the power/Rice correlation, and the distribution of Rice parameters, for the wide beam on day 77/201. In this case, there is no clear power/Rice correlation, and the distribution of Rice parameters is more consistent with a Rayleigh distributed signal. (Although there is a weak hint of some specularity, as the α = 1.5-2 column has more, and the 1-1.5 column less, than a truly Rayleigh-distributed sample).

These two graphs, then, suggest scatter from 86km comes in two forms from near the vertical - a specular component and a random component. Scatter from the off-vertical would appear to be purely random. This would explain the approximately Rayleigh distribution on the wide beam - the random scatter from the vertical and oblique directions "swamps" the vertical specular scatter. At times, on some days, a weak power/

Rice correlation can be observed on the wide beam at around 80-90km, but it is generally weaker than that for the narrow beam. It is fair to say that the signals observed with the wide beam generally show more Rayleigh-like behaviour than those observed on the narrow beam at 80-90km.

Recall, however, that powers received with the narrow beam at 0° and 11.6° from these heights are similar (chapter IV) (to within perhaps about 3-6dB). When the beam is tilted to 11.6°, the specular component would no longer contribute, so the ratio of random scatter to (random + specular) scatter should be about $10^{(-3\rightarrow-6)}/20$. Hence if this model of specular plus random scatter from the vertical, and random scatter from the off-vertical, is valid, then the specular components and random components when viewed vertically on the narrow beam, must make comparable contributions to the scattered power.

It would thus appear, then, that scatter from the ~86km layer generally consists of approximately equal components of Fresnel reflection and random scatter when observed with the vertical narrow beam. The actual ratio varies depending on the day of observation.

Fig. 5.17c shows graphs of power/Rice correlation and Rice parameter distributions when observing the ~ 86km layer at 11.6° off-vertical on the narrow beam, for day 77/201. There may be a weak specular component, as indicated by the rather large number of Rice parameters in the regime 2-2.5. However, this is questionable. Certainly there is not the same degree of specularity as at 0°. Indeed, generally observation at 11.6° do appear to suggest Rayleigh scatter, and support the above description of 86km scatter.

What about the heights below around 80km? Fig . 5.18 presents a typical case. There is not a great correlation between powers and Rice parameters in this case. However, the histogram of Rice parameters

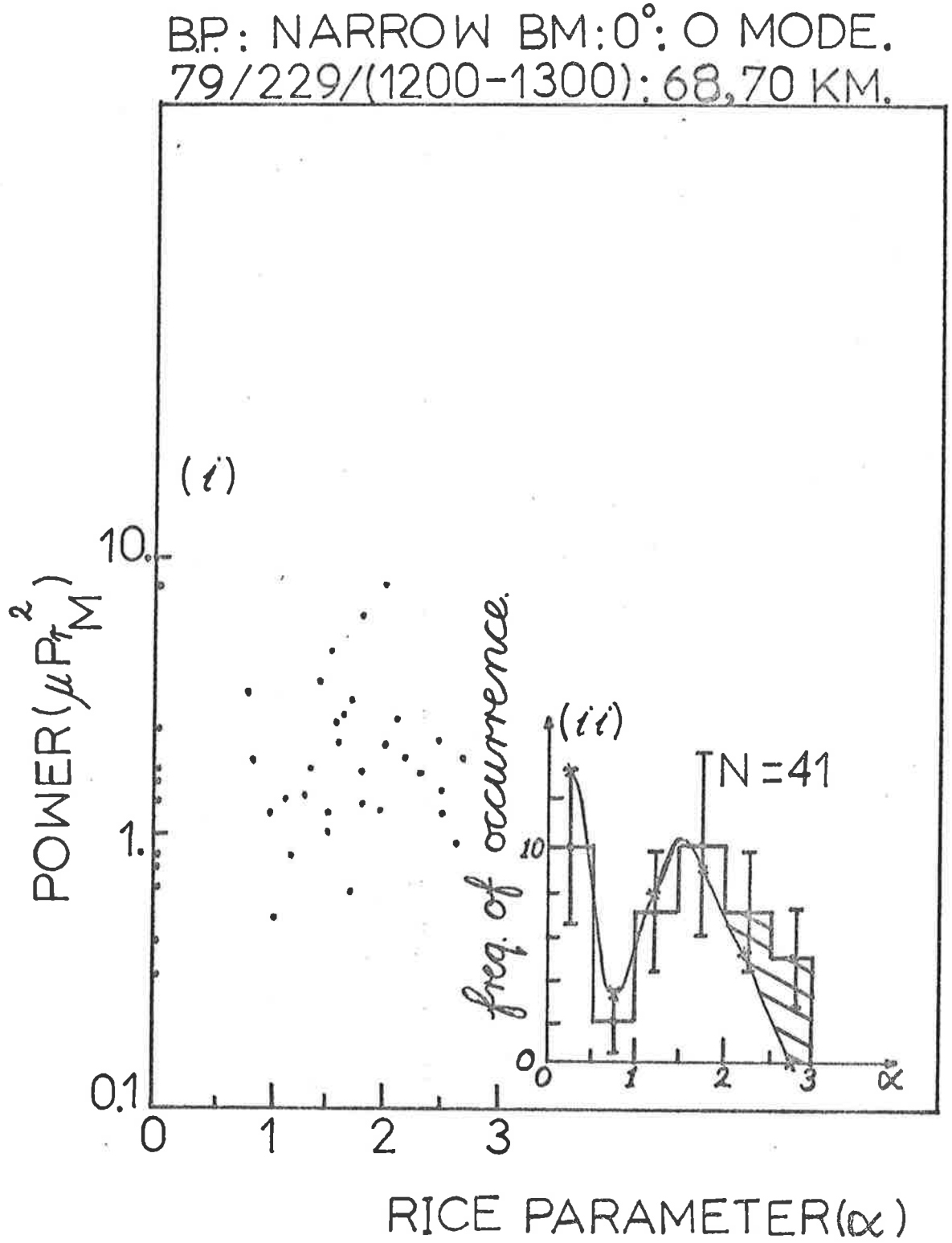

Fig. 5.18: (i) Correlation of 1 min. mean powers and 1 min. Rice parameters at 68-70km for day 79/229 at Buckland Park using the vertical narrow beam.
(ii) Distribution of the 1 min. Rice parameters, with error bars equal to $\sqrt{n}$. The solid line represents the expected distribution of Rice parameters for a Rayleigh-distributed signal with $T/\tau_{\frac{1}{2}} \sim 16$ (see section 5.3).

Fig. 5.19: Profiles of power, fading time, and Rice parameter for day 79/229 at Buckland Park, using the narrow beam. The first two graphs have already been presented in Chapter IV, Fig. 4.16. The error bars associated with $\tau_{\frac{1}{2}}$ and Rice parameters are $\pm$ the standard deviation for the mean. Also plotted on the Rice profile (---) is the expected mean Rice parameter for a Rayleigh distributed series for the $T/\tau_{\frac{1}{2}}$ ratios relevant for this data. The 86km, and 70km layers, both appear Rician. The data is discussed more in the text. The data above 94km is due to the front of the E region echo, and so exhibits slow fading and large Rice parameters.

ADELAIDE . AUG 17 1979 . 1200 - 1304

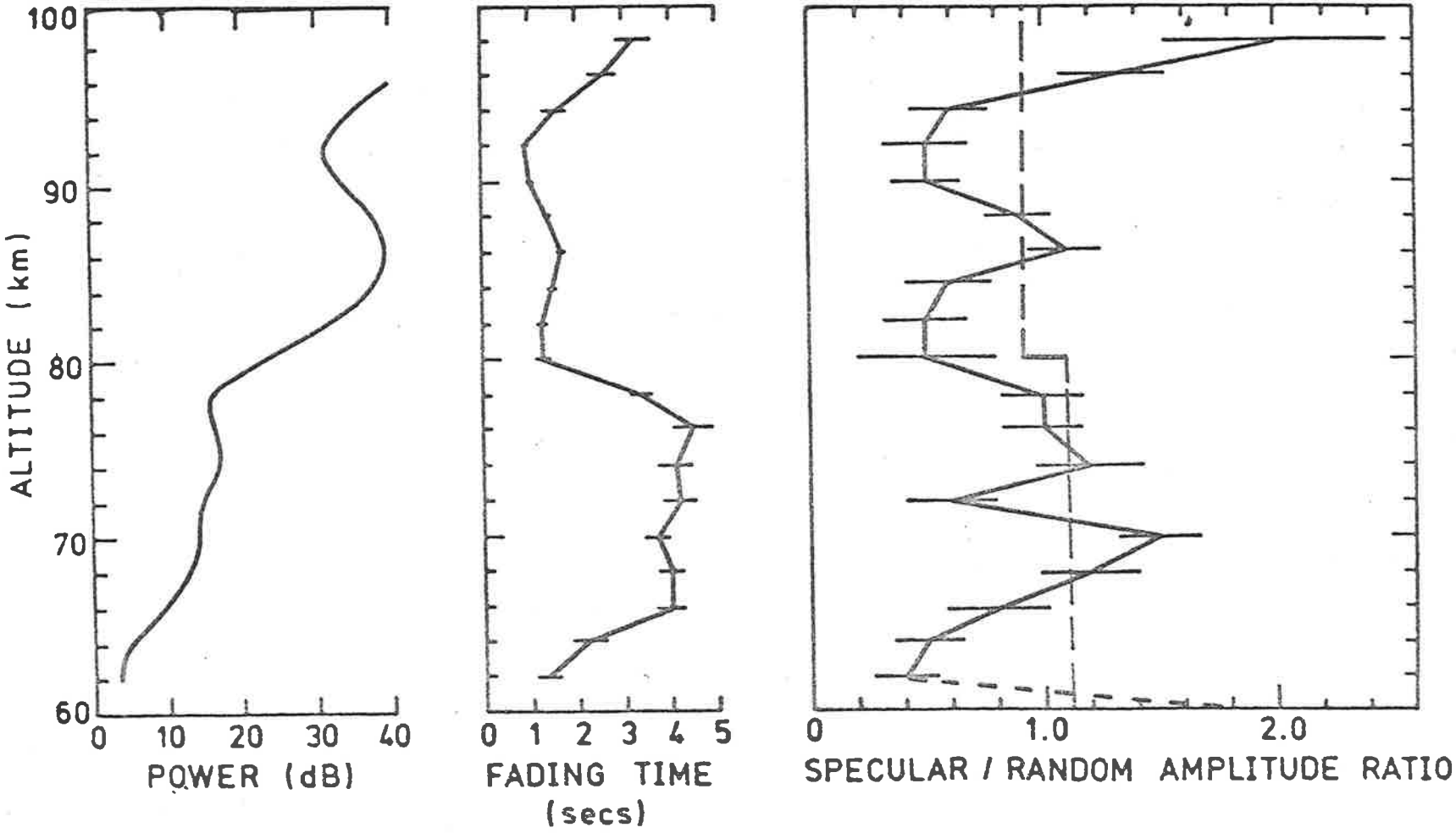

presented in Fig. 5.18(ii) definitely suggests a significant specular component, and this is generally true for the echoes from below 80km. As discussed earlier, some of the cases with $\alpha = 0.0$ at these lower heights may in fact not be Rayleigh distributed, but perhaps Hoyt distributed. This case would give $\alpha = 0.0$. The lack of a power/Rice-parameter correlation simply suggests that the scatter mechanism appears to be independent of the scattered power. At times, strong powers can be found associated with large Rice parameters, but this is not always the case. In many cases, scatter appears to be neither Rician or Rayleigh. However, it does generally appear to be specular.

The apparent specularity of these lower signals supports the evidence using beam swinging and fading times presented in Chapter IV that the scatter from below around 80km is generally due to Fresnel-reflection.

Finally, Fig. 5.19 is presented as something of a summary of Rice parameter characteristics. It refers to data taken on day 79/229 with a narrow beam at Buckland Park. It can be seen that Rice values tend to be small at the heights of minimum scattered power, as discussed. Also marked on are the expected mean α values for a Rayleigh distribution, using a data length T = 1 min. and a fading time $\tau_{\frac{1}{2}}$ of 4s below 78km, and above 80km, T = 1 min., $\tau_{\frac{1}{2}} = 2$s.

Scatter from 86km appears to contain some specular contribution. Scatter from 70km also appears to be specular. The fact that $\overline{\alpha}$ values are less than the expected means at the minima of power suggests that scatter is not really Rayleigh-like here, either. This is not surprising if much of the power is due to the beating of "tails" of the echoes from above and below.

The scatter at 74-78km may be Rayleigh distributed. However, when this data was considered in Chapter IV, it was pointed out that the

echoes from around 76→78km were temporally and spatially intermittent. Processes such as the beating of 2 specular reflectors could be important. It is the author's opinion that many of the "$\alpha = 0.0$" cases at these heights are due to non-Rician processes, as already discussed. The fact that histograms formed during large power bursts are often rejected as non-Rician, yet are often quite specular, has already been mentioned. In fact, this is possibly also true for the 70km echo.

The results of the analyses of this chapter, then, can be simply stated as follows:

Scatter from below around 76-78km is generally quite specular (and aspect sensitive (see Chapter IV)). Scatter from the $\sim$86km echo appears reasonably Rician, with both random (turbulent?) and specular scatter. It has not been possible to ascertain decisively the nature of echoes from $\gtrsim$ 90km, but it is felt the scatter is largely Rayleigh.

End of Volume I . . .

Completed in Volume II.